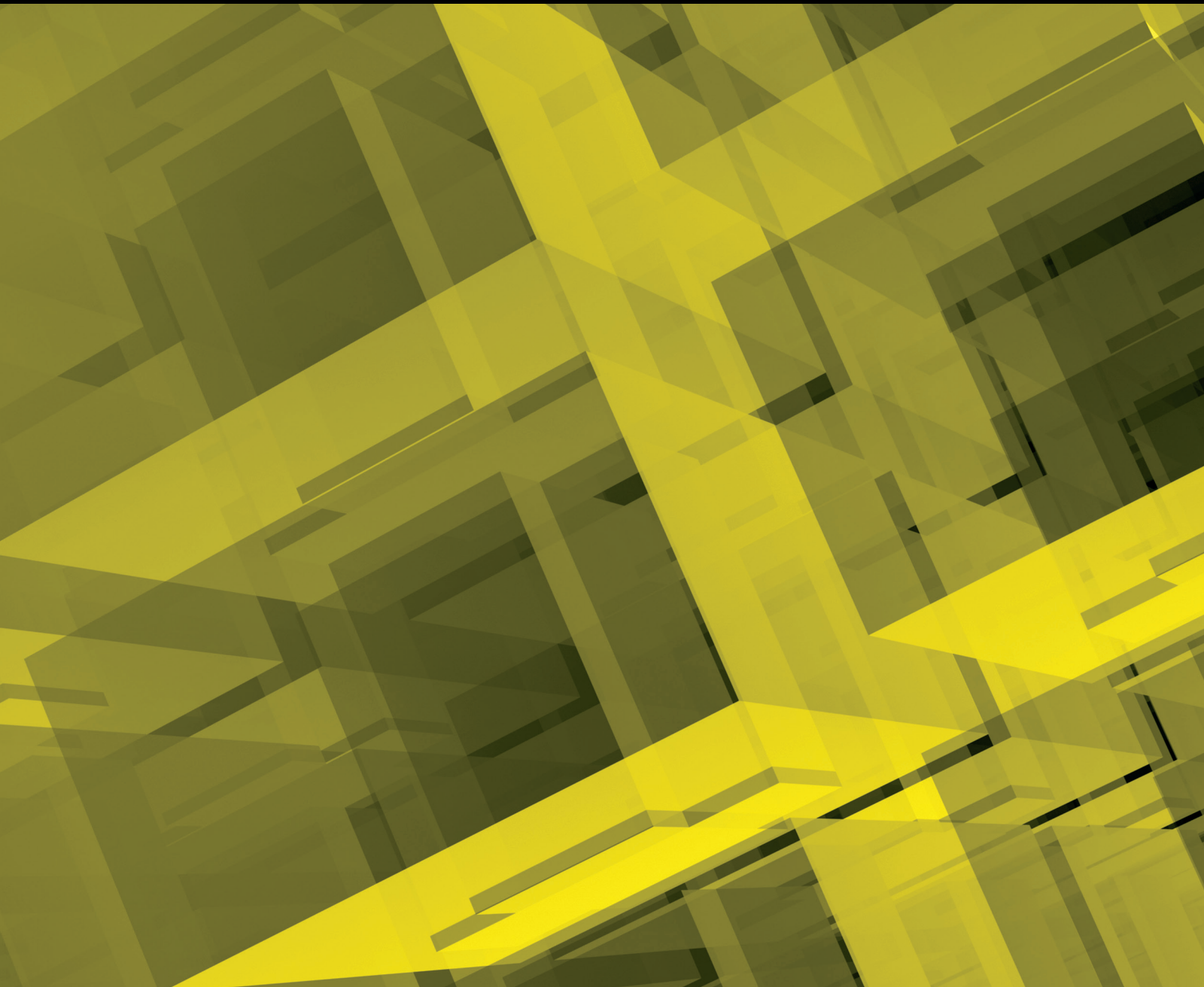


Journal of Applied Mathematics

# Mathematical and Numerical Modeling of Flow and Transport 2013

Guest Editors: Shuyu Sun, Mohamed Fathy El-Amin, and Bo Yu





---

**Mathematical and Numerical Modeling  
of Flow and Transport 2013**

Journal of Applied Mathematics

---

**Mathematical and Numerical Modeling  
of Flow and Transport 2013**

Guest Editors: Shuyu Sun, Mohamed Fathy El-Amin,  
and Bo Yu



---

Copyright © 2014 Hindawi Publishing Corporation. All rights reserved.

This is a special issue published in "Journal of Applied Mathematics." All articles are open access articles distributed under the Creative Commons Attribution License, which permits unrestricted use, distribution, and reproduction in any medium, provided the original work is properly cited.

## Editorial Board

- Saeid Abbasbandy, Iran  
Mina B. Abd-El-Malek, Egypt  
Mohamed A. Abdou, Egypt  
Subhas Abel, India  
Janos Abonyi, Hungary  
Sergei Alexandrov, Russia  
M. Montaz Ali, South Africa  
Mohammad R. Aliha, Iran  
Carlos J. S. Alves, Portugal  
Mohamad Alwash, USA  
Gholam R. Amin, Oman  
Saiied Aminossadati, Australia  
Igor Andrianov, Germany  
Boris Andrievsky, Russia  
Whye-Teong Ang, Singapore  
Abul-Fazal M. Arif, Saudi Arabia  
Sabri Arik, Turkey  
Ali R. Ashrafi, Iran  
Allaberen Ashyralyev, Turkey  
Francis T. K. Au, Hong Kong  
Francesco Aymerich, Italy  
Jalel Azaiez, Canada  
Seungik Baek, USA  
Hamid Bahai, UK  
Olivier Bahn, Canada  
Antonio Bandera, Spain  
Jean-Pierre Barbot, France  
Mostafa Barigou, UK  
Roberto Barrio, Spain  
Henri Baudrand, Brazil  
Alfredo Bellen, Italy  
Vasile Berinde, Romania  
Jafar Biazar, Iran  
Anjan Biswas, Saudi Arabia  
Abdellah Bnouhachem, Morocco  
Gabriele Bonanno, Italy  
Stphane P. A. Bordas, USA  
Walter Bricc, France  
James Robert Buchanan, USA  
Humberto Bustince, Spain  
Alberto Cabada, Spain  
Xiao Chuan Cai, USA  
Piermarco Cannarsa, Italy  
Jinde Cao, China  
Yijia Cao, China
- Zhenfu Cao, China  
B. Carpentieri, The Netherlands  
Ana Carpio, Spain  
Alexandre Carvalho, Brazil  
Song Cen, China  
Shih-sen Chang, China  
Tai-Ping Chang, Taiwan  
Wei-Der Chang, Taiwan  
Shuenn-Yih Chang, Taiwan  
Kripasindhu Chaudhuri, India  
Ru-Dong Chen, China  
Zhang Chen, China  
Zhi-Zhong Chen, Japan  
Jianbing Chen, China  
Yuming Chen, Canada  
Xinkai Chen, Japan  
Rushan Chen, China  
Ke Chen, UK  
Eric Cheng, Hong Kong  
Ching-Hsue Cheng, Taiwan  
Qi Cheng, USA  
Chin-Hsiang Cheng, Taiwan  
Jin Cheng, China  
Hui Cheng, China  
Francisco Chiclana, UK  
Jen-Tzung Chien, Taiwan  
Chongdu Cho, Korea  
Han H. Choi, Republic of Korea  
S. H. Chowdhury, Malaysia  
Yu-Ming Chu, China  
Hung-Yuan Chung, Taiwan  
Angelo Ciaramella, Italy  
Pedro J. Coelho, Portugal  
Carlos Conca, Chile  
Vitor Costa, Portugal  
Lirong Cui, China  
Jie Cui, USA  
Livija Cveticanin, Serbia  
Gaoliang Dai, Germany  
Hua Dai, China  
Binxiang Dai, China  
Michael Defoort, France  
Hilmi Demiray, Turkey  
Ming-Cong Deng, Japan  
Youjun Deng, France
- Orazio Descalzi, Chile  
Raffaele Di Gregorio, Italy  
Kai Diethelm, Germany  
Daniele Dini, UK  
Urmila Diwekar, USA  
Vit Dolejsi, Czech Republic  
BoQing Dong, China  
Rodrigo W. dos Santos, Brazil  
Wenbin Dou, China  
Rafael Escarela-Perez, Mexico  
Magdy A. Ezzat, Egypt  
Meng Fan, China  
Ya Ping Fang, China  
Istvn Farag, Hungary  
Didier Felbacq, France  
Ricardo Femat, Mexico  
Antonio J. M. Ferreira, Portugal  
George Fikioris, Greece  
Michel Fliess, France  
Marco A. Fontelos, Spain  
Dimitris Fotakis, Greece  
Tomonari Furukawa, USA  
Maria Gandarias, Spain  
Xiao-wei Gao, China  
Naiping Gao, China  
Huijun Gao, China  
Xin-Lin Gao, USA  
Laura Gardini, Italy  
Winston Garira, South Africa  
Leonidas N. Gergidis, Greece  
Bernard J. Geurts, The Netherlands  
Sandip Ghosal, USA  
Dibakar Ghosh, India  
Pablo Gonzlez-Vera, Spain  
Alexander N. Gorban, UK  
Keshlan S. Govinder, South Africa  
Said R. Grace, Egypt  
Jose L. Gracia, Spain  
Maurizio Grasselli, Italy  
Zhi-Hong Guan, China  
Nicola Guglielmi, Italy  
Frédéric Guichard, Canada  
Kerim Guney, Turkey  
Shu-Xiang Guo, China  
Vijay Gupta, India

Saman K. Halgamuge, Australia  
Ridha Hambli, France  
Abdelmagid S. Hamouda, Qatar  
Bo Han, China  
Maoan Han, China  
Pierre Hansen, Canada  
Ferenc Hartung, Hungary  
Jesper H. Hattel, Denmark  
Xiao-Qiao He, China  
Yuqing He, China  
Nicolae Herisanu, Romania  
O. H.-Lerma, Mexico  
Luis J. Herrera, Spain  
Thomas Höhne, Germany  
Wei-Chiang Hong, Taiwan  
Sun-Yuan Hsieh, Taiwan  
Ying Hu, France  
Ning Hu, Japan  
Jianguo Huang, China  
Dan Huang, China  
Zhilong L. Huang, China  
Ting-Zhu Huang, China  
Zhenkun Huang, China  
Asier Ibeas, Spain  
Mustafa Inc, Turkey  
Gerardo Iovane, Italy  
Anuar Ishak, Malaysia  
Takeshi Iwamoto, Japan  
George Jaiani, Georgia  
GunHee Jang, Korea  
Zhongxiao Jia, China  
Daqing Jiang, China  
Haijun Jiang, China  
Jianjun Jiao, China  
Xing Jin, China  
Zhen Jin, China  
Lucas Jodar Snchez, Spain  
Zlatko Jovanoski, Australia  
Tadeusz Kaczorek, Poland  
Dongsheng Kang, China  
Sangmo Kang, USA  
Ido Kanter, Israel  
Abdul Hamid Kara, South Africa  
H.R. Karimi, Germany  
Dimitrios A. Karras, Greece  
Ihsan Kaya, Turkey  
Dogan Kaya, Turkey  
C. M. Khaliq, South Africa  
Waqar A. Khan, Pakistan  
Khalil Khanafer, USA  
Adem Kılıçman, Malaysia  
Hyunsung Kim, Korea  
Younjea Kim, Republic of Korea  
Jong Hae Kim, Republic of Korea  
Svein Kleiven, Sweden  
Kazutake Komori, Japan  
Vassilis Kostopoulos, Greece  
Jisheng Kou, China  
Roberto A. Kraenkel, Brazil  
Kannan Krithivasan, India  
Vadim A. Krysko, Russia  
Jin L. Kuang, Singapore  
Gennady M. Kulikov, Russia  
V. Kumaran, India  
Mirosław Lachowicz, Poland  
Hak-Keung Lam, UK  
Tak-Wah Lam, Hong Kong  
Heung-Fai Lam, Hong Kong  
Luciano Lamberti, Italy  
Peter G L Leach, Cyprus  
Jaehong Lee, Republic of Korea  
Usik Lee, Korea  
Myung-Gyu Lee, Korea  
Wen-Chuan Lee, Taiwan  
Jinsong Leng, China  
Xiang Li, China  
Yongkun Li, China  
Wan-Tong Li, China  
Qingdu Li, China  
Hua Li, Singapore  
Lixiang Li, China  
Wenlong Li, Hong Kong  
Shuai Li, Hong Kong  
Shiyong Li, China  
Qin Li, China  
Yan Liang, China  
Jin Liang, China  
Dongfang Liang, UK  
Ching-Jong Liao, Taiwan  
Teh-Lu Liao, Taiwan  
Gao Lin, China  
Yiping Lin, China  
Yong-Cheng Lin, China  
Chong Lin, China  
Ignacio Lira, Chile  
Peide Liu, China  
Meiqin Liu, China  
Pengfei Liu, China  
Sheng Liu, Australia  
Zhuangjian Liu, Singapore  
Zhengrong Liu, China  
Chein-Shan Liu, Taiwan  
Kang Liu, USA  
Zhijun Liu, China  
Yansheng Liu, China  
Peter Liu, Taiwan  
Weiqing Liu, China  
Tao Liu, China  
Shutian Liu, China  
Fei Liu, China  
Chongxin Liu, China  
Jose L. López, Spain  
Shiping Lu, China  
Hongbing Lu, China  
Benzhuo Lu, China  
Henry Horng-Shing Lu, Taiwan  
Yuan Lu, China  
Hao Lu, USA  
Gilles Lubineau, Saudi Arabia  
Zhen Luo, China  
Shuping Ma, China  
Changfeng Ma, China  
Ruyun Ma, China  
Li Ma, China  
Lifeng Ma, China  
Krzysztof Magnucki, Poland  
Nazim I. Mahmudov, Turkey  
Oluwole Daniel Makinde, South Africa  
Flavio Manenti, Italy  
Francisco J. Marcelln, Spain  
Vasile Marinca, Romania  
Giuseppe Marino, Italy  
Guiomar Martín-Herrán, Spain  
Carlos Martín-Vide, Spain  
Alessandro Marzani, Italy  
Nikos E. Mastorakis, Bulgaria  
Nicola Mastronardi, Italy  
Panayotis Takis Mathiopoulos, Greece  
Gianluca Mazzini, Italy  
Marta Mazzocco, UK  
Michael McAleer, The Netherlands  
Stephane Metens, France  
Michael Meylan, Australia  
Efrén Mezura-Montes, Mexico

Fan Min, China  
 Alain Miranville, France  
 Ram N. Mohapatra, USA  
 S. A. Mohiuddine, Saudi Arabia  
 Gisele Mophou, France  
 José Morais, Portugal  
 Cristinel Mortici, Romania  
 Emmanuel Moulay, France  
 Jaime E. Munoz Rivera, Brazil  
 Javier Murillo, Spain  
 Roberto Natalini, Italy  
 Srinivasan Natesan, India  
 Tatsushi Nishi, Japan  
 Mustapha Nourelfath, Canada  
 Andreas Öchsner, Australia  
 Wlodzimierz Ogryczak, Poland  
 Roger Ohayon, France  
 Javier Oliver, Spain  
 Soontorn Oraintara, USA  
 Donal O'Regan, Ireland  
 Martin Ostoja-Starzewski, USA  
 Turgut Öziş, Turkey  
 Claudio Padra, Argentina  
 Vincent Pagneux, France  
 Reinaldo Martinez Palhares, Brazil  
 Quanke Pan, China  
 Endre Pap, Serbia  
 Sehie Park, Korea  
 Manuel Pastor, Spain  
 Giuseppe Pellicane, South Africa  
 Francesco Pellicano, Italy  
 Juan Manuel Peña, Spain  
 Jian-Wen Peng, China  
 Ricardo Perera, Spain  
 Fernando Perez-Cruz, Spain  
 Malgorzata Peszynska, USA  
 Allan C. Peterson, USA  
 Vu Ngoc Phat, Vietnam  
 Andrew Pickering, Spain  
 Somyot Plubtieng, Thailand  
 Hector Pomares, Spain  
 Kerehalli V. Prasad, India  
 Radu-Emil Precup, Romania  
 Mario Primicerio, Italy  
 Morteza Rafei, The Netherlands  
 P. Rattanadecho, Thailand  
 Laura Rebollo-Neira, UK  
 Mahmoud M. Reda Taha, USA  
 Roberto Renò, Italy  
 J. A. Rodriguez-Velzquez, Spain  
 Ignacio Rojas, Spain  
 Carla Roque, Portugal  
 Debasish Roy, India  
 Imre J. Rudas, Hungary  
 Abbas Saadatmandi, Iran  
 Kunihiko Sadakane, Japan  
 Samir Saker, Egypt  
 Rathinasamy Sakthivel, Korea  
 Juan J. S. González, Spain  
 Miguel A. F. Sanjuan, Spain  
 Bogdan Sasu, Romania  
 Richard Saurel, France  
 Wolfgang Schmidt, Germany  
 Mehmet Sezer, Turkey  
 Naseer Shahzad, Saudi Arabia  
 Pengjian Shang, China  
 M. Shariyat, Iran  
 Hui-Shen Shen, China  
 Jian Hua Shen, China  
 Yong Shi, China  
 Yasuhide Shindo, Japan  
 Patrick Siarry, France  
 Fernando Simões, Portugal  
 Theodore E. Simos, Greece  
 Georgios Sirakoulis, Greece  
 Robert J. Smith, Canada  
 Francesco Soldovieri, Italy  
 Abdel-Maksoud A. Soliman, Egypt  
 Qiankun Song, China  
 Xinyu Song, China  
 Yuri N. Sotskov, Belarus  
 Ivanka Stamova, USA  
 Niclas Strömberg, Sweden  
 Ray K.L. Su, Hong Kong  
 Housheng Su, China  
 Jitao Sun, China  
 Wenyu Sun, China  
 Chengjun Sun, Hong Kong  
 W.Y. Szeto, Hong Kong  
 Toshio Tagawa, Japan  
 Ying Tan, China  
 San-Yi Tang, China  
 XianHua Tang, China  
 Nasser-Eddine Tatar, Saudi Arabia  
 Zhidong Teng, China  
 Engang Tian, China  
 Alexander Timokha, Norway  
 Aydin Tiryaki, Turkey  
 Yiyong Tong, USA  
 Hossein Torkaman, Iran  
 Mariano Torrisi, Italy  
 Juan J. Trujillo, Spain  
 Jung-Fa Tsai, Taiwan  
 George Tsiatas, Greece  
 Ch. Tsitouras, Greece  
 Antonia Tulino, USA  
 Stefano Ubertini, Italy  
 Alexandrina Untaroiu, USA  
 Sergey Utyuzhnikov, UK  
 Kuppalapalle Vajravelu, USA  
 Alvaro Valencia, Chile  
 Olaf van der Sluis, The Netherlands  
 Erik Van Vleck, USA  
 Ezio Venturino, Italy  
 Jesus Vigo-Aguiar, Spain  
 Michael N. Vrahatis, Greece  
 Michael Vynnycky, Sweden  
 Dongqing Wang, China  
 Youqing Wang, China  
 Xiang Wang, China  
 Yuh-Rau Wang, Taiwan  
 Peiguang Wang, China  
 Shuming Wang, Singapore  
 Heng Wang, Singapore  
 Yaonan Wang, China  
 Qing-Wen Wang, China  
 Guangchen Wang, China  
 Baolin Wang, China  
 Mingxin Wang, China  
 Junzo Watada, Japan  
 Jinjia Wei, China  
 Wei Wei, China  
 Guoliang Wei, China  
 Junjie Wei, China  
 Li Weili, China  
 Martin Weiser, Germany  
 Frank Werner, Germany  
 Man Leung Wong, Hong Kong  
 Yuqiang Wu, China  
 Min-Hsien Wu, Taiwan  
 Wei Wu, China  
 Xiangjun Wu, China  
 Qingbiao Wu, China  
 Xian Wu, China

Shi-Liang Wu, China  
Cheng Wu, China  
Shanhe Wu, China  
Yonghui Xia, China  
Tiecheng Xia, China  
Xian Xian-Yong, China  
Xuejun Xie, China  
Gongnan Xie, China  
Daoyi Xu, China  
Zhiqiang Xu, China  
Yuesheng Xu, USA  
Wei Xu, China  
Fuzhen Xuan, China  
Gregory S. Yablonsky, USA  
Chao Yan, USA  
Chao Yang, China  
Suh-Yuh Yang, Taiwan  
Bin Yang, China  
Chao-Tung Yang, Taiwan  
Na Yang, China  
Guowei Yang, China  
Chunyu Yang, China

Zhichun Yang, China  
Xiao-Jun Yang, China  
Dar-Li Yang, Taiwan  
Her-Terng Yau, Taiwan  
Wei-Chang Yeh, Taiwan  
Guan H. Yeoh, Australia  
Chih-Wei Yi, Taiwan  
Simin Yu, China  
Bo Yu, China  
Xiaohui Yuan, China  
Jinyun Yuan, Brazil  
Gonglin Yuan, China  
Rafal Zdunek, Poland  
Ashraf Zenkour, Egypt  
Guisheng Zhai, Japan  
Jianming Zhan, China  
Meng Zhan, China  
Long Zhang, China  
Ke Zhang, China  
Zhengqiu Zhang, China  
Sheng Zhang, China  
Jifeng Zhang, China

Heping Zhang, China  
Henggui Zhang, UK  
Liang Zhang, China  
Jiangang Zhang, China  
Jingxin Zhang, Australia  
Zihua Zhang, China  
Shan Zhao, USA  
Chongbin Zhao, Australia  
Yun-Bo Zhao, UK  
Baosheng Zhao, China  
Renat Zhdanov, USA  
Dong Zheng, USA  
Huaichun Zhou, China  
Huamin Zhou, China  
Shangbo Zhou, China  
Bin Zhou, China  
William Zhu, China  
Xinqun Zhu, Australia  
Quanxin Zhu, China  
Goangseup Zi, Korea  
Zhiqiang Zuo, China  
J. C. D. Hoenderkamp, The Netherlands

# Contents

**Mathematical and Numerical Modeling of Flow and Transport 2013**, Shuyu Sun, Mohamed Fathy El-Amin, and Bo Yu  
Volume 2014, Article ID 320831, 2 pages

**An Efficient Methodology for Calibrating Traffic Flow Models Based on Bisection Analysis**, Enzo C. Jia, Jianqiang Wang, and Daiheng Ni  
Volume 2014, Article ID 949723, 12 pages

**Similarity Solution of Marangoni Convection Boundary Layer Flow over a Flat Surface in a Nanofluid**, Norihan Md. Arifin, Roslinda Nazar, and Ioan Pop  
Volume 2013, Article ID 634746, 8 pages

**Design and Simulation of a Fused Silica Space Cell Culture and Observation Cavity with Microfluidic and Temperature Controlling**, Shangchun Fan, Jinhao Sun, Weiwei Xing, Cheng Li, and Dongxue Wang  
Volume 2013, Article ID 378253, 13 pages

**Flow Patterns Transition Law of Oil-Water Two-Phase Flow under a Wide Range of Oil Phase Viscosity Condition**, Wei Wang, Wei Cheng, Kai Li, Chen Lou, and Jing Gong  
Volume 2013, Article ID 291217, 8 pages

**Multiobjective Optimization of Low-Specific-Speed Multistage Pumps by Using Matrix Analysis and CFD Method**, Qiaorui Si, Shouqi Yuan, Jianping Yuan, Chuan Wang, and Weigang Lu  
Volume 2013, Article ID 136195, 10 pages

**Proposal of Damping Function for Low-Reynolds-Number  $k-\varepsilon$  Model Applicable in Prediction of Turbulent Viscoelastic-Fluid Flow**, Takahiro Tsukahara and Yasuo Kawaguchi  
Volume 2013, Article ID 197628, 15 pages

**Multiphase, Multicomponent Simulation for Flow and Transport during Polymer Flood under Various Wettability Conditions**, Ji Ho Lee and Kun Sang Lee  
Volume 2013, Article ID 101670, 8 pages

**Link-Based Signalized Arterial Progression Optimization with Practical Travel Speed**, Wu Xianyu, Hu Peifeng, and Yuan Zhenzhou  
Volume 2013, Article ID 197313, 13 pages

**A Mathematical Model for the Flow Resistance and the Related Hydrodynamic Dispersion Induced by River Dunes**, Marilena Pannone, Annamaria De Vincenzo, and Francesco Brancati  
Volume 2013, Article ID 432610, 9 pages

**Hydraulic Transients Induced by Pigging Operation in Pipeline with a Long Slope**, Tao Deng, Jing Gong, Haihao Wu, Yu Zhang, Siqi Zhang, Qi Lin, and Huishu Liu  
Volume 2013, Article ID 231260, 9 pages

**Dynamic Characteristics of Rotating Stall in Mixed Flow Pump**, Xiaojun Li, Shouqi Yuan, Zhongyong Pan, Yi Li, and Wei Liu  
Volume 2013, Article ID 104629, 12 pages

**New Analytical and Numerical Solutions for Mixed Convection Boundary-Layer Nanofluid Flow along an Inclined Plate Embedded in a Porous Medium**, Emad H. Aly and Abdelhalim Ebaid  
Volume 2013, Article ID 219486, 7 pages

**Pressure Transient Analysis of Dual Fractal Reservoir**, Xiao-Hua Tan, Xiao-Ping Li, Jian-Yi Liu, Chuan Tang, and Jin-man Li  
Volume 2013, Article ID 137518, 9 pages

**MHD Forced Convection Laminar Boundary Layer Flow of Alumina-Water Nanofluid over a Moving Permeable Flat Plate with Convective Surface Boundary Condition**, S. M. AbdEl-Gaied and M. A. A. Hamad  
Volume 2013, Article ID 403210, 8 pages

**Simulation of Evacuation Characteristics Using a 2-Dimensional Cellular Automata Model for Pedestrian Dynamics**, Liqiang Ji, Yongsheng Qian, Junwei Zeng, Min Wang, Dejie Xu, Yan Yan, and Shuo Feng  
Volume 2013, Article ID 284721, 8 pages

**Study on the Convective Term Discretized by Strong Conservation and Weak Conservation Schemes for Incompressible Fluid Flow and Heat Transfer**, Peng Wang, Bo Yu, Jianyu Xie, Yu Zhao, Jingfa Li, and Qianqian Shao  
Volume 2013, Article ID 630517, 10 pages

**Mathematical Analysis of Casson Fluid Model for Blood Rheology in Stenosed Narrow Arteries**, J. Venkatesan, D. S. Sankar, K. Hemalatha, and Yazariah Yatim  
Volume 2013, Article ID 583809, 11 pages

**Optimized Weighted Essentially Nonoscillatory Third-Order Schemes for Hyperbolic Conservation Laws**, A. R. Appadu and A. A. I. Peer  
Volume 2013, Article ID 428681, 12 pages

**The Fractal Dimension of River Length Based on the Observed Data**, Ni Zhihui, Wu Lichun, Wang Ming-hui, Yi Jing, and Zeng Qiang  
Volume 2013, Article ID 327297, 9 pages

**Simulation of Stress Distribution near Weld Line in the Viscoelastic Melt Mold Filling Process**, Binxin Yang, Jie Ouyang, and Fang Wang  
Volume 2013, Article ID 856171, 8 pages

**Comparison Study on the Performances of Finite Volume Method and Finite Difference Method,**

Renwei Liu, Dongjie Wang, Xinyu Zhang, Wang Li, and Bo Yu

Volume 2013, Article ID 596218, 10 pages

**Numerical Simulation on Flow Field of Oilfield Three-Phase Separator,** Yong-tu Liang, Sheng-qiu Zhao,

Xia-xue Jiang, Xian-qi Jia, and Wang Li

Volume 2013, Article ID 298346, 6 pages

**Mixed Platoon Flow Dispersion Model Based on Speed-Truncated Gaussian Mixture Distribution,**

Weitiao Wu, Wenzhou Jin, and Luou Shen

Volume 2013, Article ID 480965, 9 pages

## Editorial

# Mathematical and Numerical Modeling of Flow and Transport 2013

Shuyu Sun,<sup>1</sup> Mohamed Fathy El-Amin,<sup>2</sup> and Bo Yu<sup>3</sup>

<sup>1</sup> Computational Transport Phenomena Laboratory, King Abdullah University of Science and Technology, Thuwal 23955, Saudi Arabia

<sup>2</sup> Department of Mathematics, Aswan University, Aswan 81528, Egypt

<sup>3</sup> Department of Oil and Gas Storage and Transportation Engineering, China University of Petroleum-Beijing, Changping, Beijing 102249, China

Correspondence should be addressed to Shuyu Sun; [shuyu.sun@kaust.edu.sa](mailto:shuyu.sun@kaust.edu.sa)

Received 5 May 2014; Accepted 5 May 2014; Published 10 August 2014

Copyright © 2014 Shuyu Sun et al. This is an open access article distributed under the Creative Commons Attribution License, which permits unrestricted use, distribution, and reproduction in any medium, provided the original work is properly cited.

Application areas of flow and transport phenomena vary widely; however, accurate mathematical and numerical simulation of flow and transport remains a challenging topic from many aspects of physical modeling, numerical analysis, and scientific computation. This annual issue concerns numerical and mathematical analysis that are very important for all scientific, engineering, and environmental applications. Rapid progress has been seen in the analysis of flow and transport phenomena especially in recent years because of the significance of flow and transport to science and engineering. The list of papers published in this issue covers a wide range of applications using different approaches and analysis. The list of papers includes nanofluids transport, reservoir modeling, optimization problems, river flow, complex dynamic flow, traffic flow, and finally numerical scheme testing that may be stated as follows.

The first group of papers is devoted to investigate flow and transport of nanofluids. The paper entitled “*Similarity solution of Marangoni convection boundary layer flow over a flat surface in a nanofluid*” by N. Md. Arifin et al. introduced that the problem of steady Marangoni boundary layer flow and heat transfer over a flat plate in a nanofluid is studied using different types of nanoparticles. E. H. Aly and A. Ebaid presented two different analytical and numerical methods in the paper “*New analytical and numerical solutions for mixed convection boundary-layer nanofluid flow along an inclined plate embedded in a porous medium*” to solve the problem of mixed convection boundary-layer nanofluids flow

along an inclined plate embedded in a porous medium. The paper “*MHD forced convection laminar boundary layer flow of alumina-water nanofluid over a moving permeable flat plate with convective surface boundary condition*” by S. M. AbdEl-Gaied and M. A. A. Hamad studied the problem of two-dimensional steady forced convection boundary layer viscous incompressible flow of alumina-water nanofluid over a moving permeable vertical flat plate under the effect of a magnetic field normal to the plate. P. Wang et al. have discretized the convective term by two different schemes, namely, strong and weak conservation schemes, in a paper entitled “*Study on the convective term discretized by strong conservation and weak conservation schemes for incompressible fluid flow and heat transfer*.” The paper “*Design and simulation of a fused silica space cell culture and observation cavity with microfluidic and temperature controlling*” by S. Fan et al. focuses on a principle prototype of space animal cell perfusion culture and observation.

The second group concerns oil reservoir problems. W. Wang et al. in the paper “*Flow patterns transition law of oil-water two-phase flow under a wide range of oil phase viscosity condition*” have introduced that a systematic work on the prediction of flow patterns transition of the oil-water two-phase flows is carried out under a wide range of oil phase viscosities, where four main flow regimes are considered including stratified, dispersed, core-annular, and intermittent flow. Also, a paper entitled “*Multiphase, multicomponent simulation for flow and transport during polymer flood under*

*various wettability conditions*” by J. H. Lee and K. S. Lee concerns accurate assessment of polymer flood which requires the understanding of flow and transport of fluids involved in the process under different wettability of reservoirs. Finally, the paper “*Pressure transient analysis of dual fractal reservoir*” by X.-H. Tan et al. discusses the semianalytical model of a dual fractal reservoir transient flow. In the paper “*Numerical simulation on flow field of oilfield three-phase separator*,” Y.-t. Liang et al. have studied the flow field of three-phase separator numerically with taking into consideration the production situation of PetroChina Huabei Oilfield.

Some fluid optimization problems are studied in the following group of papers. T. Tsukahara and Y. Kawaguchi presented a paper entitled “*Proposal of damping function for low-Reynolds-number  $k-\epsilon$  model applicable in prediction of turbulent viscoelastic-fluid flow*” to study the problem of low-Reynolds-number  $k-\epsilon$  model for viscoelastic fluid to predict the frictional-drag reduction and the turbulence modification in a wall-bounded turbulent flow. In another paper “*Link-based signalized arterial progression optimization with practical travel speed*” by W. Xianyu et al., the authors propose an algorithm on how to obtain an optimal coordinated signal timing plan with both optimal link bandwidth and optimal arterial bandwidth considering practical vehicles’ speed. Q. Si et al. in the paper “*Multiobjective optimization of low-specific-speed multistage pumps by using matrix analysis and CFD method*” have studied multiobjective optimization problems in low-specific-speed pumps. In the paper “*Optimized weighted essentially nonoscillatory third-order schemes for hyperbolic conservation laws*,” A. R. Appadu and A. A. I. Peer have derived a third-order weighted essentially nonoscillatory (WENO) scheme by coupling a WENO spatial discretization scheme with a temporal integration scheme.

This group focuses on the river flow problems. In the paper “*The fractal dimension of river length based on the observed data*,” N. Zhihui et al. have used some variable dimension fractal analysis methods to study river flow discharge. M. Pannone et al. in another paper entitled “*A mathematical model for the flow resistance and the related hydrodynamic dispersion induced by river dunes*” have derived equation for the total flow resistance associated with river bedforms with focusing on the effect induced by the out-of-phase free surface undulations appearing in presence of sand dunes.

Complex flows problems are also presented in the following articles. T. Deng et al. in their paper “*Hydraulic transients induced by pigging operation in pipeline with a long slope*” have proposed a model for the dynamic simulation of the pigging process after water pressure testing in a long slope pipeline. The paper “*Dynamic characteristics of rotating stall in mixed flow pump*” by X. Li et al. is devoted to investigate prerotation generated at the upstream of the impeller, leakage flow at the tip clearance between the casing and the impeller, and strong reserve flow at the inlet of the diffuser. L. Ji et al. have studied the people-people interaction and the people-environment interaction in the occupants’ evacuation process, in the paper “*Simulation of evacuation characteristics using a 2-dimensional cellular automata model for pedestrian dynamics*.” In the paper “*Mathematical analysis of Casson*

*fluid model for blood rheology in stenosed narrow arteries*,” J. Venkatesan et al. have investigated the flow of blood through a narrow artery with bell-shaped stenosis.

Traffic flow problems are studied in two papers. W. Wu et al. in their paper “*Mixed platoon flow dispersion model based on speed-truncated Gaussian mixture distribution*” have presented a macroscopic mixed platoon flow dispersion model (MPFDM) based on field data, to simulate the platoon dispersion process along the road section between two adjacent intersections from the flow view. In the paper “*An efficient methodology for calibrating traffic flow models based on bisection analysis*” by E. C. Jia et al., results are presented for a pedestrian walkway for pedestrian flow up to 108 persons/min and the limitations of the implemented system are enumerated.

Finally some numerical issues are discussed in the following papers. Vorticity-stream function method and MAC algorithm are adopted to systemically compare the finite volume method (FVM) and finite difference method (FDM) in the paper “*Comparison study on the performances of finite volume method and finite difference method*” by R. Liu et al. The finite volume methods on nonstaggered grids are used to solve the viscoelastic-Newtonian two-phase model in the paper “*Simulation of stress distribution near weld line in the viscoelastic melt mold filling process*” by B. Yang et al.

In conclusion, this special issue presents and highlights new applications and new challenges in different five important research areas of flow and transport. This special issue is not intended to be an exhaustive collection nor a survey of all of the current trends in flow and transport research; many additional significant research areas of flow and transport still exist and remain to be explored, but multidisciplinary research effort remains a clear trend.

## Acknowledgments

The authors would like to thank the participants of the special issue for their inspiring contributions and the anonymous reviewers for their diligent work, which led to the high quality of the special issue. The lead guest editor S. Sun would like to acknowledge KAUST Faculty Baseline Research Fund for supporting his research in flow and transport.

Shuyu Sun  
Mohamed Fathy El-Amin  
Bo Yu

## Research Article

# An Efficient Methodology for Calibrating Traffic Flow Models Based on Bisection Analysis

Enzo C. Jia,<sup>1</sup> Jianqiang Wang,<sup>2</sup> and Daiheng Ni<sup>1</sup>

<sup>1</sup> Department of Civil Engineering, University of Massachusetts, Amherst, MA 01003, USA

<sup>2</sup> State Key Laboratory of Automotive Safety and Energy, Tsinghua University, Beijing 100084, China

Correspondence should be addressed to Jianqiang Wang; [wjqlws@tsinghua.edu.cn](mailto:wjqlws@tsinghua.edu.cn)

Received 19 July 2013; Accepted 22 December 2013; Published 18 February 2014

Academic Editor: Bo Yu

Copyright © 2014 Enzo C. Jia et al. This is an open access article distributed under the Creative Commons Attribution License, which permits unrestricted use, distribution, and reproduction in any medium, provided the original work is properly cited.

As urban planning becomes more sophisticated, the accurate detection and counting of pedestrians and cyclists become more important. Accurate counts can be used to determine the need for additional pedestrian walkways and intersection reorganization, among other planning initiatives. In this project, a camera-based approach is implemented to create a real-time pedestrian and cyclist counting system which is regularly accurate to 85% and often achieves higher accuracy. The approach retasks a state-of-the-art traffic camera, the Autoscope Solo Terra, for pedestrian and bicyclist counting. Object detection regions are sized to identify multiple pedestrians moving in either direction on an urban sidewalk and bicyclists in an adjacent bicycle lane. Collected results are processed in real time, eliminating the need for video storage and postprocessing. In this paper, results are presented for a pedestrian walkway for pedestrian flow up to 108 persons/min and the limitations of the implemented system are enumerated. Both pedestrian and cyclist counting accuracy of over 90% is achieved.

## 1. Introduction

*1.1. Introduction to a Severe Highway Safety Problem.* Every year around 1.2 million people are killed in road accidents all over the world, and another 50 million get injured [1]. Among these tragedies, many are caused by aggressive driving in severe conditions that require extra carefulness, like bad weather, road sections near work zone or crash site, and so forth. Usually people have their consistent driving styles, which can be described by a traffic flow model, and under a special situation it is not guaranteed a driver adjusts his/her style properly in correspondence to the change of situations which happened on road. For example, a proportion of drivers failed to drive more carefully near work zones, and this is a remarkable source of accidents [2]. And during conditions of light precipitation, friction between tyres and pavement deteriorates significantly, but drivers not experienced enough might be not sure how careful they should be. Under such a circumstance an unexperienced driver has a high probability to drive in an overly aggressive style. As a result, an investigation conducted by FHWA [3] suggests that an average annual rate for weather-related crashes from 1995

to 2008 is approximately 1.5 million; this number accounts for 24% of all vehicle crashes annually. And during the same period more than 7 thousand people were killed on road every year, which accounts for 17% of all crash fatalities. These statistics can be found in Table 1.

*1.2. Existing Solutions.* Currently there are several methods deployed by the highway administration to improve traffic safety under severe weather conditions:

- (1) reshaping dangerous sections of road network to improve on-road safety condition. By analysing crash history, administration departments can identify road sections with relatively higher accident/fatality rates, and it is helpful to redesign and reconstruct such sections;
- (2) deploying more roadside information board, including LED display board, so the highway administration can edit information displayed;
- (3) delivering postcrash care including temporary information board and guidance by police cars.

TABLE 1: Weather-related crash statistics (annual averages 1995–2008) [3].

Road weather conditions	Annual rates (approximately)	Weather-related crash statistics	
		Percentages	
Wet pavement	1,128,000 crashes	18% of vehicle crashes	75% of weather-related crashes
	507,900 persons injured	17% of crash injuries	81% of weather-related crash injuries
	5,500 persons killed	13% of crash fatalities	77% of weather-related crash fatalities
Rain	707,000 crashes	11% of vehicle crashes	47% of weather-related crashes
	330,200 persons injured	11% of crash injuries	52% of weather-related crash injuries
	3,300 persons killed	8% of crash fatalities	46% of weather-related crash fatalities
Snow/sleet	225,000 crashes	4% of vehicle crashes	15% of weather-related crashes
	70,900 persons injured	2% of crash injuries	11% of weather-related crash injuries
	870 persons killed	2% of crash fatalities	12% of weather-related crash fatalities
Icy pavement	190,100 crashes	3% of vehicle crashes	13% of weather-related crashes
	62,700 persons injured	2% of crash injuries	10% of weather-related crash injuries
	680 persons killed	2% of crash fatalities	10% of weather-related crash fatalities
Snow/slushy pavement	168,300 crashes	3% of vehicle crashes	11% of weather-related crashes
	47,700 persons injured	2% of crash injuries	8% of weather-related crash injuries
	620 persons killed	1% of crash fatalities	9% of weather-related crash fatalities
Fog	38,000 crashes	1% of vehicle crashes	3% of weather-related crashes
	15,600 persons injured	1% of crash injuries	2% of weather-related crash injuries
	600 persons killed	1% of crash fatalities	8% of weather-related crash fatalities
Weather-related	<b>1,511,200 crashes</b>	<b>24% of vehicle crashes</b>	
	<b>629,300 persons injured</b>	<b>21% of crash injuries</b>	
	<b>7,130 persons killed</b>	<b>17% of crash fatalities</b>	

Obviously methods mentioned above are helping in improving road safety significantly; however, as we are discussing safety issues under severe conditions, there is more we can do with specially designed technologies for further help. Among methods mentioned above, solution 1 requires years of crash record, which might not be available for new road sections. And usually highway segments are designed and constructed by considering specific shapes of landscape, so it is not easy to make significant modifications. What is more, highway construction requires huge budget and amount of time, and this makes it even more difficult to reshape a segment. Regarding solutions 2 and 3, they work well in hazardous situations, but the problem we are facing is, these applications distract travellers' attention from normal driving, and this can be a remarkable cause of accidents like tailgating. When drivers are careful enough for on-going incidents on road, say, drizzle or slight accidents, distracting methods like LED displays and large-scale police car manipulation would contribute to troubling consequences. However, when severe situations like snowstorm or heavy accidents happen, it is much more possible that drivers' average aggression is too high to keep traffic safe. So here we need a supporting system to point out whether drivers are driving too aggressively to keep them safe on road or a system tells degree of drivers' aggression at the moment of observation. By deploying such a system it is possible to apply administrating strategies like solutions 2 and 3 accordingly to help modify drivers' aggression.

## 2. An Efficient Methodology

*2.1. Drivers' Aggression.* Thus, we raised the idea of developing an aggression surveillance system; intuitively the following question is how to rate a driver's aggression. The most efficient way would be finding a parameter or constant which denotes drivers' aggression in a traffic flow model, and by calibrating this model we get a quantified value of average aggression. By comparing this value with the normal aggression value under similar situations, it is helpful in making decisions of whether to intervene with on-road traffic.

### *2.2. Introduction to Traffic Flow Models and Calibration Methods*

*2.2.1. Previous Works in Traffic Flow Modelling and Calibrating.* Pursuing of a precise mathematical model to describe traffic flow behaviours has lasted for more than half a century, and there are models successfully developed and applied. Greenshields' model [4] applies a simple linear relationship to traffic density and average speed, which is not precise enough but worked as the very beginning of research on modelling traffic flow characters. Newell's model [5, 6] has a much more precise description of traffic behaviours. General Motors model [7, 8] was developed as a car-following model but can be used as a tool for research on macroscopic traffic flow theories. Similarly Gipps' model [9] is a successful

development on drawing how traffic's flow, density, and average speed depend on each other. In Kosonen's Ph.D. dissertation [10], a rule-based model was applied in simulating traffic behaviours in urban environment, and this was based on previous research on utilizing fuzzy decision rules to simulate traffic flow [11]. As the latest achievement on modelling traffic flows, Daiheng Ni et al. [12–14] utilized field theory to simulate behaviours of vehicles on road and got the longitudinal control model (LCM), which we will introduce in detail.

On the calibration part, there are also previous works trying to locate sufficient and precise methods for finding values of parameters in traffic flow models. This field of research was initiated by Chandler et al. [7], Gazis et al. [8], and Herman et al. [15] in the late 1950s and early 1960s. GM model was opted for by Chandler's team and field data was studied for obtaining parameter values in the model. With development of computational technology, simulation tools are utilized in studying traffic phenomena and calibrating models, as revealed by Brackstone and McDonald [16]. In the past decade there are several research projects improving calibration methods. Using field data obtained on IH-10 in Houston, Texas, Schultz and Rilett [17] evaluated the parameter values they calculated with microscopic traffic simulation tools. In 2008, Kesting and Treiber [18] tested a method that minimized the difference between field data and model prediction. They resulted with errors lower than 30%. Also some ideas from computer science helped getting a higher accuracy. S. P. Hoogendoorn and R. Hoogendoorn [19] implemented genetic algorithm for calculating parameter values in traffic flow models in 2010.

### 2.2.2. Traffic Flow Models for Evaluating Drivers' Aggression.

A suitable model for finding average aggression is longitudinal control model (LCM) [12–14]. In this macroscopic model we define relationship between traffic density and speed as follows:

$$k = \frac{1}{(\gamma v^2 + \tau v + l) \left[ 1 - \ln \left( 1 - \left( v/v_f \right) \right) \right]}, \quad (1)$$

where  $k$  is traffic density,  $v$  is space-mean speed,  $\gamma$  denotes degree of aggression that characterizes the driving population,  $\tau$  is average response time that characterizes the driving population,  $l$  is average effective vehicle length, and  $v_f$  is free flow speed. So if we get the value of  $\gamma$  against field data under a specific situation, current degree of aggression on road is found.

Also we use Newell's model as an enhancement for modelling drivers' behaviours in this research.

So if we set a live camera at roadside to collect real-time traffic data and use these data to calibrate LCM model and Newell's model, it is possible to get current value of average aggression or other related parameters. However, calibration tasks lead to optimization problems, which usually costs huge amounts of time finding solutions. In order to clear this challenge, an efficient algorithm developed for calibrating traffic flow models against empirical data is demonstrated in the following sections.

**2.3. Essential Points of This Methodology.** To achieve an approach for such a system, three requirements are pointed out:

- (1) this approach should be able to precisely reflect traffic conditions at the specific moment on a chosen segment of highway;
- (2) computation should not be a significant burden so the system can react to changing situations immediately;
- (3) algorithm adopted by this system must have a rigorous mathematical derivation of evaluating criterion.

Item 1 is intuitive since precision is fundamental for a research on calibration. In item 2, by emphasizing efficiency of the algorithm this system adopts, it is necessary to get it to react quickly, and this fact further strengthens to the system's ability to reflect real situation on assigned location and time. Also we design the third item because such a system is supposed to work in various environments, regardless of different traffic flow, density, speed, or such rates affected by abnormal situations.

To achieve these objectives, the following ideas are raised:

- (1) aggregating raw observation data to reduce the algorithm's running time and applying coefficients on aggregated observation points to offset loss on accuracy because of data aggregation;
- (2) using bisection method to reach a solution of optimized parameters rapidly.

## 3. Principle of Methodology

**3.1. Background.** Generally speaking, calibration problems lead to optimization problems. However, under most circumstances people solve optimization problems by applying numeration methods, considering that it is not easy to find a universal method for a kind of problems. So even successful commercial optimization packages, like IBM ILOG CPLEX Optimizer, work in an extremely time-consuming way. Meanwhile, most root-finding problems have corresponding well-defined solving methods, either analytical or numerical or both. And among these methods a lot are time efficient, such as bisection method and Newton's method for solving linear equations and Crank-Nicolson method for partial differential equations.

Based on facts mentioned above, we determine principle of this research as converting an optimization problem into a root-finding problem. However, the challenge here is that an optimization problem requires a solution which achieves the minimized value of its objective function, whilst what a root-finding problem needs is a solution to get the value of a function equal to zero. So regarding this particular calibration problem, we establish a function (12). And when value of this function goes towards zero, a traffic flow model gets better accuracy. In this way we convert an optimization problem into a root-finding problem, and then it is possible to apply numerical methods for solutions. Method of establishing this variable is introduced in Section 4.2.

3.2. *An Introduction to Bisection Method.* In engineering applications, there are usually complex computing tasks that require high amount of resources on both time and hardware. This leads to an obvious conflict between efficiency and cost. As a compromised solution, scientists in applied mathematics developed a series of algorithms to approximate solutions of specified computing problems. In this way an algorithm, which we call a numerical method, is designed to deliver an approximated solution to a computing problem with a high enough and thus adjustable accuracy.

Among the most well-known numerical algorithms, bisection method, also known as binary search method, is widely used because of its simplicity and robustness. As most other numerical algorithms, this method is applied to solve root-finding problems  $f(x) = 0$ , where the continuous function  $f$  is defined on interval  $[a, b]$  as sign of  $f(a)$  is opposite to  $f(b)$ 's. Thus, such a problem can be described as

$$\begin{aligned} f(x) = 0, \quad x \in [a, b] \quad a < b \\ f(a) \times f(b) \leq 0. \end{aligned} \tag{2}$$

A loop is designed to solve the problem described in (2) where, in every iteration of the loop, we divide the interval  $[a, b]$  into two halves  $[a, (a + b)/2]$  and  $[(a + b)/2, b]$ . By computing value of function  $f$  at midpoint  $(a + b)/2$ , we can determine which half of the interval a root of  $f(x) = 0$  lies in. If  $f((a + b)/2)$  has the same sign as  $f(a)$ , then it's certain that there is a root of  $f(x) = 0$  in interval  $[(a + b)/2, b]$  or if  $f((a + b)/2)$  has the same sign as  $f(b)$ , then this root can be found in  $[a, (a + b)/2]$ . Also it is theoretically possible, but very unlikely, that  $f((a + b)/2) = 0$  which leads to an exact solution  $(a + b)/2$ . As this loop going interval  $[a, b]$  keeps shrinking and this method makes sure that there is a root which lies in this interval. So when length of  $[a, b]$  is smaller than expected error  $\epsilon$ , either  $a$  or  $b$  can be final result of this looping as approximated solution to the problem expressed in (2). This means we can take  $c = (a + b)/2$  as final result when length of  $[a, b]$  is smaller than  $2\epsilon$ , since in this way one less loop is computed to get a better performance on running time. So determination of the result from this method can be described in (3), as  $s$  denotes approximated solution for above root-finding problem and  $\epsilon$  is the maximum error allowed:

$$s = \frac{a + b}{2} \quad \text{when } |a - b| < \epsilon. \tag{3}$$

Though there are many methods providing faster convergence, we still adopt bisection method instead of other options. And the reason is, our problem is finding root for a function defined in (12), and this function is not a definite mathematical function, so simplicity of a root-finding method is essential to guarantee robustness under any possible situation of input data provided. For example, Newton's method is more advanced compared to bisection method but requires derivation operations, and in this case derivation leads to unpredictable results. After testing repeatedly, we see that bisection method delivers both time efficiency and robustness we need.

And Figure 1 shows principle of how this method works.

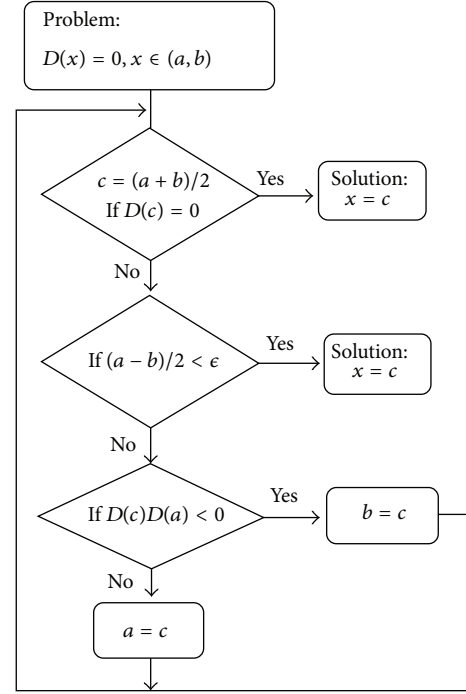


FIGURE 1: Flow chart for bisection method.

#### 4. Structure of Algorithm

Structure of our methodology is a nested two-level looping. The inner looping is a collection of evaluating results for a particular set of parameters of a traffic flow model, and the outer looping is an implementation of bisection method for search of a set of optimized parameters. And before the nested looping we aggregated data first.

4.1. *Data Aggregation.* To reduce running time of this algorithm, aggregation of empirical data should be the first step. We aggregate raw field observation data by averaging 3D data values along an axis. For example, a set of speed-density-flow data are aggregated by averaging speed, density, and flow values of all observations which fall into a section  $k^{(i)} < k < k^{(i+1)}$ , where  $k^{(i)}$  and  $k^{(i+1)}$  are lower and upper bounds of  $i$ th density section. And this procession can be expressed as

$$\begin{aligned} \bar{v}_i &= \frac{1}{n} \sum_{j=1}^{n_i} (v_{ij}), \\ \bar{k}_i &= \frac{1}{n} \sum_{j=1}^{n_i} (k_{ij}), \\ \bar{q}_i &= \frac{1}{n} \sum_{j=1}^{n_i} (q_{ij}), \end{aligned} \tag{4}$$

where footnote  $i$  means this calculation is for  $i$ th density slice,  $n_i$  is number of raw observations in this slice,  $\bar{v}_i$ ,  $\bar{k}_i$ , and  $\bar{q}_i$  are averaged values of  $v$ ,  $k$ , and  $q$  for  $i$ th slice, respectively, and  $v_{ij}$ ,  $k_{ij}$ , and  $q_{ij}$  are coordinates for  $j$ th raw observation in  $i$ th slice of  $v$ - $k$ - $q$  coordinate system.

#### 4.2. Inner Looping: Evaluation of Parameters

4.2.1. *Derivation of Objective Function.* A calibration criterion has been raised by Rakha and Arafeh [20] and is formulated as

$$\text{Min } E = \sum_i \left\{ \left( \frac{v_i - \hat{v}_i}{\bar{v}} \right)^2 + \left( \frac{q_i - \hat{q}_i}{\bar{q}} \right)^2 + \left( \frac{k_i - \hat{k}_i}{\bar{k}} \right)^2 \right\}, \quad (5)$$

where  $q_i$ ,  $k_i$ , and  $v_i$  are flow, density, and average speed data from field tests, respectively.  $\hat{q}$ ,  $\hat{k}$ , and  $\hat{v}$  are flow, density, and average speed derived from a model, as  $\bar{q}$ ,  $\bar{k}$ , and  $\bar{v}$  are maximum value of flow, density, and speed observed in filed. This is a very good estimation for models simulating traffic flows; however, two concerns are still worth more research for solutions:

- (1) there is still room for improvement on time and resource efficiency. It is acceptable to compromise on accuracy of an algorithm in order to get it faster;
- (2) all aggregated data dots receive the same treatment, while in fact some of the dots are aggregated from more raw field observations than others, as there are many more vehicles travelling around 60 mph than those opt 30 mph on the same section of highway.

Regarding issue 1, since  $q_i = k_i \times v_i$ , also approximately  $\hat{q}_i \approx \hat{k}_i \times \hat{v}_i$  and  $\bar{q}_i \approx \bar{k}_i \times \bar{v}_i$ , thus we consider flow  $q$  in this evaluation criterion redundant, which means we can get the same result by switching to criterion 6 instead of 5:

$$\text{Min } E = \sum_i \left\{ \left( \frac{v_i - \hat{v}_i}{\bar{v}} \right)^2 + \left( \frac{k_i - \hat{k}_i}{\bar{k}} \right)^2 \right\}. \quad (6)$$

As shown in Section 4.1, we make narrow slices on  $k$ - $v$  coordinate system to get groups of data for aggregation, and here we presume it is  $k$ -axis we slice to group data, so each observation which falls into  $i$ th group satisfies  $k^{(i)} < k \leq k^{(i+1)}$ , where  $k^{(i)}$  and  $k^{(i+1)}$  are lower and upper bounds of  $i$ th density section. According to (4), we get aggregated dot's coordinate on  $k$ -axis by averaging all raw observations' corresponding coordinates; thus, if we opt for middle point between  $k^{(i+1)}$  and  $k^{(i)}$ , instead of  $\bar{k}_i$ , to approach  $k_i$  the corresponding error would be

$$\begin{aligned} \text{err} &\leq \frac{\epsilon}{2}, \\ \epsilon &= k^{(i+1)} - k^{(i)} \\ \text{when } k_i &= \frac{k^{(i+1)} + k^{(i)}}{2}, \end{aligned} \quad (7)$$

where  $\text{err}$  is error derived from approximation for  $k_i$  by middling  $i$ th slice and  $\epsilon$  is width of  $i$ th slice. So obviously if we set  $\epsilon$  to be a small enough number it is possible to opt for (7) as approximation for  $k_i$  without losing too much accuracy. In our simulation we choose  $\epsilon = 0.5$  vehicle/km. In this way

we avoid calculating average value of a set of observations as shown in (4).

By narrowing slices on  $k$ -axis, another obvious strategy is intuitive that, in calculation for (6), we can ignore the second term which is square of relative difference for density  $k$ . This is because in a slice relative difference between densities of a raw observation and the aggregated dot is very small, especially compared to that between speeds of the same dots. This can be proved by computing curve of the following function (8), which is the relationship between two terms in (6):

$$f = \frac{\sum_i ((v_i - \hat{v}_i) / \bar{v})^2}{\sum_i ((k_i - \hat{k}_i) / \bar{k})^2}. \quad (8)$$

This curve is shown in Figure 2. Also this figure perfectly explains drivers' different behaviour patterns corresponding to different density rates. When density is very low (lower than 7 vehicles per km), drivers opt for different speeds freely according to their own preferences, so speeds under such situations are distributed widely because of big variance on people's personal preferences. When there are some more vehicles on road but still not too many (8 to 24 vehicles per km), traffic flows travel fast, so under such circumstances drivers who prefer driving slowly are encouraged to drive faster to follow the flow. And as density grows higher to around 40 vehicles per km, average speed decreases remarkably. Actually average speed at this stage is so low that a significant proportion of drivers opt for fast lanes for higher speed and overtaking, and this causes a peak at 40 vehicles per km. As density goes up, there is less room for drivers' maneuvers including lane changing, accelerating, and braking; thus, there are less people driving aggressively, and this makes the curve go down gradually at density higher than 40 vehicles per km.

Thus, we can delete second term in criterion 6 without losing too much on precision of a model. In this way we improve it

$$\text{Min } E = \sum_i \left( \frac{v_i - \hat{v}_i}{\bar{v}} \right)^2. \quad (9)$$

Actually here we do not need the denominator  $\bar{v}$ , as for an optimization problem, dividing its objective function by a constant does not make any difference to the result. Similarly, replacing square operation by calculating absolute value will not affect optimization result since minimizing an equation's square leads to the same point of that by minimizing its absolute value. Thus, (10) reflects exactly the same criterion as (9):

$$\text{Min } E = \sum_i |v_i - \hat{v}_i|. \quad (10)$$

Here  $v_i$  is speed value for an aggregated field observation and  $\hat{v}_i$  is the estimated speed which corresponds to density value of the same aggregated observation. This estimation of speed is done by applying macroscopic traffic flow simulation models.

By opting for (10) as objective function, it is convenient to calculate its value without any other looping, whilst Rakda's

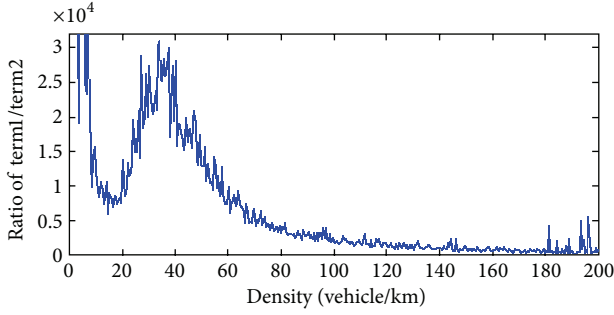


FIGURE 2: Curve computed from function (8).

method with objective function (5) requires another level of optimization to find a point  $(q'_i, k'_i, v'_i)$  which is the nearest one on a curve to an aggregated observation  $(q_i, k_i, v_i)$ . Usually this kind of optimization uses a looping to try a series of points on the curve; after calculating distance from every one of this series of points to the observation  $(q_i, k_i, v_i)$ , the point with the least distance is considered as the nearest point from the curve to  $(q_i, k_i, v_i)$ . In our algorithm this level of optimization can be avoided; thus, a considerable amount of time is saved from this step.

**4.2.2. Conversion to a Root-Finding Problem.** In order to implement bisection method in later Section 4.3, it's necessary to convert this optimization problem into a root-finding problem. Key to this conversion is finding a function which has a root in a domain of its parameters, and such a root should be very near, if not the same, to solution of the optimization problem solved with objective function (10). Thus, we assign positive and negative signs to results of inner looping. In the case discussed above, if an aggregated observation point locates at left side of corresponding speed-density curve we multiply the result of its objective function by  $-1$ , and if it sits at right side then we keep it as positive. Actually this strategy can be applied simply by removing absolute value calculation in objective function (10). So the root-finding problem is as follows:

$$F = \sum_i v_i - \hat{v}_i. \quad (11)$$

In this function every aggregated observation is considered equally important; however, in reality we do not agree with this assumption, since during most time vehicles travel in traffic with density less than 50 vehicles per km. Our observation data reveals that more than 60% traffic happens with density lower than 50 vehicles per km, and this can be found in following Figure 3.

So it is appropriate to multiply every aggregated observation with a term of weight which is number of raw observations it is aggregated from. So we have the final version of the root-finding problem as

$$F = \sum_i n_i (v_i - \hat{v}_i), \quad (12)$$

where  $n_i$  is the number of raw observations which fall into  $i$ th slice of  $k$ - $v$  plane, and these raw observations are used to

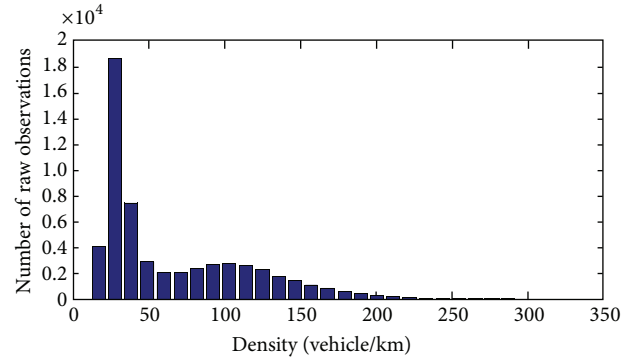


FIGURE 3: Number of raw observations which happened at different density levels.

produce  $i$ th aggregated observation by applying (4). Here we name result of this function degree of satisfaction for a set of parameters, and purpose of inner looping is to find degree of satisfaction for a specific set of parameters, whilst outer looping explained in Section 4.3 is to find a set of parameters which has its degree of satisfaction the nearest one to zero.

**4.3. Outer Looping: Bisection Method.** As we get degree of satisfaction of every set of parameters in inner looping, different parameter sets get evaluated by running outer looping. Goal of this evaluation is to find a set of model parameters which let right side of (12) equal 0. So the problem here is to find a root for this function, and intuitively numerical analysis methods can help because it is not a simple linear function. Here we adopt bisection method because of its simplicity and robustness. Using LCM model as an example to calibrate,

$$k = \frac{1}{(\gamma v^2 + \tau v + l) [1 - \ln(1 - (v/v_f))]}, \quad (13)$$

where  $k$  is traffic density,  $v$  is space-mean speed,  $\gamma$  denotes aggressiveness that characterizes the driving population,  $\tau$  is average response time that characterizes the driving population,  $l$  is average effective vehicle length, and  $v_f$  is free flow speed. So in this model we need to allocate four parameters  $\gamma$ ,  $\tau$ ,  $l$ , and  $v_f$ . As an example, steps of this bisection algorithm to optimize  $\gamma$  include the following.

- (i) Step 1: if any of  $\tau$ ,  $l$ , and  $v_f$  has already been optimized before  $\gamma$ , set these parameters as their calibrated values. And for those that have not been calibrated, set default parameter values. Default values are best guesses based on common sense and earlier experience. For  $\gamma$  we set lower bound  $\gamma_l$  and upper bound  $\gamma_u$ . Set acceptable largest error of gamma  $\epsilon$ .
- (ii) Step 2: if  $\gamma_u - \gamma_l < \epsilon$ , then return  $\gamma = (\gamma_l + \gamma_u)/2$  as result of this algorithm and quit algorithm. Otherwise, run inner looping with  $\gamma = (\gamma_l + \gamma_u)/2$  and other parameter values as set in step 1 for LCM model; get degree of satisfaction for this set of parameters with new  $\gamma$  value.
- (iii) Step 3: if degree of satisfaction value got in step 2 is greater than 0, it means we underestimated drivers'

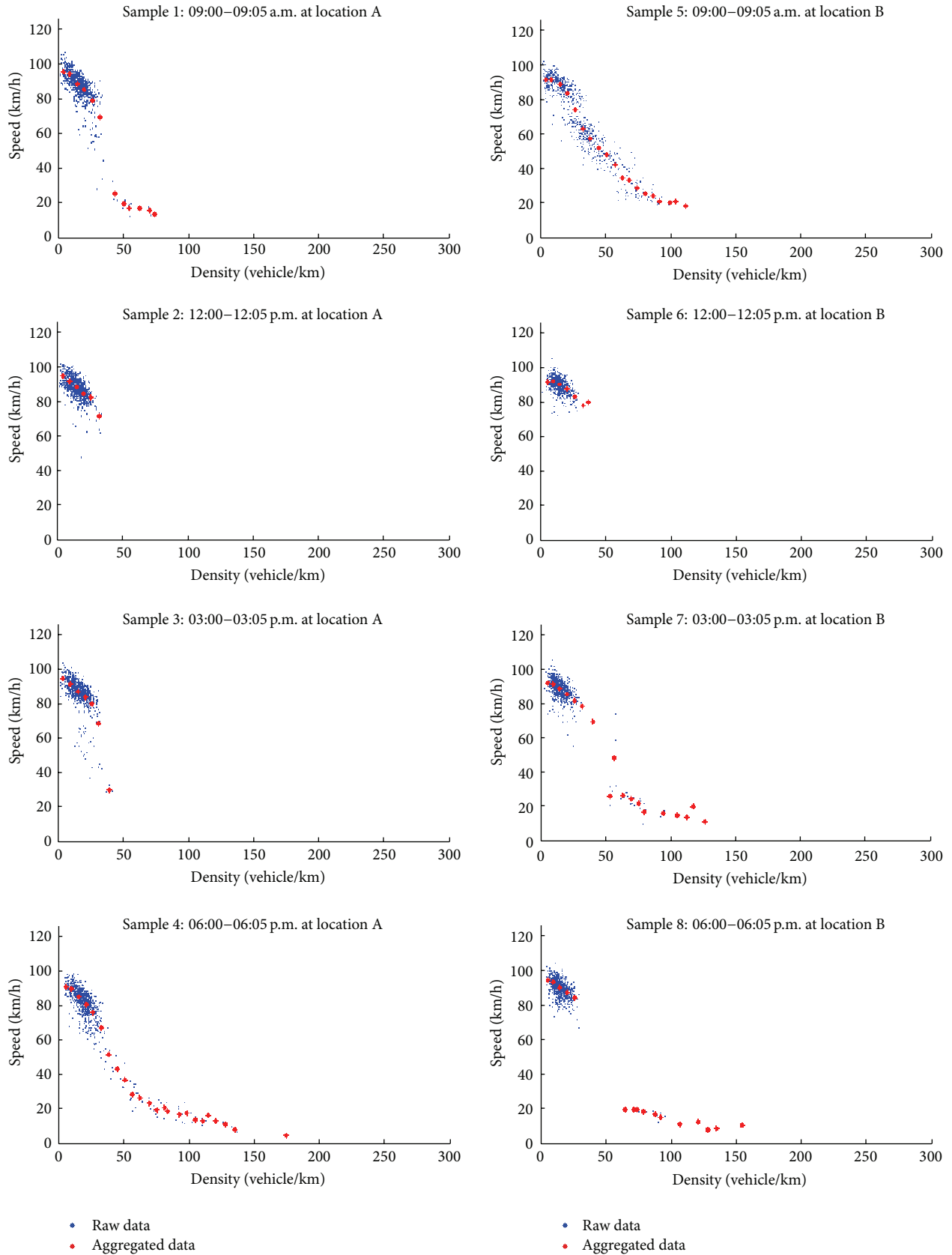


FIGURE 4: Raw and aggregated observation points.

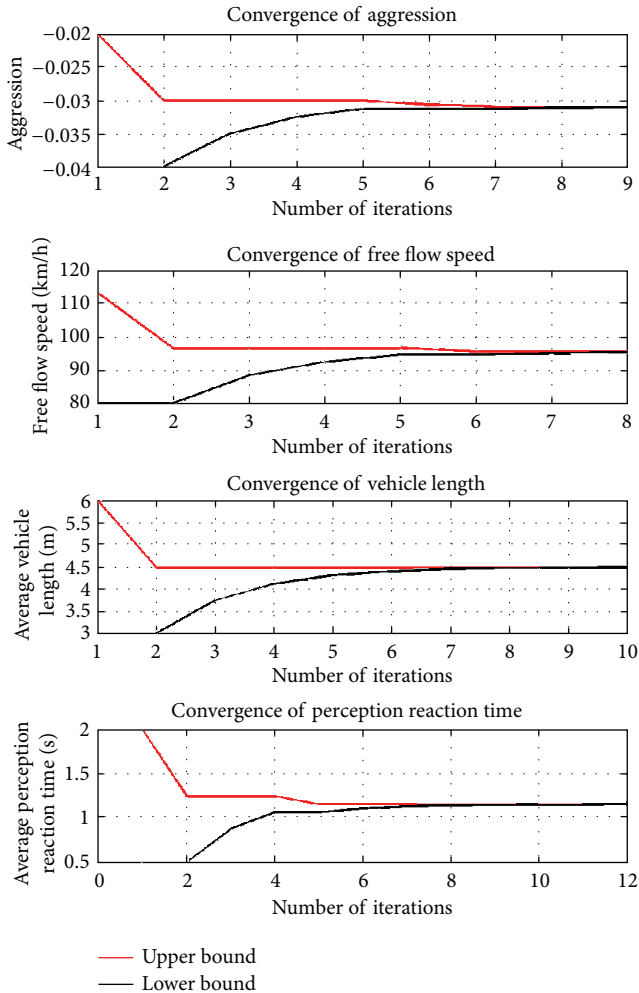


FIGURE 5: Steps for parameters to converge in bisection calibrating method.

aggression at this particular time and location; thus, reset lower bound of aggressiveness as  $\gamma_l = (\gamma_l + \gamma_u)/2$ , keep other parameters unchanged, and go to step 2. Otherwise, it means we overestimated drivers' aggressiveness so reset upper bound as  $\gamma_u = (\gamma_l + \gamma_u)/2$  and go to step 2.

With this bisection algorithm we will finally get a calibrated  $\gamma$  value when sum of signed distances is very near to 0, which means our calibration criterion is approximately satisfied. And repeat this for every model parameter.

## 5. Verification and Analysis

To verify and analyse the approach introduced in Sections 3 and 4, we pick eight sample sets of 5-minute traffic data to verify and analyse our algorithm. These samples are cut from a set of traffic flow data logs for route 400 in Georgia in July 2003, containing information collected by two roadside cameras. Four of the 5-minute samples derived from logs were collected by camera 1106 near North Old Milton Parkway, Alpharetta, GA (location A), and the other

four are related to logs of camera 1134 near South Hammond Drive, Sandy Springs, GA (location B). These traffic data logs contain raw observations of flow, density, and speed with time stamps. Every raw observation was for a 20-second period, so information contained by an observation is average rate of flow, density, and speed of traffic which went through a camera's shooting area during a specific 20-second period. Thus, this data set is capable of simulating traffic situation in real time except one fact that, size of data log in reality would be much bigger than our data set since we assume real-time data stream is observations for individual vehicles, not averaged traffic during periods. To solve this problem we aggregate data from logs of different days in July into one sample. For example, in order to get a sample for traffic during 9:00–9:05 am at camera 1106, we aggregate all traffic data for this site and this time of day on all days in July into one single file as a simulation of real-time observation of individual vehicles. Since traffic flow characters should be consistent for the same site under the same illumination, it is reasonable to simulate by aggregating.

In order to get samples without any preference, for each site we pick four 5-minute segments of the logs with a 3-hour step; that is, these four samples are log segments of traffic data at 9:00–9:05 am, 12:00–12:05 pm, 3:00–3:05 pm, and 6:00–6:05 pm, respectively.

**5.1. Data Aggregation and Weighting.** As the first step, data aggregation contributes remarkably to saving running time. 150 slices on  $k$ -axis are made on interval  $k \in [0, 300]$ ; however, consider that there are slices where no raw observations fall in; actual number of aggregated observation points is less than 150. As shown in Figure 4, there are 15–70 aggregated points that depend on span of raw data's density value. Also from this figure we see obvious patterns of traffic flow in different time of a day. In the morning majority of traffic travelled at density  $k < 30$  vehicles per km; higher density happened sometimes and was not ignorable, especially for camera 1134 at location B. This is just the normal situation on highway; sequences of vehicles come with considerable high internal density but there are long distances between different sequences. And sometimes slow leading vehicles of sequences make traffic slow down. During noon time traffic was more concentrated to density under 30, sparse points exist at higher density and lower speed, so it is still normal situation with minor differences. Traffic situation in afternoon was significantly different. For sample data at 3 pm, there are, but not many, observations with densities higher than 30 vehicles per km, so we consider that most vehicles were travelling in smooth and confident maneuvers. However, traffic at 6 pm at location A was a contrast, with a large proportion of observations distributed with high density and low speed, so this is a rush hour situation.

Patterns for location A and location B are not exactly the same, and this might be because a camera is only for surveillance of one side of highway, as well as the fact that camera 1106 is at the side of location A which is more congested during afternoon rush hour, and camera 1134 occupies the side of location B that accommodates morning crowds.

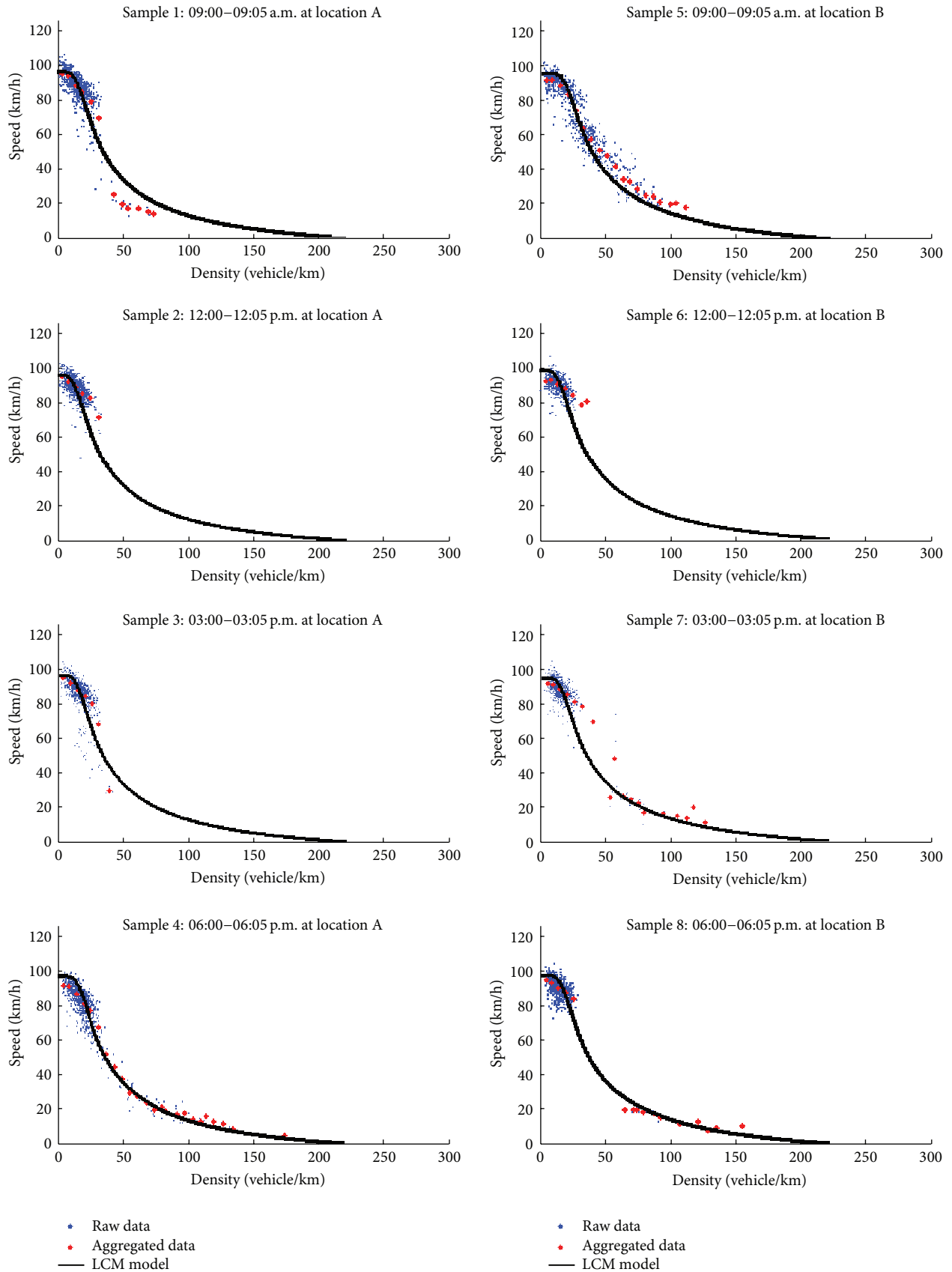


FIGURE 6: Calibration results for sample data sets by bisection based algorithm.

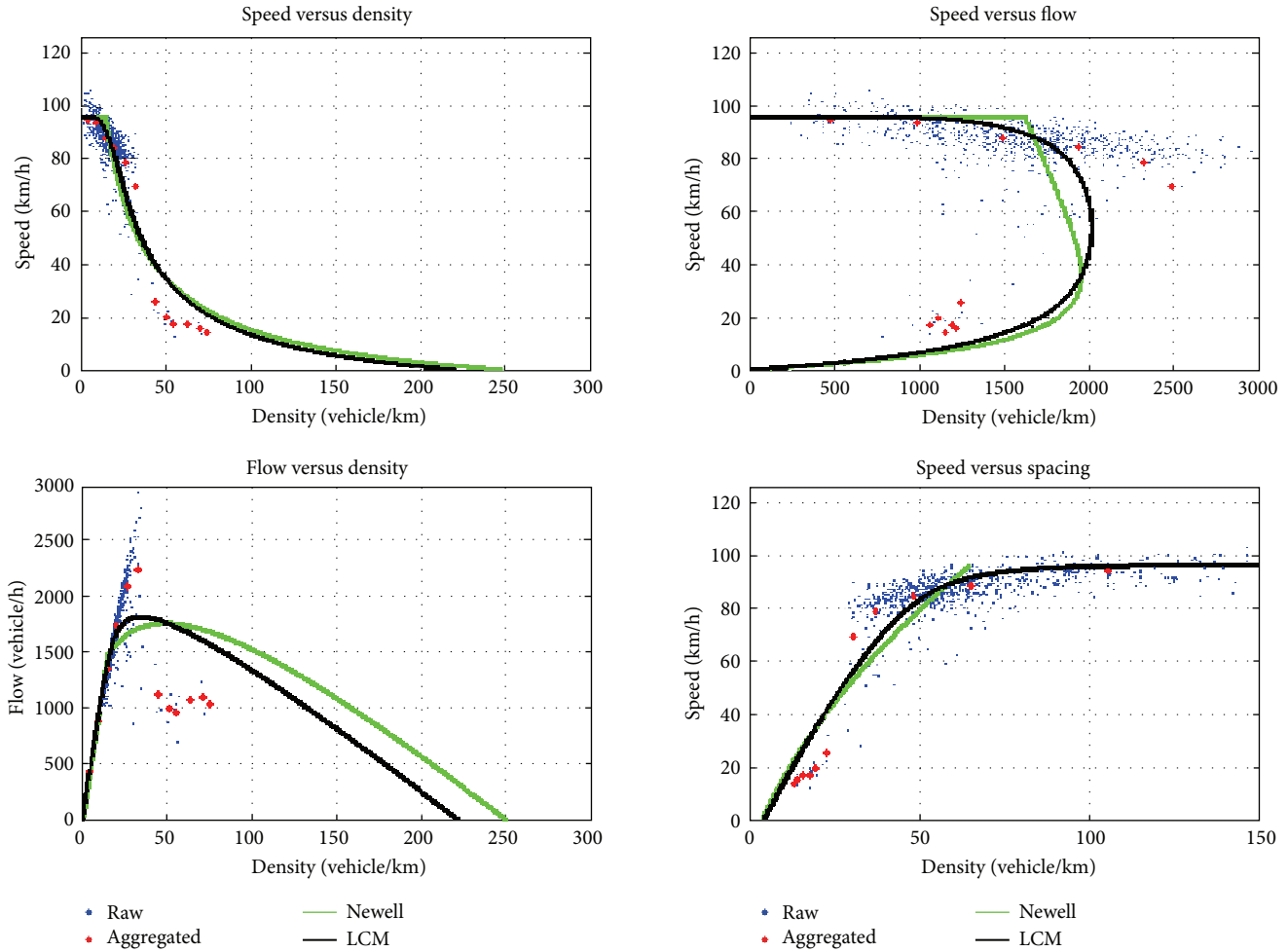


FIGURE 7: LCM and Newell's model calibrated by bisection algorithm.

Also from above Figure 4 we see importance of applying weights to aggregated observation points. Take noon sample at location B as an example; the red point with density at 39 vehicles per km is aggregated from only 1 raw observation, while another red point at 16 vehicles per km is aggregated from 33 raw observations, so intuitively these two points should have different effects on shape of a flow model. In order to generate a weight for an aggregated point, we use the number of raw observations from which this aggregated point is calculated. By adapting this definition of weights for points, inputs from different situations are reasonable.

**5.2. Convergence Speed for Bisection Method.** Though bisections are not the most advanced numerical analytical method, consider its time complexity as  $O(\log_2 n)$ ; it meets our requirement of performing in real time for transportation engineering and administration purpose. As shown in Figure 5, to calibrate against location B 9 am sample data, every parameter of LCM model converges in at most 12 iterations, so its guaranteed running time is less than a second. Compared to other nonnumerical methods, it is a very fast algorithm for calibrating traffic flow models, and practically this calculating system reacts in real time.

**5.3. Calibration Result.** In Table 2, we get quantified patterns for sample data sets by calibrating LCM model. As we assumed, parameters of LCM model appear to be consistent for a specific location, and for these two cases, as there are both near-straight sections without any obvious curve, there is no significant difference between values of their parameters. Driving patterns at location A are especially more consistent compared to that of location B, considering that location B is near conjunction of route 285 and route 400, so there is more interference coming from the complicated structure of this conjunction.

Thus, calibration result of our algorithm meets common sense, and Figure 6 demonstrates how speed-density curve of LCM model fits field data after calibration. This figure further proves role of weighting aggregated points as discussed in Section 5.1, especially in sample 1 for location A at 9 am; six red points between density 40 and 75 vehicles per km are considered less important so curve of final result does not go through these points perfectly; however, this makes overall precision of the model optimized.

A more comprehensive visualized result for this bisection based algorithm is shown in a following page in Figure 7. Sample 2 for location B at 9 am is opted for this demonstration

TABLE 2: Calibration results for sample data sets by bisection based algorithm.

Samples	Parameters				
	Free flow speed (km/h)	Vehicle length (m)	P-R time (sec)	Aggression ( $s^2/m$ )	
Location A	9:00–9:05 a.m.	96.1628	4.5088	1.2438	-0.0305
	12:00–12:05 p.m.	95.6600	4.5088	1.3331	-0.0311
	3:00–3:05 p.m.	96.4143	4.5029	1.2892	-0.0301
	6:00–6:05 p.m.	96.6655	4.5029	1.1903	-0.0300
Location B	9:00–9:05 a.m.	95.4087	4.4971	1.1544	-0.0310
	12:00–12:05 p.m.	98.1741	4.4912	1.2240	-0.0286
	3:00–3:05 p.m.	95.9115	4.4971	1.2592	-0.0305
	6:00–6:05 p.m.	97.6712	4.5029	1.1720	-0.0290

because its data points are better spread; thus, it is easier to read how calibration results fit field and aggregated data. Also Newell's model is calibrated to prove versatility of our algorithm.

## 6. Conclusion

Consider its time complexity as  $O(\log_2 n)$ ; this bisection based algorithm has a theoretical high performance. In practice, we run this algorithm on a personal laptop with a T7300 CPU and 2 GB ram; calibration for LCM model against every sample completes in 0.5 seconds, and calibration for Newell's model runs for less than 1 second. Also because of aggregation procedure, this algorithm is not sensitive to size of sample, as it calibrates both models against a 24-hour data set with 56,000 observations in less than 2 seconds. Also by verifying and analysing the algorithm's procedures and results in Section 5, we see it has good accuracy in both calculating parameters of a model and drawing statistical relationships between traffic flow, density, and speed. Thus, it is reasonable to use this calibration algorithm on real-time surveillance of drivers' behaviours.

## Conflict of Interests

The authors declare that they have no conflict of interests regarding the publication of this paper.

## References

- [1] NHTSA's National Center for Statistics and Analysis, "Traffic safety facts 2009 data, pedestrians part," Tech. Rep., U.S. Department of Transportation, National Highway Traffic Safety Administration, Washington, DC, USA, 2010.
- [2] J. G. Pigman and K. R. Agent, "Highway accidents in construction and maintenance work zones," *Transportation Research Record*, no. 1270, pp. 12–21, 1990.
- [3] Federal Highway Administration, *How Do Weather Events Impact Roads?*, 2011.
- [4] B. D. Greenshields, J. R. Bibbins, W. S. Channing, and H. H. Miller, "A study of traffic capacity," in *Proceedings of the 14th Annual Meeting of the Highway Research Board*, vol. 14, pp. 448–477, Highway Research Board, Washington, DC, USA, 1935.
- [5] G. F. Newell, "Nonlinear effects in the dynamics of car following," *Operations Research*, vol. 9, no. 2, pp. 209–229, 1961.
- [6] G. F. Newell, "A simplified theory of kinematic waves in highway traffic, part II: queueing at freeway bottlenecks," *Transportation Research B*, vol. 27, no. 4, pp. 289–303, 1993.
- [7] R. E. Chandler, R. Herman, and E. W. Montroll, "Traffic dynamics: studies in car following," *Operations Research*, vol. 6, no. 2, pp. 165–184, 1958.
- [8] D. C. Gazis, R. Herman, and R. B. Potts, "Car-following theory of steady-state traffic flow," *Operations Research*, vol. 7, no. 4, pp. 499–505, 1959.
- [9] P. G. Gipps, "A behavioural car-following model for computer simulation," *Transportation Research B*, vol. 15, no. 2, pp. 105–111, 1981.
- [10] I. Kosonen, *HUTSIM—urban traffic simulation and control model: principles and applications [M.S. thesis]*, Helsinki University of Technology, Espoo, Finland, 1999.
- [11] S. Kikuchi and P. Chakroborty, "Car-following model based on fuzzy inference system," *Transportation Research Record*, no. 1365, pp. 82–91, 1992.
- [12] D. Ni, C. Zhang, and H. Wang, "A unified perspective on traffic flow theory, part III: validation and benchmarking," in *Proceedings of the 11th International Conference of Chinese Transportation Professionals (ICCTP '11)*, pp. 4264–4286, ASCE, Nanjing, China, August 2011.
- [13] D. Ni, "A unified perspective on traffic flow theory, part II: the unified diagram," in *Proceedings of the 11th International Conference of Chinese Transportation Professionals (ICCTP '11)*, pp. 4244–4263, ASCE, Nanjing, China, August 2011.
- [14] D. Ni, "A unified perspective on traffic flow theory, part I: the field theory," in *Proceedings of the 11th International Conference of Chinese Transportation Professionals (ICCTP '11)*, pp. 4227–4243, ASCE, Nanjing, China, August 2011.
- [15] R. Herman, E. W. Montroll, R. B. Potts, and R. W. Rothery, "Traffic dynamics: analysis of stability in car following," *Operations Research*, vol. 7, no. 1, pp. 86–106, 1959.
- [16] M. Brackstone and M. McDonald, "Car-following: a historical review," *Transportation Research F*, vol. 2, no. 4, pp. 181–196, 1999.
- [17] G. G. Schultz and L. R. Rilett, "Analysis of distribution and calibration of car-following sensitivity parameters in microscopic traffic simulation models," *Transportation Research Record*, vol. 1876, pp. 41–51, 2004.

- [18] A. Kesting and M. Treiber, "Calibrating car-following models by using trajectory data methodological study," *Transportation Research Record*, vol. 2088, pp. 148–156, 2008.
- [19] S. P. Hoogendoorn and R. Hoogendoorn, "Generic calibration framework for joint estimation of car-following models by using microscopic data," *Transportation Research Record*, vol. 2188, pp. 37–45, 2010.
- [20] H. Rakha and M. Arafah, "Calibrating steady-state traffic stream and car-following models using loop detector data," *Transportation Science*, vol. 44, no. 2, pp. 151–168, 2010.

## Research Article

# Similarity Solution of Marangoni Convection Boundary Layer Flow over a Flat Surface in a Nanofluid

Norihan Md. Arifin,<sup>1</sup> Roslinda Nazar,<sup>2</sup> and Ioan Pop<sup>3</sup>

<sup>1</sup> *Institute for Mathematical Research and Department of Mathematics, Universiti Putra Malaysia, 43400 Serdang, Selangor, Malaysia*

<sup>2</sup> *School of Mathematical Sciences, Faculty of Science & Technology, Universiti Kebangsaan Malaysia, 43600 Bangi, Selangor, Malaysia*

<sup>3</sup> *Department of Mathematics, Babeş-Bolyai University, 400084 Cluj-Napoca, Romania*

Correspondence should be addressed to Norihan Md. Arifin; [norihanarifin@yahoo.com](mailto:norihanarifin@yahoo.com)

Received 21 June 2013; Accepted 10 December 2013

Academic Editor: Mohamed Fathy El-Amin

Copyright © 2013 Norihan Md. Arifin et al. This is an open access article distributed under the Creative Commons Attribution License, which permits unrestricted use, distribution, and reproduction in any medium, provided the original work is properly cited.

The problem of steady Marangoni boundary layer flow and heat transfer over a flat plate in a nanofluid is studied using different types of nanoparticles. The general governing partial differential equations are transformed into a set of two nonlinear ordinary differential equations using unique similarity transformation. Numerical solutions of the similarity equations are obtained using the Runge-Kutta-Fehlberg (RKF) method. Three different types of nanoparticles are considered, namely, Cu, Al<sub>2</sub>O<sub>3</sub>, and TiO<sub>2</sub>, by using water as a base fluid with Prandtl number Pr = 6.2. The effects of the nanoparticle volume fraction  $\phi$  and the constant exponent  $m$  on the flow and heat transfer characteristics are obtained and discussed.

## 1. Introduction

A nanofluid is a colloidal mixture of nanosized particles (<100 nm) in a base fluid. It is known that nanofluid can tremendously enhance the heat transfer characteristics of the original (base) fluid. One such characteristic of nanofluid is the anomalous high thermal conductivity at very low concentration of nanoparticles and the considerable enhancement of convective heat transfer. Thus, nanofluids have many applications in industry such as coolants, lubricants, heat exchangers, and microchannel heat sinks. Nanoparticles are made of various materials such as oxide ceramics, and nitride ceramics. The objective of nanofluids is to achieve the best possible thermal properties with the least possible (<1%) volume fraction of nanoparticles in the base fluid [1]. There have been many studies in the literature to better understand the mechanism behind the enhanced heat transfer characteristics. An excellent collection of papers on this topic can be found in the book by Das et al. [2] and in several review papers ([3–8]). There are also several experimental studies to better understand the mechanism

of heat transfer enhancement for natural convection heat transfer in nanofluids ([1, 9–12]).

Marangoni flow induced by surface tension along a liquid surface causes undesirable effects in crystal growth melts in the same manner as buoyancy-induced natural convection [13]. These undesirable effects also occur in space-based crystal growth experiments since Marangoni flow is involved in microgravity as well as in earth gravity. An excellent view of the Marangoni effect from the perspective of all three possible interfaces as motion inducing agents has been done by Tadmor [14]. It is worth mentioning that there are two existing models for Marangoni boundary layer that have been studied, namely, model for nonisobaric Marangoni boundary layer as discussed by Golia and Viviani [15] and model for Marangoni boundary layer over a flat plate studied by Christopher and Wang [13]. Marangoni boundary layer studied by Golia and Viviani [15] has been extended by Pop et al. [16] where they included the concentration equation. Chamkha et al. [17] studied the same model with Golia and Viviani [15] in which they considered the gravity effects. Hamid et al. [18] extended the problem of the thermosolutal

Marangoni forced convection boundary layer flow by Pop et al. [16] when the wall is permeable. Very recently, Mat et al. [19] discussed the radiation effects on the problem of Marangoni boundary layer with permeable surface. On the other hand, nanofluid equations model as proposed by Tiwari and Das [20] has been used by Arifin et al. [21] for the Marangoni boundary layer problem by Golia and Viviani [15]. They found that the numerical results also indicate that, for both a regular fluid ( $\varphi = 0$ ) and a nanofluid ( $\varphi \neq 0$ ), dual solutions exist when  $\beta < 0.5$ . These dual solutions were not discussed by Golia and Viviani [15]. This problem has been extended by Remeli et al. [22] to the problem with suction and injection effects. Mat et al. [23] also extended the problem of Marangoni boundary layer in a nanofluid by Arifin et al. [21] to the radiation effect.

It is worth mentioning that Christopher and Wang [13] considered the Marangoni boundary layer over a flat plate where the term  $u_e(x)$ , which is the velocity of the external flow in Golia and Viviani [15], has been neglected. The similarity solutions of the Christopher and Wang [13] problem are also different from the Golia and Viviani [15] problem. The problem of Christopher and Wang [13] has been extended by several researchers such as Al-Mudhaf and Chamkha [24] where they have presented the similarity solutions for MHD Marangoni convection in the presence of heat generation or absorption effects and Magyari and Chamkha [25] reported the exact analytical solutions of thermosolutal Marangoni flows in the presence of temperature-dependent volumetric heat source/sinks as well as of a first-order chemical reaction. Recently, Hamid et al. [26] studied the two-dimensional Marangoni convection flow past a flat plate in the presence of thermal radiation, suction, and injection effects. Further MHD thermosolutal Marangoni convection boundary layer over a flat surface considering the effects of the thermal diffusion and diffusion-thermo with fluid suction and injection has been examined by Hamid et al. [27].

It should be highlighted that the present paper presents a similarity solution for the steady Marangoni convection boundary layer flow over a static semi-infinite flat plate due to an imposed temperature gradient in a nanofluid, which extends the problem by Christopher and Wang [13] to the case of nanofluid. The nanofluid equations model proposed by Tiwari and Das [20] has been used. This model has been very successfully used in several papers [21, 28–32]. Thus, we wish to highlight that this present study is original and all the results are new. To the best of our knowledge, the present problem has not been considered before. The study of nanofluid is still at its early stage and it seems difficult to have a precise idea on the way the use of nanoparticles acts in heat transfer. A clear picture on the boundary layer flows of nanofluid is yet to emerge.

## 2. Problem Formulation

We consider the steady two-dimensional boundary layer flow past a semi-infinite flat plate in a water-based nanofluid containing different types of nanoparticles, namely, copper (Cu), alumina ( $\text{Al}_2\text{O}_3$ ), and titania ( $\text{TiO}_2$ ), with Marangoni

effects. The nanofluid is assumed incompressible and the flow is assumed to be laminar. It is also assumed that the base fluid (i.e., water) and the nanoparticles are in thermal equilibrium and no slip occurs between them. The thermophysical properties of the nanofluids are given in Table 1 (see Oztop and Abu-Nada [29]). Further, we consider a Cartesian coordinate system  $(x, y)$ , where  $x$  and  $y$  are the coordinates measured along the plate and normal to it, respectively, and the flow takes place at  $y \geq 0$ . It is also assumed that the temperature of the plate is  $T_w(x)$  and that of the ambient nanofluid is  $T_\infty$ . Following [15–17, 25, 33, 34] the surface tension  $\sigma$  is assumed to vary linearly with temperature as follow:

$$\sigma = \sigma_0 [1 - \gamma(T - T_0)], \quad (1)$$

where  $\sigma_0$  and  $T_0$  are the characteristics surface tension and temperature, respectively, and we assume that  $T_0 \equiv T_\infty$ . Equation (1) is a commonly made assumption [34]. For most liquids, the surface tension decreases with temperature; that is,  $\gamma$  is a positive fluid property.

The steady boundary layer equations for a nanofluid in the coordinates  $\bar{x}$  and  $\bar{y}$  are ([13, 20])

$$\frac{\partial u}{\partial x} + \frac{\partial v}{\partial y} = 0, \quad (2)$$

$$u \frac{\partial u}{\partial x} + v \frac{\partial u}{\partial y} = \frac{\mu_{\text{nf}}}{\rho_{\text{nf}}} \frac{\partial^2 u}{\partial y^2}, \quad (3)$$

$$u \frac{\partial T}{\partial x} + v \frac{\partial T}{\partial y} = \alpha_{\text{nf}} \frac{\partial^2 T}{\partial y^2} \quad (4)$$

subject to the boundary conditions

$$\begin{aligned} v = 0, \quad T = T_0 + Ax^{m+1}, \quad \mu_{\text{nf}} \frac{\partial u}{\partial y} = \frac{\partial \sigma}{\partial T} \frac{\partial T}{\partial x} \quad \text{at } y = 0, \\ u = 0, \quad T = T_\infty \quad \text{as } y \rightarrow \infty. \end{aligned} \quad (5)$$

Here,  $u$  and  $v$  are the velocity components along the  $x$ - and  $y$ -axes, respectively,  $T$  is the temperature of the nanofluid,  $m$  is the constant exponent of the temperature,  $\alpha_{\text{nf}}$  is the thermal diffusivity of the nanofluid,  $\rho_{\text{nf}}$  is the effective density of the nanofluid,  $k_{\text{nf}}$  is the effective thermal conductivity of the nanofluid, and  $\mu_{\text{nf}}$  is the effective viscosity of the nanofluid, which are given by

$$\begin{aligned} \alpha_{\text{nf}} &= \frac{k_{\text{nf}}}{(\rho C_p)_{\text{nf}}}, \quad \rho_{\text{nf}} = (1 - \phi) \rho_f + \phi \rho_s, \\ \mu_{\text{nf}} &= \frac{\mu_f}{(1 - \phi)^{2.5}}, \quad (\rho C_p)_{\text{nf}} = (1 - \phi) (\rho C_p)_f + \phi (\rho C_p)_s, \\ \frac{k_{\text{nf}}}{k_f} &= \frac{(k_s + 2k_f) - 2\phi(k_f - k_s)}{(k_s + 2k_f) + \phi(k_f - k_s)}, \end{aligned} \quad (6)$$

where  $\phi$  is the nanoparticle volume fraction,  $\rho_f$  is the reference density of the fluid fraction,  $\rho_s$  is the reference

velocity of the solid fraction,  $\mu_f$  is the viscosity of the fluid fraction,  $k_f$  is the thermal conductivity of the fluid,  $k_s$  is the thermal conductivity of the solid, and  $(\rho C_p)_{nf}$  is the heat capacity of the nanofluid.

We look now for a similarity solution of (2)–(4) subject to the boundary conditions (5) of the following form:

$$\psi = C_1 x^{(2+m)/3} f(\eta), \quad \theta(\eta) = \frac{T - T_\infty}{Ax^{1+m}}, \quad (7)$$

$$\eta = C_2 x^{(m-1)/3} y,$$

where  $\psi$  is the stream function which is defined as  $u = \partial\psi/\partial y$  and  $v = -\partial\psi/\partial x$ . Further,  $m$ ,  $A$ ,  $C_1$ , and  $C_2$  are constants with  $A$ ,  $C_1$ , and  $C_2$  given by

$$A = \frac{\Delta T}{L^{m+1}}, \quad C_1 = \sqrt[3]{\frac{\sigma_0 \gamma A \mu_f}{\rho_f^2}}, \quad (8)$$

$$C_2 = \sqrt[3]{\frac{\sigma_0 \gamma A \rho_f}{\mu_f^2}},$$

with  $L$  being the length of the surface and  $\Delta T$  being the constant characteristic temperature. Substituting (7) into (2) and (3), we get the following ordinary differential equations:

$$\frac{1}{(1-\phi)^{2.5} (1-\phi + \phi \rho_s / \rho_f)} f''' + \frac{2+m}{3} f f'' - \frac{1+2m}{3} f'^2 = 0, \quad (9)$$

$$\frac{1}{\text{Pr} \left( 1 - \phi + \phi (\rho C_p)_s / (\rho C_p)_f \right)} \theta'' + \frac{2+m}{3} f \theta - (1+m) f' \theta = 0,$$

and the boundary conditions (5) become

$$f(0) = 0, \quad \frac{1}{(1-\phi)^{2.5}} f''(0) = -1, \quad \theta(0) = 1, \quad (10)$$

$$f'(\infty) = 0, \quad \theta(\infty) = 0.$$

We can now determine the surface velocity  $u(x, 0) = u_w(x)$  as

$$u_w(x) = \sqrt[3]{\frac{(\sigma_0 \gamma A)^2}{\rho_f \mu_f}} x^{(1+2m)/3} f'(0). \quad (11)$$

A quantity of interest is the local Nusselt number  $\text{Nu}_x$  which is defined as

$$\text{Nu}_x = \frac{x q_w(x)}{k_f [T(x, 0) - T(x, \infty)]}, \quad (12)$$

where  $q_w(x)$  is the heat flux from the surface of the plate and it is given by

$$q_w(x) = -k_{nf} \left( \frac{\partial T}{\partial y} \right)_{y=0}. \quad (13)$$

Using (7), (12), and (13), we get

$$\text{Nu}_x = -\frac{k_{nf}}{k_f} C_2 x^{(2+m)/3} \theta'(0). \quad (14)$$

The average Nusselt number  $\text{Nu}_L$  based on the average temperature difference between the temperature of the surface and the temperature far from the surface (ambient fluid) is given by

$$\text{Nu}_L = -\frac{6+3m}{5+4m} \frac{k_{nf}}{k_f} \text{Ma}_L^{1/3} \text{Pr}^{-1/3} \theta'(0), \quad (15)$$

where  $\text{Ma}_L$  is the Marangoni based on  $L$  and is defined as

$$\text{Ma}_L = \frac{\sigma_T A L^{2+m}}{\mu_f \alpha_f} = \frac{\sigma_T \Delta T L}{\mu_f \alpha_f}. \quad (16)$$

Also, the total mass flow  $\dot{m}$  in the boundary layer per unit width is given by

$$\dot{m} = \int_0^\infty \rho_f u dy = \sqrt[3]{\sigma_0 \gamma \rho_f \mu_f} x^{(2+m)/3} f(\infty). \quad (17)$$

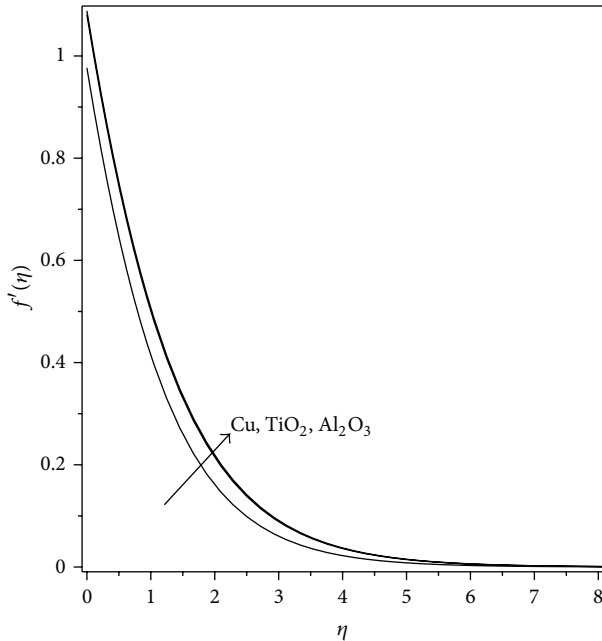
### 3. Results and Discussion

The nonlinear ordinary differential equation (9) subject to the boundary conditions (10) forms a two-point boundary value problem (BVP) and is solved numerically using the Runge-Kutta-Fehlberg fourth-fifth-order (RKF45) method using Maple 12- and the algorithm RKF45 in Maple has been well tested for its accuracy and robustness [35]. In this method, it is most important to choose the appropriate finite value of the edge of boundary layer,  $\eta \rightarrow \infty$  (say  $\eta_\infty$ ) that is between 4 and 10, which is in accordance with the standard practice in the boundary layer analysis. We begin with some initial guess value of  $\eta_\infty$  and solve (9) subject to the boundary conditions (10) with some particular set of parameters to obtain the surface velocity  $f'(0)$  and the temperature gradient  $-\theta'(0)$ . The solution process is repeated until further changes (increment) in  $\eta_\infty$  would not lead to any changes in the values of  $f'(0)$  and  $-\theta'(0)$ , or in other words, the results are independent of the value of  $\eta_\infty$ . The initial step size employed is  $h = \Delta\eta = 0.1$ . Following Oztop and Abu-Nada [29], we considered the range of nanoparticles volume fraction  $\phi$  as  $0 \leq \phi \leq 0.2$ . The Prandtl number of the base fluid (water) is kept constant at 6.2. Further, it should also be pointed out that the thermophysical properties of fluid and nanoparticles (Cu,  $\text{Al}_2\text{O}_3$ , and  $\text{TiO}_2$ ) used in this study are given in Table 1. It is worth mentioning that, the present study reduces to that of a classical viscous (regular) fluid studied by Christopher and Wang [13] when  $\phi = 0$ .

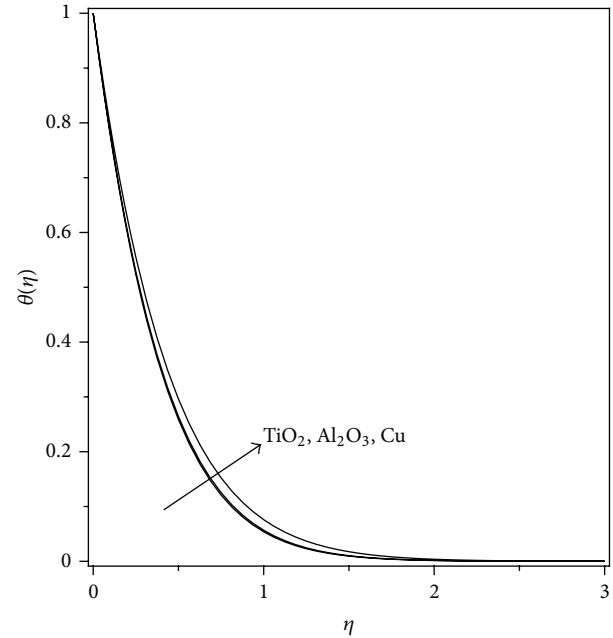
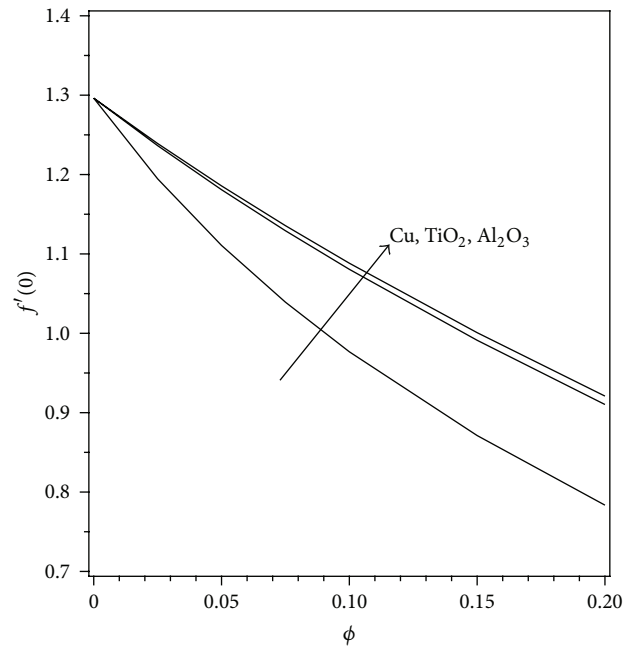
Figures 1 and 2 show the distribution of the dimensionless velocity  $f'(\eta)$  and temperature  $\theta(\eta)$  profiles for the three types of the nanoparticles considered when the solid volume fraction of the nanofluid parameter  $\phi = 0.1$  and  $m = 0$  (which corresponds to a linear variation of the surface temperature with the distance  $x$  measured along the flat plate), while Figures 3 and 4 display the variation with  $\phi$  of the reduced

TABLE 1: Thermophysical properties of fluid and nanoparticles [29].

Physical properties	Fluid phase (water)	Cu	Al <sub>2</sub> O <sub>3</sub>	TiO <sub>2</sub>
$C_p$ (J/kg K)	4179	385	765	686.2
$\rho$ (kg/m <sup>3</sup> )	997.1	8933	3970	4250
$k$ (W/mK)	0.613	400	40	8.9538

FIGURE 1: Dimensionless velocity profiles  $f'(\eta)$  for different types of nanoparticles when  $\phi = 0.1$  and  $m = 0$ .

surface velocity,  $f'(0)$ , and reduced temperature gradient,  $-\theta'(0)$ , respectively. It is seen from Figure 1 that the velocity profiles in Figure 1 for Al<sub>2</sub>O<sub>3</sub> and TiO<sub>2</sub> are almost identical while the profile for Cu is smaller. This is consistent with the variation of the reduced surface velocity  $f'(0)$  as shown in Figure 3. In Figure 2, it is shown that the temperature profile is the highest for higher thermal diffusivity nanoparticle (Cu). On the other hand, the thermal boundary layer thickness as shown in Figure 2 decreases with a decrease in thermal diffusivity, which in turn gives rise to the  $-\theta'(0)$  as illustrated in Figure 4. Figures 3 and 4 display the surface velocity,  $f'(0)$ , and the surface temperature gradient,  $-\theta'(0)$ , respectively, for different types of nanoparticles (Cu, Al<sub>2</sub>O<sub>3</sub>, and TiO<sub>2</sub>) when  $m = 0$ . One can see that the surface velocity,  $f'(0)$  and the surface temperature gradient,  $-\theta'(0)$  decrease as  $\phi$  increases for all three nanoparticles (Cu, Al<sub>2</sub>O<sub>3</sub>, TiO<sub>2</sub>). It should be noticed that the entire values of  $-\theta'(0)$  are always positive; that is, the heat is transferred from hot surface to the cold surface. In Figure 4, we are looking at the variation of temperature gradient with the nanoparticle volume fraction  $\phi$ . It is observed that the reduced value of thermal diffusivity leads to higher temperature gradients and, therefore, higher enhancements in heat transfer. Nanoparticles with low thermal diffusivity, TiO<sub>2</sub>, have better enhancement on heat transfer compared to Cu and Al<sub>2</sub>O<sub>3</sub>. Further, Figure 5 shows the variations of the reduced surface velocity  $f'(0)$  with  $m$ ,

FIGURE 2: Dimensionless temperature profiles  $\theta(\eta)$  for different types of nanoparticles when  $\phi = 0.1$  and  $m = 0$ .FIGURE 3: Variation of surface velocity  $f'(0)$  with  $\phi$  for different types of nanoparticles when  $Pr = 6.2$  and  $m = 0$ .

where  $m = 0$  refers to a linear variation of the surface temperature with the distance  $x$  measured along the flat plate and  $m = 1$  is a quadratic variation of the surface temperature with  $x$ , while  $m = -0.5$  refers to a temperature variation relative to the square root of  $x$ . It should also be noticed that for  $\phi = 0$  (regular fluid), we reproduced the variations of surface velocity obtained by Christopher and Wang [13] as illustrated by dashed lines in the figure.

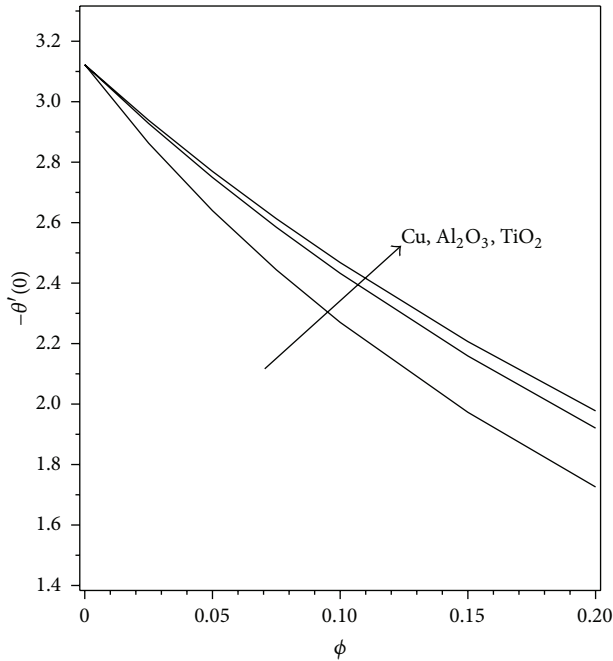


FIGURE 4: Variation of  $-\theta'(0)$  with  $\phi$  for different types of nanoparticles when  $Pr = 6.2$  and  $m = 0$ .

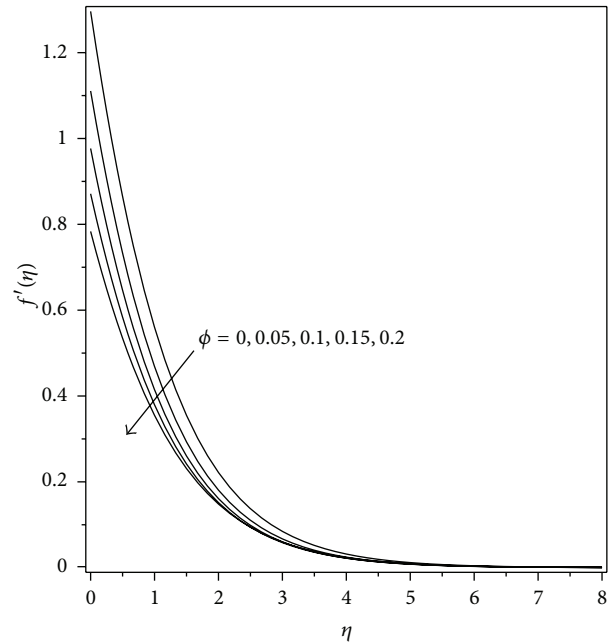


FIGURE 6: Dimensionless velocity profiles  $f'(\eta)$  for Cu nanoparticles with  $m = 0$  and various values of  $\phi$ .

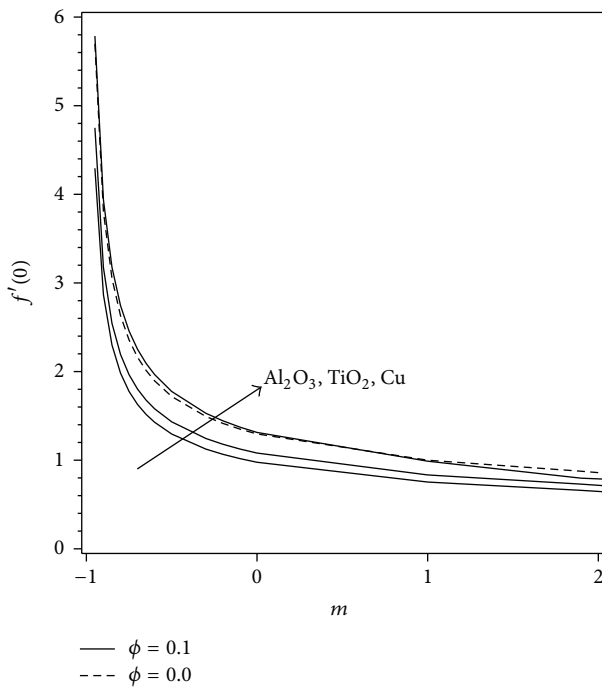


FIGURE 5: Variation of surface velocity  $f'(0)$  with  $m$  for different types of nanoparticles when  $Pr = 6.2$ ,  $\phi = 0$  (regular fluid), and  $\phi = 0.1$ .

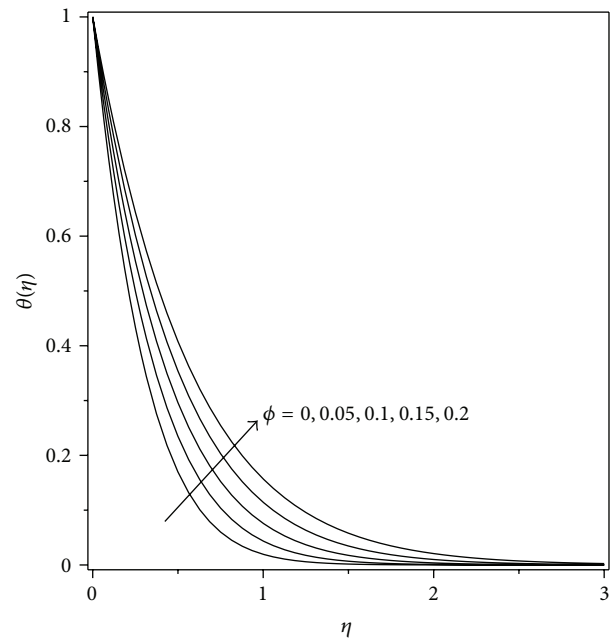


FIGURE 7: Dimensionless temperature profiles  $\theta(\eta)$  for Cu nanoparticles with  $m = 0$  and various values of  $\phi$ .

Figures 6 to 11 show the dimensionless velocity  $f'(\eta)$  and temperature  $\theta(\eta)$  profiles for different values of  $\phi$  in the range  $0 \leq \phi \leq 0.2$  when  $m = 0$  with different types of nanoparticles, namely, Cu,  $Al_2O_3$ , and  $TiO_2$ , respectively. It is worth mentioning that nanoparticle volume fraction is a key parameter for studying the effect of nanoparticles on flow fields and

temperature distributions. More fluid is heated for higher values of nanoparticle volume fraction. Flow strength also increases with increasing of nanoparticle volume fraction. As the nanoparticle volume fraction increases, movements of particles become irregular and random due to increasing of energy exchange rates in the fluid (see [29]). It is observed from these figures that, for any type of nanoparticles, as the nanoparticle volume fraction  $\phi$  increases, both the surface velocities and the temperature gradients decrease, which is

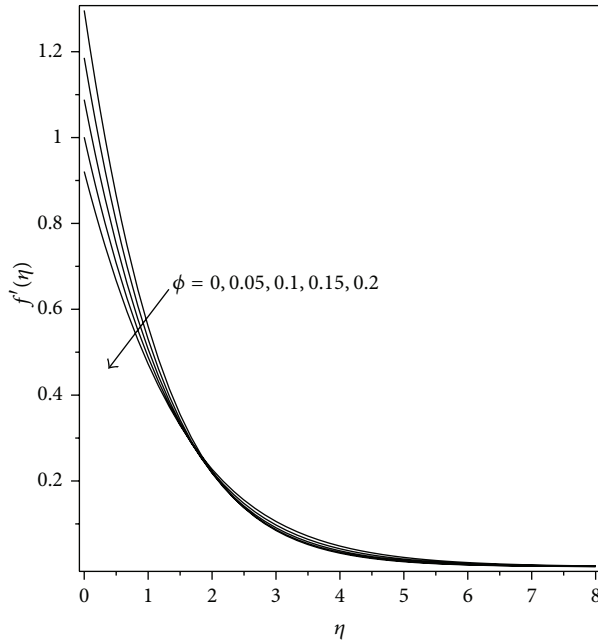


FIGURE 8: Dimensionless velocity profiles  $f'(\eta)$  for  $\text{Al}_2\text{O}_3$  nanoparticles with  $m = 0$  and various values of  $\phi$ .

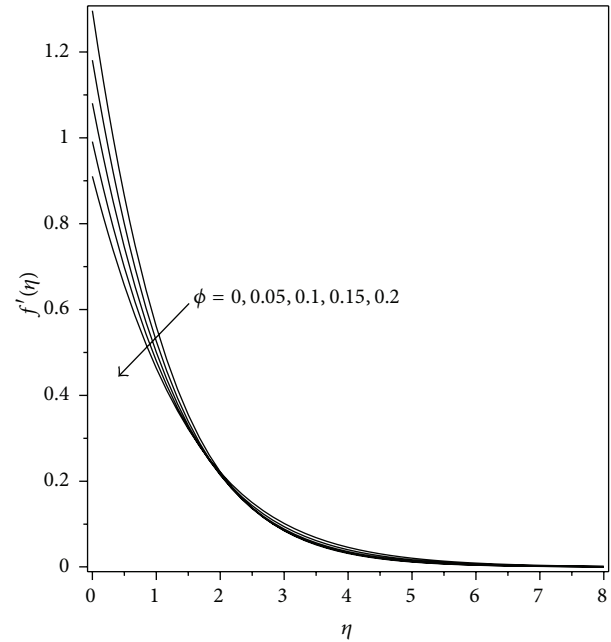


FIGURE 10: Dimensionless temperature profiles  $\theta(\eta)$  for  $\text{TiO}_2$  nanoparticles with  $m = 0$  and various values of  $\phi$ .

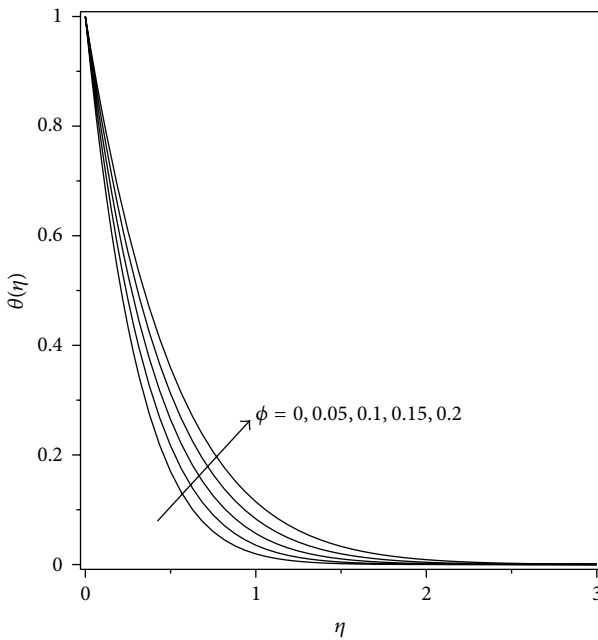


FIGURE 9: Dimensionless temperature profiles  $\theta(\eta)$  for  $\text{Al}_2\text{O}_3$  nanoparticles with  $m = 0$  and various values of  $\phi$ .

again in agreement with Figures 3 and 4. It should also be noticed again, that for  $\phi = 0$  (regular fluid), we reproduced the velocity and temperature profiles obtained by Christopher and Wang [13].

#### 4. Conclusion

We have theoretically and numerically studied the problem of steady two-dimensional laminar Marangoni-driven boundary layer flow in nanofluids. It is worth mentioning that the

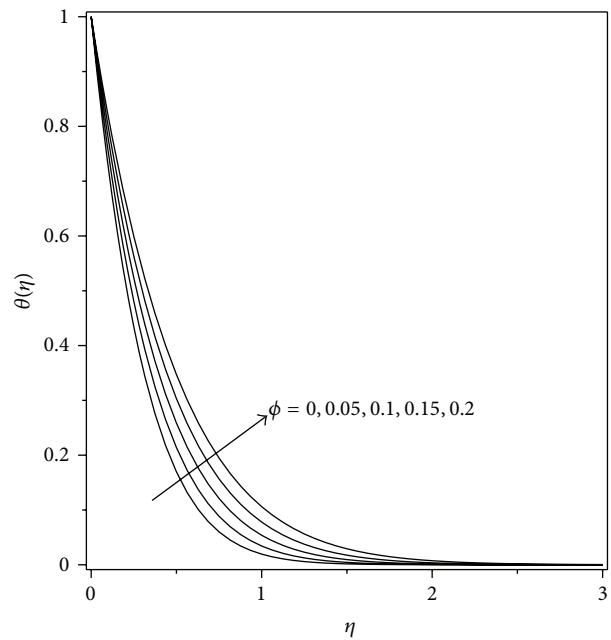


FIGURE 11: Dimensionless velocity profiles  $f'(\eta)$  for  $\text{TiO}_2$  nanoparticles with  $m = 0$  and various values of  $\phi$ .

novelty of the present paper is to study numerically the heat transfer in a liquid layer driven by Marangoni flow with various types of nanoparticles ( $\text{Cu}$ ,  $\text{Al}_2\text{O}_3$ , and  $\text{TiO}_2$ ) in the base fluid which has not been considered before. The nonlinear ordinary differential equation (9) subject to the boundary conditions (10) forms a two-point boundary value problem (BVP) and is solved numerically using the Runge-Kutta-Fehlberg fourth-fifth-order (RK45) method using Maple 12,

and the algorithm RKF45 in Maple has been well tested for its accuracy and robustness. Similarity solutions are obtained for the surface velocity  $f'(0)$  and the surface temperature gradient  $-\theta'(0)$  as well as the velocity and temperature profiles for some values of the governing parameters, namely, the solid volume fraction of the nanofluid  $\phi$  ( $0 \leq \phi \leq 0.2$ ), the constant exponent  $m$ , and the Prandtl number  $Pr$ . It was found that nanoparticles with low thermal diffusivity ( $TiO_2$ ) have better enhancement on heat transfer compared to  $Al_2O_3$  and  $Cu$ .

## Acknowledgments

The authors gratefully acknowledge the financial support received in the form of a FRGS Research Grant from the Ministry of Higher Education, Malaysia, and a Research University Grant (AP-2013-009) from the Universiti Kebangsaan Malaysia. They also wish to express their sincere thanks to the reviewers for the valuable comments and suggestions.

## References

- [1] L. Godson, B. Raja, D. M. Lal, and S. Wongwises, "Enhancement of heat transfer using nanofluids—an overview," *Renewable and Sustainable Energy Reviews*, vol. 14, no. 2, pp. 629–641, 2010.
- [2] S. K. Das, S. U. S. Choi, W. Yu, and T. Pradeep, *Nanofluids: Science and Technology*, Wiley, Hoboken, NJ, USA, 2007.
- [3] J. Buongiorno, "Convective transport in nanofluids," *Journal of Heat Transfer*, vol. 128, no. 3, pp. 240–250, 2006.
- [4] W. Daungthongsuk and S. Wongwises, "A critical review of convective heat transfer of nanofluids," *Renewable and Sustainable Energy Reviews*, vol. 11, no. 5, pp. 797–817, 2007.
- [5] V. Trisaksri and S. Wongwises, "Critical review of heat transfer characteristics of nanofluids," *Renewable and Sustainable Energy Reviews*, vol. 11, no. 3, pp. 512–523, 2007.
- [6] X.-Q. Wang and A. S. Mujumdar, "Heat transfer characteristics of nanofluids: a review," *International Journal of Thermal Sciences*, vol. 46, no. 1, pp. 1–19, 2007.
- [7] X.-Q. Wang and A. S. Mujumdar, "A review on nanofluids—part I: theoretical and numerical investigations," *Brazilian Journal of Chemical Engineering*, vol. 25, no. 4, pp. 613–630, 2008.
- [8] S. Kakaç and A. Pramuanjaroenkij, "Review of convective heat transfer enhancement with nanofluids," *International Journal of Heat and Mass Transfer*, vol. 52, no. 13–14, pp. 3187–3196, 2009.
- [9] N. Putra, W. Roetzel, and S. K. Das, "Natural convection of nano-fluids," *Heat and Mass Transfer*, vol. 39, no. 8–9, pp. 775–784, 2003.
- [10] D. Wen and Y. Ding, "Formulation of nanofluids for natural convective heat transfer applications," *International Journal of Heat and Fluid Flow*, vol. 26, no. 6, pp. 855–864, 2005.
- [11] K. S. Hwang, J.-H. Lee, and S. P. Jang, "Buoyancy-driven heat transfer of water-based  $Al_2O_3$  nanofluids in a rectangular cavity," *International Journal of Heat and Mass Transfer*, vol. 50, no. 19–20, pp. 4003–4010, 2007.
- [12] X.-Q. Wang and A. S. Mujumdar, "A review on nanofluids—part II: experiments and applications," *Brazilian Journal of Chemical Engineering*, vol. 25, no. 4, pp. 631–648, 2008.
- [13] D. M. Christopher and B. Wang, "Prandtl number effects for Marangoni convection over a flat surface," *International Journal of Thermal Sciences*, vol. 40, no. 6, pp. 564–570, 2001.
- [14] R. Tadmor, "Marangoni flow revisited," *Journal of Colloid and Interface Science*, vol. 332, no. 2, pp. 451–454, 2009.
- [15] C. Golia and A. Viviani, "Non isobaric boundary layers related to Marangoni flows," *Meccanica*, vol. 21, no. 4, pp. 200–204, 1986.
- [16] I. Pop, A. Postelnicu, and T. Grosan, "Thermosolutal Marangoni forced convection boundary layers," *Meccanica*, vol. 36, no. 5, pp. 555–571, 2001.
- [17] A. J. Chamkha, I. Pop, and H. S. Takhar, "Marangoni mixed convection boundary layer flow," *Meccanica*, vol. 41, no. 2, pp. 219–232, 2006.
- [18] R. A. Hamid, N. M. Arifin, R. Nazar, F. M. Ali, and I. Pop, "Dual Solutions on thermosolutal Marangoni forced convection boundary layer with suction and injection," *Mathematical Problems in Engineering*, vol. 2011, Article ID 875754, 19 pages, 2011.
- [19] N. Mat, N. M. Arifin, R. Nazar, F. Ismail, and I. Pop, "Radiation effects on Marangoni convection boundary layer over a permeable surface," *Meccanica*, vol. 48, pp. 83–89, 2013.
- [20] R. K. Tiwari and M. K. Das, "Heat transfer augmentation in a two-sided lid-driven differentially heated square cavity utilizing nanofluids," *International Journal of Heat and Mass Transfer*, vol. 50, no. 9–10, pp. 2002–2018, 2007.
- [21] N. M. Arifin, R. Nazar, and I. Pop, "Non-Isobaric Marangoni boundary layer flow for  $Cu$ ,  $Al_2O_3$  and  $TiO_2$  nanoparticles in a water based fluid," *Meccanica*, vol. 46, no. 4, pp. 833–843, 2011.
- [22] A. Remeli, N. M. Arifin, R. Nazar, F. Ismail, and I. Pop, "Marangoni-driven boundary layer flow in a nanofluid with suction and injection," *World Applied Sciences Journal*, vol. 17, pp. 21–26, 2012.
- [23] N. A. A. Mat, N. M. Arifin, R. Nazar, and F. Ismail, "Radiation effect on Marangoni convection boundary layer flow of a nanofluid," *Mathematical Sciences*, vol. 6, article 21, 2012.
- [24] A. Al-Mudhaf and A. J. Chamkha, "Similarity solutions for MHD thermosolutal Marangoni convection over a flat surface in the presence of heat generation or absorption effects," *Heat and Mass Transfer*, vol. 42, no. 2, pp. 112–121, 2005.
- [25] E. Magyari and A. J. Chamkha, "Exact analytical results for the thermosolutal MHD Marangoni boundary layers," *International Journal of Thermal Sciences*, vol. 47, no. 7, pp. 848–857, 2008.
- [26] R. A. Hamid, N. M. Arifin, R. Nazar, and F. M. Ali, "Radiation effects on Marangoni convection over a flat surface with suction and injection," *Malaysian Journal of Mathematical Sciences*, vol. 5, no. 1, pp. 13–25, 2011.
- [27] R. A. Hamid, W. M. K. A. W. Zaimi, N. M. Arifin, N. A. A. Bakar, and B. Bidin, "Thermal-diffusion and diffusion-thermo effects on MHD thermosolutal Marangoni convection boundary layer flow over a permeable surface," *Journal of Applied Mathematics*, vol. 2012, Article ID 750939, 14 pages, 2012.
- [28] E. Abu-Nada, "Application of nanofluids for heat transfer enhancement of separated flows encountered in a backward facing step," *International Journal of Heat and Fluid Flow*, vol. 29, no. 1, pp. 242–249, 2008.
- [29] H. F. Oztop and E. Abu-Nada, "Numerical study of natural convection in partially heated rectangular enclosures filled with nanofluids," *International Journal of Heat and Fluid Flow*, vol. 29, no. 5, pp. 1326–1336, 2008.
- [30] E. Abu-Nada and H. F. Oztop, "Effects of inclination angle on natural convection in enclosures filled with  $Cu$ -water nanofluid," *International Journal of Heat and Fluid Flow*, vol. 30, no. 4, pp. 669–678, 2009.

- [31] M. Muthamilselvan, P. Kandaswamy, and J. Lee, "Heat transfer enhancement of copper-water nanofluids in a lid-driven enclosure," *Communications in Nonlinear Science and Numerical Simulation*, vol. 15, no. 6, pp. 1501–1510, 2010.
- [32] N. Bachok, A. Ishak, R. Nazar, and N. Senu, "Stagnation-point flow over a permeable stretching/shrinking sheet in a copper-water nanofluid," *Boundary Value Problems*, vol. 2013, article 39, 2013.
- [33] C. Golia and A. Viviani, "Marangoni buoyant boundary layers," *Aerotecnica Missili e Spazio*, vol. 64, pp. 29–35, 1985.
- [34] B. S. Dandapat, B. Santra, and H. I. Andersson, "Thermocapillarity in a liquid film on an unsteady stretching surface," *International Journal of Heat and Mass Transfer*, vol. 46, no. 16, pp. 3009–3015, 2003.
- [35] A. Aziz, "A similarity solution for laminar thermal boundary layer over a flat plate with a convective surface boundary condition," *Communications in Nonlinear Science and Numerical Simulation*, vol. 14, no. 4, pp. 1064–1068, 2009.

## Research Article

# Design and Simulation of a Fused Silica Space Cell Culture and Observation Cavity with Microfluidic and Temperature Controlling

Shangchun Fan,<sup>1,2,3</sup> Jinhao Sun,<sup>1,2,3</sup> Weiwei Xing,<sup>1,2,3</sup> Cheng Li,<sup>1,2,3</sup> and Dongxue Wang<sup>1,2,3</sup>

<sup>1</sup> School of Instrument Science and Opto-Electronics Engineering, Beihang University, 37 Xueyuan Road, Haidian District, Beijing 100191, China

<sup>2</sup> Key Laboratory of Precision Opto-Mechatronics Technology, Ministry of Education, Beihang University, Beijing 100191, China

<sup>3</sup> Key Laboratory of Inertial Science and Technology for National Defence, Beihang University, Beijing 100191, China

Correspondence should be addressed to Jinhao Sun; [maomao9242@163.com](mailto:maomao9242@163.com)

Received 11 June 2013; Accepted 27 September 2013

Academic Editor: Bo Yu

Copyright © 2013 Shangchun Fan et al. This is an open access article distributed under the Creative Commons Attribution License, which permits unrestricted use, distribution, and reproduction in any medium, provided the original work is properly cited.

We report a principle prototype of space animal cell perfusion culture and observation. Unlike previous work, our cell culture system cannot only realize microfluidic and temperature controlling, automatic observation, and recording but also meet an increasing cell culture at large scale operation and overcome shear force for animal cells. A key component in the system is ingenious structural fused silica cell culture cavity with the wedge-shaped connection. Finite volume method (FVM) is applied to calculate its multipoint flow field, pressure field, axial velocity, tangential velocity, and radial velocity. In order to provide appropriate flow rate, temperature, and shear force for space animal cell culture, a closed-loop microfluidic circuit and proportional, integrating, and differentiation (PID) algorithm are employed. This paper also illustrates system architecture and operating method of the principle prototype. The dynamic culture, autofocus observation, and recording of M763 cells are performed successfully within 72 h in the laboratory environment. This research can provide a reference for space flight mission that carries an apparatus with similar functions.

## 1. Introduction

The increasing demand of recombinant therapeutic proteins, monoclonal antibodies, and vaccines produced by mammalian cells has stimulated the development of space cell culture technology, for which almost all space powers have a huge interest. In order to make an in-depth research of space cell culture characteristics, some space powers have developed various space cell culture devices [1–4]. Many of these have completed space flight mission that are shown in Table 1 and Figure 1. Such space cell culture apparatus not only provides appropriate temperature, adequate nutrition and oxygen, low concentration of toxic secretions, and reasonable mechanical property but also records details of cell proliferation [5]. However, space perfusion cultures require more efficient and advanced system, the most frequently reported based on microfluidic chip with kinds of sensors [6–10] and aerospace heat transfer [11]. Rotating wall bioreactor

is widely used because the internal spin-filters are conducive to perfusion rates and reproductive rate at large-scale operation [12, 13]. In this case, the defects such as high energy consumption, noise, low space utilization, and shear force have been considered as limitation of culture duration and process performance.

Despite the great importance of cell culture data after space flight, many studies have been carried out mainly to recognize the differences between original ground data before space flight experiment and new character after it. These studies apparently cannot meet the current research requirements today [14, 15]. Early efforts indicate that microfluidic technology plays an important role in large-scale cell operation, real-time observation, and recording. Dynamical culture in space biological experiments becomes increasingly needed [16, 17]. Dynamical culture can ensure that cells always get enough fresh nutrient solution and metabolic waste is moved out during culture process and construct

TABLE 1: Space cell culture instruments development at home and abroad.

Name	Country	Flight plan	Time
Woodlawn wanderer-9	US	Salyut-3	1978
Biotherm	Switzerland	Salyut-4; Salyut-5	1982
Cytos I	France	Salyut-6	1982
Biorack	Germany	D-1	1983
Carry-on	Switzerland	STS-8	1984
Cytos II	France	Salyut-7	1986
Dynamic cell culture system	Switzerland	IML-1	1988
Static training device	China	Jian-yi-yi satellite	1989
Cell culture device	Japan	IML-2	1994
Improved CCS	China	Jian-yi-yi satellite	1994
Miniature space cell culture device (SBRI)	Switzerland	STS-65; S/MM-03	1994
Cell culture device	China	Shen Zhou 3	2002

a more suitable environment for long-term cell culture. Furthermore, compared with the conventional cell culture techniques [18], the combination of microfluidic chip and cell culture techniques will benefit long-term cell culture and improve cell biology research levels. However, only a certain aspect but not the complete system is introduced in the majority of reports in this field, not to mention considering the impact of the acceleration of gravity.

The study presented in this paper involves fused silica cell culture cavity's simulation, design, and perfusion experiment, which is carried out under realistic operating conditions of temperature and flow rate, using M763 cells. With a wedge-shaped connection, the newly designed cavity is free from the effects of gravitational acceleration before entering orbit and is better sealed. Fused silica is adopted for its outstanding optical property, insulating property, thermal conductivity, and stability, all of which enable the cavity to be isolated from harsh outside environment. In this paper, firstly the creatively designed cavity structure, simulation, and experimental verification of microflow FVM are presented. Then a description of hardware circuits and software design is given. At last, a complete space cell system is conducted and characteristics are listed. The research has some theoretical and engineering value on the design and implementation of space cell culture system.

## 2. Materials and Methods

Our automatic guided space cell culture system mainly includes cell culture unit, observation and record unit, and intelligent control unit; still all outer space conditions need to be overcome. In the outer space, the equipment is expected to executive automatically operations presetted. The experimental apparatus for cell perfusion simulations is shown in Figure 2.

*2.1. Design and Fabrication of the Cavity.* Entire cell culture cavity adopts fused silica, which has the following advantages: perfect thermal stability, low deformation, resistance to high acid and contamination, high hardness, and excellent light transmittance.

Cell culture cavity (Figure 3) is mainly made up of two parts: the upper cover and the lower cover. The upper and the lower covers are pressed together to form a hollow cell culture cavity. Cell suspension and reagent and metabolic waste go in and out through the three wedge-shaped cylindrical pipes welded to the lower cover. Both the upper and the lower covers have 50 mm diameter circular photic zone; the rest part is made as matte at roughness 3.2 and fastened via eight through-bolts in uniform distribution. The upper cover, lower cover, micro pressure sensor cavity, and three wedge-shaped catheters are shown in the assembly drawing of cell culture cavity (Figure 4).

To make the structure better sealed, the three wedge-shaped cylindrical pipes in the lower cover and three independent catheters are connected to micro pressure sensor cavity through the wedge connection, which contributes to overcoming the overload when entering orbit. Using Polytetrafluoroethylene (PTFE) tube connects inlet and outlet into a rotary valve, and then the rotary valve is connected to micropump, thus making it easy for the system to control micro fluid. The pipe in between serves as a waste export as well as a biochemical detection port. The overall structural design is ingenious and highly modularized.

The system allows automatically real-time observation and recording in dynamical culture process through circular photic zone, which facilitates light irradiation and benefits the microscopic observation. The practical parameters of cell culture cavity are shown in Figure 5. Heating coil (Figure 6) is designed in lower cover surface to provide a suitable temperature.

What matters most in this experiment is how to design a perfect cell culture cavity and locate it precisely. A three-dimensional servo platform with high precision is designed to cooperate with microscopic observation. The top of the servo platform is the fixed device of cell culture cavity (Figure 7).

*2.2. The Theory of the Computational Fluid Dynamics.* Continuous equation, namely, the conversation of mass equation, means that any liquidity issue must agree with the law of conversation of mass. In accordance with the law of conversation of mass, the sum of the fluid rest mass out of

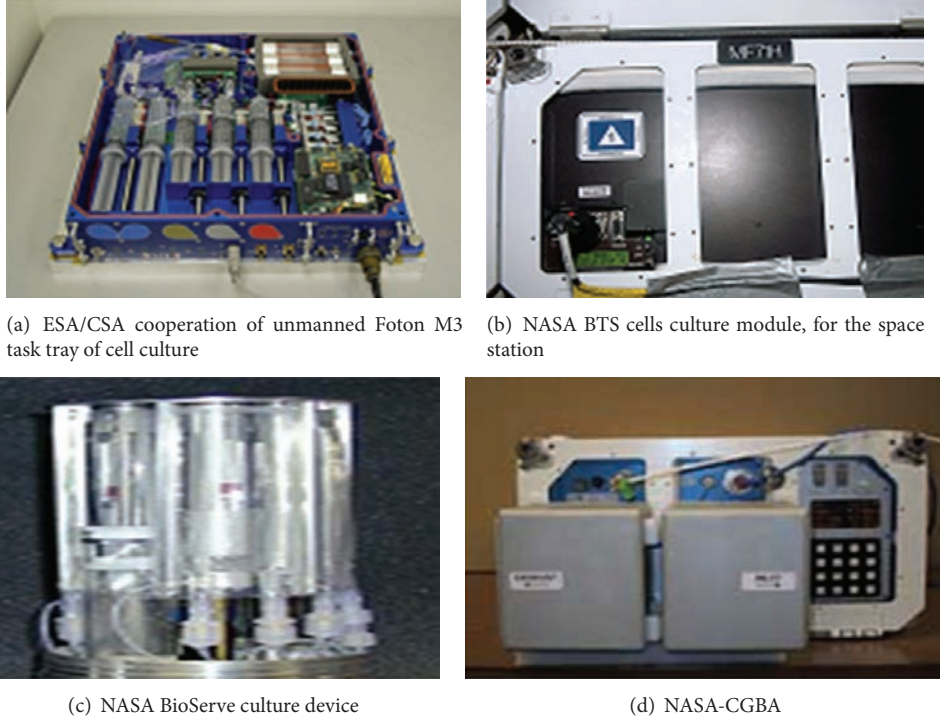


FIGURE 1: Successful applications of space cell culture instruments.

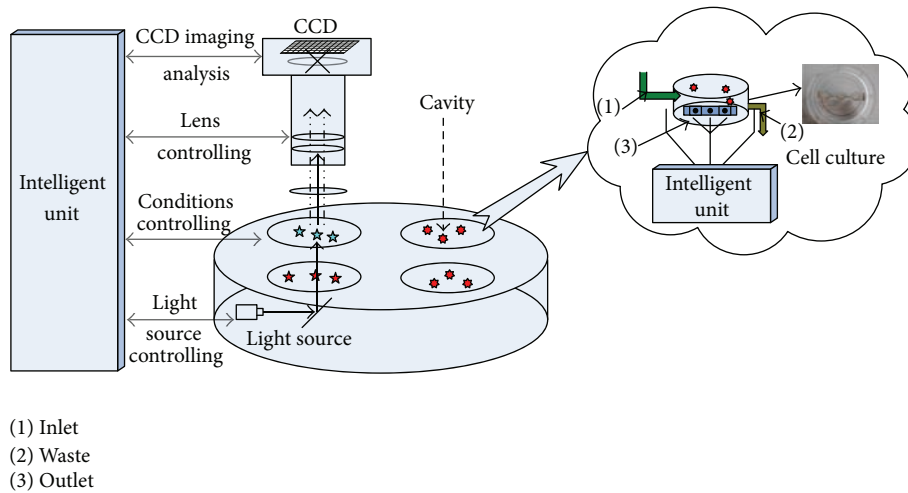


FIGURE 2: Experimental set-up for cell perfusion simulations.

control interval in unit time should be equal to the reducing quality caused by density variations in control interval in the same unit time. Based on that, the differential form of fluid flow continuous equation can be derived as

$$\frac{\partial \rho}{\partial t} + \frac{\partial(\rho u_x)}{\partial x} + \frac{\partial(\rho u_y)}{\partial y} + \frac{\partial(\rho u_z)}{\partial z} = 0, \quad (1)$$

where  $u_x$ ,  $u_y$ , and  $u_z$  are, respectively, the component of velocity (m/s) for three directions,  $t$  is time(s), and  $\rho$  is density ( $\text{kg/m}^3$ ).

The Hamiltonian differential operator is derived

$$\nabla = i \frac{\partial}{\partial x} + j \frac{\partial}{\partial y} + k \frac{\partial}{\partial z}. \quad (2)$$

Equation (1) can be expressed as (3) and divergence form (4):

$$\frac{\partial \rho}{\partial t} + \nabla \cdot (\rho \vec{u}) = 0, \quad (3)$$

$$\frac{\partial \rho}{\partial t} + \text{div}(\rho \vec{u}) = 0. \quad (4)$$

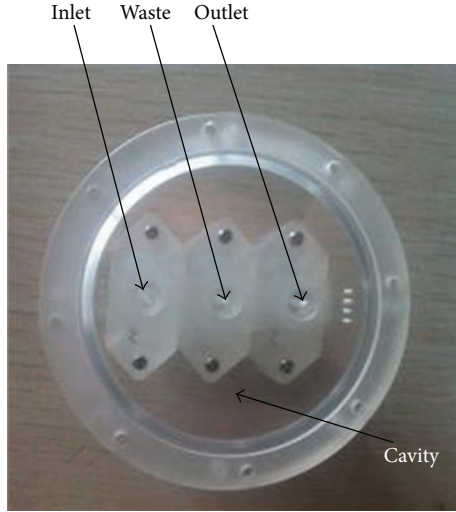


FIGURE 3: A photograph of cell culture cavity.

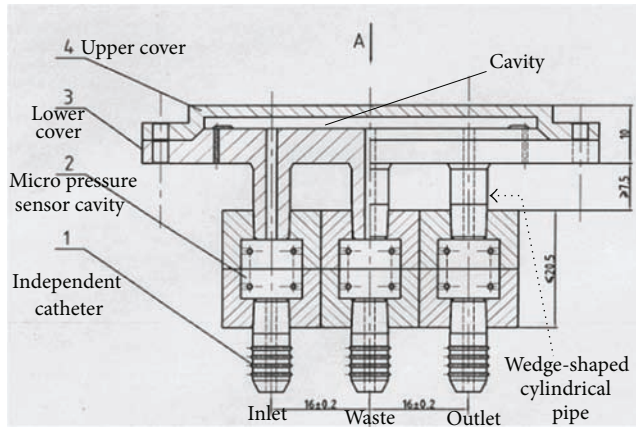


FIGURE 4: The assembly drawing of cell culture cavity.

The form of the continuity equation is expressed as (5) in a cylindrical coordinate system:

$$\frac{\partial \rho}{\partial t} + \frac{\rho u_r}{r} + \frac{\partial(\rho u_r)}{\partial r} + \frac{\partial(\rho u_\theta)}{r \partial \theta} + \frac{\partial(\rho u_z)}{\partial z} = 0. \quad (5)$$

Equation (5) is the normal continuity equation for general use. If for steady flow  $\partial \rho / \partial t = 0$ , its form should be changed to

$$\frac{\partial(\rho u_x)}{\partial x} + \frac{\partial(\rho u_y)}{\partial y} + \frac{\partial(\rho u_z)}{\partial z} = 0. \quad (6)$$

For incompressible flow, in the flow process, the density  $\rho$  of each dot is always unchanged, that is,  $\partial \rho / \partial t = 0$  and  $\rho \neq 0$ ; the form of the continuity equation of incompressible fluid can be derived as

$$\frac{\partial u_x}{\partial x} + \frac{\partial u_y}{\partial y} + \frac{\partial u_z}{\partial z} = 0. \quad (7)$$

Cylindrical coordinate's form of (7) is

$$\frac{u_r}{r} + \frac{\partial u_r}{\partial r} + \frac{\partial u_\theta}{r \partial \theta} + \frac{\partial u_z}{\partial z} = 0. \quad (8)$$

The motion equation of viscous fluid was first proposed in 1827 by Navier who only took the flow of incompressible fluid into account. Poisson proposed the equation of the compressible fluid in 1831. Saint-Venant and Stokes, respectively, in 1843 and 1845, independently proposed the form in which viscosity coefficient was a constant, now known as Navier-Stokes equation, referred to as the N-S equation.

For incompressible viscous fluid, the N-S equation is

$$\frac{\partial \vec{u}}{\partial t} + (\vec{u} \cdot \nabla) \vec{u} = f - \frac{1}{\rho} \nabla p + \frac{\mu}{\rho} \nabla^2 \vec{u}. \quad (9)$$

In (9),  $\vec{u}$  (vector symbol) represents velocity (m/s),  $p$  represents pressure (Pa),  $\mu$  represents the viscosity of fluid ( $\text{kg/m}^3$ ), and the pressure gradient  $\nabla p$  is expressed as and

$$\nabla p = i \frac{\partial p}{\partial x} + j \frac{\partial p}{\partial y} + k \frac{\partial p}{\partial z}, \quad (10)$$

$\nabla^2$  in (9) is Laplacian operator described as (11). The left part of (9) represents the inertia force; in the right part, they represent inturn mass force, pressure (or pressure gradient), and the viscous force:

$$\nabla^2 = \frac{\partial^2}{\partial x^2} + \frac{\partial^2}{\partial y^2} + \frac{\partial^2}{\partial z^2}, \quad (11)$$

N-S equation accurately describes the actual flow. Viscous fluid flow analysis usually refers to researching N-S equation. Because of its rather complex form, only a handful can find the exact solution. The study of numerical solving is usually applied. N-S equation is also the basic equation for calculating the computational fluid dynamics. It can be said that all flow problems revolve around solving N-S equation.

**2.3. Perfusion Numerical Simulations.** According to the animal cells growth requirements, we need to endow micro fluid in the cell cavity with low shear force, good transmission effect, and so on. The truth is that there are always some mutual restraint factors among these principles. For example, a fully hybrid environment is required to strengthen its transmission effect during the dynamical culture process, while the vulnerability of animal cells restrict the formation of such an environment. Therefore theoretical analysis on the nature of the fluid mechanics of the design structure is carried out to optimize the constraints among the above-mentioned principles. The authors in [19] indicate that apart from some simple cases, it is difficult to give analytical solution to the most fluid mechanics problems, so computational fluid dynamics (CFD) is adopted in their analysis.

In a calculation of CFD, the cell suspension is usually regarded as incompressible and homogeneous Newtonian fluid so that Turbulent Navier-Stokes mathematical model is applied to solve [20]. Reynolds number represents the ratio

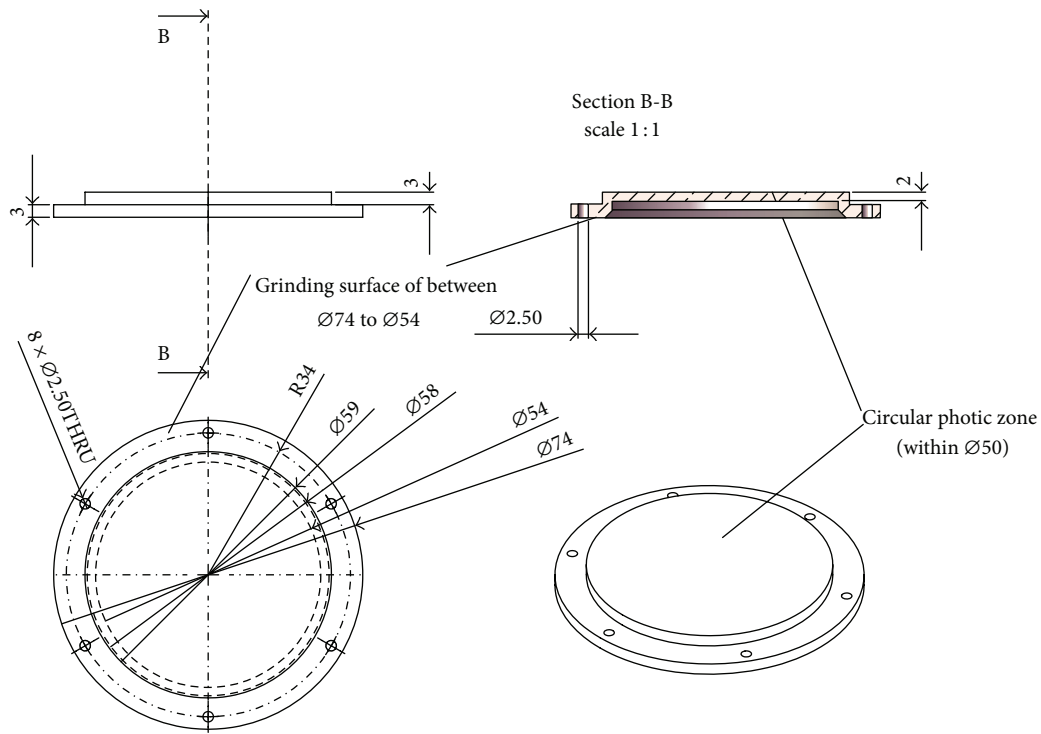


FIGURE 5: The engineering drawing for upper cover of cell culture cavity.

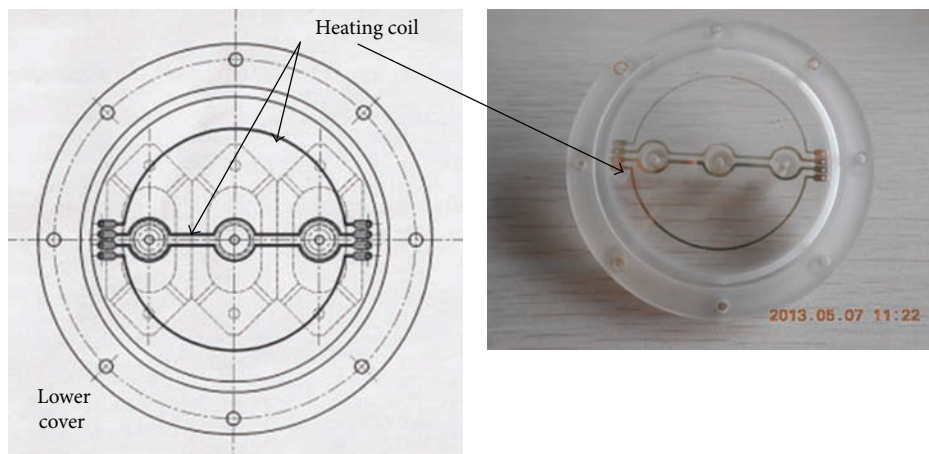


FIGURE 6: The engineering drawing for lower cover of cell culture cavity.

of fluid inertial force of unit mass and viscous force, discriminating the laminar and turbulent flow. Since Reynolds number in microfluidic scale is relatively smaller than 0.01 ( $Re < 0.01$ ), the pressure-driven flow through the cell culture unit is laminar flow [21]. Reynolds number can be calculated by

$$Re = \frac{\rho V d}{\mu}, \tag{12}$$

where  $V$  stands for the average flow rate,  $d$  is equal to characteristic length, also equal to hydraulic diameter, and then equal to 4 multiplies by overcurrent cross-sectional area divided by wetted perimeter. The relationship between the

flow velocity and flow rate in working fluid inlet port is described as

$$v = \frac{w}{A}, \tag{13}$$

where  $v$  stands for flow rate,  $w$  is the inlet flow, and  $A$  is the cross-sectional area of the micro channel.

We check the validity of the number of grids. We perform numerical simulation for five different grids at 604160, 791808, 946096, 1144500, and 1529928, respectively, with same inlet total pressures. We have the curve result of the flow rate for outlet total pressure loss as shown in Figure 8(b). Three curves of grid nodes at 946096, 1144500 and 1529928

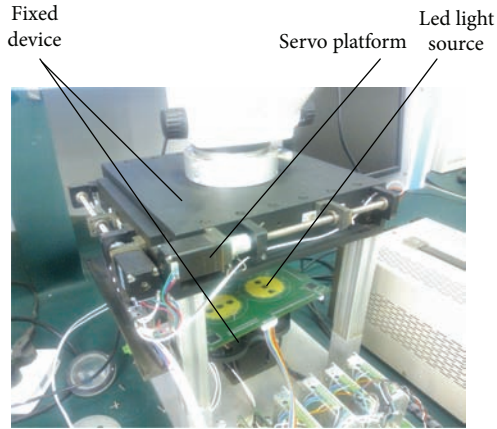


FIGURE 7: A photograph of cell culture cavity three-dimensional servo platform.

were almost overlapped, as could be seen in Figure 8(b). Thus it is demonstrated that the flow field is independent of the number of grids when the grid nodes are greater than or equal to 946096. Finally, the 1144500 grid nodes are applied, and that is in line with grid independency.

Based on the above discussion, “Numeca” software and Fine-solver are adopted in the simulation. Finite volume method (FVM) is employed to study flow and pressure distribution of micro fluid during perfusion in the microfluidic cell culture cavity. The streamline field and pressure field distribution in the cell culture cavity under different flow velocity and inlet static pressure are calculated by applying Numeca simulation analysis software. The height of the cell culture cavity is 2 mm, diameter 50 mm, and volume  $15,708 \text{ mm}^3$ . The diameter of the fluid inlet and fluid outlet pipes is 1.7 mm. During establishing a physical mesh this cavity is divided into 1,144,500 griddings as shown in Figure 8, among which 1,020,285 grid nodes are used for cavity and 41,405 grid nodes for inlet and outlet pipes. We also increase the density of the solid wall mesh, and the mesh width of first layer is 0.001 mm. For the convenience of calculation, the material parameters of the working fluid adopt the material parameters of water (density at  $998.3 \text{ kg/m}^3$ ; the viscosity at  $1.003 \times 10^{-3} \text{ kg/(m}\cdot\text{s)}$ ). Apart from inlet and outlet, the rest of cavity is seen as the solid wall boundaries of adiabatic and no-slip boundary. Firstly, simulation of large flow under the temperature at  $15^\circ\text{C}$  is carried out at inlet total pressures of 110,000, 120,000, and 150,000 Pa and the outlet static pressure is 101,000 Pa. The result is as shown in Figure 9. At the same time the simulation of the condition in greater pressure and larger flow rate is carried out and the result is shown in Figure 10.

The results indicate that when the outlet static pressure and temperature keep unchanged, the flow correlates with pressure: total inlet pressure of 110,000 Pa corresponds to flow rate of 2.791 g/s, 120,000 Pa corresponds to 5.279 g/s, 150,000 Pa corresponds to 10.03 g/s, and 200,000 Pa corresponds to 15.31 g/s. Secondly, the other things being equal, a simulation analysis at the flow rate 200 mg/s is carried out again. It can be seen from Figure 11 that both the

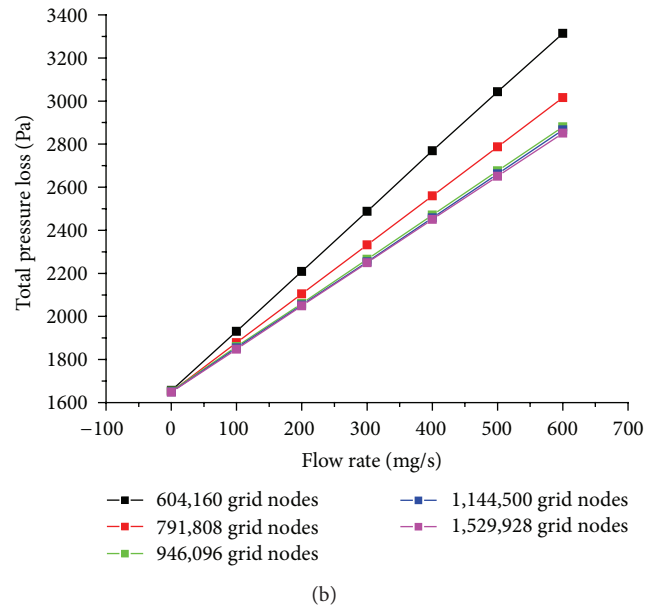
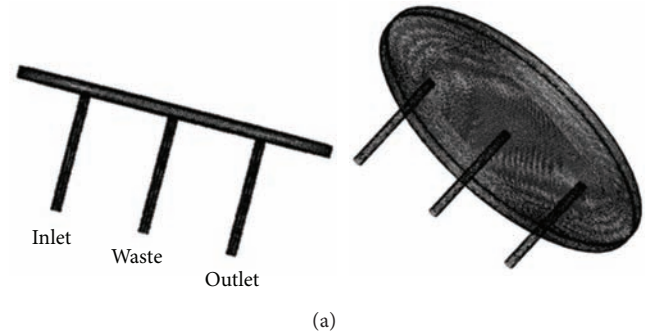


FIGURE 8: The grids method: (a) the side view of mesh division for cell culture internal cavity, (b) the curve result of the flow rate for outlet total pressure loss.

pressure field and the streamline field meet the requirements. Finally, the micro flow simulation result is shown in Figure 12.

It can be seen from the streamline distribution graph (Figure 9) that ejection happens in both of the two entrances. The differential pressure (or flow rate) is so great that the fluid injects to the inner wall of the upper cover. Obviously, this is against the protection of the cell structure, because the well-distributed streamline field means establishment of the cycle process of dynamical culture. It can be seen from the middle surface pressure filed distribution (Figure 10(a)) that the max differential pressure value in the cell culture cavity is 2000 Pa, which is too great to be conducive to cell culture. When the flow rate is  $2 \times 10^{-4} \text{ kg/s}$ , the max differential pressure value is only 12 Pa (Figure 10(b)) and the pressure field in the cavity is well distributed. Sharp change on differential pressure only happens in the fluid inlet and outlet. This meets the requirements. It can be seen, from the streamline distributions (Figures 12(b), 12(c), 12(d)), that there is no infinite loop in the whole cavity area. Infinite loop emerges in the cell cavity when the flow rate is  $3 \times 10^{-7} \text{ kg/s}$

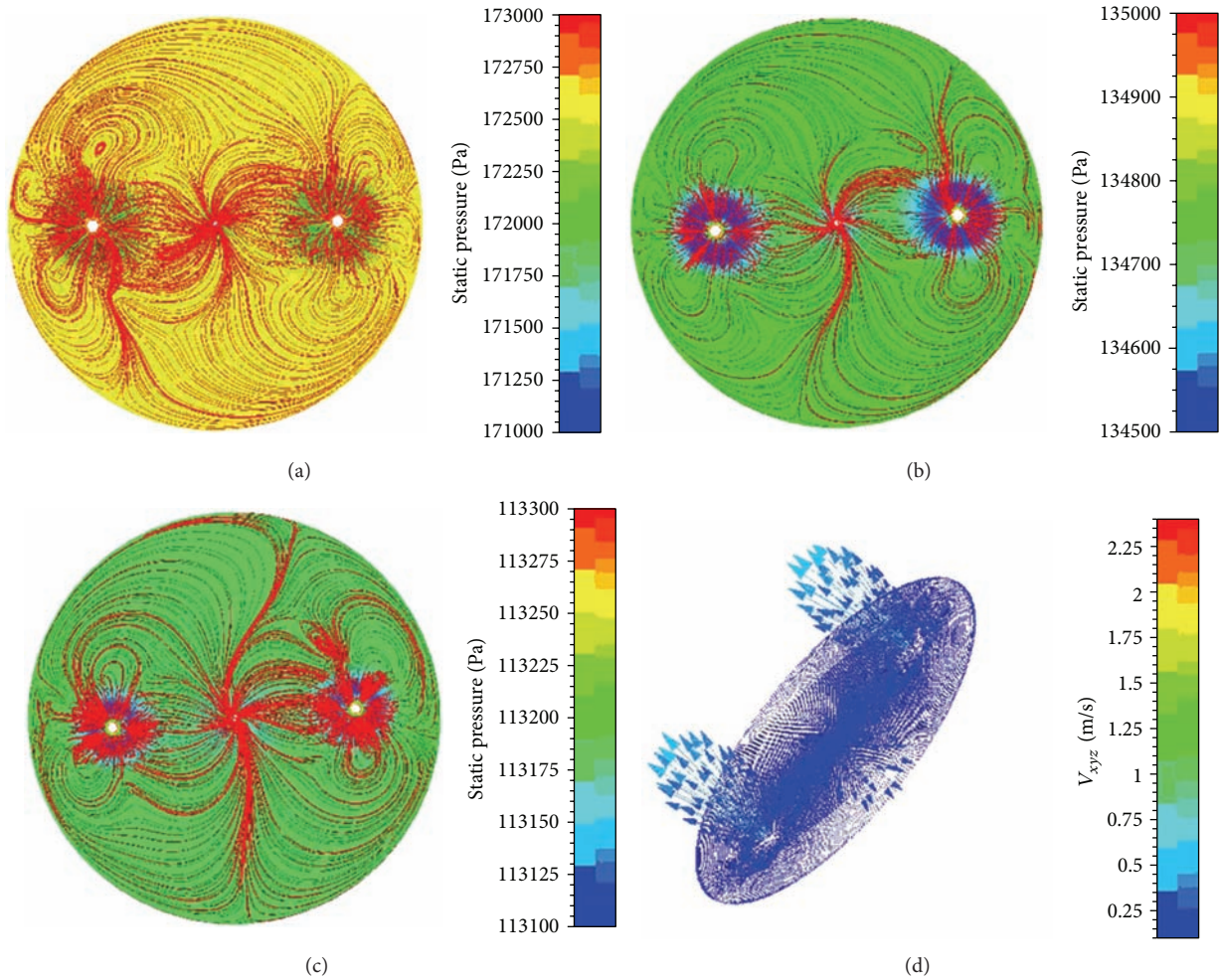


FIGURE 9: The simulation results in large flow: (a) the middle surface streamline chart in inlet static pressure of 200,000 Pa, (b) the middle surface streamline chart in inlet static pressure of 150,000 Pa, (c) the middle surface streamline chart in inlet static pressure of 120,000 Pa, (d) the middle surface vector of cavity in inlet static pressure of 150,000 Pa.

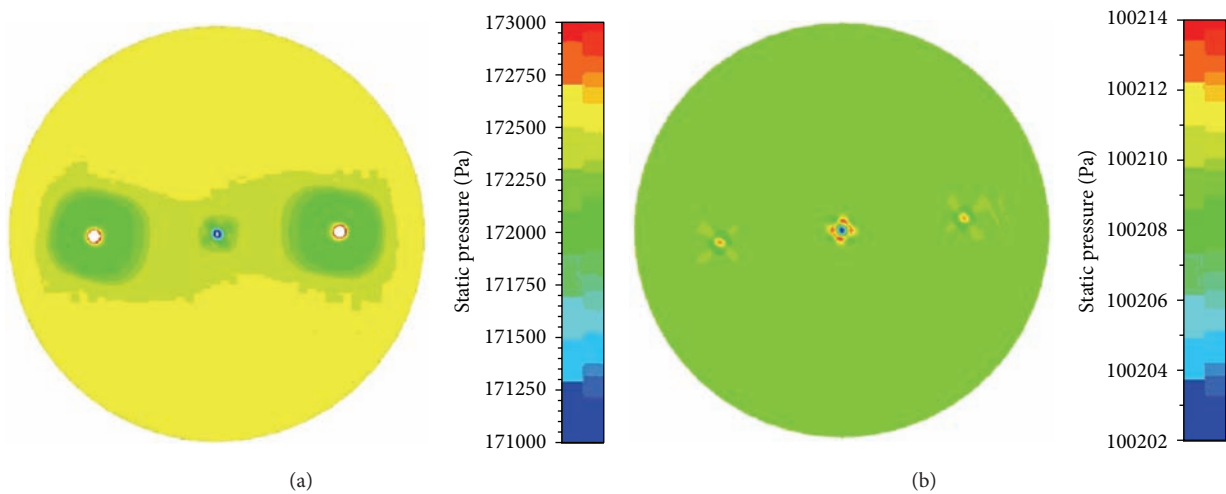


FIGURE 10: The pressure distribution graph of cell culture cavity: (a) the middle surface pressure distribution graph in inlet static pressure of 200,000 Pa, (b) the pressure field distribution when the flow rate is  $2 \times 10^{-4}$  kg/s.

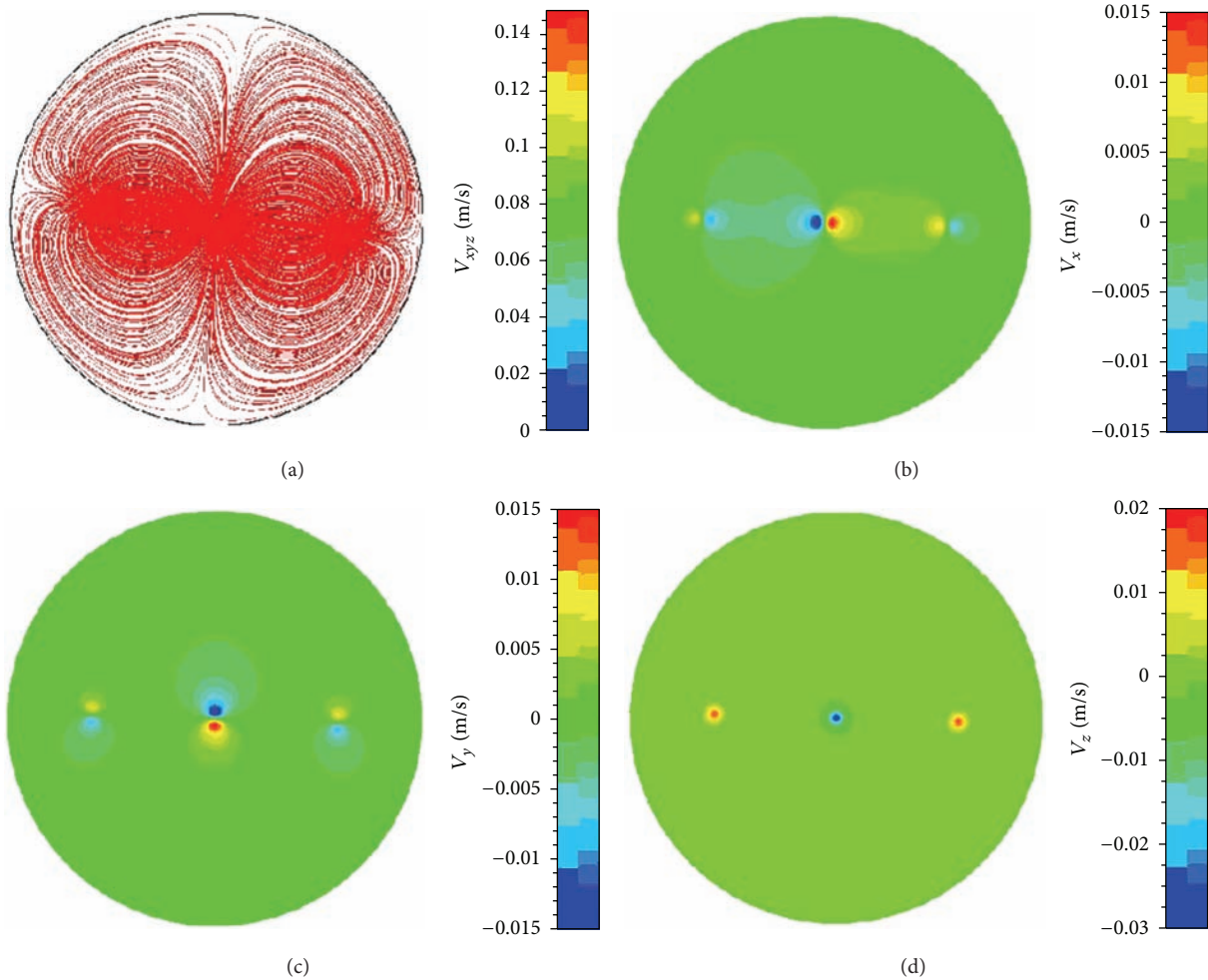


FIGURE 11: The simulation analysis when the flow rate is 200 mg/s. (a) Streamline distribution, (b) velocity distribution in  $x$  direction, (c) velocity distribution in  $y$  direction, (d) velocity distribution in  $z$  direction.

(Figure 12(a)) and there is hardly pressure difference, which is regarded as the minimum flow rate of the designed cavity. Of course, further calibration is supposed to be in line with the actual experimental environment and the overall equipment characteristics.

The different cell culture and experimental design demand different flow rate, for they have different cell culture volumes and different days in culture. Based on the experimental experience, the simulation of the feature points sampling is carried out to work out the maximum value and the minimum value, thus estimating the flow rate control range. So we roughly select the minimum of flow rate, that is,  $3 \times 10^{-7}$  kg/s, and the maximum of flow rate 200 mg/s according to the animal cells growth requirements. The result of Numeca analysis software also identifies that the structure design program of cell culture cavity is reasonable and the flow field is well distributed.

**2.4. Experimental Device for Perfusion Cell Culture.** Automatic guided space cell culture system aims to realize unattended cell culture, observation, and recording with

microfluidic and temperature control circuits. This system involves high-speed analog signal synchronous sampling technique, embedded technology, intelligent power technology, servo control technology, multisensors information fusion, dedicated bus technology, SCADA technology, microfluidic hardware and software technology, and intelligence analysis technique. Major circuit diagram is shown in Figure 13 consisting of Synchronous differential pressure sampling circuit, controller area network (CAN) and RS485 bus circuit, embedded control board, cell culture circuit, PCI-104 data acquisition module, the serial port expansion module, and processing analysis software. Cell culture and the extended port in the back panel of observation platform are as shown in Figure 14. These ports are mainly used to connect microscope, motor, and multisensor circuit board. As is shown in Figure 15, the multisensor data is used to acquire sampling unit pressure, temperature, biochemical parameter, and lighting control; the motor with CAN bus and RS232 port is used to control valve and micropump. The microscope of observation system has three grating rulers to control displacement in three directions. When we want to

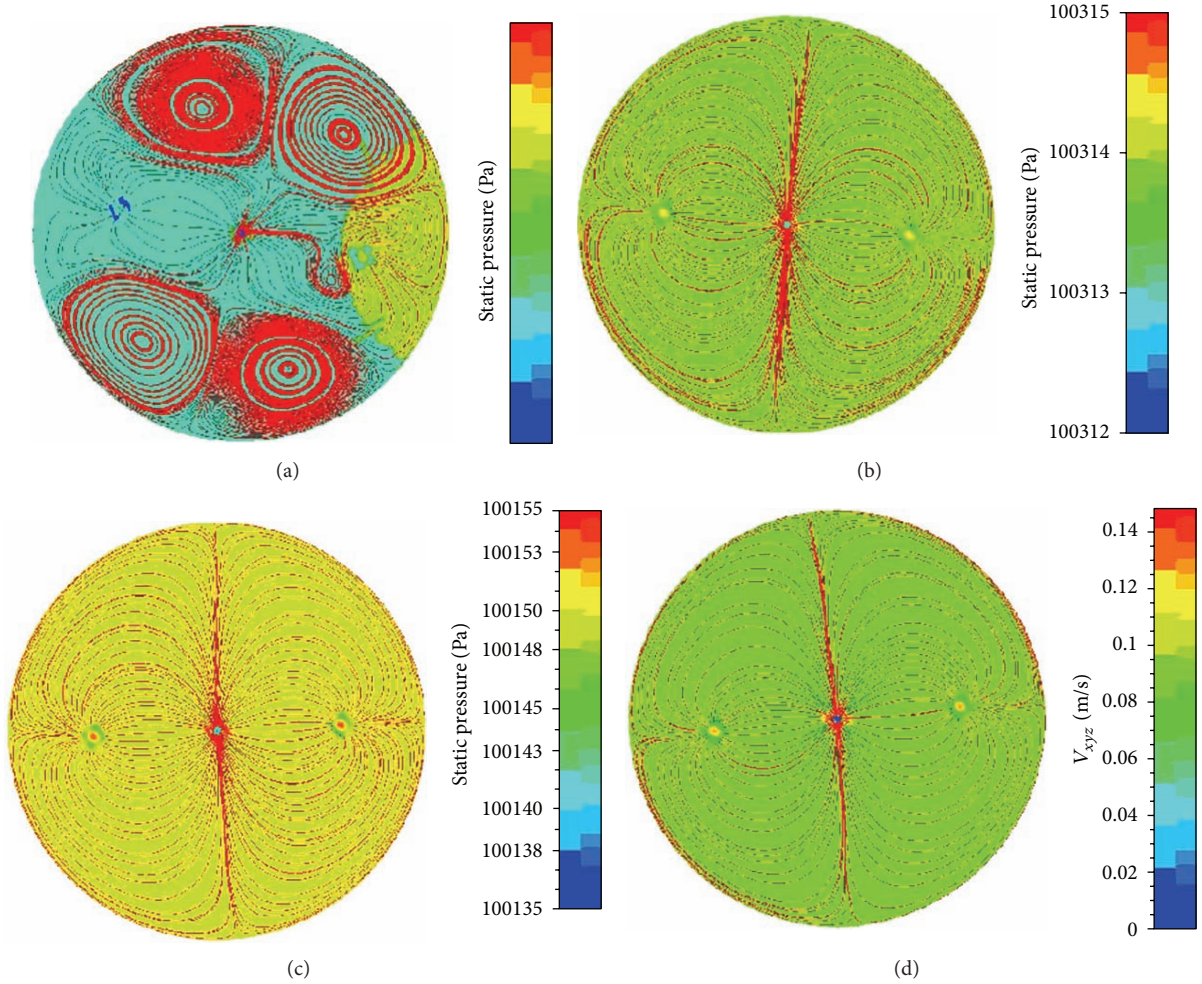


FIGURE 12: The simulation results of micro flow: (a) the flow field distribution when the flow rate is  $3 \times 10^{-7}$  kg/s, (b) the flow field distribution when the flow rate is  $3 \times 10^{-5}$  kg/s, (c) the flow field distribution when the flow rate is  $3 \times 10^{-4}$  kg/s, (d) the flow field distribution when the flow rate is  $2 \times 10^{-7}$  kg/s.

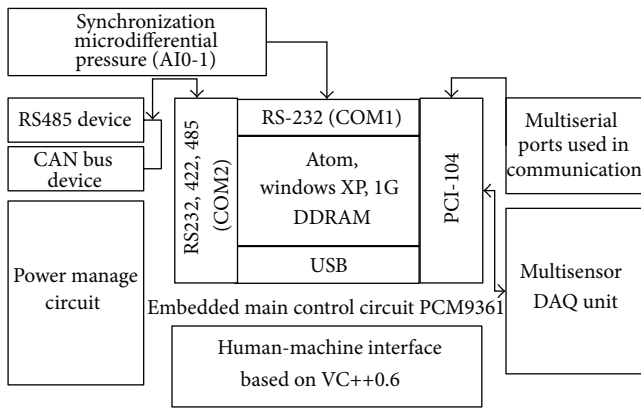


FIGURE 13: Cell culture and observation system platform diagram.

move over a direction for a certain distance, the servo motor powers it. The grating rulers acquire RS232 outputs pulse to calculate the precise displacement location, so that the

microscope performs autofocus observation, other direction way similar. The communication between cell culture and observation system platform and microscope observation system uses three RS232 serial ports for the displacement controlling in  $x$ ,  $y$ , and  $z$  directions and one USB port for the transmission of image data. Moreover, the micro pump closed-loop controlling of microfluidic system needs pressure sensor sampling value and two motors with RS232 and CAN. According to the simulation results and discussion of cell culture cavity, the microfluidic software flow chart is designed as shown in Figure 16. Temperature controlling system consists of temperature sensor PT100, micro controller C8051F, heating coil, and so on. and adopts PID algorithm. It adjusts the cavity temperature to cell culture.

The human-machine interaction interface of cell culture and observation system platform adopts a 10.5 inch touch screen and then fixes it on the front panel of cabinet. Microsoft Visual C++ is adopted for its software programming.

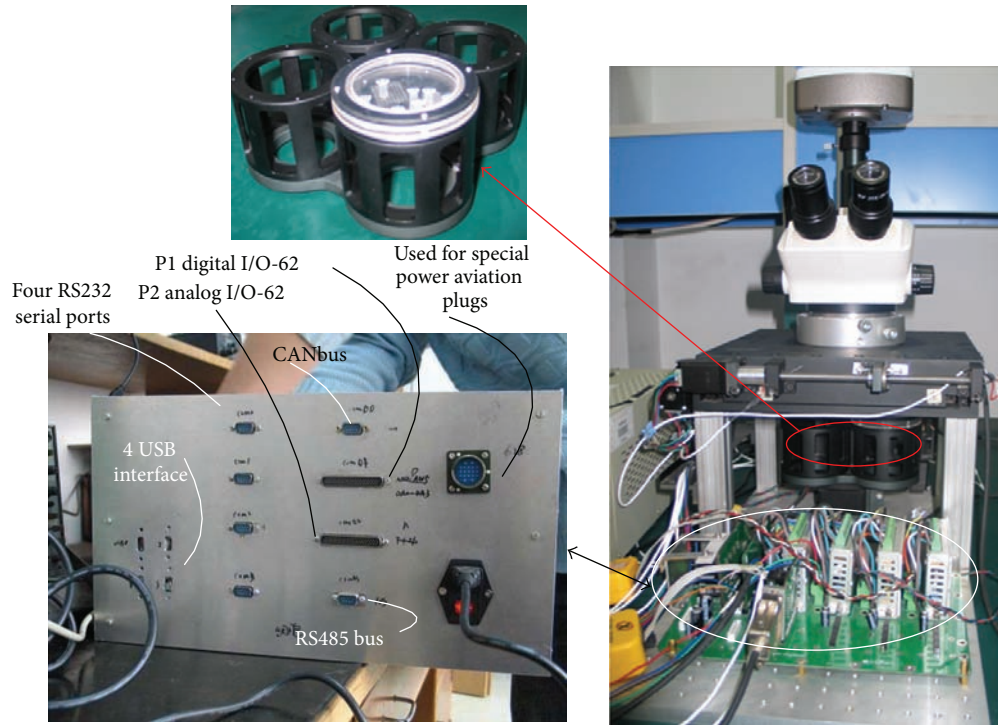


FIGURE 14: A photograph of cell culture and observation system platform.

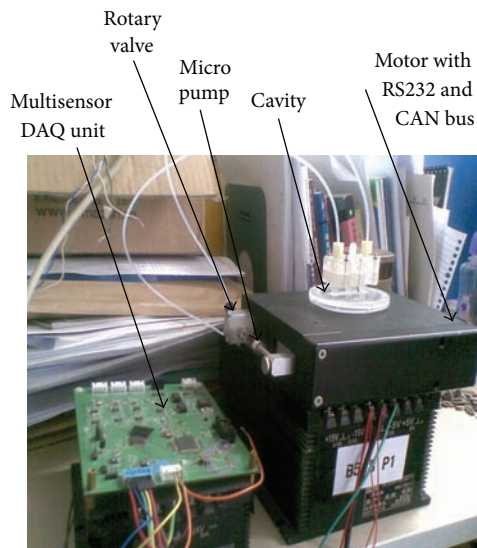


FIGURE 15: A photograph of micro pump and multisensor data acquisition unit.

### 3. Results and Discussion

In the present system, the cell's requirement for nutrients and dissolved oxygen is met by the replacement of the culture medium in the cell culture cavity. When the flow rate is too large, it will not only cause the waste of the culture medium, but also the shear force and vortex that is bad for cells. The determination of the flow rate mainly relates to nutrients

and dissolved oxygen supply and shear force. The supply of nutrients and dissolved oxygen is estimated empirically according to the required culture solution replacement time, which mainly depends on the structure and capacity of the culture vessel and cell type. The size of the shear force is related to the size of the flow rate as well as the structure of the culture vessel. Therefore, the flow rate of the culture solution is first estimated empirically according to required replacement time, and then we calculate whether the shear force caused by the flow rate meets the requirements. The appropriate flow rate is ultimately determined by experiment. Since M763 cells are cultured at  $36.5 \pm 0.5^\circ\text{C}$ , temperature controlling circuits are expected to perform with a high-speed response and in a permitted error range. Adhering to the distance metering principle, traditional focusing technology mainly employs the distance system to drive the lens to find the best observation location, while this method needs additional equipment. Considering that space flight mission asks the equipment to be as small and light as possible, the initiative technology is employed. This technology uses image information to analyze focus direction and adjust the focal length to the best position. Since the focusing quality is decided by algorithm of the initiative technology [22], we adopt the morphological wavelet decomposition pyramid for microscopy system autofocus.

**3.1. Measurements.** Two experiments are carried out on the temperature control unit and the result shows that the temperature of the cavity can be stabled. In experiment 1, the initial temperature is set as  $27.68^\circ\text{C}$ , the target temperature as  $36.5^\circ\text{C}$ , and temperature rising curve is as shown in Figure 17.

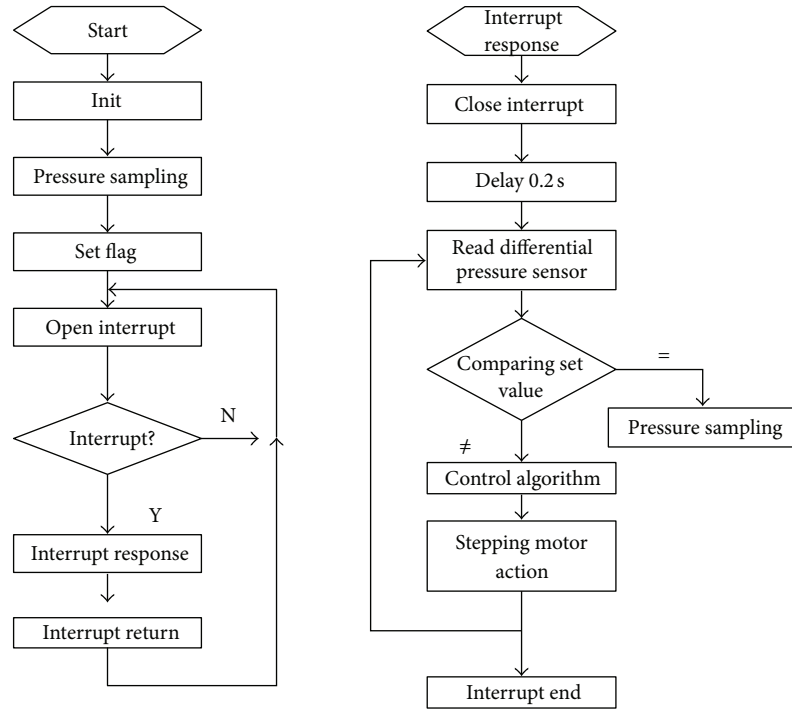


FIGURE 16: Micro fluid controlling software flow chart.

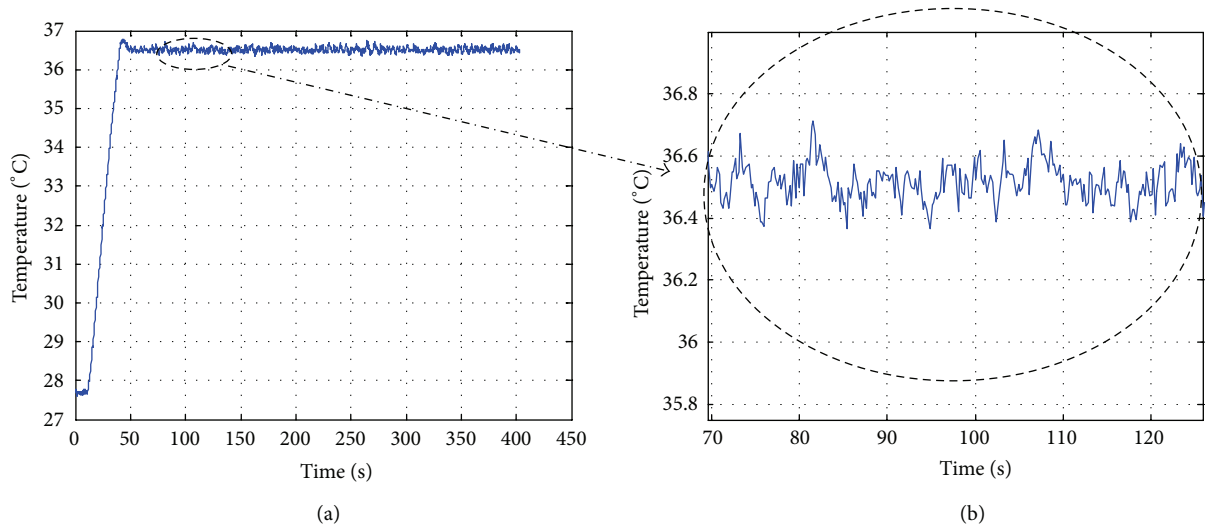


FIGURE 17: (a) Temperature characteristic of temperature closed-loop control circuit with start temperature at 27.68°C. (b) Temperature characteristic partial enlarged detail.

It can be seen that the time from the initial temperature to the target temperature is about 38 s and the temperature error is in the range of  $\pm 0.5^{\circ}\text{C}$ . In experiment 2, the initial temperature is set as  $31.65^{\circ}\text{C}$ , the target temperature  $36.5^{\circ}\text{C}$ , temperature rising curve is as shown in Figure 18. It can be seen that the temperature remains stable after 25 s, so it is concluded that the rising of environmental temperature leads to the reduction of rising time.

72-hours-cell culture and observation are carried out with the aid of the culture cavity. Microscope (Nikon ECLIPSE Ti-S, Nikon Corporation, Japan), CCD (Olympus), and the cell culture and observation system platform form a cell image observation system. Figure 19 is the growth records of M763 in the cavity captured by the image observation system. We can see that the cells in 24 hours, have stuck to the wall and unfolded completely. In 48 hours, apparent cell division

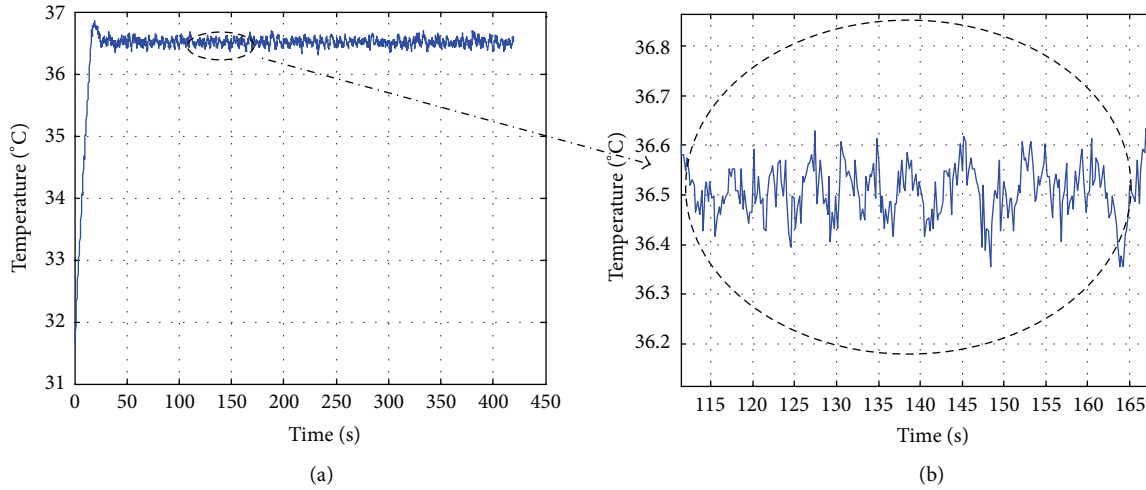


FIGURE 18: (a) Temperature characteristic of temperature closed-loop control circuit with start temperature at 31.65°C. (b) Temperature characteristic partial enlarged detail.

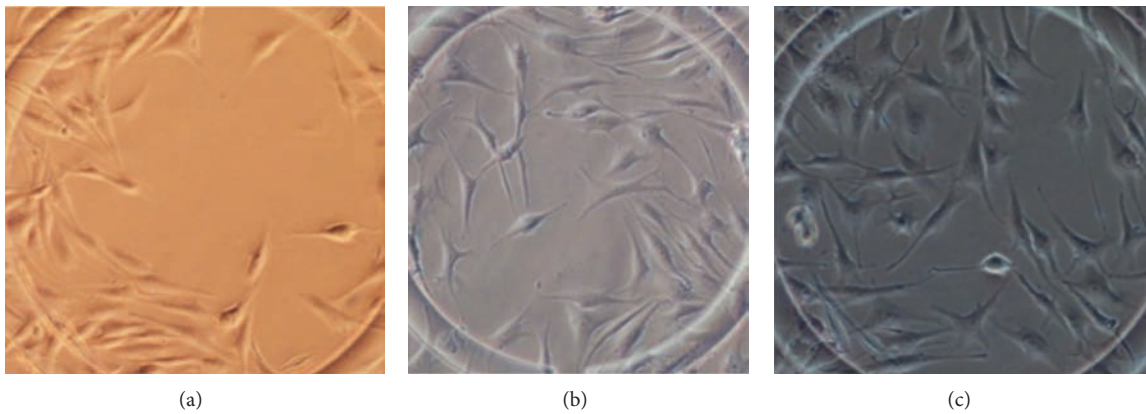


FIGURE 19: Growth image of M763 cells for different time steps. (a), (b), and (c) are, respectively, growth images of 24 h, 48 h, and 72 h.

TABLE 2: The part index of automatic guided space cell culture system.

Parameter	Index
Microscopic image system resolution	0.98 $\mu\text{m}$
Maximum pixel	2048 * 1536
Image pixel equivalent	horizontal $C_x = 138.7 \text{ nm/pixel}$ ; Vertical $C_y = 139.7 \text{ nm/pixel}$
Frame rate	5 frame/s
Mobile platform x direction resolution	0.5 $\mu\text{m}$
Mobile platform y direction resolution	0.6 $\mu\text{m}$
Compression rate (for umbilical vein living cells image)	39.4 : 1
Range of recommended flow-rate	0.3 $\mu\text{L/s}$ ~200 $\mu\text{L/s}$
Precision of temperature control	$\pm 1^\circ\text{C}$

happens. In 72 hours, the process continues. All these indicate that the system design in this paper is successful.

3.2. *System Performance.* The automatic guided space cell culture system has been calibrated. Part of its performance indexes are as shown in Table 2.

#### 4. Conclusion

In this paper, a fused silica space cell culture cavity is designed, simulated, and tested. This culture cavity with circular photic zone for autoobservation and heating coil for adjusting temperature realizes in-place culturing, observing and recording, with the aid of automatic control system having microfluidic and temperature control circuits. The efficacy of the wedge-shaped connection is demonstrated; however, for future space flight mission it should be more robust to perform better leakproofness and be better resistant to the impact of the gravitational acceleration caused by the duration of carrier rocket into orbit. It has also been demonstrated that automatic guided space cell culture system with microfluidic and temperature control circuits is successful in laboratory environment.

The system aims to be used in the future space experiment, and extensive ground testing has been done to verify its functions. It performs perfectly during the test. The only flaw is that the system is too bulky for a space experiment. The future work will focus on the miniaturization of the apparatus.

#### Acknowledgments

This work was supported by the Research Program Biological Smart Sensor Technology and Application from the Ministry of Industry and Information Technology of China and by the 863 National High-tech Research and Development Program (2008AA12A20).

#### References

- [1] B. van der Schoot, M. Boillat, and N. de Rooij, "Micro-instruments for life science research," *IEEE Transactions on Instrumentation and Measurement*, vol. 50, no. 6, pp. 1538–1542, 2001.
- [2] I. Walther, B. van der Schoot, M. Boillat, and A. Cogoli, "Performance of a miniaturized bioreactor in space flight: microtechnology at the service of space biology," *Enzyme and Microbial Technology*, vol. 27, no. 10, pp. 778–783, 2000.
- [3] V. D. Kern, S. Bhattacharya, R. N. Bowman et al., "Life sciences flight hardware are development for the international space station," *Advances in Space Research*, vol. 27, no. 5, pp. 1023–1030, 2001.
- [4] Commercial Generic Bioprocessing Apparatus (CGBA) [EB/OL], 2009, <http://www.nasa.gov/centers/marshall/news/background/facts/cgba.html>.
- [5] Y. Tan, X. G. Yuan, J. B. Rui, and J. R. Yu, "Research progress of cell culture apparatus," *Space Medicine & Medical Engineering*, vol. 15, no. 5, pp. 383–386, 2002.
- [6] M. Huang, S. Fan, W. Xing, and C. Liu, "Microfluidic cell culture system studies and computational fluid dynamics," *Mathematical and Computer Modelling*, vol. 52, no. 11–12, pp. 2036–2042, 2010.
- [7] N. Hu, X. Zhang, J. Yang, S. W. Joo, and S. Qian, "A cell electrofusion microfluidic chip with micro-cavity microelectrode array," *Microfluidics and Nanofluidics*, vol. 15, no. 2, pp. 151–160, 2013.
- [8] K. Lei, M. H. Wu, P. Y. Liao, Y. M. Chen, and T. M. Pan, "Development of a micro-scale perfusion 3D cell culture biochip with an incorporated electrical impedance measurement scheme for the quantification of cell number in a 3D cell culture construct," *Microfluidics and Nanofluidics*, vol. 12, no. 1–4, pp. 117–125, 2012.
- [9] S. Sharma, A. R. B. Moniz, I. Triantis et al., "An integrated silicon sensor with microfluidic chip for monitoring potassium and pH," *Microfluidics and Nanofluidics*, vol. 10, no. 5, pp. 1119–1125, 2011.
- [10] S. K. Yoo, J. H. Lee, S. S. Yun, M. B. Gu, and J. H. Lee, "Fabrication of a bio-MEMS based cell-chip for toxicity monitoring," *Biosensors and Bioelectronics*, vol. 22, no. 8, pp. 1586–1592, 2007.
- [11] B. S. Elkins, M. Huang, and J. I. Frankel, "Higher-time derivative of in-depth temperature sensors for aerospace heat transfer," *International Journal of Thermal Sciences*, vol. 52, pp. 31–39, 2012.
- [12] F. Vallez-Chetreau, L. G. Fraisse Ferreira, R. Rabe, U. von Stockar, and I. W. Marison, "An on-line method for the reduction of fouling of spin-filters for animal cell perfusion cultures," *Journal of Biotechnology*, vol. 130, no. 3, pp. 265–273, 2007.
- [13] D. Voisard, F. Meuwly, P. A. Ruffieux, G. Baer, and A. Kadouri, "Potential of cell retention techniques for large-scale high-density perfusion culture of suspended mammalian cells," *Biotechnology and Bioengineering*, vol. 82, no. 7, pp. 751–765, 2003.
- [14] B. J. Klement and B. S. Spooner, "Utilization of microgravity bioreactors for differentiation of mammalian skeletal tissue," *Journal of Cellular Biochemistry*, vol. 51, no. 3, pp. 252–256, 1993.
- [15] I. Walther, B. van der Schoot, M. Boillat, and A. Cogoli, "Performance of a miniaturized bioreactor in space flight: microtechnology at the service of space biology," *Enzyme and Microbial Technology*, vol. 27, no. 10, pp. 778–783, 2000.
- [16] C. Yi, C. W. Li, S. Ji, and M. Yang, "Microfluidics technology for manipulation and analysis of biological cells," *Analytica Chimica Acta*, vol. 560, no. 1–2, pp. 1–23, 2006.
- [17] J. H. Yeon and J. K. Park, "Microfluidic cell culture systems for cellular analysis," *Biochip Journal*, vol. 1, no. 1, pp. 17–27, 2007.
- [18] J. El-Ali, P. K. Sorger, and K. F. Jensen, "Cells on chips," *Nature*, vol. 442, no. 7101, pp. 403–411, 2006.
- [19] L. Kim, Y. C. Toh, J. Voldman, and H. Yu, "A practical guide to microfluidic perfusion culture of adherent mammalian cells," *Lab on a Chip*, vol. 7, no. 6, pp. 681–694, 2007.
- [20] D. W. Huttmacher and H. Singh, "Computational fluid dynamics for improved bioreactor design and 3D culture," *Opinion Trends in Biotechnology*, vol. 26, no. 2, pp. 166–172, 2008.
- [21] H. Singh, S. H. Teoh, H. T. Low, and D. W. Huttmacher, "Flow modelling within a scaffold under the influence of uni-axial and bi-axial bioreactor rotation," *Journal of Biotechnology*, vol. 119, no. 2, pp. 181–196, 2005.
- [22] W. Xia, S. Fan, W. Xing, C. Liu, T. Li, and J. Wang, "A mathematical morphological approach for region of interest coding of microscopy image compression," *Journal of Harbin Institute of Technology*, vol. 19, no. 3, pp. 115–121, 2012.

## Research Article

# Flow Patterns Transition Law of Oil-Water Two-Phase Flow under a Wide Range of Oil Phase Viscosity Condition

Wei Wang, Wei Cheng, Kai Li, Chen Lou, and Jing Gong

*Beijing Key Laboratory of Urban Oil & Gas Distribution Technology, Department of Mechanical and Transportation Engineering, China University of Petroleum, Beijing 102249, China*

Correspondence should be addressed to Jing Gong; [ydgj@cup.edu.cn](mailto:ydgj@cup.edu.cn)

Received 16 July 2013; Accepted 13 September 2013

Academic Editor: Bo Yu

Copyright © 2013 Wei Wang et al. This is an open access article distributed under the Creative Commons Attribution License, which permits unrestricted use, distribution, and reproduction in any medium, provided the original work is properly cited.

A systematic work on the prediction of flow patterns transition of the oil-water two-phase flows is carried out under a wide range of oil phase viscosities, where four main flow regimes are considered including stratified, dispersed, core-annular, and intermittent flow. For oil with a relatively low viscosity, VKH criterion is considered for the stability of stratified flow, and critical drop size model is distinguished for the transition of o/w and w/o dispersed flow. For oil with a high viscosity, boundaries of core-annular flow are based on criteria proposed by Bannwart and Strazza et al. and neutral stability law ignoring that the velocity of the viscous phase is introduced for stratified flow. Comparisons between predictions and quantities of available data in both low and high viscosity oil-water flow from literatures show a good agreement. The framework provides extensive information about flow patterns transition of oil-water two-phase flow for industrial application.

## 1. Introduction

Oil-water two-phase systems abound in many applications in the petroleum industry including emulsions preparation, oil-water mixture separation, and transportation. Accurate prediction of oil-water flow characteristics, such as flow pattern transition, is important in many engineering applications. Despite the importance, however, oil-water flow has not been explored to the same extent as gas-liquid flow. The density difference between the two phases is relatively small, while the viscosity ratio encountered can extend over several orders of magnitude, both of which bring great complexities and difficulties to the study of oil-water flow transitions.

Various experimental works have been proposed in the literature to enhance the understanding of oil-water flow transitions [1–4] in horizontal pipes with the flow pattern being classified as stratified, dispersed, and mixed flow. Trallero [4] conducted extensive experimental and theoretical studies on oil-water flow patterns, where segregated and dispersed flow were mainly focused and a total of six patterns were identified.

For the transition law of the flow patterns, Brauner and Maron [5] first developed a two-fluid model to characterize

the transition from stratified flow to other flow patterns. Trallero [4] proposed that VKH criterion could predict the transition between stratified flow and unstable wavy stratified flow. Brauner [6] suggested an approach for the transition to dispersed flow pattern. Recently, Sharma et al. [7] introduced the energy minimization concept, a principle that a system can be stabilized to its minimum total energy, into oil-water flow pattern transition.

Most of the published works focus on low viscosity oil-water flows. However, when the viscosity of oil increases, new characteristics could be observed. For heavy oil-water dispersions, core-annular flow, especially oil core-water annular flow, becomes dominant. Moreover, drop entrainment as well as oil clot and slug can easily be found in such flow.

For the transition of core-annular flow pattern, Bannwart [8] argued that core-annular flow is prone to occur in a pipe where the two fluids have very dissimilar viscosities but relatively close densities. In this case, however, it is proposed that velocity difference of the two phases should be small. Grassi et al. [9] found that the extension of theoretical models for low viscosity ratio to high viscosity ratio flows should not be straightforward. Rodriguez et al. [10] developed a refined

pressure-loss prediction model which includes a slip ratio term that implicitly accounts for the buoyancy of the oil core.

From the previous literature, it could be gained that systematic work for the prediction of flow pattern transition is still demanded. This paper aims to establish a framework for flow pattern transition prediction especially over a wide range of oil viscosity, which is expected to provide extensive support for the industrial application of oil-water flow pattern transition theories. Results are validated with a wide range of existing published data, even that of heavy crude oils.

## 2. Theoretical Models of Flow Pattern Transition

**2.1. Flow Pattern Classification.** Although large amounts of experiments on oil-water two-phase flow in horizontal pipe have been conducted by scholars, there still lacks overall consensus about how the flow patterns could be classified. This may be due to the fact that experimental conditions differ and ways to observe flow regimes are not identical. In spite of that, the common regimes without drop entrainment are mainly considered here. Combine Taitel and Dukler's gas-liquid flow pattern classification method with oil-water pipe flow

characteristics, the flow patterns of low viscosity oil-water two-phase flow are classified as stratified flow, w/o dispersed flow, o/w dispersed flow, and intermittent flow.

### 2.2. Transition of Stratified Flow

**2.2.1. Transition of Stratified Flow for Low Viscosity Ratio.** Recent researches of stratified flow stability are all based on momentum and continuity equation of double fluid model by introducing the influence of small disturbance on the interface. It is common that ways of treating the stability equations could be classified into two categories: ZNS (zero neutral stability)/ZRC (zero real characteristics) criterion and Kelvin-Helmholz (IKH and VKH) instability theory. Brauner and Moalem Maron [11] used ZNS/ZRC criterion to predict the transition criterion of smooth stratified flow pattern to other flow patterns. ZNS line is set as the boundary of smooth stratified and stratified wavy and ZRC line as the upper limit of smooth stratified. Trallero [4] argued that the VKH equation determines the transition between stable stratified flow and either unstable stratified with wavy interface or some other flow patterns and may be used to predict onset of entrainment, which is suitable for low viscosity oil-water systems. The equations are as follows:

$$\overbrace{(C_V - C_{IV})^2 + \frac{\rho_w \rho_o}{\rho H_w H_o} (U_w - U_o)^2 - \frac{(\rho_w - \rho_o) g \cos \beta A}{\rho S_i}}^{\text{VKH}} - \underbrace{\frac{\sigma A}{\rho S_i} k^2}_{\text{IKH}} + \frac{\rho_f (U_w - U_o)^2 C_S A}{\rho} \left( \frac{1}{A_w} - \frac{1}{A_o} \right) < 0 \quad (1)$$

$$\overbrace{J_\mu + J_U - J_g - J_o + J_s}_{\text{IKH}} < 0 \quad (2)$$

$$C_V = \frac{\partial F / \partial H_w}{\partial F / \partial U_{so} - \partial F / \partial U_{sw}} \quad (3)$$

$$F = -\frac{\tau_w S_w}{A_w} + \frac{\tau_o S_o}{A_o} + \tau_i S_i \left( \frac{1}{A_w} + \frac{1}{A_o} \right) = 0 \quad (4)$$

$$C_{IV} = \frac{\rho_w U_w H_w + \rho_o U_o H_o}{\rho_w H_w + \rho_o H_o} \quad (5)$$

$$\rho = A \left( \frac{\rho_w}{A_w} + \frac{\rho_o}{A_o} \right), \quad (6)$$

where  $\rho_w$  and  $\rho_o$  are the density of water and oil, respectively;  $H_w$  and  $H_o$  are the holdup of water and oil, respectively;  $U_{sw}$  and  $U_{so}$  are superficial velocity of water and oil, respectively;  $U_w$  and  $U_o$  are real mean velocity of water and oil, respectively;  $\tau_w$ ,  $\tau_o$ , and  $\tau_i$  are water, oil, and interfacial shear stresses;  $S_w$ ,  $S_o$ , and  $S_i$  are water, oil, and interface wet perimeter;  $A_w$ ,  $A_o$ , and  $A$  are cross-sectional area of water, oil, and the pipe;  $C_V$  and  $C_{IV}$  are interface wave velocity and critical interface wave velocity, and  $k$  is the wave number.

The first item on the left of (1) is the viscous instability, depending on  $\tau_w$ ,  $\tau_o$ , and  $\tau_i$ ; the second item is the velocity

instability, related to velocity difference of the two phases; the third item is the gravity stability; the fourth item is interface tension stability, related to interface tension and interface wave number; the fifth is a correction term which stands for the influence of other interface instable factors.  $C_S$  is the correction coefficient.

In order to apply the stratified flow criterion, the in-situ water and oil velocities as well as cross-section parameters must be resolved firstly as in-situ water and oil velocities as well as cross-section parameters can be regarded as a function of liquid level,  $h_w$ .

Fairuzov [12] found that, while solving the steady state parameters of (4) for gas-liquid horizontal stratified flow, there may appear more than one solution, but, for oil-water stratified flow, there exists only one solution in the global scope. Therefore, in the current study, liquid level  $h_w$  is obtained by varying the parameter from 0 to  $D$ .

**2.2.2. Transition of Stratified Flow for High Viscosity Ratio.** In derivation of the neutral stability equation of stratified liquid-liquid flow, Brauner [13] found that the lower fluid of stratified flow is sometimes much faster, so the velocity of the upper phase may be neglected in neutral stability condition. Such an extreme situation may be of practical relevance, for example, in the transportation of high viscosity oil-water system. Ignoring the time and space variations in the upper fluid velocity yields

$$U_{sw}^2 \left( \frac{C_{rn}}{U_w} - 1 \right)^2 < \frac{16}{\pi^2} \frac{D \bar{A}_w^3}{\rho_b \bar{A}'_w} (\Delta \rho g + \sigma k^2) \quad (7)$$

$$C_{rn} = \frac{U_w (\partial F / \partial U_w) - (A_w / A'_w) (\partial F / \partial H)}{(\partial F / \partial U_w)}, \quad (8)$$

where  $C_{rn}$  is the real neutral stable wave velocity.

**2.3. Transition of Dispersed Flow.** Dispersed flow exists on the condition that the continuous phase is turbulent and the turbulent kinetic energy in the whole region is sufficiently intense to break the dispersed droplets into drops smaller than the critical diameter:

$$\begin{aligned} d_{\max} < d_{cr}, \quad \text{Re}_C \geq 2100, \\ 1.82 \text{Re}_C^{-0.7} < \frac{d_{crit}}{D} < 0.1, \end{aligned} \quad (9)$$

where  $D$  is the inner diameter of the pipe.

**2.3.1. Phase Inversion Point.** It is important to introduce the phase inversion point. Factors that influence phase inversion vary, including two-phase density, viscosity, interfacial tension, and other physical properties and operation conditions. At the same time, temperature, oil-water system formation, and mixture container wettability also play an impact. The inversion point aims to provide a probable range of distinction between continuous and disperse phase where Decarre and Fabre [14] model is introduced:

$$\varphi_{inv} = \left[ 1 + \left( \frac{\mu_o}{\mu_w} \right)^{1/6} \left( \frac{\rho_o}{\rho_w} \right)^{1/6} \right]^{-1}, \quad (10)$$

where  $\varphi_{inv}$  stands for water content of inverting point.

**2.3.2. Maximum Diameter.** In the turbulent field, the dispersed droplet is dominately affected by the turbulent inertia shear. Therefore, the maximum stable drop is the balance

between turbulent kinetic energy and droplet interface energy [6]:

$$\text{We}_{crit} = \frac{\tau d_{\max}}{\sigma}, \quad (11)$$

$$\frac{\rho_c u^2}{2} \approx \frac{4\sigma}{d_{\max}}. \quad (12)$$

In Chen's work [15], maximum drop size of dilute oil-water dispersed flow depends on the energy dissipation rate of the continuous phase and is directly proportional to  $(\varepsilon^{-0.4})$ . Meanwhile, by introducing Barnea's [16] idea of gas-liquid bubbly flow, the dispersed volume fraction is taken into consideration, which gives

$$d_{\max} = (1 + a\varphi^s) \left( \frac{\rho_c}{\rho_d} \right)^{0.33} \left( \frac{\sigma}{\rho_c} \right)^{0.6} \varepsilon^{-0.4}, \quad (13)$$

$$\varepsilon = \frac{2fU_m^3}{D}, \quad (14)$$

where  $\varepsilon$  is the energy dissipation rate,  $U_m$  is the mixture velocity,  $f$  is the friction coefficient, and the subscripts  $c$  and  $d$  stand for continuous phase and dispersed phase, respectively.

The higher the concentration of the dispersed phase, the more the energy needed by the continuous phase. Brauner [6] supposed that the incoming flow of the continuous phase should carry sufficient turbulent energy to disrupt the tendency to coalescence and to disperse the other phase. So the maximum droplet diameter can be expressed as

$$\begin{aligned} d_{\max} &= 2.22 C_H^{3/5} \left( \frac{\rho_c U_c^2 D}{\sigma} \right)^{-0.6} \\ &\times \left( \frac{\varepsilon_w}{1 - \varepsilon_w} \right)^{0.6} \left[ \frac{\rho_m}{\rho_c (1 - \varepsilon_w)} f \right]^{-0.4} D, \end{aligned} \quad (15)$$

where  $C_H$  is a constant,  $C_H = O(1)$ .  $\varepsilon_w$  is the water holdup.  $\rho_m$  is the density of mixture.

**2.3.3. Critical Diameter.** Due to the gravity or buoyancy effect, droplets will be separated from the mainstream, migrating to the wall. Considering the equilibrium of gravity and turbulent forces only, the droplet of critical dimension can be obtained through

$$\frac{d_{cb}}{D} = \frac{3\rho_c f U_c^2}{8|\rho_c - \rho_d| Dg}. \quad (16)$$

By assuming the buoyancy force is strong enough to overcome interfacial tension and break a dispersed drop, the critical size can be expressed through the balance between interfacial tension and buoyancy forces:

$$\frac{d_{c\sigma}}{D} = \left[ \frac{0.4\sigma}{|\rho_c - \rho_d| g D^2} \right]^{0.5}. \quad (17)$$

The practical critical diameter is the minimum between the two conditions including oil-water two-fluid system and operation condition:

$$\frac{d_{\text{crit}}}{D} = \text{Min} \left( \frac{d_{c\sigma}}{D}, \frac{d_{cb}}{D} \right). \quad (18)$$

**2.4. Transition of Core-Annular Flow.** Joseph et al. [17] used the hydrodynamic stability theory and concluded that a fully developed laminar-laminar core flow having the same density could stay stable when more viscous fluid is placed at the core and occupies most of the cross-section. Considering the stability of a viscous liquid flowing in the core, which was surrounded by a turbulent annulus, Bannwart [8] extended the previous model by using effective viscosity:

$$\mu_{o,\text{eff}} > \mu_{w,\text{eff}}, \quad \mu_o > \mu_w + 0.0005\rho_w U_{\text{sw}} D, \quad (19)$$

where  $\mu_{\text{eff}}$  is the effective viscosity which is the sum of the absolute molecular viscosity with the turbulent viscosity. To obtain the predicted transition boundary, it is necessary to find the critical  $U_{\text{sw}}$ . Through a two-fluid model, Brauner [13] proposed an expression for calculating the core diameter,  $D_c$ , as a function of  $U_{\text{sw}}$  and  $U_{\text{so}}$ , given the setup conditions and fluid properties. Considering a laminar core-turbulent annular flow, the expression that includes the influence of drop entrainment is given as

$$\frac{D_c}{D} = \left\{ \phi \times \left( \chi \phi \left[ \frac{\mu_o \rho_w}{\mu_w \rho_b} \left( \frac{\nu_w}{\nu_b} \right)^2 \frac{G(\phi)^{1.8}}{F(\phi)} \right]^{1/2} + \phi + \frac{G(\phi)}{F(\phi)} \right)^{-1} \right\}^{1/2}, \quad (20)$$

where  $\phi = U_{\text{so}}/U_{\text{sw}}$  and  $\chi$  is the Lockhart-Martinelli parameter which is fully based on superficial variables:

$$F(\phi) = \frac{\alpha_w \phi - (1 - \alpha_w)}{\phi(\alpha_w + \alpha_c - 1)}, \quad (21)$$

$$G(\phi) = \frac{\alpha_c - (1 - \alpha_c)\phi}{\alpha_w + \alpha_c - 1}, \quad (22)$$

where  $\alpha_w$  and  $\alpha_c$  stand for water volume fraction in the annular and oil volume fraction in the core. Once the oil superficial velocity  $U_{\text{so}}$  and  $H_o = H_o$  are fixed, the critical water velocity corresponding to the transition from core-annular flow is obtained.

### 3. Results and Discussion

**3.1. Model Diagram.** The oil-water flow pattern transition prediction is based on sound results of fluid properties, certain pipelines, and operation parameters. Thus the criterion can be integrated as given in Figure 1.

Figure 2(a) indicates how the diameter affects the stability of the stratified flow and dispersed flow. The diameters are 1, 2, and 3 inches, respectively. Viscosity ratio of oil to water ( $\bar{\mu}$ ) is 29.6 and interface tension is 0.036 N/m. Prediction indicates that the scope of stratified flow becomes broader when the diameter increases, but the scope of o/w and w/o dispersed flow becomes narrower. It can be concluded that, for oil-water two-phase flows, stratified flow pattern is more likely to form in a large-diameter pipe, as the effect of gravity stable term (1) is more obvious, which, to a certain extent, hinders the growth of interface wave and stabilizes the two-phase flow while, in smaller pipes, dispersed oil-water flow is relatively common, due to the fact that flow energy dissipation rate and turbulent kinetic energy are large though mixing velocity is unchanged. In addition, under the same diameter and internal phase concentration, the velocity needed to maintain a complete o/w dispersed flow pattern is bigger than that of a complete w/o dispersed flow pattern.

Figure 2(b) shows the influence of viscosity on stability of stratified and dispersed flow. The viscosities are 10, 50, and 80 mPa·s, respectively, while pipe diameter is 2 inch, and the interfacial tension is 0.036 N/m. Prediction indicates that the scope of stratified flow becomes narrower with larger oil viscosity while the scope of w/o dispersed flow becomes broader, and the sensitivity of o/w dispersed flow boundary is weaker.

The more viscous the oil, the stronger the influence of viscous instability and the smaller the superficial velocity needed to maintain the two phases stratified. From (9) and (12), dispersed viscosity plays no impact on maximum droplet diameter and critical droplet diameter. Therefore, for o/w dispersed flow, the model does not provide the trend of boundary changes with oil viscosity. This is due to the present model neglecting the effect of dispersed drop viscosity.

**3.2. Discussions.** Models are validated against available experimental data. Two cases of low viscosity oil (viscosity ratio of oil/aqueous phase <100) and two higher ones (viscosity ratio >100) are selected and compared. Comparisons with Oglesby [1] and Trallero [4] results are chosen as a representation of low viscosity.

Figure 3(a) is a comparison between predicted results and Trallero [4] experimental data (viscosity ratio 29.6), which indicates a good agreement between the predicted results of o/w and w/o transition boundaries and the experimental data. The scope of stratified flow with mixed interface (stratified wavy flow) in experiment is very large; the proper explanation is that the low viscosities of both phases make it easier for drop entrainment to take place. Actually this flow pattern is a transitional flow pattern from stratified flow to dispersed flow. The predicted transition boundary of stratified flow includes some stratified flows with mixed interface.

Figure 3(b) compares the predicted boundaries with the experimental data from Oglesby [1] (viscosity ratio 62.8). The prediction of w/o boundary fits well with experimental data. The prediction of o/w dispersed flow boundary is narrower than experimental results. This is partly because the sensitivity of the o/w dispersed flow criterion is weak (discussed above). Another explanation is that oil and water were

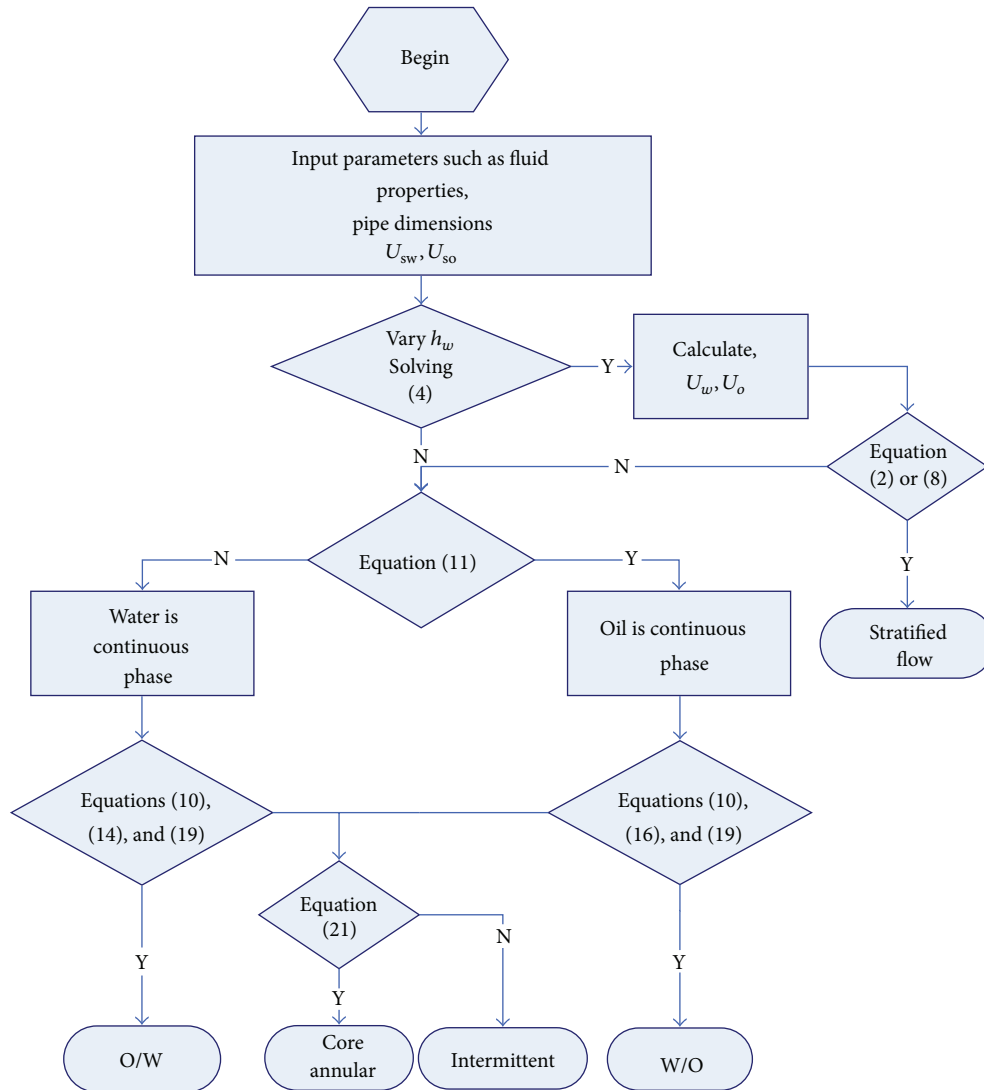


FIGURE 1: Diagram of flow pattern transition program.

mixed before entering the experimental system. The premix process makes o/w dispersed flow scope larger and stratified flow scope narrower. In addition, the predicted scope of stratified flow is narrow, and this is because the viscous instability becomes stronger.

Figure 4(a) is a comparison between predicted results and Yao and Gong [18] experimental data (viscosity ratio 325.4), while Figure 4(b) compares the predicted boundaries and experimental data from Wang et al. [19] (viscosity ratio 620). Core-annular, stratified, w/o dispersed, and intermittent flow are considered.

Both figures show that the stratified flow transition criterion fail to predict the accurate region. This may be caused by drop entrainment in viscous oil. And pure single phase in certain region of the pipe cross-section rarely exists. It should be noted that (7) does not take into account the drop entrainment in both phases, whose regime actually is Dw/o and Do/w. In addition, the core-annular/Do/w transition boundary agrees well with experimental data. This boundary is the

lowest oil holdup requirement, beyond which the oil core will be broken and finally dispersed in the water. As water drop is easily entrained into the viscous oil phase, the flow regime of Dw/o becomes dominant when phase inversion occurs. Phase inversion point can be perfectly regarded as a criterion for Dw/o transition boundary.

#### 4. Conclusions

In current work, theoretical models concerning systems with both low and high viscosity ratio are introduced for criterion of flow pattern transition of oil-water horizontal flow. The main flow regimes considered include water stratified flow, core-annular flow, w/o dispersed flow, o/w dispersed flow, and intermittent flow. A systematic work is carried out for flow pattern transition with oil viscosity varying in a wide range.

It is concluded that stability of the oil-water stratified flow in horizontal pipe is strongly related to oil viscosity, gravity,

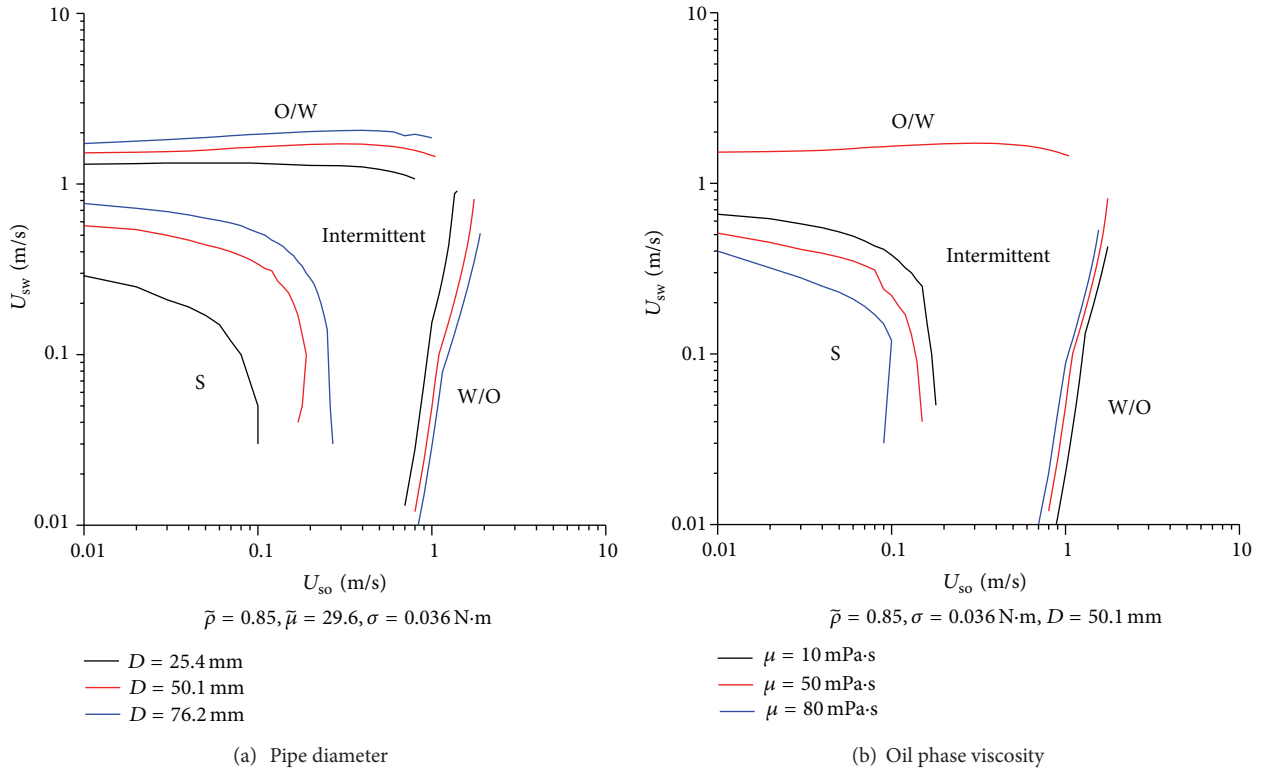


FIGURE 2: Prediction of flow pattern transition.

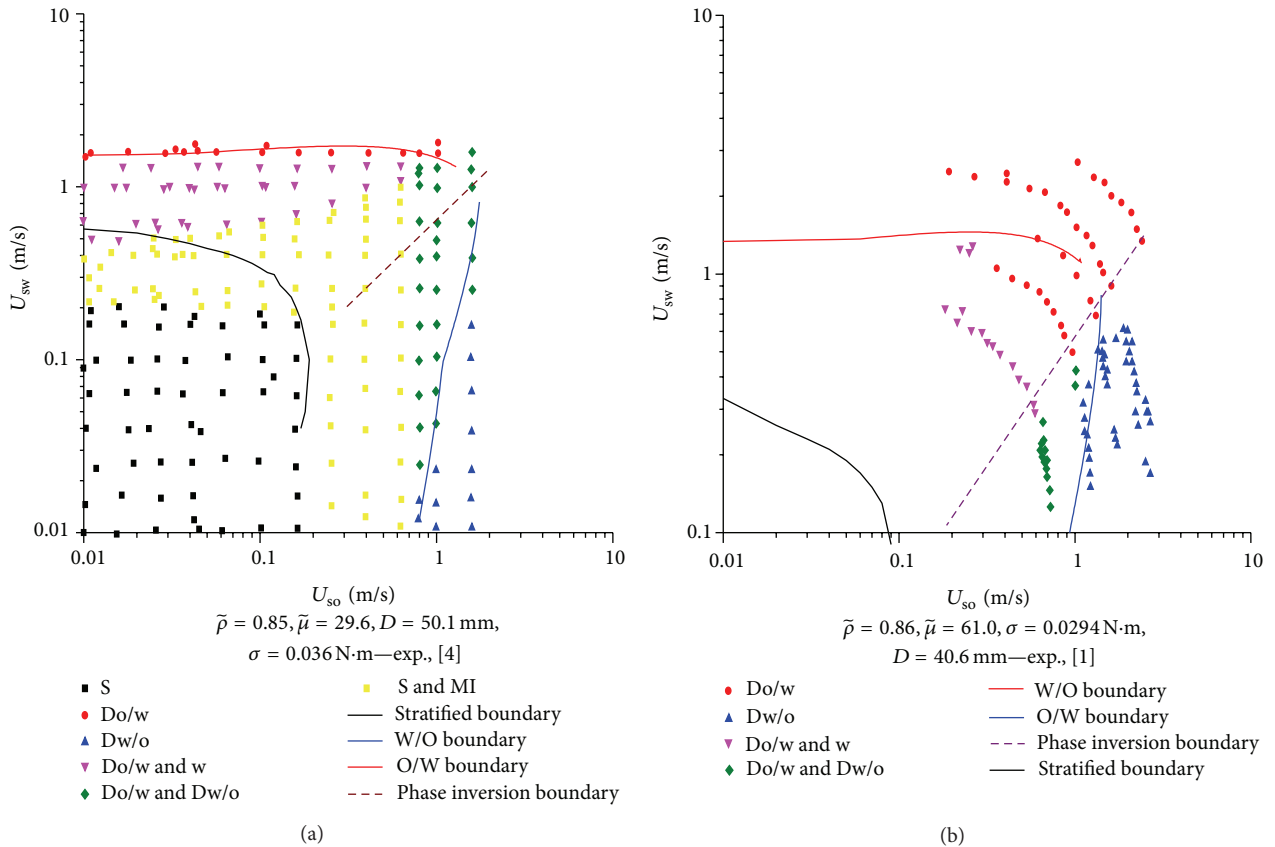


FIGURE 3: Comparison of experimental data (symbols) and prediction (lines) of oil-water two phase flow pattern transition.

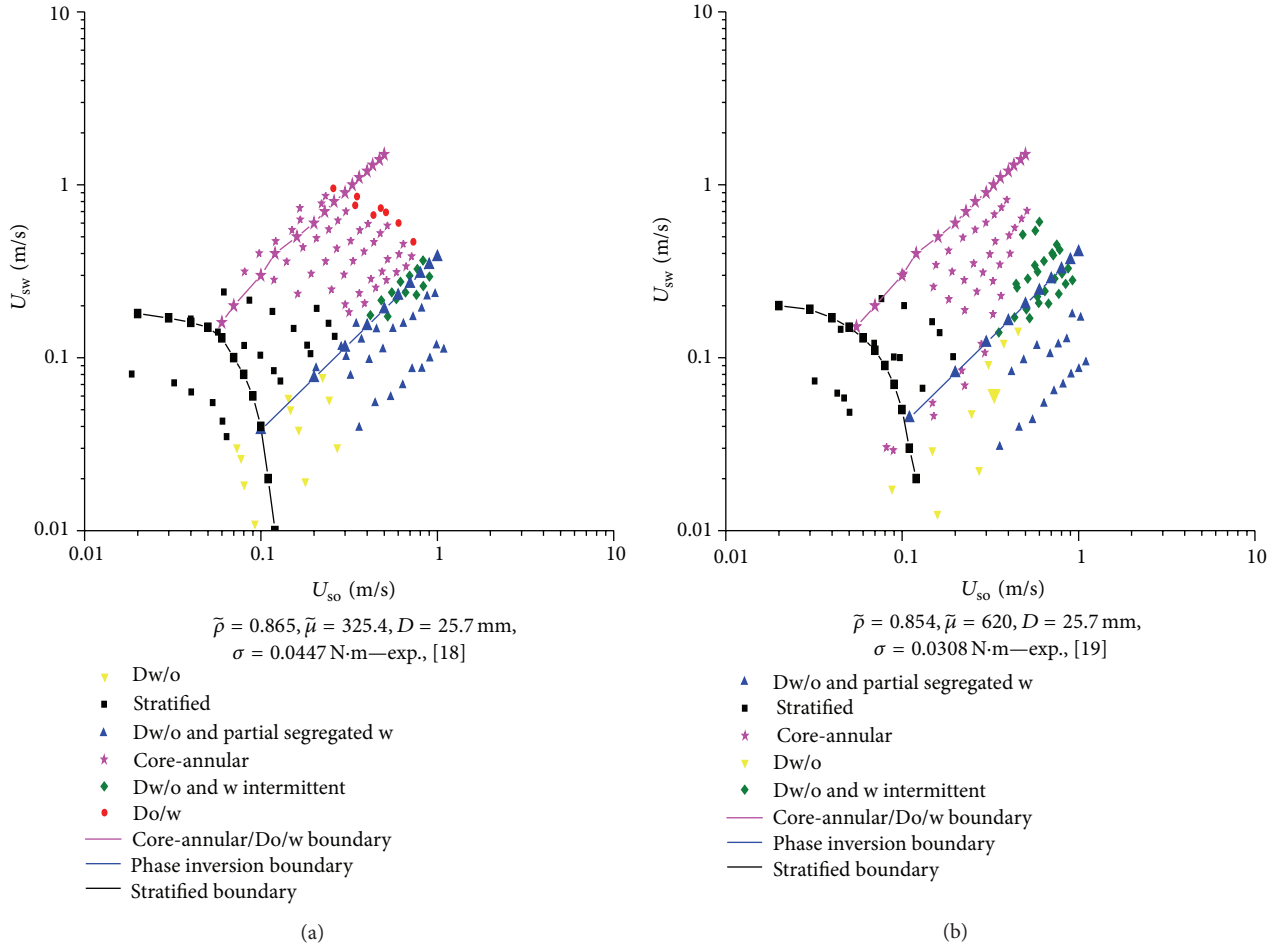


FIGURE 4: Comparison between prediction (lines) and experimental data (symbols) of oil-water flow.

and interfacial tension. For viscous oils, the influence of shear stress becomes much more obvious and can be characterised by ignoring the velocity of the viscous phase while, in dispersed flow, as the viscosity increases, oil droplets become harder to breakup, meaning that the ability of droplets to recover deformation becomes stronger. It is more difficult for o/w dispersed flow to be formed in viscosity oil. Additionally, core-annular flow tends to occur in a pipe where the two fluids have much different viscosities but relatively close densities. Drop entrainment occurs easily in core-annular flow and must be taken into consideration in the transition criterion.

## Acknowledgments

The authors wish to thank the National Natural Science Foundation of China (51104167), the program for New Century Excellent Talents in University (NCET-12-0969), the Foundation for the Author of National Excellent Doctoral Dissertation of PR China (201254), the National Science and Technology Specific Program of China (2011ZX05026-004-03), and the Foundation of China University of Petroleum-Beijing (BJ-2011-02) for the financial support for this work.

## References

- [1] K. D. Oglesby, *An experimental study on the effects of oil viscosity, mixture velocity and water fraction on horizontal oil water flow* [M.S. thesis], The University of Tulsa, Tulsa, Okla, USA, 1979.
- [2] S. Arirachakaran, K. D. Oglesby, M. Malinowsky, M. S. O. Shoham, and J. P. Brill, "An analysis of oil water flow phenomena in horizontal pipes," in *Proceedings of the SPE Production Operations Symposium*, 1989.
- [3] T. Al-Wahaibi and P. Angeli, "Transition between stratified and non-stratified horizontal oil-water flows. Part I: stability analysis," *Chemical Engineering Science*, vol. 62, no. 11, pp. 2915–2928, 2007.
- [4] J. L. Trallero, *Oil-water flow pattern in horizontal pipes* [Ph.D. thesis], The University of Tulsa, Tulsa, Okla, USA, 1995.
- [5] N. Brauner and D. M. Maron, "Two phase liquid-liquid stratified flow," *Physicochemical Hydrodynamics*, vol. 11, no. 4, pp. 487–506, 1989.
- [6] N. Brauner, "The prediction of dispersed flows boundaries in liquid-liquid and gas-liquid systems," *International Journal of Multiphase Flow*, vol. 27, no. 5, pp. 885–910, 2001.
- [7] A. Sharma, A. Al-Sarkhi, C. Sarica, and H. Zhang, "Modeling of oil-water flow using energy minimization concept," *International Journal of Multiphase Flow*, vol. 37, no. 4, pp. 326–335, 2011.

- [8] A. C. Bannwart, "Modeling aspects of oil-water core-annular flows," *Journal of Petroleum Science and Engineering*, vol. 32, no. 2-4, pp. 127-143, 2001.
- [9] B. Grassi, D. Strazza, and P. Poesio, "Experimental validation of theoretical models in two-phase high-viscosity ratio liquid-liquid flows in horizontal and slightly inclined pipes," *International Journal of Multiphase Flow*, vol. 34, no. 10, pp. 950-965, 2008.
- [10] O. M. H. Rodriguez, A. C. Bannwart, and C. H. M. de Carvalho, "Pressure loss in core-annular flow: modeling, experimental investigation and full-scale experiments," *Journal of Petroleum Science and Engineering*, vol. 65, no. 1-2, pp. 67-75, 2009.
- [11] N. Brauner and D. Moalem Maron, "Stability analysis of stratified liquid-liquid flow," *International Journal of Multiphase Flow*, vol. 18, no. 1, pp. 103-121, 1992.
- [12] Y. V. Fairuzov, "Stability analysis of stratified oil/water flow in inclined pipelines," *SPE Production and Facilities*, vol. 16, no. 1, pp. 14-21, 2001.
- [13] N. Brauner, "Two-phase liquid-liquid annular flow," *International Journal of Multiphase Flow*, vol. 17, no. 1, pp. 59-76, 1991.
- [14] S. Decarre and J. Fabre, "Phase inversion behavior for liquid-liquid dispersions," *Revue de l'Institut Francais du Petrole*, vol. 52, no. 4, pp. 415-424, 1997.
- [15] J. Chen, *Experimental study on horizontal oil water pipe flow [Ph.D. thesis]*, China University of Petroleum, Beijing, China, 2003.
- [16] D. Barnea, "Transition from annular flow and from dispersed bubble flow-unified models for the whole range of pipe inclinations," *International Journal of Multiphase Flow*, vol. 12, no. 5, pp. 733-744, 1986.
- [17] D. D. Joseph, M. Renardy, and Y. Renardy, "Instability of the flow of immiscible liquids with different viscosities in a pipe," *Journal of Fluid Mechanics*, vol. 141, pp. 309-317, 1984.
- [18] H. Y. Yao and J. Gong, "An Experimental investigation on flow patterns and pressure gradient of heavy oil-water flows in horizontal pipes," *Advances in Multiphase Flows*, vol. 2, pp. 359-361, 2004.
- [19] W. Wang, J. Gong, and P. Angeli, "Investigation on heavy crude-water two phase flow and related flow characteristics," *International Journal of Multiphase Flow*, vol. 37, no. 9, pp. 1156-1164, 2011.

## Research Article

# Multiobjective Optimization of Low-Specific-Speed Multistage Pumps by Using Matrix Analysis and CFD Method

Qiaorui Si, Shouqi Yuan, Jianping Yuan, Chuan Wang, and Weigang Lu

Research Center of Fluid Machinery Engineering and Technology, Jiangsu University, Zhen Jiang 212013, China

Correspondence should be addressed to Qiaorui Si; siqiaoruijsu@163.com

Received 16 June 2013; Revised 22 August 2013; Accepted 22 August 2013

Academic Editor: Mohamed Fathy El-Amin

Copyright © 2013 Qiaorui Si et al. This is an open access article distributed under the Creative Commons Attribution License, which permits unrestricted use, distribution, and reproduction in any medium, provided the original work is properly cited.

The implementation of energy-saving and emission-reduction techniques has become a worldwide consensus. Thus, special attention should be provided to the field of pump optimization. With the objective of focusing on multiobjective optimization problems in low-specific-speed pumps, 10 parameters were carefully selected in this study for an  $L_{27}(3^{10})$  orthogonal experiment. The parameters include the outlet width of the impeller blade, blade number, and inlet setting angle of the guide vane. The numerical calculation appropriate for forecasting the performance of multistage pumps, such as the head, efficiency, and shaft power, was analyzed. Results were obtained after calculating the two-stage flow field of the pump through computational fluid dynamics (CFD) methods. A matrix method was proposed to optimize the results of the orthographic experiment. The optimal plan was selected according to the weight of each factor. Calculated results indicate that the inlet setting angle of the guide vane influences efficiency significantly and that the outlet angle of blades has an effect on the head and shaft power. A prototype was produced with the optimal plan for testing. The efficiency rating of the prototype reached 58.61%; maximum shaft power was within the design requirements, which verifies that the proposed method is feasible for pump optimization.

## 1. Introduction

Pumps are widely utilized in various fields of the national economy [1]. Where there is water, there are pumps. Low-specific-speed centrifugal pumps are commonly employed in sewage treatment and well pumping because of their small flow and high head. They consume large amounts of energy and have a potential for energy saving. Low efficiency and overload tendency in long-term large-flow operations are the two obstacles in designing such pumps; the impeller diameter of low-specific-speed centrifugal pumps is relatively large, and the flow channel is long and narrow, resulting in significant disc friction and hydraulic loss. Thus, the efficiency of low-specific-speed centrifugal pumps is relatively low; the shaft power curves of such pumps increase sharply. The greater flow method is usually adopted in the design of low-specific-speed pumps to enhance flow efficiency. Thus, the ratio of macroshaft power to designed power becomes much higher than that of common centrifugal pumps. A motor whose export pipeline has no valve burns out easily [2, 3]. Pumps are usually designed in multistages to increase the amount of pressure because of limitations imposed by costs

or diameter, such as the case of well pumps. Increasing the single-stage head may decrease the number of stages to save costs, energy, and materials. High efficiency in maintaining the head and low power are the two goals of multistage pump designs. Thus, the study on multitarget optimal pump designs is important in implementing energy saving and emission reduction.

Mathematical methods, such as neural networks, orthographic experiments, genetic algorithms, and grey theory, are often adopted in multitarget optimization design [4, 5]. An orthographic experiment design can optimize the experimental conditions to achieve the target with fewer experiments [6, 7]. It has been widely adopted in pump design. Shouqi et al. [8] employed an orthogonal table  $L_8(2^7)$  to thoroughly study the effect of impeller geometric parameters and the throat area on pump performance. He proposed a practical framework for a centrifugal pump without overload and its design method. Wang et al. [9] focused on the effect of main impeller geometric parameters on deep-geometric performance via orthographic experiments. Shen et al. [10] designed nine models of complex impeller centrifugal pumps with orthographic experiments and discovered the effect

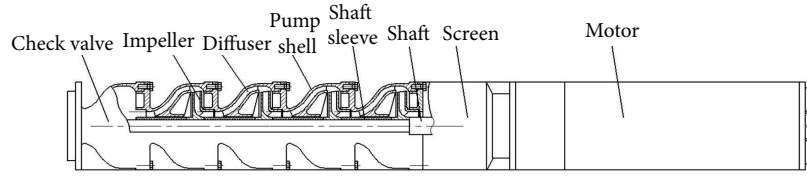


FIGURE 1: Model structure chart.

TABLE 1: Data structure of the multi-target orthogonal test.

First level	Experimental index											
Second level	Factor $A_1$			Factor $A_2$				Factor $A_l$				
Third level	$A_{11}$	...	$A_{1m-1}$	$A_{1m}$	$A_{21}$	...	$A_{2m-1}$	$A_{2m}$	$A_{l1}$	...	$A_{lm-1}$	$A_{lm}$

order of geometric parameters on pump performance. Zhou et al. [11] identified the key factors that affect the performance of guiding blades by studying conduit guiding blades and by conducting orthographic experiments and designing high-performance guiding blades. The orthogonal experiment method is therefore a multivariate and multilevel optimization method suitable for pump design. The studies mentioned above examined the influence of parameters on the impeller or guiding blades separately; however, the factors were not enough to completely reflect the effect of geometric parameters on the experiment. Furthermore, the multiobjective test was usually transformed into a single-objective test in the experimental analysis. Plans were then comprehensively selected through single-index analyses, including intuitive analysis and variance analysis. These methods neglect the significance and differences of indexes.

QS10-68, a typical multistage electric submersible pump (ESP), was regarded as an example in the present study. A method that combines orthogonal experimentation and numerical simulation was applied for optimization. A simple matrix method was also introduced to calculate the effect of factors on each index and to directly decide the factor order according to weight, which would perfectly solve the issue of selecting an optimal plan in an orthographic experiment design. The effect of 10 geometric parameters of the impeller and guiding vane on the multistage head, efficiency, and shaft power was also studied. Lastly, a set of optimum geometric parameters was obtained based on weight calculation. A prototype that employs the optimal plan was then tested for verification.

## 2. Pump Model

The structure of the multistage ESP is displayed in Figure 1. The figure shows a multistage centrifugal pump operating in a vertical position [12]. The pump shaft is connected to the protector by a mechanical coupling at the bottom of the pump. Fluids from the well enter the pump through an intake screen and are lifted by the pump stages. Produced liquids, after being subjected to great centrifugal forces caused by the high rotational speed of the impeller, lose their kinetic energy in the diffuser. Kinetic energy is converted to pressure energy in the diffuser. The design parameters for this pump are as follows: flow rate  $Q_d = 10 \text{ m}^3/\text{h}$ , total head  $H_d = 68 \text{ m}$ ,

speed  $n = 2850 \text{ r/min}$ , four stages, and the efficiency of the necessary electric motor is 4 kW.

## 3. Matrix Analysis Model and Experimental Scheme

In a multiobjective optimization problem, engineers adopt an orthographic experimental method as a solvent. The orthographic experimental method is a scientific method utilized to arrange and analyze multiple factor experiments by means of a table based on orthogonal principles. Through scientific arrangement and analysis of the result, a study can discover the ideal production conditions and techniques. However, problems, including large calculated amounts and confirming the weights unreasonably, exist in the multitarget orthogonal test method. A matrix analysis model was presented to solve this problem. In this model, a three-layer structure and the layer structure matrix of the orthogonal test are established first. The weight matrix of the test index is then calculated by multiplying the matrix of each layer. The weights of the factors and levels that affect the tests results are calculated. Finally, the optimal plan and the importance order of the factors that influence the test index values are determined according to the weights.

**3.1. Matrix Analysis Model.** An orthographic experiment was designed (ignoring the interaction for the first). The three-layer structural model based on data structure was established. The first layer in Table 1 is the investigation index, the second layer is the factor layer, and the last one is the level layer. The data of each layer determine the definition of the matrix as follows.

**Definition 1.** The following is the matrix of the experimental investigation index. The study order is  $K_{ij} = k_{ij}$ . The matrix is established on the conditions that  $l$  factors exist in the experiment, each factor has  $m$  levels,  $k_{ij}$  is the average index of factor  $A_i$  at  $j$  level, and the investigation index is good when it is high. A low investigation index is considered good when the study establishes a matrix supposing  $K_{ij} = 1/k_{ij}$ .

**Definition 2.** The matrix of the factor layer:  $T_i = 1/\sum_{j=1}^m K_{ij}$  to build (2) matrix.

**Definition 3.** The matrix of the level layer: the range of  $A_i$  in the orthographic experiment is set as  $s_i$ . The study order is  $S_i = s_i / \sum_{i=1}^l s_i$ . Equation (3) matrix is then established.

**Definition 4.** The weight matrix that may affect the test index:  $\omega^T = MTS$ .

$$M = \begin{bmatrix} K_{11} & 0 & 0 & \cdots & 0 \\ K_{12} & 0 & 0 & \cdots & 0 \\ \cdots & \cdots & \cdots & \cdots & \cdots \\ K_{1m} & 0 & 0 & \cdots & 0 \\ 0 & K_{21} & 0 & \cdots & 0 \\ 0 & K_{22} & 0 & \cdots & 0 \\ \cdots & \cdots & \cdots & \cdots & \cdots \\ 0 & K_{2m} & \cdots & \cdots & \cdots \\ \cdots & \cdots & \cdots & \cdots & \cdots \\ 0 & 0 & 0 & \cdots & K_{l1} \\ 0 & 0 & 0 & \cdots & K_{l2} \\ \cdots & \cdots & \cdots & \cdots & \cdots \\ 0 & 0 & 0 & \cdots & K_{lm} \end{bmatrix}, \quad (1)$$

$$T = \begin{bmatrix} T_1 & 0 & 0 & 0 \\ 0 & T_2 & 0 & 0 \\ \cdots & \cdots & \cdots & \cdots \\ 0 & 0 & 0 & T_l \end{bmatrix}, \quad (2)$$

$$S = \begin{bmatrix} S_1 \\ S_2 \\ \cdots \\ S_l \end{bmatrix}, \quad (3)$$

$$\omega^T = [\omega_1, \omega_2, \dots, \omega_m]. \quad (4)$$

In the matrix above mentioned,  $\omega_1 = K_{11}T_1S_1, K_{11}T_1$  refers to the ratio of  $A_1$ 's first level index to the sum of all  $A_1$ 's level indexes.  $S_1$  is the ratio of  $A_1$ 's range to the sum of all ranges. The product of these two data reflects the effect of the first level of  $A_1$  on the index and range of  $A_1$ . The other factors and levels are identical. The weight of each factor and level was obtained after calculation. The optimal plan and the factor order in the index were established based on the weight value.

**3.2. Experimental Scheme.** According to Euler equations, theoretical head  $H_t$  is

$$H_t = \frac{u_2 v_{u2} - u_1 v_{u1}}{g} = \frac{u_2}{g} \left( u_2 h_0 - \frac{Q_t}{F_2 \tan \beta_2} \right), \quad (5)$$

where  $u_1$  (m/s) is peripheral speed at the inlet;  $v_{u1}$  is the peripheral velocity component of the blade inlet;  $v_{u1} = 0$  in the straight cone suction chamber;  $u_2$  (m/s) refers to the circular velocity at the impeller outlet;  $g$  ( $m^2/s$ ) is acceleration because of gravity;  $h_0 = 1 - (\pi/z)$  is the stodal slip coefficient;  $z$  represents blade numbers;  $Q_t$  ( $m^3/h$ ) is the theoretical flow;  $F_2 = \pi D_2 b_2 \psi_2$  is the cross-section area of the impeller outer;  $\psi_2$  is the blade expelling coefficient;  $b_2$  (m) is the width of the blade outlet;  $\beta_2$  is the blade outlet angle.  $P'$ , the hydraulic power input, can be deduced by the following equation:

$$P' = \rho g H_t Q_t = \rho u_2^2 Q_t \left( h_0 - \frac{Q_t}{u_2 F_2 \tan \beta_2} \right). \quad (6)$$

TABLE 2: Factor level table.

Level	Factor									
	A	B	C	D	E	F	G	H	I	J
1	122	8	10	6	2	88	34	5	0	15
2	124	9	15	7	3	89	36	10	5	20
3	126	10	20	8	4	90	38	15	10	25

$A-d_{2min}/mm, B-b_2/mm, C-\beta_2/(\circ), D-z, E-S_2/mm, F-\alpha_2/(\circ), G-d_1/mm, H-\Delta\beta_1/(\circ), I-\gamma_3/(\circ), J-\beta_3/(\circ)$ .

In (6),  $\rho$  ( $kg/m^3$ ) refers to water density. The equation shows that both theoretical head and hydraulic input power are determined by the impeller. However, rolling flow causes  $P_m$ , additional shaft power, as it enters the guiding blade channel. Hence, shaft power  $P = P' + P_m$  and pump efficiency  $\eta = P'/P$ . Pump shaft power and efficiency are determined by both the impeller and the guide vane in hydraulics.

The following are the main geometric parameters of the model: width of the blade outlet  $b_2$ , suction diameter of impeller  $d_1$ , inclination of the back cover board  $\alpha_2$ , inlet attack angle  $\Delta\beta_1$ , inlet angle in axial plane  $\gamma_3$ , blade outlet angle  $\beta_2$ , blade number  $z$ , outer diameter of the back cover  $d_{2min}$ , blade thickness  $S_2$ , inlet angle of the guide vane  $\beta_3$ , outlet angle of the guide vane  $\alpha_3$ , import width of the guide vane  $b_3$ , blade number of the guide vane  $z_1$ , axial length of the guide vane  $\gamma_3$ , inlet diameter of the guide vane  $D_2$ , and outlet diameter of the guide vane  $D_1$ .  $\alpha_3$  is equal to  $90^\circ$  to eliminate the rotation component. The last five factors were determined by the basic geometric parameters of the impeller. The first 10 geometric parameters were selected as testing factors.

According to the specific speed equation,

$$n_s = \frac{3.65n\sqrt{Q}}{H^{3/4}}, \quad (7)$$

where  $Q$  refers to the flow and  $H$  refers to the head of the pump. The design-specific speed of the pump is low, namely, 65.6, because it is lower than 80. Relative parameters can be obtained with the velocity-coefficient method under structure demand; these factors are shown in Table 2. Three levels were selected in each factor. The experimental scheme, shown in Table 3, is based on the  $L_{27}(3^{10})$  orthogonal table. In the 27 group tests, different numerals appear at the same frequency in any column, and any two-digit number appears equivalent in any row. After deciding the experimental plan, tests were implemented in numerical order without any arbitrary changes.

## 4. Numerical Simulation

In traditional orthogonal experiments, research procedures involve manufacturing prototypes, performance tests, and results analyses. However, creating prototypes from the 27 groups of impellers and guide vanes would be a waste of time and money; moreover, a large number of prototype tests would inevitably cause significant manufacturing and test errors. The prediction of pump performance has become

TABLE 3: Orthogonal test schemes.

Test number	A/mm	B/mm	C/(°)	D/	E/mm	F/(°)	G/mm	H/(°)	I/(°)	J/(°)
1	122	8	10	6	2	88	34	5	0	15
2	122	8	10	6	3	89	36	10	5	20
3	122	8	10	6	4	90	38	15	10	25
4	122	9	15	7	2	88	34	10	5	20
5	122	9	15	7	3	89	36	15	10	25
6	122	9	15	7	4	90	38	5	0	15
7	122	10	20	8	2	88	34	15	10	25
8	122	10	20	8	3	89	36	5	0	15
9	122	10	20	8	4	90	38	10	5	20
10	124	8	15	8	2	89	38	5	5	25
11	124	8	15	8	3	90	34	10	10	15
12	124	8	15	8	4	88	36	15	0	20
13	124	9	20	6	2	89	38	10	10	15
14	124	9	20	6	3	90	34	15	0	20
15	124	9	20	6	4	88	36	5	5	25
16	124	10	10	7	2	89	38	15	0	20
17	124	10	10	7	3	90	34	5	5	25
18	124	10	10	7	4	88	36	10	10	15
19	126	8	20	7	2	90	36	5	10	20
20	126	8	20	7	3	88	38	10	0	25
21	126	8	20	7	4	89	34	15	5	15
22	126	9	10	8	2	90	36	10	0	25
23	126	9	10	8	3	88	38	15	5	15
24	126	9	10	8	4	89	34	5	10	20
25	126	10	15	6	2	90	36	15	5	15
26	126	10	15	6	3	88	38	5	10	20
27	126	10	15	6	4	89	34	10	0	25

possible in engineering applications owing to the rapid development of computational fluid dynamics (CFD) [13]. Reasonable CFD calculations reflect the actual internal flow of the pump and accurately predict the pump head performance, efficiency, shaft power, and so forth at specific conditions [14, 15]. Therefore, the use of CFD technology is more feasible than the use of a prototype in pump design optimization and in the establishment of a preliminary forecast of pump performance.

*4.1. Governing Equations and Boundary Conditions.* The flow field information of pumps can be described by Navier-Stokes equations. A numerical simulation is performed to solve the following governing equations [16]:

$$\begin{aligned} \frac{\partial \rho}{\partial t} + \frac{\partial}{\partial x_i} (\rho u_i) &= 0, \\ \frac{\partial (\rho u_i)}{\partial t} + \frac{\partial (\rho u_i u_j)}{\partial x_j} &= -\frac{\partial p}{\partial x_i} + \frac{\partial e_{ij}}{\partial x_j}. \end{aligned} \quad (8)$$

Fluent 6.2 was utilized in this study. The 3D unsteady flow of centrifugal pumps was calculated based on Reynolds-averaged equations that resemble the standard renormalization group  $k-\varepsilon$  turbulence model. Velocity, turbulent kinetic

TABLE 4: Head at design flow contrast of different stages (m).

Stage	1st head	2nd head	3rd head	4th head	Total head
1	16.93				16.56
2	16.89	16.53			32.17
3	16.87	16.62	16.77		48.87
4	16.79	16.60	16.92	16.84	64.50

energy, and eddy viscosity coefficients were provided as a first-order upwind scheme. The velocity at the inlet and free flow at the outlet were selected with boundary conditions. A solid wall was set as the no-slip condition, and a smooth wall condition was employed as the near-wall function. The convergence precision was set to  $10^{-5}$ .

*4.2. Computational Domain.* The flow domain of the submersible pump is composed of the inlet, a multistage distorting impeller, a multistage space diffuser, and an outlet. Its flow pattern is more complex than that of a single-stage pump. A rotational flow exists at the impeller inlet, but the first stage and flow in the channel are similar. Demands on computer performance would be made if all stages are considered in the calculation. Therefore, selecting only the appropriate stages is important. Four kinds of computational domains in different

TABLE 5: Shaft power at design flow contrast of different stages (kW).

Stage	1st Shaft power	2nd Shaft power	3rd Shaft power	4th Shaft power	Total shaft power
1	0.853				0.853
2	0.855	0.856			1.711
3	0.857	0.854	0.851		2.562
4	0.851	0.854	0.858	0.861	3.424

TABLE 6: Efficiency at design flow contrast of different stages (%).

Stage	1st efficiency	2nd efficiency	3rd efficiency	4th efficiency	Total efficiency
1	59.25				58.38
2	59.34	61.77			60.78
3	59.47	61.73	61.79		60.81
4	59.41	61.82	61.93	61.87	60.85

stages are simulated for scheme 1. The relevant results are presented in Tables 4, 5, and 6.

Tables 4 and 5 indicate that the head and shaft power of each stage in the pump are very similar that the two-stage values can be regarded as the corresponding values of the pump. Table 6 shows that only a few differences exist in terms of efficiency; however, many differences were noted between the first stage and other stages after the second. No changes were observed after stage two. In summary, it is appropriate to select two full-flow models to analyze pump performance. Similarly, the use of the head and shaft power of two stages as well as the efficiency of stage two to predict performance is also feasible. The computational domain composed of the inlet, the distorting impeller of two stages, the space diffusers, and the outlet is shown in Figure 2. The first pump water chamber is not shown in the figure.

**4.3. Model Meshing.** The quantity and quality of the grid are two important factors that affect computation accuracy and duration. The unstructured tetrahedral mesh provided by GAMBIT, the professional software for grid generation, was utilized on the entire basin. The mesh has strong adaptability. Encryption and nonequidistance were processed in the near-wall region. Five different mesh sizes were selected to determine the appropriate number of grids and to conduct a grid-independent analysis. Scheme 1 at  $Q_d$  was regarded as an example. The calculated results are shown in Table 7.

Table 7 shows that the difference between pump head does not exceed 0.5%, efficiency does not exceed 0.06%, and shaft power does not exceed 0.3% when the mesh size is smaller than 2.0 mm.  $y^+$ , which was utilized to examine the closest node to the surface, is not greater than 150. Thus, the criteria of standard renormalization group  $k - \epsilon$  turbulence model calculation were met. Therefore, numerical simulation grid size of 2.0 mm was selected after considering computation accuracy and duration. The grid view of computational domain is shown in Figure 3.

One of the convergence plots is shown in Figure 4; this plot can be used to justify the ultimate choice of grid

TABLE 7: Results of different mesh sizes.

Parameter	Mesh size/mm				
	1.6	1.8	2.0	2.2	2.4
Grids/ $10^4$	184	129	91	69.4	53.4
Head/m	32.58	32.33	32.17	32.03	31.87
Efficiency $\eta$ /%	61.82	61.81	61.77	61.46	60.53
Shaft Power $P$ /kW	1.716	1.706	1.711	1.694	1.686

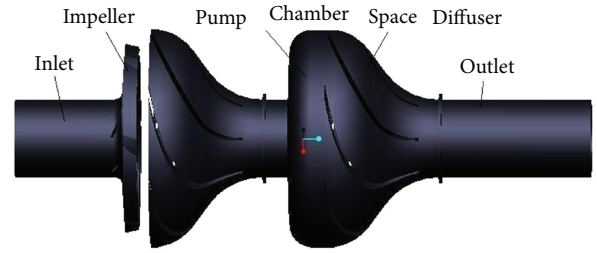


FIGURE 2: Schematic of the computational domain.

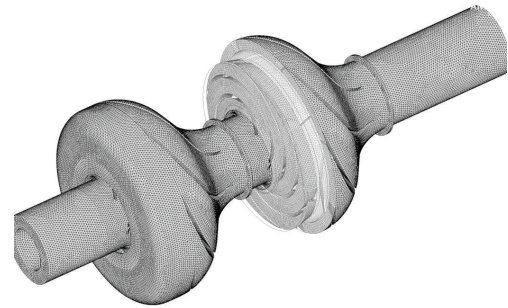


FIGURE 3: Grid view of computational domain.

for the analysis. According to Figure 4, all the convergence precisions reached  $10^{-5}$ , which satisfied the requirement of the calculation.

## 5. Results Analysis

Given that the shaft power of low-specific-speed centrifugal pumps increases rapidly with the enlargement of flow, the shaft power at  $1.5Q_d$  was selected as the monitoring value for overload judging. An electric pump works safely at the range of  $0.7Q_d$  to  $1.3Q_d$ . If the shaft power at  $1.5Q_d$  is less than the motor power, then the pump will not experience an overload. A total of 27 numerical simulations were performed. The results of two-stage head  $H$  under the rated condition, shaft power  $P$  at  $1.5Q_d$ , and efficiency  $\eta$  of stage two under the rated condition are shown in Table 8.

**5.1. Visual Analysis.** Orthographic experimental data were analyzed. With the first column of rated point head index  $H$  as an example,

$$\begin{aligned}
 k_{1A} &= (32.17 + 32.81 + 30.25 + 38.08 \\
 &\quad + 34.97 + 35.22 + 35.94 + 36.78 + 38.56) \\
 &\quad \times (9)^{-1} = 34.977,
 \end{aligned}$$



TABLE 9: Range analysis of orthogonal test data.

Index	A	B	C	D	E	F	G	H	I	J
<i>H/m</i>										
$k_1$	34.977	34.401	33.862	34.625	35.784	35.473	35.281	35.366	35.412	35.087
$k_2$	35.627	35.355	35.831	36.045	35.295	35.252	35.447	35.656	35.434	36.535
$k_3$	35.513	36.362	36.424	35.447	35.038	35.393	35.389	35.096	35.271	34.495
$s$	0.650	1.961	2.562	1.420	0.746	0.221	0.167	0.560	0.163	2.040
<i><math>\eta/\%</math></i>										
$k_1$	60.795	60.935	61.059	61.116	60.630	60.739	60.285	60.530	60.678	60.600
$k_2$	60.661	60.838	60.754	60.965	60.747	60.755	60.920	60.897	60.713	61.795
$k_3$	60.571	60.254	60.214	59.946	60.650	60.532	60.822	60.601	60.636	59.632
$s$	0.224	0.681	0.844	1.170	0.117	0.223	0.635	0.367	0.077	2.163
<i>P/kW</i>										
$k_1$	1.963	1.927	1.855	1.936	2.033	2.027	2.009	2.015	2.017	2.018
$k_2$	2.033	2.007	2.045	2.053	2.017	2.000	2.008	2.022	2.031	2.025
$k_3$	2.038	2.101	2.134	2.045	1.985	2.007	2.017	1.998	1.987	1.992
$s$	0.075	0.174	0.279	0.116	0.048	0.027	0.009	0.024	0.043	0.033

$$\omega = \frac{(\omega_1 + \omega_2 + \omega_3)}{3} = \begin{pmatrix} 0.0204 \\ 0.0208 \\ 0.0207 \\ 0.0606 \\ 0.0623 \\ 0.0641 \\ 0.0779 \\ 0.0825 \\ 0.0838 \\ 0.0442 \\ 0.046 \\ 0.0452 \\ 0.024 \\ 0.0237 \\ 0.0235 \\ 0.007 \\ 0.007 \\ 0.007 \\ 0.0053 \\ 0.0053 \\ 0.0053 \\ 0.0178 \\ 0.018 \\ 0.0177 \\ 0.0052 \\ 0.0052 \\ 0.0052 \\ 0.0643 \\ 0.0669 \\ 0.0632 \end{pmatrix} + \begin{pmatrix} 0.0115 \\ 0.0115 \\ 0.0115 \\ 0.0351 \\ 0.035 \\ 0.0347 \\ 0.0436 \\ 0.0433 \\ 0.043 \\ 0.0604 \\ 0.0603 \\ 0.0593 \\ 0.006 \\ 0.006 \\ 0.006 \\ 0.0115 \\ 0.0115 \\ 0.0114 \\ 0.0323 \\ 0.0327 \\ 0.0326 \\ 0.0188 \\ 0.0189 \\ 0.0188 \\ 0.0039 \\ 0.0039 \\ 0.0039 \\ 0.1107 \\ 0.1129 \\ 0.109 \end{pmatrix} + \begin{pmatrix} 0.0151 \\ 0.0146 \\ 0.0146 \\ 0.035 \\ 0.0336 \\ 0.0321 \\ 0.0573 \\ 0.052 \\ 0.0498 \\ 0.0238 \\ 0.0224 \\ 0.0225 \\ 0.0097 \\ 0.0097 \\ 0.0099 \\ 0.0053 \\ 0.0054 \\ 0.0054 \\ 0.0018 \\ 0.0018 \\ 0.0018 \\ 0.0048 \\ 0.0048 \\ 0.0048 \\ 0.0087 \\ 0.0087 \\ 0.0088 \\ 0.0066 \\ 0.0066 \\ 0.0067 \end{pmatrix} \times (3)^{-1} = \begin{pmatrix} 0.015667 \\ 0.015633 \\ 0.0156 \\ 0.043567 \\ 0.043633 \\ 0.043623 \\ 0.0596 \\ 0.059267 \\ 0.058867 \\ 0.0428 \\ 0.0429 \\ 0.042333 \\ 0.013233 \\ 0.013132 \\ 0.013133 \\ 0.007933 \\ 0.007967 \\ 0.007933 \\ 0.013133 \\ 0.013267 \\ 0.013233 \\ 0.0138 \\ 0.0139 \\ 0.013767 \\ 0.005933 \\ 0.005932 \\ 0.005967 \\ 0.060533 \\ 0.062133 \\ 0.059633 \end{pmatrix} = \begin{pmatrix} A_1 \\ A_2 \\ A_3 \\ B_1 \\ B_2 \\ B_3 \\ C_1 \\ C_2 \\ C_3 \\ D_1 \\ D_2 \\ D_3 \\ E_1 \\ E_2 \\ E_3 \\ F_1 \\ F_2 \\ F_3 \\ G_1 \\ G_2 \\ G_3 \\ H_1 \\ H_2 \\ H_3 \\ I_1 \\ I_2 \\ I_3 \\ J_1 \\ J_2 \\ J_3 \end{pmatrix} \quad (14)$$

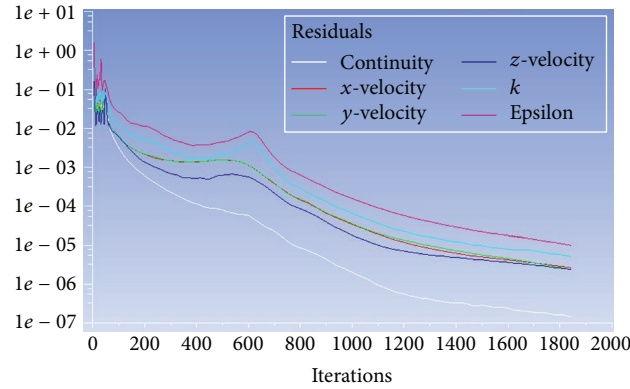


FIGURE 4: Convergence plots of the CFD calculation.

The calculations provide the weight of the result of each factor with three levels. Hence, the optimal plan for orthographic experiments is determined quickly. The optimal plan is  $A_1B_2C_2D_2E_1F_2G_2H_2I_3J_2$ , and the importance order of the index is  $JDCGHEABFI$ .

## 6. Experimental Verification

The optimal model,  $J_2D_2C_2G_2H_2E_1A_1B_2F_2I_3$ , was prototyped for the experiment to test the optimized programs. The geometric parameters of the hydraulic model were as follows: width of the blade outlet  $b_2 = 9$  mm, inclination of back cover board  $\alpha_2 = 89^\circ$ , inlet attack angle  $\Delta\beta_1 = 10^\circ$ , inlet angle in axial plane  $\gamma_3 = 10^\circ$ , blade outlet angle  $\beta_2 = 15^\circ$ , blades number  $z = 7$ , outer diameter of back cover  $d_{2\min} = 122$  mm, blade thickness  $S_2 = 2$  mm, inlet angle of guide vane  $\beta_3 = 20^\circ$ , and axial length of the guide vane  $\gamma_3 = 10^\circ$ . The test was performed in accordance with the national standards GB/T 12785-2002 of China. Figure 5 presents the results of the experiment and the entire flow field simulation.

Comparison of the simulation and experimental results indicates that the simulated head and efficiency are slightly higher than those of the experiment; however, the simulated power is slightly lower. Error analysis indicates the following: (1) the numerical simulation did not consider the loss of leakage at the oral ring and between stages; (2) small differences exist because of limitations imposed by casting accuracy, casting errors, casting model (particularly the impeller), and simulated model; these differences can cause disparity between experimental and simulated values. However, the error is less than 5%, and both experimental and simulated values exhibit similar trends when the flow changes. Hence, the simulation methods employed in this study can meet the demand of practical usage in programs for design optimization.

The efficiency of QS10-68/4 based on the national standard of China is 51%. After optimization, the pump's rated head is 68.9 m and rated efficiency is 58.61%, which is approximately 7% higher than the national standard. The maximum shaft power is 3.83 kW. The performance of nonoverload also

meets the demand, which is 4 kW. All of the above data indicate that optimization was successful.

## 7. Conclusions

The influence of 10 factors and three levels on the head, efficiency, and shaft power was analyzed by conducting 27 orthographic experiments through numerical simulation. Weight matrix analysis was then performed to determine the optimal model. The principal conclusions drawn from this research are as follows.

- (1) The simulation results indicate that the inlet setting angle of the guide vane  $\beta_3$  significantly affects the efficiency and that the outlet angle of blades  $\beta_2$  has a significant effect on the head and shaft power.
- (2) The importance order of the index for the head is  $\beta_2\beta_3b_2zS_2d_{2\min}\Delta\beta_1\alpha_2d_1\gamma_3$ , and the geometric parameters of optimal plan are as follows:  $d_{2\min} = 124$  mm,  $b_2 = 10$  mm,  $\beta_2 = 20^\circ$ ,  $z = 7$ ,  $S_2 = 2$  mm,  $\alpha_2 = 88^\circ$ ,  $d_1 = 36$  mm,  $\Delta\beta_1 = 10^\circ$ ,  $\gamma_3 = 5^\circ$ , and  $\beta_3 = 20^\circ$ . The importance order of the index for efficiency is  $\beta_3z\beta_2b_2d_1\Delta\beta_1d_{2\min}\alpha_2S_2\gamma_3$ , and the geometric parameters of optimal plan are as follows:  $d_{2\min} = 122$  mm,  $b_2 = 8$  mm,  $\beta_2 = 10^\circ$ ,  $z = 6$ ,  $S_2 = 3$  mm,  $\alpha_2 = 89^\circ$ ,  $d_1 = 36$  mm,  $\Delta\beta_1 = 10^\circ$ ,  $\gamma_3 = 5^\circ$ , and  $\beta_3 = 20^\circ$ . For shaft power, the importance order of the index is  $\beta_2b_2zd_{2\min}S_2\gamma_3\beta_3\alpha_2\Delta\beta_1d_1$ , and the geometric parameters of optimal plan are as follows:  $d_{2\min} = 122$  mm,  $b_2 = 8$  mm,  $\beta_2 = 10^\circ$ ,  $z = 6$ ,  $S_2 = 4$  mm,  $\alpha_2 = 89^\circ$ ,  $d_1 = 36$  mm,  $\Delta\beta_1 = 15^\circ$ ,  $\gamma_3 = 10^\circ$ , and  $\beta_3 = 25^\circ$ .
- (3) By performing weight matrix analysis, optimal model was obtained based on the influence of factors and levels on the head, efficiency, and shaft power. The geometric parameters of the hydraulic model were as follows:  $b_2 = 9$  mm,  $\alpha_2 = 89^\circ$ ,  $\Delta\beta_1 = 10^\circ$ ,  $\gamma_3 = 10^\circ$ ,  $\beta_2 = 15^\circ$ ,  $z = 7$ ,  $d_{2\min} = 122$  mm,  $S_2 = 2$  mm,  $\beta_3 = 20^\circ$ , and  $\gamma_3 = 10^\circ$ . The performance of the prototype in the test indicates that efficiency at the rated point is 7% higher than the national standard

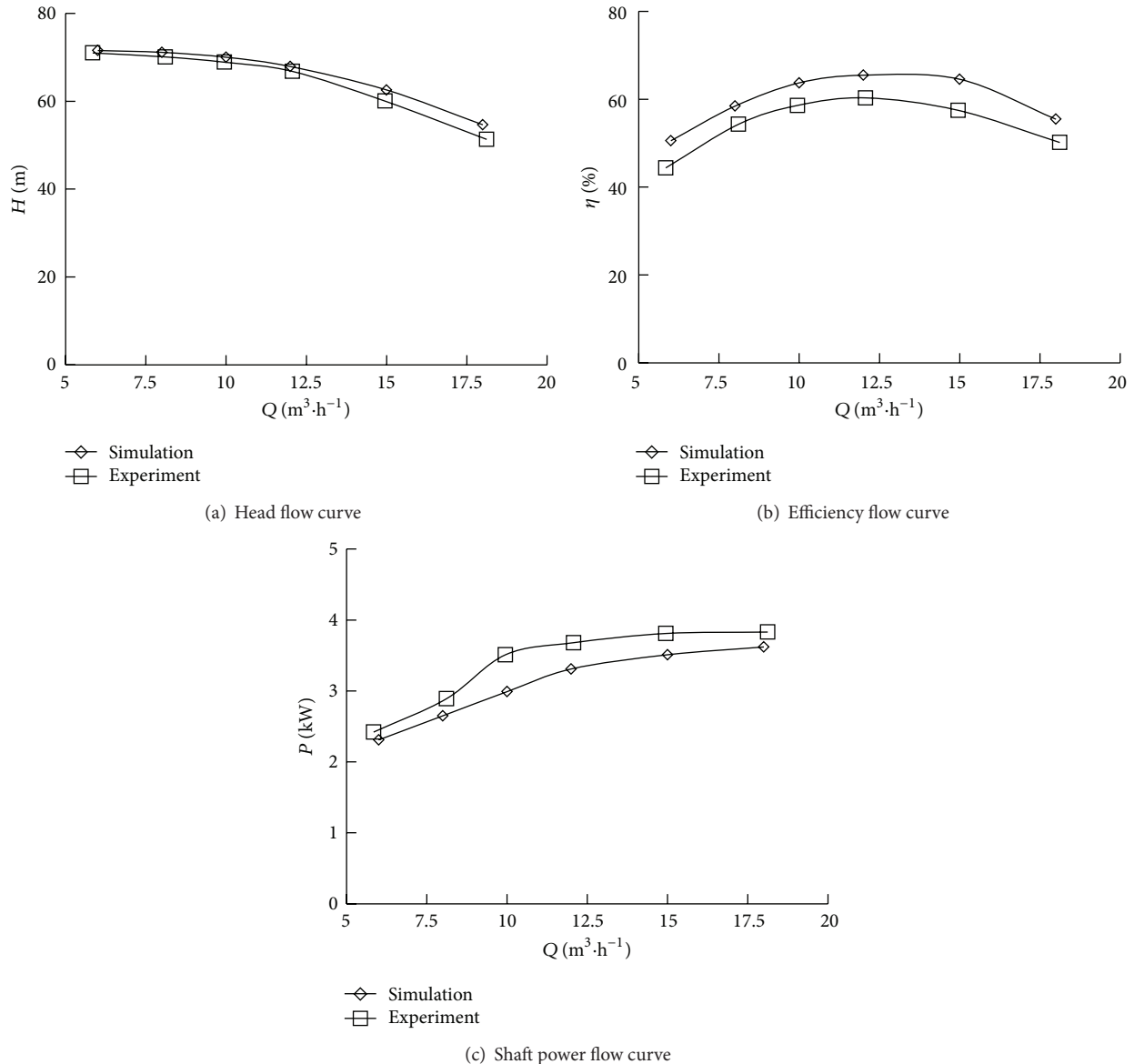


FIGURE 5: Contrast diagram between the simulation and experiment.

of China. This result verifies the potential use of the orthographic design combined matrix analysis with numerical simulation in pump optimization.

- (4) The changes in the head, efficiency, and shaft power determined from the simulation are in accordance with the test results. The error between numerical simulation and test result is less than 5% in the rated flow, which further verifies the possibility of forecasting the performance of multistage pumps through numerical simulation.

### Acknowledgments

This work was financially supported by the State Key Program of National Natural Science of China (Grant no. 51239005) and the National Science & Technology Pillar Program

(Grant no. 2011BAF14B04) of China. This research was also sponsored by the Research and Innovation Project for College Graduates of Jiangsu Province (CXZZ12\_0679).

### References

- [1] F. G. Johann, *Centrifugal Pumps*, Springer, New York, NY, USA, 2008.
- [2] Y. Shouqi, C. Wuling, and L. Shiyang, "Theory and design method of non-overload centrifugal pumps," *Chinese Journal of Mechanical Engineering*, vol. 5, no. 4, pp. 252–260, 1992.
- [3] Z. peifang, Y. Shouqi, and X. Jianqiang, "Present status and development trends of low-specific-speed centrifugal pumps," *Drainage and Irrigation Machinery*, vol. 21, no. 6, pp. 42–45, 2003.
- [4] M. A. Moreno, J. I. Córcoles, D. A. Moraleda, A. Martinez, and J. M. Tarjuelo, "Optimization of underground water pumping,"

- Journal of Irrigation and Drainage Engineering*, vol. 136, no. 6, pp. 414–420, 2010.
- [5] M. Moradi-Jalal, S. I. Rodin, and M. A. Marino, “Use of genetic algorithm in optimization of irrigation pumping stations,” *Journal of Irrigation and Drainage Engineering*, vol. 130, no. 5, pp. 357–365, 2004.
- [6] A. S. Hedayat, N. J. A. Sloane, and J. Stufken, *Orthogonal Arrays, Theory and Applications*, Springer, New York, NY, USA, 1999.
- [7] Z. Lixue, S. Yaozhen, L. Qingsheng et al., “Mathematic model of seed peeling efficiency with critical structure parameters based on orthogonal multinomial tests,” *Transactions of the CSAE*, vol. 19, no. 5, pp. 22–26, 2003.
- [8] Y. Shouqi, Z. Jinfeng, Y. Jianping et al., “Orthogonal experimental study effect of main geometry factors of splitter blades on pump performance,” *And Irrigation Machinery*, vol. 26, no. 2, pp. 1–5, 2008.
- [9] H. Wang, W. Shi, W. Lu, L. Zhou, and C. Wang, “Optimization design of deep well pump based on latin square test,” *Transactions of the Chinese Society of Agricultural Machinery*, vol. 41, no. 5, pp. 56–63, 2010 (Chinese).
- [10] Y. Shen, S. Yuan, W. Lu, J. Zhang, and J. Yuan, “Orthogonal test design method based on numerical simulation for non-overload centrifugal pump with complex impeller,” *Transactions of the Chinese Society of Agricultural Machinery*, vol. 41, no. 9, pp. 22–26, 2010 (Chinese).
- [11] L. Zhou, W. Shi, W. Lu, R. Xu, and C. Wang, “Orthogonal test and optimization design of submersible pump guide vanes,” *Journal of Drainage and Irrigation Machinery Engineering*, vol. 29, no. 4, pp. 312–342, 2011.
- [12] W. Shi, T. Jiang, W. Cao, W. Lu, D. Zhang, and B. Chen, “Optimal design and experiment on a high-head non-overload submersible sewage pump,” *Transactions of the Chinese Society of Agricultural Engineering*, vol. 27, no. 5, pp. 151–155, 2011.
- [13] S. N. Shukla and J. T. Kshirsagar, “Numerical experiments on a centrifugal pump,” in *Proceedings of the 2002 ASME Joint U.S.-European Fluids Engineering Division Conference (FEDSM '02)*, pp. 709–720, July 2002.
- [14] R. K. Byskov, C. B. Jacobsen, and N. Pedersen, “Flow in a centrifugal pump impeller at design and off-design conditions. Part II: large eddy simulations,” *Journal of Fluids Engineering*, vol. 125, no. 1, pp. 73–83, 2003.
- [15] R. Spence and J. Amaral-Teixeira, “A CFD parametric study of geometrical variations on the pressure pulsations and performance characteristics of a centrifugal pump,” *Computers and Fluids*, vol. 38, no. 6, pp. 1243–1257, 2009.
- [16] J. H. Ferziger, *Computational Methods for Fluid Dynamics*, Springer, Berlin, Germany, 2002.

## Research Article

# Proposal of Damping Function for Low-Reynolds-Number $k$ - $\epsilon$ Model Applicable in Prediction of Turbulent Viscoelastic-Fluid Flow

**Takahiro Tsukahara and Yasuo Kawaguchi**

*Department of Mechanical Engineering, Tokyo University of Science, 2641 Yamazaki, Noda-shi, Chiba 278-8510, Japan*

Correspondence should be addressed to Takahiro Tsukahara; [tsuka@rs.tus.ac.jp](mailto:tsuka@rs.tus.ac.jp)

Received 24 June 2013; Revised 12 September 2013; Accepted 13 September 2013

Academic Editor: Mohamed Fathy El-Amin

Copyright © 2013 T. Tsukahara and Y. Kawaguchi. This is an open access article distributed under the Creative Commons Attribution License, which permits unrestricted use, distribution, and reproduction in any medium, provided the original work is properly cited.

A low-Reynolds-number  $k$ - $\epsilon$  model applicable for viscoelastic fluid was proposed to predict the frictional-drag reduction and the turbulence modification in a wall-bounded turbulent flow. In this model, an additional damping function was introduced into the model of eddy viscosity, while the treatment of the turbulent kinetic energy ( $k$ ) and its dissipation rate ( $\epsilon$ ) is an extension of the model for Newtonian fluids. For constructing the damping function, we considered the influence of viscoelasticity on the turbulent eddy motion and its dissipative scale and investigated the frequency response for the constitutive equation based on the Giesekus fluid model. Assessment of the proposed model's performance in several rheological conditions for drag-reduced turbulent channel flows demonstrated good agreement with DNS (direct numerical simulation) data.

## 1. Introduction

It is known that minute amount of additives, such as polymer and surfactant, can reduce the frictional drag in wall-bounded turbulent flows at high Reynolds numbers. This effect, often referred to as “Toms effect” or “turbulent drag reduction (DR),” has been focused as an efficient energy-saving technology for a large variety of applications (e.g., oil pipelines and district heating/cooling systems). The possibility of substantially decreasing the energy consumption for the transport of liquids stimulated intensive studies of this effect. Many investigators have considered the Toms effect to be a phenomenon that is closely related to a viscoelasticity of the dilute polymer (or surfactant) solution and to a modification of the turbulent structures in the flow. Predictions of the level of DR as well as the modulated turbulent flow of viscoelastic liquids are nontrivial issues to apply the Toms effect in practical situations.

Since the direct numerical simulation (DNS) is one of the important tools to investigate turbulence phenomena qualitatively and quantitatively, DNSs of viscoelastic flows have been increasingly performed by a number of researchers after the pioneering works in 1997-1998 [1, 2]; see reviews [3, 4].

They used several kinds of viscoelastic models for a rheological constitutive equation, such as the FENE-P (finitely extensible nonlinear elastic-Peterlin) model, the Oldroyd-B model, and the Giesekus model, to describe the behaviour of viscoelastic fluids. Most DNS studies aimed at understanding the mechanism of DR and actually revealed some important characteristics common to turbulent channel and pipe flows subject to DR. For instance, Kim and Sureshkumar [5] recently proposed a plausible mechanism associated with the effect of dynamic interactions between turbulent vortical structures and viscoelastic stress on DR. One of their interesting conclusions is the fact that the interplay between the turbulent-eddy (turnover) time scale and the relaxation time of viscoelastic fluid produces the differences in the flow characteristics between low DR regime and high DR regime, which are, respectively, observed at low and high Weissenberg numbers. In viscoelastic flows with a relaxation time that is small but larger than the vortex time scale in the vicinity of a wall, near-wall vortices can be affected by the viscoelastic stress, whereas weaker and larger vortices in the outer layer remain unaffected. With increasing relaxation time, the eddies with longer time scales would interact with

the viscoelasticity and the outer-layer modification would be more pronounced. A reason of the existence of maximum DR limit was also explained by Kim and Sureshkumar: the viscoelastic effects eventually encompass all dynamically relevant vortex time scales with very high Weissenberg numbers and, hence, the DR saturates. This result exemplifies the Lumley's time criteria [6].

As for high Reynolds number simulations, the available information on the viscoelastic turbulent flow is even more scarce than for the Newtonian turbulence, despite of the development of computer resources in the recent decades. A noticeable exception is the DNS performed by Thais et al. [7, 8], where high DR flows at the friction Reynolds number  $Re_\tau = 1000$  was achieved and the Reynolds number similarity was investigated systematically. Viscoelastic flows through complex geometries are also of practically importance and interesting subjects. In flows around bluff bodies, the fluid viscoelasticity would significantly distort the streamlines of the mean flow, regardless of either laminar or turbulent state. Tsukahara et al. [9, 10] demonstrated the flow modification as well as the turbulence modulation in an orifice flow of the viscoelastic fluid, by means of DNS. However, both the Reynolds number and the Weissenberg number examined by the existing DNS studies are still lower than typical level in industrial applications. Therefore, the prediction based on the physics (or the governing equation) of the viscoelastic turbulent flow should be improved for applying the practical flows. Although the use of DNS can be extremely computationally expensive for most engineering applications, DNS databases are useful as calibration/comparison database when considering the application of Reynolds-averaged Navier-Stokes (RANS) simulations. The development of mathematical and computational models for viscoelastic flow is not sufficiently well advanced to allow RANS simulation to be undertaken. With this background, it is then a matter of interest to build more physically-based turbulence closures for the prediction of flows with drag-reducing additives with the aid of the DNS database and the already-proposed mechanism of DR.

Several researchers have attempted to develop more general eddy viscosity or Reynolds stress transport closures for viscoelastic fluids. Leighton et al. [11] developed a Reynolds stress model for the drag-reducing viscoelastic fluids described by the FENE-P rheological constitutive equation, as motivated by the need for robust predictive tools. Their modeling approach focused on two kinds of expected polymer effects on the turbulent flow: one is what they call the "explicit" effect that would be expressed as a new term containing the interactions between fluctuations of the polymer stress and kinematic quantities; the other is the "implicit" effect pertaining to the slow pressure-strain (redistribution) term in the Reynolds-stress transport equation. Pinho and coworkers [12–14] have developed a  $k$ - $\varepsilon$  model for the FENE-P fluid, using the Reynolds averaged form of the conformation tensor equation to determine the average polymer stress. They devoted their efforts to devise the closures for the new terms appearing in the governing equations, especially, the nonlinear turbulence distortion term (represented by  $\Lambda_{ij}$  in this paper) in the averaged equation of the conformation tensor. Their closure models were

calibrated well on the basis of DNS database, Iaccarino et al. [15] employed the  $v^2$ - $f$  approach to treat the intensified wall damping of wall-normal turbulence in the drag-reduced flow. Moreover, they modelled directly the Reynolds-averaged polymer stress without solving the constitutive equation for the conformation tensor, resulting in less coefficients and functions. The results predicted by these models were generally in good agreement with DNS database for low and intermediate DR. More recently, Resende et al. [16] proposed a  $k$ - $\omega$  model based on the model of Bredberg et al. [17] for Newtonian fluids. Some improvement was achieved for predictions in the intermediate DR region, but still not enough to estimate  $k$  and the high DR (in which the drag reduction rate is more than 60%).

The present objective is to construct RANS that can be applied for the viscoelastic turbulent flow by adding corrections to a low Reynolds number  $k$ - $\varepsilon$  model of Newtonian-fluid flow (here,  $k$  and  $\varepsilon$  are the turbulent kinetic energy and its dissipation rate, resp.). Two major corrections to be applied to the low Reynolds number  $k$ - $\varepsilon$  model, which has been well designed and employed widely in commercial softwares, are the addition of a damping function based on the Lumley's time criteria and the simultaneous calculation of the constitutive equation of the Giesekus model. The first correction is proposed from the fact that one of the most important effects of the fluid viscoelasticity on turbulence is suppression of small-scale vortical motions near the wall. Hence, the knowledge of scales of eddies that are suppressed by additives is indispensable to discuss the form of the present model. We have obtained this information from existing DNS database [18] enabling a priori development of turbulence closures. To analyze the data, we performed an investigation of frequency response of the Giesekus model and considered the relationship between the shift of the dissipation scale and the viscoelastic behavior of the fluid.

The following section provides a brief introduction of the currently adopted model, which is originally for the Newtonian flow. Thereafter, the scale shifts of the dissipation range and of the viscoelastic behavior are considered and the present constitutive equation as well as the  $k$  and  $\varepsilon$  equations are then developed. Finally, the proposed model will be tested in comparison with DNS results.

## 2. Introduction of Low-Re $k$ - $\varepsilon$ Model

The present section commences with a brief review of established models for turbulent flows of Newtonian fluid using two-equation turbulent viscosity closures. In the following, the vector  $x_i = (x_1, x_2, x_3) \equiv (x, y, z)$  denotes the coordinate directions;  $u_i = (u_1, u_2, u_3) \equiv (u, v, w)$  is the velocity fluctuating component, while those capital letters represent the mean components. The overbar indicates an ensemble average over all homogeneous directions and time.

The low Reynolds number  $k$ - $\varepsilon$  model for a turbulent flow relates the Reynolds stress to the mean strain field as follows:

$$-\overline{u_i u_j} = \nu_t \left( \frac{\partial U_i}{\partial x_j} + \frac{\partial U_j}{\partial x_i} \right) - \frac{2}{3} k \delta_{ij}, \quad (1)$$

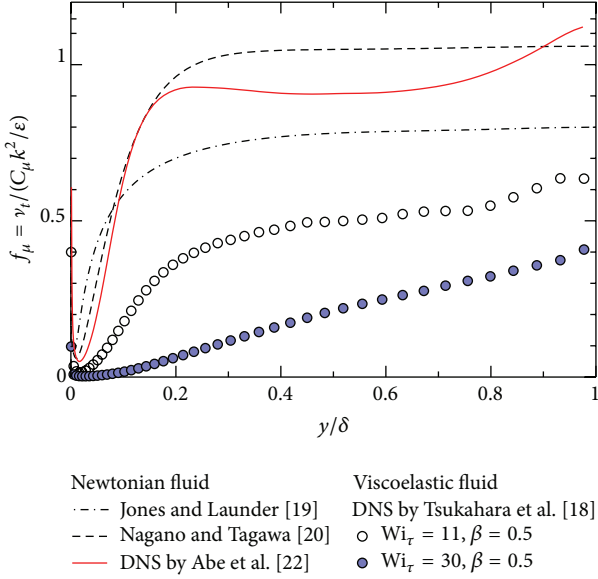


FIGURE 1: Comparison of damping function  $f_\mu$  for turbulent channel flow at  $Re_\tau = 395$ .

where  $\delta_{ij}$  is the Kronecker delta and the turbulent kinematic viscosity is expressed as

$$\nu_t = C_\mu f_\mu \frac{k^2}{\epsilon}. \quad (2)$$

Here,  $C_\mu$  is a constant with value equal to 0.09. A number of proposals for the damping function  $f_\mu$  have been made; for instance, Jones and Launder [19] functionalized  $f_\mu$  using a turbulent Reynolds number  $Re_t$  as follows:

$$f_\mu = \exp\left(-\frac{2.5}{1 + Re_t/50}\right). \quad (3)$$

On the other hand, some researchers introduced the wall-normal distance normalized in wall unit,  $y^+ = y\rho\mu_\tau/\mu_0$ , as a parameter of  $f_\mu$ . A typical example is the one proposed by Nagano and Tagawa [20] as follows:

$$f_\mu = \left\{1 - \exp\left(-\frac{y^+}{26}\right)\right\} \left\{1 + \frac{4.1}{Re_t^{3/4}}\right\}. \quad (4)$$

Their damping function is based on the van Driest wall-damping formula [21]. They considered the behavior of turbulence on an infinite flat plate with a simple harmonic oscillation parallel to the plate. The amplitude of the motion of the fluid in each position was examined to describe the damping function. Figure 1 shows the  $f_\mu$  distribution of these individual models when applied to the turbulent channel flow at a given Reynolds number. The model proposed by Nagano and Tagawa [20] is in better agreement with the DNS data for the Newtonian flow [22], especially, in the near-wall region.

As for a viscoelastic-fluid flow accompanied by DR, both timescale and lengthscale of turbulent-eddy motions are known to be different from those in Newtonian flows. Therefore, a modification of  $f_\mu$  for viscoelastic flow is necessarily

required. Here, we have investigated the predictive values of  $f_\mu$  for viscoelastic fluids using our DNS database [18], which provides various statistical data of the drag-reducing turbulent channel flow for several different rheological properties. Figure 1 shows that  $f_\mu$  is dramatically suppressed in any drag-reducing condition. Such aspect is attributed to diminishing turbulent-eddy motions due to the elasticity of fluid. Cruz and Pinho [12] proposed a damping function for a pipe flow of the viscoelastic fluid. They deduced the damping function in the similar way with van Driest [21] and devised an equation including two damping functions to take into account both the fluid rheology and the wall effect into the eddy viscosity. Their function is written as

$$\begin{aligned} f_\mu &= f_{\mu v} \cdot f_{\mu e} \\ &= \left\{1 - \left[1 + \left|\frac{1-n}{1+n}\right| y^+\right]^{-\frac{(1/26.5)(1+n)}{(1-n)}}\right\} \\ &\quad \cdot \left\{1 - \left[1 + \left|\frac{q-1}{3-q}\right| y^+ C_n^{(1-q)/(2-q)}\right]^{-\frac{(1/26.5)(3-q)}{(q-1)}}\right\}, \end{aligned} \quad (5)$$

where  $n$  is the viscosity power index of the shear behavior,  $q$  is the viscosity power index of the Trouton-ratio behavior, and  $C_n$  is a parameter dependent on the additive. In the present paper, we also propose a new additional damping function based on the Lumley's time criteria [6] for the Giesekus viscoelastic-fluid model.

### 3. Shift of Dissipative Scale

**3.1. Lumley's Consideration of Time Criteria.** As many existing studies show, the turbulent eddy motions and ordered structures in drag-reducing viscoelastic flows are known to exhibit time and spatial scales that are different from those of Newtonian flows [3, 4]. As inspired by the work of Kim and Sureshkumar [5], it is clear that a knowledge of scales (especially, dissipation scale of turbulent kinetic energy) of turbulent eddy motions should be useful and indispensable to construct a turbulence model for predicting the drag-reduced flow. The theoretical concepts [6, 23] about the eddy-scale range that can be shifted in the drag-reduced turbulent flow have not yet been utilized fully and, as far as the authors know, none has been tested against DNS quantitatively. This provides the motivation for re-examining this issue. According to Lumley's consideration in terms of turbulent energy spectrum [6], we discuss here the energy spectra and the scale shift for the turbulent channel flow.

It is assumed that the mean pressure gradient is constant and the turbulent flow field is fully developed, where the channel width is  $2\delta$ . The one-dimensional energy spectrum of the streamwise velocity fluctuation is defined as

$$\int_0^\infty E_{uu}(\kappa) d\kappa = \overline{uu}, \quad (6)$$

where  $\kappa$  is a wave number. In the logarithmic layer, there is no relevant length other than the wall-normal height

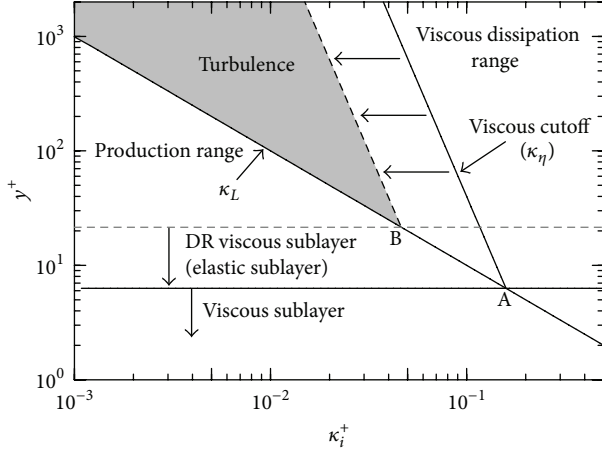


FIGURE 2: Scaling relation in a wall-bounded turbulence: Lumley's concept [6].

$y$  according to the mixing length theory [24] and, hence, the energy-containing large-scale eddies should be scaled roughly with  $y$ . With respect to the energy spectrum, its peak is expected to occur at a wave number  $\kappa_L$  given by

$$\kappa_L \cdot y \simeq 1, \quad (7)$$

which then represents the limit of the production range of the spectrum. On the other hand, the scale of dissipative small-scale eddies can be estimated from the energy dissipation spectrum, described as  $\kappa_i^2 E_{uu}(\kappa)$  [25]. Lumley [6] assumed that the peak of the dissipation spectrum for the Newtonian-fluid turbulence would occur at

$$\kappa_\eta \eta \simeq 0.2, \quad (8)$$

where  $\eta = (\nu^3/\varepsilon)^{1/4}$  is the Kolmogorov scale. Here, if the turbulence production and the viscous dissipation rate  $\varepsilon$  are locally balanced for each flow unit, we have

$$\varepsilon \simeq \frac{u_\tau^3}{\kappa_K \cdot y}, \quad (9)$$

using the von Kármán constant  $\kappa_K$  and the friction velocity  $u_\tau$  [24]. Therefore, the relation between  $y$  and  $\kappa_\eta$  is rewritten from (8) as

$$\kappa_\eta^+ (\kappa_K \cdot y^+)^{1/4} \simeq 0.2. \quad (10)$$

The size of turbulent fluctuations (or eddies) ranges between  $\kappa_L$  and  $\kappa_\eta$ . Figure 2 shows both wave numbers of  $\kappa_L$  and  $\kappa_\eta$  as a function of  $y^+$  in the ordinate. If  $\kappa_K = 0.4$ , the lines of (7) and (10) intersect at  $y^+ = 6.3$ . Here, we call this point as A. Above the point A, the momentum transport by turbulent vortical motions is active. As  $y^+$  being very close to A, the energy productive scale and the dissipative one become comparable with each other, resulting in the unsustainable turbulence at the relevant heights. It can be believed that the upper bound of the viscous sublayer corresponds to the point A, below which the viscous stress is dominant in the total stress.

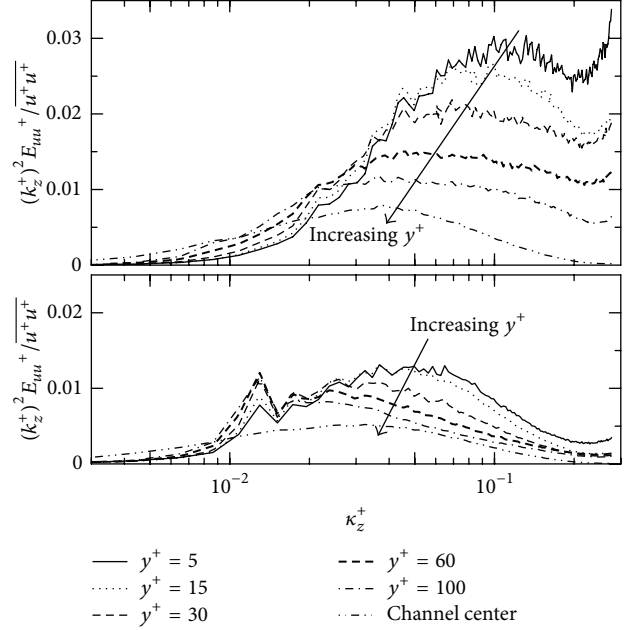


FIGURE 3: Premultiplied one-dimensional spanwise energy spectra of streamwise velocity fluctuation in drag-reducing viscoelastic flow at  $Re_\tau = 395$ . (a)  $Wi_\tau = 10$ ,  $\beta = 0.8$  and (b)  $Wi_\tau = 30$ ,  $\beta = 0.5$ .

In the drag-reducing viscoelastic flow, the relationship of  $\kappa_L$  and  $\kappa_\eta$  is expected to be changed as shown with broken lines in Figure 2, according to Lumley [6]. He reasoned that less difference between  $\kappa_L^+$  and  $\kappa_\eta^+$  as a result of decreased  $\kappa_\eta^+$  might lead to the expanding of the viscous sublayer. The intersection of  $\kappa_L^+$  and  $\kappa_\eta^+$ , therefore, shifts from A to a higher position labeled as B. Assuming that B is the shifted bound of the viscous sublayer in the relevant flow, the viscous sublayer of the viscoelastic fluid should be enlarged. In other words, the new region, so-called the elastic layer [26], arises in the vicinity of the wall with the upper bound at the height of B.

In order to verify this concept of DR, we reexamine the existing DNS data of the turbulent channel flow accompanied by DR [18], as shown in Figure 3. The value of  $\kappa_\eta$  is determined from the peak of the spanwise energy-dissipation spectrum function of  $\kappa_z^2 E_{uu}(\kappa_z)$ . For a viscoelastic flow at the friction Weissenberg number  $Wi_\tau = 30$ , the  $\kappa_\eta$  is remarkably decreased at every height, especially in the near-wall region, compared to the case of  $Wi_\tau = 10$ . As a result, the intersection of the  $\kappa_L$  line and the  $\kappa_\eta$  line moves to a higher position of about  $y^+ = 12$ , as given in Figure 4. The  $\kappa_\eta$  is prone to shift leftwards as the Weissenberg number is increasing consistent to the above Lumley's drag-reduction model.

**3.2. Dynamic Characterization of Viscoelastic Fluid.** In this section, we investigate the dynamic characterization of the viscoelastic fluid, in order to discuss the effect of its viscoelasticity on turbulent fluctuations (eddies). A model fluid for this study is based on the Giesekus model [27], which is one of the typical viscoelastic models to describe the relationship between stress and strain exerted on the fluid of

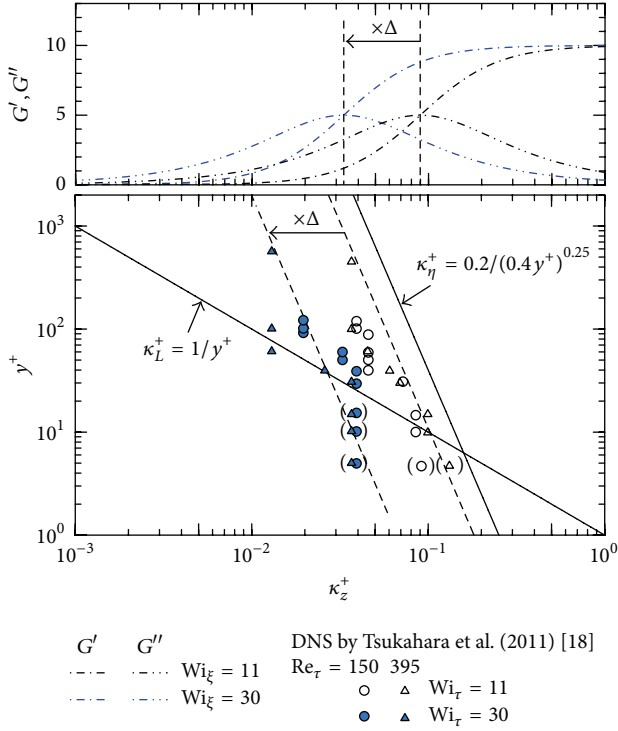


FIGURE 4: (a) Dependence of the storage modulus and loss modulus on a frequency for the viscoelastic fluid of Giesekus model. (b) Scaling relation in the turbulent channel flow with/without drag reduction: shifting in the wave number of the energy-dissipative range by viscoelastic effects.

interest. The rheological constitutive equation with respect to the viscoelastic stress tensor  $\tau_{ij}^p$  is written as

$$\begin{aligned} \tau_{ij}^p + \lambda \left\{ \frac{D\tau_{ij}^p}{Dt} - \tau_{ik}^p \frac{\partial u_j}{\partial x_k} - \frac{\partial u_i}{\partial x_k} \tau_{kj}^p + \frac{\alpha}{\mu_\alpha} (\tau_{ik}^p \tau_{kj}^p) \right\} \\ = \mu_0 \left( \frac{\partial u_i}{\partial x_j} + \frac{\partial u_j}{\partial x_i} \right), \end{aligned} \quad (11)$$

where  $\lambda$  is the relaxation time,  $\mu_0$  is the zero shear rate viscosity of the solution, and  $\alpha$  is the mobility factor to indicate the level of nonlinearity.

It is generally known that a measurement under a small amplitude oscillatory flow is a powerful tool for describing the microscopic state of the test fluid. Therefore, we consider here a small fluid volume under a simple shear flow whose shear rate varies periodically with time as

$$\dot{\gamma} = \dot{\gamma}_{\max} \exp(i\kappa t), \quad (12)$$

where  $\kappa$  is the frequency of the oscillatory shear stress. The dimensionless complex modulus as one of rheological material functions is obtained from

$$G = \frac{c_{12}}{\dot{\gamma}_{\max}}, \quad (13)$$

where the nondimensional conformation tensor  $c_{12}$  is derived explicitly from the viscoelastic stress tensor; that is,

$\tau_{ij}^p = \mu_0(c_{ij} - \delta_{ij})/\lambda$ . Note that the complex shear modulus  $G$  consists of the dynamic storage modulus  $G'$  and the dynamic loss modulus  $G''$  as follows:

$$G = G'(\kappa) + iG''(\kappa). \quad (14)$$

In the case of an elastic body, there is no phase difference between strain and stress, while in a viscous body the phase difference is  $\pi/2$ . Therefore,  $G'$  and  $G''$  can be used as barometers of elasticity and viscosity, respectively.

Typical  $G'$  and  $G''$  versus frequency data for the viscoelastic fluid described by the Giesekus model are shown in the top panel of Figure 4, where the horizontal axis represents the wave number  $\kappa$ . Both moduli clearly depend only on the Weissenberg number, and they would not depend on any other flow parameter, such as the Reynolds number and the maximum shear rate  $\dot{\gamma}_{\max}$ , for the laminar simple shear flow. Here, the Weissenberg number  $Wi_\xi$  is defined as the product of  $\lambda$  and  $\dot{\gamma}_{\max}$ . The most obvious consequence of the increasing Weissenberg number on the frequency sweep in the figure is to decrease the crossover frequency, at which  $G' = G''$ , thereby extending the high plateau in  $G'(\kappa)$  to lower frequencies. As  $Wi_\xi$  varies from 11 to 30, the frequency of the crossover point shifts from  $\kappa_1^+ \approx 0.090$  to  $\kappa_2^+ \approx 0.033$ . This shift factor corresponds to the ratio of the two Weissenberg numbers; that is,  $\Delta = \kappa_2/\kappa_1 = 11/30$ . The magnitude of the plateau modulus is essentially unchanged against the Weissenberg number.

From the above facts, it can be conjectured that, as the Weissenberg number increases, the behavior of relevant fluid becomes elastic against high-frequency inputs associated with small-scale eddies in the near-wall turbulence. Correspondingly, the relationship between the energy-dissipation range and the frequency response of the Giesekus model reveals that the shift in wave number of the energy dissipation is consistent with the change of viscoelastic behavior, as shown in Figure 4. From this result, it can be said that viscoelastic fluid should behave more elastically against high-frequency eddy motions in turbulence and suppress them.

#### 4. Model Development

While some details of the present model differ from Jones and Launder [19], their low-Reynolds-number  $k$ - $\epsilon$  model will be applied unaltered in most respects. As for the effect of viscoelastic fluid, the above observation has driven us to consider the time-scale ratio between the characteristic time scale of turbulent eddy motions and the relaxation time  $\lambda$  of the relevant fluid, and we employ it to describe the diminished values of  $\nu_t$ . In the drag-reducing viscoelastic fluid that has a relaxation time comparable to some scale of turbulent eddies, the smaller eddies, if larger than the Kolmogorov scale, should be damped due to the elastic behavior of the fluid. Using the Kolmogorov time  $t_\eta$  as the characteristic time scale in turbulence, the time-scale ratio can be proposed as

$$\frac{\lambda}{t_\eta} = \frac{\lambda}{\sqrt{\nu_s/\epsilon}} = \frac{Wi_\tau}{\sqrt{\beta Re_\tau/\epsilon^*}}, \quad (15)$$

where  $\nu_s$ ,  $\text{Re}_\tau$ , and  $\beta$  are defined as the solvent kinematic viscosity ( $\mu_s/\rho$ ), the Reynolds number based on the friction velocity and the channel half width, and the ratio of the solvent viscosity  $\mu_s$  to the zero-shear-rate viscosity of the solution  $\mu_0$ , respectively. Then, replacing (2), let us modify  $\nu_t$  by introducing an additional damping function  $f_v$  based on this time-scale ratio, as follows:

$$\nu_t = C_\mu f_\mu f_v \frac{k^2}{\bar{\varepsilon}}, \quad (16)$$

$$f_v = \exp \left[ -\psi_0 \frac{\text{Wi}_\tau}{\sqrt{\beta \text{Re}_\tau / \bar{\varepsilon}^*}} \left( \frac{1-\beta}{\beta} \right)^{0.1} \right]. \quad (17)$$

Here, the ‘‘homogeneous’’ dissipation rate  $\bar{\varepsilon}$  ( $= \varepsilon - \hat{\varepsilon}$ ) is introduced, while

$$\hat{\varepsilon} = \begin{cases} 2\nu_s \left( \frac{\partial \sqrt{k}}{\partial y} \right)^2, & \text{when } \left( \frac{\partial \sqrt{k}}{\partial y} \right) \geq 0, \\ 0, & \text{when } \left( \frac{\partial \sqrt{k}}{\partial y} \right) < 0, \end{cases} \quad (18)$$

is defined with an assumption that  $y$  is normal to the wall. To accommodate the effect of  $\beta$  on DR, the form of  $(\beta^{-1} - 1)^{0.1}$  was chosen *ad hoc* and adopted to  $f_v$ . The presently optimized value of the additional model coefficient  $\psi_0$  is 0.36.

The conventional damping function  $f_\mu$ , that is used for the low-Reynolds-number turbulence model to comply with the damping effect of the wall, remains the same as for a Newtonian fluid. For  $f_\mu$  in (15), we adopt the function proposed by Kawashima and Kawamura [28] as follows:

$$f_\mu = 1.0 - \exp \left[ - \left( \frac{y_\eta}{285} \right) - \left( \frac{y_\eta}{20} \right)^3 \right], \quad (19)$$

where  $y_\eta$  is the wall-normal distance normalized by the Kolmogorov length scale,  $\eta = (y_s^3/\varepsilon)^{1/4}$ . The model of  $\nu_t$  by (17) and (19) satisfies the following two assumptions: first, very small-scale eddies are damped by the elastic behavior of the fluid and thereby the eddy viscosity decreases ( $\nu_t \rightarrow 0$  when  $t_\eta \ll \lambda$ ); secondly, the eddy viscosity for less elastic fluid is close to be that for the Newtonian case ( $\nu_t \rightarrow (2)$  when  $t_\eta \gg \lambda$ ).

The following equations are the Reynolds equation and the ensemble-averaged constitutive equation, which govern the incompressible viscoelastic-fluid flow as follows:

$$\frac{DU_i}{Dt} = -\frac{1}{\rho} \frac{\partial P}{\partial x_i} + \nu_s \frac{\partial^2 U_i}{\partial x_j^2} - \frac{\partial \overline{u_i u_j}}{\partial x_j} + \frac{\nu_a}{\lambda} \frac{\partial C_{ij}}{\partial x_j}, \quad (20)$$

$$\begin{aligned} \frac{DC_{ij}}{Dt} + \frac{\partial \overline{c_{ij} u_k}}{\partial x_k} - C_{ik} \frac{\partial U_j}{\partial x_k} - \frac{\partial U_i}{\partial x_k} C_{kj} \\ - \underbrace{\left( \frac{\partial \overline{u_i}}{\partial x_k} c_{kj} + c_{ik} \frac{\partial \overline{u_j}}{\partial x_k} \right)}_{\Lambda_{ij}} \\ + \frac{1}{\lambda} \left[ C_{ij} - \delta_{ij} + \alpha \left( C_{ik} C_{kj} + \overline{c_{ik} c_{kj}} - 2C_{ij} + \delta_{ij} \right) \right] = 0. \end{aligned} \quad (21)$$

In (21), the terms which include the  $c_{ij}$ , which represent the fluctuating part of the conformation tensor, should be modeled. The second term and the term of  $\overline{c_{ik} c_{kj}}$  (included in the last term) in the left-hand side of (21) are small enough to be ignored. The term labeled as  $\Lambda_{ij}$  in the left-hand side is modeled in the following form:

$$\Lambda_{ij} \equiv c_{ik} \frac{\partial \overline{u_j}}{\partial x_k} + \frac{\partial \overline{u_i}}{\partial x_k} c_{kj} = \psi_1 \frac{1}{t_\eta} \frac{\lambda}{\nu_a} \overline{u_i u_j} + \psi_2 \frac{1}{t_\eta} (C_{ij} - \delta_{ij}), \quad (22)$$

where  $\psi_1 = 0.001(1 - \exp(-y_\eta/100))$  and  $\psi_2 = -0.001(1 - \exp(-y_\eta/5))$  are given based on the DNS data [18]. This form was originally proposed by Leighton et al. [11].

From the Navier-Stokes equation, the transport equation of turbulent kinetic energy is obtained and modeled as

$$\begin{aligned} \frac{Dk}{Dt} &= D_k + P_k - (\bar{\varepsilon} + \hat{\varepsilon}) + \pi_k + E_k^d + E_k^\varepsilon, \\ D_k &= \frac{\partial}{\partial x_j} \left[ \left( \nu_s + \frac{\nu_t}{\sigma_k} \right) \frac{\partial k}{\partial x_j} \right], \\ P_k &= - \left[ \nu_t \left( \frac{\partial U_i}{\partial x_j} + \frac{\partial U_j}{\partial x_i} \right) + \frac{2}{3} \delta_{ij} k \right] \frac{\partial U_i}{\partial x_j}, \\ \pi_k &= -\frac{1}{2} \nu_s \frac{\partial}{\partial x_k} \left[ \frac{k}{\varepsilon} \left( \frac{\partial \hat{\varepsilon}}{\partial x_k} \right)^2 \right], \\ E_k^d &= \frac{\partial}{\partial x_k} \left( \frac{\nu_a}{\lambda} \overline{u_i c_{ik}} \right) \approx 0, \\ E_k^\varepsilon &= -\frac{\nu_a}{\lambda} \left( c_{ik} \frac{\partial \overline{u_i}}{\partial x_k} \right) = -\frac{\nu_a}{2\lambda} \Lambda_{ii}, \end{aligned} \quad (23)$$

and the transport equation of the dissipation of turbulent kinetic energy is written as

$$\begin{aligned} \frac{D\bar{\varepsilon}}{Dt} &= D_\varepsilon + (P_\varepsilon - Y) + E + E_\varepsilon \\ &= \frac{\partial}{\partial x_j} \left[ \left( \nu_s + \frac{\nu_t}{\sigma_\varepsilon} \right) \frac{\partial \bar{\varepsilon}}{\partial x_j} \right] \\ &\quad + \frac{\bar{\varepsilon}}{k} (C_{\varepsilon 1} P_k - C_{\varepsilon 2} \bar{\varepsilon} - \hat{\varepsilon}) + E + E_\varepsilon, \\ E &= C_{\varepsilon 3} \nu_s \nu_t \left( \frac{\partial^2 U}{\partial x_k^2} \right)^2, \\ E_\varepsilon &= 2 \frac{\nu_s \nu_a}{\lambda} \frac{\partial \overline{u_i}}{\partial x_k} \frac{\partial}{\partial x_k} \left( \frac{\partial C_{ij}}{\partial x_j} \right) \approx 0, \end{aligned} \quad (24)$$

where  $E_k^d$  and  $E_\varepsilon$  are assumed to be negligible compared to the other terms. Numerical studies of these terms showed them indeed to be small [7, 18]. Their omission in this model simplified the formulation of a stable numerical scheme. We can obtain the value of  $E_k^\varepsilon$  by applying (22). Following

TABLE 1: Percentage drag reduction DR%.

Reynolds number $Re_\tau$	150	150	150	150	150	395	395
Weissenberg number $Wi_\tau$	10	11	30	30	40	11	30
Shear-viscosity ratio $\beta$	0.8	0.5	0.5	0.3	0.5	0.5	0.5
Present model	15%	1%	57%	63%	68%	4%	60%
DNS [18]	13%	23%	58%	64%	67%	27%	58%

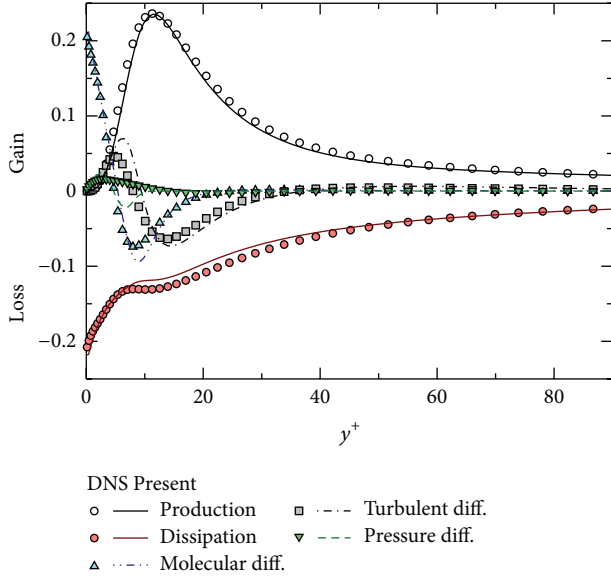


FIGURE 5: Budget of turbulent kinetic energy for Newtonian fluid in turbulent channel flow at  $Re_\tau = 395$  with emphasis on the near-wall region.

Kawashima and Kawamura [28], the model constants in the above equations are taken as  $C_{\varepsilon 1} = 1.44$ ,  $C_{\varepsilon 2} = 1.92$ ,  $C_{\varepsilon 3} = 0.6$ , and

$$\sigma_k = \sigma_\varepsilon = 1.0 - 0.5 \exp \left[ - \left( \frac{y_\eta}{20} \right)^2 \right]. \quad (25)$$

Prior to discussion on the feasibility of the present model for the drag-reducing viscoelastic fluid, Figure 5 shows the computed budget of the turbulent kinetic energy for the Newtonian fluid. The results of DNS by Abe et al. [22] are also shown for comparison. The agreement can be regarded as excellent everywhere in the turbulent channel flow at  $Re_\tau = 395$ .

## 5. Results

Results are presented below for drag-reduced turbulent channel flows. The tested range of the flow and rheological parameters were set to be  $Re_\tau = 150$  and  $395$ ,  $\beta = 0.3$ – $0.8$ ,  $\alpha = 0.001$ , and  $Wi_\tau = 10$ – $40$ . Note that we tested four different values of the Weissenberg number (10, 11, 30, and 40), at which Tsukahara et al. [18] executed a series of DNS at the same Reynolds number. The numerical solutions of the

proposed model equations were obtained using the second-order central-difference scheme for discretization, while convergence calculation was performed by the successive over-relaxation (SOR) method. We used nonuniform grids, which divide the half length of channel into 128 parts. The wall boundary conditions are  $U = k = \varepsilon = 0$  and the zero gradient boundary condition is applied to all variables at the channel center (except  $V = 0$ ). In this paper, the superscript  $(+)$  describes a nondimensionalized quantity by the friction velocity  $u_\tau$ , the effective viscosity [1], and the density of solution  $\rho$ , while  $(*)$  describes a nondimensionalized quantity by the channel half-width  $\delta$ ,  $u_\tau$ , and  $\rho$ . The friction Reynolds and Weissenberg numbers to be used in the following are defined as  $Re_\tau = \rho u_\tau \delta / \mu_0$  and  $Wi_\tau = \rho u_\tau^2 \lambda / \mu_0$ , respectively.

As an illustration of the performance of the present model, we present some results of the predicted rate of DR in several cases, in which the DNS database is available, see Table 1. Here, the percent drag reduction is determined as

$$DR\% = \left( 1 - \frac{C_{f,visc}}{C_{f,Newt}} \right) \times 100 (\%), \quad (26)$$

where the suffixes “visc” and “Newt” stand for the friction-coefficient values in the viscoelastic and Newtonian flows, respectively, at the same bulk Reynolds number. The model predicts DR% and its parameter dependence quite well in the region from low to high DR flows, as shown in Table 1. At both Reynolds numbers, the parameter combination of  $(Wi_\tau, \beta) = (11, 0.5)$  results in quite low DR%, while the DNS demonstrated moderate DR. This defect occurs in very low Weissenberg numbers with a low value of  $\beta$  and, moreover, the model has predicted that a near-zero  $Wi_\tau$  would produce a negative DR%, as shown later. This issue is not serious, because such a combination of low  $Wi_\tau$  and low  $\beta$  should not be impractical rheological condition; usually, dilute polymer solutions should be equivalent to viscoelastic fluids with low  $Wi_\tau$  and high  $\beta$  ( $\approx 1$ ).

**5.1. Mean Flow Statistics.** Figure 6 shows the mean velocity profiles, as a function of  $y^+$ , computed using the present model together with DNS data. Note again that, for the drag-reduced flows,  $y^+$  is normalized by the effective viscosity of each case, whose values are described in Table 2. Also shown in Figure 6 is the MDR asymptote, where the log-law profile for maximum drag reduction is that proposed by Virk [26]. At each Weissenberg number, the present model was in good agreement with the DNS data. Especially, the model applied for  $Wi_\tau = 10$  and  $30$  exhibited a better performance as  $y$  is close to the channel center. Small discrepancies are noticeable in the elastic layer and at the channel center, as  $Wi_\tau$  increases

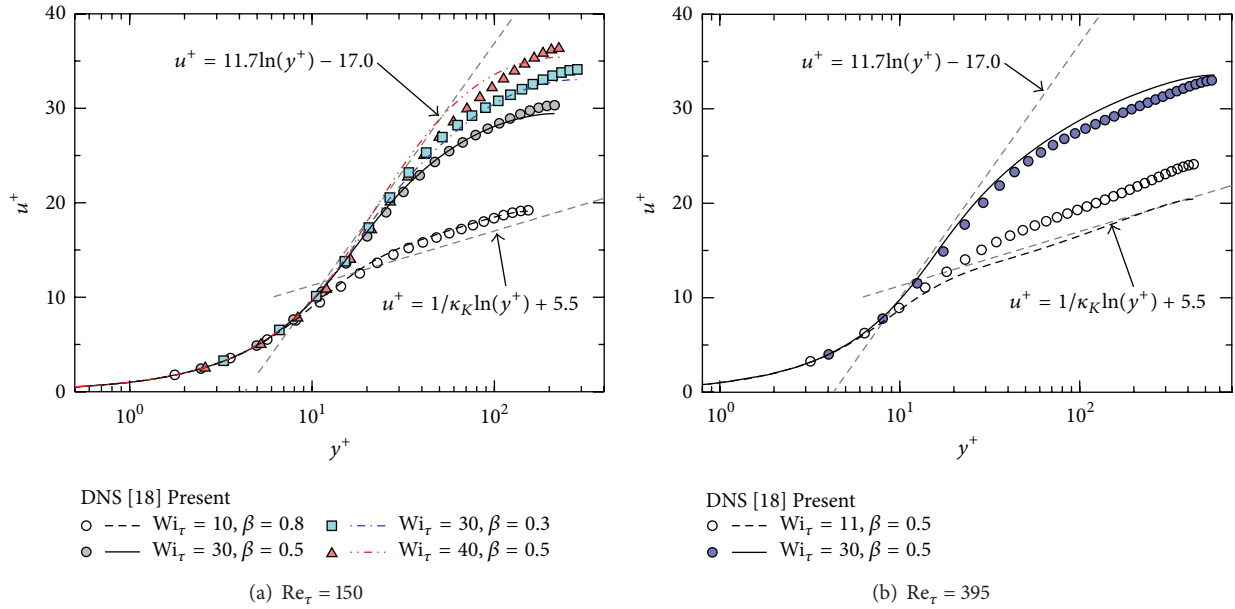


FIGURE 6: Mean velocity profiles in wall coordinates. Comparison between the model prediction and the corresponding DNS data [18].

TABLE 2: Effective wall viscosity normalized by  $\mu_0$ .

Reynolds number $Re_\tau$	150	150	150	150	150	395	395
Weissenberg number $Wi_\tau$	10	11	30	30	40	11	30
Shear-viscosity ratio $\beta$	0.8	0.5	0.5	0.3	0.5	0.5	0.5
Present model	0.961	0.880	0.697	0.527	0.654	0.880	0.697
DNS [18]	0.962	0.870	0.690	0.518	0.654	0.870	0.690

to 40, at which the achieved drag-reduction rate is close to MDR. However, in the elastic layer, the present model successfully demonstrates the profile that coincides with the MDR asymptote. The vertical displacements of the velocity profiles for high Weissenberg numbers are consistent with the DNS and the aforementioned results of DR%.

From the above assessments, it can be said that the Weissenberg-number dependence of the mean velocity is well described by the present model in a range of parameters including high DR cases, except for the combination of low  $Wi_\tau$  and low  $\beta$ . The model provided an underestimated velocity for  $Wi_\tau = 11$  and  $\beta = 0.5$ , as shown in Figure 6(b), while the result of a set of  $Wi_\tau = 10$  and  $\beta = 0.8$  seems to be predicted well, as given in Figure 6(a).

Figures 7 and 8 compare the predictions of  $C_f-Re_m$  and DR%- $Re_m$  with data from DNS [18]. The computations were made in a range of  $Wi_\tau$  from low DR to the maximum DR for the three values of  $\beta$  ( $=0.3, 0.5$ , and  $0.8$ ), at two Reynolds numbers. For reference, the MDR asymptote of Virk [26] is also plotted. As seen in the figures, the Weissenberg number dependences of  $C_f$  and DR% are demonstrated, enabling us to estimate the maximum  $Wi_\tau$  that gives rise to the maximum DR. For example, according to the model predictions at  $Re_\tau = 395$ , the MDR would be achieved at  $Wi_\tau \approx 45, 50$ , and  $60$  for  $\beta = 0.3, 0.5$ , and  $0.8$ , respectively. However, it is not necessarily the case that those critical states of MDR should be corresponding to the limiting conditions of the

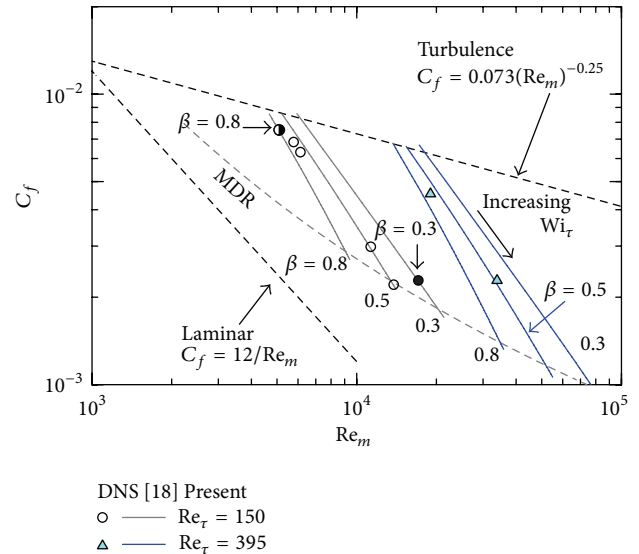


FIGURE 7: Frictional coefficient.

model prediction. The present model may provide a result with both lower  $C_f$  and higher DR% than those for MDR as the Weissenberg number increases further (not shown in Figures 7 and 8). With too high  $Wi_\tau$ , the mean velocity

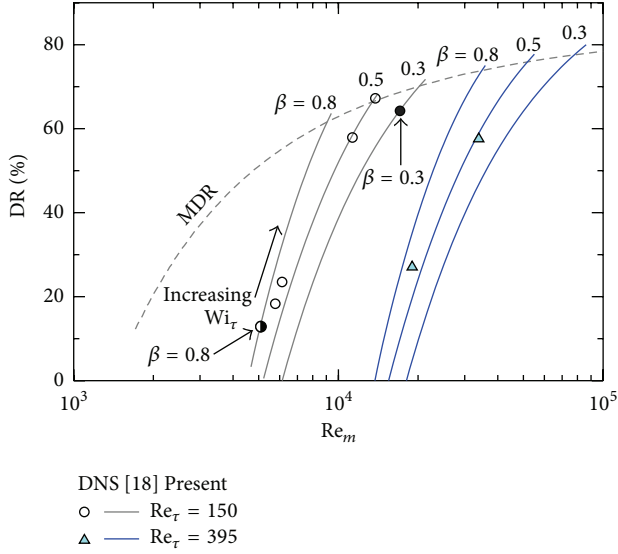


FIGURE 8: Drag reduction rate.

obtained by the model reveals that it exceeds the profile for the MDR asymptote [26] and, in addition, the Reynolds shear stress of  $-\overline{u'v'}$  still remains to be nonzero value. This result argues against the experimental fact that the contribution of  $-\overline{u'v'}$  would be almost absent in the highly drag-reduced turbulent channel flows by polymer/surfactant [4, 29, 30]. The reproducibility of the MDR state by means of RANS would be an interesting and challenging issue.

As can be seen in Figures 9 and 10, the predicted  $k^+$  and  $C_{11}$  follow those trends in the DNS data, although the near-wall peak value reveals clearly  $k^+$  to be overestimated. The discrepancy becomes large as the Weissenberg number increases. As for the wall-normal height of the peak, the model shows almost good agreements with the DNS data. It would be difficult to improve this aspect in the framework of the isotropic  $k$ - $\epsilon$  model, because highly drag-reduced viscoelastic flows should be inevitably accompanied by enhanced anisotropy in the near-wall region.

5.2. Reynolds and Conformation Stresses. The total shear stress can be obtained as

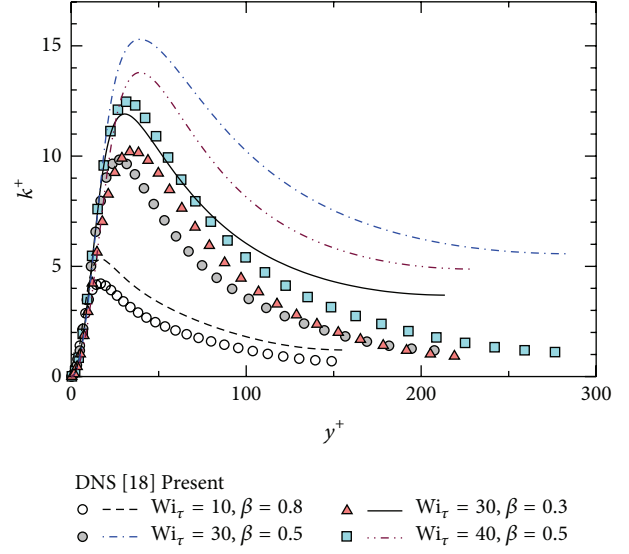
$$\tau_{total}^+ = \frac{\beta}{Re_\tau} \frac{\partial U^+}{\partial y^*} - \overline{u^+v^+} + \frac{1-\beta}{Wi_\tau} C_{12}. \quad (27)$$

Here, the terms are (in order from left to right of the right-hand side) the viscous shear stress, the Reynolds shear stress, and the viscoelastic shear stress. Figure 11 shows the wall-normal distributions of these stresses in several conditions chosen from Table 1. In all the test cases, the obtained total shear stress is in accordance with the theoretical value as follows:

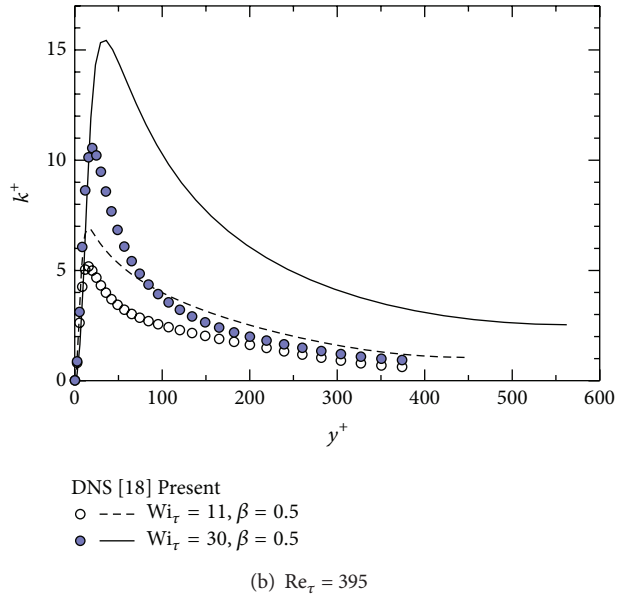
$$\tau_{total}^+ = 1 - y^*, \quad (28)$$

proving the validity of the model calculation.

The viscous shear stress is well represented by the present model throughout the entire channel, as shown in Figure 11.



(a)  $Re_\tau = 150$



(b)  $Re_\tau = 395$

FIGURE 9: Same with Figure 6, but with respect to turbulent kinetic energy,  $k^+$ .

All the shear stresses for  $Wi_\tau = 10$  are considerably close to the DNS data, indicating that nearly Newtonian fluid calculations would be also executed adequately, as can be seen in Figure 11(a). However, the other three cases shown in the figure have resulted in the overestimated peaks of  $-\overline{u^+v^+}$  and their shifts towards the channel center, compared with those by the DNS. As for the viscoelastic stress, the model exhibits tendencies to overestimate it in  $10 < y^+ < 70$  in the buffer and elastic layers and to underestimate it significantly in the outer layer. The model does, however, correctly show the dependence of the drag-reduction rate on the Weissenberg number, as given in Table 1.

To obtain a better agreement with DNS, it is necessary to further improve the modeling of the viscoelastic contribution

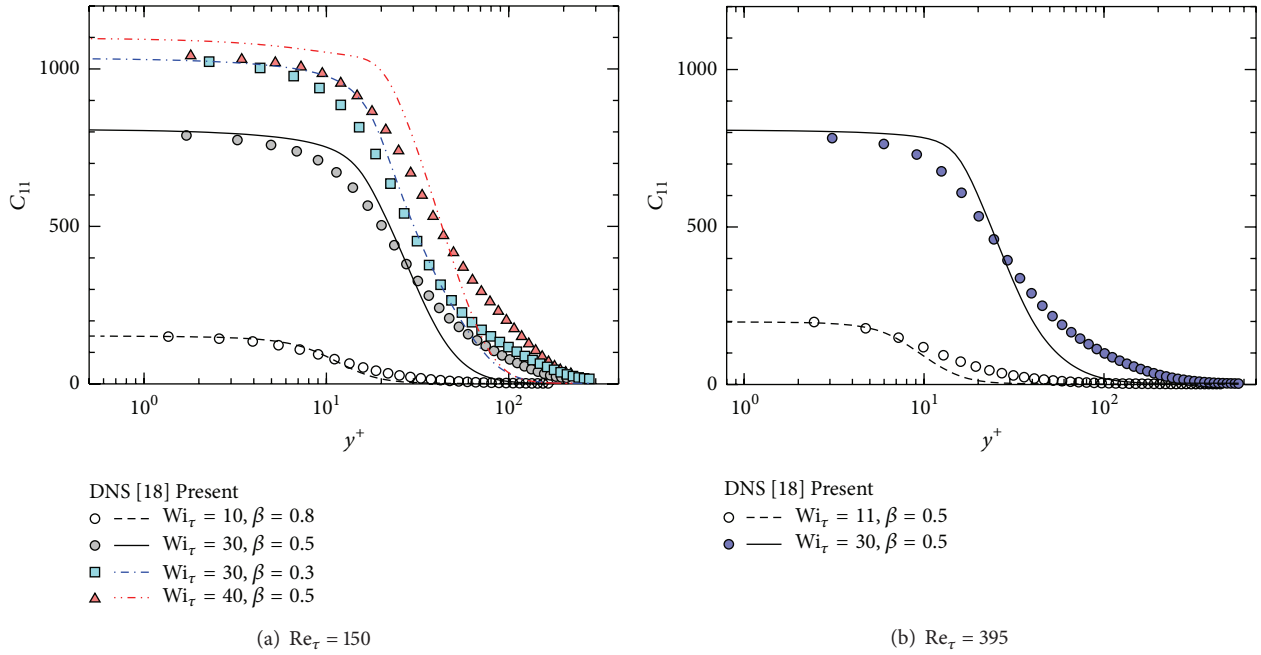


FIGURE 10: Same with Figure 6, but with respect to a conformation normal stress,  $C_{11}^+$ .

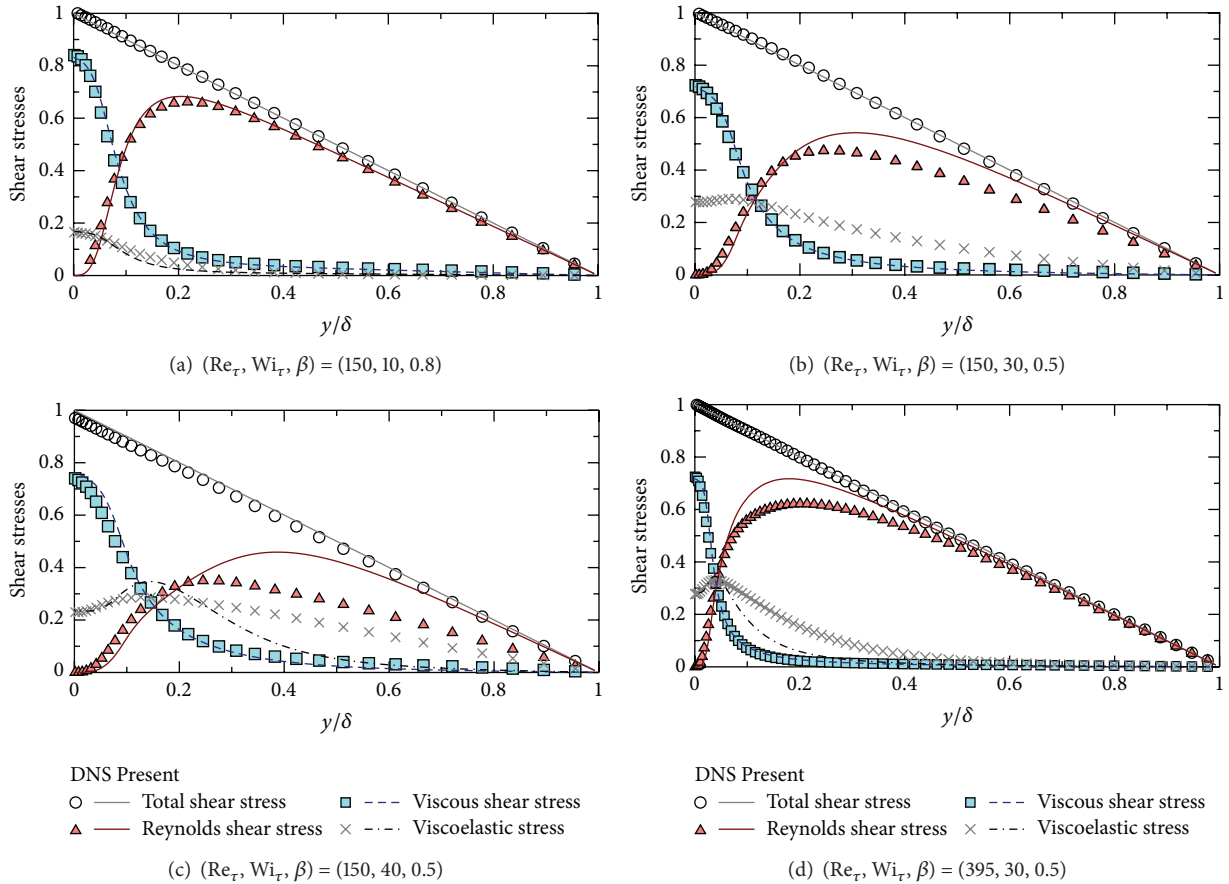


FIGURE 11: Shear stress profiles of drag-reducing viscoelastic flow in channel.

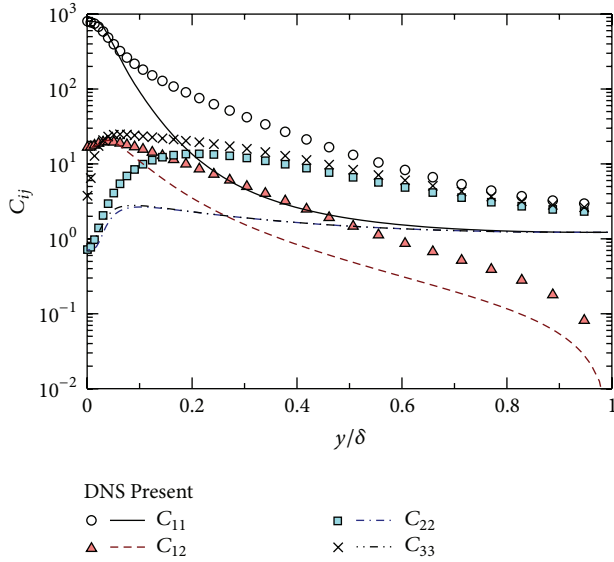


FIGURE 12: Mean conformation tensor for  $Re_\tau = 395$ ,  $Wi_\tau = 30$ , and  $\beta = 0.5$ .

in the region above the buffer layer for high Weissenberg numbers, where the drag-reduction rate is being close to the maximum drag reduction. A typical result about the profiles of  $C_{ij}$  computed by the present model is shown in Figure 12. As noted above with respect to  $C_{12}$ , the comparison with DNS data shows the present model to underestimate the conformation stresses throughout the channel except for the near-wall region.

Figure 13 shows the budget in the  $k$  transport equation of the viscoelastic fluid flow at  $Wi_\tau = 30$  and  $\beta = 0.5$ , with a moderate DR, for both the present model and the DNS data. The level of the production term calculated by the model agrees well with that of the DNS data, both in terms of its magnitude and the general shape of the curve. There is a similar agreement for the molecular diffusion, but its negative peak at  $y^+ \approx 18$  is slightly overestimated. Due to both this overestimation and the false negative peak in the pressure diffusion, the turbulent diffusion is enhanced considerably around  $y^+ = 15$ . The dissipation rate  $\varepsilon$  is in good agreement near the wall, but in the other region it is two or three times too high. This should be a deficiency due to the characteristic of the  $k$ - $\varepsilon$  model to be applied to the strongly anisotropic turbulence, as similar to that observed already in the overprediction of  $k$ . The viscoelastic contribution  $E_k^\varepsilon$  is found to be inadequately predicted as being very small compared to the other terms. This also might cause the overestimated value of  $\varepsilon$  that would compensate the unbalance (in the budget of  $k$ ) due to too small  $E_k^\varepsilon$ .

**5.3. Damping Function.** It is well known that DR is associated with a decrease in the Reynolds shear stress [4]. By adopting (16), this reduction in the Reynolds shear stress can be achieved through a decrease in  $k$ , an increase in  $\bar{\varepsilon}$ , and/or a decrease of  $f_v$ . Since, as shown already, both variations of  $k$  and  $\bar{\varepsilon}$  might not provide a significant cause of the reduction,

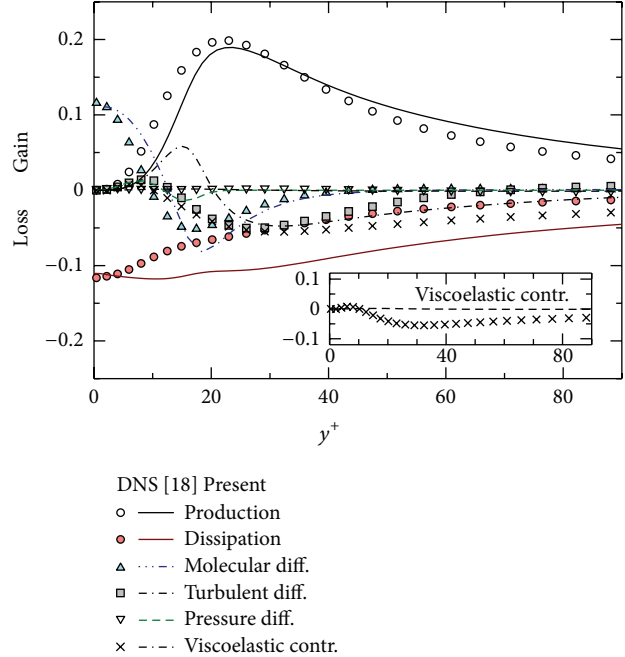


FIGURE 13: Budget of turbulent kinetic energy for drag-reducing viscoelastic fluid in turbulent channel flow at  $Re_\tau = 395$ ,  $Wi_\tau = 30$ , and  $\beta = 0.5$ .

the DR predicted well by the model must be accompanied by a large decrease of the damping function  $f_v$ . Figure 14 shows the damping function, the product of  $f_\mu$  and  $f_v$ , both for the present model and the estimated value via DNS, indicating that the present model has yielded fairly close agreement with the DNS result. It can be confirmed that the near-wall asymptotic behavior of the product of the damping functions has been well predicted via the present model. In terms of the Reynolds shear stress (Figure 11), the deviations from the DNS results are detected in the outer layer, that is,  $y/\delta > 0.1-0.2$ , and probably attributed to the inaccuracy (overestimation) of the turbulent kinetic energy in the highly turbulent region.

## 6. Conclusion

A new low-Reynolds-number  $k$ - $\varepsilon$  model including an additional damping function in the eddy viscosity was applied to predict the viscoelastic flow accompanied by turbulent drag reduction. The proposed model was constructed, based on the energy-dissipative range and the dynamic characterization of the viscoelastic fluid, and was tested by comparison with the DNS data for the drag-reduced channel flow.

The analysis of frequency response of the Giesekus model revealed that, for a high Weissenberg number, the elastic behavior of fluid should have influence on the diminishing turbulent eddy motions. Consequently, with the increasing relaxation time of the fluid, the dissipation scale of turbulent kinetic energy is increased and the viscous sublayer is thickened. The mean velocity and the drag-reduction rate were well reproduced by the present model (at least for the

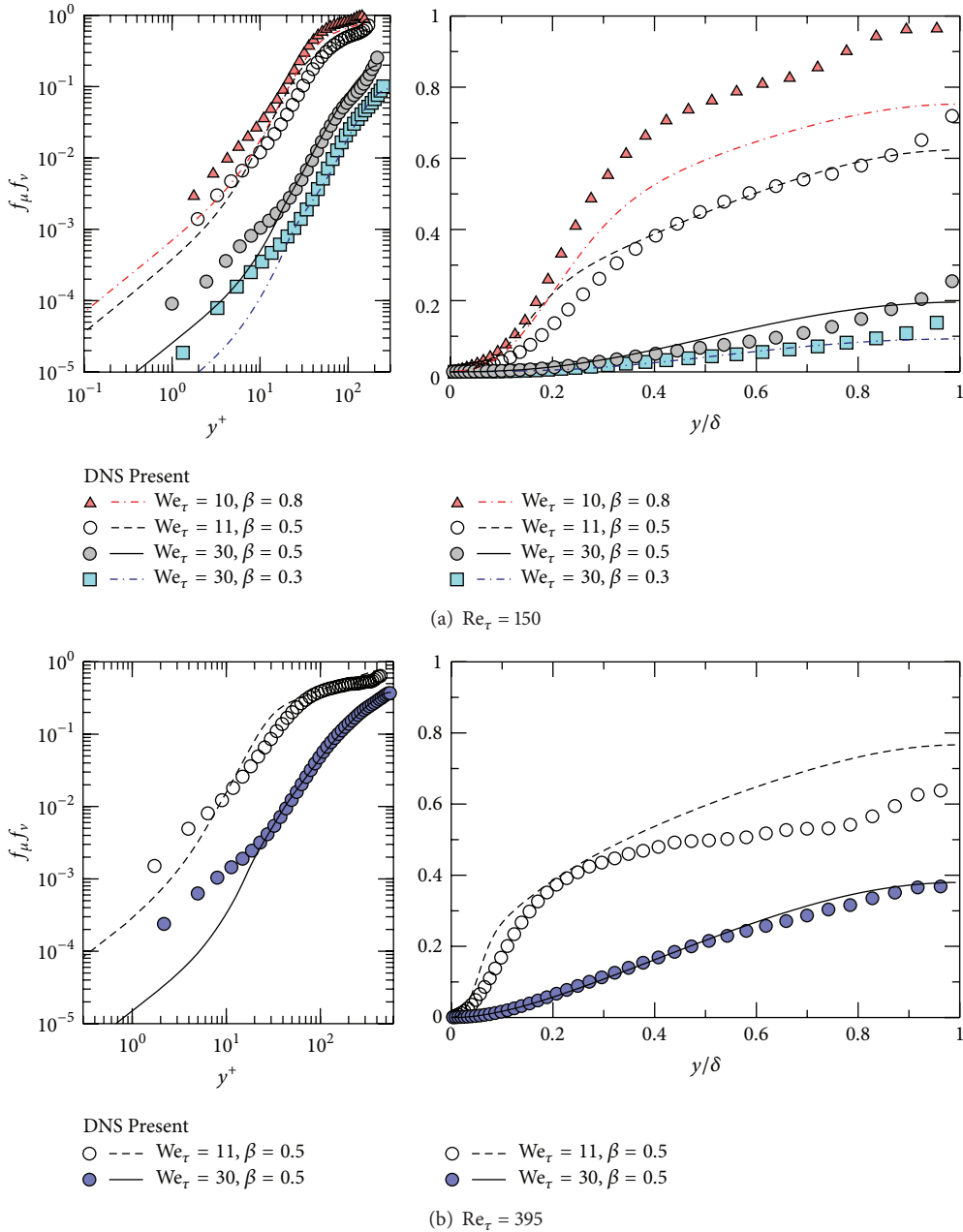


FIGURE 14: Validation of damping function, the product of  $f_\mu$  and  $f_\nu$ .

present parameters). The present model, however, showed some significant deviations from the DNS data with respect to the Reynolds shear and viscoelastic stresses, when applied for high Weissenberg numbers.

The most serious deficiency found in the present comparisons with DNS data was the overpredicted dissipation rate, which compensated the underestimated term pertaining to the viscoelastic contribution. This error in the overpredictions of the dissipation rate as well as the turbulent kinetic energy would occur in other situations relating to strongly anisotropic turbulence. One cause of this may be the insufficient model for the viscoelastic contribution in the  $k$  transport equation. It seems that the deficiency is associated

with also the inadequacy in the isotropic  $k$ - $\epsilon$  model for highly drag-reducing viscoelastic flows, although the drag-reduction phenomena in terms of bulk flows were predicted well by the present model. Hence, the model predictions should be improved further also in the framework of other models including the anisotropic/nonlinear  $k$ - $\epsilon$  model and the Reynolds stress model. In addition, the reproducibility of the MDR state and the application of the present model to practical flows and situations will be investigated in the near future.

In this paper, our discussion is restricted to the case of  $\alpha = 0.001$ . The present damping function model of (17) takes into account the inertia (through the Reynolds number),

the viscoelastic relaxation effect (through the dependence on the Weissenberg number), and the polymer/surfactant concentration in solution (through the viscosity ratio). However, any dependence on the maximum polymer effect on extensional thickening has not been explicitly involved in the model formulation. For the Giesekus model used here, the dependence on the shear thinning/thickening is controlled through the mobility factor  $\alpha$ . Only one value of that parameter has been used throughout this work because of the limited DNS database. Although not shown in this paper, some comparative verifications with DNS data at different values of  $\alpha$  [31, 32] were carried out. We confirmed the present model would work well and drew the same conclusions, at least, in the range of  $\alpha = 0.001-0.01$ . We should consider the key effect depending on  $\alpha$  further to improve the model applicable to dilute-to-dense solutions.

## Appendix

For fully-developed channel flows, some terms including the spatial derivatives in the horizontal directions can be neglected. In the following, the reduced equations for obtaining time-averaged values in the channel flow are given with being nondimensionalized by the channel half width  $\delta$ , the friction velocity  $u_\tau = \sqrt{-(\delta/\rho)\partial P/\partial x}$ , and the solution zero-shear-rate kinematic viscosity  $\nu$ .

The momentum equation

$$1 + \frac{\beta}{\text{Re}_\tau} \frac{\partial^2 U^+}{\partial y^{*2}} - \frac{\overline{\partial u^+ \nu^+}}{\partial y^*} + \frac{1-\beta}{\text{Wi}_\tau} \frac{\partial C_{12}}{\partial y^*} = 0, \quad (\text{A.1})$$

the constitutive equation

$$\begin{aligned} C_{11} &= \frac{1}{(1-2\alpha)} \\ &\times \left[ (1-\alpha) - \alpha (C_{1k} C_{k1}) \right. \\ &\quad \left. + \frac{\text{Wi}_\tau}{\text{Re}_\tau} \left( 2C_{12} \frac{\partial U^+}{\partial y^*} + \Lambda_{11}^* \right) \right], \\ C_{12} &= \frac{1}{(1-2\alpha)} \left[ -\alpha (C_{1k} C_{k2}) + \frac{\text{Wi}_\tau}{\text{Re}_\tau} \left( C_{22} \frac{\partial U^+}{\partial y^*} + \Lambda_{12}^* \right) \right], \\ C_{13} &= \frac{1}{(1-2\alpha)} \left[ -\alpha (C_{1k} C_{k3}) + \frac{\text{Wi}_\tau}{\text{Re}_\tau} \left( C_{23} \frac{\partial U^+}{\partial y^*} + \Lambda_{13}^* \right) \right], \\ C_{22} &= \frac{1}{(1-2\alpha)} \left[ (1-\alpha) - \alpha (C_{2k} C_{k2}) + \frac{\text{Wi}_\tau}{\text{Re}_\tau} \Lambda_{22}^* \right], \\ C_{23} &= \frac{1}{(1-2\alpha)} \left[ -\alpha (C_{2k} C_{k3}) + \frac{\text{Wi}_\tau}{\text{Re}_\tau} \Lambda_{23}^* \right], \\ C_{33} &= \frac{1}{(1-2\alpha)} \left[ (1-\alpha) - \alpha (C_{3k} C_{k3}) + \frac{\text{Wi}_\tau}{\text{Re}_\tau} \Lambda_{33}^* \right], \end{aligned} \quad (\text{A.2})$$

where

$$\begin{aligned} \Lambda_{ij}^* &= \frac{\psi_1 \text{Wi}_\tau}{(1-\beta) \sqrt{\beta/(\text{Re}_\tau \tilde{\varepsilon}^*)}} \overline{u_i^+ u_j^+} \\ &\quad + \frac{\psi_2}{\sqrt{\beta/(\text{Re}_\tau \tilde{\varepsilon}^*)}} (C_{ij} - \delta_{ij}), \end{aligned} \quad (\text{A.3})$$

the transport equation of  $k$ , normalized by  $\delta/u_\tau^3$ ,

$$\begin{aligned} \frac{\partial}{\partial y^*} \left[ \left( \frac{\beta}{\text{Re}_\tau} + \frac{\nu_t^*}{\sigma_k} \right) \frac{\partial k^+}{\partial y^*} \right] + \nu_t^* \left( \frac{\partial U^+}{\partial y^*} \right)^2 \\ - (\tilde{\varepsilon}^* + \varepsilon^*) - \frac{1}{2} \frac{\beta}{\text{Re}_\tau} \frac{\partial}{\partial y^*} \\ \times \left[ \frac{k^+}{\varepsilon^*} \left( \frac{\tilde{\varepsilon}^*}{\varepsilon^*} \right)^2 \frac{\partial \tilde{\varepsilon}^*}{\partial y^*} \right] - \frac{1-\beta}{2\text{Wi}_\tau} \Lambda_{ii} = 0, \end{aligned} \quad (\text{A.4})$$

and the transport equation of  $\tilde{\varepsilon}^*$ , normalized by  $\delta^2/u_\tau^4$ ,

$$\begin{aligned} \frac{\partial}{\partial y^*} \left[ \left( \frac{\beta}{\text{Re}_\tau} + \frac{\nu_t^*}{\sigma_\varepsilon} \right) \frac{\partial \tilde{\varepsilon}^*}{\partial y^*} \right] \\ + \frac{\tilde{\varepsilon}^*}{k^+} \left[ C_{\varepsilon 1} \nu_t^* \left( \frac{\partial U^+}{\partial y^*} \right)^2 - C_{\varepsilon 2} \tilde{\varepsilon} - \tilde{\varepsilon} \right] \\ + C_{\varepsilon 3} \frac{\beta}{\text{Re}_\tau} \nu_t^* \left( \frac{\partial^2 U^+}{\partial y^{*2}} \right)^2 = 0. \end{aligned} \quad (\text{A.5})$$

The Reynolds stress  $\overline{u_i^+ u_j^+}$  is given by (1) and (16).

## Nomenclature

$C_f$ :	Skin friction coefficient, $= 2\tau_w/[\rho(\int_0^1 u dy^*)^2]$
$C_{ij}$ :	Mean conformation tensor
$c_{ij}$ :	Fluctuation of conformation tensor
$C_\mu, C_{\varepsilon i}$ :	Model coefficients
DR%:	Percentage of drag reduction
$f_\nu, f_\mu$ :	Damping functions
$G$ :	Complex shear modulus
$G'$ :	Dynamic storage modulus
$G''$ :	Dynamic loss modulus
$k$ :	Turbulent kinetic energy, $= \overline{u_i u_i}/2$
$p$ :	Pressure
$\text{Re}_m$ :	Bulk Reynolds number, $= 2\rho(\int_0^1 u dy^*)\delta/\mu_0$
$\text{Re}_t$ :	Turbulence Reynolds number, $= \rho k^2/(\mu_0 \tilde{\varepsilon})$
$\text{Re}_\tau$ :	Friction Reynolds number, $= \rho u_\tau \delta/\mu_0$

$t$ :	Time
$t_\eta$ :	Kolmogorov time scale
$U_i$ :	Mean velocity vector
$u_i$ :	Fluctuation of velocity vector
$u_\tau$ :	Friction velocity, $= \sqrt{\tau_w/\rho}$
$Wi_\xi$ :	Weissenberg number, $= \lambda \dot{\gamma}_{\max}$
$Wi_\tau$ :	Friction Weissenberg number, $= \rho u_\tau^2 \lambda / \mu_0$
$x$ :	Streamwise coordinate
$y$ :	Wall-normal coordinate
$z$ :	Spanwise coordinate
$\alpha$ :	Anisotropic mobility factor
$\beta$ :	Ratio of shear viscosities, $= \mu_s / \mu_0$
$\dot{\gamma}$ :	Shear rate
$\delta$ :	Channel half width
$\varepsilon$ :	Dissipation rate of $k$
$\eta$ :	Kolmogorov length scale
$\kappa$ :	Wave number or frequency
$\kappa_K$ :	Wave number or frequency
$\lambda$ :	Relaxation time
$\mu_0$ :	Solution zero-shear-rate shear viscosity, $= \mu_s + \mu_a$
$\mu_a, (\nu_a)$ :	Shear (kinematic) viscosity of additive contribution
$\mu_s, (\nu_s)$ :	Shear (kinematic) viscosity of solvent contribution
$\mu_t, (\nu_t)$ :	Turbulent (kinematic) viscosity
$\rho$ :	Density
$\sigma_k, \sigma_\varepsilon$ :	Model coefficients
$\psi_i$ :	Model functions
$\tau_{i,j}$ :	Viscoelastic stress tensor
$\tau_w$ :	Mean wall shear stress
$(\ )^*$ :	Normalized by $u_\tau$ and $\delta$
$(\ )^+$ :	Normalized by $u_\tau$ and the effective viscosity
$(\ )$ :	Statistically averaged.

## Acknowledgments

The authors are grateful to Professor H. Kawamura (Tokyo University of Science, Suwa) for fruitful discussions and comments, and to Mr. H. Kawamoto (who was a master's course student at Tokyo University of Science) for his work. The DNS database we utilized here to assess results predicted by the present model was acquired using supercomputing resources at the Cyberscience Center at Tohoku University. This work was partially supported by Grants-in-Aid for Scientific Research (C) no. 25420131 from Japan Society for the Promotion of Science (JSPS).

## References

- [1] R. Sureshkumar, A. N. Beris, and R. A. Handler, "Direct numerical simulation of the turbulent channel flow of a polymer solution," *Physics of Fluids*, vol. 9, no. 3, pp. 743–755, 1997.
- [2] C. D. Dimitropoulos, R. Sureshkumar, and A. N. Beris, "Direct numerical simulation of viscoelastic turbulent channel flow exhibiting drag reduction: effect of the variation of rheological parameters," *Journal of Non-Newtonian Fluid Mechanics*, vol. 79, no. 2-3, pp. 433–468, 1998.
- [3] C. M. White and M. G. Mungal, "Mechanics and prediction of turbulent drag reduction with polymer additives," *Annual Review of Fluid Mechanics*, vol. 40, pp. 235–256, 2008.
- [4] F. C. Li, B. Yu, J. J. Wei, and Y. Kawaguchi, *Turbulent Drag Reduction by Surfactant Additives*, Wiley, 2012.
- [5] K. Kim and R. Sureshkumar, "Spatiotemporal evolution of hair-pin eddies, Reynolds stress, and polymer torque in polymer drag-reduced turbulent channel flows," *Physical Review E*, vol. 87, Article ID 063002, 11 pages, 2013.
- [6] J. Lumley, "Drag reduction by additives," *Annual Review of Fluid Mechanics*, vol. 1, pp. 367–384, 1969.
- [7] L. Thais, T. B. Gatski, and G. Mompean, "Some dynamical features of the turbulent flow of a viscoelastic fluid for reduced drag," *Journal of Turbulence*, vol. 13, no. 12, 26 pages, 2012.
- [8] L. Thais, G. Mompean, and T. B. Gatski, "Spectral analysis of turbulent viscoelastic and Newtonian channel flows," *Journal of Non-Newtonian Fluid Mechanics*, vol. 200, pp. 165–176, 2003.
- [9] T. Tsukahara, T. Kawase, and Y. Kawaguchi, "DNS of viscoelastic turbulent channel flow with rectangular orifice at low Reynolds number," *International Journal of Heat and Fluid Flow*, vol. 32, no. 3, pp. 529–538, 2011.
- [10] T. Tsukahara, M. Motozawa, D. Tsurumi, and Y. Kawaguchi, "PIV and DNS analyses of viscoelastic turbulent flows behind a rectangular orifice," *International Journal of Heat and Fluid Flow*, vol. 41, pp. 66–79, 2013.
- [11] R. Leighton, D. T. Walker, T. Stephens, and G. Garwood, "Reynolds stress modeling for drag reducing viscoelastic flows," in *Proceedings of the 4th ASME/JSME Joint Fluids Engineering Conference*, pp. 735–744, Honolulu, Hawaii, USA, July 2003.
- [12] D. O. A. Cruz and F. T. Pinho, "Turbulent pipe flow predictions with a low Reynolds number  $k$ - $\varepsilon$  model for drag reducing fluids," *Journal of Non-Newtonian Fluid Mechanics*, vol. 114, no. 2-3, pp. 109–148, 2003.
- [13] F. T. Pinho, C. F. Li, B. A. Younis, and R. Sureshkumar, "A low Reynolds number turbulence closure for viscoelastic fluids," *Journal of Non-Newtonian Fluid Mechanics*, vol. 154, no. 2-3, pp. 89–108, 2008.
- [14] P. R. Resende, K. Kim, B. A. Younis, R. Sureshkumar, and F. T. Pinho, "A FENE-P  $k$ - $\varepsilon$  turbulence model for low and intermediate regimes of polymer-induced drag reduction," *Journal of Non-Newtonian Fluid Mechanics*, vol. 166, no. 12-13, pp. 639–660, 2011.
- [15] G. Iaccarino, E. S. G. Shaqfeh, and Y. Dubief, "Reynolds-averaged modeling of polymer drag reduction in turbulent flows," *Journal of Non-Newtonian Fluid Mechanics*, vol. 165, no. 7-8, pp. 376–384, 2010.
- [16] P. R. Resende, F. T. Pinho, B. A. Younis, K. Kim, and R. Sureshkumar, "Development of a Low-Reynolds-number  $k$ - $\omega$  Model for FENE-P Fluids," *Flow Turbulence and Combustion*, vol. 90, pp. 89–108, 2013.
- [17] J. Bredberg, S.-H. Peng, and L. Davidson, "An improved  $k$ - $\omega$  turbulence model applied to recirculating flows," *International Journal of Heat and Fluid Flow*, vol. 23, no. 6, pp. 731–743, 2002.
- [18] T. Tsukahara, T. Ishigami, B. Yu, and Y. Kawaguchi, "DNS study on viscoelastic effect in drag-reduced turbulent channel flow," *Journal of Turbulence*, vol. 12, article N13, pp. 1–25, 2011.
- [19] W. P. Jones and B. E. Launder, "The prediction of laminarization with a two-equation model of turbulence," *International Journal of Heat and Mass Transfer*, vol. 15, no. 2, pp. 301–314, 1972.
- [20] Y. Nagano and M. Tagawa, "An improved  $k$ - $\varepsilon$  model for boundary layer flows," *Journal of Fluids Engineering*, vol. 112, no. 1, pp. 33–39, 1990.

- [21] E. R. van Driest, "On turbulent flow near a wall," *Journal of the Aeronautical Sciences*, vol. 23, no. 11, pp. 1007–1011, 1956.
- [22] H. Abe, H. Kawamura, and Y. Matsuo, "Direct numerical simulation of a fully developed turbulent channel flow with respect to the Reynolds number dependence," *Journal of Fluids Engineering*, vol. 123, pp. 382–393, 2001.
- [23] K. R. Sreenivasan and C. M. White, "The onset of drag reduction by dilute polymer additives, and the maximum drag reduction asymptote," *Journal of Fluid Mechanics*, vol. 409, pp. 149–164, 2000.
- [24] H. Tennekes and J. L. Lumley, *A First Course in Turbulence*, MIT Press, Cambridge, Mass, USA, 1972.
- [25] S. B. Pope, *Turbulent Flows*, Cambridge University Press, Cambridge, Mass, USA, 2000.
- [26] P. S. Virk, "An elastic sublayer model for drag reduction by dilute solutions of linear macromolecules," *Journal of Fluid Mechanics*, vol. 45, pp. 417–440, 1971.
- [27] H. Giesekus, "A simple constitutive equation for polymer fluids based on the concept of deformation-dependent tensorial mobility," *Journal of Non-Newtonian Fluid Mechanics*, vol. 11, no. 1-2, pp. 69–109, 1982.
- [28] N. Kawashima and H. Kawamura, "Reconstruction of  $k$ - $\varepsilon$  model with relevance to the wall- asymptotic behavior," *Transactions of the Japan Society of Mechanical Engineers B*, vol. 62, no. 597, pp. 1700–1708, 1996 (Japanese).
- [29] M. D. Warholic, D. K. Heist, M. Katcher, and T. J. Hanratty, "A study with particle-image velocimetry of the influence of drag-reducing polymers on the structure of turbulence," *Experiments in Fluids*, vol. 31, no. 5, pp. 474–483, 2001.
- [30] M. Motozawa, T. Watanabe, W. Gu, and Y. Kawaguchi, "Experimental investigation on zonal structure in drag-reducing channel flow with surfactant additives," *Advances in Mechanical Engineering*, vol. 2011, Article ID 120438, 12 pages, 2011.
- [31] B. Yu and Y. Kawaguchi, "Direct numerical simulation of visco-elastic drag-reducing flow: a faithful finite difference method," *Journal of Non-Newtonian Fluid Mechanics*, vol. 116, no. 2-3, pp. 431–466, 2004.
- [32] B. Yu, F. Li, and Y. Kawaguchi, "Numerical and experimental investigation of turbulent characteristics in a drag-reducing flow with surfactant additives," *International Journal of Heat and Fluid Flow*, vol. 25, no. 6, pp. 961–974, 2004.

## Research Article

# Multiphase, Multicomponent Simulation for Flow and Transport during Polymer Flood under Various Wettability Conditions

**Ji Ho Lee and Kun Sang Lee**

*Department of Natural Resources and Environmental Engineering, Hanyang University, Seoul 133-791, Republic of Korea*

Correspondence should be addressed to Kun Sang Lee; [kunslee@hanyang.ac.kr](mailto:kunslee@hanyang.ac.kr)

Received 10 June 2013; Accepted 21 October 2013

Academic Editor: Shuyu Sun

Copyright © 2013 J. H. Lee and K. S. Lee. This is an open access article distributed under the Creative Commons Attribution License, which permits unrestricted use, distribution, and reproduction in any medium, provided the original work is properly cited.

Accurate assessment of polymer flood requires the understanding of flow and transport of fluids involved in the process under different wettability of reservoirs. Because variations in relative permeability and capillary pressure induced from different wettability control the distribution and flow of fluids in the reservoirs, the performance of polymer flood depends on reservoir wettability. A multiphase, multicomponent reservoir simulator, which covers three-dimensional fluid flow and mass transport, is used to investigate the effects of wettability on the flow process during polymer flood. Results of polymer flood are compared with those of waterflood to evaluate how much polymer flood improves the oil recovery and water-oil ratio. When polymer flood is applied to water-wet and oil-wet reservoirs, the appearance of influence is delayed for oil-wet reservoirs compared with water-wet reservoirs due to unfavorable mobility ratio. In spite of the delay, significant improvement in oil recovery is obtained for oil-wet reservoirs. With respect to water production, polymer flood leads to substantial reduction for oil-wet reservoirs compared with water-wet reservoirs. Moreover, application of polymer flood for oil-wet reservoirs extends productive period which is longer than water-wet reservoir case.

## 1. Introduction

After primary and secondary oil recovery, there remains lots of oil in place in the reservoirs. To gain unrecovered oil in the reservoirs, additional flood, called enhanced oil recovery (EOR) method, is needed to be applied. Polymer flood has been known as one of the most widely used chemical EOR method. Increased viscosity of displacing fluid by adding low concentrations of water soluble and high molecular weight polymer into water produces the lower mobility ratio. Favorable mobility ratio improves the sweep efficiency so that oil recovery is increased.

Craig defined wettability as the tendency of one fluid to spread on or adhere to a solid surface in the presence of other immiscible fluids [1]. The influences of reservoir wettability on multiphase flow on porous medium and hence on oil recovery have been well known. The wettability of a rock controls the location, flow, and distribution of fluids within reservoir rocks [2], which affects the relative permeability and capillary pressure [3, 4]. Therefore, the recovery of

polymer flood in oil-wet reservoirs is totally different from that in water-wet reservoirs. Also, considerable hydrocarbon reserves are remained in mixed-wet or oil-wet reservoirs. Consequently, there is a necessity to better understand the effects of wettability on the oil recovery during polymer flood. Most of polymer flood studies have been carried out without considering wettability effect or focused on water-wet reservoirs with respect to field scale [5–7]. The investigations on the role of wettability on the various aspects of oil recovery during polymer flooding have been mainly based on the experimental works [8–10]. Therefore, there is need to conduct comprehensive numerical study on the flow and transport of aqueous and oleic phases during polymer flood under various wetting conditions on field scale.

## 2. Mathematical Formulation

Simulations of polymer flood were conducted with UTCHEM, which is a 3D, multicomponent, multiphase,

compositional model of chemical flooding processes considering complex phase behavior, chemical and physical transformation, and heterogeneous porous media properties [11].

The basic mass conservation equation for components can be written as follows:

$$\frac{\partial}{\partial t} (\phi \bar{C}_\kappa \rho_\kappa) + \nabla \cdot \left[ \sum_{l=1}^{n_p} \rho_\kappa (C_{\kappa l} \mathbf{u}_l - \mathbf{D}_{\kappa l}) \right] = R_\kappa, \quad (1)$$

where  $\kappa$  is the component index,  $j$  is the phase index including aqueous ( $w$ ) and oleic ( $o$ ) phases,  $\phi$  is the porosity,  $\bar{C}_\kappa$  is the overall concentration of component  $\kappa$  (volume fraction),  $\rho_\kappa$  is the density of component  $\kappa$  [ $\text{ML}^{-3}$ ],  $n_p$  is the number of phases,  $C_{\kappa j}$  is the concentration of component  $\kappa$  in phase  $j$  (volume fraction),  $\mathbf{u}_j$  is Darcy velocity of phase  $j$  [ $\text{LT}^{-1}$ ],  $R_\kappa$  is the total source/sink term for component  $\kappa$  (volume of component  $\kappa$  per unit volume of porous media per unit time),  $\mathbf{D}_{\kappa j}$  is the dispersion tensor.

The phase flux from Darcy's law is

$$\mathbf{u}_j = -\frac{\mathbf{k}k_{rj}}{\mu_j} \nabla (p_j - \gamma_j h), \quad (2)$$

where  $\mathbf{k}$  is the intrinsic permeability tensor,  $h$  is the vertical depth,  $k_{rj}$  is the relative permeability,  $\mu_j$  is the viscosity, and  $\gamma_j$  is the specific weight of phase  $j$ .

To predict the reservoir behavior under multiphase condition, it is important to understand relative permeability of a reservoir rock to each of the fluids flowing through it. Relative permeability is assumed to be solely determined by own saturation and residual saturations and investigated by experimental and analytical methods [12]. Extensive studies have been conducted resulting in representative correlations between relative permeability, saturation, and other factors [12]. In this study, multiphase relative permeabilities are modeled with Corey-type functions [11]. Corey-type relative permeability is expressed with relative permeability on residual saturation, exponent defining the curvature of relative permeability, and residual saturation determining normalized saturation. Corey-type relative permeability equation is given as follows:

$$k_{rj} = k_{rj}^o S_{nj}^{n_j} \quad \text{for } j = w, o, \quad (3)$$

where  $k_{rj}^o$  is the end point of relative permeability meaning relative permeability at residual saturation,  $n_j$  is the exponent of relative permeability of phase  $j$  determining the curvature of relative permeability,  $S_{nj}$  represents the normalized saturation of phase  $j$  calculated as follows:

$$S_{nj} = \frac{S_j - S_{jr}}{1 - \sum_{j=1}^{n_p} S_{jr}}, \quad (4)$$

where  $S_j$  is the saturation of phase  $j$  and  $S_{jr}$  is the residual saturation of phase  $j$ .

Whether oil displaces water or water displaces oil through flow channels in reservoirs, flow phenomenon for immiscible

fluid phases, oil and water, is involved with the pressure difference between these phases. Brooks and Corey observed a large number of data on consolidated rock cores and analyzed them by plotting the logarithm of effective saturation versus the logarithm of capillary pressure [13]. Due to this study, linear relationship between logarithm of effective saturation and logarithm of capillary pressure has been revealed and is shown as follows:

$$\ln S_e = -\lambda \ln p_c + \lambda \ln p_b \quad \text{for } p_c \geq p_b, \quad (5)$$

where  $S_e$  is the effective saturation calculated with residual saturations,  $\lambda$  and  $p_b$  are constants realized from intercept and slope,  $\lambda$  means pore size distribution,  $p_b$  is interpreted as maximum capillary pressure, the  $p_c$  is the capillary pressure which represents pressure difference between wetting phase pressure and nonwetting phase pressure.

Capillary pressure is strong function of saturation as presented by (5). Leverett derived capillary pressure scaled by soil permeability and porosity for homogeneous reservoirs [11, 14]. Reflected on previous relations, Brooks and Corey capillary pressure-saturation is calculated as follows:

$$p_c = p_b \sqrt{\frac{\phi}{k}} \quad \text{for } j = w, o, \quad (6)$$

$$p_b = C_{pc} (1 - S_{nj})^{E_{pc}},$$

where  $E_{pc}$  is equivalent to  $-(1/\lambda)$ ,  $C_{pc}$  is constant, and  $k$  and  $\phi$  are the permeability and the porosity of the reservoirs.

### 3. Numerical Modeling

This study analyzes the effect of wettability on flow and transport of fluids during polymer flood. Reservoir wettability is implemented in the numerical model by changing relative permeability and capillary pressure curves simultaneously. The reservoir depth is 2,000 ft and initial reservoir pressure is maintained at 400 psi. Horizontal area is  $360 \times 360 \text{ ft}^2$  and vertical thickness of reservoir is 25 ft. The simulation domain consists of 10 layers and each layer is discretized into  $15 \times 15$  grid blocks in horizontal direction. As close to production and injection wells, grid block has smaller size comparing with blocks which are away from wells to assess pressures and saturations more accurately near wells. The model assumes that the reservoir is homogeneous so the porosity and permeability are constant everywhere as 0.2 and 300 md for horizontal direction and 30 md for vertical direction. The initial saturations of oil and water are assumed to be constant for 0.62 and 0.38, respectively. Properties of water and oil in reservoir are listed in Table 1. Water for injection is assumed to be identical as water in reservoir. Viscosity of polymeric solution including salinity and mechanical effects is considered as listed in Table 1.

The simulation was continued over 1,000 days. Injection designs for water and polymeric solution with conditions of constant rate are assumed to be identical for both water-wet and oil-wet reservoirs cases to access the performance of polymer flood quantitatively. To prevent high injection

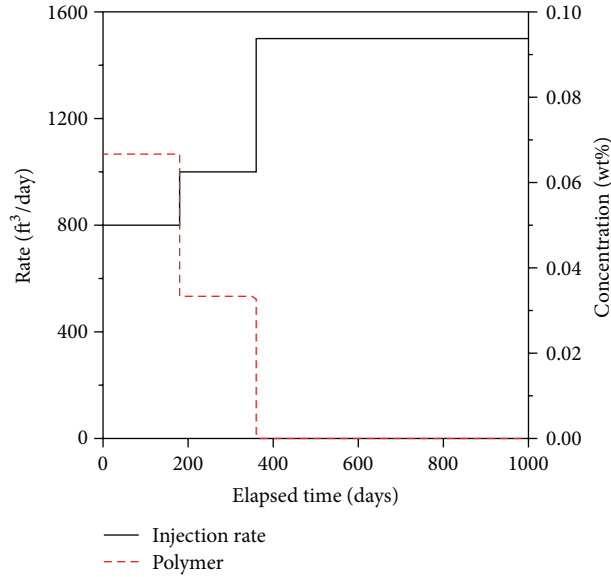


FIGURE 1: History of injection rate and polymer concentration.

TABLE 1: Properties of water and oil and viscosity of polymeric solution.

Fluid		
Viscosity ( $\mu$ )	Water	0.73 cp
	Oil	40 cp
Density ( $\rho$ )	Water	0.43353 psi/ft
	Oil	0.385839 psi/ft
Compressibility ( $C_f$ )	Water	0 psi <sup>-1</sup>
	Oil	0 psi <sup>-1</sup>
Polymer viscosity		
Parameters for zero shear viscosity	$A_{p1}$	38.47 wt% <sup>-1</sup>
	$A_{p2}$	1,600 wt% <sup>-2</sup>
	$A_{p3}$	0 wt% <sup>-3</sup>
Parameters for effective salinity	$\beta_p$ for $C_{SEP}$	20
	$C_{SEP,min}$	0.01 meq/mL
	Slope of $\mu_p^o$ versus $C_{SEP}$	-0.3
Parameters for shear rate dependence	$\dot{\gamma}_c$	130 day (darcy) <sup>0.5</sup> /ft·s
	$\dot{\gamma}_{1/2}$	280
	$P_a$	2.2

pressure due to increased viscosity of polymeric solution, injection of water and polymeric solution was operated in three steps as given in Figure 1. The flow rate of solution was constant at each step. In the first step, with 0.1% of polymer, injection was operated at low rate as 800 ft<sup>3</sup>/day to prevent fractures on the injection well until 180 days. In the next step, the concentration of polymer was reduced to 0.05%, whereas the flow rate of injection was increased to 1,000 ft<sup>3</sup>/day by 360 days. In the last step, from 360 to 1,000 days, only water was injected through well by the end of operation. The reservoir

fluids were recovered from the production well constrained with at 200 psi.

In order to analyze the effect of wettability on the flow and transport of fluids during polymer flood, comparisons were made for results from simulations implementing different relative permeability curves and capillary pressure curves. Relative permeability and capillary pressure are the most important factors that show the different performances of polymer flood applied to water-wet and oil-wet reservoirs. To model wettability effect, data for different relative permeabilities and capillary pressure curves are attained from several studies. Anderson derived an equation of Corey-type functions by curve fitting the data measured by Morrow et al. [15–17]. Table 1 lists fitted relative permeability parameters and Figure 2(a) shows relative permeability curves generated with the parameters.

Calculation of capillary pressure is based on Brooks and Corey equation as previously explained. Capillary pressure end point,  $C_{pc}$ , and capillary pressure exponent,  $E_{pc}$ , for water-wet and oil-wet reservoirs are listed in Table 2 [17]. Capillary pressures are also calculated with the data as shown in Figure 2(b).

## 4. Results and Discussion

Based on the simulation results, comparisons were made between the performances of polymer flood and waterflood applied to water-wet and oil-wet reservoirs. The results were presented with cumulative oil recovery, water-oil ratio, and oil saturation distribution of the fifth (middle) layer. To decide whether application of polymer flood for oil-wet reservoirs is effective or not, water cut was also analyzed.

Figures 3(a) and 3(b) present the cumulative oil recovery and water-oil ratio which was obtained from the application of waterflood and polymer flood to water-wet reservoirs. As

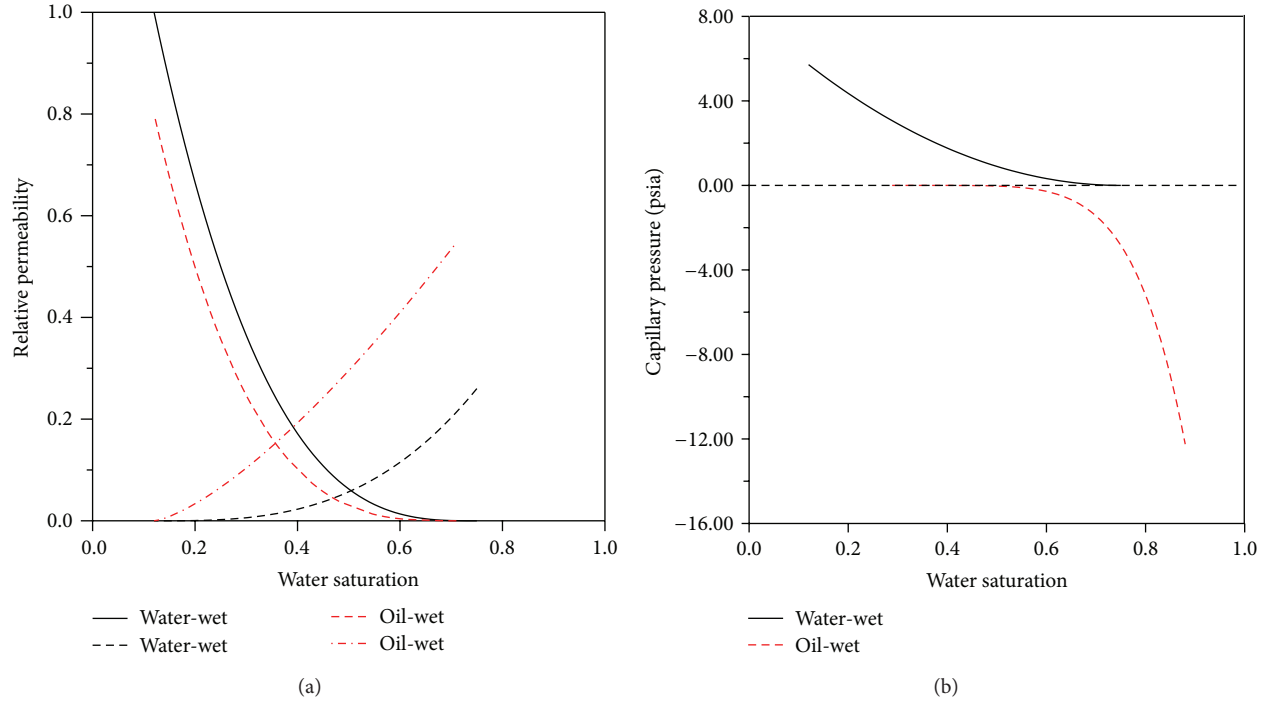


FIGURE 2: Properties of water-wet and oil-wet reservoirs: (a) relative permeability curves and (b) capillary pressure curves.

TABLE 2: Input parameters for capillary pressure and relative permeability depending on wettability.

Parameters	$S_{wr}$	$S_{or}$	$k_{rw}^o$	$k_{ro}^o$	$n_w$	$n_o$
Relative permeability						
Water-wet	0.12	0.25	0.26	1	3	1.3
Oil-wet	0.12	0.28	0.56	0.8	1.4	3.3
Parameters	$C_{pc}$		$E_{pc}$			
Capillary pressure						
Water-wet	7		2			
Oil-wet	-15		6			

can be seen, the cumulative oil recovery by polymer flood is 0.58, which is considerably higher than the oil recovery by waterflood, 0.40, at the end of production. In terms of water-oil ratio, polymer flood results in lower water-oil ratio from 70 to 850 days, not from the initiation of injection. Even though polymeric solution is injected with a start of simulation, it takes time, 70 days in this model, to manifest the effect of polymer flood so that no improvement can be seen until 70 days. After 850 days, polymer flood already recovers almost movable oil in reservoirs, so that significant water production and lower increment of oil recovery are obtained. These improvements, higher oil recovery and lower water-oil ratio, during 70 days to 850 days result from increased viscosity of polymeric solution leading to lower or favorable mobility ratio. Furthermore, productive period is calculated to prove the influence of polymer flood applied to water-wet reservoir compared with waterflood case. The life span of

production is determined with the assumption that producer is valid until it produces 90% of water cut. Considering results shown in Figure 5(a), polymer flood for water-wet reservoir sustains productive period of 160 days longer than that of waterflood case.

In attempts to study the effectiveness of polymer flood in oil-wet reservoirs, relative permeability and capillary pressure curves are set to be as Figures 2(a) and 2(b). Figures 4(a) and 4(b) compare the cumulative oil recovery and water-oil ratio between numerical simulations of polymer flood and waterflood for oil-wet reservoir. Application of polymer flood to oil-wet reservoir increases cumulative recovery as much as 0.36 which is higher than the result of waterflood case, 0.08, and decreases water-oil ratio significantly. According to the calculation of productive period, while production by waterflood seems invalid for whole production period due to higher water cut as much as 90%, polymer flood extends the life span of the well as much as 315 days as shown Figure 5(b). From the analysis of the average reservoir pressure in application of polymer flood shown in Figure 6, pressure profile for oil-wet reservoir has been maintained to be lower than water-wet reservoir. Due to the high viscosity of polymeric solution, pressure starts to be increased initially regardless of wettability. After post-flush as waterflood is applied, it is going to be decreased.

Despite of these effective performances of polymer flood for oil-wet reservoirs, utilization of polymer flood has not widely fulfilled. As shown in Figures 3 and 4, lower recovery and higher water-oil ratio are observed than those of water-wet reservoirs when both waterflood and polymer flood are applied to oil-wet reservoirs. In agreement with previous

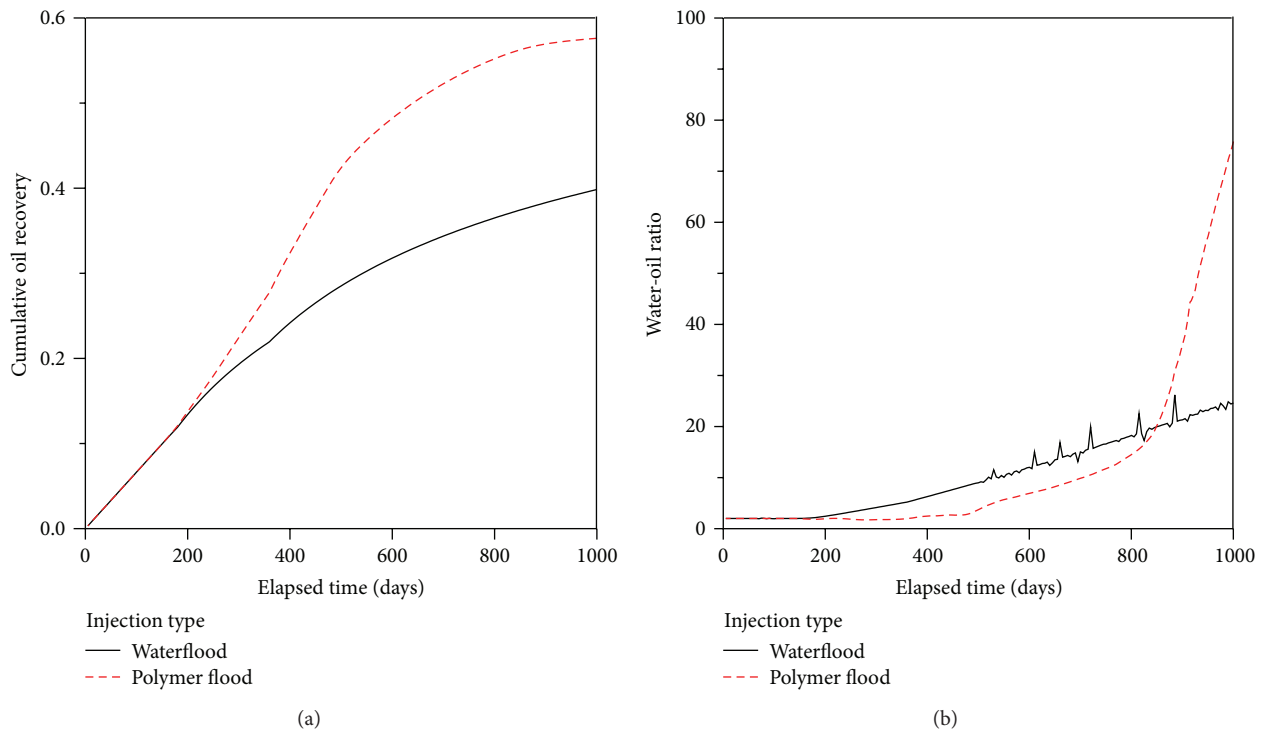


FIGURE 3: Comparison of waterflood and polymer flood for water-wet reservoir: (a) cumulative oil recovery and (b) water-oil ratio.

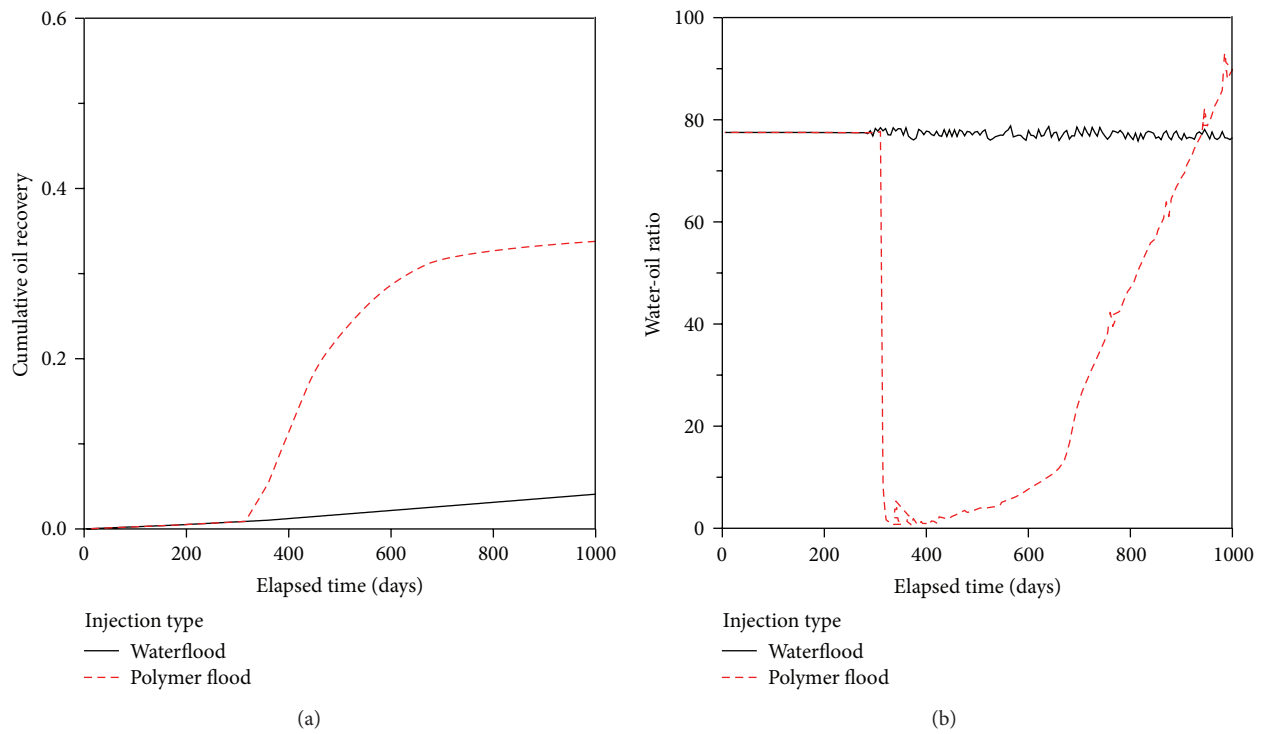


FIGURE 4: Comparison of waterflood and polymer flood for oil-wet reservoir: (a) cumulative oil recovery and (b) water-oil ratio.

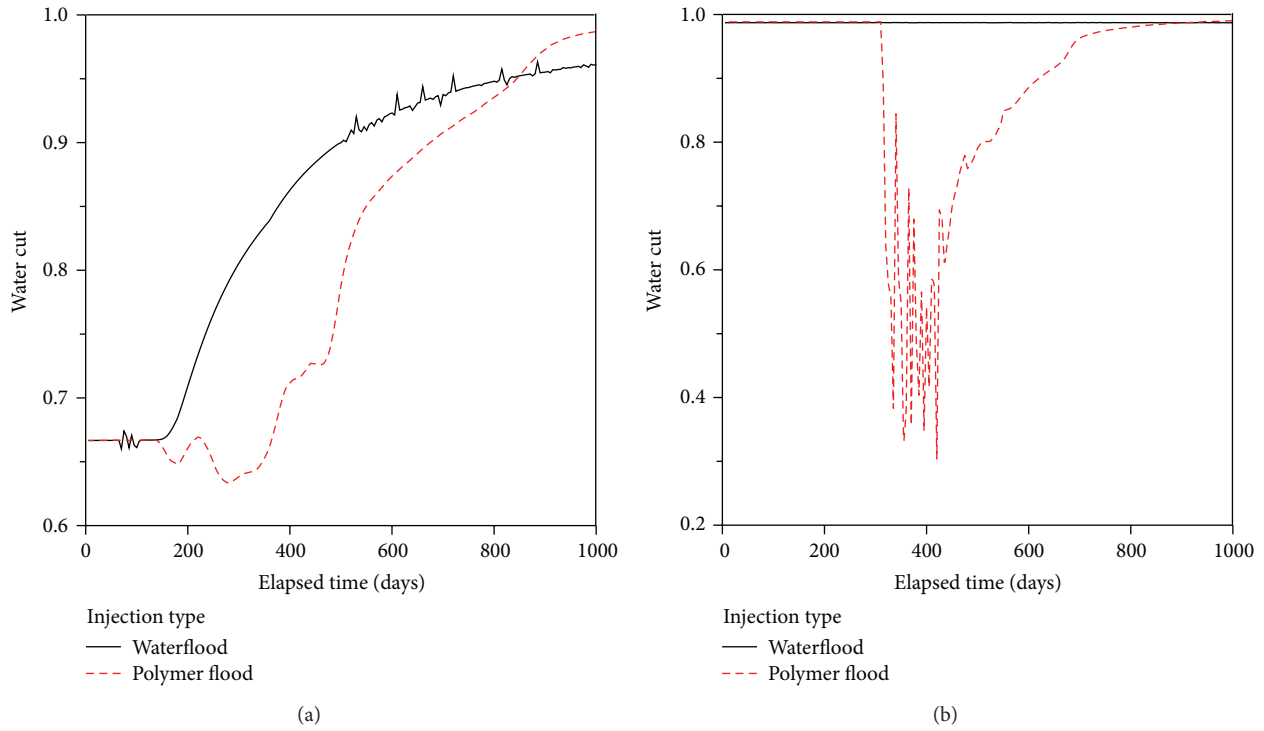


FIGURE 5: Water cut of waterflood and polymer flood depending on wettability: (a) water-wet and (b) oil-wet.

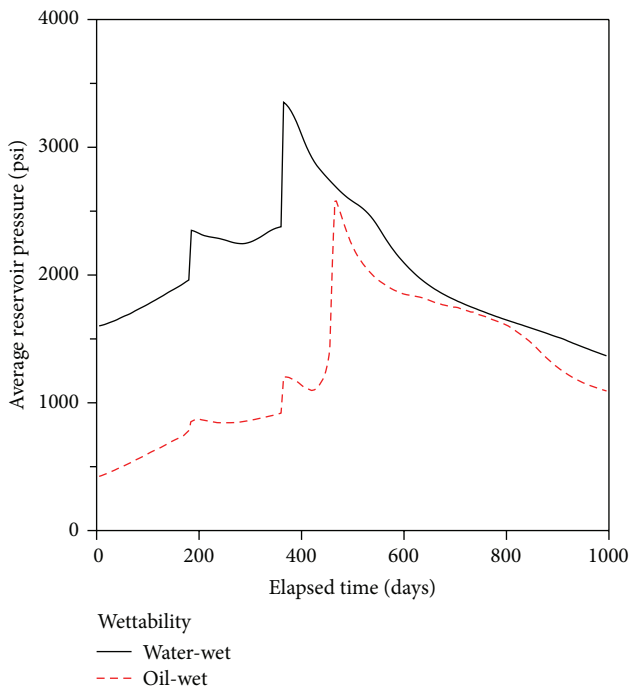


FIGURE 6: Average reservoir pressure profiles for polymer flood depending on wettability.

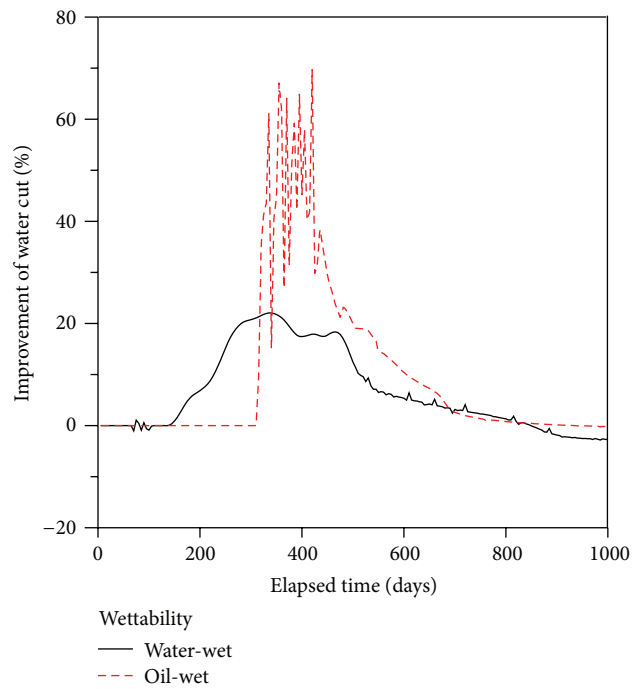


FIGURE 7: Improvement of water cut depending on wettability.

studies, the performance of polymer flood in oil-wet reservoir seems less effective than that in water-wet reservoir. These results could draw the conclusion that the application of

polymer flood to oil-wet seems not very effective and may not be recommended because it still shows low performance. However, not only the absolute value of oil recovery and water-oil ratio but also the improvement should be analyzed

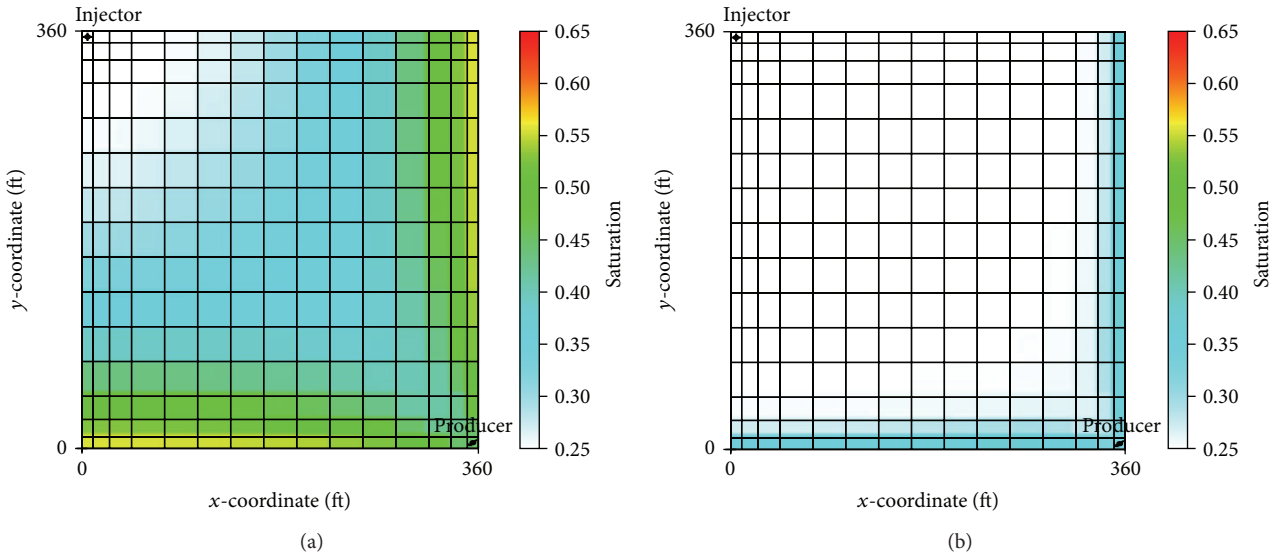


FIGURE 8: Comparison of oil saturation distribution in the fifth layer at 1,000 days for water-wet reservoir: (a) waterflood and (b) polymer flood.

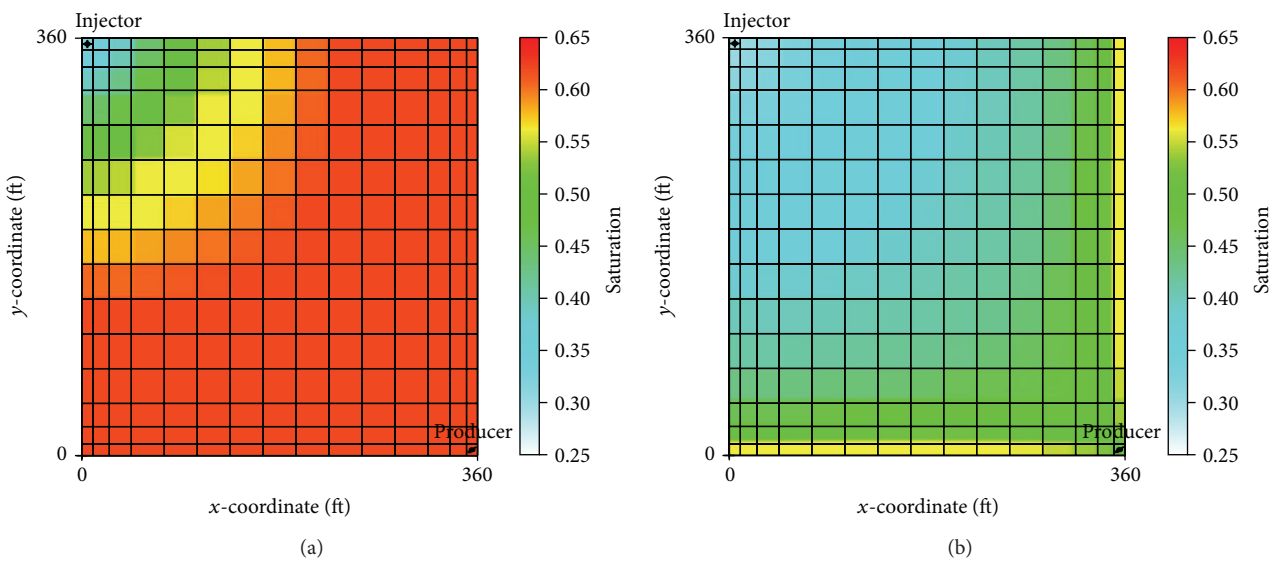


FIGURE 9: Comparison of oil saturation distribution in the fifth layer at 1,000 days for oil-wet reservoir: (a) waterflood and (b) polymer flood.

to consider efficiency of polymer flood. Therefore, additional analysis was repeated with respect to improvement by polymer flood. For water-wet reservoirs, polymer flood increases cumulative oil recovery up to 45% than that of waterflood from 0.40 to 0.58. Polymer flood also reduces water-oil ratio at least 50% less than the waterflood case. If there is enough capability for waterflood to produce high performance, these improvements attained by polymer flood may not be so significant. Whereas, for the oil-wet reservoirs, the application of polymer flood leads to substantial improvement of oil recovery and extensive reduction of water-oil ratio compared with waterflood case due to low performance of waterflood. As shown in Figure 5(b), when waterflood is applied to oil-wet reservoirs, it already exceeds 90% water cut

at the early stage and it increases up to 99%. Because of high water production, waterflood should be suspended for oil-wet reservoir. However, polymer flood reduces water-oil ratio as much as maximum 90% compared with waterflood case, so that it makes oil-wet reservoirs as fruitful. Moreover, polymer flood leads to increment of oil recovery as much as 351% at the end of production as shown in Figure 4. Additionally, analysis on improvements of water cut by polymer flood for different wettability is calculated and shown in Figure 7. Even though polymer flood for water-wet reservoirs represents the maximum reduction of water cut as much as 22%, it results in reduction of as much as 80% for oil-wet reservoirs. Also, it sustains longer productive period as much as 315 days compared with that of water-wet reservoirs, 160 days,

as shown in Figures 5 and 7. Therefore, the application of polymer flood results in more significant improvement in the case of oil-wet reservoir than in the case of water-wet reservoir.

Figure 8 compares remained oil saturation in the fifth layer in application of waterflood and polymer flood to water-wet reservoirs at 1,000 days or 1.98 pore volumes injected. Due to the favorable mobility ratio by polymer flood, relatively higher contrast of oil saturation between swept and unswept regions exists in reservoir. On the other hand, Figure 9 shows simulated oil saturation in the same condition like Figure 8, except for wettability as oil-wet reservoir. The overall oil saturation of polymer-flooded water-wet reservoirs is lower than that of water-flooded scheme and is almost close to residual oil saturation. For oil-wet reservoirs, remained oil saturation is still higher than residual oil saturation after polymer flood is applied. Nevertheless, the contrast of oil saturation distribution between before and after polymer flood is applied is clearly seen in oil-wet reservoirs rather than water-wet reservoirs.

## 5. Conclusions

According to multiphase, multicomponent simulation, polymer flood allows the mobility ratio between aqueous and oleic fluids to be favorable, which increases oil recovery and decreases water-oil ratio in both water-wet and oil-wet reservoir conditions. The efficiency of polymer flood is remarkably affected by reservoir wettability. Performance of polymer flood for water-wet condition seems better than that for oil-wet condition. Because polymer flood is kind of modified waterflood, polymeric solution can displace oil out of the pore easily in water-wet scheme so that it sweeps lots of mobile oil and leaves just a little oil including residual oil saturation. This mechanism results in higher recovery for water-wet reservoir than oil-wet one. It could mislead us that polymer flood for oil-wet reservoirs is not effective as much as that for water-wet reservoirs. If anything, application of polymer flood to oil-wet reservoirs clearly shows higher improvement of oil recovery, water-oil ratio, and productive period than that of water-wet reservoirs. These results demonstrate that oil-wet reservoirs seem good candidates for the application of polymer flood because the technique is very effective in terms of the improvement of performance. Therefore, reliable evaluation of polymer flood should take into account wettability of reservoirs.

## Acknowledgments

This work was supported by the Energy Efficiency and Resources of the Korea Institute of Energy Technology Evaluation and Planning (KETEP) Grant funded by the Korean government, Ministry of Trade, Industry and Energy (20122010300020).

## References

- [1] F. F. Craig, *The Reservoir Engineering Aspects of Waterflooding*, vol. 3 of *SPE Monograph Series*, Society of Petroleum Engineers, 1971.
- [2] W. G. Anderson, "Wettability literature survey—part 1: rock/oil/brine interactions and the effects of core handling on wettability," *Journal of Petroleum Technology*, vol. 38, no. 11, pp. 1125–1144, 1986.
- [3] W. G. Anderson, "Wettability literature survey—part 5: the effects of wettability on relative permeability," *Journal of Petroleum Technology*, vol. 39, no. 11, pp. 1453–1468, 1987.
- [4] W. G. Anderson, "Wettability literature survey—part 4: effects of wettability on capillary pressure," *Journal of Petroleum Technology*, vol. 39, no. 10, pp. 1283–1300, 1987.
- [5] Y. Du and L. Guan, "Field-scale polymer flooding: lessons learnt and experiences gained during past 40 years," in *Proceedings of the SPE International Petroleum Conference*, pp. 383–388, Puebla, Mexico, November 2004, SPE 91787-MS.
- [6] X. Zhang, W. Guan, and F. Pan, "Polymer flooding for middle and low permeability sandstone reservoirs," in *Proceedings of the 6th International Petroleum Technology Conference*, Beijing, China, March 2013, SPE 16536-MS.
- [7] Y. Wang, Y. Pang, Z. Shao et al., "The polymer flooding technique applied at high water cut stage in daqing oilfield," in *Proceedings of the the North Africa Technical Conference & Exhibition*, Cairo, Egypt, April 2013, SPE 164595.
- [8] H. Xia, D. Wang, J. Wu, and F. Kong, "Elasticity of HPAM solutions increases displacement efficiency under mixed wettability conditions," in *Proceedings of the SPE Asia Pacific Oil and Gas Conference and Exhibition*, pp. 103–110, Perth, Australia, October 2004, SPE 88456.
- [9] H. Dong, Y. Hong, W. Rui, and D. Fan, "The effect of wettability on oil recovery of alkaline/surfactant/polymer flooding," in *Proceedings of the SPE Annual Technical Conference and Exhibition*, pp. 2396–2403, San Antonio, Tex, USA, September 2006, SPE 102564.
- [10] Y. Zhu, Y. Zhang, Q. Hou, H. Yuan, and G. Jian, "Effect of main factors on oil recovery of surfactant-polymer flooding," in *Proceedings of the 6th International Petroleum Technology Conference (IPTC '13)*, Beijing, China, March 2013, IPTC16433.
- [11] Center for Petroleum and Geosystems Engineering, *UTCHEM-9.0, a Three-Dimensional Chemical Flood Simulator*, University of Texas at Austin, Austin, Tex, USA, 2000.
- [12] A. T. Corey, "The interrelation between gas and oil relative permeabilities," *Production Monthly*, vol. 19, no. 1, pp. 38–41, 1954.
- [13] R. H. Brooks and A. T. Corey, "Properties of porous media affecting fluid flow," *Journal of the Irrigation and Drainage Division*, vol. 92, no. 2, pp. 61–90, 1966.
- [14] M. C. Leverett, "Capillary behavior on porous solids," *Transactions of the AIME*, vol. 142, no. 1, pp. 152–169, 1941.
- [15] G. A. Anderson, *Simulation of chemical flood enhanced oil recovery processes including the effects of reservoir wettability [M.S. thesis]*, University of Texas at Austin, Austin, Tex, USA, 2006.
- [16] N. R. Morrow, P. J. Cram, and F. G. McCaffery, "Displacement studies in dolomite with wettability control by octanoic acid," *SPE Journal*, vol. 13, no. 4, pp. 221–232, 1973.
- [17] M. Delshad, N. F. Najafabadi, G. A. Anderson, G. A. Pope, and K. Sepehrnoori, "Modeling wettability alteration in naturally fractured reservoirs," in *Proceedings of the 15th SPE-DOE Improved Oil Recovery Symposium*, pp. 1132–1140, Tulsa, Okla, USA, April 2006, SPE 100081.

## Research Article

# Link-Based Signalized Arterial Progression Optimization with Practical Travel Speed

Wu Xianyu,<sup>1</sup> Hu Peifeng,<sup>2</sup> and Yuan Zhenzhou<sup>1</sup>

<sup>1</sup> MOE Key Laboratory for Urban Transportation Complex Systems Theory and Technology,  
Beijing Jiaotong University, Beijing 100044, China

<sup>2</sup> Center for Advanced Transportation Education and Research (CATER), UNR, MS 258, Reno, NV 89557, USA

Correspondence should be addressed to Wu Xianyu; wuxy@bjtu.edu.cn

Received 17 June 2013; Revised 6 September 2013; Accepted 6 September 2013

Academic Editor: Mohamed Fathy El-Amin

Copyright © 2013 Wu Xianyu et al. This is an open access article distributed under the Creative Commons Attribution License, which permits unrestricted use, distribution, and reproduction in any medium, provided the original work is properly cited.

Bandwidth is defined as the maximum amount of green time for a designated movement as it passes through an arterial. In most previous studies, bandwidth has been referred to arterial bandwidth. In practice, a balance between link bandwidth and arterial bandwidth has proven to be important in optimizing coordinated signal timing plans, because not all drivers need to pass through all the intersections on an arterial. This study proposes an algorithm on how to obtain an optimal coordinated signal timing plan with both optimal link bandwidth and optimal arterial bandwidth considering practical vehicles' speed. The weighted link bandwidth attainability is introduced as an additional measure of effectiveness for assessing the optimization results. The link bandwidth optimization is built based on the improvement of Messer's algorithm about bandwidth optimization. The arterial bandwidth optimization algorithm takes into consideration the weighted link bandwidth attainability while selecting phase sequences. The proposed algorithm is demonstrated in a case study, and many improvements are archived when a balanced consideration is given to both link bandwidth and arterial bandwidth. Fine-tuning of initial signal timing plan is done using practical travel speed. The evaluation results show a rather significant improvement which is achieved.

## 1. Introduction

The objective of a signalized arterial progression is to provide continuous movement of vehicles and/or minimize the delay along an arterial. Bandwidth is defined as the maximum amount of green time for a designated movement as it passes through an arterial. It is an outcome of the signal timing plan that is determined by the offsets between intersections and the allotted green time for the coordinated phase at each intersection. Bandwidth (measured in seconds) can be defined in terms of two consecutive intersections (referred to as link bandwidth) or in terms of an entire arterial (referred to as arterial bandwidth). Bandwidth and with its associated measures of efficiency and attainability are measures that are often used to assess the effectiveness of a coordinated signal timing plan [1].

A larger progression bandwidth implies that more traffic on an arterial can progress through the signals without stops [2, 3]. Furthermore, bandwidth-based signal timing

is preferred because it better meets drivers' expectations. A signal timing solution without a good progression band, no matter how well it may claim to minimize system delays and stops, may not be acceptable to traffic engineers and travelers [4]. A study conducted by Yang indicated that bandwidth-based solutions generally outperform delay-based solutions based on several field studies [5].

From the late 1960s to the early 1980s, many researchers, including Little, Messer, and Brooks, made a significant progress and developed a series of bandwidth optimization algorithms [6]. Messer et al. developed a variable-sequence program to form the core of the PASSER software. They modified traditional green bandwidth method and added variable phase sequence operation in the software [7, 8]. Little et al. developed the MAXBAND, using a more complicated mixed integer linear programming model [9]. Besides MAXBAND and PASSER, there are several other models that have been introduced. Gartner et al. developed MULTI-BAND to improve the original MAXBAND [10]. In 1996, they

published MULTIBAND-96 to further improve the model and applied to realistic networks [11]. Efforts to improve bandwidth-based optimization models and their computing algorithms continued up to the late 1990s [12–15]. Feng [16] developed the projection algorithm (PA) to optimize signal offsets and cycle length while considering start-up delay, residual queues, and unbalanced traffic volumes.

In these studies mentioned above, bandwidth is always defined in terms of an entire arterial. Arterial bandwidth is commonly used to describe capacity or maximized vehicle throughput. While arterial bandwidth is a good indicator for progression opportunities, it may not fully capture the overall arterial operation. For example, on an arterial with 10 signalized intersections, an arterial bandwidth solution allows vehicles to travel through the entire system. In reality, one must consider how many vehicles actually travel through all the intersections. In some cases, link bandwidth is more important than arterial bandwidth because of high volumes (especially in the case of high left-turn volumes) between some links. Therefore both link and arterial bandwidth should be considered in optimizing coordinated signal timing plans. In 2002, Gartner and Stamatiadis provided mathematical programming models for the development of optimal arterial-based progression schemes considering an individually weighted band that can be adapted to the prevailing traffic flows on that link [17]. Their models began to pay more attention to link bandwidth; however they did not consider the impact of speed variation and could not obtain the signal timing plan with both optimal arterial bandwidth and optimal link bandwidth. Although software tools, such as SYNCHRO and TRANSYT7F, can depict both arterial bands and link bands, their optimization objective is network delay instead of bandwidth. A signal timing plan with both optimized link bandwidth and arterial bandwidth is normally difficult to be obtained [18]. To overcome the limitations of previous studies, this study focuses on an algorithm that can obtain a best signal timing plan with both optimal link bandwidth and optimal arterial bandwidth.

In an ideal coordinated system with optimal bandwidth, platoons with desired travel speed from an upstream intersection at the start of green should arrive at downstream intersection near start of the green indication. In reality, vehicle's speed might be lower or higher than the desired speed. Speed limit is generally used when the actual speed data are not available. Recently, transportation professionals have new technologies and instruments to collect traffic data. The use of Global Positioning Systems (GPS) has become a springboard for many transportation related projects. GPS tools can capture, store, and transfer real-time traffic data on the field. Vehicle counts, speed, time, and delay are the key components of information to develop proper signal coordination timing plan. The expanding Geographic Information System (GIS) and GPS technologies have made it easy to collect spatial data (latitude, longitude) with attributes of time and velocity [19–22]. Considering the impact of practical travel speed, Feng [16] has developed a corridor signal optimization method called projection algorithm (PA). It does not introduce the fine-tuning of initial signal timing plan with practical travel speed.

This study proposes an arterial progression optimization approach using link-based bandwidth optimization algorithm and a GPS tool on an arterial. The rest of paper is organized as follows. Section 2 introduces some notations of the bandwidth optimization methodology and provides a link bandwidth optimization algorithm with eight situations to calculate upper/lower interferences and six cases to calculate relative offset between two consecutive intersections. Section 3 presents the new link-based arterial bandwidth optimization algorithm. Section 4 presents a case study to demonstrate the proposed algorithm and compare the performance index of signal timing plans on different speeds, especially the practical vehicles' speed, with simulation models. Finally, Section 5 provides the summary and conclusions.

## 2. Link Bandwidth Optimization

**2.1. Notations.**  $N$ : number of intersections on an arterial;  $C$ : signal cycle length;  $i$ : intersection;  $L_{i,i+1}$ : the link between  $i$  and  $i + 1$ ;  $G_{IBT,i}$ : inbound through movement green time of  $i$ ;  $G_{IBL,i}$ : inbound left-turn movement green time of  $i$ ;  $G_{OBT,i}$ : outbound through movement green time of  $i$ ;  $G_{OBL,i}$ : outbound left-turn movement green time of  $i$ ;  $\beta_i$ : phase sequence of  $i$  for left-turn in the arterial direction, whose value can be 1, 2, 3, and 4, in which (1) "Lead/Lead," meaning IBL, is leading phase and OBL is leading phase, (2) "Lead/Lag," (3) "Lag/Lead," (4) "Lag/Lag";  $O_i$ : offset of  $i$ , start of green time of outbound through movement;  $O_{i,i+1}$ : relative offset between  $i$  and  $i + 1$ ;  $RO_{i,\beta_i}$ : relative offset of  $G_{IBT,i}$  with respect to  $G_{OBT,i}$  at  $i$  with sequence  $\beta_i$ . Figure 1 shows the calculation of  $RO_{i,\beta_i}$ .

$T_{i,i+1}$ : travel time from  $i$  to  $i + 1$ ;  $T_{i+1,i}$ : travel time from  $i + 1$  to  $i$ ;  $LI_{\beta_i,\beta_{i+1}}$ : lower interference between  $i$  and  $i + 1$ ;  $UI_{\beta_i,\beta_{i+1}}$ : upper interference between  $i$  and  $i + 1$ ;  $VI_{\beta_i,\beta_{i+1}}$ : valid interference between  $i$  and  $i + 1$ ;  $Os_{i,i+1}$ —slack time between  $G_{OBT,i}$  and  $G_{OBT,i+1}$ , and  $Os_{i,i+1} = G_{OBT,i} - G_{OBT,i+1}$ ;  $Is_{i,i+1}$ : slack time between  $G_{IBT,i}$  and  $G_{IBT,i+1}$ , and  $Is_{i,i+1} = G_{IBT,i} - G_{IBT,i+1}$ ;  $B^i$ : link bandwidth of  $L_{i,i+1}$ ;  $B_O^i$ : outbound link bandwidth of  $L_{i,i+1}$ ;  $B_I^i$ : inbound link bandwidth of  $L_{i,i+1}$ ;  $V_{OBT,i}$ : traffic volume of outbound through movement at  $i$ ;  $V_{IBT,i}$ : traffic volume of inbound through movement at  $i$ .

**2.2. Calculation of Upper/Lower Interference.** The bandwidth optimization algorithm developed by Brooks and Little establishes the primary principles of bandwidth optimization. The algorithm was originally developed for two-phase signals. Messer et al. [7] enhanced the original algorithm to handle multiphase signals with left-turn phases, which formed the core of PASSER II [8]. One major limitation of the algorithm is to get the optimal progression bandwidth for an arterial with high number of signalized intersections (e.g., >10). Messer's paper did not include how to calculate relative offsets and did not consider the relative locations of intersections. This section provides detailed descriptions on all possible situations to calculate upper/lower interferences and offset for two consecutive intersections.

Figure 2 illustrates the basic concepts of bandwidth optimization algorithm for three signals with left-turn phases. The maximum progression bandwidth is the sum of outbound bandwidth and inbound bandwidth. The value of

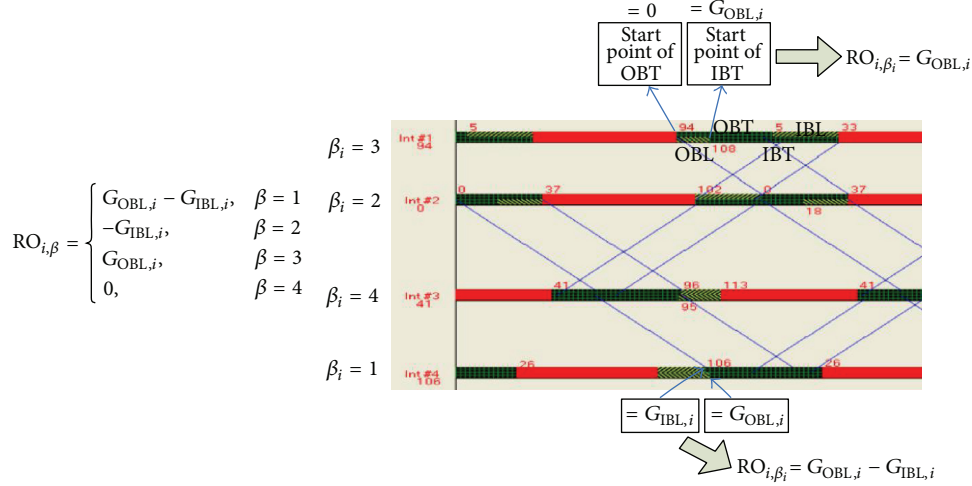


FIGURE 1: Relative offset of  $G_{IBT,i}$  with respect to  $G_{OBT,i}$ .

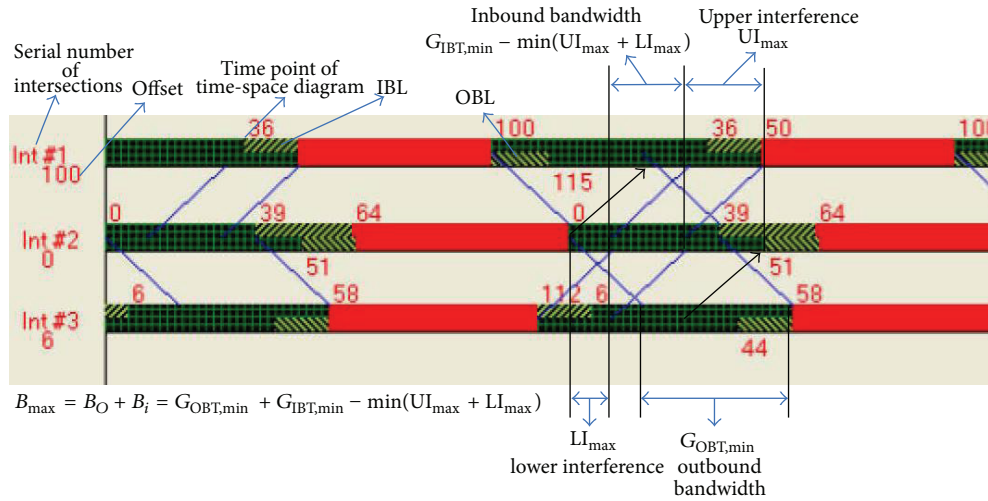


FIGURE 2: Illustration of bandwidth optimization algorithm.

outbound bandwidth is a constant, which equals the minimum outbound through green time  $G_{OBT,min}$ . And the inbound bandwidth is determined by minimum total valid interference from other intersections. In Figure 2, the second intersection is the master intersection, which has minimum inbound through green time  $G_{IBT,min}$ . A valid upper interference is by the first intersection,  $UI_{max}$ , and a valid lower interference is by the third intersection,  $LI_{max}$ . Therefore the inbound bandwidth is  $G_{IBT,min} - \min(UI_{max} + LI_{max})$ .

The bandwidth optimization principle reveals that the location of  $i$  with respect to  $i + 1$  plays an important role in calculating upper and lower interferences for two consecutive intersections. On the other hand, according to comparison of inbound and outbound through movement green time, there are four situations that ensure correct upper and lower interference calculations.

After calculating upper/lower interferences, there are four additional cases to adjust these upper/lower interferences and

obtain the valid interferences, as shown in Table 1. Figure 3 graphically illustrates the calculation of upper interference for the situation 4. In this situation, the intersection  $i$  has the minimum inbound through movement green time, meaning that the master intersection is on the left side of intersection  $i + 1$ .

In Figure 3, phase sequence of the first intersection no.  $i$  is "IBL:Lag/OBL:Lead,"  $\beta_i = 3$ , and phase sequence of the second intersection no.  $i + 1$  is "IBL:Lead/OBL:Lag,"  $\beta_{i+1} = 2$ . To calculate upper/lower interference between these two intersections, there are other 15 conditions with different combinations of phase sequences, as shown in Table 2.

**2.3. Valid Upper/Lower Interference and Link Bandwidth.** All upper/lower interferences to be valid must be less than the minimum inbound through movement green time and greater than the slack time between  $G_{IBT,i}$  and  $G_{IBT,i+1}$ , as

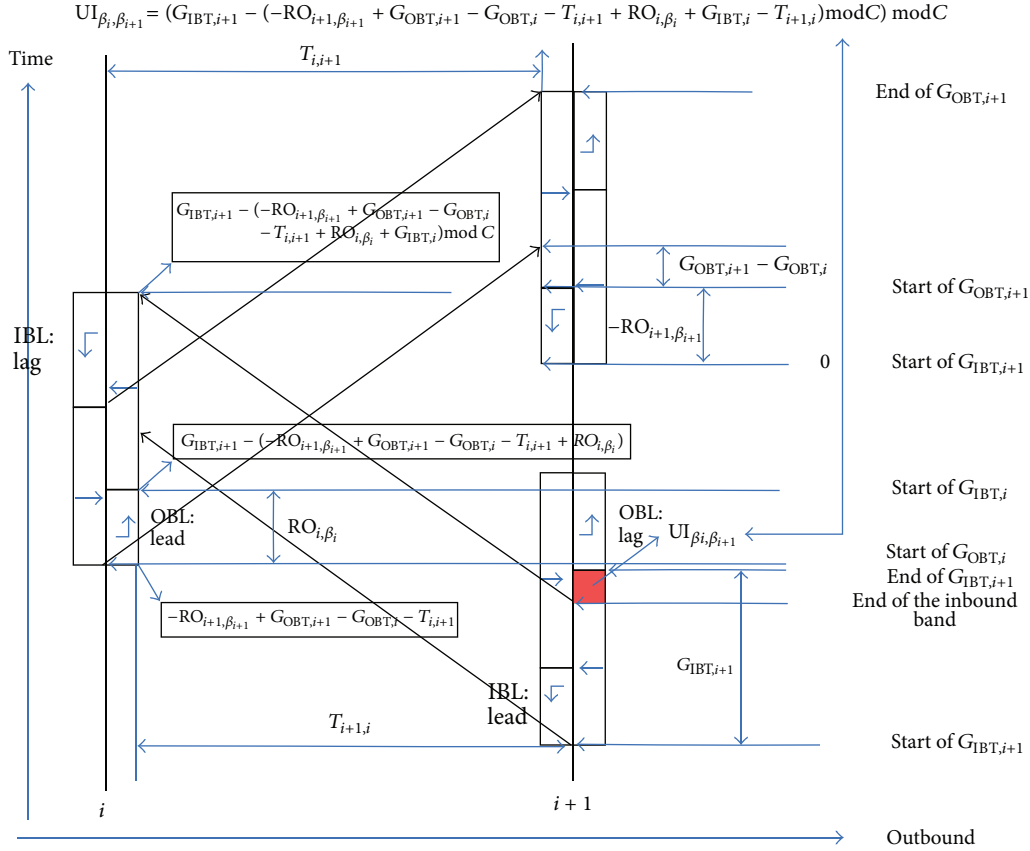


FIGURE 3: The calculation of upper interference for situation 4.

TABLE 1: Calculation of upper/lower interference for link bandwidth.

Common situation	Upper interference	Lower interference
$G_{OBT, i} \leq G_{OBT, i+1}$ $G_{IBT, i+1} > G_{IBT, i}$	$UI_{\beta_i, \beta_{i+1}} = G_{IBT, i} - (-RO_{i, \beta_i} + T_{i, i+1} + RO_{i+1, \beta_{i+1}} + G_{IBT, i+1} + T_{i+1, i}) \bmod C$	$LI_{\beta_i, \beta_{i+1}} = (-RO_{i, \beta_i} + T_{i, i+1} - Os_{i+1, i} + RO_{i+1, \beta_{i+1}} + T_{i+1, i}) \bmod C$
$G_{OBT, i} > G_{OBT, i+1}$ $G_{IBT, i+1} > G_{IBT, i}$	$UI_{\beta_i, \beta_{i+1}} = (G_{IBT, i} - (-RO_{i, \beta_i} + G_{OBT, i} - G_{OBT, i+1} + T_{i, i+1} + RO_{i+1, \beta_{i+1}} + G_{IBT, i+1} + T_{i+1, i})) \bmod C \bmod C$	$LI_{\beta_i, \beta_{i+1}} = (-RO_{i, \beta_i} + T_{i, i+1} - Os_{i+1, i} + RO_{i+1, \beta_{i+1}} + T_{i+1, i}) \bmod C$
$G_{OBT, i+1} \leq G_{OBT, i}$ $G_{IBT, i+1} \leq G_{IBT, i}$	$UI_{\beta_i, \beta_{i+1}} = (G_{IBT, i+1} - (-RO_{i+1, \beta_{i+1}} - T_{i, i+1} + RO_{i, \beta_i} + G_{IBT, i} - T_{i+1, i})) \bmod C \bmod C$	$LI_{\beta_i, \beta_{i+1}} = (-RO_{i+1, \beta_{i+1}} - T_{i, i+1} - Os_{i+1, i} + RO_{i, \beta_i} - T_{i+1, i}) \bmod C$
$G_{OBT, i+1} > G_{OBT, i}$ $G_{OBT, i+1} \leq G_{OBT, i}$	$UI_{\beta_i, \beta_{i+1}} = (G_{IBT, i+1} - (-RO_{i+1, \beta_{i+1}} + G_{OBT, i+1} - G_{OBT, i} - T_{i, i+1} + RO_{i, \beta_i} + G_{IBT, i} - T_{i+1, i})) \bmod C \bmod C$	$LI_{\beta_i, \beta_{i+1}} = (-RO_{i+1, \beta_{i+1}} - T_{i, i+1} - Os_{i+1, i} + RO_{i, \beta_i} - T_{i+1, i}) \bmod C$
Special situation	Upper/lower interference	Interference adjustment
$Is_{i+1} < 0$	$C + Is_{i+1} \leq LI_{\beta_i, \beta_{i+1}} \leq C$	$LI_{\beta_i, \beta_{i+1}} = LI_{\beta_i, \beta_{i+1}} - C$
$LI_{\beta_i, \beta_{i+1}} < 0$	$C + LI_{\beta_i, \beta_{i+1}} \leq \min\{G_{IBT, i}, G_{IBT, i+1}\}$	$LI_{\beta_i, \beta_{i+1}} = LI_{\beta_i, \beta_{i+1}} + C$
$Is_{i+1} < 0$	$C + Is_{i+1} \leq UI_{\beta_i, \beta_{i+1}} \leq C$	$UI_{\beta_i, \beta_{i+1}} = UI_{\beta_i, \beta_{i+1}} - C$
$UI_{\beta_i, \beta_{i+1}} < 0$	$C + UI_{\beta_i, \beta_{i+1}} \leq \min\{G_{IBT, i}, G_{IBT, i+1}\}$	$UI_{\beta_i, \beta_{i+1}} = UI_{\beta_i, \beta_{i+1}} + C$

shown in

$$Is_i \leq LI_{\beta_i, \beta_{i+1}} \leq \min\{G_{IBT, i}, G_{IBT, i+1}\},$$

$$Is_i \leq UI_{\beta_i, \beta_{i+1}} \leq \min\{G_{IBT, i}, G_{IBT, i+1}\}.$$
(1)

Additionally, because the master intersection has the minimum green time, only one interference (cannot be both) could occur for one combination phase sequence at two intersections, as shown in

$$VI_{\beta_i, \beta_{i+1}} = \{UI_{\beta_i, \beta_{i+1}}, LI_{\beta_i, \beta_{i+1}}\}.$$
(2)

TABLE 2: Phase sequence combinations of two consecutive intersections.

Phase sequence combination	No. $i$ intersection			No. $i + 1$ intersection		
	IBL	OBL	$\beta$	IBL	OBL	$\beta$
1				Lead	Lead	$\beta_{i+1} = 1$
2	Lead	Lead	$\beta_i = 1$	Lead	Lag	$\beta_{i+1} = 2$
3				Lag	Lead	$\beta_{i+1} = 3$
4				Lag	Lag	$\beta_{i+1} = 4$
5				Lead	Lead	$\beta_{i+1} = 1$
6	Lead	Lag	$\beta_i = 2$	Lead	Lag	$\beta_{i+1} = 2$
7				Lag	Lead	$\beta_{i+1} = 3$
8				Lag	Lag	$\beta_{i+1} = 4$
9				Lead	Lead	$\beta_{i+1} = 1$
10 (Figure 2)	<b>Lag</b>	<b>Lead</b>	$\beta_i = 3$	<b>Lead</b>	<b>Lag</b>	$\beta_{i+1} = 2$
11				Lag	Lead	$\beta_{i+1} = 3$
12				Lag	Lag	$\beta_{i+1} = 4$
13				Lead	Lead	$\beta_{i+1} = 1$
14	Lag	Lag	$\beta_i = 4$	Lead	Lag	$\beta_{i+1} = 2$
15				Lag	Lead	$\beta_{i+1} = 3$
16				Lag	Lag	$\beta_{i+1} = 4$

Then, a link bandwidth can be gained using

$$B^i = B_O^i + B_I^i$$

$$= \min \{G_{OBT,i}, G_{OBT,i+1}\} + \min \{G_{IBT,i}, G_{IBT,i+1}\} - VI_{\beta_i, \beta_{i+1}}. \quad (3)$$

**2.4. Calculation of Relative Offset.** Assume that the referencing phase is the start of green time of outbound through movement, there are six cases to calculate the relative offset of two consecutive intersections.

**Case 1.** Consider  $G_{OBT,i} \leq G_{OBT,i+1}$ ,  $G_{IBT,i+1} > G_{IBT,i}$ , and  $VI_{\beta_i, \beta_{i+1}} = UI_{\beta_i, \beta_{i+1}}$ , as shown in Figure 4(a).

Then

$$O_i = 0, \quad O_{i+1} = T_{i,i+1} \bmod C. \quad (4)$$

**Case 2.** Consider  $G_{OBT,i} > G_{OBT,i+1}$  and  $G_{IBT,i+1} > G_{IBT,i}$ .

Then

$$O_i = 0, \quad O_{i+1} = (T_{i,i+1} + G_{OBT,i} - G_{OBT,i+1}) \bmod C. \quad (5)$$

**Case 3.** Consider  $G_{OBT,i} \leq G_{OBT,i+1}$ ,  $G_{IBT,i+1} > G_{IBT,i}$ , and  $VI_{\beta_i, \beta_{i+1}} = LI_{\beta_i, \beta_{i+1}}$ , as shown in Figure 4(b).

Then

$$O_i = 0,$$

$$O_{i+1} = (T_{i,i+1} + G_{OBT,i} - G_{OBT,i+1} + K * C) \bmod C, \quad (6)$$

where  $K$  is an integer. If  $T_{i,i+1} + G_{OBT,i} - G_{OBT,i+1} < 0$ , then  $K = 1$  or else  $K = 0$ .

**Case 4.** Consider  $G_{OBT,i+1} \leq G_{OBT,i}$ ,  $G_{IBT,i+1} \leq G_{IBT,i}$ , and  $VI_{\beta_i, \beta_{i+1}} = UI_{\beta_i, \beta_{i+1}}$ .

Then

$$O_i = K * C - T_{i,i+1}, \quad O_{i+1} = 0. \quad (7)$$

**Case 5.** Consider  $G_{OBT,i+1} > G_{OBT,i}$  and  $G_{IBT,i+1} \leq G_{IBT,i}$ .

Then

$$O_i = K * C - T_{i,i+1} + G_{OBT,i+1} - G_{OBT,i}, \quad O_{i+1} = 0. \quad (8)$$

**Case 6.** Consider  $G_{OBT,i+1} \leq G_{OBT,i}$ ,  $G_{IBT,i+1} \leq G_{IBT,i}$ , and  $VI_{\beta_i, \beta_{i+1}} = LI_{\beta_i, \beta_{i+1}}$ .

Then

$$O_i = K * C - T_{i,i+1} + G_{OBT,i+1} - G_{OBT,i}, \quad O_{i+1} = 0. \quad (9)$$

**2.5. Example of Link Bandwidth Optimization Algorithm.** The signal timing plans of two intersections are shown below. The distance between them is 2015 ft, and the speed limit is 40 mph; then travel time is 34 s and cycle length is 130 s:

$$\begin{aligned} G_{IBT,i} &= 51, & G_{OBT,i} &= 49, \\ G_{IBL,i} &= 20, & G_{OBL,i} &= 18, \\ G_{IBT,i+1} &= 45, & G_{OBT,i+1} &= 36, \\ G_{IBL,i+1} &= 29, & G_{OBL,i+1} &= 20. \end{aligned} \quad (10)$$

Then,  $G_{OBT,i+1} \leq G_{OBT,i}$  and  $G_{IBT,i+1} \leq G_{IBT,i}$  are fit for common situation 3 in Table 1. Table 3 shows the results of upper/lower interference calculation, including 16 phase sequence combinations.

According to the rule of valid interference in Section 2.3 and calculation of offset in Section 2.4, we can get the valid interference, link bandwidth, and offset relative to phase sequences, as shown in Table 3 (bold text), including 10 phase sequence combinations (not all 16 combinations have valid interference).

TABLE 3: Upper/lower interferences of two consecutive intersections.

Phase sequence									
Intersection $i + 1$	1	1	1	1	2	2	2	2	
Intersection $i$	1	2	3	4	1	2	3	4	
Interference of intersection $i + 1$ from intersection $i$									
Upper interference	55	Common: $45 - (-(20 - 29) - 34 + (-20) + 51 - 34) = 73$	35	53	35	53	15	33	
Lower interference	-74	Common: Special: $-92 + 130 = 38 < 45$ valid interference	-54	-72	-54	-72	-34	-52	
Link bandwidth	—	$45 + 36 - 38 = 43$	$45 + 36 - 35 = 46$	—	46	—	66	48	
Offset of intersection $i$	—	$130 - 34 + 36 - 49 = 83$	$130 - 34 = 96$	—	96	—	96	96	
Phase sequence									
Intersection $i + 1$	3	3	3	3	4	4	4	4	
Intersection $i$	1	2	3	4	1	2	3	4	
Interference									
Upper interference	84	102	64	82	64	82	44	62	
Lower interference	27	9	-83	29	-83	29	-63	-81	
Link bandwidth	54	72	—	52	—	52	37	—	
Offset of intersection $i$	83	83	—	83	—	83	96	—	

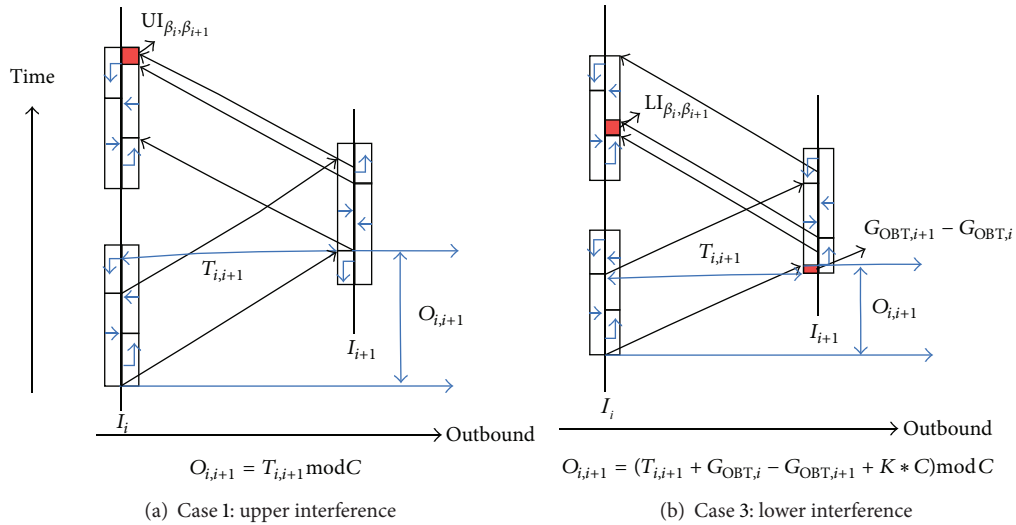


FIGURE 4: The calculation of relative offset.

### 3. Link-Based Arterial Bandwidth Optimization Algorithm

3.1. Measures of Effectiveness (MOE). Bandwidth efficiency and attainability are two measures to describe the quality of a coordinated signal timing plan. Both are computed from a time-space diagram that represents the signal timing plan.

The two parameters are first defined by Messer et al. [7, 8], as shown in

$$E_B = \frac{(B_{out} + B_{in})}{2C} \times 100\%,$$

$$A_c = \frac{B_{out} + B_{in}}{G_{OBT,min} + G_{IBT,min}} \times 100\%, \quad (11)$$

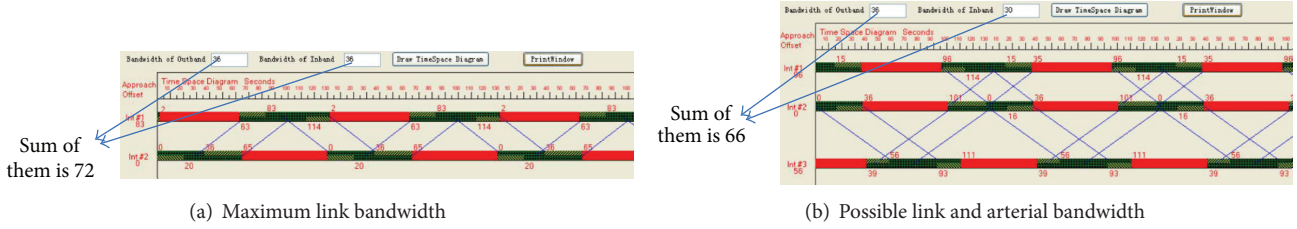


FIGURE 5: Example of maximum and possible link bandwidth and arterial bandwidth.

where  $E_B$  arterial bandwidth efficiency,  $B_{out}$  arterial bandwidth of outbound,  $B_{in}$  arterial bandwidth of inbound, and  $A_c$  the attainability for a given cycle length.

Besides the arterial bandwidth efficiency and attainability, maximum link bandwidth, possible link bandwidth, and link bandwidth attainability are first proposed as additional measures of effectiveness in our research. Maximum link bandwidth is the maximum value of a link bandwidth obtained using link bandwidth optimization algorithm. Possible link bandwidth is the value of a link bandwidth when the signal system has the optimal arterial progression bandwidth. In this case, the link bandwidth may not be the best solution to get the arterial bandwidth. In Figure 5, the maximum link bandwidth between the first and the second intersections is 72 seconds, while the possible link bandwidth is only 66 seconds to obtain the optimal arterial bandwidth (offset and phase sequence have been changed).

$B_{max}^i$  is maximum link bandwidth of  $L_i$ ,  $B_i$  possible link bandwidth of  $L_i$ , and  $\alpha_i$  link bandwidth attainability, defined as ratio of  $B_i$  over  $B_{max}^i$ , shown in

$$\alpha_i = \frac{B_i}{B_{max}^i}. \quad (12)$$

**3.2. Calculation of Link Bandwidth.** After the outbound direction is determined, link bandwidth  $B^i$  with phase sequence  $\beta_i$ ,  $\beta_{i+1}$ , and offset  $O_{i,i+1}$  can be calculated. The optimized results of  $L_{i,i+1}$  are shown in Table 4 and are sorted in a descending order by  $B^i$ . Both  $\beta_i$  and  $\beta_{i+1}$  can be 1, 2, 3, and 4; therefore the total number of possible solutions is 16. It is noted that not all 16 solutions yield a valid upper or lower interference. Only 9 valid solutions are included in Table 4, using two intersections on Kietzke Lane, Reno, NV, USA.

Similarly, the link bandwidth  $B^{i+1}$  with phase sequence  $\beta'_{i+1}$  (intermediate variable to differentiate it from  $\beta_{i+1}$ ),  $\beta_{i+2}$  and offset  $O_{i+1,i+2}$  can be calculated. The optimized results of  $L_{i+1,i+2}$  are shown in Table 5 and sorted in a descending order by  $B^{i+1}$ .

Using the same approach, the link bandwidth  $B^{i+2}$  with phase sequence  $\beta'_{i+2}$ ,  $\beta_{i+3}$  and offset  $O_{i+2,i+3}$  can be calculated. The optimized results of  $L_{i+2,i+3}$  are shown in Table 6 and sorted in a descending order by  $B^{i+2}$ .

**3.3. Selection of Phase Sequence.** Using the conditions  $\beta_{i+1} = \beta'_{i+1}$  and  $\beta_{i+2} = \beta'_{i+2}$ , one can get many solutions of phase

sequences for the intersections on this arterial. Importance of each link bandwidth may be different from one another on an arterial. There are many factors that impact the value of the importance, such as traffic volumes (through movement, left-turn), road configuration, and passing pedestrians. If traffic volume of through movement from  $i$  and  $i + 1$  is more than others, then link bandwidth of  $L_{i,i+1}$  is more important than others.  $\omega_i$  is defined as a weighted factor that reflects the importance of link bandwidth attainability.  $E_m$  is defined as the efficiency for solution  $m$  of a coordinated signal timing plan

$$E_m = \sum_i^N \omega_i \alpha_i, \quad (13)$$

$$\omega_i = \frac{(V_{OBT,i} + V_{IBT,i+1})}{\sum_i (V_{OBT,i} + V_{IBT,i+1})}.$$

The best solution is the one that has the maximum efficiency  $E_m$ . In this example,

$$\begin{aligned} \omega_1 &= \frac{(V_{OBT,i} + V_{IBT,i+1})}{\sum_i (V_{OBT,i} + V_{IBT,i+1})} \\ &= \frac{(820 + 492)}{(820 + 492) + (903 + 625) + (971 + 6483)} \\ &= 0.3055, \end{aligned} \quad (14)$$

$$\omega_2 = 0.3559, \quad \omega_3 = 0.3386.$$

Table 7 shows five solutions of different phase sequences, based on the data in Tables 4, 5, and 6. The weighted factor of each link is calculated using through traffic volumes. As can be seen, solution 2 is the best solution, which has an efficiency of 0.9755. The number of solutions is dependent on the optimized result. Table 7 just shows five of the solutions.

**3.4. Calculation of Offset.** The inbound through movement green time determines which intersection is the reference intersection for one link and how the relative offset of each intersection is calculated. According to the value of inbound through movement green time, there are four cases to calculate the offsets of  $i$ ,  $i + 1$ , and  $i + 2$ .

*Case 1.* Consider  $G_{IBT,i+1} > G_{IBT,i}$  and  $G_{IBT,i+2} > G_{IBT,i+1}$ ; then

$$O_i = 0, \quad O_{i+1} = O_{i,i+1}, \quad O_{i+2} = O_{i,i+1} + O_{i+1,i+2}. \quad (15)$$

TABLE 4: Optimized results for  $L_{i,i+1}$  on Kietzke Lane ( $G_{IBT,i+1} < G_{IBT,i}$ , 2nd Steet and Mill Street).

Timing parameter	Valid solutions								
	1	2	3	4	5	6	7	8	9
$\beta_i$	2	3	1	4	2	4	3	1	2
$\beta_{i+1}$	3	2	3	3	4	2	1	2	1
$B^i$	72	66	54	52	52	48	46	46	43
$\alpha_i$	1.0	0.92	0.75	0.72	0.72	0.67	0.64	0.64	0.60
$O_{i,i+1}$	83	96	83	83	83	96	96	96	83

TABLE 5: Optimized results for  $L_{i+1,i+2}$  on Kietzke Lane ( $G_{IBT,i+2} > G_{IBT,i+1}$ , Mill Street and Vassar Street).

Timing parameter	Valid solutions														
	1	2	3	4	5	6	7	8	9	10	11	12	13	14	15
$\beta'_{i+1}$	1	1	1	2	2	2	4	4	4	2	3	1	4	3	3
$\beta'_{i+2}$	1	3	4	1	2	4	3	1	4	3	3	2	2	1	4
$B^{i+1}$	81	81	81	81	81	81	81	73	72	71	70	64	55	53	52
$\alpha_{i+1}$	1.0	1.0	1.0	1.0	1.0	1.0	1.0	0.90	0.89	0.88	0.86	0.79	0.68	0.65	0.64
$O_{i+1,i+2}$	56	56	56	37	56	37	56	56	56	37	56	56	56	56	56

TABLE 6: Optimized results for  $L_{i+2,i+3}$  on Kietzke Lane ( $G_{IBT,i+3} < G_{IBT,i+2}$ , Vassar Street and Plumb Lane).

Timing parameter	Valid solutions											
	1	2	3	4	5	6	7	8	9	10	11	12
$\beta'_{i+2}$	2	4	1	2	2	3	4	1	4	1	2	3
$\beta'_{i+3}$	3	3	3	1	4	3	1	1	4	4	2	2
$B^{i+2}$	98	83	82	80	78	65	63	62	61	60	58	54
$\alpha_{i+2}$	1.0	0.85	0.84	0.82	0.80	0.63	0.64	0.63	0.62	0.61	0.59	0.55
$O_{i+2,i+3}$	81	81	81	81	81	81	81	81	81	81	81	86

Case 2. Consider  $G_{IBT,i+1} > G_{IBT,i}$  and  $G_{IBT,i+2} \leq G_{IBT,i+1}$ ; then

$$\begin{aligned} O_i &= 0, & O_{i+1} &= O_{i,j+1}, \\ O_{i+2} &= O_{i,i+1} - O_{i+1,i+2} + K * C, \end{aligned} \quad (16)$$

where  $K$  is an integer. If  $O_{i,i+1} - O_{i+1,i+2} < 0$ , then  $K = 1$  or else  $K = 0$ .

Case 3. Consider  $G_{IBT,i+1} \leq G_{IBT,i}$  and  $G_{IBT,i+2} > G_{IBT,i+1}$ ; then

$$O_i = O_{i,i+1}, \quad O_{i+1} = 0, \quad O_{i+2} = O_{i+1,i+2}. \quad (17)$$

Case 4. Consider  $G_{IBT,i+1} \leq G_{IBT,i}$  and  $G_{IBT,i+2} \leq G_{IBT,i+1}$ ; then

$$O_i = O_{i,i+1}, \quad O_{i+1} = 0, \quad O_{i+2} = C - O_{i+1,i+2}. \quad (18)$$

In Table 7, solution 2 is the best solution of phase sequences on this arterial. Using the algorithm of calculating the above offset, one can get the offset for each intersection.

(1) Consider  $G_{IBT,i+1} < G_{IBT,i}$ ,  $G_{IBT,i+2} > G_{IBT,i+1}$ ; then

$$O_i = O_{i,i+1} = 96, \quad O_{i+1} = 0, \quad O_{i+2} = O_{i+1,i+2} = 56. \quad (19)$$

(2) Consider  $G_{IBT,i+3} < G_{IBT,i+2}$ ; then

$$O_{i+2} = O_{i+1,i+2} = 56,$$

$$O_{i+3} = K * C + (O_{i+1,i+2} - O_{i+2,i+3}) = 130 + (56 - 81) = 105. \quad (20)$$

## 4. Case Study

**4.1. Site Description.** A Windows program bandwidth optimization and time space diagram (BOTSD) was developed based on the proposed algorithm. Time-space diagrams can be produced by BOTSD with additional information to show the start and end of each phase. This information is useful for field implementation of signal timing plans, providing easiness of verifying that the current plan is running.

Kietzke Lane, an arterial in Reno, NV, USA, is selected as a case study to check the performance of the proposed bandwidth optimization algorithm. There are eight intersections (E 2nd Street no. 1, Mill Street no. 2, Vassar Street no. 3, Plumb Lane no. 4, Grove Street no. 5, Gentry Way no. 6, Moana Lane no. 7, and Peckham Lane no. 8) on the Kietzke Lane selected in this study. The coordinated cycle length of this arterial is 130 seconds (16:00 pm–18:00 pm) and speed limit is 40 mph. Table 8 shows lengths of phase split in the initial signal timing plan of Kietzke Lane. This plan is suitable for real traffic volumes of each isolated intersection,

TABLE 7: Selected solutions of different phase sequences on Kietzke Lane (2nd Street → Plumb Lane).

$m$	1		2		3		4		5	
$I_i$	$\beta_i$	$\alpha_i$	$\beta_i$	$\alpha_i$	$\beta_i$	$\alpha_i$	$\beta_i$	$\alpha_i$	$\beta_i$	$\alpha_i$
1	2	1	3	0.92	3	0.92	3	0.92	1	0.75
2	3	0.86	2	1	2	1	2	1	3	0.86
3	3	0.63	2	1	4	0.85	1	0.84	3	0.63
4	3	—	3	—	3	—	3	—	3	—
$E_m$	—	0.8249	—	<b>0.9755</b>	—	0.9247	—	0.9214	—	0.7485

TABLE 8: Phase splits in the initial signal timing plan of Kietzke Lane (2nd Street → Peckham Lane).

INTID	SBL	NBT	WBL	EBT	NBL	SBT	EBL	WBT	Distance (ft)
1	<b>18</b>	<b>51</b>	20	41	<b>20</b>	<b>49</b>	30	31	
2	<b>20</b>	<b>45</b>	25	40	<b>29</b>	<b>36</b>	25	40	2015
3	<b>18</b>	<b>54</b>	23	35	<b>17</b>	<b>55</b>	18	40	3294
4	<b>22</b>	<b>48</b>	18	42	<b>20</b>	<b>50</b>	22	38	2600
5	<b>16</b>	<b>79</b>	—	35	<b>16</b>	<b>79</b>	—	35	1841
6	<b>15</b>	<b>80</b>	—	35	<b>18</b>	<b>77</b>	—	—	2180
7	<b>22</b>	<b>40</b>	20	48	<b>18</b>	<b>44</b>	19	49	724
8	<b>36</b>	<b>41</b>	21	32	<b>16</b>	<b>61</b>	19	34	2168

TABLE 9: Traffic volumes of every intersection in the Kietzke Lane from field data.

INTID	NBL	NBT	NBR	SBL	SBT	SBR	EBL	EBT	EBR	WBL	WBT	WBR
1	<b>226</b>	820	169	<b>56</b>	430	54	248	585	143	160	418	63
2	<b>220</b>	903	259	<b>120</b>	492	121	166	684	134	318	742	146
3	<b>96</b>	971	120	<b>109</b>	625	146	149	238	100	200	408	256
4	<b>253</b>	780	313	<b>299</b>	483	143	230	870	244	282	757	168
5	<b>89</b>	1193	72	<b>6</b>	800	148	113	71	70	128	98	30
6	<b>119</b>	1143	51	<b>30</b>	883	79	170	56	170	61	66	46
7	<b>166</b>	897	168	<b>296</b>	738	140	250	631	111	257	681	176
8	<b>71</b>	845	249	<b>305</b>	633	168	81	419	19	—	514	300
Total	<b>1240</b>	7552	1401	<b>1221</b>	5084	999	1407	3554	991	1406	3684	1185

shown in Table 9, not fit for the whole arterial. Left-turn traffic volumes were much lower than through movement traffic volumes, so the optimal arterial progression bandwidth can enable more drivers pass through the arterial systems without stops. In this case study, based on this timing plan, we optimized phase sequences and offsets to obtain best solution of signal timing plan with optimal link bandwidth and arterial bandwidth.

**4.2. Optimized Results Using Messer's Algorithm.** Figure 6 shows time-space diagram of Kietzke Lane drawn by BOTSD, using Messer's algorithm when southbound is the outbound direction. The outbound arterial bandwidth is 36 seconds and 14 seconds for the inbound. If northbound is selected as the outbound direction, then the second intersection is the master intersection, which has the minimum through movement green time. The outbound arterial bandwidth is 40 seconds and 13 seconds for the inbound. If a vehicle arrives

at intersection no. 1 at the beginning of outbound through movement, it will stop and wait at intersection no. 1 and the offset of intersection no. 1 can be adjusted, as shown in Figure 6.

**4.3. Optimized Results Using the Proposed Algorithm.** Southbound is the outbound direction. Figure 7 shows time-space diagram for this arterial drawn by BOTSD using the new proposed method in southbound. The arterial outbound bandwidth is 30 seconds, and 28 seconds for the inbound. Arterial bandwidth efficiency is 22.31%, and bandwidth attainability is 75.32%, which means a fair progression according to the guidelines of bandwidth efficiency [1].

Using the same method of fine-tuning, we have got time-space diagrams with other travel speeds, which are less than the speed limit and same for every link. In this case study, the speed limit is 40 mph; we can use 38 mph, 35 mph, and 32 mph to design the signal timing plans with

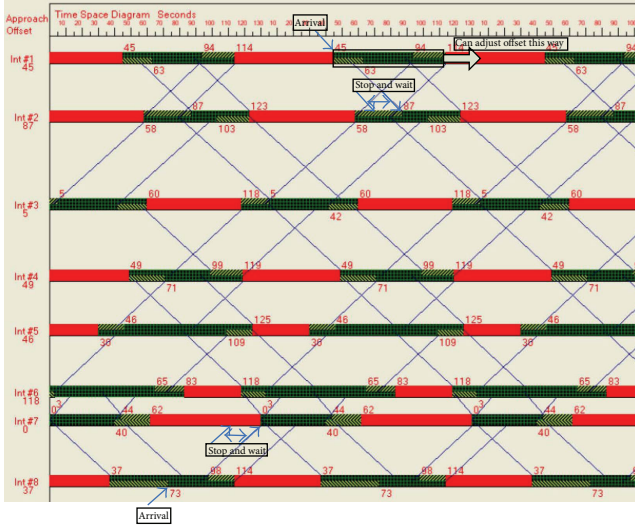


FIGURE 6: TSD of signal timing plan with Messer's algorithm.

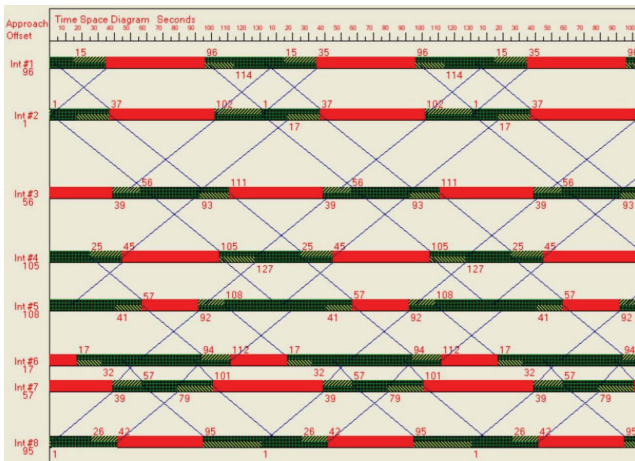


FIGURE 7: TSD of signal timing plan with proposed algorithm.

the proposed bandwidth optimization algorithm and get the TSD with maximum progression of arterial bandwidth and link bandwidth for comparison.

#### 4.4. Fine-Tuning of Signal Timing Plan with Practical Travel Speed

**4.4.1. Travel Time Data Collection with GPS Tool.** We have collected more than ten study runs of GPS data at the PM peak hours, using GPS receiver and GPS2LT [23]. Then, the actual travel time and speed can be obtained by the PC travel for Windows [24]. Based on the results of the actual travel time and speed for links shown in Figure 8, the actual travel speeds for most links are less than speed limit. Additionally, all the standard deviations of travel speed for ten runs are less than 3 mph.

**4.4.2. Analysis of Initial Signal Timing.** Using the GPS and TS tool and the collected GPS data, we have drawn the GPS

trajectory on the TSD for three types of study runs for PM peak hours (16:00 pm–18:00 pm). In Figure 9, the arterial road progression bandwidth of southbound is 12 seconds and 29 seconds in northbound. The car can go through all the 8 intersections on the TSD with the speed of 40 mph in the southbound for just two of ten runs. However, on the northbound, the car must stop at least one time no matter when it entered the system.

**4.4.3. Signal Timing with Practical Speed.** According to the results of fine-tuning of initial signal timing plan link by link, we have got the best solution of TSD for the arterial. The arterial progression bandwidth of southbound is 28 seconds, and 39 seconds in northbound. The bandwidth efficiency is 25.8%. Attainability of every link is more than 85% and three of them are equal to 100%, as shown in Figure 10.

#### 4.5. Comparison of Results

**4.5.1. MOE Results.** Table 10 shows the link bandwidth attainability and arterial bandwidth efficiency of eight intersections on Kietzke Lane with Messer's algorithm and the proposed algorithm.

According to arterial bandwidth efficiency and attainability in Figures 9 and 10, and link bandwidth attainability in Table 10, the solution of coordinated signal timing plan from the proposed algorithm is much better than that from Messer's algorithm whether the outbound direction is southbound or northbound. If a vehicle arrives at intersection no. 1 at the beginning of outbound through movement, it will stop and wait at intersection no. 1, the offset of intersection no. 1 can be adjusted, as shown in Figure 9. However, the time-space diagrams in Figure 10 have improved these problems.

In the other way, simulation results from SYNCHRO show that the proposed algorithm is better than Messer's algorithm. Total intersection control delay of 8 intersections with optimized signal timing plan with proposed algorithm is 266.2 s, less than that of Messer's algorithm 288 s. Total Link delay in arterial direction with proposed algorithm is 401.3 s, less than that of Messer's algorithm 445.2 s.

Additionally, when the number of signals in a system increases, it becomes more difficult to obtain a good bandwidth solution using Messer's algorithm. In some cases there is no valid solution with arterial bandwidth. However, the new proposed algorithm can be used to obtain an optimal solution of coordinated signal timing plan with both optimal link bandwidth and optimal arterial bandwidth.

**4.5.2. Simulation Results Comparison of Speed Limit and Practical Speed.** The simulation model of this arterial is built up in VISSIM 5.30. Individual parameters in VISSIM 5.30 were adjusted and tuned with model calibration and validation. To reduce stochastic variation, ten random-seeded runs were conducted in VISSIM 5.30 for the case study. At the same time, the signal timing plan has been input into SYNCHRO 7.0 to get the control delay for the intersections and links on the arterial and check the traffic flow lines on the TSD. Average speed and delay per vehicle for the whole network,

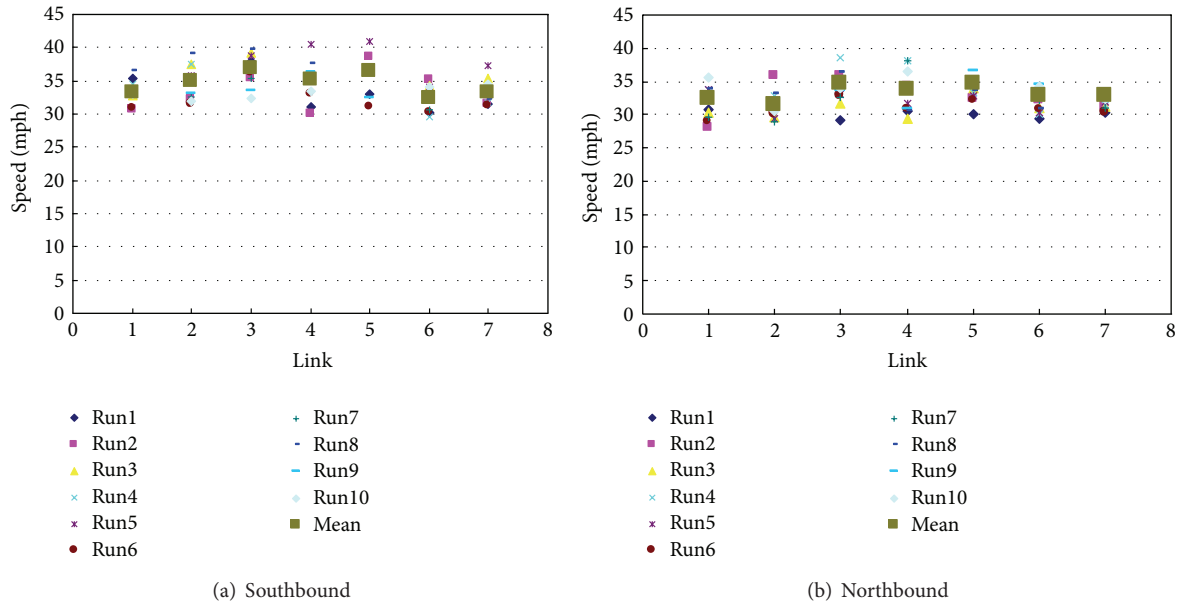


FIGURE 8: Average practical travel speeds for links.

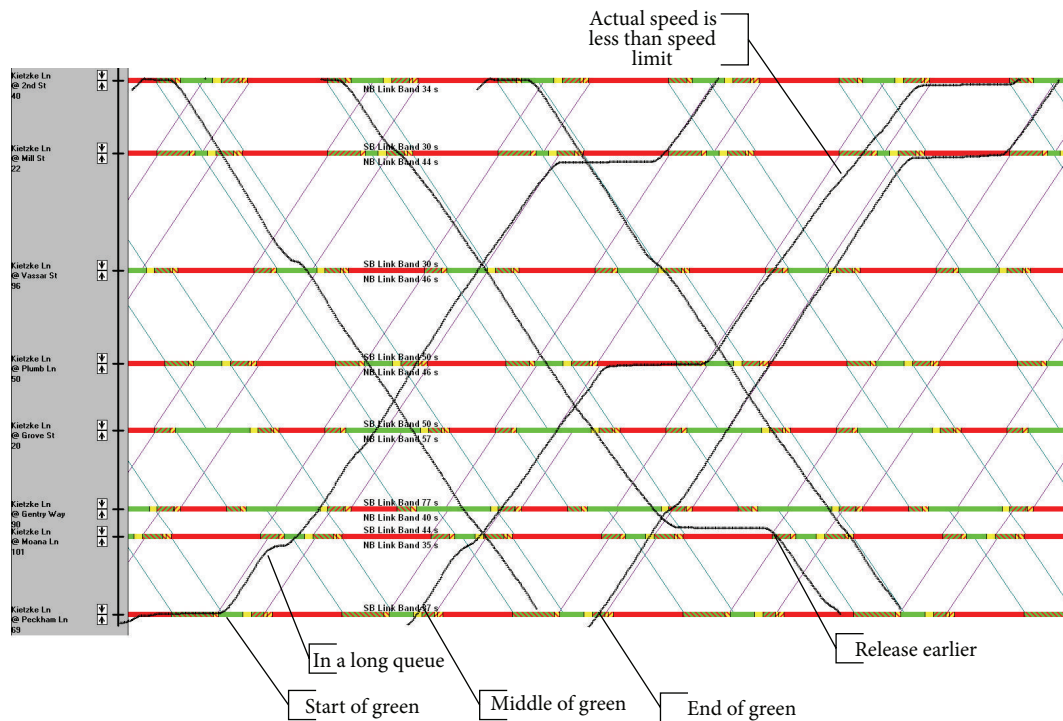


FIGURE 9: GPS trajectory on initial TSD on the speed of 40 mph.

average delay and queue length for the nodes, and average delay for the links are the main simulation results, shown in Table 11.

The results show that a rather significant improvement is achieved after the fine-tuning of signal timing plan with practical travel speed data is done.

## 5. Conclusion

Bandwidth can be defined in terms of two consecutive intersections (link bandwidth) or in terms of an entire arterial (arterial bandwidth). In most previous studies, bandwidth is always referred to as arterial bandwidth. In practice, a balance

TABLE 10: Attainability of link bandwidth on Kietzke Lane with two algorithms.

Link		1	2	3	4	5	6	7	Arterial MOE		
Max link bandwidth (s)		72	81	98	98	134	84	84			
Weighted factor of link		0.1155	0.1345	0.1280	0.1391	0.1827	0.1656	0.1347			
Link bandwidth attainability											
Algorithm	Outbound	$\alpha_1$	$\alpha_2$	$\alpha_3$	$\alpha_4$	$\alpha_5$	$\alpha_6$	$\alpha_7$	$E_m$	$E_b$	$A_c$
Proposed	SB	0.89	1.00	1.00	1.00	1.00	1.00	0.99	0.9855	0.2231	0.7532
	NB	0.89	1.00	1.00	1.00	1.00	1.00	0.99	0.9856		
Messer	SB	0.81	0.94	0.96	0.94	0.84	0.99	0.77	0.8903	0.1923	0.6494
	NB	0.89	0.99	0.85	0.97	0.83	0.99	0.73	0.8915	0.2038	0.6883

TABLE 11: Performance index of signal timing plans with different speeds.

Type	Index	32	Practical speed	35	38	40 (speed limit)
Network performance	Average speed (mph)	18.01	<b>19.12</b>	17.95	17.9	17.69
	Average delay (s)	57.25	<b>53.2</b>	57.91	58.29	61.83
Nodes	Total average delay (s)	210.7	<b>190.6</b>	209.1	213.2	221.4
	Total average queue (ft)	519.8	<b>505.1</b>	527.6	532.8	548.2
	Total intersection control delay	257.2	<b>235.8</b>	260.6	267.2	266.2
Links	Delay from VISSIM	378.7	<b>350.6</b>	370.3	382.1	392.7
	Delay from SYNCHRO	378.3	<b>364.3</b>	382.6	397.6	401.3

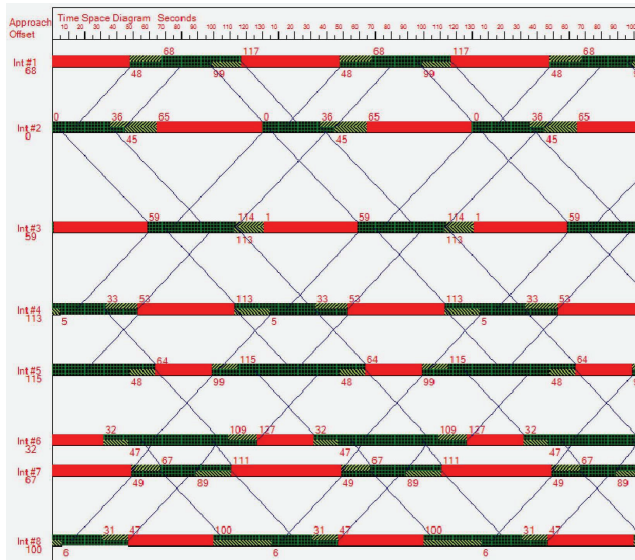


FIGURE 10: TSD of signal timing plan with practical travel speed.

between link bandwidth and arterial bandwidth has proven to be important in optimizing coordinated signal timing plans, because not all drivers need to pass through all the intersections on an arterial. This paper proposes an algorithm on how to obtain an optimal coordinated signal timing plan with both optimized link and arterial bandwidth. The proposed algorithm has two parts: link bandwidth optimization and arterial bandwidth optimization. Link bandwidth attainability is defined as an additional measure of effectiveness for assessing

the optimized results. In the link bandwidth optimization, there are eight cases to calculate upper/lower interference and six cases to calculate offset between two consecutive intersections, based on the improvement of Messer's research. The arterial bandwidth optimization has 3-fold processes, such as calculation of link bandwidth, selection of phase sequence, and calculation of offset, generally link by link. Weighted means of link bandwidth attainability is defined as another measure of effectiveness for selecting the best solution of different phase sequences. The results in the case study show that the proposed algorithm can be used to get a much better signal timing plan than that from Messer's algorithm. Additionally when the number of signals in a system increases, it becomes more difficult to obtain a good bandwidth solution with Messer's algorithm. There is no valid solution of arterial bandwidth using Messer's algorithm when the number of signals is very high. However, the proposed algorithm of this paper can be used to obtain an optimal coordinated signal timing plan with both optimal link bandwidth and arterial bandwidth. Fine-tuning of initial signal timing plan is done to improve link and arterial progression bandwidth using practical travel speed compared to speed limit. The evaluation results show that a rather significant improvement is achieved. In future, we will continue our research on optimizing coordinated signal timing plans under the consideration of the traffic volumes of left-turns and earlier release of left-turn phase.

### Conflict of Interests

There is no known conflict of interests associated with this paper and there has been no significant financial support for

this work that could have influenced its outcome. The authors do not have any possible conflict of interests.

## Acknowledgments

This study is supported by Project “The Fundamental Research Funds for the Central Universities (no. 2013JBM049)” and “National Basic Research Program of China (no. 2012CB725403).”

## References

- [1] Federal Highway Administration and USDOT, *Traffic Signal Timing Manual*, United States Department of Transportation, Washington, DC, USA, 2008.
- [2] J. Bonneson, S. Sunkari, and M. Pratt, *Traffic Signal Operations Handbooks*, Texas Transportation Institute, Texas DOT, Texas, Tex, USA, 2009.
- [3] Minnesota DOT, *Mn/DOT Traffic Signal Timing and Coordination Manual*, Minnesota Department of Transportation, Saint Paul, Minn, USA, 2009.
- [4] Z. Tian and T. Urbanik, “System partition technique to improve signal coordination and traffic progression,” *Journal of Transportation Engineering*, vol. 133, no. 2, pp. 119–128, 2007.
- [5] X. K. Yang, “Comparison among computer packages in providing timing plans for Iowa arterial in Lawrence, Kansas,” *Journal of Transportation Engineering*, vol. 127, no. 4, pp. 311–318, 2001.
- [6] K. G. Baass, “Another look at bandwidth maximization,” *Transportation Research Record*, no. 905, pp. 38–47, 1983.
- [7] C. J. Messer, R. H. Whitson, C. Dudek, and E. J. Romano, “A variable -sequence multiphase progression optimization program,” *Highway Research Record*, no. 445, pp. 24–33, 1973.
- [8] C. J. Messer, H. E. Haenel, and E. A. Koeppel, “A report on the user’s manual for progression analysis and signal system evaluation routine-PASSER II,” Research Report 165-14, Texas Transportation Institute, College Station, Tex, USA, 1974.
- [9] J. D. C. Little, M. D. Kelson, and N. H. Gartner, “MAXBAND: a program for setting signals on arteries and triangular networks,” *Transportation Research Record*, no. 795, pp. 40–46, 1981.
- [10] N. H. Gartner, S. F. Assmann, F. Lasaga, and D. L. Hou, “MULTI-BAND: a variable-bandwidth arterial progression scheme,” *Transportation Research Record*, vol. 1287, pp. 212–222, 1990.
- [11] C. Stamatiadis and N. H. Gartner, “MULTIBAND-96: a program for variable-bandwidth progression optimization of multiarterial traffic networks,” *Transportation Research Record*, no. 1554, pp. 9–17, 1996.
- [12] N. Papola, “Bandwidth maximization: split and unsplit solutions,” *Transportation Research Part B*, vol. 26, no. 5, pp. 341–356, 1992.
- [13] N. Papola and G. Fusco, “Maximal bandwidth problems: a new algorithm based on the properties of periodicity of the system,” *Transportation Research B*, vol. 32, no. 4, pp. 277–288, 1998.
- [14] H. K. Sripathi, N. H. Gartner, and C. Stamatiadis, “Uniform and variable bandwidth arterial progression schemes,” *Transportation Research Record*, no. 1494, pp. 135–145, 1995.
- [15] R. S. Pillai, A. K. Rathi, and S. L. Cohen, “A restricted branch-and-bound approach for generating maximum bandwidth signal timing plans for traffic networks,” *Transportation Research B*, vol. 32B, no. 8, pp. 517–529, 1998.
- [16] C. Feng, *Projection algorithm for improved corridor signal coordination [M.S. thesis]*, Master of Science in Engineering, University of Akron, Civil Engineering, Akron, Ohio, USA, 2009.
- [17] N. H. Gartner and C. Stamatiadis, “Arterial-based control of traffic flow in urban grid networks,” *Mathematical and Computer Modelling*, vol. 35, no. 5-6, pp. 657–671, 2002.
- [18] D. Husch and J. Albeck, *Synchro 6: Traffic Signal Software, User Guide*, Trafficware, Albany, Calif, USA, 2003.
- [19] S. Rhyne, “Utilizing GPS and GIS in traffic signal coordination,” in *Proceedings of the Annual Meeting and Exhibit Compendium of Technical Papers (ITE ’05)*, vol. 8, 2005.
- [20] C. A. Quiroga and D. Bullock, “Travel time studies with global positioning and geographic information systems: an integrated methodology,” *Transportation Research C*, vol. 6C, no. 1-2, pp. 101–127, 1998.
- [21] H. Rakha, F. Dion, and H. Sin, “Using global positioning system data for field evaluation of energy and emission impact of traffic flow improvement projects: issues and proposed solutions,” *Transportation Research Record*, no. 1768, pp. 210–223, 2001.
- [22] Z. A. Sabra, *Global Positioning System for Time-Based Signal Coordination: Benefit-Cost Analysis*, Baltimore Regional Traffic Signal Forum, Baltimore, Md, USA, 2nd edition, 2005.
- [23] JAMER Technologies, *GPS Travel Time Reference Manual-Travel Time and Delay Data Collection Software*, JAMER Technologies, Hatfield, Pa, USA, 2004.
- [24] JAMER Technologies, *PC-Travel for Windows Reference Manual-Travel Time and Delay Analysis Software*, JAMER Technologies, Hatfield, Pa, USA, 2004.

## Research Article

# A Mathematical Model for the Flow Resistance and the Related Hydrodynamic Dispersion Induced by River Dunes

**Marilena Pannone, Annamaria De Vincenzo, and Francesco Brancati**

*School of Engineering, University of Basilicata, Viale dell'Ateneo Lucano 10, 85100 Potenza, Italy*

Correspondence should be addressed to Marilena Pannone; [marilena.pannone@unibas.it](mailto:marilena.pannone@unibas.it)

Received 5 July 2013; Revised 1 October 2013; Accepted 1 October 2013

Academic Editor: Mohamed Fathy El-Amin

Copyright © 2013 Marilena Pannone et al. This is an open access article distributed under the Creative Commons Attribution License, which permits unrestricted use, distribution, and reproduction in any medium, provided the original work is properly cited.

Present work is aimed at the derivation of a simply usable equation for the total flow resistance associated with river bedforms, by a unifying approach allowing for bypassing some of the limiting restrictions usually adopted in similar types of studies. Specifically, we focused on the effect induced by the out-of-phase free surface undulations appearing in presence of sand dunes. The proposed expression, obtained by combining the balance of momentum referred to the control volume whose longitudinal dimension coincides with the dune wavelength and the energy balance integrated between its extreme sections, was tested by comparison with some laboratory experimental measurements available in the literature and referred to steady flow past fixed, variably rough bedforms. In terms of shear stress or friction factor, the proposed theory provides estimates in good agreement with the real data, especially if evaluated against the performances provided by other classical similar approaches. Moreover, when analyzed in terms of hydrodynamic dispersive properties as a function of the skin roughness on the basis of a previously derived analytical solution, the dune-covered beds seem to behave like meandering channels, responsible for a globally enhanced fluid particles longitudinal spreading, with a relatively reduced effect in the presence of less pronounced riverbed modelling.

## 1. Introduction

Stream flow along undulated beds has been widely studied in the past, both analytically and experimentally, in terms of resistance factors [1–12]. Several more recent experimental-analytical works have dealt with the fluid-dynamical aspect of the problem through innovative techniques (e.g., [13–16]).

Indeed, for a long time it has been commonly accepted that large-scale bedforms like dunes and bars are generated by large-scale turbulence, vertical or horizontal, respectively [17–20] through the so-called bursting processes [19–26]. Bursting process, or simply burst, is synonym of evolution of a large macroturbulent eddy. In the zone of highest resistance, that is, near the flow solid boundaries, very large values of fluctuating shear stresses make the fluid rolling-up into eddies. The so-generated vortices move away from river bed or banks as they are conveyed downstream by the flow, in the meantime diffusing, coalescing, eventually breaking-up

at the borders of the domain, and thus generating a space-time rhythmic sequence [27].

The periodic (or, more realistically, pseudoperiodic) distortion of the velocity field, in its turn, triggers off the deformation of the mobile bed and, therefore, the creation of typical bedforms. From turbulence measurements, it has been found that the fully-developed dune wavelength  $\Lambda$  scales with the average flow depth  $H$ :  $\Lambda \sim 6H$ . Unavoidably these bedforms, which constitute the physical imprint of the turbulent flow, are affected by the strong and ubiquitous random element characterizing the high Reynolds number processes and should be therefore analyzed by resorting to suitable stochastic approaches (e.g., [28–31]). In any case, even leaving aside the random aspect, in turbulent flow conditions and in presence of solid transport, there is a wide set of elements from whose interaction the total resistance opposed by the river bed to the water flux is determined. For instance, the skin roughness, commonly identified with

shape and dimensions of the material constituting the wetted contour, can incorporate other factors whose quantitative effect can not be evaluated with the same accuracy, that is, the concentration and the distribution of the grains, or the vegetation. The latter, which is usually present both on the bottom and the banks of the channel, is associated with a sometimes considerable reduction of the bed capacity, slowing down the flow in a more or less pronounced fashion depending on type, height, density, and distribution of the arboreal species. To the skin roughness, it is then necessary to add the resistance induced by the geometric bed irregularities, like those represented by particularly uneven wetted contours and, obviously, those deriving from the continuously evolving bed configuration and related to the specific type of solid load (ripples, dunes, and anti-dunes up to a limit grain size and macroroughness for larger grains dimensions). Furthermore, one should account for the dynamical influence of the solid transport itself, either as bed or suspended load, which tends to highlight the effect of the bed irregularities and to increase the flow resistance and, finally, for the changes that the transported solid particles cause on the physical-chemical characteristics of the stream. Even restricting the investigation field to the uniform or on average-uniform flows, and therefore neglecting the contributions to the resistance represented by obstacles and obstructions (i.e., bridge piers, dams and alluvial fans), as well as those attributable to the flow rate oscillations, it is clearly difficult to quantify the effects due to so many factors.

The aim of present work is represented by the analytical derivation of a closed-form solution for the estimation of the total resistance in presence of river dunes (a typically two-dimensional sand bed pattern) in perfect equilibrium conditions, that is, neglecting the effects of their downstream migration, based on the elaboration of the global momentum and energy balances. The final expression accounts for skin and shape roughness in a nontrivially additive way, and for the free surface undulation as a function of Froude number; the intrinsically nonstationary phenomenon of the flow separation near the dune crest is evaluated in terms of resistance resorting to an equivalent steady flow configuration.

The proposed approach is then tested by comparing the analytical estimates of the total friction factor with the laboratory measurements provided by Engel and Lau [9], and the analytical estimates of the total shear stress with the laboratory measurements documented in McLean et al. [15]. Moreover, based on a previously derived closed-form solution for the hydrodynamic dispersion coefficient [31], the data by Engel and Lau [9] are utilized to investigate the relationship between the flow resistance and the dispersive properties of streams flowing past undulated sand beds.

## 2. Mathematical Formulation

Consider steady and periodically uniform two-dimensional streams. For weak curvatures of the fluid particles trajectory determined by bottom and free surface undulations, the pressure can be assumed as hydrostatically distributed along all the verticals. Note that, in the separated flow zone

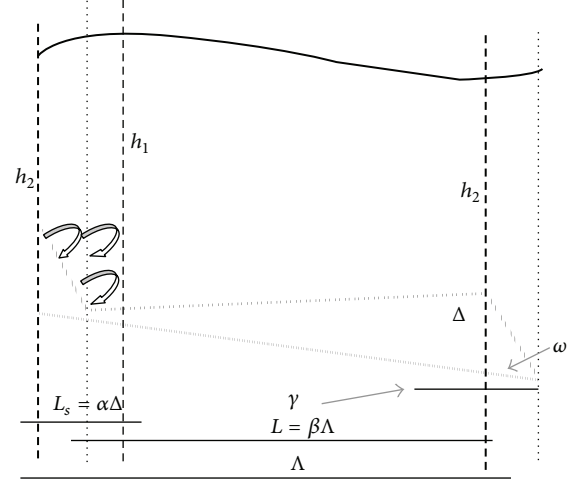


FIGURE 1: Sketch of the physical model.

downstream the dune crest, the validity of the assumption is guaranteed by Helmholtz theory and by the substantial immobility of the fluid subject to the geopotential. In the same zone, the shear stresses are usually neglected due to their very small negative values. Finally, in the low Froude number regime flows, water and bed sediment waves are commonly out of phase. Specifically, it is reasonable to expect the maximum drop of the free surface near the dune peak, due to the acceleration induced by its upstream positive slope, and the maximum rise in the separated and highly turbulent zone where the flow, after having achieved the minimum velocity, realigns and accelerates again (see Figure 1). In the most standard situations, with the basic geometric parameters assuming the most common values, the separation length  $L_s$  ranges from about  $4\Delta$  to about  $6\Delta$ , where  $\Delta$  indicates the dune height measured along the vertical [9]. Generally,  $L_s = \alpha\Delta$ . In order to estimate the total friction factor in such circumstances, we have applied the momentum balance equation to the control volume (basically, the flow domain identified by the dunes sequence wavelength) delimited in Figure 1 by the free surface, the dune contour, and the vertical bold dashed lines:

$$\mathbf{I} + \mathbf{M}_o - \mathbf{M}_i = \mathbf{G} + \mathbf{\Pi}, \quad (1)$$

where  $\mathbf{I}$  indicates the local inertia,  $\mathbf{M}_o$  and  $\mathbf{M}_i$  the outflow and inflow momentum flux, respectively,  $\mathbf{G}$  the control volume weight and  $\mathbf{\Pi}$  the resultant of the applied surface forces (isotropic pressures plus shear stresses). In turbulent steady conditions, and because of the periodicity of the peculiar velocity field, the projection of that equation along the horizontal direction  $x$  yields

$$\Pi_x = \tau' L + p_b (\Delta - i_f L) - p_s [\Delta + i_f (\Lambda - L)] = 0 \quad (2)$$

with

$\tau'$ : shear stress due to the skin roughness only;

$\Lambda$ : horizontal length of the sand wave;

$L = \beta\Lambda = \{1 - \Delta/\Lambda[\cos(\omega + \gamma)\cos\gamma/\sin\omega]\}\Lambda$ :  
horizontal length of the dune back;

$i_f = \tan\gamma$ : bottom slope (generally weak);

$\omega$ : angle of the downstream slope;

$p_b$ : average pressure acting on the dune back;

$p_s$ : average pressure acting on the dune in the separation zone ( $L_s$ ).

It is worth noting that in (2) the length of the control volume where the skin shear stress is considered active coincides with the whole upstream dune surface. That assumption is justified for bed disturbances characterized by relatively small amplitude (small  $L_s$ ). Considering an approximately linear variation of the free surface profile associated with not exceedingly steep bedforms, and  $\omega \rightarrow \pi/2$ , we obtain

$$p_b = \gamma_w H \quad p_s \cong \gamma_w \left( H - \frac{\delta}{2} \right), \quad (3)$$

where  $\delta = h_1 - \Delta - h_2$  represents the difference between maximum and minimum free surface elevation and  $\gamma_w$  is the water specific weight. Actually, the second of the previous identities should be rewritten as:

$$p_s = \gamma_w (H - b), \quad (4)$$

$$b = \frac{\delta}{2} \left[ \frac{\beta}{1 - \alpha(\Delta/\Lambda)} - \frac{(1 - \beta)}{\alpha(\Delta/\Lambda)} \right].$$

However, (4) tends to its approximate counterpart for small  $\Delta/\Lambda$  and  $\omega \rightarrow \pi/2$ . The relationship linking  $\delta$  to the flow kinematic parameters can be derived by considering the energy balance (1D Saint Venant equation) integrated between Sections 1 and 2, characterized by maximum and minimum flow depths  $h_1$  and  $h_2$ , respectively. Under the above-mentioned conditions,

$$i_f L + h_1 + \frac{U_1^2}{2g} - \frac{\tau' L}{\gamma_w H} = \Delta + h_2 + \frac{U_2^2}{2g} \quad (5)$$

with  $U_1$  and  $U_2$  indicating the inflow and outflow section averaged velocities, respectively, and  $\tau' L/\gamma_w H$  the unit weight energy loss. The result reads

$$\delta = \frac{U_2^2 - U_1^2}{2g} - \left( i_f - \frac{\tau'}{\gamma_w H} \right) L. \quad (6)$$

Now, by virtue of continuity:  $UH = U_1 h_1 = U_2 h_2$ , and assuming  $H$  as the geometric mean of the extreme flow depth values:  $H \sim (h_1 h_2)^{1/2}$ , one obtains

$$\delta = \frac{\Delta F_r^2}{1 - F_r^2} - \left( i_f - \frac{\tau'}{\gamma_w H} \right) \frac{L}{1 - F_r^2}, \quad (7)$$

where  $F_r = U/(gH)^{1/2}$  indicates the average Froude number (kinetic index). Finally, the combination of (2), (3) and (7) yields the following expression for the total shear stress

$\tau = \gamma H i_f$  as a function of Froude number and geometric bedforms parameters:

$$\tau = \beta \left\{ 1 + \frac{\Lambda}{2H(1 - F_r^2)} \left[ \frac{\Delta}{\Lambda} + (1 - \beta) i_f \right] \right\} \tau' \quad (8)$$

$$+ \frac{\gamma_w}{2} \left[ \frac{\Delta}{\Lambda} + (1 - \beta) i_f \right] \left( \frac{\Delta F_r^2}{1 - F_r^2} - \frac{\beta \Lambda i_f}{1 - F_r^2} \right).$$

Equation (8) can straightforwardly be transformed in terms of friction factors invoking the well-known relationships:

$$f = \frac{8\tau}{\rho U^2} \quad f' = \frac{8\tau'}{\rho U^2}, \quad (9)$$

where  $\rho$  is the water density, leading to

$$f = Af' + B, \quad (10)$$

$$A = \beta \left\{ 1 + \frac{\Lambda}{2H(1 - F_r^2)} \left[ \frac{\Delta}{\Lambda} + (1 - \beta) i_f \right] \right\},$$

$$B = 4 \left[ \frac{\Delta}{\Lambda} \frac{1}{1 - F_r^2} - \frac{\Lambda}{H} \frac{\beta i_f}{F_r^2(1 - F_r^2)} \right].$$

As (10) clearly suggests, the proposed approach produces an analytical expression for the total friction factor which is not the mere superposition of the effects of skin roughness and bed modelling, as it happens in all the previous works dealing with the same topic by analytical tools. On the contrary, besides a term dependent on the bed geometric parameters and on the Froude number only ( $B$ ), which essentially accounts for the contribution to the flow resistance coming from the macroscopic bed deformation, it includes a coefficient ( $A$ ) which modulates the skin friction factor  $f'$  on the basis of the same characteristics and, therefore, accounts for the declining contribution of the grain roughness when the bottom undergoes a transition from flat to mildly steep. The derivation of the hydrodynamic dispersion coefficient in presence of sand dunes sequences was carried out based on a stochastic Lagrangian model [31], extensively discussed in the next section, when the corresponding solution is analyzed in terms of dependence on the dunes flow resistance.

### 3. Results and Discussion

In order to test the proposed formulation, we employed the experimental data provided by Engel and Lau [9], because they cover, in our opinion, a rather meaningful and well controlled range of geometrical and hydrodynamical parameters for approximately two-dimensional flow in presence of dunes. In their laboratory surveys, the authors utilized artificial and fixed bedforms characterized by a constant height  $\Delta$  equal to 3 cm, a variable slope  $\Delta/\Lambda$  ranging from 0.02 to 0.07, and a downstream angle  $\omega = 30^\circ$ . The skin roughness was made by a fixed grain layer with a  $D_{50}$  varying between 0.35 and 9 mm. Furthermore, based on what was recommended by Yalin [4] and others, flow conditions and

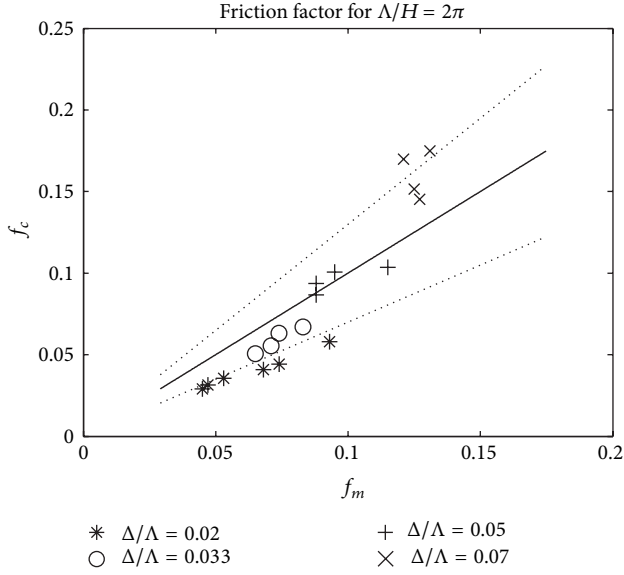


FIGURE 2: Comparison between measured [9] and calculated friction factors. The dotted lines correspond to the 70% confidence interval.

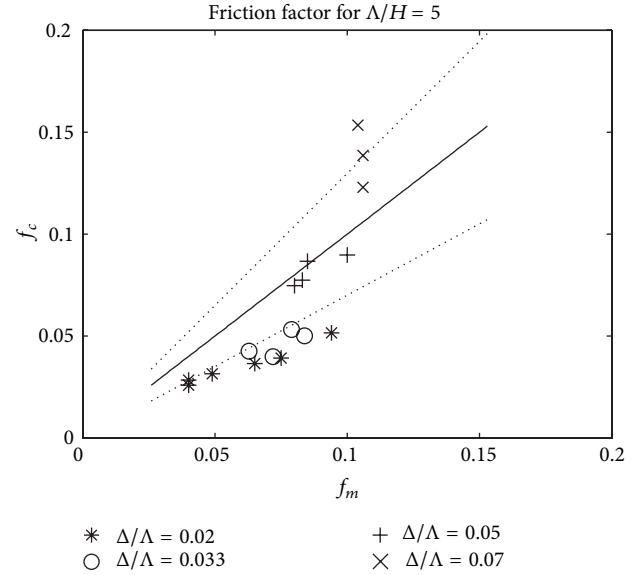


FIGURE 3: Comparison between measured [9] and calculated friction factors. The dotted lines correspond to the 70% confidence interval.

effects were analyzed for ratios of wavelength to average depth  $\Lambda/H$  equal to  $2\pi$  (which is almost 6) and 5; the average bed slope  $i_f$  and the Froude number  $Fr$  varied in a nonsystematic fashion, from  $4.16 \times 10^{-4}$  to 0.022 and from 0.22 to 0.42, respectively. Finally, the estimation of the skin friction factor was carried out based on the following logarithmic formula:

$$f' = 1.28 \left( \ln \frac{11H}{K_s} \right)^{-2}, \quad (11)$$

where  $K_s$ , sand-equivalent roughness index, can be approximated by  $2D_{50}$ . Figures 2 and 3 illustrate, for  $\Lambda/H$  equal to  $2\pi$  and 5, respectively, the comparison between the values of the total friction factor experimentally measured and those mathematically obtained through the combination of momentum and energy balances (10). As already mentioned, for each of the subcategories representing the different dunes slopes,  $i_f$  and  $Fr$  vary in a non systematic fashion, while the relative roughness  $D_{50}/H$  increases along with both the calculated and the measured friction factors, ranging from 0.0016 to 0.0513 for  $\Lambda/H = 2\pi$  and from 0.0013 to 0.0402 for  $\Lambda/H = 5$ . The grain Reynolds number  $u_* K_s / \nu$ , with  $u_*$  indicating the shear velocity and  $\nu$  the kinematic water viscosity, is always larger than 70, conventionally meaning rough fully turbulent flow.

As Figures 2 and 3 (which display the 70% confidence intervals also) clearly show, the best agreement is obtained for  $\Delta/\Lambda = 0.05$ , that is, for mildly steep dunes. Conversely, the theoretical formula underestimates the total friction factor for the flatter bedforms ( $\Delta/\Lambda = 0.02$  e  $0.033$ ) and overestimates that for the steeper ones ( $\Delta/\Lambda = 0.07$ ). Given the hypotheses at the basis of (10), it is reasonable to expect a deterioration of the performance of the equation as the dune slope increases, whereas it is worth discussing the discrepancy detected in the field of the flatter bedforms.

Indeed, it is possible that the proposed formula is not able to completely account for the greater or lesser relevance to be attributed to the skin roughness as a function of the dune slope and, although it is not a simple effects superposition, it should perhaps incorporate a modulation coefficient of  $f'$  which could vary with the magnitude of the flow dragging action and, presumably, in a nonlinear way with the dune slope. In any case, considering the possibility of measurement errors, the assumptions underlying the closed form solution (which, for instance, unavoidably neglects the pulsatile and crucial phenomenon of the vortex shedding at the dune crest), and a percentage error which is on average smaller than 20–25%, we can conclude that (10) incorporates within a reasonable degree of approximation the influence of bottom and free surface undulations on the flow resistance in riverbeds. On the other hand, the comparison with the performances provided by other compact expressions for the total  $f$  (Engelund [5]; Garde and Ranga Raju [6]; Vanoni and Hwang [7], resp.):

$$f = f' + 4 \frac{\Delta}{\Lambda} \frac{\Delta}{H},$$

$$f = \frac{8}{\left[ 3.2(H/D_{50})^{1/6} \right]^2}, \quad (12)$$

$$f = \frac{8}{(9.3 \log(\Lambda H / \Delta^2) - 6.5)^2}$$

effectively demonstrates (see Figure 4, displaying the histograms of the percentage errors for the 4 available equations, including (10)) the interpretative improvement represented by the present study.

Figure 5 shows the behaviour of (10) as a function of Froude for  $\Lambda/H = 2\pi$ ,  $i_f = 0.0012$ ,  $H = 0.17$  m,  $D_{50} = 0.0005$  m, and the 4 sample values of  $\Delta/\Lambda$ . Note that the selected range of Froude corresponds to the interval of values detected in the Engel and Lau experiments, while the selected values of bed slope, depth, and grain size have been obtained by averaging the laboratory data. The estimates of  $f$  are obviously increasing, Fr being the same, as  $\Delta/\Lambda$  increases. The variation of  $f$  with Fr is not too pronounced for weak dune slopes, and that is in agreement with the conclusions drawn by Engel and Lau [9] themselves, which were nevertheless based on measurements carried out by letting Fr vary in a non systematic way. The substantial invariance with respect to the kinetic flow index does not hold for the steeper bedforms. Indeed, with  $\Delta/\Lambda = 0.07$  the total  $f$  ranges from about 0.12 for Fr = 0.24 to about 0.16 for Fr = 0.45. The effect of the increasing average flow velocity on the rough bedforms-induced acceleration is further highlighted in Figure 6, showing the relative free surface drop  $\delta/\Delta$  (with  $\delta$  given by (7)) as a function of the Froude number for  $\Lambda/H = 2\pi$ . The diagram seems to detect the existence of a single mathematical relationship linking  $\delta/\Delta$  to Fr regardless of the dune slope, with values up to the 18% for the faster streams.

In order to double-check the soundness of the proposed approach, (8) was tested based on the experimental measurements provided by McLean et al. [15]. In that data series (in all 8 runs) the selected dune slopes were equal to 0.05 (runs 2, 3, T5(7), and T6(8)) or 0.1 (runs 4, 5, 6, and 7). The ratio of wavelength to average flow depth was 20 or 10, respectively (thus, larger than what is considered the “expected” value ( $\sim 6$ ) of that parameter). Froude number ranged from 0.1 to 0.31. The measured quantities included the total shear stress estimated from the average flow depth  $\gamma_w Hi_f$ , the total shear stress estimated from the hydraulic ratio  $\gamma_w Ri_f$ , and the total shear stress obtained at the bottom from the Reynolds formula  $-\rho\langle uw \rangle_0$ , with  $u$  and  $w$  indicating the fluctuating component of longitudinal and vertical velocity, respectively, and the angle brackets indicating the ensemble mean. Note that, for runs from 2 to 7, with a channel width equal to 0.9 m, the percentage error in substituting the actual hydraulic radius with the average flow depth  $[(R-H)/R]$  % was  $-35.11\%$ ,  $-121.33\%$ ,  $-35.33\%$ ,  $-35.33\%$ ,  $-66.67\%$ , and  $-124.44\%$ . Thus, the experimental setup reproduced a situation considerably far from the two-dimensional flow assumed in our mathematical formulation. As Figure 7 clearly shows, although one-half of the runs was performed with a very high (almost “extreme”) value of dune slope (0.1) and the boundary effect was definitely not negligible, the shear stress estimates based on (8) (black asterisks) fall well inside the range of  $\tau$  values identified by the experimental measurements or, at the most, coincide with one/two of them, further demonstrating the robustness of present first-order analytical approach.

Finally, for the sake of completeness, Figure 8 shows the behaviour of the dimensionless hydrodynamic dispersion coefficient as a function of the skin friction factor for the four different dune slopes whose effects were analyzed in the present work. The dimensionless coefficient  $D_x$  was evaluated on the basis of the analytical solution proposed by Pannone

[31], starting from the Lagrangian stochastic interpretation of the fluid particles spreading process:

$$D_x(t) = \frac{1}{2} \frac{dX_{11}}{dt} = \int_0^t \langle U' [X(t)] U' [X(\tau)] \rangle d\tau, \quad (13)$$

where the primes indicate the random fluctuations,  $X = X(t)$  is the longitudinal particle trajectory,  $X_{11}(t) = \langle X'(t)^2 \rangle$  is the particle trajectory covariance, and  $\langle U' [X(t)] U' [X(\tau)] \rangle$  the Lagrangian velocity covariance. Incidentally, the (periodic) random nature of the Lagrangian velocity field derives from the sampling of the section averaged velocity distribution associated with the sand waves sequence (and then represented by a strong deterministic and periodic trend), by fluid particles subject to diffusive transport mechanisms usually described by Fick’s law and Brownian paths. Thus, assuming a bed elevation covariance represented by a single cosine function, with a variance proportional to the dune height squared (e.g., [27]):

$$\langle \tilde{h}(x) \tilde{h}(x + \xi) \rangle = C_h(\xi) = \left(\frac{\Delta}{2}\right)^2 \cos\left(\frac{2\pi\xi}{\Lambda}\right) \quad (14)$$

and relying on the continuity condition for not exceedingly high and steep dunes, that is, for relatively small depth deviations  $\tilde{h}$ :

$$U(x) = \frac{UH}{h(x)} = \frac{UH}{H + \tilde{h}(x)} \cong U \left(1 - \frac{\tilde{h}(x)}{H}\right), \quad (15)$$

the following first order solution for small  $\Delta/\Lambda$  was obtained [31]:

$$D_x(t) = \frac{(\Delta^2/16)(U/H)^2}{(\pi^2/\Lambda^2)((4\pi^2\varepsilon_x^2/\Lambda^2) + U^2)} \times \left\{ \frac{4\pi^2\varepsilon_x}{\Lambda^2} \left[ 1 - \exp\left(-\frac{4\pi^2\varepsilon_x t}{\Lambda^2}\right) \cos\left(\frac{2\pi U}{\Lambda}t\right) \right] + \frac{2\pi U}{\Lambda} \exp\left(-\frac{4\pi^2\varepsilon_x t}{\Lambda^2}\right) \sin\left(\frac{2\pi U}{\Lambda}t\right) \right\}. \quad (16)$$

With  $D_x = D_x(\infty)/U\Lambda$  and  $\varepsilon_x = 5.93u_*'H = 5.93\sqrt{\tau'/\rho H}$  defining the flat bed turbulent mixing coefficient [32], one can finally write

$$D_x \cong \frac{1}{8\pi^2} \left(\frac{\Delta}{H}\right)^2 \frac{\sqrt{2/f'}}{(1 + (2/\pi^2 f'))}. \quad (17)$$

As Figure 8 explains, the regime value of the dimensionless longitudinal dispersion coefficient (which practically represents one-half of the time-derivative of the solute cloud inertia moment and is then a measure of the rate at which the cloud is dispersed and diluted by the flow in the given direction) generated by the dune-like periodical nonuniformity is strongly affected by the bed-form steepness, raising with  $\Delta/\Lambda$  everything else being the same (more intense

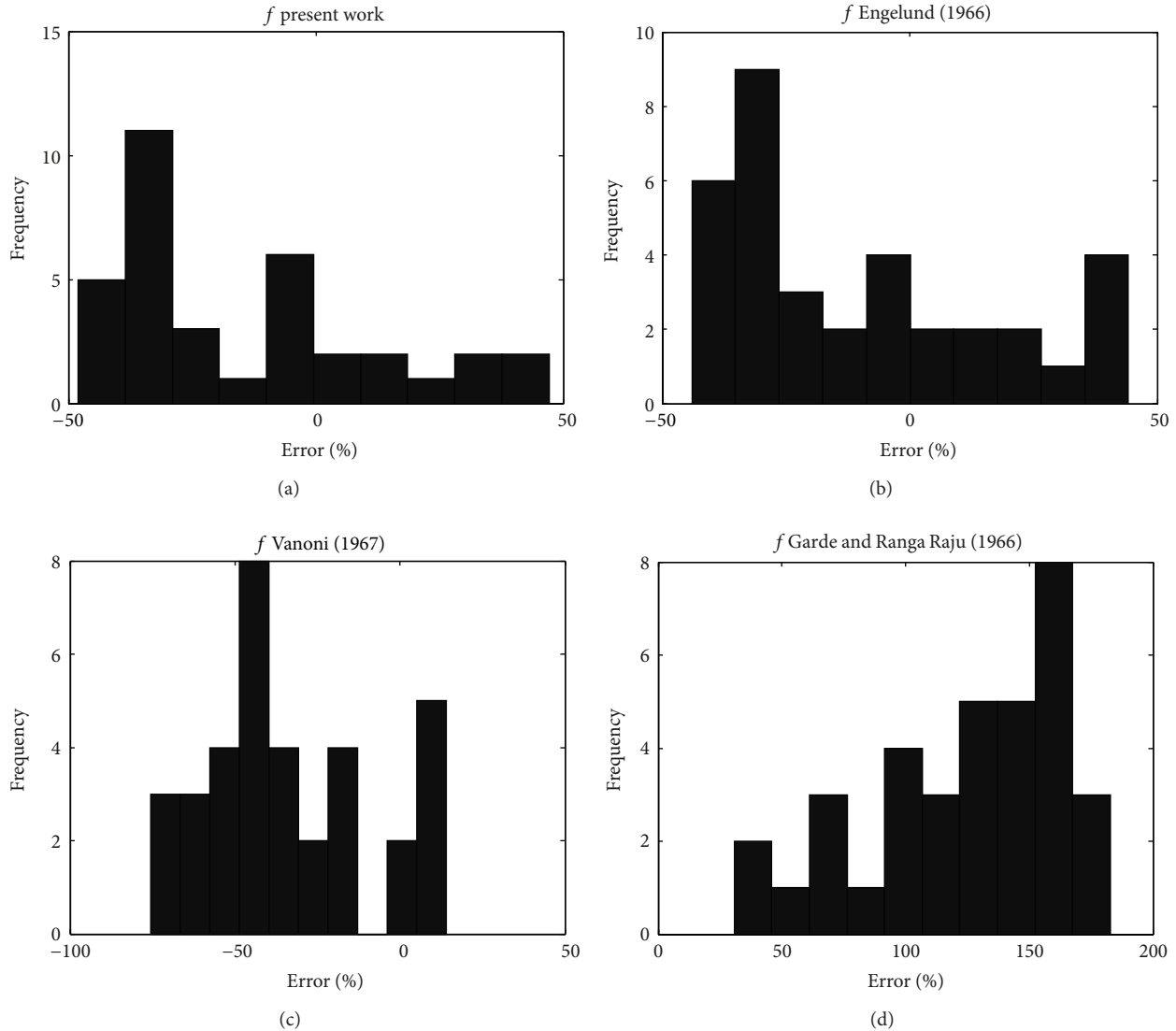


FIGURE 4: Histograms of percentage errors corresponding to the use of (10) and (12).

macrovortices dissipation). Furthermore, whereas for low values of  $\Delta/\Lambda$  the coefficient is almost independent of the degree of wall turbulence depending on  $f'$ , as  $\Delta/\Lambda$  increases the asymptotic  $D_x$  is more and more influenced by the skin friction factor, to which it is directly related. We could say that, in terms of hydrodynamic dispersion, the inclined planes of upstream and downstream faces of the dune seem to have the same function of the river meanders. Indeed, less rough flow field contours induce less turbulent (and, therefore, less uniform) time-mean velocity profiles due to the slower transverse mixing. Less uniform wall velocity profiles in turn cause a more pronounced solute hydrodynamic dispersion along the local flow direction and, by continuity, a consequent reduced dispersion along the orthogonal ones. If the local flow direction is considerably different from the straight horizontal direction characterizing straight-axis flat-bed rivers (highly meandering rivers = horizontal deviations; highly undulated beds = vertical deviations), the longitudinal

dispersion diminishes. That would explain why, as  $\Delta/\Lambda$  increases, the longitudinal dispersion coefficient becomes more sensitive to the skin roughness variations.

#### 4. Conclusions

Present work has proposed the analytical derivation of a simple and easily usable closed-form solution for the estimation of the total flow resistance in presence of river dunes, based on the application of the global equilibrium equations. The final expression accounts for skin and shape roughness in a non trivially additive way and for the free surface undulation as a function of the Froude number; the intrinsically non stationary phenomenon of flow separation at the dune crest is handled in terms of resistance based an equivalent steady flow configuration.

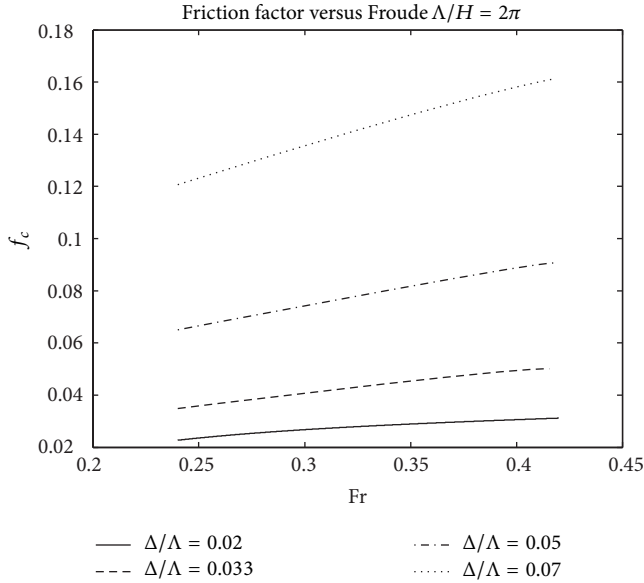


FIGURE 5: Behaviour of the calculated friction factor as a function of Froude number.

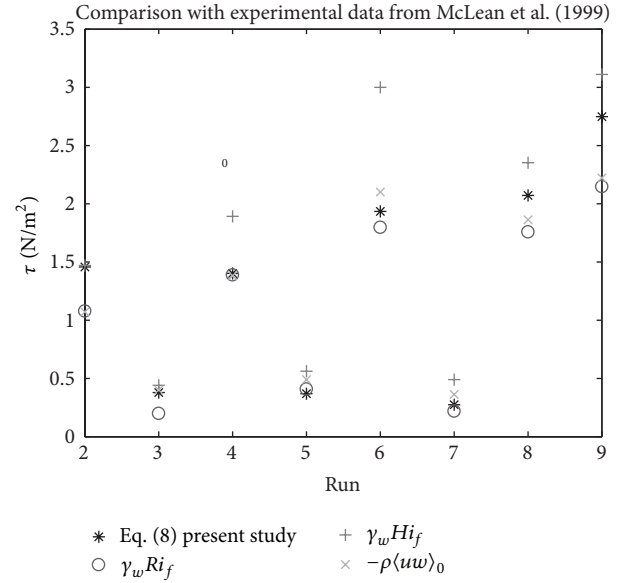


FIGURE 7: Comparison between measured [15] and calculated total shear stresses.

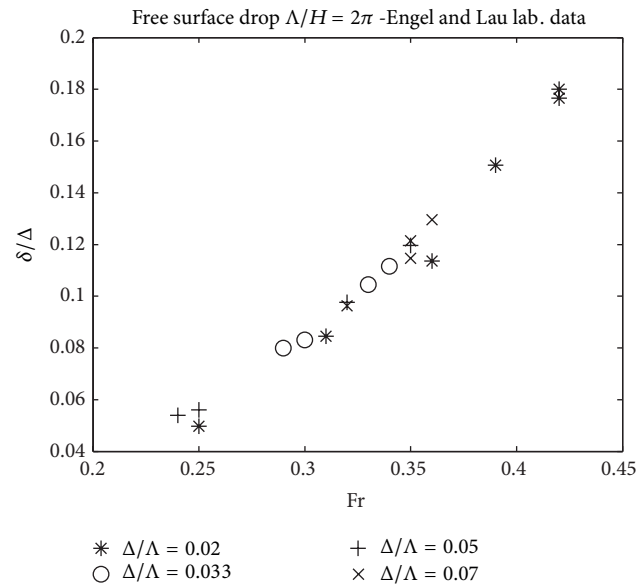


FIGURE 6: Effect of Froude number on the free surface relative drop.

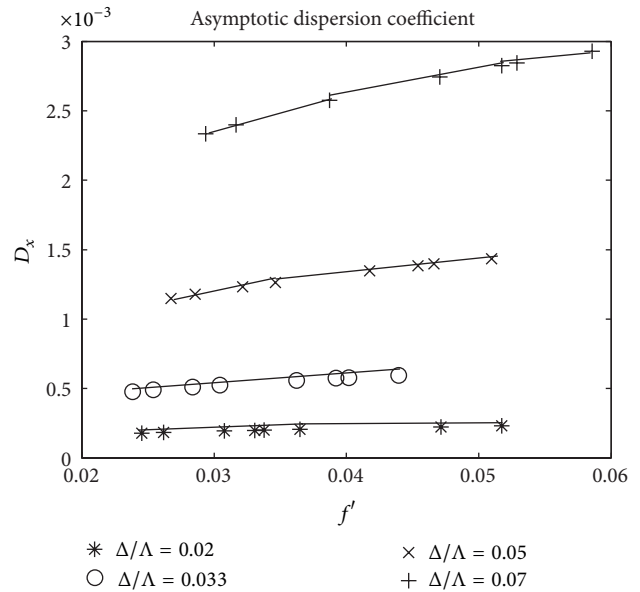


FIGURE 8: Behaviour of the dimensionless asymptotic dispersion coefficient as a function of the skin friction factor for different dune slopes.

That expression is tested by comparing the analytical estimates of the total friction factor with the laboratory measurements provided by Engel and Lau [9], against the equations proposed by classical literature works [5–7]. In the sampled conditions (for varying average flow velocity and everything else being the same), the three classical formulas rewritten in terms of dimensionless friction factor (12) are not able to account for the effect of the free surface undulation and would provide a constant value for  $f$  regardless of the Froude number. Conversely, (10), as shown by Figures 2 and 3, seems to be able to capture the influence systematic and separated of that crucial parameter by providing friction

factor values rather close to the measured ones, especially for the mildly steep case  $\Delta/\Lambda = 0.05$ . On the other hand, the comparison of the performances provided by the 4 equations (Figure 4) in terms of percentage error histograms reveals the considerable interpretative improvement of the phenomenon represented by (10). Figure 5 highlights a definite increase of the flow resistance with the Froude number that is more pronounced in presence of steeper bedforms, as one would expect due to the more intense disturbances induced within the core of the turbulent flow. The analysis of the relative free

surface drop in Figure 6 shows the substantial independence of that parameter on the dune slope and its monotonic increase with the Froude number. A further development of the research could address the comprehension and the mathematical modelling of the mechanisms through which the skin roughness resistance is modulated when added to the shape resistance, not only as a function of the geometric characteristics of the sand waves sequence but also as a consequence of the effective cross-sectional velocity profiles, which should be reasonably different from the flat bed logarithmic functions constituting the outcome of the classic Prandtl theory and which justify equations like (11).

In order to double-check the soundness of the proposed approach, (8) was tested based on the experimental measurements presented by McLean et al. [15] and including the total shear stress estimated from the flow dept, the total shear stress estimated from the hydraulic ratio, and the turbulent Reynolds shear stress detected at the bottom. Although one half of the runs was performed with a quite high value of dune slope (0.1) and, therefore, theoretically in contrast with the hypotheses characterizing the proposed approach, the shear stress estimates obtained by (8) fall well inside the range of  $\tau$  values provided by the experimental measurements or, at the most, coincide with one/two of them, demonstrating the robustness of our analytical approach even in quite extreme conditions.

Finally, when analyzed in terms of hydrodynamic dispersive properties as a function of the skin roughness on the basis of a previously derived analytical solution, the dune-covered beds seem to behave like meandering channels, responsible for a globally enhanced hydrodynamic solute particles spreading, though with a relatively reduced effect in presence of a less pronounced riverbed modelling.

## References

- [1] H. A. Einstein, *The Bed-Load Function for Sediment Transportation in Open Channel Flows*, U.S. Department of Agriculture, Soil Conservation Service, Washington, DC, USA, 1950.
- [2] H. A. Einstein and N. L. Barbarossa, "River channel roughness," *Transactions of the American Society of Civil Engineers*, vol. 117, pp. 1121–1146, 1952.
- [3] H. K. Liu and S. Y. Hwang, "Discharge formula for straight alluvial channels," *Journal of the Hydraulic Division*, vol. 85, article HY11, 1959.
- [4] M. S. Yalin, "Geometrical properties of sand waves," *Journal of Hydraulic Engineering*, vol. 90, article HY5, pp. 105–120, 1964.
- [5] F. Engelund, "Hydraulic resistance of alluvial streams," *Journal of the Hydraulic Division*, vol. 92, article NY2, pp. 315–326, 1966.
- [6] R. J. Garde and K. G. Ranga Raju, "Resistance relationship for alluvial channel flow," *Journal of the Hydraulic Division*, vol. 94, article HY4, 1966.
- [7] V. A. Vanoni and L. S. Hwang, "Relation between bed forms and friction in streams," *Journal of the Hydraulic Division*, vol. 93, article HY3, pp. 121–144, 1967.
- [8] C. G. Ilo, "Resistance to flow in alluvial channels," *Journal of Hydraulic Engineering*, vol. 101, article HY6, pp. 665–679, 1975.
- [9] P. Engel and Y. L. Lau, "Friction factor for two-dimensional dune roughness," *Journal of Hydraulic Research*, vol. 18, no. 3, pp. 213–225, 1980.
- [10] M. I. Haque and K. Mahmood, "Analytical study on steepness of ripples and dunes," *Journal of Hydraulic Engineering*, vol. 112, no. 3, pp. 229–236, 1986.
- [11] C. Colosimo, V. A. Copertino, and M. Veltri, "Friction factor evaluation in gravel-bed rivers," *Journal of Hydraulic Engineering*, vol. 114, no. 8, pp. 861–876, 1988.
- [12] H. W. Shen, H. M. Fehelman, and C. Mendoza, "Bed form resistances in open channel flows," *Journal of Hydraulic Engineering*, vol. 116, no. 6, pp. 799–815, 1990.
- [13] S. R. McLean, J. M. Nelson, and S. R. Wolfe, "Turbulence structure over two-dimensional bed forms: implications for sediment transport," *Journal of Geophysical Research*, vol. 99, no. 6, pp. 727–747, 1994.
- [14] T. B. Maddux, S. R. McLean, and J. M. Nelson, "Turbulent flow over three-dimensional dunes: 2. Fluid and bed stresses," *Journal of Geophysical Research*, vol. 108, no. 1, 2003.
- [15] S. R. McLean, S. R. Wolfe, and J. M. Nelson, "Spatially averaged flow over a wavy boundary revisited," *Journal of Geophysical Research C*, vol. 104, no. 7, pp. 15743–15753, 1999.
- [16] S. R. McLean, V. I. Nikora, and S. E. Coleman, "Double-averaged velocity profiles over fixed dune shapes," *Acta Geophysica*, vol. 56, no. 3, pp. 669–697, 2008.
- [17] G. H. Matthes, "Macroturbulence in natural stream flows," *Transactions, American Geophysical Union*, vol. 28, no. 2, pp. 255–265, 1947.
- [18] M. A. Velikanov, *Dynamics of Alluvial Streams*, vol. 2, Sediment and bed flow, State Publishing House for Theoretical and Technical Literature, Moscow, Russia, 1955.
- [19] K. V. Grishanin, *Dynamics of Alluvial Streams*, Gidrometeoizdat, Leningrad, Russia, 1979.
- [20] N. Kondratiev, I. Popov, and B. Snishchenko, *Foundations of Hydromorphological Theory of Fluvial Processes*, Gidrometeoizdat, Leningrad, Russia, 1982.
- [21] M. A. Dementiev, "Investigation of flow velocities fluctuations and their influences on the flow rate of mountainous rivers," Technical Report of the State Hydrogeological Inst. (GGI), vol. 98, 1962.
- [22] S. Yokosi, "The structure of river turbulence," *Bulletin of the Disaster Prevention Research Institute, Kyoto University*, vol. 17, no. 12, 1967.
- [23] A. B. Klaven, "Investigation of structure of turbulent streams," Technical Report of the State Hydrogeological Inst. (GGI), vol. 136, 1966.
- [24] A. B. Klaven and Z. D. Kopaliani, "Laboratory investigations of the kinematic structure of turbulent flow past a very rough bed," Technical Report of the State Hydrogeological Inst. (GGI), vol. 209, 1973.
- [25] R. G. Jackson, "Sedimentological and fluid-dynamic implications of the turbulent bursting phenomenon in geophysical flows," *Journal of Fluid Mechanics*, vol. 77, no. 3, pp. 531–560, 1976.
- [26] M. S. Yalin, *River Mechanics*, Pergamon Press, Oxford, UK, 1992.
- [27] M. S. Yalin and A. M. Ferreira da Silva, *Fluvial Processes*, IAHR, Delft, 2001.
- [28] A. Robert, "Statistical properties of sediment bed profiles in alluvial channels," *Mathematical Geology*, vol. 20, no. 3, pp. 205–225, 1988.
- [29] S.-G. Li, L. Venkataraman, and D. McLaughlin, "Stochastic theory for irregular stream modeling. Part I: flow resistance," *Journal of Hydraulic Engineering*, vol. 118, no. 8, pp. 1079–1090, 1992.

- [30] S.-G. Li and X. Zhou, "Stochastic theory for irregular stream modeling. II: solute transport," *Journal of Hydraulic Engineering*, vol. 123, no. 7, pp. 610–616, 1997.
- [31] M. Pannone, "Transient hydrodynamic dispersion in rough open channels: theoretical analysis of bed-form effects," *Journal of Hydraulic Engineering*, vol. 136, no. 3, pp. 155–164, 2010.
- [32] J. W. Elder, "The dispersion of marked fluid in turbulent shear flow," *Journal of Fluid Mechanics*, vol. 5, pp. 544–560, 1959.

## Research Article

# Hydraulic Transients Induced by Pigging Operation in Pipeline with a Long Slope

Tao Deng,<sup>1</sup> Jing Gong,<sup>1</sup> Haihao Wu,<sup>1</sup> Yu Zhang,<sup>2</sup> Siqi Zhang,<sup>1</sup> Qi Lin,<sup>1</sup> and Huishu Liu<sup>1</sup>

<sup>1</sup> Beijing Key Laboratory of Urban Oil and Gas Distribution Technology, China University of Petroleum, Beijing 102249, China

<sup>2</sup> South East Asia Pipeline Company Limited, China National Petroleum Corporation, Beijing 100028, China

Correspondence should be addressed to Jing Gong; ydgi@cup.edu.cn

Received 14 July 2013; Revised 22 August 2013; Accepted 9 September 2013

Academic Editor: Bo Yu

Copyright © 2013 Tao Deng et al. This is an open access article distributed under the Creative Commons Attribution License, which permits unrestricted use, distribution, and reproduction in any medium, provided the original work is properly cited.

Pigging in pipelines basically performs operations for five reasons including cleaning the pipe interior, batching or separating dissimilar products, displacement, measurement, and internal inspection. A model has been proposed for the dynamic simulation of the pigging process after water pressure testing in a long slope pipeline. In this study, an attempt has been made to analyze two serious accidents during pigging operation in 2010 by the model which is developed by the method of characteristic (MOC) by Wylie et al. (1993) and the two-phase homogeneous equilibrium vaporous cavitation model developed by Shu (2003) for vaporous cavitation. Moreover, simulation results of the third operation show good agreement with field data from the previous field trial. After investigation, it was showed that the impulse pressures produced during collapse of a vapor cavity result in severe damage of tubes.

## 1. Introduction

Modern hydraulic systems are widely applied to various industrial fields. Routinely, for pressure testing of segmental pigging, pigs are usually employed to remove liquids and deposits after the pressure testing. Although there are a large number of variations and special applications, pigs are basically utilized in pipelines to perform operations for five reasons including cleaning the pipe interior, batching or separating dissimilar products, displacement, measurement, and internal inspection. Pressure testing, which includes strength tests and tightness tests, is an important part of the guarantee for the safe operation of oil and gas pipelines. As, air is accessible and inexpensive, it was utilized as a medium and the pressure is increased gradually to values that the pressure testing requires. However, operation staffs have difficulty to find quality defects for small spills. For a long pipeline, once a pipeline leakage takes place, pressure would not decrease dramatically due to the compressibility of air. Moreover, there is also the risk of getting pipes burst by pressurized air. Thus, air pressure testing has been out of use since the 1970s. Fortunately, water pressure testing can cover up those problems. The pipelines of thousands

of kilometers in length are divided into segments varying in length according to elevation profiles and maximum allowable differences. B 31.8 Code Committee and American Gas Association jointly made great contribution to promote water pressure testing for decades. Pressure testing gradually took advantage of water for its safety and stability. Generally, pigging process is safe under low pressure because after pressure testing, operation staffs will decrease pressure by discharging the water through the valves at the end of pipes. However, due to varying elevation profiles, there are always some segments with a long slope, especially in a mountainous area and pigging operation, that should deal with new problems. More specifically, for full-flow pipes with a long slope, valves opening and moving pigs may cause liquid transients in a pipeline. Pigging process is subject to rapid pressure transients, resulting in water-hammer events.

In a system, any change in flow velocity causes a change of pressure instantaneously. Large pressure variations and distributed cavitation (bubble flow) may be involved due to the sudden shutdown of a pump or closure of a valve. Column separation therefore may occur and may have a significant impact on subsequent transients in the system [1].

During the course of a transient, usually at high point, the pressure in a pipeline falls to the vapor pressure of water, resulting in a localized liquid column separation [2–5] or vaporous cavitation. Streeter and Wylie, in their textbooks [4, 6] (Wylie and Streeter 1978a), summarized previous work on column separation in detail. Beuthe [7] provided an extensive general review with emphasis on steam condensation. For vaporous cavitation, vapor is distributed along a portion of a pipeline, rather than being concentrated at one location as for a localized liquid column separation. However, the formation and collapse of a vapor cavity in a pipeline may lead to unexpectedly high pressure rises in the form of short-duration pressure pulses. Angus [8], emphasized that the damage done to pipes as a result of water hammer is so serious that no engineer can afford to neglect it in the design of long pipes, particularly those under low heads. Most of the early efforts in liquid transients in pipelines emphasized particularly on the prediction of the maximum pressure rise due to closure of a valve [9–11] or shutdown of hydropower turbines [12]. Joukowsky's simple water hammer formula is used to determine the maximum head rise due to the instantaneous closure of a valve without consideration of liquid column separation or linepack during a transient event. When a local column separation forms, the pressure magnitude produced by the collapse of the cavity is greater than the Joukowsky rise which is referred to as a short-duration pressure pulse. Previous analytical studies [8, 13–15] predicted that the pressure rise, due to the collapse of a vapor cavity, may exceed the Joukowsky pressure rise. Much previous experimental data showed strong attenuation of the maximum pressure rise upon the first collapse of a cavity at a valve [16–18]. Jaeger et al. [19], Martin [20], and Thorley [21] were devoted to comprehensive bibliographies of the historical development of many aspects of water hammer including column separation. As previously mentioned, column separation is a common approach in transmission line modeling. However, such an approach is oversimplistic and can lead to unrealistic results. Shu [22] proposed the two-phase homogeneous equilibrium vaporous cavitation model which could avoid unrealistically high pressure spikes with consideration of frequency-dependent friction.

A pipe is divided in to two parts including the upstream air section and the downstream liquid section by a pig. Because water directly discharges into atmospheric environment, the liquid flow will be under depressurized condition. Additionally, compressed air at upstream is to be at low pressure. In order to ensure that the pig is moving forward, the pressure is just greater than the resisting force acting on the pig. The pig slowly moves and has great influence on the hydrodynamic pressure of the downstream flow. Accordingly, the pressure downstream may drop to or below vapor pressure and it would result in a large cavity of vapor usually at high points. In previous researches [23, 24], cavities were assumed to form only at high points, at changes in pipeline slope (convex up), and at system boundaries. Moreover, the gas and liquid two-phase flow may appear in the sloping pipe where the hydraulic grade line is found to be at or below the elevation of vapor pressure head. Ultimately, sever accident may occur when column separation collapses

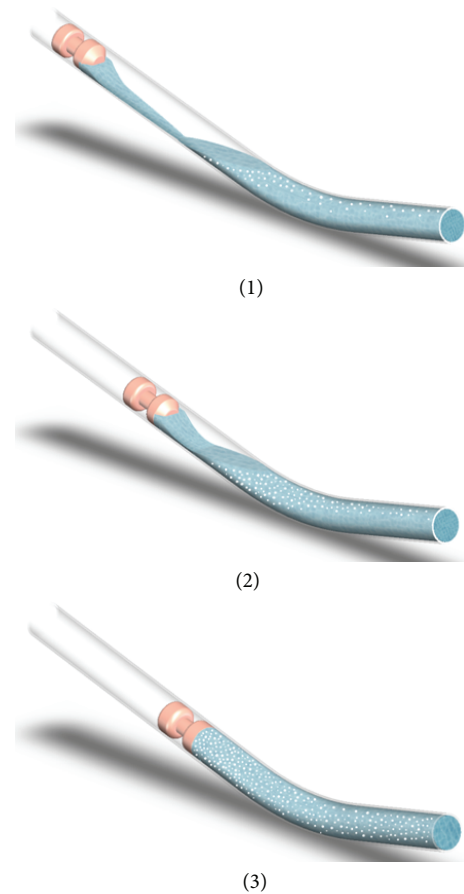


FIGURE 1: Schematic diagram of collapse of a cavity by a pig.

by the heavy pig at high speed. Due to the factors such as the terrains, a large number of bubbles will be produced, and the flow pattern is the bubbly flow with the intense pressure oscillations at the end of the pipeline. The large cavity of vapor and air between the pig and downhill liquid-filled pipe will be compressed at the downhill when the pig runs fast after the high point. The compression is an isothermal process, and the gas would undergo the extrusion process at the end of the outlet. Eventually the gas is dispersed into water in the form of bubbles as shown in Figure 1.

## 2. Mathematical Methods

*2.1. Conventional MOC.* One-dimensional continuity and momentum equations are applied to analyze the hydraulic transients. A number of approaches have been introduced for the simulation of the pipeline transients including the method of characteristics (MOC), wave characteristics method (WCM), finite volume method (FVM) [25], finite element method (FEM), and finite difference method (FDM). Among these methods, MOC is extensively used due to its simplicity. It is an explicit method and a powerful tool to analyze hydraulic transients in pipeline flow. With the method of characteristics (MOC), the partial differential equations can be converted into ordinary differential equations.

The method of characteristics is a technique that takes advantage of the known physical information at each point of the regular rectangular grid. Therefore, the results of physical characteristics can be quickly calculated in every time step.

For a fixed cross-sectional area, the mass conservation equation can be written as follows:

$$\frac{\partial H}{\partial t} + V \frac{\partial H}{\partial x} + \left( \frac{a^2}{gA} \right) \frac{\partial Q}{\partial x} = 0. \quad (1)$$

The momentum conservation equation can be expressed by:

$$\frac{1}{gA} \left( \frac{\partial Q}{\partial t} + V \frac{\partial Q}{\partial x} \right) + \frac{\partial H}{\partial x} + fQ|Q|^{1-m} = 0, \quad (2)$$

where

$$f = 0.0246 \frac{\nu^m}{D^{5-m}}. \quad (3)$$

The MOC approach transforms the above partial differential equations into the ordinary differential equations along the characteristic lines and is defined as

$$C^+ \begin{cases} \frac{dx}{dt} = V + a \\ \frac{a}{gA} dQ + dH + fQ|Q|^{1-m} adt = 0, \end{cases} \quad (4)$$

$$C^- \begin{cases} \frac{dx}{dt} = V - a \\ \frac{a}{gA} dQ - dH + fQ|Q|^{1-m} adt = 0. \end{cases}$$

Due to the fact that  $V \ll a$ , the term of  $V$  can be omitted from the equations. Flow rate  $Q$  is unknown and difficult to determine between time steps  $t$  and  $t + \Delta t$ , because it varies with time and space. Therefore, it is impossible to identify the value of  $Q_P$ . However, the term of  $\int_B^P fQ|Q|^{1-m} dx$  can be dealt with approximately by the method of Streeter and Wylie. So we assume that

$$|Q|^{1-m} = Q_P |Q_A|^{1-m}, \quad (5)$$

$$|Q|^{1-m} = Q_P |Q_B|^{1-m}.$$

Due to the above simplification, these equations are integrated on the characteristic lines between time steps  $t$  and  $t + \Delta t$ , as shown in Figure 2, and solved by the known variables:

$$C^+ : \begin{cases} \frac{\Delta x}{\Delta t} = +a \\ \frac{a}{gA} (Q_P - Q_A) + (H_P - H_A) + fQ_P |Q_A|^{1-m} a \Delta t = 0, \end{cases}$$

$$C^- : \begin{cases} \frac{\Delta x}{\Delta t} = -a \\ \frac{a}{gA} (Q_P - Q_B) - (H_P - H_B) + fQ_P |Q_B|^{1-m} a \Delta t = 0. \end{cases} \quad (6)$$

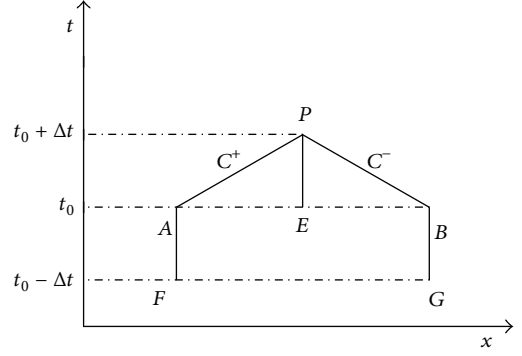


FIGURE 2: Characteristic lines in  $x-t$  plan.

These equations can be written in the simplified forms as follows:

$$C^+ : H_P = R_A - S_A Q_P, \quad (7)$$

$$C^- : H_P = R_B + S_B Q_P,$$

where

$$R_A = H_A + C_W Q_A,$$

$$R_B = H_B - C_W Q_B,$$

$$S_A = C_W + f|Q_A|^{1-m} a \Delta t, \quad (8)$$

$$S_B = C_W + f|Q_B|^{1-m} a \Delta t,$$

$$C_W = \frac{a}{gA},$$

where the  $Q_P$  is unknown flow at point  $P$  at time  $t + \Delta t$ ,  $H_P$  is the unknown hydraulic head at point  $P$  at time  $t + \Delta t$ ,  $Q_A$  and  $Q_B$  are flows at neighboring sections of  $P$  at the previous time  $t$ , and  $H_A$  and  $H_B$  are heads at neighboring sections of  $P$  at the previous time  $t$ .

**2.2. The Two-Phase Homogeneous Equilibrium Vaporous Cavitation.** When vaporous cavities are locally incipient, the local pressures may be less than or greater than the vapor pressure of the liquid. However, for modeling purposes in engineering, it is assumed that the local pressures are equal to the vapor pressure when vaporous cavitation is occurring. During the pigging process, vaporization occurs and vapor cavities may be physically dispersed homogeneously in the form of bubbles. Due to the factors such as the terrains, a large number of bubbles will be produced, and the flow pattern is the bubbly flow with the intense pressure oscillations along the pipeline. The behavior of the flow should be described by the two-phase flow theory. Otherwise, water hammer equations solved by the MOC can be adopted for the single-phase flow.

The basic equations for the unsteady homogeneous equilibrium flow model in a tube are

$$\frac{1}{a^2} \frac{\partial P}{\partial t} + (\rho_l - \rho_v) \frac{\partial \alpha}{\partial t} + \frac{\rho_m}{\pi r_0^2} \frac{\partial}{\partial x} \left( \frac{Q}{\alpha} \right) = 0, \quad (9)$$

$$\frac{\rho_m}{\pi r_0^2} \frac{\partial}{\partial t} \left( \frac{Q}{\alpha} \right) + \frac{\partial P}{\partial x} + F_0 \left( \frac{Q}{\alpha}, \alpha \right) + \rho_m g \sin \theta_0 = 0. \quad (10)$$

In terms of the volumetric fraction  $\alpha$  of liquid and vapor phase density  $\rho_v$ , the mean density  $\rho_m$  can be written as

$$\rho_m = \alpha \rho_l + (1 - \alpha) \rho_v. \quad (11)$$

In the above equations, the second term in (9) describes the interfacial mass transfer rate and the term  $Q/\alpha$  in (9), and (11) shows the flow rate differences between the liquid and the vapor phase. Using the Darcy-Weisbach friction factor  $f$ , the term  $F_0(Q/\alpha, \alpha)$  can be expressed as follows:

$$F_0 \left( \frac{Q}{\alpha}, \alpha \right) = \frac{f \rho_m Q |Q|}{4\pi^2 \alpha^2 r_0^5}. \quad (12)$$

The method of characteristics is used to transform the above equations to four ordinary differential equations:

$$C^+ : \begin{cases} \frac{1}{\pi r_0^2} \frac{d}{dt} \left( \frac{Q}{\alpha} \right) + \frac{1}{\rho_l a} \frac{d}{dt} (P - p_v) + a \frac{\partial}{\partial t} \left( \ln \frac{\rho_m}{\rho_l} \right) \\ + \frac{fQ|Q|}{4\pi^2 \alpha^2 r_0^5} + g \sin \theta_0 = 0 \\ \frac{dx}{dt} = a, \end{cases} \quad C^- : \begin{cases} \frac{1}{\pi r_0^2} \frac{d}{dt} \left( \frac{Q}{\alpha} \right) - \frac{1}{\rho_l a} \frac{d}{dt} (P - p_v) - a \frac{\partial}{\partial t} \left( \ln \frac{\rho_m}{\rho_l} \right) \\ + \frac{fQ|Q|}{4\pi^2 \alpha^2 r_0^5} + g \sin \theta_0 = 0 \\ \frac{dx}{dt} = -a. \end{cases} \quad (13)$$

The equations needed to solve the variables at each time step are

$$C^+ : \frac{1}{\pi r_0^2} \frac{Q_p}{\alpha_p} + \frac{1}{\rho_l a} (P_p - P_V) + \frac{a}{2} \ln \frac{\rho_{mp}}{\rho_l} = C_A, \quad (14)$$

$$C^- : \frac{1}{\pi r_0^2} \frac{Q_p}{\alpha_p} - \frac{1}{\rho_l a} (P_p - P_V) - \frac{a}{2} \ln \frac{\rho_{mp}}{\rho_l} = C_B, \quad (15)$$

where  $Q_p$ ,  $P_p$ , and  $\alpha_D = (\rho_{mD} - \rho_v)/(\rho_l - \rho_v)$  can be solved by the above equations,  $C_A$  and  $C_B$  are constant:

$$C_A = \frac{1}{\pi r_0^2} \left( \frac{Q_A}{\alpha_A} \right) + \frac{1}{\rho_l a} (P_A - P_V) + \frac{a}{2} \ln \frac{\rho_{mE} \rho_{mF}}{\rho_l \rho_{mA}} \\ - \frac{f \Delta x Q_A |Q_A|}{4\pi^2 \alpha_A^2 r_0^5 a} - \frac{g \Delta x \sin \theta_0}{a}, \quad (16)$$

$$C_B = \frac{1}{\pi r_0^2} \left( \frac{Q_B}{\alpha_B} \right) + \frac{1}{\rho_l a} (P_B - P_V) + \frac{a}{2} \ln \frac{\rho_{mE} \rho_{mG}}{\rho_l \rho_{mB}} \\ - \frac{f \Delta x Q_B |Q_B|}{4\pi^2 \alpha_B^2 r_0^5 a} - \frac{g \Delta x \sin \theta_0}{a},$$

The two-phase homogeneous equilibrium vaporous cavitation model has no conflict between negative cavity sizes and pressures below the vapor pressure.

If  $C_A \geq C_B$ , then  $\alpha_p = 1$ ,

$$P_p = \frac{\rho_l a}{2} (C_A - C_B) + P_V. \quad (17)$$

If  $C_A < C_B$ ,  $P_p = P_V$ , then

$$\alpha_p = \frac{\rho_l \exp((C_A - C_B)/a) - \rho_v}{\rho_l - \rho_v}. \quad (18)$$

In either case,

$$Q_p = \frac{\pi r_0^2 \alpha_p}{2} (C_A + C_B). \quad (19)$$

Numerical results show that the volume rate range is from 0 to 0.95 m<sup>3</sup>/s. According to the present study,  $\rho_l = 1000$  kg/m<sup>3</sup>,  $\rho_v = 1.293$  kg/m<sup>3</sup>,  $a = 1100$  m/s,  $A = 1.099$  m<sup>2</sup>,  $\theta_0 \approx 0$ ,  $f = 0.00035$ ,  $P_V = 2340$  Pa, and  $\Delta x = 110$  m are given; then we assume that the volumetric fraction of liquid  $\alpha$  varies between 0.999 and 0.5. Therefore, it is possible to identify the values of  $C_A$  and  $C_B$  by our program, and the range is from  $-380.837$  m/s to  $22.864$  in the present study.

**2.3. Boundary Conditions.** Boundaries include the inlet of pipeline, the outlet of pipeline, the tail of the pig, and nose of the pig. In order to solve the flow dynamic equations, boundaries conditions must be given. Boundaries at the pipeline inlet and outlet are constant flow rate and constant pressure, respectively. In addition, it is assumed that pressure and flow rate at the tail of the pig are the same as they are in the upstream fluid, close to the pig. We assume that the pig is a moving boundary with no thickness compared with the length of the pipeline, but its weight would be considered. Based on the above assumptions, the behavior of the pig is taken into account to solve the flow dynamics equations.

The behavior of the pig in the pipeline is determined by a balance of forces acting on the pig as shown in Figure 3. The pig will move forward if the drag force is less than the driving force, but it will stop when the drag force is dominant:

$$P_1 = P_2 + \Delta P_s + \frac{1}{A} M \cdot g \cdot \sin \theta_0 + \frac{M}{A} \frac{dV}{dt}, \quad (20)$$

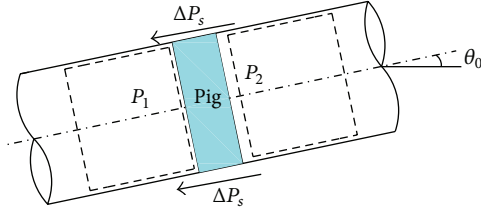


FIGURE 3: Forces acting on the pig.

TABLE 1: Summary of basic parameters for field operations.

Parameters	Values
The length of pipeline	6.93 Km
Pipe size	$\Phi 1219 \times 18.4$ mm
The maximum elevation difference	178.5 m
Wall equivalent roughness	0.01 mm
Mass of pig	700.0 kg
Frictional resistance between pig and pipe wall	0.03 MPa
Static friction resistance between pig and pipe wall	0.04 MPa
Type of compressor	XHP1070
Rated operating pressure	2.2 MPa
Air displacement	30.0 Nm <sup>3</sup> /min

where  $V$ ,  $M$ ,  $P_1$ ,  $P_2$ , and  $\theta_0$  are the pig velocity, pig mass, the pressure on the upstream, downstream faces of the pig, and angle between axis and horizontal direction. Term  $\Delta P_s$  represents the axial contact force between the pig and the pipe wall, acting in opposition to the pig motion, in the direction of the pig axis. The axial contact force between the pig and the pipe wall is obtained from the contact force equation.

### 3. Results and Discussion

For the convenience of analysis, the main stages (labeled with roughness of back line in Figure 4) of the pigging process are defined as follows, according to the pig position during the process:

- (1) the pig flat-segment movement stag,
- (2) the pig gully-segment movement stage,
- (3) the pig downhill-segment movement stage,
- (4) the pig near outlet-segment movement and overpressure stage.

As shown in Figure 4, the pipeline with a long slope is nearly 7 kilometers long and 1219 millimeters in diameter. Air compressors and a valve were installed at the high point and the low point, respectively. A pig was put into pipeline from the high point before air compressors started to work to make the pig move and drain away water at the low point.

Table 1 summarizes some important information of the pigging process in practice including pipeline, pig, and air compressor.

TABLE 2: Summary of two accidents.

	The first accident	The second accident
Number of compressor	2	1
Total time of pigging process	20 Hours	39.5 Hours
The length of drainage pipe	150.0 m	150.0 m
The drainage pipe size	$\Phi 159.0 \times 8.7$ mm	$\Phi 159.0 \times 8.7$ mm
The length of rupture	2.6 m	2.5 m
Maximum of air pressure		1.01 MPa
Bursting pressure of tube	20.83 MPa	20.83 MPa

#### 3.1. Numerical Simulation of Two Accidents

**3.1.1. The First Accident Description.** On July 19, a couple of XHP1070 air compressors and a DN150 valve were installed for dewatering after water pressure testing. All the preparations for the pigging process were completed and the pig was put in the pipeline. At nine o'clock in the morning, the compressors started to work and the valve was simultaneously opened. At five o'clock in the next morning, an eruption of the mixture of water and gas occurred at the outlet of the pipeline, and the pigging operation had taken nearly twenty hours. Finally, a fracture of 2.6 m in length was found at the last piece of steel tube.

**3.1.2. The Second Accident Description.** On September 21, an air compressor and a DN150 valve were installed for dewatering after water pressure testing. At three o'clock in the morning, a pig was put in the pipe before the compressor started to work, while the valve was opened. At half past six in the next afternoon, the second accident happened, and a fracture of 2.5 m in length was about 5 m away from the first fracture. The pigging operation had totally taken nearly thirty nine hours and half an hour. During this period of time, according to the records, the maximum of air pressure was about 1.01 MPa.

After investigation, however, the tubes have no quality default, and the rated operating pressure of the air compressor is 2.2 MPa so that the compressed air unlikely caused the damages. Additionally, bursting pressure is determined from Barlow's equation that instantaneous pressure for severe rupture of the tube should be over 20.83 MPa as shown in Table 2.

A mathematical model has been suggested for simulating the pigging process, based on our own previous work. Meanwhile, these results were obtained from simulating the process by our own program.

The simulated time of the first pigging operation was 19.6 hours. During the pig downhill-segment movement stage, some amount of water was gathered in the part of low elevation near the outlet due to the gravity. When the pig was close to the end of the pipe, some amount of gas downstream would undergo extrusion process and eventually was dispersed into water as shown in Figure 1. Consequently, the gas cavity collapsed resulting in an impulse pressure up

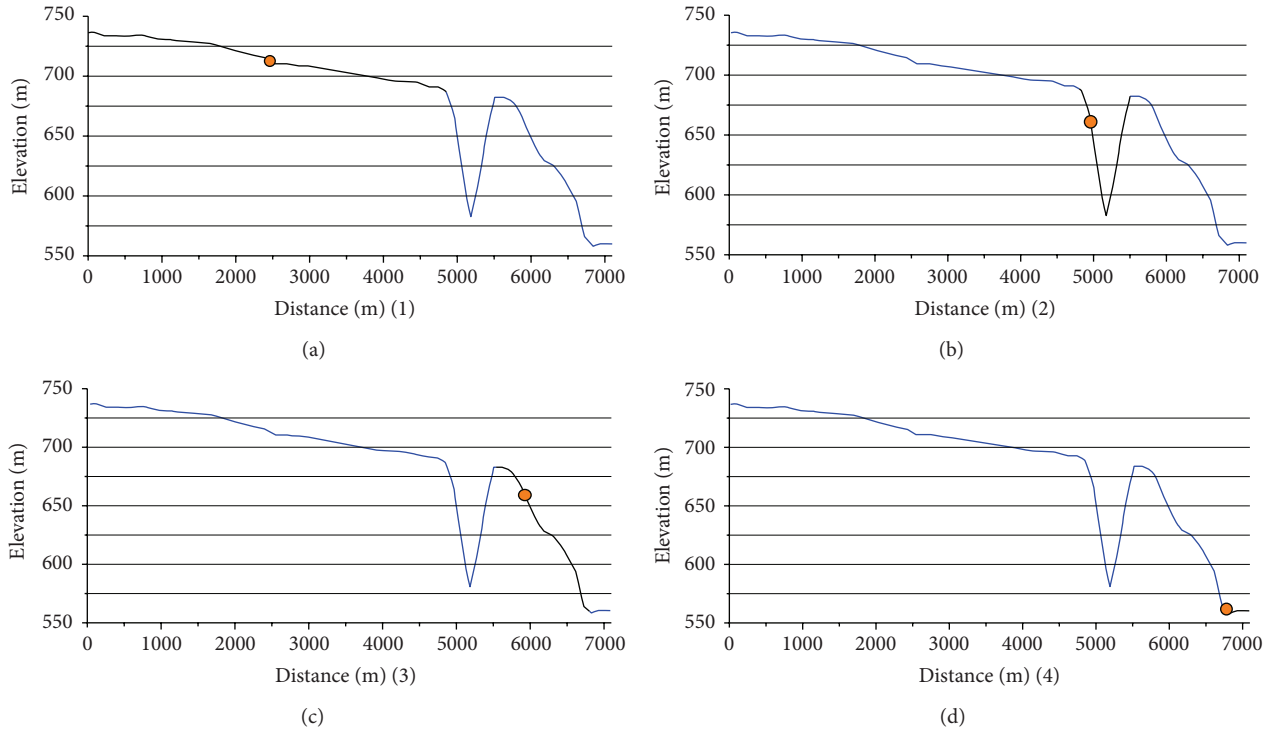


FIGURE 4: Four stages for pigging process.

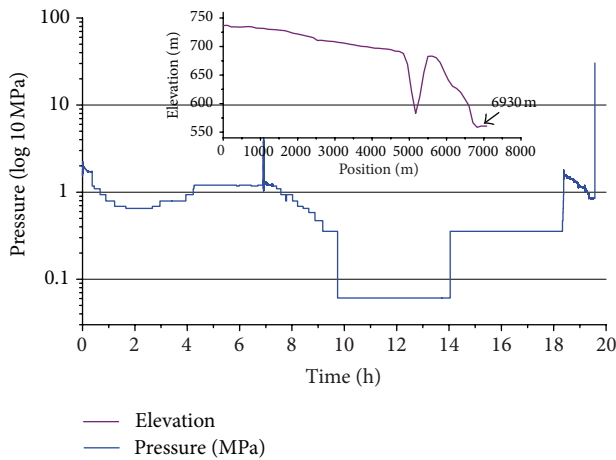


FIGURE 5: Numerical result of pressure at the end of pipe for the first accident.

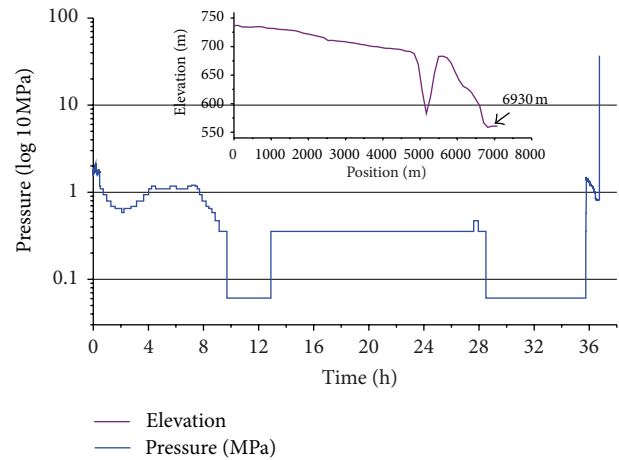


FIGURE 6: Numerical result of pressure at the end of pipe for the second accident.

to 30.50 MPa as shown in Figure 5. The value of the impulse pressure is larger than the bursting pressure of the tube, and therefore it caused the rupture.

There is a large slope at the end of pipe so that pressure varied with the liquid level in the pipe. In other words, pressure would decrease when the liquid level dropped, and pressure would increase when the liquid level rose. According to the results, the liquid level quickly dropped near 9 h and 28 h, and the liquid level rose near 11 h because the flow rate of outlet and top was varying during the pigging process. The flow rate at the outlet was much larger than that at the top

when the liquid level quickly dropped. On the contrary, the flow rate of top was much larger than that at the outlet when the liquid level quickly rose.

The simulated time of the first pigging operation was 19.6 hours. During this period of time, the maximum pressure of compressed air was as much as 1.03 MPa as shown in Figure 7. Finally, the gas cavity collapsed resulting in an impulse pressure up to 37.03 MPa as shown in Figure 6. The value of the impulse pressure is also larger than the bursting pressure of the tube, and the second accident occurred as shown in Table 3.

TABLE 3: Summary of numerical simulation of the two accidents.

	The first accident	The second accident
Number of compressor	2	1
Total time of pigging process	19.6 Hours	36.7 Hours
Maximum of air pressure		1.03 MPa
Maximum of outlet pressure	30.50 MPa	37.03 MPa
Bursting pressure	20.83 MPa	20.83 MPa

TABLE 4: Summary of the field trial and numerical simulation.

	The field trial	Numerical simulation
Number of compressor	1	1
Total time of pigging process	36 Hours	35.5 Hours
Value of the impulse pressure	1.576 MPa	1.51 MPa
Bursting pressure	20.83 MPa	20.83 MPa

**3.2. Comparison of Field Results to Simulating Predictions.** To study the variation of outlet pressure due to the pigging process, a field trial was conducted in 2011 by Luo [26] from China National Petroleum Corporation (CNPC). After two accidents, the third operation was conducted and transient pressures were recorded by two pressure transducers which were installed at the third and fourth tubes from the end, respectively. In this experiment, the NS-B pressure transducers are 50 MPa in measurement range and 0.3% in precision installed with an angle of 90 degrees to assure the results validity. While the drainage tube is 159 mm in diameter for the first two pigging processes, the last tube of pipe which is 1219 mm in diameter has four bores of 600 mm in diameter for drainage, and the total area of the cross sections of the four bores will be equal to the area of the cross section of the tube.

As Figure 8 and Figure 9 show, the simulated time of the first pigging operation was 19.6 hours, and the maximum pressure was as much as 1.51 MPa. However, the pressure at the end was constantly kept in lower level for most of the time. Because the pressure at the location of cavitation is usually below the saturated vapor pressure, the vapor pressure of the liquid is adopted as the cavitation inception pressure in this mathematical model for transient cavitation. When the pressure is under the saturated vapor pressure, the water would change into vapor. Furthermore, as it was below the vapor pressure for a long period of time, the air dissolved in the water is released, and thus there would be a large cavity of the water vapor and air. When the pig was close to the end of the pipe, some amount of gas downstream would undergo extrusion process, and eventually an eruption of the mixture of water and gas appeared at the outlet according to field records.

With comparison between model prediction and field data, it was found that the amplitudes of the impulse pressures induced by the collapse of the cavity were nearly the same, and their total time was 36 hours, and 35.5 hours (see Figure 10) respectively as shown in Table 4.

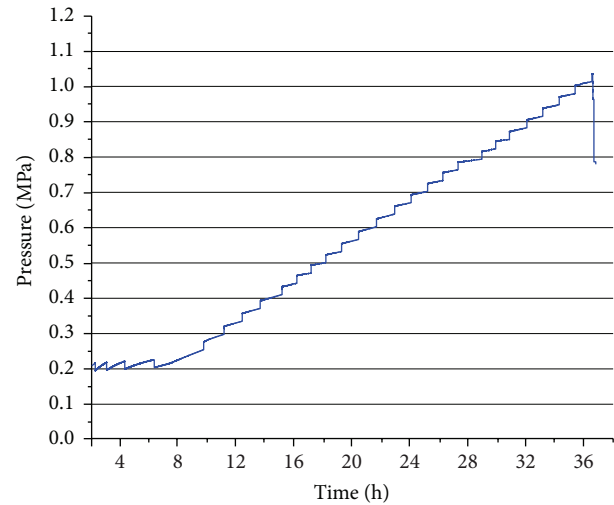


FIGURE 7: Numerical result of air pressure for the second accident.

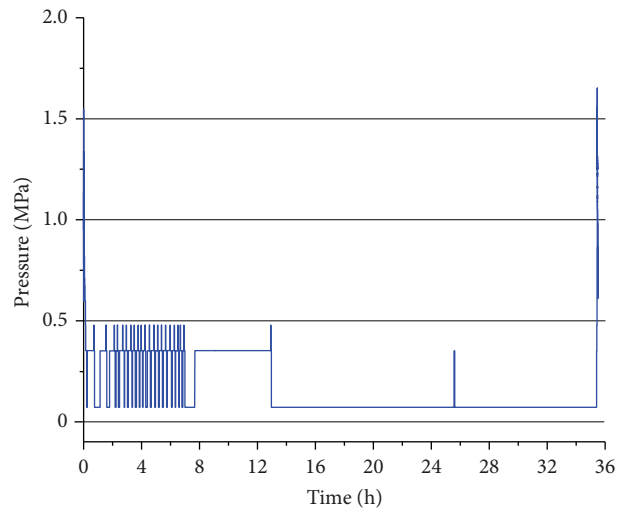


FIGURE 8: Numerical result of pressure at the end of pipe for the field trial.

## 4. Conclusions

The model proposed for the pigging process was employed to understand the flow dynamics in the pipeline and to obtain transient pressures for the two accidents and the field trial. The large cavity of water vapor and air was in the down-slope pipe following the peak and slack line flow that exited for a long period of time. When the pig was close to the outlet, the cavity was compressed, and gas underwent the extrusion process and eventually was dispersed into water in the form of bubbles. Finally, the cavity collapsed by the pig, and the serious collision resulted in considerable impulse pressures. The results of the simulation illustrate that the impulse pressures caused the severe damages during the pigging process. Additionally, our model predictions for the third operation showed good agreement with field data, and the diameter of drainage had a significant effect on impulse

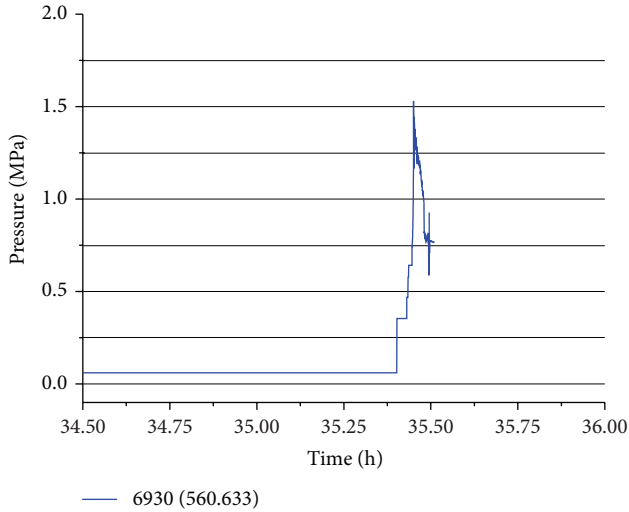


FIGURE 9: Numerical result of the impulse pressure for the field trial.

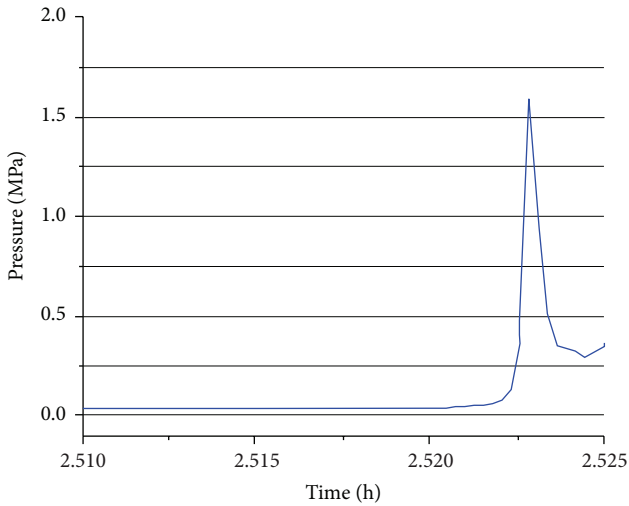


FIGURE 10: Result of the impulse pressure for the field trial.

pressures. Generally, the terrain of pipeline is a key factor for the liquid-fill flow behavior, and slack line flow may appear in a long-slope pipeline. Then, column separation would occur as a common phenomenon for a hilly pipeline, and it can cause devastating effects such as severe damages. Therefore, preventive measures are of a critical significance for practical reasons.

## Nomenclature

- $f$ : Friction factor  
 $x$ : Distance along the pipeline (m)  
 $g$ : Gravity acceleration ( $\text{m} \cdot \text{s}^{-2}$ )  
 $t$ : Time (s)  
 $A$ : Cross-section area of pipeline ( $\text{m}^2$ )  
 $m$ : The index number of Darcy formula  
 $H$ : Water head of fluid (m)  
 $a$ : Acoustic speed of fluid (m/s)

- $Q$ : Volume rate of fluid ( $\text{m}^3/\text{s}$ )  
 $Q_A, Q_B$ : Volume rates for given points ( $\text{m}^3/\text{s}$ )  
 $H_A, H_B$ : Water heads for given points (m)  
 $Q_P$ : Volume rate for unknown point ( $\text{m}^3/\text{s}$ )  
 $H_P$ : Volume rate for unknown point (m)  
 $V$ : Velocity (m/s)  
 $D$ : Diameter of the pipeline (mm)  
 $\nu$ : Kinematic viscosity of liquid ( $\text{m}^2/\text{s}$ )  
 $P_V$ : Saturated vapor pressure at liquid temperature (Pa)  
 $\rho$ : Density of liquid ( $\text{kg}/\text{m}^3$ )  
 $M$ : Pig mass (kg)  
 $P_1$ : The pressure on the upstream faces of the pig (Pa)  
 $P_2$ : The pressure on the downstream faces of the pig (Pa)  
 $\beta$ : A angle between axis and horizontal direction (rad)  
 $\Delta P_s$ : The axial contact force (Pa)  
 $\alpha$ : The volumetric fraction of liquid  
 $\rho_v$ : Vapor phase density ( $\text{kg}/\text{m}^3$ )  
 $\rho_l$ : Liquid phase density ( $\text{kg}/\text{m}^3$ )  
 $\rho_m$ : The mean density ( $\text{kg}/\text{m}^3$ ).

## Abbreviations

- MOC: The method of characteristic  
IAHR: International Association For Hydraulic Research  
HC: Hydrodynamic cavitation.

## Acknowledgments

The authors thank the National Science & Technology Specific Project (Grant no. 2011ZX05039-002), and the Key National Science and Technology Specific Project (2011ZX05026-004-03), the National Natural Science Foundation of China (51104167) for their financial support.

## References

- [1] A. Bergant, A. R. Simpson, and A. S. Tijsseling, "Water hammer with column separation: a historical review," *Journal of Fluids and Structures*, vol. 22, no. 2, pp. 135–171, 2006.
- [2] R. A. Baltzer, *A study of column separation accompanying transient flow of liquid in pipes [Ph.D. thesis]*, The University of Michigan, Ann Arbor, Mich, USA, 1967.
- [3] R. A. Baltzer, "Column separation accompanying liquid transients in pipes," *ASME Journal of Basic Engineering D*, vol. 89, pp. 837–846, 1967.
- [4] V. L. Streeter and E. B. Wylie, *Hydraulic Transients*, McGraw-Hill Book Company, New York, NY, USA, 1967.
- [5] J. A. Swaffield, "A study of column separation following valve closure in a pipeline carrying aviation kerosine," *Proceedings of the Institution of Mechanical Engineers*, vol. 184, no. 7, pp. 57–64, 1969.
- [6] E. B. Wylie, V. L. Streeter, and L. SuoJones, *Fluid Transients in Systems*, chapter 3, Prentice Hall, Englewood Cliffs, NJ, USA, 1993.

- [7] T. G. Beuthe, "Review of two-phase water hammer," in *Proceedings of the 18th Canadian Nuclear Society Conference*, p. 20, Toronto, Canada, 1997.
- [8] R. W. Angus, "Simple graphical solution for pressure rise in pipes and discharge lines," *Journal of Engineering Institute of Canada*, vol. 18, no. 2, pp. 72–81, 1935.
- [9] N. E. Joukowsky, "Water Hammer," *Proceedings of the American Water Works Association*, vol. 24, pp. 314–424, 1904.
- [10] L. Allievi, *General Theory of Perturbed Flow of Water in Pressure Conduits*, Annali della Societa degli Ingegneri ed architetti italiani, Milano, Italy, 1903.
- [11] L. Allievi, *Theory of Water Hammer. Notes I to V*, ASME, New York, NY, USA, 1913.
- [12] N. R. Gibson, "Pressure in penstocks caused by gradual closing of turbine gate," *Transactions of the American Society of Civil Engineers*, vol. 83, pp. 707–775, 1919.
- [13] R. W. Angus, "Water hammer in pipes, includin those supplied by centrifugal pumps: graphical treatment," *Proceedings of the Institution of Mechanical Engineers*, vol. 136, pp. 245–331, 1937.
- [14] I. C. O'Neill, *Water Hammer in Simple Pipe Systems [M.S. thesis]*, Department of civil Engineering, University of Melbourne, Victoria, Australia, 1959.
- [15] A. R. Simpson and E. B. Wylie, "Problems encountered in modeling vapor column separation," in *Proceedings of the Symposium on Fluid Transients in Fluid-Structure Interaction*, pp. 103–107, ASME, Miami Beach, Fla, USA, November 1985.
- [16] J. P. Kalkwijk and C. Kranenburg, "Cavitation in horizontal pipelines due to water hammer," *ASCE Journal of the Hydraulics Division*, vol. 97, no. 10, pp. 1585–1605, 1971.
- [17] C. Kranenburg, "Transient cavitation in pipelines," Report 73-2, Laboratory of Fluid Mechanics, Communications on Hydraulics, Department of Civil Engineering, Delft University of Technology, 1973.
- [18] C. Kranenburg, "Gas release during transient cavitation in pipes," *ASCE Jouranl of the Hydraulic Division*, vol. 100, no. 10, pp. 1383–1398, 1974.
- [19] C. Jaeger, L. S. Kerr, and E. B. Wylie, "Selected bibliography," in *Proceedings of the International Symposium on Water Hammer in Pumped Storage Projects*, ASME Winter Annual Meeting, pp. 233–241, Chicago, ILL, USA, 1965.
- [20] C. S. Martin, "Status of fluid transients in W estern Europe and the United Kingdom: report on laboratory visits by Freeman scholat," *ASME Journal of Fluids Engineering*, vol. 95, pp. 301–318, 1973.
- [21] A. R. D. Thorley, *A Survey of Investigations into Pressure Surge Phenomena*, The City University, Department of Mechanical Engineering, London, UK, 1976.
- [22] J.-J. Shu, "Modelling vaporous cavitation on fluid transients," *International Journal of Pressure Vessels and Piping*, vol. 80, no. 3, pp. 187–195, 2003.
- [23] C. Kranenburg, "The effect of gas release on column separation," Report 74-3, Delft University of Technology, Department of Civil Engineering, 1974, Communication on Hydraulics.
- [24] V. L. Streeter, "Transient cavitation pipe flow," *ASCE Journal of Hydraulic Engineering*, vol. 109, no. 11, pp. 1407–1423, 1983.
- [25] M. H. Afshar and M. Rohani, "Water hammer simulation by implicit method of characteristic," *International Journal of Pressure Vessels and Piping*, vol. 85, no. 12, pp. 851–859, 2008.
- [26] J. Luo, "An analysis of the problems of fracture at new great drop line pipe," *Oil and Gas Storage and Transportation*, pp. 1000–8241, 2011.

## Research Article

# Dynamic Characteristics of Rotating Stall in Mixed Flow Pump

Xiaojun Li,<sup>1</sup> Shouqi Yuan,<sup>1</sup> Zhongyong Pan,<sup>1</sup> Yi Li,<sup>2</sup> and Wei Liu<sup>1</sup>

<sup>1</sup> Research Center of Fluid Machinery Engineering and Technology, Jiangsu University, Zhenjiang, Jiangsu 212013, China

<sup>2</sup> School of Mechanical Engineering and Automation, Zhejiang Sci-Tech University, Hangzhou, Zhejiang 310018, China

Correspondence should be addressed to Xiaojun Li; [lixiaojun530@163.com](mailto:lixiaojun530@163.com)

Received 3 June 2013; Accepted 21 August 2013

Academic Editor: Bo Yu

Copyright © 2013 Xiaojun Li et al. This is an open access article distributed under the Creative Commons Attribution License, which permits unrestricted use, distribution, and reproduction in any medium, provided the original work is properly cited.

Rotating stall, a phenomenon that causes flow instabilities and pressure hysteresis by propagating at some fraction of the impeller rotational speed, can occur in centrifugal impellers, mixed impellers, radial diffusers, or axial diffusers. Despite considerable efforts devoted to the study of rotating stall in pumps, the mechanics of this phenomenon are not sufficiently understood. The propagation mechanism and onset of rotating stall are not only affected by inlet flow but also by outlet flow as well as the pressure gradient in the flow passage. As such, the complexity of these concepts is not covered by the classical explanation. To bridge this research gap, the current study investigated prerotation generated at the upstream of the impeller, leakage flow at the tip clearance between the casing and the impeller, and strong reverse flow at the inlet of the diffuser. Understanding these areas will clarify the origin of the positive slope of the head-flow performance curve for a mixed flow pump. Nonuniform pressure distribution and adverse pressure gradient were also introduced to evaluate the onset and development of rotating stall within the diffuser.

## 1. Introduction

Gopalakrishnan pointed out that the three primary requirements of pump research and development can be broadly divided into three categories: hydraulic (with emphasis on improving the prediction of performance and improvement of impeller life), vibrations (with the aim of providing cost-effective capability for problem solving/avoidance), and pump design [1]. Flow instabilities and unsteadiness, flow-induced noise, and flow-induced vibration in pumps have been continuously studied for years [2–4]. Advanced diagnostics for pump performance and failure must be provided attention to analyze flow fields and their responses [5]. Various studies that focused on these issues have contributed to the development and production of pumps [2–7]. In the last two years, researchers have focused on an unsteady flow feature called rotating stall [8–11], which is one of the most important sources of unsteadiness at partial flow rates for pumps. Unsteadiness occurs when the pressure increase in the rotor which exhibits a positive slope. Predicting the dynamic characteristics of rotating stall and gaining detailed information on the head-flow performance curve of pumps are very important as vibration and noise increase

at partial flow rates where the positive slope of a head-flow performance curve appears easily.

This study attempts to illustrate the relationship between pump characteristic instability and the rotating stall. Rotating stall is briefly summarized, including its causes, propagation mechanism, and onset, as well as the structure of the stall cell. A mixed flow pump with a positive slope in the head-flow performance curve is then investigated, and the relationship between the head-flow characteristic instability and design parameters is discussed in detail. The change in flow topology in the diffuser is related to the positive slope; reverse flow and adverse pressure gradient are thereby introduced to evaluate the onset and development of rotating stall within the diffuser.

## 2. Review of Rotating Stall in Pumps

The stable operating range of a pump is limited at the part-load flow rate. With decreasing flow rate, the relative velocity of the incoming fluid in the impeller throat is decelerated, whereas the incidence angle at the impeller leading edge (LE), which is the difference between the incoming flow angle

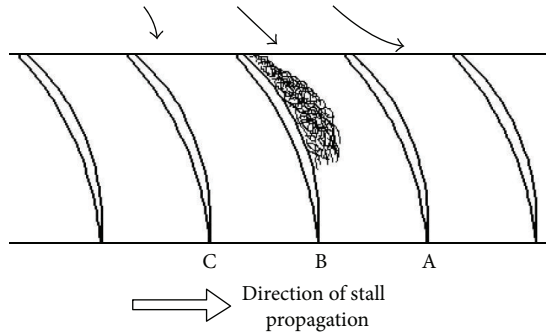


FIGURE 1: Rotating stall phenomenon in a diffuser.

and the blade angle, is accelerated. If the flow rate is further reduced, the flow would become unstable and would separate from the blade suction surface. A stall may occur and block the passage of the impeller. When a rotating stall occurs, one or more stall cells rotate around the axis and propagate at some fraction of the impeller's rotational speed; standing stall cells have been observed in the passage of the impeller in several cases [12].

The common method of explaining the onset and development of rotating stall in a diffuser is illustrated in Figure 1. In a row of blades operating at a high angle of incidence, if blade B is stalled, a separate wake is generated that blocks the flow in the passage between blades B and A. The blockage in the passage will divert the flow away from blade B, thereby increasing the angle of incidence on blade A and reducing that on blade C. Thus, blade A would stall, whereas any stall on blade C would diminish. The stall will therefore propagate from left to right in the figure if conditions are suitable. This case is seen in the diffuser, whereas that in the rotating impeller is slightly different [11].

Although Emmons et al. presented a coherent explanation of propagating stall in compressors in 1955 [13], understanding of the mechanism of this phenomenon remains limited. Rotating stall is frequently observed and widely studied in compressors, and an important issue is predicting both the onset and consequence of a rotating stall. A useful criterion is that rotating stall occurs when the stall approaches the maximum in the total head rise and the flow coefficient decreases. This condition is, however, no more than a crude approximation, and Greitzer quoted a number of cases in which rotating stall occurs while the slope of the performance curve is still negative [14]. A more sophisticated criterion widely used is from Leiblein and involves the diffusion factor,  $D_f$ , defined as

$$D_f = 1 - \frac{w_2}{w_1} + \frac{v_{\theta 2} - v_{\theta 1}}{2s w_1}, \quad (1)$$

where  $s$  is solidity. Rotating stall may begin when  $D_f$  is increased to a value of about 0.6. Rotating stall has not, however, been reported in axial pumps with a small number of blades, perhaps because  $D_f$  will not approach 0.6 in typical axial pumps or inducers with a small number of blades.

As for pumps, several studies of rotating stall have been made in which rotating stall causes the positive slope of

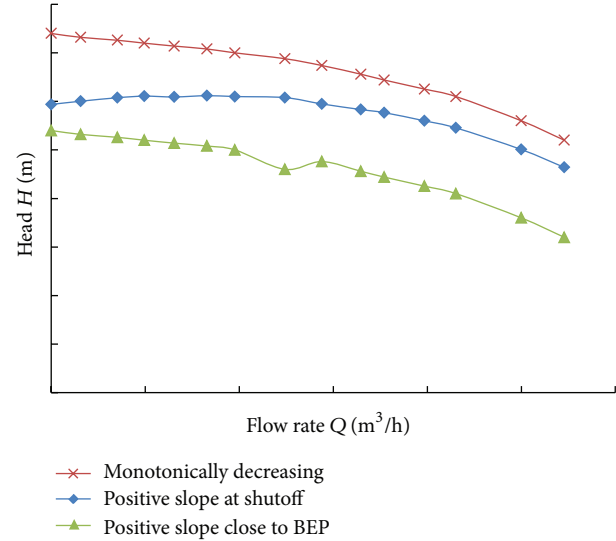


FIGURE 2: Typical pumping characteristics.

a head-flow performance curve. Three typical head-flow characteristics are presented in Figure 2. Curve 1 satisfies most end-users' needs for its characteristic of a monotonically negative slope. Curve 2 is a characteristic with a positive slope close to shutoff, which is caused by resistance at that operating point. The positive slope of characteristic occurs close to the best efficiency point (BEP) for curve 3, which is typical for axial and mixed flow pumps and high specific-speed centrifugal pumps. A theoretical analysis was carried out by Greitzer to explain the fundamental mechanisms and characteristics of a rotating stall [14]. He concluded that a rotating stall is flow instability caused by a positive slope of the head-flow rate performance curve, whereby the rotational frequency of rotating stall depends on the performance and the geometry of the rotor. Miyabe et al. visualized the unsteady internal flow in diffuser with Dynamic PIV [15, 16]. The authors clarified that the diffuser rotating stall causes the positive slope of a head-flow characteristic, and the backflow (i.e., a stall cell or a vortex) at the hub side of the diffuser plays an important role in the onset of a diffuser rotating stall. Anchored on the investigation of the behavior of a rotating stall in a diffuser mixed flow pump, Miyabe et al. enlarged the diameter of the hub at the diffuser inlet and found that the flow rate at which characteristic instability occurs is lower [15]. Pan et al. also enlarged the diameter of the hub at the diffuser inlet and obtained a similar result [10]. Although the method mentioned above does not suppress the positive slope of the head-flow performance curve completely, it still provides insight that an appropriate diffuser will eliminate the positive slope area while the rotating stall still occurs. That is, the situation quoted by Greitzer may also be found in pumps.

### 3. Unstable Head-Flow Characteristic Generation Mechanism

A typical positive slope of the head-flow performance curve close to BEP is represented in Figure 2 (curve 3), and

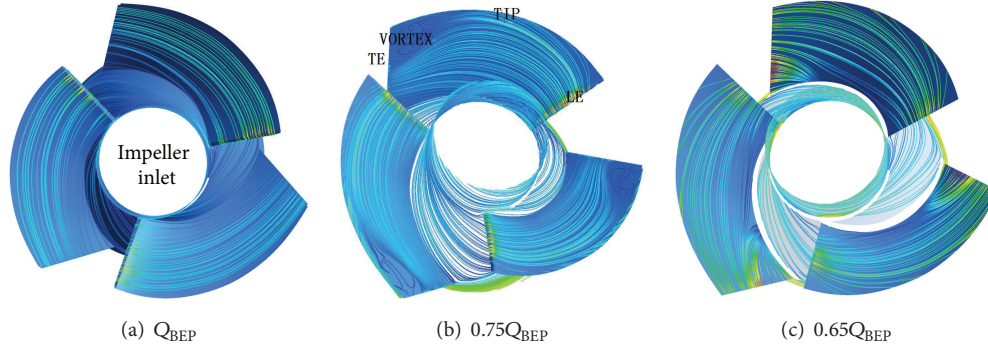


FIGURE 3: Velocity streamlines near the surface of impeller blades.

the mechanism of the head-flow curve instability can be explained as follows [10, 11, 17]. As shown in Figure 3, the streamline distribution near the blade surface is applied to provide a measure of flow separation and losses for the impeller [18]. At a partial flow rate, the flow angle decreases because of a tip leakage flow developed from the pressure surface (PS) to the suction surface (SS) near the trailing edge (TE) of the impeller; meanwhile, the generated vortices, which decrease the effective diameter of the impeller TE, mainly cause the abrupt head drop (Figure 3(b)). The prerotation upstream of the impeller LE at the casing also causes a decrease in pressure [19].

Further decrease in the flow rate causes the flow on the vane diffuser hub side to become unstable from the adverse pressure gradient and strong reserve flow. The reserve flow, which may change flow pattern in the impeller from the axial type to the centrifugal type and cause a slight increase of the head, returns to the impeller and blocks the passage flow from the impeller (Figure 3(c)).

To suppress the positive slope in a head-flow characteristic, feasibility should be studied to eliminate the three cases mentioned above. To investigate the flow structures and the head-flow curve instability for a mixed flow pump, a computation fluid dynamic is used in this study. The tested pump is a three-blade impeller and a seven-blade diffuser with a specific speed of  $n_s = 472$  at the best efficiency point ( $n_s = 3.65nQ^{0.5}H^{-0.75}/60$ ,  $Q_{BEP} = 887.76 \text{ m}^3/\text{h}$ ,  $H = 5.86 \text{ m}$ ,  $n = 980 \text{ r/min}$ ). Figure 4 shows the computational model for this study, which involves suction casing, impeller, diffuser, and discharge casing. The tip clearance between the impeller and the casing with a clearance of 3 mm is also included. Relevant details on the pump geometry are shown in Figure 5.

The mesh is generated using the commercial software ICEM-CFD v12.0, a grid independence study used seven different sizes of grids with elements from 1,200,000 to 2,400,000 nodes. As the differences of the CFD results were less than 0.2% with the meshes having more than 1,800,000 nodes and finer grid is needed to capture the flow structure, hence, the meshes with 2,000,000 nodes were adapted for the calculations.

In the present study, three-dimensional, steady and unsteady, Reynolds-averaged Navier-Stokes equations are solved by using the SST  $k-\omega$  turbulence model derived by

Menter [20]. Boundary conditions and the convergence criteria of the steady flow simulation are set according to [9, 10]. As for the unsteady calculation, 11 revolutions of the impeller for each operating condition in this case were conducted, and 3 deg of impeller rotation per step was adopted for the revolutions; therefore, 120 transient results are included for one impeller revolution. Within each time step, the number of iterations has been chosen to 15, and the iteration stops when the RMS (root mean square) residual dropped below  $4 \times 10^{-5}$ . The inlet boundary condition is set to mass flow rate, while a constant total pressure (1.1 atm) in the stationary frame is applied as the outlet condition. The interface between the impeller and the diffuser is set to “transient rotor-stator” to capture the transient flow.

Figure 5 shows the experimental results of the head-flow performance in comparison with CFD results. The maximum difference between the two methods is  $\pm 4.8$  percent, which indicates that the result of the CFD in this study is reliable.

### 3.1. Factors for the Abrupt Head Drop

**3.1.1. Prerotation at the Impeller Inlet.** Prerotation is assumed to be responsible for a head drop at part-load operating points, as proven in earlier studies [21]. Figure 6 shows the streamline at the upstream of the impeller, where prerotation occurs at partial flow rate. Muggli et al. used the standard  $k-\epsilon$  turbulence model to calculate a mixed flow pump characteristic from shutoff to maximum flow [19]. They clarified that the prerotation upstream of the impeller LE at the casing causes a decrease in pressure. However, more details on the drastic head drop were not presented. In other words, further study is needed to determine whether prerotation is an important factor in characteristic instability.

To analyze the influence of prerotation on the positive slope of the head-flow performance curve, a swirl-stop is placed upstream of the impeller. The velocity streamline of the impeller inlet with a swirl-stop is presented in Figure 7.

Head curves with two different conditions are presented in Figure 8. Although prerotation is eliminated at  $0.75Q_{BEP}$  in the presence of the swirl-stop, the positive slope region does not disappear. As the prerotation appears at  $0.65Q_{BEP}$ , the influence of the swirl-stop on pump performance at this point cannot be concluded. The prerotation may be no more than

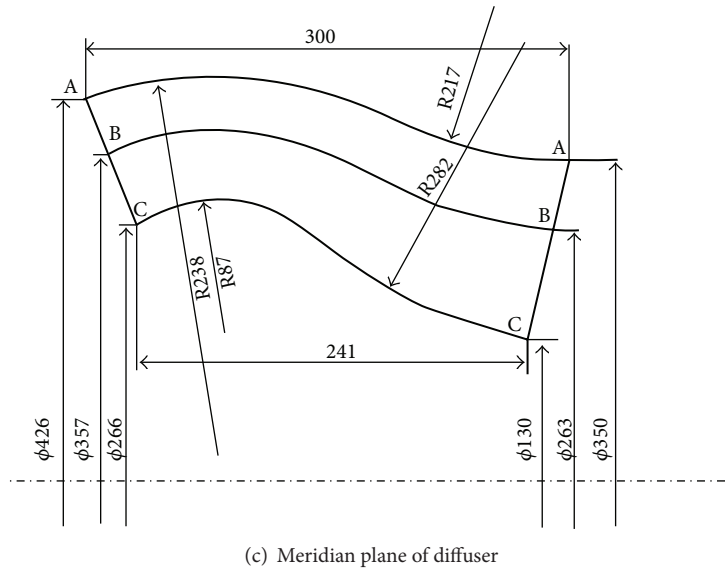
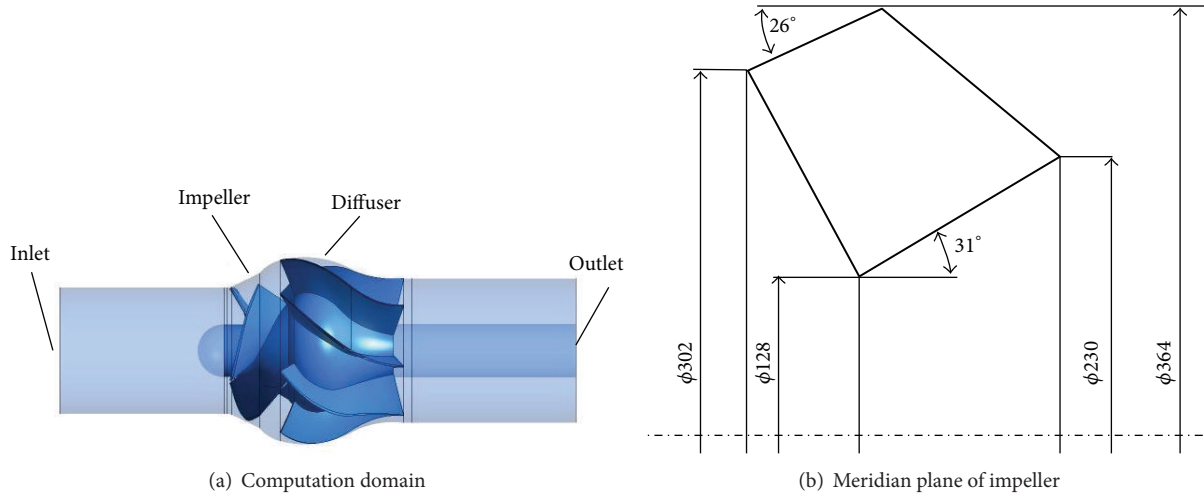


FIGURE 4: Overview of the investigated pump.

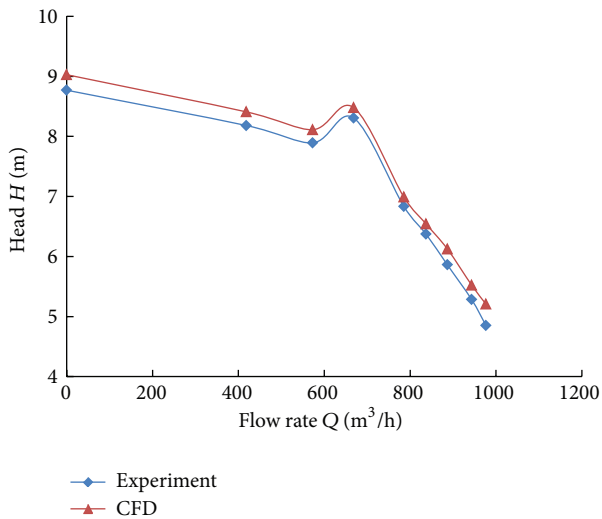


FIGURE 5: Measured and calculated head (total pressure) curves.

the result of flow rate change rather than the reason for the positive slope of the head-flow performance curve. Therefore, eliminating the prerotation of the impeller inlet is not a viable approach for inhibiting the performance curve instability.

The following examples can support the above mentioned conclusion. Sinha et al. used a converging nozzle and a flow straightener (honeycombs and screen) at the entrance of a centrifugal pump with a vane diffuser to smooth the inflow: no rotating stall was found in the impeller compared with that in a vane passage at the beginning of the volute, and the abrupt head drop occurred at  $0.51Q_{BEP}$  [22]. To suppress the rotating stall in the diffuser, Miyabe et al. enlarged the diameter of the hub at the diffuser inlet and placed a swirl stop at the pump entrance. The positive slope of the head-flow performance still occurred at partial flow rate [16].

**3.1.2. Leakage Flow in the Tip Clearance.** Figure 9 shows the flow pattern in the tip clearance. The leakage flow flows from the PS to the SS, and the interaction between the leakage flow

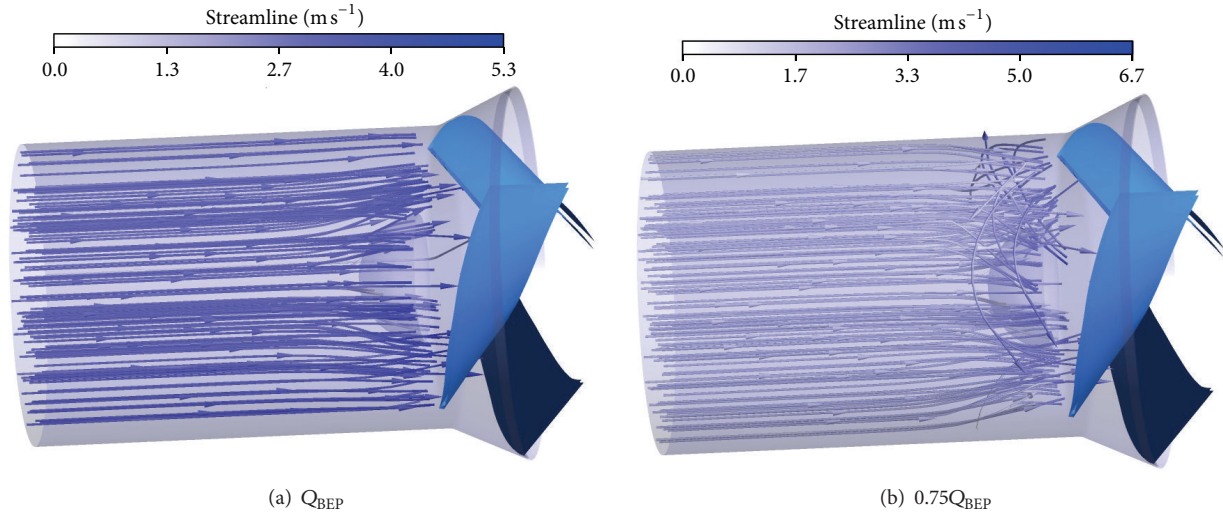


FIGURE 6: Velocity streamline at the upstream of the impeller.

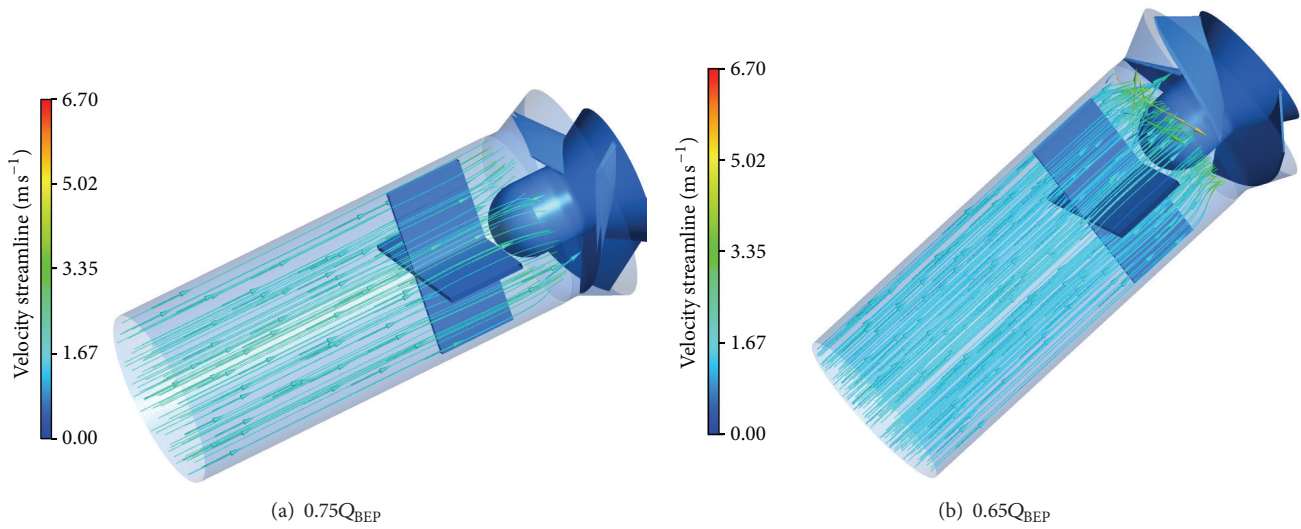


FIGURE 7: Velocity streamline at the upstream of the impeller with a swirl-stop.

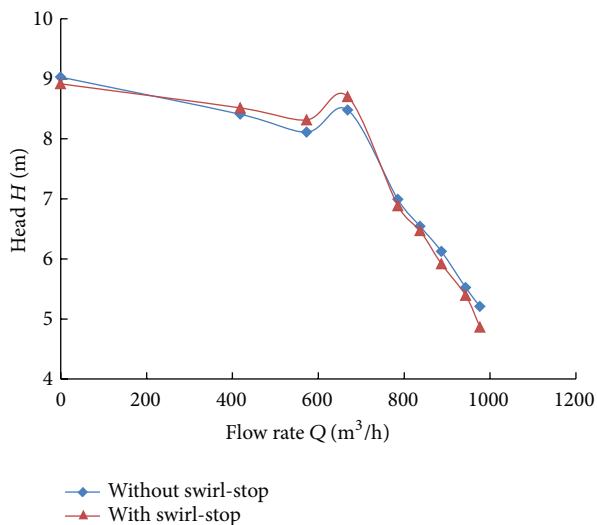


FIGURE 8: Head curves of the pump with and without swirl-stop.

in the tip clearance and the passage flow in the impeller generates a vortex. The leakage flow gradually increases, and a separate flow is generated on the suction surface with the decreasing flow. Yamade et al. also clarified that the drastic change of flow structures at the impeller outlet has a significant effect on the positive slope of the head-flow performance curve [23].

A mixed flow pump without tip clearance is then adopted to analyze the influence of leakage flow on the positive slope of the head-flow performance curve. The predicted pump characteristic is plotted in Figure 10, which is compared with the numerical simulation result of a conventional pump. The positive slope region is shown to be eliminated for the pump without tip clearance. Moreover, a positive slope region is not seen in the head-flow characteristic at  $0.75Q_{BEP}$ , which appears in the case of a conventional pump.

The velocity streamlines of the impeller blade surface and the impeller inlet at  $0.75Q_{BEP}$  are shown in Figure 11. The vortices caused by the leakage flow near the TE of the impeller tip have been suppressed, and prerotation at the impeller inlet

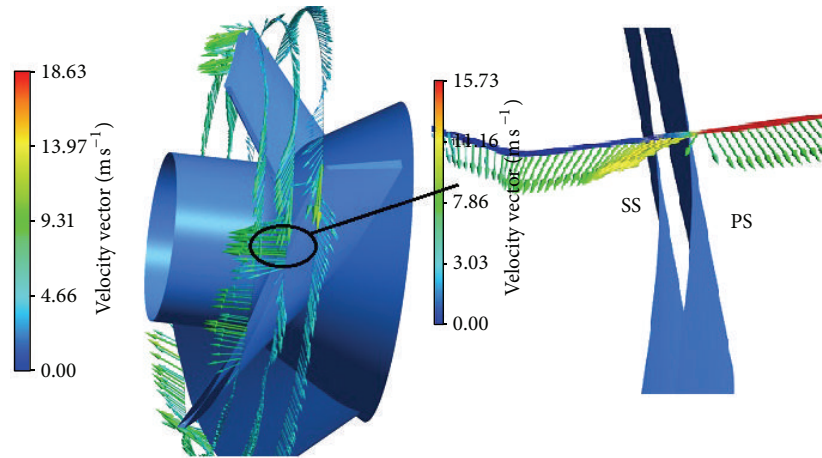


FIGURE 9: Relative velocity vectors of the leakage flow in the tip clearance at  $0.75Q_{BEP}$ .

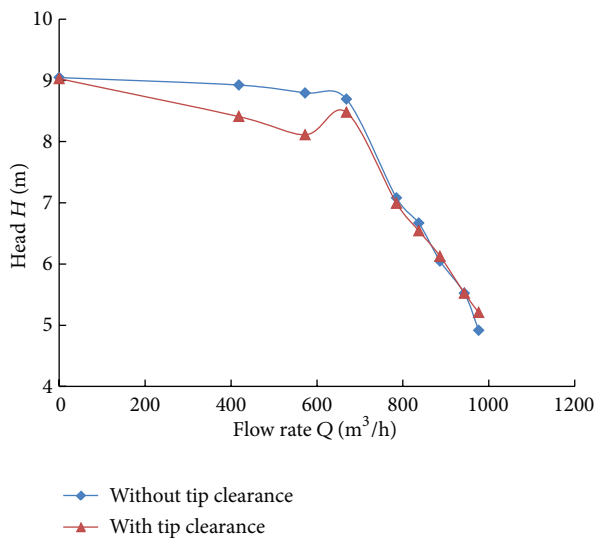


FIGURE 10: Head curves of the pump with and without tip clearance.

are also restricted in comparison with Figures 3(b) and 6(b). As the prerotation at the impeller inlet has no obvious effect on the positive slope of the head-flow performance curve, the vortices caused by leakage flow near the TE of the impeller tip can be concluded as the main reason for the abrupt head drop.

Although the mixed flow pump without tip clearance has a stable head-flow characteristic, this pump cannot be produced, as the gap between the impeller tip and the casing is a necessity to ensure the normal operation of the pump. In fact, zero leakage in the tip clearance is the reason that the head-flow characteristic of a mixed flow pump is stable, that is, tangential velocity of the leakage flow is zero in this case. Certain methods could be used to minimize the velocity of the leakage flow, which will suppress the positive slope of the head-flow performance curve despite the presence of the tip clearance. Installing shallow grooves on the casing wall near the impeller tip is such a method.

Figure 12 shows the velocity streamline in the shallow groove at  $0.75Q_{BEP}$ . Two kinds of grooves are presented. J-Groove, the shallow groove installed in the axial direction on the casing wall, has a rectangular cross-sectional area. Both J-Grooves have the same configuration with 30 grooves, each with a width of 4 mm and length of 45 mm; the depths of the grooves differ. Groove 1 has a depth of 4 mm, and Groove 2 has a depth of 2 mm.

J-Grooves can suppress the rotating stall by controlling mainstream angular momentum. Although the grooves are very shallow, the decrease in the tangential velocity of the leakage flow is significant. As seen in Figure 12, Groove 1, which has a lower velocity of groove flow, can suppress the head-flow characteristic instability (Figure 12(b)). With the decrease in depth, the ability of the J-Grooves to control the angular momentum of the main flow is weakened. Thus, Groove 2, which is half as deep as Groove 1, has less effect on the positive slope of the head-flow performance curve (Figure 12(c)).

*3.2. Factors for the Slight Rise of the Head.* As mentioned above, reverse flow occurring near the inlet of the hub surface of the vane diffuser is the main reason for the slight rise of the head-flow characteristic instability. To illustrate this phenomenon, the internal flow in the vane diffuser at different flow rates is analyzed and then presented in Figure 13.

The slope of the performance curve changes at  $0.75Q_{BEP}$ ; a vortex is generated at the tip of the impeller outlet, and the reverse flow occurs near the TE of the diffuser (Figures 3(b) and 13(c)). As the flow rate decreases further, a strong vortex is generated near the inlet of the hub surface of the vane diffuser, and the velocity profiles change at both the inlet and outlet of the impeller. Reverse flow takes place at the inlet-tip and outlet-hub, and the flow pattern changes from the axial type to centrifugal type in the passage of the impeller, which leads to a slight increase of the head-flow characteristic instability. As in [24], the current study ignores the detail of

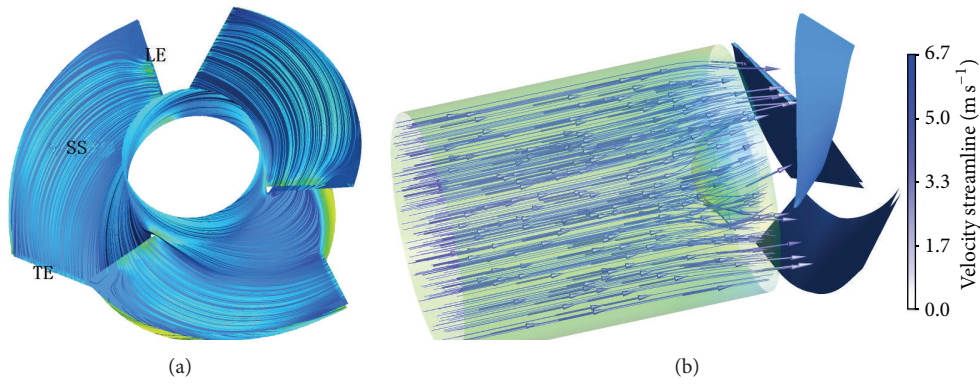


FIGURE 11: Velocity streamlines of the pump without tip clearance at  $0.75Q_{\text{BEP}}$ .

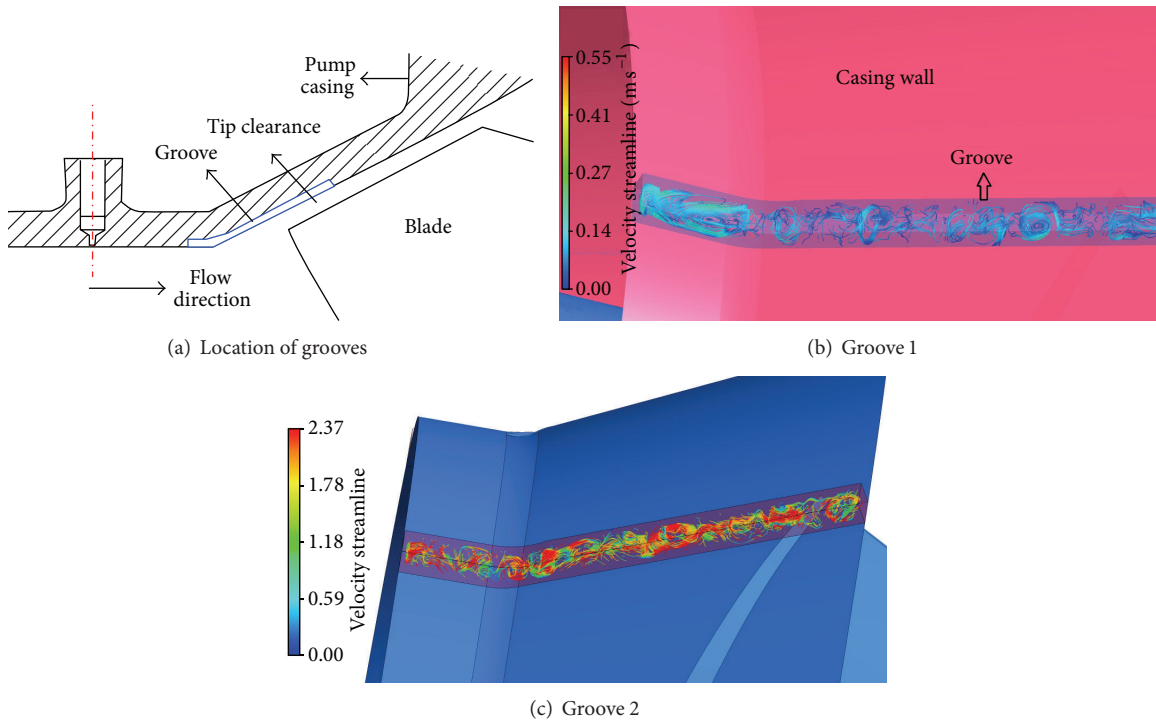


FIGURE 12: Velocity streamlines in the shallow groove ( $0.75Q_{\text{BEP}}$ ).

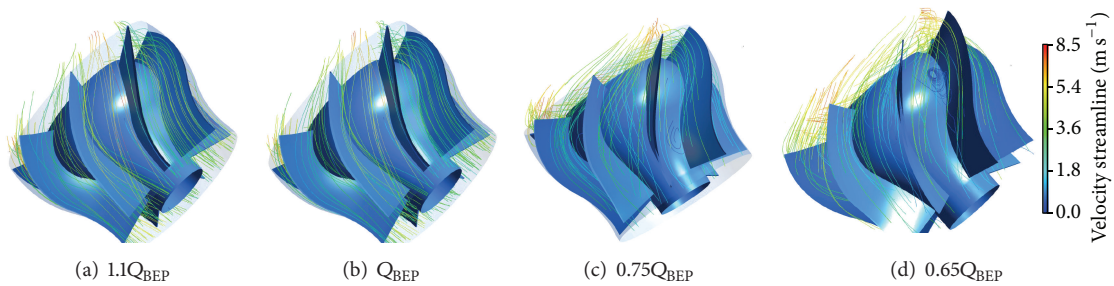


FIGURE 13: Three-dimensional streamlines in the vane diffuser.

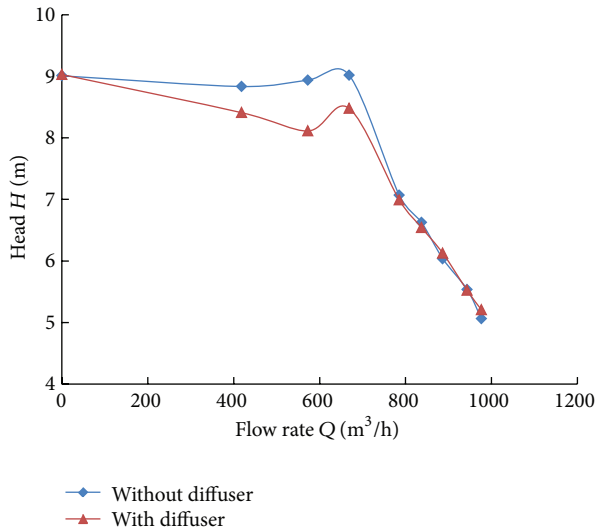


FIGURE 14: Comparison of performance curve when the pump is with and without diffuser.

the rotating stall although the instabilities are related to the stall behavior.

To verify the relation between the head-flow characteristic instability and the flow structure in the diffuser, the diffuser is removed and a new pump is obtained. The predicted pump characteristic is presented in Figure 14, which shows that the pump head is higher than the conventional one over the entire flow rate range. Energy loss is generated when the fluid flows through the diffuser, and interaction between the impeller and the diffuser also causes an energy loss. At partial flow rates, an abrupt head drop appears on the head curve at  $0.75Q_{BEP}$ , but the region of slight head rise is eliminated at  $0.65Q_{BEP}$ .

Figure 15 presents the velocity streamlines at the meridional section of the impeller passage without a diffuser; the reserve flow region at the TE of the impeller hub is restricted in comparison with that in Figure 3(c). The reserve flow at the outlet of the impeller is caused by a strong vortex at the LE of the diffuser that blocks the downstream flow from the impeller. Further study on flow patterns of the diffuser may help reveal the mechanism of the slight rise in the head-flow characteristic instability.

#### 4. Dynamic Characteristics of Rotating Stall within the Diffuser

Several studies have focused on the relationship between pump characteristic instability and internal flow in a pump. The positive slope of head-flow performance curve mentioned in Section 3 is an example of this research inquiry. As for the pump with a diffuser, the diffuser rotating stall causes the positive slope of head-flow characteristic, and the backflow at the hub side of the diffuser plays an important role in the onset of the diffuser rotating stall [9, 15, 25]. The onset and developed state of rotating stalls within a vane diffuser was illustrated in Section 2. However, Ogata and

Ichiro found that the propagation mechanism of a stall cell from one vane passage to another is more complex than that covered in the conventional explanation [26]. The inception of characteristic instability can be analyzed as follows [15, 22]: at partial flow rate, low energy fluids are accumulated in the corner between the hub surface and the convex surface of the diffuser vane. As the flow rate further decreases, the region of low energy fluids at the corner axis asymmetrically expands along the hub and becomes unstable because of the adverse pressure gradient. Then, strong backflow occurs, which impinges against passage flow from the impeller at the inlet of the vane diffuser. Therefore, flow separation occurs near the inlet of the vane diffuser, and a stall is generated.

**4.1. Effect of Flow Rate and Onset of the Stall.** Figure 16 shows the contour of axial velocity distributed at the cross-sections of the vane diffuser at partial flow rates. The flow rates are selected to show the transition of decreasing flow rate from a flow where no stall occurs to conditions of massive stall in the diffuser passage. At  $0.8Q_{BEP}$ , the flow is clearly not stalled, compared with the head-flow curve provided in Figure 5. With the decrease in the flow rate, an obvious difference is seen in the axial velocity and the static pressure distribution between adjacent diffuser passages (Figures 16(b) and 17(b)), which may be the reason for the flow separation near the outlet of the vane diffuser, shown in Figure 13(c). As the flow further decreases, the axial velocity becomes negative in the corner between the hub surface and the suction surface of the diffuser inlet at  $0.65Q_{BEP}$ , hence, flow separates from the suction surface at the LE of the diffuser, and the stall core is generated (Figures 13(d) and 16(d)).

**4.2. Propagation Mechanism of a Rotating Stall.** As seen in Figure 17, the adverse pressure gradient is increased in the diffuser passage where a stall is developed. A difference in static pressure distribution is observed in the adjacent diffuser passages at partial flow rates, but the detailed flow pattern is far more than is known. Relative velocity vectors near the LE of the diffuser is presented at  $0.65Q_{BEP}$  where a vortex is developed toward the inlet of the diffuser and blocks the passage flow from the impeller, near the diffuser inlet. The adverse pressure gradient is then increased in the diffuser passage, which causes the strong reserve flow in the entire area of one diffuser passage (Figures 16(d) and 18(a)).

In our previous studies, we found that the propagation mechanism and onset of rotating stall are more complicated than described in the classical explanation. The stall is not only affected by the inlet flow but also influenced by the outlet flow, as well as the pressure gradient in the flow passage. The nonuniform pressure distribution in the diffuser outlet or inlet causes the stall to propagate [11]. Sinha et al. attributed the nonuniform pressure distribution in the diffuser inlet to high-speed leakage flow (jet-flow) in the gap between the impeller and the diffuser [22]. Yoshida et al. observed a seven-bladed centrifugal impeller operating with a variety of diffusers with and without vanes. Rotating stall occurs in the vane diffuser at a speed less than 10% of the impeller speed. The clearance between the impeller and the diffuser vanes is

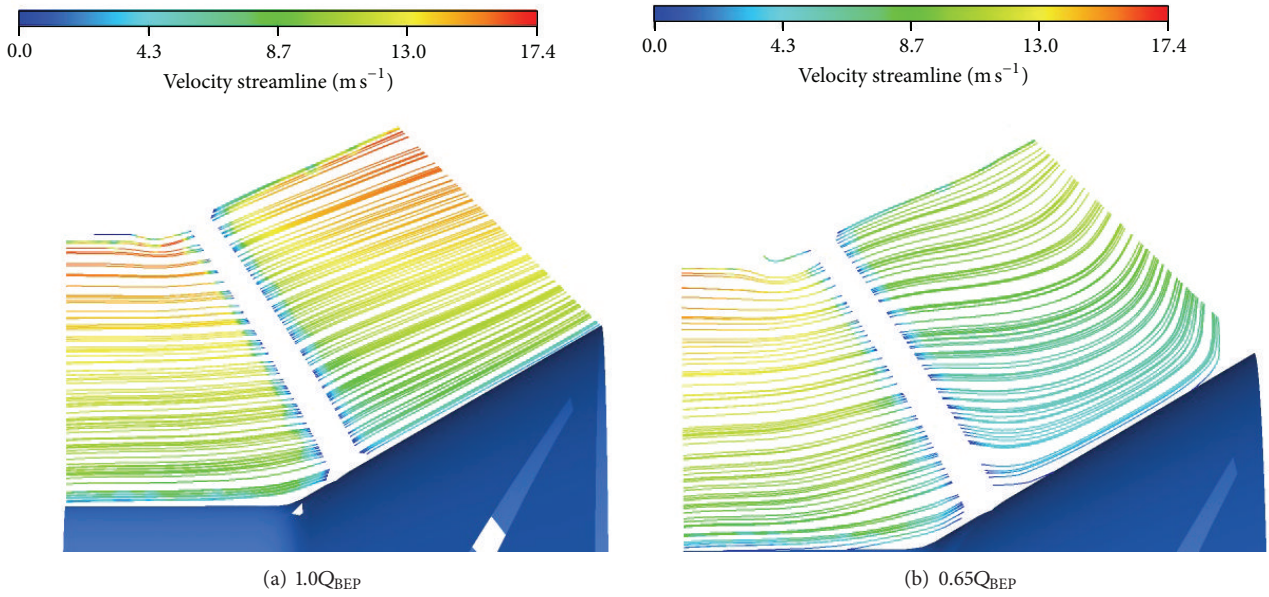


FIGURE 15: Velocity streamlines at the meridional section of impeller the passage without diffuser.

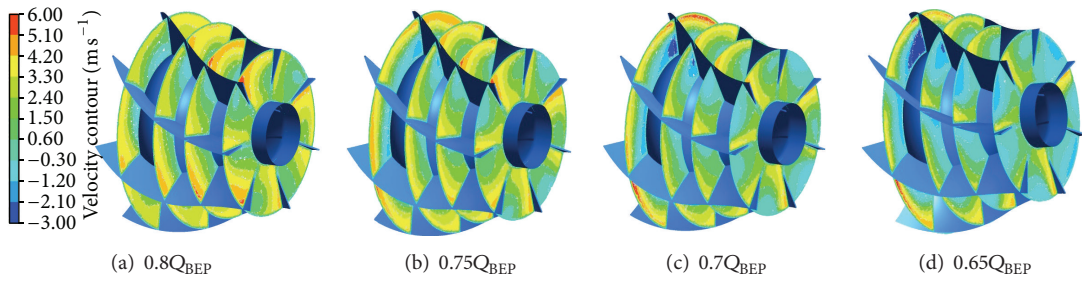


FIGURE 16: Axial velocity contour in the vane diffuser at partial flow rate.

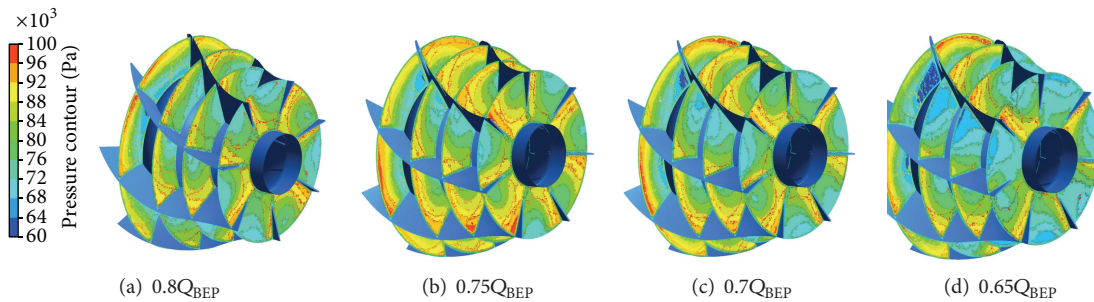


FIGURE 17: Pressure contour in the vane diffuser at partial flow rate.

large. As this clearance decreases, the diffuser rotating stall tends to disappear [27]. The jet flow also occurs near the TE of the vane, and alternate jet flow and reverse flow appear when a rotating stall occurs, as shown in Figure 19.

As the propagation mechanism and onset of rotating stall is more complicated than described in the classical explanation, an accurate propagation velocity is difficult to achieve. The speed is clearly a fraction of the circumferential component of the relative velocity, that is, either  $v_{\theta 1}$  in the

case of a stator or  $w_{\theta 1}$  in the case of a rotor. In the case of a rotor, the stall rotates in the same direction as the rotor but with 50% to 70% (other reports indicate 50% to 90%) of the rotor angular velocity. In the case of a stator, the fraction is between 10% and 25% [9, 12]. Figure 20 shows a period of stall propagation at  $0.65Q_{\text{BEP}}$ , where the propagation speed is about 20% of the impeller speed. Additional information cannot be obtained as the stall does not finish one complete circle of propagation.

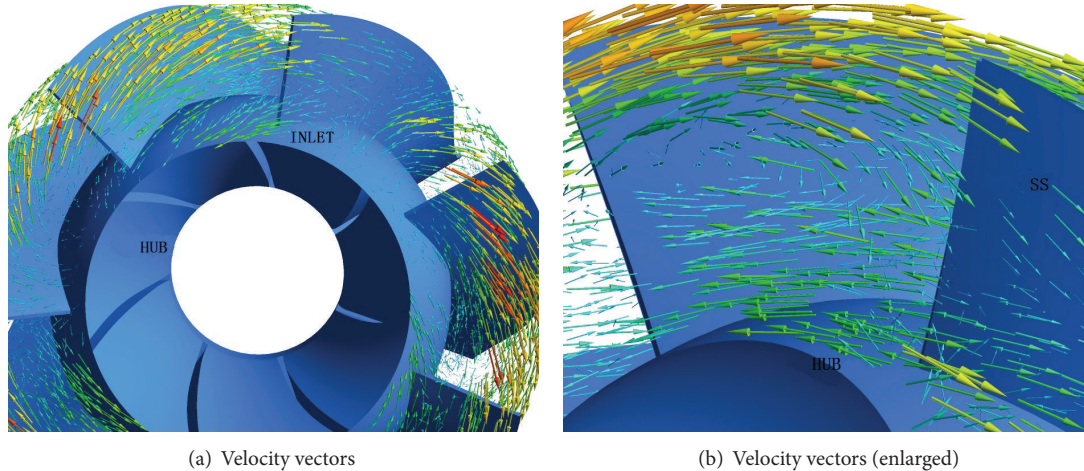


FIGURE 18: Relative velocity vectors near the LE of diffuser at  $0.65Q_{BEP}$ .

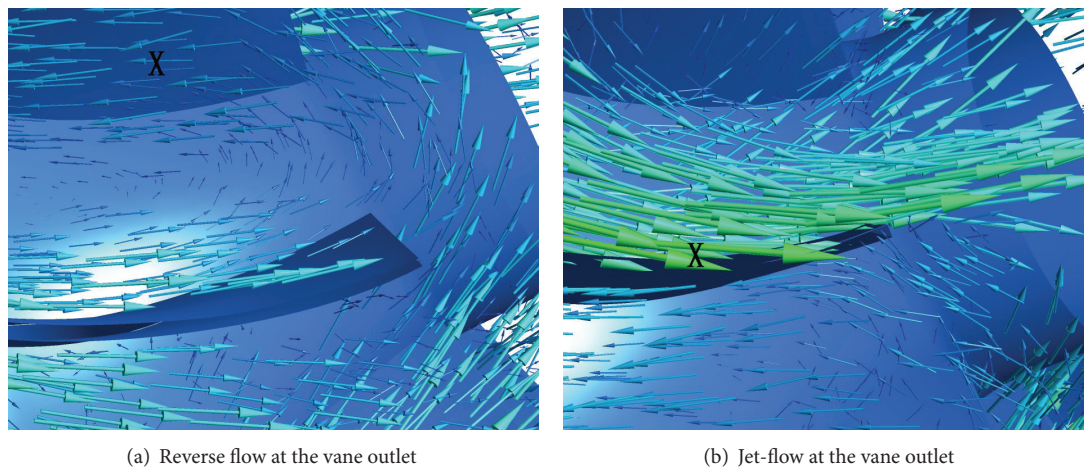


FIGURE 19: Instantaneous velocity vectors near the TE of the diffuser at  $0.65Q_{BEP}$ .

## 5. Conclusions

- (1) The appearance of pump characteristic instability is associated with the unstable flow pattern at partial flow rate. The leakage flow occurs at the tip clearance between the casing and the impeller. The reserve flow at the inlet of the diffuser contributes to the head-flow characteristic instability. Prerotation may cause a head drop, but it has no effect on the positive slope of a head-flow performance curve.
- (2) At partial flow rate, the flow angle decreases because of the leakage flow near the LE of the impeller tip and generated vortices, which are the main reason to the abrupt head drop. This conclusion is verified by the pump without tip clearance and by the J-Grooves mounted on the casing.
- (3) The flow pattern in the impeller changes from the axial type to the centrifugal type because of the reserve flow near the inlet of the hub surface of the vane diffuser. The stall is generated at the diffuser inlet and causes a slight increase of the head-flow characteristic instability.
- (4) The propagation mechanism and onset of rotating stalls are more complicated than described in the classical explanation. A rotating stall is not only effected by the inlet flow but also influenced by the outlet flow, as well as the pressure gradient in the flow passage. The pressure phase determines the stall propagation. However, the factor that determines the pressure phase is a further concern.
- (5) Alternate jet-flow and reverse flow appear in the passage of a diffuser or an impeller when a rotating stall occurs. The nonuniform pressure distribution in the impeller/diffuser outlet or inlet causes the stall to propagate. Lower identical frequencies exist and are dependent on flow rate and rotational speed. A discrepancy is observed in the performance curve, and as a result, it is believed that the pump is closed to the onset condition of a rotating stall.

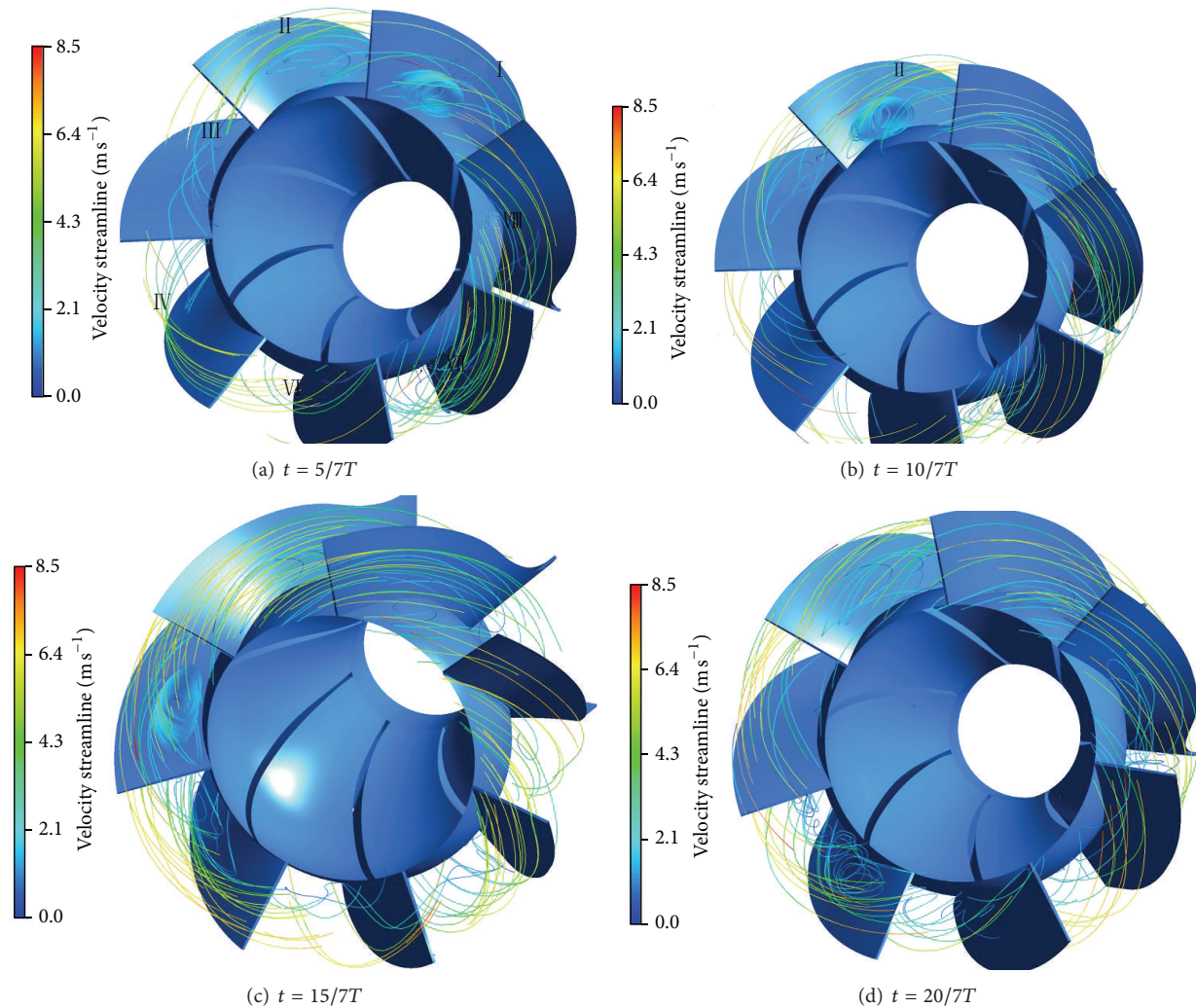


FIGURE 20: Period of stall propagation at  $0.65Q_{BEP}$ .

## Acknowledgments

This work was supported by the National Natural Science Foundation of China (Grant Nos. 51076144 and 51239005), National Science and Technology Pillar Program of China (Grant no. 2011BAF14B04), and Jiangsu Provincial Projects for Innovative Postgraduates of China (Grant no. CXZZ11.0564). The support provided by these institutions is gratefully acknowledged.

## References

- [1] S. Gopalakrishnan, "Pump research and development: past, present, and future—an American perspective," *ASME Journal of Fluids Engineering*, vol. 121, no. 2, pp. 237–253, 1999.
- [2] Z. Y. Pan, Y. Y. Ni, J. Ho, and S. Q. Yuan, "Flow structures and pressure fluctuations in a centrifugal pump at design and off-design conditions," in *Proceedings of the ASME Fluids Engineering Division Summer Conference (FEDSM '09)*, pp. 137–145, Vail, Colo, USA, August 2009.
- [3] S. Q. Yuan, J. Yang, J. P. Yuan, Y. Luo, and J. Pei, "Measurement on the flow-induced noise under variable conditions for centrifugal pumps," *Chinese Journal of Mechanical Engineering*, vol. 25, pp. 456–462, 2012.
- [4] Y. Y. Ni, S. Q. Yuan, Z. Y. Pan, and J. P. Yuan, "Detection of cavitation in centrifugal pump by vibration methods," *Chinese Journal of Mechanical Engineering*, vol. 21, no. 5, pp. 46–49, 2008.
- [5] T. Yamamoto, J. Ho, and Z. Y. Pan, "Development of pump performance monitor (Part I)," in *Symposium on Evaluation and Diagnosis (Section 5)*. Japan, pp. 105–112, 2005.
- [6] Z. Y. Pan, J. J. Li, S. Li, and S. Q. Yuan, "Study on radial forces of centrifugal pumps with various collectors," in *Proceedings of the ASME-JSME-KSME Joint Fluids Engineering Conference*, Hamamatsu, Japan, 2011.
- [7] S. Q. Yuan, Y. Y. Ni, Z. Y. Pan, and J. P. Yuan, "Unsteady turbulent simulation and pressure fluctuation analysis for centrifugal pumps," *Chinese Journal of Mechanical Engineering*, vol. 22, no. 1, pp. 64–69, 2009.
- [8] Z. Y. Pan, J. J. Li, H. Li, and W. Liu, "Overview for research on rotating stall of pump," *Fluid Machinery*, vol. 39, pp. 35–39, 2011.

- [9] Z. Y. Pan, J. J. Li, X. J. Li, and S. Q. Yuan, "Performance curve instability and rotating stall," *Transactions of the Chinese Society for Agricultural Machinery*, vol. 43, pp. 64–68, 2012.
- [10] Z. Y. Pan, T. T. Wu, J. J. Li, and Y. J. Li, "Mechanism of characteristic instability and its suppression in mixed flow pump," *Transactions of the Chinese Society for Agricultural Machinery International Journal of Comprehensive Engineering C*, vol. 1, pp. 1–7, 2012.
- [11] S. Q. Yuan, W. Liu, Z. Y. Pan, and X. J. Li, "Review on rotating stall in pumps," *Transactions of the Chinese Society for Agricultural Machinery International Journal of Comprehensive Engineering C*, vol. 1, pp. 28–38, 2012.
- [12] N. Krause, K. Zähringer, and E. Pap, "Time-resolved particle imaging velocimetry for the investigation of rotating stall in a radial pump," *Experiments in Fluids*, vol. 39, no. 2, pp. 192–201, 2005.
- [13] H. W. Emmons, C. E. Pearson, and H. P. Grant, "Compressor surge and stall propagation," *ASME Journal of Fluids Engineering*, vol. 79, pp. 237–253, 1955.
- [14] E. M. Greitzer, "The stability of pumping systems—the 1980 Freeman scholar lecture," *ASME Journal of Fluids Engineering*, vol. 103, no. 2, pp. 193–242, 1981.
- [15] M. Miyabe, A. Furukawa, H. Maeda, I. Umeki, and Y. Jittani, "On improvement of characteristic instability and internal flow in mixed flow pumps," *Journal of Fluid Science and Technology*, vol. 3, pp. 732–743, 2008.
- [16] M. Miyabe, A. Furukawa, H. Maeda, and I. Umeki, "Rotating stall behavior in a diffuser of mixed flow pump and its suppression," in *Proceedings of the ASME Fluids Engineering Division Summer Conference (FEDSM '08)*, pp. 1147–1152, Jacksonville, Fla, USA, August 2008.
- [17] M. Miyabe, H. Maeda, I. Umeki, and Y. Jittani, "Unstable head-flow characteristic generation mechanism of a low specific speed mixed flow pump," *Journal of Thermal Science*, vol. 15, no. 2, pp. 115–144, 2006.
- [18] H. W. Oh, "Design parameter to improve the suction performance of mixed-flow pump impeller," *Proceedings of the Institution of Mechanical Engineers A*, vol. 224, no. 6, pp. 881–887, 2010.
- [19] F. A. Muggli, P. Holbein, and P. Dupont, "CFD calculation of a mixed flow pump characteristic from shutoff to maximum flow," *ASME Journal of Fluids Engineering*, vol. 124, no. 3, pp. 798–802, 2002.
- [20] F. R. Menter, "Two-equation eddy-viscosity turbulence models for engineering applications," *AIAA journal*, vol. 32, no. 8, pp. 1598–1605, 1994.
- [21] R. Xie, Z. Y. Pan, J. J. Li, and J. R. Liu, "Influences of various inlet flow structure on the pump performance," in *Proceedings of the 3rd International Conference on Information and Computing, ICIC 2010*, vol. 2, pp. 86–89, Wuxi, China, June 2010.
- [22] M. Sinha, A. Pinarbasi, and J. Katz, "The flow structure during onset and developed states of rotating stall within a vaned diffuser of a centrifugal pump," *ASME Journal of Fluids Engineering*, vol. 123, no. 3, pp. 490–499, 2001.
- [23] Y. Yamade, C. Kato, H. Shimizu, and T. Nagahara, "Large eddy simulation of internal flow of a mixed-flow pump," in *Proceedings of the ASME Fluids Engineering Division Summer Conference (FEDSM '09)*, pp. 407–416, Vail, Colo, USA, August 2009.
- [24] R. K. Byskov, C. B. Jacobsen, and N. Pedersen, "Flow in a centrifugal pump impeller at design and off-design conditions—part II: large eddy simulations," *ASME Journal of Fluids Engineering*, vol. 125, no. 1, pp. 73–83, 2003.
- [25] S. H. Stenning, "Rotating stall and surge," *ASME Journal of Fluids Engineering*, vol. 102, no. 1, pp. 14–20, 1980.
- [26] M. Ogata and A. Ichiro, "An experimental study of rotating stall in a radial vaned diffuser," in *Proceedings of the International Symposium on Unsteady Aerodynamics and Aeroelasticity of Turbomachines*, pp. 625–641, 1995.
- [27] Y. Yoshida, Y. Murakami, T. Tsurusaki, and Y. Tsujimoto, "Rotating stalls in centrifugal impeller/vaned diffuser systems," in *Proceedings of the 1st ASME/JSME Joint Fluids Engineering Conference*, vol. FED-107, pp. 125–130, Portland, Ore, USA.

## Research Article

# New Analytical and Numerical Solutions for Mixed Convection Boundary-Layer Nanofluid Flow along an Inclined Plate Embedded in a Porous Medium

Emad H. Aly<sup>1,2</sup> and Abdelhalim Ebaid<sup>3</sup>

<sup>1</sup> Department of Mathematics, Faculty of Science, King Abdulaziz University, Jeddah 21589, Saudi Arabia

<sup>2</sup> Department of Mathematics, Faculty of Education, Ain Shams University, Roxy, Cairo 11757, Egypt

<sup>3</sup> Department of Mathematics, Faculty of Science, University of Tabuk, Tabuk 71491, Saudi Arabia

Correspondence should be addressed to Emad H. Aly; [emad-aly@hotmail.com](mailto:emad-aly@hotmail.com)

Received 17 July 2013; Accepted 23 August 2013

Academic Editor: Mohamed Fathy El-Amin

Copyright © 2013 E. H. Aly and A. Ebaid. This is an open access article distributed under the Creative Commons Attribution License, which permits unrestricted use, distribution, and reproduction in any medium, provided the original work is properly cited.

Two different analytical and numerical methods have been applied to solve the system describing the mixed convection boundary-layer nanofluids flow along an inclined plate embedded in a porous medium, namely, homotopy perturbation method (HPM) and Chebyshev pseudospectral differentiation matrix (ChPDM), respectively. Further, ChPDM is used as a control method to check the accuracy of the results obtained by HPM. The analytical method is applied using a new way for the deformed equations, and the resulted solution was expressed in terms of a well-known entire error function. In addition, using only two terms of the homotopy series, the approximate analytical solution is compared with the numerical solution obtained by the accurate ChPDM approach. The results reveal that good agreements have been achieved between the two approaches for various values of the investigated physical parameters.

## 1. Introduction

The concept of nanofluids is put into practice particularly after the tremendous development of nanotechnologies in the last decade, as they are of great importance in many industrial and engineering applications, especially in heat transfer enhancement [1–4]. Nanofluids are produced by dispersing nanometer-scale solid particles into base liquids such as water, ethylene glycol, and oils. Normally, if the particle sizes are in the 1–100 nm ranges, they are generally called nanoparticles.

Recently, the boundary-layer flow of nanofluids has attracted much attention [5–8]. The flow field of such problems is governed at first by a system of linear and nonlinear partial differential equations which are then transformed into a new system of linear and non-linear ordinary differential equations with applying the appropriate transformations. Due the difficulties that arise in obtaining the analytical

solutions for the resulted system, most of the authors resort to numerical methods.

Although the numerical methods have the upper hand over the analytical methods in solving the complex systems of differential equations, the analytical solutions can be viewed as an optimal choice when available. In addition, the obtained solutions can be directly used for getting the required plots without needing subprograms as in the numerical methods. In conclusion, one can say that each of the two approaches has its own advantage over the other. Therefore, comparing the results obtained by two different analytical and numerical approaches is generally of great importance in the applied sciences. Two different analytical methods (homotopy perturbation method, HPM) [9–18] and numerical method (Chebyshev pseudospectral differentiation matrix, ChPDM) [19–21] are proposed in this paper for the mixed convection boundary-layer nanofluids flow along an inclined plate embedded in a porous medium.

More details about these techniques and their advantages are introduced in the next two paragraphs.

The homotopy perturbation method (HPM) was proposed by He [9–15] as an analytical technique to solve nonlinear differential equations. This method has been widely used by many authors to investigate various models [16–18]. Unlike, the requirement for the regular perturbation techniques [19], the homotopy perturbation method is always valid no matter whether there exists small physical parameter or not. It combines the traditional perturbation method and the homotopy technique to deform a nonlinear problem into a simple solving one. The solution using this method is expressed as the summation of an infinite series, which usually converges rapidly to the exact solution in most cases. Several terms of the series solution can be used for approximating the exact solution with a high degree of accuracy.

On the other hand, the ChPDM is a known highly accurate numerical approach which was introduced and successfully applied by Aly et al. [20] to analyze the two-dimensional MHD boundary-layer flow over a permeable surface with a power law stretching velocity in the presence of a magnetic field applied normally to the surface. Under certain circumstances, it is shown that the problem has an infinite number of solutions which were examined by this technique. Further, Guedda et al. [21] have applied this method to validate and evidence the analysis of two-dimensional mixed convection boundary-layer flow over a vertical flat plate embedded in a porous medium saturated with water at 4°C (maximum density) and applied magnetic field. Both cases of the assisting and opposing flows are considered. Multiple similarity solutions are obtained and investigated by ChPDM under the power law variable wall temperature, or variable heat flux, or variable heat transfer coefficient. Recently, Aly and Ebaid [22] have applied this technique to solve the current problem in the absence of the magnetic and permeability of parameters. They found that the ChPDM results are very accurate in an excellent manner compared to those published in the literature using the homotopy analysis [23]. It is then successfully applied to validate and evidence the resulted exact solutions for different positive and negative values of the investigated parameters.

The motivation of presenting this paper is therefore to extend the applicability of both HPM and ChPDM approaches. The suggested procedure is based first on obtaining all the possible exact solutions. Then, the second step of the suggested procedure is to validate these results numerically to explore the effectiveness and efficiency of the proposed numerical approach. Besides, comparisons with other published results are also presented, where a full agreement is observed. In addition, it is shown that the solution up to the first order is sufficient to obtain accurate results.

## 2. The Physical Model

Rana et al. [24] considered the steady, incompressible, laminar, boundary-layer flow of a nanofluid along a semi-infinite inclined flat plate in a nanofluid-saturated porous medium

with an acute angle  $\alpha$  to the vertical. The mathematical model is governed by the following system of nonlinear ordinary differential equations:

$$f'' = \frac{Ra_x}{Pe_x} (\theta' - N_r \phi') \cos(\alpha), \quad (1)$$

$$\theta'' + \frac{1}{2} f \theta' + N_b \phi' \theta' + N_t (\theta')^2 = 0, \quad (2)$$

$$\phi'' + \frac{1}{2} Le f \phi' + \frac{N_t}{N_b} \theta'' = 0,$$

which has to be solved, subject to the boundary conditions:

$$f(0) = 0, \quad f'(\infty) = 1, \quad (3)$$

$$\theta(0) = 1, \quad \theta(\infty) = 0, \quad (4)$$

$$\phi(0) = 1, \quad \phi(\infty) = 0, \quad (5)$$

where primes denoting differentiation with respect to  $\eta$  and  $Le$ ,  $N_r$ ,  $N_b$ ,  $N_t$ ,  $Ra_x$ , and  $Pe_x$  are the Lewis number, buoyancy ratio parameter, Brownian motion parameter, thermophoresis parameter, local Darcy-Rayleigh number, and local Péclet number, respectively. On integrating (1) with respect to  $\eta$  from  $\infty$  to  $\eta$  and using the boundary conditions in (3)–(4), we have

$$f' = 1 + \Omega (\theta - N_r \phi), \quad \text{where } \Omega = \frac{Ra_x}{Pe_x} \cos(\alpha). \quad (6)$$

## 3. Application of the HPM

In this section, the homotopy perturbation method (HPM) is applied to search for the approximate analytical solutions for the system of (6) and (2) with the boundary conditions (3)–(5). In order to apply this method, we rewrite the investigated system in terms of an embedding parameter  $p$  as

$$\begin{aligned} f' &= 1 + p [\Omega (\theta - N_r \phi)], \\ \theta'' + \frac{1}{2} f \theta' &= -p [N_b \phi' \theta' + N_t (\theta')^2], \\ \phi'' + \frac{1}{2} Le f \phi' &= -p \left[ \frac{N_t}{N_b} \theta'' \right]. \end{aligned} \quad (7)$$

According to the HPM, the following assumptions are assumed:

$$\begin{aligned} f(\eta) &= \sum_{n=0}^{\infty} p^n f_n(\eta), \\ \theta(\eta) &= \sum_{n=0}^{\infty} p^n \theta_n(\eta), \\ \phi(\eta) &= \sum_{n=0}^{\infty} p^n \phi_n(\eta). \end{aligned} \quad (8)$$

Substituting (8) into (7) and by comparing the like powers of the embedding parameter  $p^0$ , we get the following systems:

$$\begin{aligned} f_0'(\eta) &= 1, & f_0(0) &= 0, \\ \theta_0'' + \frac{1}{2}f_0\theta_0' &= 0, & \theta_0(0) &= 1, & \theta_0(\infty) &= 0, \\ \phi_0'' + \frac{1}{2}f_0\phi_0' &= 0, & \phi_0(0) &= 1, & \phi_0(\infty) &= 0, \end{aligned} \tag{9}$$

and for  $p^n, n \geq 0$ , we have

$$\begin{aligned} f_{n+1}'(\eta) &= \theta_n - N_r\phi_n, \\ \theta_{n+1}'' + \frac{1}{2}f_0\theta_{n+1}' &= -\sum_{k=0}^n \left[ \frac{1}{2}f_{n+1-k}\theta_k' + N_b\phi_{n-k}'\theta_k' \right. \\ &\quad \left. + N_t\theta_{n-k}'\theta_k' \right], \\ \phi_{n+1}'' + \frac{1}{2}Le f_0\phi_{n+1}' &= -\frac{N_t}{N_b}\theta_n'' - \frac{1}{2}Le \sum_{k=0}^n f_{n+1-k}\phi_k'. \end{aligned} \tag{10}$$

The last systems are subjected to the boundary conditions:

$$\begin{aligned} f_{n+1}(0) &= 0, \\ \theta_{n+1}(0) &= 0, & \theta_{n+1}(\infty) &= 0, \\ \phi_{n+1}(0) &= 0, & \phi_{n+1}(\infty) &= 0. \end{aligned} \tag{11}$$

**3.1. Solution of the Zeroth-Order System.** The exact solutions of the zeroth-order system are given as

$$\begin{aligned} f_0(\eta) &= \eta, \\ \theta_0(\eta) &= 1 - \operatorname{erf}\left(\frac{1}{2}\eta\right), \\ \phi_0(\eta) &= 1 - \operatorname{erf}\left(\sqrt{\frac{Le}{4}}\eta\right), \end{aligned} \tag{12}$$

where erf is the error function; see Abramowitz and Stegun [25]. These exact solutions can be verified by the direct substitution.

**3.2. Solution of the First-Order System.** The system of first-order is obtained by considering  $n = 0$  in (10) and given by

$$\begin{aligned} f_1'(\eta) &= \theta_0 - N_r\phi_0, \\ \theta_1'' + \frac{1}{2}f_0\theta_1' &= -\frac{1}{2}f_1\theta_0' - \left[ N_b\phi_0'\theta_0' + N_t(\theta_0')^2 \right], \\ \phi_1'' + \frac{1}{2}Le f_0\phi_1' &= -\frac{1}{2}Le f_1\phi_0' - \frac{N_t}{N_b}\theta_0'', \end{aligned} \tag{13}$$

where the appropriated boundary conditions are

$$\begin{aligned} f_1(0) &= 0, \\ \theta_1(0) &= 0, & \theta_1(\infty) &= 0, \\ \phi_1(0) &= 0, & \phi_1(\infty) &= 0. \end{aligned} \tag{14-16}$$

On using the initial condition (14), the exact solution of the  $f_1$ -equation in system (13) is given as follows:

$$\begin{aligned} f_1(\eta) &= \Omega \int_0^\eta [\theta_0(\sigma) - N_r\phi_0(\sigma)] d\sigma \\ &= (1 - N_r)\Omega\eta \\ &\quad + \Omega \int_0^\eta \left[ N_r \operatorname{erf}\left(\sqrt{\frac{Le}{4}}\sigma\right) - \operatorname{erf}\left(\frac{1}{2}\sigma\right) \right] d\sigma \\ &= \sqrt{\frac{4}{\pi}} \left( 1 - \frac{N_r}{\sqrt{Le}} \right) \Omega \\ &\quad + \Omega \left[ (\theta_0 - N_r\phi_0)\eta + \sqrt{\frac{4}{\pi}} \right. \\ &\quad \left. \times \left( \frac{N_r}{\sqrt{Le}} e^{-(1/4)Le\eta^2} - e^{-(1/4)\eta^2} \right) \right]. \end{aligned} \tag{17}$$

Regarding the view of  $\theta_1$ -equation in (13) and boundary conditions (15), we obtain  $\theta_1$  in the following closed form:

$$\theta_1(\eta) = I_1(\eta) - I_1(\infty) \operatorname{erf}\left(\frac{1}{2}\eta\right), \tag{18}$$

where  $I_1(\eta)$  is given by

$$I_1(\eta) = \int_0^\eta e^{-(1/4)\sigma^2} d\sigma \int_0^\sigma e^{(1/4)\xi^2} \psi_1(\xi) d\xi, \tag{19}$$

where

$$\psi_1(\xi) = -\left[ \frac{1}{2}f_1(\xi) + N_b\phi_0'(\xi)\theta_0'(\xi) + N_t(\theta_0'(\xi))^2 \right]. \tag{20}$$

The double integral in (19) can be expressed in terms of single integrations by using the integral identity:

$$\int_0^\eta g(\sigma) d\sigma \int_0^\sigma h(\xi) d\xi = \int_0^\eta h(\xi) d\xi \int_\xi^\eta g(\sigma) d\sigma, \tag{21}$$

and hence,

$$\begin{aligned} I_1(\eta) &= \int_0^\eta e^{(1/4)\xi^2} \psi_1(\xi) d\xi \int_\xi^\eta e^{-(1/4)\sigma^2} d\sigma \\ &= \sqrt{\pi} \int_0^\eta \left[ \operatorname{erf}\left(\frac{1}{2}\eta\right) - \operatorname{erf}\left(\frac{1}{2}\xi\right) \right] e^{(1/4)\xi^2} \psi_1(\xi) d\xi \\ &= \sqrt{\pi} \operatorname{erf}\left(\frac{1}{2}\eta\right) \int_0^\eta e^{(1/4)\xi^2} \psi_1(\xi) d\xi \\ &\quad - \sqrt{\pi} \int_0^\eta e^{(1/4)\xi^2} \operatorname{erf}\left(\frac{1}{2}\xi\right) \psi_1(\xi) d\xi. \end{aligned} \tag{22}$$

In a similar way, we obtain the solution of the  $\phi_1$ -equation in (13) with the boundary conditions (16) in closed form as follows:

$$\phi_1(\eta) = I_2(\eta) - I_2(\infty) \operatorname{erf}\left(\sqrt{\frac{Le}{4}}\eta\right), \tag{23}$$

where  $I_2(\eta)$  is given by

$$I_2(\eta) = \int_0^\eta e^{-(1/4)Le\sigma^2} d\sigma \int_0^\sigma e^{(1/4)Le\xi^2} \psi_2(\xi) d\xi, \quad (24)$$

where

$$\psi_2(\xi) = - \left[ \frac{1}{2} Le f_1(\xi) \phi_0'(\xi) + \frac{N_t}{N_b} \theta_0''(\xi) \right]. \quad (25)$$

Following the above analysis of  $I_1(\eta)$  in (22),  $I_2(\eta)$  can be given as

$$I_2(\eta) = \sqrt{\frac{\pi}{Le}} \operatorname{erf} \left( \sqrt{\frac{Le}{4}} \eta \right) \int_0^\eta e^{(1/4)Le\xi^2} \psi_2(\xi) d\xi - \sqrt{\frac{\pi}{Le}} \int_0^\eta e^{(1/4)Le\xi^2} \operatorname{erf} \left( \sqrt{\frac{Le}{4}} \xi \right) \psi_2(\xi) d\xi. \quad (26)$$

Therefore, at  $p = 1$ , the approximate solutions for the temperature distribution  $\theta(\eta)$  and the nanoparticle concentration  $\phi(\eta)$  up to the first order are given by

$$\theta(\eta) \approx 1 - \operatorname{erf} \left( \frac{1}{2} \eta \right) + I_1(\eta) - I_1(\infty) \operatorname{erf} \left( \frac{1}{2} \eta \right),$$

$$\phi(\eta) \approx 1 - \operatorname{erf} \left( \sqrt{\frac{Le}{4}} \eta \right) + I_2(\eta) - I_2(\infty) \operatorname{erf} \left( \sqrt{\frac{Le}{4}} \eta \right). \quad (27)$$

The current approximate solution obtained in this section is checked via comparing with those obtained in the literature.

**3.3. Special Case: Horizontal Plate.** At  $\alpha = \pi/2$ , we have the following simple expressions for the temperature distribution  $\theta(\eta)$  and the nanoparticle concentration distribution  $\phi(\eta)$ :

$$\theta(\eta) = 1 - \operatorname{erf} \left( \frac{1}{2} \eta \right) + [N_b I_3(\infty) + N_t] \operatorname{erf} \left( \frac{1}{2} \eta \right) - N_b I_3(\eta) - N_t \left[ \operatorname{erf} \left( \frac{1}{2} \eta \right) \right]^2,$$

$$\phi(\eta) = 1 - \operatorname{erf} \left( \frac{\sqrt{Le}}{2} \eta \right) + \frac{2N_t}{N_b(Le-1)} \times \left[ \operatorname{erf} \left( \frac{\sqrt{Le}}{2} \eta \right) - \operatorname{erf} \left( \frac{1}{2} \eta \right) \right], \quad (28)$$

where

$$I_3(\eta) = \frac{2}{\sqrt{\pi}} \int_0^\eta e^{-\sigma^2/4} \operatorname{erf} \left( \frac{\sqrt{Le}}{2} \sigma \right) d\sigma. \quad (29)$$

#### 4. The ChPDM Technique

Chebyshev pseudospectral differentiation matrix (ChPDM) technique is briefly introduced; see Guedda et al. [21], Aly and Ebaid [22], and Van Gorder et al. [23]. On supposing

that the domain of the problem is  $[0, \eta_\infty]$ , then the following algebraic mapping  $z = 2\eta/\eta_\infty - 1$  transfers the domain to the Chebyshev one, that is  $[-1, 1]$ . It is known that the Chebyshev polynomials are usually taken with their associated collocation points in the interval  $[-1, 1]$  given by

$$z_j = \cos \left( \frac{\pi}{N} j \right), \quad j = 0, 1, \dots, N. \quad (30)$$

Therefore, the  $k$ th derivative of any function, say  $\mathbf{F}(z)$ , at these collocation points can be approximated by the equation:

$$\mathbf{F}^{(k)} = D^{(k)} \mathbf{F}, \quad (31)$$

where  $D^{(k)} \mathbf{F}$  is the Chebyshev pseudospectral approximation of  $\mathbf{F}^{(k)}$ , where  $\mathbf{F} = [F(z_0), F(z_1), \dots, F(z_N)]^T$  and  $\mathbf{F}^{(k)} = [F^{(k)}(z_0), F^{(k)}(z_1), \dots, F^{(k)}(z_N)]^T$ . The entries of the matrix  $D^{(k)}$  are given by

$$d_{i,j}^{(k)} = \frac{2\varphi_j}{N} \sum_{r=k}^N \sum_{\substack{n=0 \\ (n+r-k)\text{even}}}^{r-k} \phi_r b_{n,r}^k (-1)^{[(rj+ni)/N]} \times z_{rj-N[rj/N]} z_{ni-N[ni/N]}, \quad (32)$$

where  $\varphi_j = 1$ , except for  $\varphi_0 = \varphi_N = 1/2$ , and

$$b_{n,r}^k = \frac{2^k r}{(k-1)! c_n} \frac{(v-n+k-1)! (v+k-1)!}{(v)! (v-n)!}, \quad (33)$$

where  $2v = r + n - k$  and  $c_0 = 2, c_j = 1, j \geq 1$ . The elements  $d_{0,1}^{(k)}$  are the major elements concerning its values. Accordingly, they bear the major error responsibility when compared to the other elements. It is shown that the error in  $d_{0,1}^{(1)}$  is of order  $O(N^2 \varepsilon_r)$ , where  $\varepsilon_r$  is the machine precision [26].

On the view of [21–23], derivatives of the function  $f(\eta)$ ,  $\theta(\eta)$ , and  $\phi(\eta)$  at the points  $z_i$  are given by

$$\chi^{(k)}(z_i) = \sum_{j=0}^N d_{i,j}^{(k)} \chi(z_j), \quad \chi \equiv f, \theta, \phi, \quad k = 1, 2, 3, \quad (34)$$

$$i = 1, 2, \dots, N.$$

Therefore, (1)–(5) become, respectively,

$$\begin{aligned} \sum_{j=0}^N d_{i,j}^{(2)} f(z_j) &= \frac{Ra_x}{Pe_x} \left[ \sum_{j=0}^N d_{i,j}^{(1)} \theta(z_j) - N_r \sum_{j=0}^N d_{i,j}^{(1)} \phi(z_j) \right] \cos \alpha, \\ \sum_{j=0}^N d_{i,j}^{(2)} \theta(z_j) + \frac{1}{2} f(z_i) \left( \frac{\eta_\infty}{2} \right) \sum_{j=0}^N d_{i,j}^{(1)} \theta(z_j) + N_b \sum_{j=0}^N d_{i,j}^{(1)} \theta(z_j) \\ &\times \sum_{j=0}^N d_{i,j}^{(1)} \phi(z_j) + N_t \left( \sum_{j=0}^N d_{i,j}^{(1)} \theta(z_j) \right)^2 = 0, \\ \sum_{j=0}^N d_{i,j}^{(2)} \phi(z_j) + \frac{1}{2} Le f(z_i) \left( \frac{\eta_\infty}{2} \right) \sum_{j=0}^N d_{i,j}^{(1)} \phi(z_j) \\ &+ \frac{N_t}{N_b} \sum_{j=0}^N d_{i,j}^{(2)} \theta(z_j) = 0, \\ f(z_N) &= 0, \quad \sum_{j=0}^N d_{0,j}^{(1)} f(z_j) = 0, \\ \theta(z_N) &= 1, \quad \theta(z_0) = 0, \\ \phi(z_N) &= 1, \quad \phi(z_0) = 0. \end{aligned} \tag{35}$$

### 5. Results and Discussion

In Sections 3 and 4, mixed convection boundary-layer nanofluid flow along an inclined plate embedded in a porous medium has been solved analytically using two terms of the HPM and numerically by the ChPDM technique, respectively. The solutions were obtained for the temperature distribution  $\theta$  and nano-particle concentration distribution  $\phi$ . In the current section, we aim to compare the results derived from HPM by those obtained by the ChPDM, which may be considered as a reference approach because it was successfully compared before with homotopy analysis method in [22]. In each forthcoming figure, it should be noted that solid and dotted curves refer to the results obtained by ChPDM and HPA, respectively.

Figure 1 shows the comparison between the HPM and ChPDM solutions for the nanoparticle concentration distribution  $\phi(\eta)$  at different values of Brownian motion parameter  $N_b$ , where  $N_t = 0.5$ ,  $N_r = 0.5$ ,  $Le = 10$ ,  $Ra_x/Pe_x = 0.5$ , and  $\alpha = \pi/6$ . From this figure, it is clear that the profiles of  $\phi(\eta)$  are very close to each other and to those obtained in Figure 3 by Rana et al. [24].

The temperature distribution  $\theta$  is depicted against  $\eta$  at different values of thermophoresis parameter  $N_t$  for  $N_b = 0.5$ ,  $N_r = 0.5$ ,  $Le = 10$ ,  $Ra_x/Pe_x = 0.5$ , and  $\alpha = \pi/6$  in Figure 2. It is also observed from it that excellent agreement is achieved on comparing with Figure 4 in [24]. These results may refer to that two terms approximate solutions of the HPM are sufficient to give accurate numerical results.

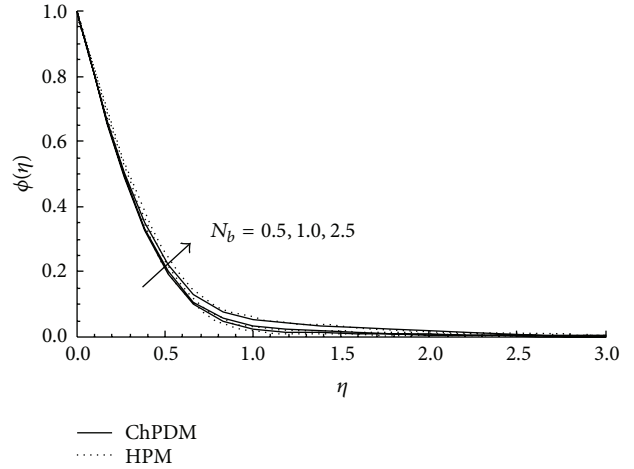


FIGURE 1: Comparison of ChPDM (solid) and HPM (dotted) for the effect of the Brownian motion parameter ( $N_b$ ) on the nanoparticle concentration distribution  $\phi(\eta)$  at  $N_t = 0.5$ ,  $N_r = 0.5$ ,  $Le = 10$ ,  $Ra_x/Pe_x = 0.5$ , and  $\alpha = \pi/6$ .

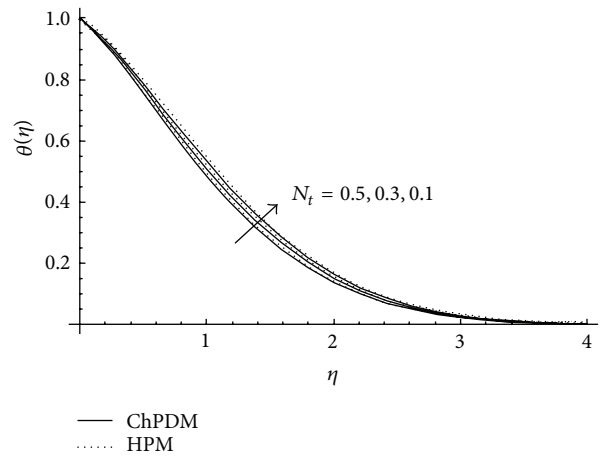


FIGURE 2: Comparison of ChPDM (solid) and HPM (dotted) for the effect of the thermophoretic parameter ( $N_t$ ) on the temperature distribution  $\theta(\eta)$  at  $N_b = 0.5$ ,  $N_r = 0.5$ ,  $Le = 10$ ,  $Ra_x/Pe_x = 0.5$ , and  $\alpha = \pi/6$ .

The last conclusion is also detected in Figure 3 for the effect of the buoyancy ratio parameter  $N_r$  and the mixed convection parameter  $Ra_x/Pe_x$  on the temperature distribution  $\theta(\eta)$  at  $N_b = 0.5$ ,  $N_t = 0.5$ ,  $Le = 10$ , and  $\alpha = \pi/6$ . From this figure, we can notice excellent agreements between the two approaches and further of those plotted in Figure 6 by Rana et al. [24].

Figure 4 indicates the effect of the inclination angle  $\alpha$  on the nanoparticle concentration distribution  $\phi$  at  $N_b = 0.5$ ,  $N_t = 0.5$ ,  $N_r = 0.5$ ,  $Le = 10$ , and  $Ra_x/Pe_x = 0.5$ . It can be easily observed from this figure that the slight difference between the curves obtained via the two approaches increases with increasing  $\alpha$ , especially at  $\alpha = \pi/2$ . A similar observation is detected from Figure 5 for the effect of Lewis number ( $Le$ ) on  $\phi$  at  $N_b = 0.5$ ,  $N_t = 0.5$ ,  $N_r = 0.5$ ,  $Ra_x/Pe_x = 0.5$ , and

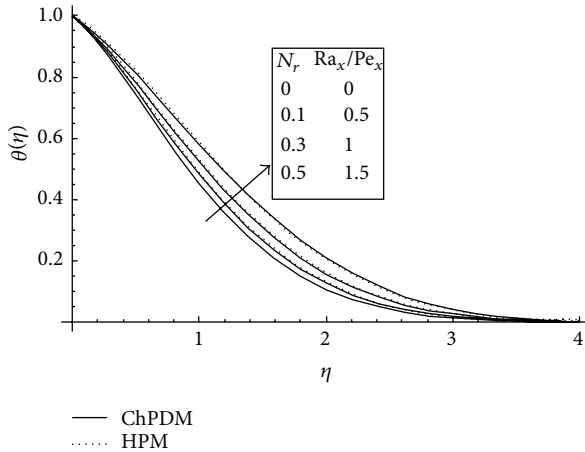


FIGURE 3: Comparison of ChPDM (solid) and HPM (dotted) for the effect of the buoyancy ratio parameter ( $N_r$ ) and the mixed convection parameter ( $Ra_x/Pe_x$ ) on the temperature distribution  $\theta(\eta)$  at  $N_b = 0.5$ ,  $N_t = 0.5$ ,  $Le = 10$ , and  $\alpha = \pi/6$ .

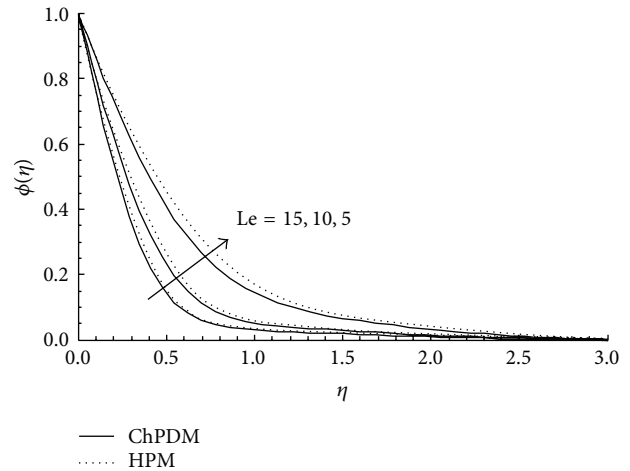


FIGURE 5: Comparison of ChPDM (solid) and HPM (dotted) for the effect of the Lewis number ( $Le$ ) on the nanoparticle concentration distribution  $\phi(\eta)$  at  $N_b = 0.5$ ,  $N_t = 0.5$ ,  $N_r = 0.5$ ,  $Ra_x/Pe_x = 0.5$ , and  $\alpha = \pi/6$ .

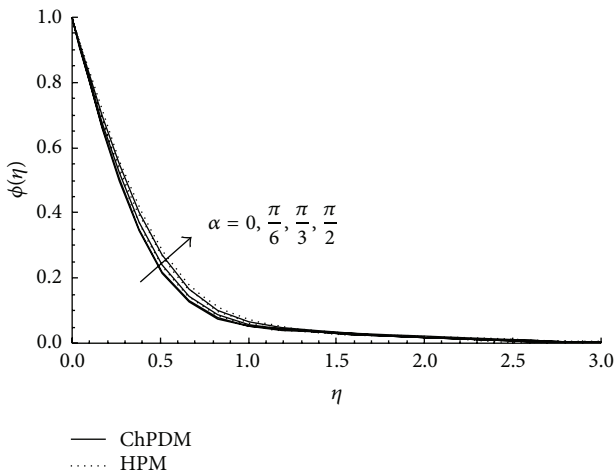


FIGURE 4: Comparison of ChPDM (solid) and HPM (dotted) for the effect of the angle of inclination ( $\alpha$ ) on the nanoparticle concentration distribution  $\phi(\eta)$  at  $N_b = 0.5$ ,  $N_t = 0.5$ ,  $N_r = 0.5$ ,  $Le = 10$ , and  $Ra_x/Pe_x = 0.5$ .

$\alpha = \pi/6$ , where the slight difference between the curves increases as Lewis number  $Le$  decreases.

From the above comparisons, one can conclude that although slight differences are observed between the two approaches in some cases, two terms approximate solutions for  $\theta(\eta)$  and  $\phi(\eta)$  are still effective and of course can be enhanced via adding more terms for the homotopy series solutions. Accordingly, the HPM can be used as a method of solution with highly trust for investigating several similar models by following the proposed analysis of the current paper.

### 6. Conclusion

In the present paper, the system of differential equations, describing the mixed convection boundary-layer nanofluids flow along an inclined plate embedded in a porous medium, has been successfully solved by applying two methods, analytically by the homotopy perturbation and numerically by Chebyshev pseudospectral differentiation matrix, which was used as a control technique. In order to obtain meaningful physical solution, a new way was deduced to formulate the deformed system of differential equations. Accordingly, the approximate solution was expressed in terms of an entire error function. This proposed way of applying HPM may be of interest for investigating similar models in the future. On applying HPM, it was found that two terms of the homotopy series are enough to achieve very good solutions when compared with the accurate results obtained numerically via ChPDM. This was investigated for various values of the appropriated physical parameters: temperature distribution  $\theta(\eta)$  and nanoparticle concentration distribution  $\phi(\eta)$  at variation of the thermophoretic parameter ( $N_t$ ), Brownian motion parameter ( $N_b$ ), buoyancy ratio parameter ( $N_r$ ), angle of inclination ( $\alpha$ ), Lewis number ( $Le$ ), and mixed convection parameter ( $Ra_x/Pe_x$ ).

### Acknowledgment

This project was funded by the Deanship of Scientific Research (DSR), King Abdulaziz University, Jeddah, under grant no. (233/965/1433). The authors, therefore, acknowledge with thanks DSR technical and financial support.

### References

[1] S. U. S. Choi, "Enhancing thermal conductivity of fluids with nanoparticles," in *Proceedings of the ASME International*

- Mechanical Engineering Congress and Exposition*, pp. 99–105, ASME, San Francisco, Calif, USA, 1995.
- [2] S. U. S. Choi, Z. G. Zhang, W. Yu, F. E. Lockwood, and E. A. Grulke, “Anomalous thermal conductivity enhancement in nanotube suspensions,” *Applied Physics Letters*, vol. 79, no. 14, pp. 2252–2254, 2001.
- [3] H. Masuda, A. Ebata, K. Teramae, and N. Hishinuma, “Alteration of thermal conductivity and viscosity of liquid by dispersing ultra-fine particles (Dispersion of g-Al<sub>2</sub>O<sub>3</sub>SiO<sub>2</sub>, and TiO<sub>2</sub> ultra-fine particles),” *Netsu Bussei*, vol. 7, pp. 227–233, 1993.
- [4] S. Lee, S. U.-S. Choi, S. Li, and J. A. Eastman, “Measuring thermal conductivity of fluids containing oxide nanoparticles,” *Journal of Heat Transfer*, vol. 121, no. 2, pp. 280–288, 1999.
- [5] A. V. Kuznetsov and D. A. Nield, “Natural convective boundary-layer flow of a nanofluid past a vertical plate,” *International Journal of Thermal Sciences*, vol. 49, no. 2, pp. 243–247, 2010.
- [6] W. A. Khan and I. Pop, “Boundary-layer flow of a nanofluid past a stretching sheet,” *International Journal of Heat and Mass Transfer*, vol. 53, no. 11-12, pp. 2477–2483, 2010.
- [7] N. Bachok, A. Ishak, and I. Pop, “Boundary-layer flow of nanofluids over a moving surface in a flowing fluid,” *International Journal of Thermal Sciences*, vol. 49, no. 9, pp. 1663–1668, 2010.
- [8] E. H. Aly and A. Ebaid, “New exact solutions for boundary-layer flow of a nanofluid past a stretching sheet,” *Journal of Computational and Theoretical Nanoscience*, vol. 10, no. 4, pp. 2591–2594, 2013.
- [9] J.-H. He, “Homotopy perturbation technique,” *Computer Methods in Applied Mechanics and Engineering*, vol. 178, no. 3-4, pp. 257–262, 1999.
- [10] J.-H. He, “A coupling method of a homotopy technique and a perturbation technique for non-linear problems,” *International Journal of Non-Linear Mechanics*, vol. 35, no. 1, pp. 37–43, 2000.
- [11] J.-H. He, “Homotopy perturbation method: a new nonlinear analytical technique,” *Applied Mathematics and Computation*, vol. 135, no. 1, pp. 73–79, 2003.
- [12] J.-H. He, “Comparison of homotopy perturbation method and homotopy analysis method,” *Applied Mathematics and Computation*, vol. 156, no. 2, pp. 527–539, 2004.
- [13] J.-H. He, “Asymptotology by homotopy perturbation method,” *Applied Mathematics and Computation*, vol. 156, no. 3, pp. 591–596, 2004.
- [14] J.-H. He, “Homotopy perturbation method for solving boundary value problems,” *Physics Letters A*, vol. 350, no. 1-2, pp. 87–88, 2006.
- [15] J.-H. He, “Application of homotopy perturbation method to nonlinear wave equations,” *Chaos, Solitons and Fractals*, vol. 26, no. 3, pp. 695–700, 2005.
- [16] P. D. Ariel, “The three-dimensional flow past a stretching sheet and the homotopy perturbation method,” *Computers & Mathematics with Applications*, vol. 54, no. 7-8, pp. 920–925, 2007.
- [17] S. Pamuk and N. Pamuk, “He’s homotopy perturbation method for continuous population models for single and interacting species,” *Computers & Mathematics with Applications*, vol. 59, no. 2, pp. 612–621, 2010.
- [18] H. Aminikhah, “The combined Laplace transform and new homotopy perturbation methods for stiff systems of ODEs,” *Applied Mathematical Modelling*, vol. 36, no. 8, pp. 3638–3644, 2012.
- [19] A. H. Nayfeh, *Perturbation Methods*, John Wiley & Sons, New York, NY, USA, 1973.
- [20] E. H. Aly, M. Benlahsen, and M. Guedda, “Similarity solutions of a MHD boundary-layer flow past a continuous moving surface,” *International Journal of Engineering Science*, vol. 45, no. 2-8, pp. 486–503, 2007.
- [21] M. Guedda, E. H. Aly, and A. Ouahsine, “Analytical and ChPDM analysis of MHD mixed convection over a vertical flat plate embedded in a porous medium filled with water at 4°C,” *Applied Mathematical Modelling*, vol. 35, no. 10, pp. 5182–5197, 2011.
- [22] E. H. Aly and A. Ebaid, “On the exact analytical and numerical solutions of nano boundary-layer fluid flows,” *Abstract and Applied Analysis*, vol. 2012, Article ID 415431, 22 pages, 2012.
- [23] R. A. van Gorder, E. Sweet, and K. Vajravelu, “Nano boundary layers over stretching surfaces,” *Communications in Nonlinear Science and Numerical Simulation*, vol. 15, no. 6, pp. 1494–1500, 2010.
- [24] P. Rana, R. Bhargava, and O. A. Bég, “Numerical solution for mixed convection boundary layer flow of a nanofluid along an inclined plate embedded in a porous medium,” *Computers & Mathematics with Applications*, vol. 64, no. 9, pp. 2816–2832, 2012.
- [25] M. Abramowitz and I. A. Stegun, *Handbook of Mathematical Functions*, Dover, New York, NY, USA, 4th edition, 1972.
- [26] E. M. E. Elbarbary and S. M. El-Sayed, “Higher order pseudospectral differentiation matrices,” *Applied Numerical Mathematics*, vol. 55, no. 4, pp. 425–438, 2005.

## Research Article

# Pressure Transient Analysis of Dual Fractal Reservoir

Xiao-Hua Tan,<sup>1</sup> Xiao-Ping Li,<sup>1</sup> Jian-Yi Liu,<sup>1</sup> Chuan Tang,<sup>1</sup> and Jin-man Li<sup>2</sup>

<sup>1</sup> State Key Laboratory of Oil and Gas Reservoir Geology and Exploitation, Southwest Petroleum University, Chengdu 610500, China

<sup>2</sup> Tianjin Exploration and Development Research Institute, CNOOC, Tanggu, Tianjin 300452, China

Correspondence should be addressed to Xiao-Hua Tan; xiaohua-tan@163.com

Received 21 May 2013; Revised 15 August 2013; Accepted 15 August 2013

Academic Editor: Bo Yu

Copyright © 2013 Xiao-Hua Tan et al. This is an open access article distributed under the Creative Commons Attribution License, which permits unrestricted use, distribution, and reproduction in any medium, provided the original work is properly cited.

A dual fractal reservoir transient flow model was created by embedding a fracture system simulated by a tree-shaped fractal network into a matrix system simulated by fractal porous media. The dimensionless bottom hole pressure model was created using the Laplace transform and Stehfest numerical inversion methods. According to the model's solution, the bilogarithmic type curves of the dual fractal reservoirs are illustrated, and the influence of different fractal factors on pressure transient responses is discussed. This semianalytical model provides a practical and reliable method for empirical applications.

## 1. Introduction

Numerous researchers have simulated the nonuniform distribution of fractures using fractal networks and have studied fluid flow behavior in fractured reservoirs. By assuming that the fracture network is fractal, Camacho-Velázquez et al. [1] studied the production decline behavior in a naturally fractured reservoir. Zhang and Tong [2] introduced a stress-sensitive coefficient and built a transient pressure analysis model for fractal reservoirs which considers stress-sensitive effects.

Jafari and Babadagli [3] illustrated the 3D permeability distribution of a reservoir using outcrop, well log, and well test data which served as the basis for applying fractal networks to a reservoir. Zhang et al. [4] solved a nonlinear flow model for a stress-sensitive dual media fractal reservoir using a finite element method.

Previous scholars often embedded fractal structures into matrix networks by using straight or intersecting lines, but this did not correctly simulate well bottom radial flow. This type of radial flow has not been sufficiently studied in the underground seepage and oil development fields.

By referring to a plant lamina's bifurcation structure, Wechsato et al. [5] used a tree-shaped fractal structure that

connected center points to different circles. The fractal network could simulate the radial flow tending toward the well bottom. Based on their research, the construction method and optimization rules for tree-shaped fractal structures [6] were formulated.

Xu and Yu [7] presented a tree-shaped fractal flow model that considered the dynamic behavior of branching tubes in a tree-shaped fractal network. Based on this model, our model's transport properties and mass transfer capabilities [8, 9] were analyzed.

Given the capillary pressure effect, the starting pressure gradient influence, and pore fractal characteristics, Yun et al. [10] developed a fractal model that describes Bingham fluid flow in porous media. Based on Yun et al. [10], Wang et al. [11] proposed a tree-shaped fractal model that considered the influence of the starting pressure gradient on Bingham fluid seepage in a porous medium.

In this paper, fractures are simulated using a tree-shaped fractal network, as it accurately simulates radial flow tending to the well bottom, and the matrix system is simulated using fractal porous media. A transient flow model of dual fractal reservoirs is then presented by embedding the fracture network into a matrix system. Factors influencing the dynamic characteristics of transient pressure responses in dual fractal

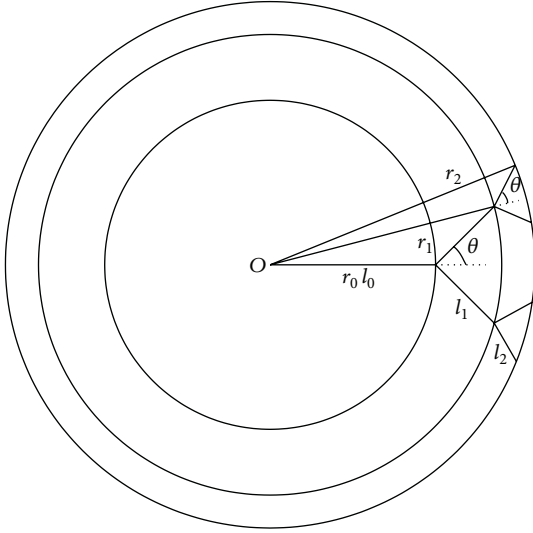


FIGURE 1: Dual fractal reservoir.

reservoirs are analyzed. This semianalytical model provides a practical and reliable method for empirical applications.

## 2. Physical Model

Figure 1 shows a well located in the reservoir center,  $O$ , with a thickness,  $h$ , and a well radius,  $r_w$ . The physical model assumptions are as follows.

- (1) The fractal porous media is divided into  $M$  annular sections in a tree-shaped fractal network.
- (2) Each fracture section's properties are different, but the fluid properties are identical. Matrix permeability is much lower than that of the fracture.
- (3) Rock and single-phase fluid are slightly compressible causing isothermal flow to be considered. Capillary pressure and gravity effects are neglected.
- (4) Fluid flows to the wellbore only through the fracture system. Fluid flow in the matrix and the fracture system of each section satisfies the linear flow rule.

## 3. Mathematical Model

**3.1. Matrix System.** According to fractal geometry theory, the fractal scaling law can be used to describe the cumulative size distribution of pores in matrix system [12]:

$$N_m(L \geq \lambda) = \left( \frac{\delta_{\max}}{\delta} \right)^{D_f}, \quad (1)$$

where  $\delta$  is pore diameter,  $\delta_{\max}$  is maximum pore diameter, and  $D_f$  is the fractal dimension of the pore space.

Tortuosity is often used to describe flow path tortuosity, as flow in porous media is tortuous. The matrix flow path tortuosity is defined as [13]:

$$T_m = \frac{L_t}{L_0}, \quad (2)$$

where  $L_t$  is the actual length of the tortuous flow path and  $L_0$  is the straight length along the macroscopic pressure gradient.

The matrix system porosity and permeability are defined as [14]:

$$\phi_m = \frac{\pi T_m D_f}{4(2 - D_f)} \frac{\delta_{\max}^2}{A_0} \left[ 1 - \left( \frac{\delta_{\min}}{\delta_{\max}} \right)^{2 - D_f} \right], \quad (3)$$

$$K_m = \frac{\pi D_f}{128 T_m (4 - D_f)} \frac{\delta_{\max}^4}{A_0}, \quad (4)$$

where  $A_0$  is the unit cell area.

**3.2. Fracture System.** Fracture system parameters are directly generated from a tree-shaped fractal network. Sets of branch structures form the tree-shaped fractal network. During network generation, the branches on each level must end up on the same circle with all circles having the same center of origin,  $O$ .  $N$  tubes which start at  $O$  make up the tree-shaped fractal network. The tube's initial length and diameter are  $l_0$  and  $d_0$ , respectively. The double branches ( $n = 2$ ), whose angles are  $\theta$  ( $\theta < \pi/2$ ) and total network branch levels are  $M$ , are applied in this network. Furthermore, two scale factors are used in this fractal network, length ratio,  $\alpha$ , and diameter ratio,  $\beta$ . The branch tube is assumed to be smooth, and tube wall thickness is ignored.

For the  $k$ th level fracture, length is given by

$$l_k = \alpha^k l_0. \quad (5)$$

For the  $k$ th level fracture, diameter is

$$d_k = \beta^k d_0. \quad (6)$$

Distance from the well to each section's boundary is defined as the radial distance, which is expressed by [8]:

$$r_k = \sum_{i=0}^k l_i \cos \theta = l_0 \left[ 1 + \frac{\alpha(1 - \alpha^k) \cos \theta}{1 - \alpha} \right]. \quad (7)$$

Xu et al. [8] proposed the  $k$ th level permeability expression of fracture system, which is expressed by

$$K_k = \frac{d_k^2}{32} \frac{1}{T_k}. \quad (8)$$

The  $k$ th section tortuosity of fracture systems can be obtained by the following expression:

$$T_k = \frac{l_k}{r_k - r_{k-1}} = \begin{cases} 1, & k = 0, \\ \frac{1}{\cos \theta}, & k > 0. \end{cases} \quad (9)$$

Substituting (6) and (9) into (8), the  $k$ th section permeability in the fracture system is

$$K_{fk} = N n^k \frac{d_k^2}{32} \frac{1}{T_k} = \begin{cases} \frac{N d_0^2}{32}, & k = 0, \\ \frac{N n^k \beta^{2k} d_0^2 \cos \theta}{32}, & k > 0. \end{cases} \quad (10)$$

For the  $k$ th section, total system volume can be calculated by

$$V_{tk} = \begin{cases} \pi h r_0^2, & k = 0, \\ \pi h (r_k^2 - r_{k-1}^2), & k > 0, \end{cases} \quad (11)$$

where  $h$  is the reservoir thickness.

For the  $k$ th section, pore volume of fracture systems can be calculated by

$$V_{ftk} = N n^k \frac{\pi l_k d_k^2}{4} = \frac{N \pi n^k \alpha^k \beta^{2k} l_0 d_0^2}{4}. \quad (12)$$

For the  $k$ th section, total system volume,  $V_{tk}$ , is expressed as  $V_{tk} = V_{mtk} + V_{ftk}$ , where  $V_{mtk}$  is total volume of the matrix system.  $V_{mtk}$  is related to the pore volume of matrix system,  $V_{mk}$ , and expressed as  $V_{mtk} = \phi_m V_{mk}$ , where  $\phi_m$  is the matrix system porosity. Thus,  $V_{mk}$  can be calculated as

$$V_{mk} = \phi_m (V_{tk} - V_{ftk}). \quad (13)$$

For the  $k$ th section, porosity of a fracture system can be obtained by dividing (12) by (11):

$$\phi_{fk} = \frac{V_{ftk}}{V_{tk}} = \begin{cases} \frac{N d_0^2}{4 h l_0}, & k = 0, \\ \frac{N n^k \alpha^k \beta^{2k} l_0 d_0^2}{4 h (r_k^2 - r_{k-1}^2)}, & k > 0. \end{cases} \quad (14)$$

For the  $k$ th section, porosity of a matrix system can be obtained by the following expression:

$$\phi_{mk} = \frac{V_{mk}}{V_{tk}} = \phi_m (1 - \phi_{fk}). \quad (15)$$

The permeability of a fracture system,  $K_f$ , and the porosity of a fracture system,  $\phi_f$ , do not change with the radial distance,  $r$ , in traditional double porosity (fracture and matrix system) reservoir transient flow models [15]. In order to compare dual fractal reservoir transient flow models with double porosity reservoir transient flow models, we have to clarify how to keep  $K_f$  and  $\phi_f$  independent of  $r$  in dual fractal reservoir transient flow models.

Under the condition of double branches ( $n = 2$ ), the permeability,  $K_{fk}$ , and porosity,  $\phi_{fk}$ , of every section in a fracture system are equal; that is,

$$\begin{aligned} K_{fk} &= K_{f(k+1)}, \\ \phi_{fk} &= \phi_{f(k+1)}. \end{aligned} \quad (16)$$

Substituting (10) and (14) into (16), we can obtain:  $n = 2$ ,  $\alpha = 1$ , and  $\beta = 0.707$ .

When  $\beta$  is smaller than 0.707, permeability of a fracture system increases with the radius of a dual fractal reservoir. When  $\beta$  is larger than 0.707, permeability of a fracture system decreases with the radius of a dual fractal reservoir.

**3.3. Dual Fractal Reservoir.** According to the physical model, the flow mathematical model of a dual fractal reservoir can be described as follows.

Governing differential equations in a dual fractal reservoir, we have the following.

For fracture system [15],

$$\frac{K_{fk}}{\mu} \left( \frac{\partial^2 p_{fk}}{\partial r^2} + \frac{1}{r} \frac{\partial p_{fk}}{\partial r} \right) + \frac{a K_m}{\mu} (p_{mk} - p_{fk}) = \frac{\varphi_{fk} C_{tf}}{3.6} \frac{\partial p_{fk}}{\partial t} \quad r_{k-1} \leq r \leq r_k. \quad (17)$$

For matrix system [15],

$$-\frac{a K_m}{\mu} (p_{mk} - p_{fk}) = \frac{\varphi_{mk} C_{tm}}{3.6} \frac{\partial p_{mk}}{\partial t} \quad r_{k-1} \leq r \leq r_k. \quad (18)$$

Initial condition:

$$p_{fk}(r, 0) = p_{mk}(r, 0) = p_i \quad (k = 0, 1, \dots, M). \quad (19)$$

Interface connecting conditions of each zone, pressure continuity [16]:

$$p_{fk} \Big|_{r=r_k} = p_{f(k+1)} \Big|_{r=r_k} \quad (k = 0, 1, \dots, M-1). \quad (20)$$

Interface connecting conditions of each zone, rate continuity [16]:

$$\frac{\partial p_{fk}}{\partial r} \Big|_{r=r_k} = \frac{k_{f(k+1)}}{k_{fk}} \frac{\partial p_{f(k+1)}}{\partial r} \Big|_{r=r_k} \quad (k = 0, 1, \dots, M-1). \quad (21)$$

Well production condition [17]:

$$q_{sf} = q + \frac{24C}{B} \frac{d p_{wf}}{dt} \quad p_{wf} = p_{f1} \Big|_{r=r_w e^{-s}}. \quad (22)$$

External boundary condition (infinite):

$$p_{fM}(r \rightarrow \infty, t) = p_i. \quad (23)$$

External boundary condition (constant pressure):

$$p_{fM}(r = r_M, t) = p_i. \quad (24)$$

External boundary condition (closed):

$$\frac{\partial p_{fM}}{\partial r} \Big|_{r=r_M} = 0. \quad (25)$$

## 4. Mathematical Model Solution

To simplify the mathematical model and its solution, dimensionless parameters are defined as follows [18, 19].

The dimensionless pressure of the fracture system of the  $k$ th section:

$$p_{Dfk} = \frac{K_{fk} h}{1.842 \times 10^{-3} q \mu B} (p_i - p_{fk}). \quad (26)$$

The dimensionless pressure of the matrix system of the  $k$ th section:

$$p_{Dmk} = \frac{K_{mk}h}{1.842 \times 10^{-3}q\mu B} (p_i - p_{mk}). \quad (27)$$

The dimensionless effective radius:

$$r_{De} = \frac{r}{r_w} e^S. \quad (28)$$

The dimensionless effective interface radius:

$$r_{Dek} = \frac{r_k}{r_w} e^S. \quad (29)$$

The dimensionless effective time:

$$t_{De} = \frac{3.6K_{f0}te^{2S}}{(\varphi C_t)_{(f+m)0}\mu r_w^2}. \quad (30)$$

The dimensionless effective wellbore storage coefficient:

$$C_{De} = \frac{Ce^{2S}}{2\pi h(\varphi C_t)_{(f+m)0}r_w^2}. \quad (31)$$

The fluid capacitance coefficient of the  $k$ th section:

$$\omega_k = \frac{\phi_{fk}C_{ft}}{\phi_{mk}C_{mt} + \phi_{fk}C_{ft}}. \quad (32)$$

The interporosity flow coefficient of the  $k$ th section:

$$\lambda_k = a \frac{K_m}{K_{fk}} r_w^2. \quad (33)$$

Substituting (26)–(33) into (17)–(25), dimensionless mathematical models are obtained [20].

For a fracture system, the governing differential equation in a dual fractal reservoir is

$$\frac{\partial^2 p_{Dfk}}{\partial r_{De}^2} + \frac{1}{r_{De}} \frac{\partial p_{Dfk}}{\partial r_{De}} + \lambda_k e^{-2S} \left( \frac{K_{fk}}{K_m} p_{Dmk} - p_{Dfk} \right) \quad (34)$$

$$= \frac{\omega_k}{C_{De}} \frac{K_{f0}}{K_{fk}} \frac{\partial p_{Dfk}}{\partial (t_{De}/C_{De})} \quad r_{De(k-1)} \leq r_{De} \leq r_{Dek};$$

For matrix system,

$$-\lambda_k e^{-2S} \left( p_{Dmk} - \frac{K_m}{K_{fk}} p_{Dfk} \right) = \frac{1 - \omega_k}{C_{De}} \frac{K_{f0}}{K_{fk}} \frac{\partial p_{Dmk}}{\partial (t_{De}/C_{De})} \quad r_{De(k-1)} \leq r_{De} \leq r_{Dek}. \quad (35)$$

Initial condition:

$$p_{Dfk}(r_{De}, 0) = p_{Dmk}(r_{De}, 0) = 0 \quad (k = 0, 1, \dots, M). \quad (36)$$

Interface connecting conditions of each zone, pressure continuity:

$$p_{Dfk}|_{r_{De}=r_{Dek}} = p_{Df(k+1)}|_{r_{De}=r_{Dek}} \quad (k = 0, 1, \dots, M-1). \quad (37)$$

Interface connecting conditions of each zone, rate continuity:

$$\frac{\partial p_{Dfk}}{\partial r_{De}} \Big|_{r_{De}=r_{Dek}} = \frac{K_{f(k+1)}}{K_{fk}} \frac{\partial p_{Df(k+1)}}{\partial r_{De}} \Big|_{r_{De}=r_{Dek}} \quad (k = 0, 1, \dots, M-1). \quad (38)$$

Well production condition:

$$\frac{dp_{wD}}{d(t_{De}/C_{De})} - \left( r_{De} \frac{\partial p_{Df0}}{\partial r_{De}} \right) \Big|_{r_{De}=1} = 1 \quad p_{wD} = p_{Df0} \Big|_{r_{De}=1}. \quad (39)$$

External boundary condition (infinite):

$$p_{DfM}(r_{De} \rightarrow \infty, t_{De}) = 0. \quad (40)$$

External boundary condition (constant pressure):

$$p_{DfM}(r_{De} = r_{DeM}, t_{De}) = 0. \quad (41)$$

External boundary condition (closed):

$$\frac{\partial p_{DfM}}{\partial r_{De}} \Big|_{r_{De}=r_{DeM}} = 0. \quad (42)$$

The flow mathematical model in Laplace space is obtained by taking the Laplace transformation of (34)–(42) based on  $t_{De}/C_{De}$ . The flow mathematical model is as follows [20].

For fracture system,

$$\frac{d^2 \bar{p}_{Dfk}}{dr_{De}^2} + \frac{1}{r_{De}} \frac{d \bar{p}_{Dfk}}{dr_{De}} + \lambda_k e^{-2S} \left( \frac{K_{fk}}{K_m} \bar{p}_{Dmk} - \bar{p}_{Dfk} \right) = \frac{\omega_k}{C_{De}} \frac{K_{f0}}{K_{fk}} z \bar{p}_{Dfk} \quad r_{De(k-1)} \leq r_{De} \leq r_{Dek}. \quad (43)$$

For matrix system,

$$-\lambda_k e^{-2S} \left( \bar{p}_{Dmk} - \frac{K_m}{K_{fk}} \bar{p}_{Dfk} \right) = \frac{1 - \omega_k}{C_{De}} \frac{K_{f0}}{K_{fk}} z \bar{p}_{Dmk} \quad r_{De(k-1)} \leq r_{De} \leq r_{Dek}. \quad (44)$$

Initial condition:

$$\bar{p}_{Dfk}(r_{De}, 0) = \bar{p}_{Dmk}(r_{De}, 0) = 0 \quad (k = 0, 1, \dots, M). \quad (45)$$

Interface connecting conditions of each zone, pressure continuity:

$$\bar{p}_{Dfk}|_{r_{De}=r_{Dek}} = \bar{p}_{Df(k+1)}|_{r_{De}=r_{Dek}} \quad (k = 0, 1, \dots, M-1). \quad (46)$$

Interface connecting conditions of each zone, rate continuity:

$$\frac{d \bar{p}_{Dfk}}{dr_{De}} \Big|_{r_{De}=r_{Dek}} = \frac{K_{f(k+1)}}{K_{fk}} \frac{d \bar{p}_{Df(k+1)}}{dr_{De}} \Big|_{r_{De}=r_{Dek}} \quad (k = 0, 1, \dots, M-1). \quad (47)$$

Well production condition:

$$z\bar{p}_{wD} - \left( r_{De} \frac{d\bar{p}_{Df0}}{dr_{De}} \right) \Big|_{r_{De}=1} = \frac{1}{z} \quad \bar{p}_{wD} = \bar{p}_{Df0} \Big|_{r_{De}=1}. \quad (48)$$

External boundary condition (infinite):

$$\bar{p}_{DfM}(r_{De} \rightarrow \infty, z) = 0. \quad (49)$$

External boundary condition (constant pressure),

$$\bar{p}_{DfM}(r_{De} = r_{DeM}, z) = 0. \quad (50)$$

External boundary condition (closed).

$$\frac{\partial \bar{p}_{DfM}}{\partial r_{De}} \Big|_{r_{De}=r_{DeM}} = 0. \quad (51)$$

In (43) and (44), the general solution of  $\bar{p}_{Dfk}$  is calculated by

$$\bar{p}_{Dfk} = A_k I_0 \left( r_{DeM} \sqrt{S_k(z)} \right) + B_k K_0 \left( r_{DeM} \sqrt{S_k(z)} \right) \quad (k = 0, 1, \dots, M). \quad (52)$$

The derivative of  $\bar{p}_{Dfk}$  in (52) is calculated by

$$\frac{d\bar{p}_{Dfk}}{dr_{De}} = \sqrt{S_k(z)} A_k I_1 \left( r_{DeM} \sqrt{S_k(z)} \right) - \sqrt{S_k(z)} B_k K_1 \left( r_{DeM} \sqrt{S_k(z)} \right) \quad (k=0, 1, \dots, M). \quad (53)$$

Substitute (52) and (53) into well production condition equation (48);

$$z\bar{p}_{wD} - \sqrt{S_0(z)} A_0 I_1 \left( \sqrt{S_0(z)} \right) + \sqrt{S_0(z)} B_0 K_1 \left( \sqrt{S_0(z)} \right) = \frac{1}{z}, \quad (54)$$

$$\bar{p}_{wD} = A_0 I_0 \left( \sqrt{S_0(z)} \right) + B_0 K_0 \left( \sqrt{S_0(z)} \right).$$

Substitute (52) and (53) into interface connecting condition equation (46);

$$\begin{aligned} & A_k I_0 \left( r_{DeM} \sqrt{S_k(z)} \right) + B_k K_0 \left( r_{DeM} \sqrt{S_k(z)} \right) \\ &= A_{k+1} I_0 \left( r_{DeM} \sqrt{S_{k+1}(z)} \right) \\ &+ B_{k+1} K_0 \left( r_{DeM} \sqrt{S_{k+1}(z)} \right) \quad (k = 0, 1, \dots, M - 1). \end{aligned} \quad (55)$$

Substitute (52) and (53) into interface connecting condition equation (47);

$$\begin{aligned} & A_k \sqrt{S_k(z)} I_1 \left( r_{DeM} \sqrt{S_k(z)} \right) - B_k \sqrt{S_k(z)} K_1 \left( r_{DeM} \sqrt{S_k(z)} \right) \\ &= \frac{K_{f(k+1)}}{K_{fk}} A_{k+1} \sqrt{S_k(z)} I_1 \left( r_{DeM} \sqrt{S_k(z)} \right) \\ &- \frac{K_{f(k+1)}}{K_{fk}} B_{k+1} \sqrt{S_k(z)} K_1 \left( r_{DeM} \sqrt{S_k(z)} \right) \end{aligned} \quad (k = 0, 1, \dots, M - 1). \quad (56)$$

Substitute (52) and (53) into external boundary condition equations (49)–(51);

$$A_M = 0, \quad (57)$$

$$A_M I_0 \left( r_{DeM} \sqrt{S_M(z)} \right) + B_M K_0 \left( r_{DeM} \sqrt{S_M(z)} \right) = 0, \quad (58)$$

$$A_M I_1 \left( r_{DeM} \sqrt{S_M(z)} \right) - B_M K_1 \left( r_{DeM} \sqrt{S_M(z)} \right) = 0. \quad (59)$$

$\bar{p}_{Dfk}$ ,  $A_k$ , and  $B_k$  ( $k = 0, 1, \dots, M$ ) can be obtained by solving the simultaneous equations (54)–(59). In (54)–(59), the tree-shaped fractal network parameters can be directly used to express the parameters of the permeability ratio,  $k_{f(k+1)}/k_{fk}$ , the dimensionless effective interface radius,  $r_{DeM}$ , and the function,  $S_k(z)$ .

The dimensionless effective interface radius expression can be derived by substituting (7) into (29):

$$r_{DeM} = \frac{l_0}{r_w} \left[ 1 + \frac{\alpha(1 - \alpha^k) \cos \theta}{1 - \alpha} \right] e^S. \quad (60)$$

The permeability ratio can be calculated using (10):

$$\frac{K_{f(k+1)}}{K_{fk}} = \begin{cases} n\beta^2 \cos \theta, & k = 0, \\ n\beta^2, & k > 0. \end{cases} \quad (61)$$

The expression of the function  $S_k(z)$  is as follows:

$$S_k(z) = \frac{(K_{f0}/K_{fk}) \lambda_k (1 - \omega_k) z}{(K_{f0}/K_{fk}) (1 - \omega_k) e^{2S} z + \lambda_k C_{De}} + \frac{K_{f0} \omega_k}{K_{fk} C_{De}} z, \quad (62)$$

where

$$\frac{K_{f0}}{K_{fk}} = (n\beta^2)^{-k}. \quad (63)$$

The interporosity flow coefficient,  $\lambda_k$ , can be obtained by substituting (4) and (10) into (33), and the fluid capacitance coefficient,  $\omega_k$ , can be obtained by substituting (3), (14), and (15) into (32).

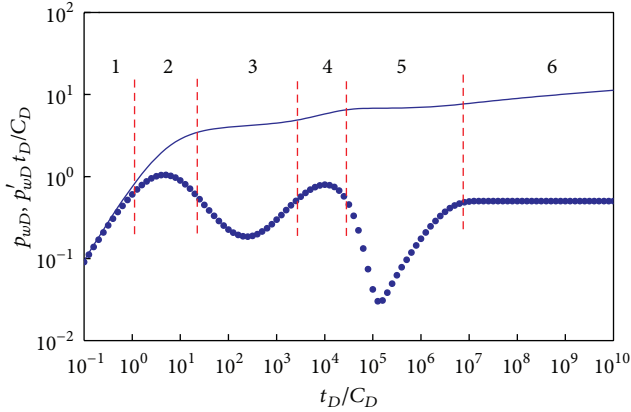


FIGURE 2: Pressure type curves of dual fractal reservoirs ( $\alpha = 1$ ,  $\beta = 0.707$ ,  $\theta = 1$ ,  $N = 4$ ,  $M = 10$ ,  $l_0 = 10$  m,  $d_0 = 0.05$  m,  $D_f = 1.5$ ,  $T_m = 4$ ,  $r_w = 0.1$  m,  $S = -1$ ,  $C_{De} = 0.0001$ ,  $h = 10$  m,  $C_{mt} = 2.2 \times 10^{-5}$  MPa $^{-1}$ , and  $C_{ft} = 1 \times 10^{-4}$  MPa $^{-1}$ ).

## 5. Analysis of Type Curve Characteristics

Dimensionless bottom hole pressure in Laplace space,  $p_{wfD}$ , is obtained by solving the linear equations (54)–(57) using the Stehfest numerical inversion method. The bilogarithmic type curves of the dual fractal reservoirs can then be illustrated.

In a condition of closed top and bottom boundary, the transient flow process, which has six flow regimes, can be clearly shown (Figure 2). The full and dashed lines represent pressure and pressure derivative curves, respectively. Regime 1 is the pure wellbore storage regime. Pressure and its derivative curves appear as upward straight lines with a slope of 1. Regime 2 is the transition flow regime. The shape of the derivative curve looks like an “arch,” which is influenced by the wellbore storage coefficient and skin factor. Regime 3 is the fracture system inter-porosity flow regime. The pressure derivative curve is V shaped, which depicts the response of inter-porosity flow between the fractures that are heterogeneously distributed. This inter-porosity flow regime is caused by spread of the pressure wave through the fracture system. Regime 4 is the fracture system radial flow regime. Slope of the pressure derivative curve is zero. In this scenario, the pressure wave spreads through the whole fracture system and begins to spread to the matrix system. Regime 5 is the inter-porosity flow regime of matrix system to fracture system. The pressure derivative curve is also V shaped. However, it is influenced by spread of the pressure wave through the matrix system. Regime 6 is the total system radial flow regime. The pressure derivative curve converges to a horizontal line, which depicts the response of the pressure dynamic balance state in the whole system.

Figure 3 shows the type curve characteristics affected by pore tortuosity,  $T_m$ . As  $T_m$  increases, the two V shaped curves deepen and shift to the right, which indicates a longer lasting inter-porosity flow regime and a delayed occurring time of the radial flow regime in the fracture system. It also indicates a delayed inter-porosity flow regime from matrix to fracture. An increase in the initial branch number,  $N$ , has a similar

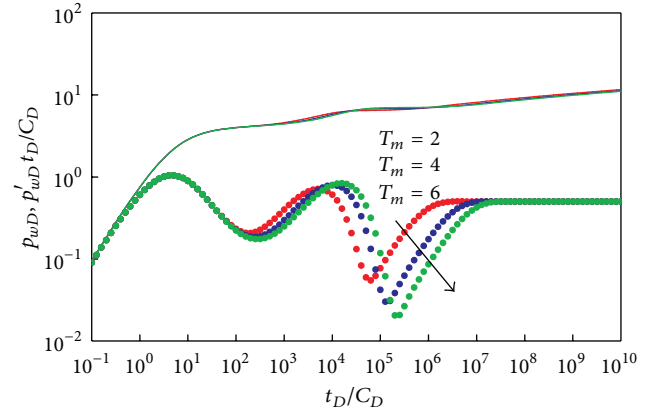


FIGURE 3: Effect of pore tortuosity ( $T_m$ ) on type curves ( $\alpha = 1$ ,  $\beta = 0.707$ ,  $\theta = 1$ ,  $N = 4$ ,  $M = 10$ ,  $l_0 = 10$  m,  $d_0 = 0.05$  m,  $D_f = 1.5$ ,  $r_w = 0.1$  m,  $S = -1$ ,  $C_{De} = 0.0001$ ,  $h = 10$  m,  $C_{mt} = 2.2 \times 10^{-5}$  MPa $^{-1}$ , and  $C_{ft} = 1 \times 10^{-4}$  MPa $^{-1}$ ).

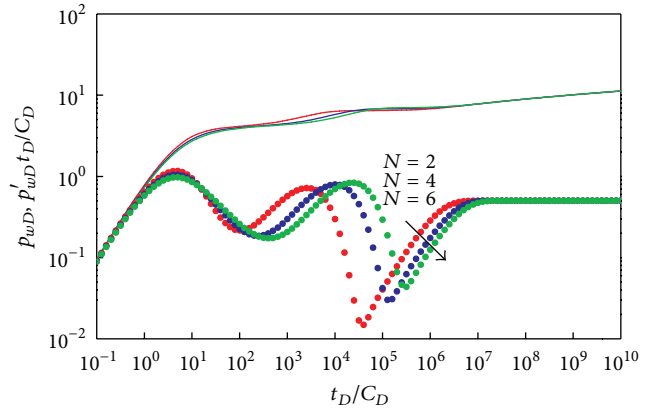


FIGURE 4: Effect of initial branch number ( $N$ ) on type curves ( $\alpha = 1$ ,  $\beta = 0.707$ ,  $\theta = 1$ ,  $M = 10$ ,  $l_0 = 10$  m,  $d_0 = 0.05$  m,  $D_f = 1.5$ ,  $T_m = 4$ ,  $r_w = 0.1$  m,  $S = -1$ ,  $C_{De} = 0.0001$ ,  $h = 10$  m,  $C_{mt} = 2.2 \times 10^{-5}$  MPa $^{-1}$ , and  $C_{ft} = 1 \times 10^{-4}$  MPa $^{-1}$ ).

influence on flow regimes 3, 4, and 5 as an increase in  $T_m$ , but the V shaped curves associated with the pressure derivative become shallower and shift to the right (Figure 4).

Figure 5 exhibits the type curve characteristics affected by pore fractal dimension,  $D_f$ . Permeability of matrix system,  $K_m$ , and porosity of matrix system,  $\phi_m$ , increase with an increase in  $D_f$ . A larger  $K_m$  leads to greater flow capacity in the matrix system with an earlier transition to regime 5. A larger  $\phi_m$  leads to a larger supplying capacity in the matrix system, and regime 5 occurs earlier and lasts longer. As  $D_f$  increases, regime 5 occurs earlier and lasts longer, which is depicted as a deeper and wider second V shaped pressure derivative curve.

Figure 6 shows the type curve characteristics affected by branch angle,  $\theta$ . Permeability of fracture system,  $K_f$ , decreases with an increase in  $\theta$ . A smaller  $K_f$  leads to lower flow capacity in the fracture system with an earlier transition to regime 5. Porosity of fracture system,  $\phi_f$ , increases with an

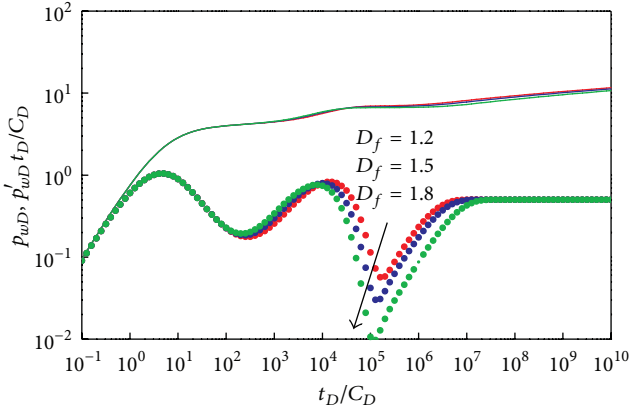


FIGURE 5: Effect of pore fractal dimension ( $D_f$ ) on type curves ( $\alpha = 1, \beta = 0.707, \theta = 1, N = 4, M = 10, l_0 = 10 \text{ m}, d_0 = 0.05 \text{ m}, T_m = 4, r_w = 0.1 \text{ m}, S = -1, C_{De} = 0.0001, h = 10 \text{ m}, C_{mt} = 2.2 \times 10^{-5} \text{ MPa}^{-1}$ , and  $C_{ft} = 1 \times 10^{-4} \text{ MPa}^{-1}$ ).

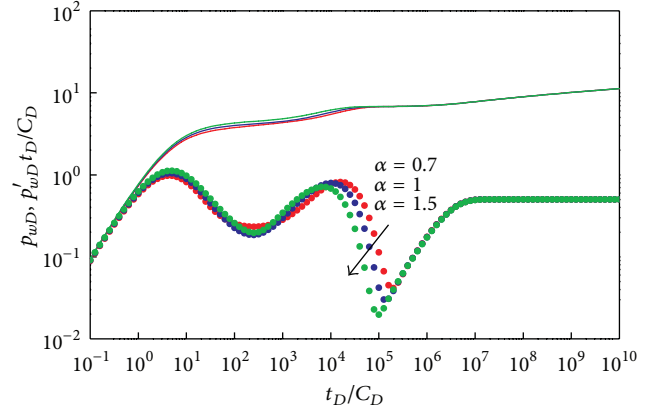


FIGURE 7: Effect of length ratio ( $\alpha$ ) on type curves ( $\beta = 0.707, \theta = 1, N = 4, M = 10, l_0 = 10 \text{ m}, d_0 = 0.05 \text{ m}, D_f = 1.5, T_m = 4, r_w = 0.1 \text{ m}, S = -1, C_{De} = 0.0001, h = 10 \text{ m}, C_{mt} = 2.2 \times 10^{-5} \text{ MPa}^{-1}$ , and  $C_{ft} = 1 \times 10^{-4} \text{ MPa}^{-1}$ ).

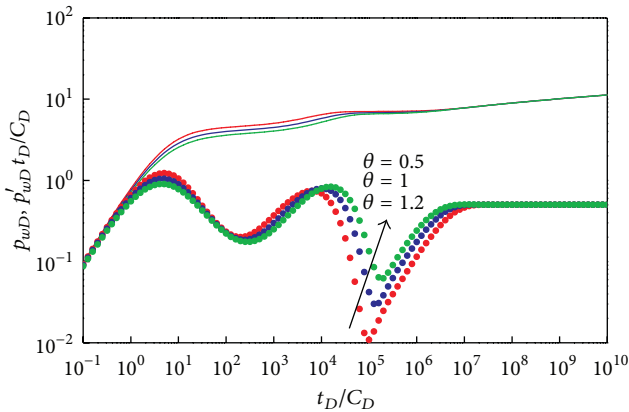


FIGURE 6: Effect of branch angle ( $\theta$ ) on type curves ( $\alpha = 1, \beta = 0.707, N = 4, M = 10, l_0 = 10 \text{ m}, d_0 = 0.05 \text{ m}, D_f = 1.5, T_m = 4, r_w = 0.1 \text{ m}, S = -1, C_{De} = 0.0001, h = 10 \text{ m}, C_{mt} = 2.2 \times 10^{-5} \text{ MPa}^{-1}$ , and  $C_{ft} = 1 \times 10^{-4} \text{ MPa}^{-1}$ ).

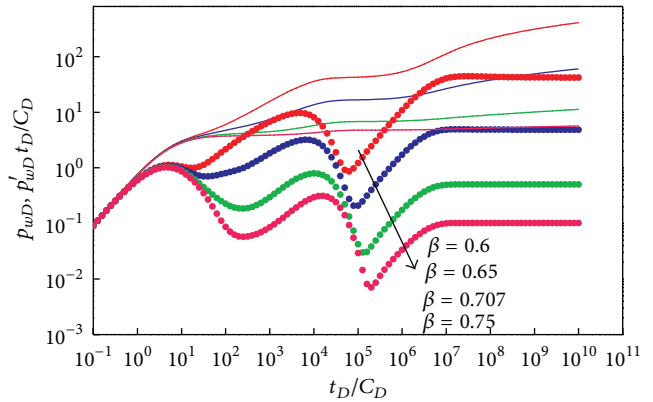


FIGURE 8: Effect of diameter ratio ( $\beta$ ) on type curves ( $\alpha = 1, \theta = 1, N = 4, M = 10, l_0 = 10 \text{ m}, d_0 = 0.05 \text{ m}, D_f = 1.5, T_m = 4, r_w = 0.1 \text{ m}, S = -1, C_{De} = 0.0001, h = 10 \text{ m}, C_{mt} = 2.2 \times 10^{-5} \text{ MPa}^{-1}$ , and  $C_{ft} = 1 \times 10^{-4} \text{ MPa}^{-1}$ ).

increase in  $\theta$ . A larger  $\phi_f$  leads to greater supplying capacity in the fracture system, and regime 5 occurs later with a shorter duration. When  $\theta$  increases, it has the opposite effect on flow regime 5 as an increase in  $D_f$ .

Figure 7 exhibits the type curve characteristics affected by the length ratio,  $\alpha$ .  $\phi_f$  decreases with an increase in  $\alpha$ . A smaller  $\phi_f$  leads to a lower supplying capacity in the fracture system and an earlier transition to a longer lasting regime 5. When a large  $\alpha$  increases, regime 5 occurs earlier, which manifests in a deeper and wider second V shaped type curve.

Figure 8 exhibits the type curve characteristics affected by diameter ratio,  $\beta$ .  $K_f$  and  $\phi_f$  increase with an increase in  $\beta$ . A larger  $K_f$  leads to larger flow capacity in the fracture system and a later transition to regime 5. A larger  $\phi_f$  leads to greater supplying capacity in the fracture system with a later and shorter regime 5. When  $\beta$  is smaller than 0.707,  $K_f$  increases with an increase in  $r$ , and when  $\beta$  is greater than 0.707,  $K_f$  decreases with  $r$ .  $\beta$  affects all regimes except for

pure wellbore storage and transition flow regime, which are not affected by  $K_f$ . A larger  $\beta$  leads to a lower location of the dimensionless pressure curve, and regime 5 occurs later, resulting in a shallower and narrower second V shaped type curve. When  $\beta$  equals the critical value of 0.707 (16), the horizontal line representing regime 6 equals 0.5.

Figures 9 and 10 exhibit the type curve characteristics affected by total branch level,  $M$ , when diameter ratio,  $\beta$ , is 0.65 and 0.75, respectively. Radius,  $r$ , increases with an increase in  $M$ . Additionally,  $r$  enhances the type curve characteristics affected by  $M$ . When  $\beta$  is less than 0.707, a large  $M$  leads to a higher dimensionless pressure curve, and vice versa, when  $\beta$  is greater than 0.707, a large  $M$  leads to a lower dimensionless pressure curve.

## 6. Conclusions

The transient flow model for pressure responses in dual fractal reservoirs is established and solved, type curves are

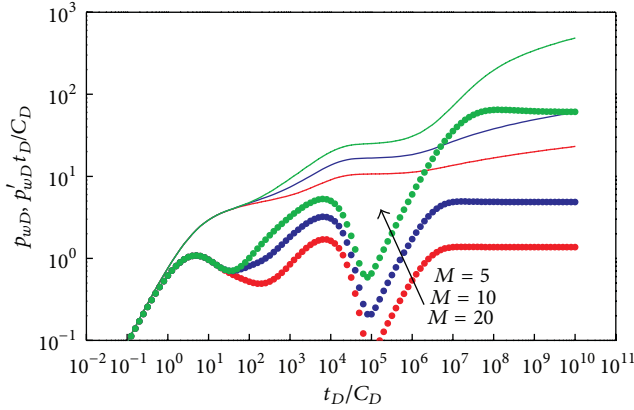


FIGURE 9: Effect of total branch level ( $M$ ) on type curves ( $\alpha = 1$ ,  $\beta = 0.65$ ,  $\theta = 1$ ,  $N = 4$ ,  $M = 10$ ,  $l_0 = 10$  m,  $d_0 = 0.05$  m,  $D_f = 1.5$ ,  $T_m = 4$ ,  $r_w = 0.1$  m,  $S = -1$ ,  $C_{De} = 0.0001$ ,  $h = 10$  m,  $C_{mt} = 2.2 \times 10^{-5}$  MPa $^{-1}$ , and  $C_{ft} = 1 \times 10^{-4}$  MPa $^{-1}$ ).

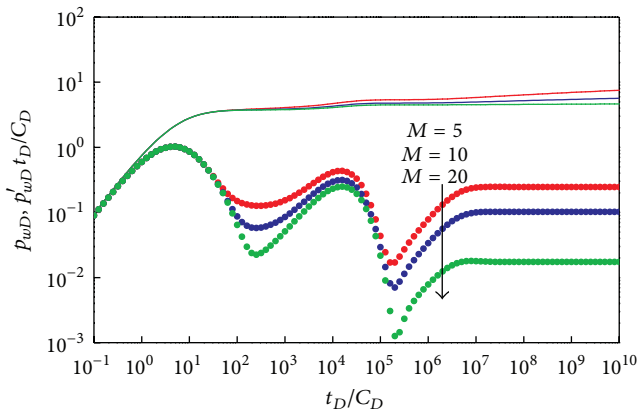


FIGURE 10: Effect of total branch level ( $M$ ) on type curves ( $\alpha = 1$ ,  $\beta = 0.65$ ,  $\theta = 1$ ,  $N = 4$ ,  $M = 10$ ,  $l_0 = 10$  m,  $d_0 = 0.05$  m,  $D_f = 1.5$ ,  $T_m = 4$ ,  $r_w = 0.1$  m,  $S = -1$ ,  $C_{De} = 0.0001$ ,  $h = 10$  m,  $C_{mt} = 2.2 \times 10^{-5}$  MPa $^{-1}$ , and  $C_{ft} = 1 \times 10^{-4}$  MPa $^{-1}$ ).

illustrated, and dual fractal flow behavior characteristics are analyzed. The following conclusions were obtained.

- (1) Fracture and matrix systems can be simulated using a tree-shaped fractal network and fractal porous media, respectively.
- (2) Six flow regimes for pressure type curves can be established. Type curves are dominated by fracture and matrix fractal parameters. These various parameters affect type curves differently.
- (3) Type curves are dominated by external boundary conditions, fractal parameters the fluid capacitance coefficient and the inter-porosity flow factor.
- (4) Semianalytical dual fractal modeling is suitable for various naturally fractured oil or gas reservoirs and provides a practical method to solve empirical cases.

## Acknowledgments

The authors are grateful for financial support from the National Science Fund for Distinguished Young Scholars of China (Grant no. 51125019), the National Key Basic Research and Development Program of China (Grant no. 2011CB201005), and the Science and Technology Innovation Fund of Southwest Petroleum University (Grant no. GIFSB0701).

## References

- [1] R. Camacho-Velázquez, G. Fuentes-Cruz, and M. Vásquez-Cruz, "Decline-curve analysis of fractured reservoirs with fractal geometry," *SPE Reservoir Evaluation and Engineering*, vol. 11, no. 3, pp. 606–619, 2008.
- [2] Y. G. Zhang and D. K. Tong, "The pressure transient analysis of deformation of fractal medium," *Journal of Hydrodynamics*, vol. 20, no. 3, pp. 306–313, 2008.
- [3] A. Jafari and T. Babadagli, "Generating 3D permeability map of fracture networks using well, outcrop, and pressure-transient data," *SPE Reservoir Evaluation and Engineering*, vol. 14, no. 2, pp. 215–224, 2011.
- [4] L. Zhang, J. Zhang, and Y. Zhao, "Analysis of a finite element numerical solution for a nonlinear seepage flow model in a deformable dual media fractal reservoir," *Journal of Petroleum Science and Engineering*, vol. 76, no. 3-4, pp. 77–84, 2011.
- [5] W. Wechsato, S. Lorente, and A. Bejan, "Tree-shaped insulated designs for the uniform distribution of hot water over an area," *International Journal of Heat and Mass Transfer*, vol. 44, no. 16, pp. 3111–3123, 2001.
- [6] W. Wechsato, S. Lorente, and A. Bejan, "Optimal tree-shaped networks for fluid flow in a disc-shaped body," *International Journal of Heat and Mass Transfer*, vol. 45, no. 25, pp. 4911–4924, 2002.
- [7] P. Xu and B. Yu, "The scaling laws of transport properties for fractal-like tree networks," *Journal of Applied Physics*, vol. 100, no. 10, Article ID 104906, 8 pages, 2006.
- [8] P. Xu, B. Yu, Y. Feng, and Y. Liu, "Analysis of permeability for the fractal-like tree network by parallel and series models," *Physica A*, vol. 369, no. 2, pp. 884–894, 2006.
- [9] P. Xu, B. Yu, M. Yun, and M. Zou, "Heat conduction in fractal tree-like branched networks," *International Journal of Heat and Mass Transfer*, vol. 49, no. 19-20, pp. 3746–3751, 2006.
- [10] M. Yun, B. Yu, and J. Cai, "A fractal model for the starting pressure gradient for Bingham fluids in porous media," *International Journal of Heat and Mass Transfer*, vol. 51, no. 5-6, pp. 1402–1408, 2008.
- [11] S. Wang, B. Yu, Q. Zheng, Y. Duan, and Q. Fang, "A fractal model for the starting pressure gradient for Bingham fluids in porous media embedded with randomly distributed fractal-like tree networks," *Advances in Water Resources*, vol. 34, no. 12, pp. 1574–1580, 2011.
- [12] B. Yu and P. Cheng, "A fractal permeability model for bi-dispersed porous media," *International Journal of Heat and Mass Transfer*, vol. 45, no. 14, pp. 2983–2993, 2002.
- [13] J. Bear, *Dynamics of Fluids in Porous Media*, American Elsevier, 1972.
- [14] M. Yun, B. Yu, and J. Cai, "Analysis of seepage characters in fractal porous media," *International Journal of Heat and Mass Transfer*, vol. 52, no. 13-14, pp. 3272–3278, 2009.

- [15] J. E. Warren and P. J. Root, "The behavior of naturally fractured reservoirs," *Society of Petroleum Engineers Journal*, vol. 3, no. 3, pp. 245–255, 1963.
- [16] R. S. Nie, J. C. Guo, Y. L. Jia, S. Q. Zhu, Z. Rao, and C. G. Zhang, "New modelling of transient well test and rate decline analysis for a horizontal well in a multiple-zone reservoir," *Journal of Geophysics and Engineering*, vol. 8, no. 3, article 464, 2011.
- [17] R. G. Agarwal, R. Al-Hussainy, and H. J. Ramey Jr., "Investigation of wellbore storage and skin effect in unsteady liquid flow-1," *Society of Petroleum Engineers Journal*, vol. 10, no. 3, pp. 279–290, 1970.
- [18] D. Bourdet and A. C. Gringarten, "Determination of fissure volume and block size in fractured reservoirs by type-curve analysis," in *Proceedings of the SPE Annual Technical Conference and Exhibition*, American Institute of Mining, Metallurgical and Petroleum Engineers, Dallas, Tex, USA, September 1980.
- [19] R. C. Earlougher, *Advances in Well Test Analysis*, Henry L. Doherty Memorial Fund of AIME, New York, NY, USA, 1977.
- [20] A. F. V. Everdingen and W. Hurst, "The application of the laplace transformation to flow problems in reservoirs," *Journal of Petroleum Technology*, vol. 1, no. 12, pp. 305–324, 1949.

## Research Article

# MHD Forced Convection Laminar Boundary Layer Flow of Alumina-Water Nanofluid over a Moving Permeable Flat Plate with Convective Surface Boundary Condition

S. M. AbdEl-Gaied and M. A. A. Hamad

Mathematics Department, Faculty of Science, Assiut University, Assiut 71516, Egypt

Correspondence should be addressed to S. M. AbdEl-Gaied; [sagaied123@gmail.com](mailto:sagaied123@gmail.com)

Received 17 July 2013; Revised 4 August 2013; Accepted 8 August 2013

Academic Editor: Mohamed Fathy El-Amin

Copyright © 2013 S. M. AbdEl-Gaied and M. A. A. Hamad. This is an open access article distributed under the Creative Commons Attribution License, which permits unrestricted use, distribution, and reproduction in any medium, provided the original work is properly cited.

This paper analyses a two-dimensional steady forced convection boundary layer viscous incompressible flow of alumina-water nanofluid over a moving permeable vertical flat plate under the effect of a magnetic field normal to the plate. Thermal convective surface boundary condition is applied. The nanofluid formulated in the present study is water dispersed with various volumetric fractions of the alumina ( $\text{Al}_2\text{O}_3$ ) nanoparticles. The plate velocity and the free stream velocities are considered to be proportional to  $x^n$ , while the magnetic field and suction velocities are taken to be proportional to  $(x)^{(n-1)/2}$ . The similarity solution of the governing problem is obtained. Numerical studies are presented to show the effect of the nanoparticle volume fraction  $\phi$ , the convective heat transfer parameter  $b$ , the power law exponent  $n$ , the wall velocity parameter  $A$ , and the suction parameter  $f_w$  on the velocity, temperature, skin-friction coefficient, and Nusselt number.

## 1. Introduction

It is known that nanofluids can tremendously enhance the heat transfer characteristics of the original (base) fluid. Thus, nanofluids have many applications in industry such as coolants, lubricants, heat exchangers, and microchannel heat sinks. Therefore, numerous methods have been taken to improve the thermal conductivity of these fluids by suspending nano-/micro-sized particle materials in liquids. Several recent studies on the modeling of free/mixed convection heat transfer in nanofluids have been published: Congedo et al. [1], Ghasemi and Aminossadati [2], and Ho et al. [3, 4]. These studies have used traditional finite difference and finite volume techniques with the tremendous call on computational resources that these techniques necessitate. Hamad et al. [5] used the application of a one-parameter group to present similarity reductions for problems of magnetic field effects on free-convection flow of a nanofluid past a semi-infinite vertical flat plate. Hamad and Pop [6] studied theoretically the similarity solution of the steady boundary layer flow near the stagnation-point flow on a permeable stretching

sheet in a porous medium saturated with a nanofluid and in the presence of internal heat generation/absorption. Hamad [7] found the analytical solutions of convective flow and heat transfer of an incompressible viscous nanofluid past a semi-infinite vertical stretching sheet in the presence of magnetic field. Abu-Nada and Chamkha [8] investigated the natural convection heat transfer characteristics in a differentially heated enclosure filled with a CuO-EG-water nanofluid for different published variable thermal conductivity and variable viscosity models. Teng et al. [9] studied the effect of particle size, temperature, and weight fraction on the thermal conductivity ratio of  $\text{Al}_2\text{O}_3$ -water nanofluid. Ho et al. [10] presented an experimental study for natural convection heat transfer of a nanofluid in vertical square enclosure of different sizes. Bachok et al. [11] studied the steady boundary-layer flow of a nanofluid past a moving semi-infinite flat plate in a uniform free stream. Hady et al. [12] studied the natural convection boundary-layer flow over a downward-pointing vertical cone in a porous medium saturated with a non-Newtonian nanofluid in the presence of heat generation or absorption. The numerical modeling

of the conjugate heat transfer and fluid flow of  $\text{Al}_2\text{O}_3$ /water nanofluid through the microchannel heat sink was presented by Lelea [13]. In this paper, the laminar flow regime was considered along with viscous dissipation effect. Also, the microchannel heat sink with square microchannels and  $Dh = 50 \mu\text{m}$  was considered. Nandy and Mahapatra [14] analyzed the effects of velocity slip and heat generation/absorption on magnetohydrodynamic (MHD) stagnation-point flow and heat transfer over a stretching/shrinking surface, with convective boundary conditions, in the presence of nanoparticle fractions. They considered also the effects of Brownian motion and thermophoresis. Numerical study for the effects of thermal radiation and viscous dissipation on hydromagnetic mixed convection flow over a nonlinear stretching and shrinking sheets in nanofluids was presented by Pal et al. [15]. Rohni et al. [16] theoretically investigated the steady two-dimensional boundary-layer flow past a moving semi-infinite flat plate in a water-based nanofluid containing three different types of nanoparticles: copper (cuprum), alumina (aluminium oxide), and titania (titanium dioxide). For more information, see also Das et al. [17], Wang and Mujumdar [18–20], and Kakaç and Pramuanjaroenkij [21].

Heat transfer due to forced convection occurs in many areas. Examples include chemical process, biochemical process, and engineering. Its study is important due to the need to improve the efficiency of the heat transfer. Ali [22] studied the effect of temperature dependent viscosity on laminar mixed convection boundary layer flow and heat transfer on a continuously moving vertical isothermal surface and obtained local similarity solutions. According to previous studies, the forced convection flow over moving plate has many practical engineering applications such as liquid films in condensation process and in aerodynamics. Similarity solutions about moving plate were investigated by many authors. Among them, Ishak et al. [23] studied the boundary layer flow on a moving permeable plate parallel to a moving stream and concluded that dual solutions exist if the plate and the free stream move in the opposite directions. Magyari [24] studied the moving plate thermometer with uniform velocity. His approach was based on a series solution of the problem using the Merkin transformation method. Hoernel [25] investigated similarity solution for steady laminar boundary layer equations governing MHD flow near forward stagnation point of two dimensional moving axisymmetric bodies. Recently, Pal and Mondal [26] studied MHD forced convection and heat transfer of an incompressible Newtonian electrically conducting and heat generating/absorbing fluid having temperature-dependent viscosity over a nonisothermal permeable wedge in the presence of thermal radiation. In all of the above studies, convective thermal boundary conditions (either prescribed heat flux or prescribed surface temperature) were used.

According to previous scholars, the MHD flow has received the attention of many researchers due to its engineering applications. In metallurgy, for example, some processes involve the cooling of many continuous strips by drawing them through an electrically conducting fluid subject to a magnetic field (Kandasamy and Muhaimin [27]). This allows the rate of cooling to be controlled and final product with

the desired characteristics to be obtained. Another important application of hydromagnetic flow in metallurgy is in the purification of molten metals from nonmetallic inclusions through the application of a magnetic field. Research has also been carried out by previous researchers on the flow and heat transfer effects of electrically conducting fluids such as liquid metals, water mixed with a little acid and other equivalent substances in the presence of a magnetic field. The studies have involved different geometries and different boundary conditions. Herdricha et al. [28] studied MHD flow control for plasma technology applications. They identified potential applications for magnetically controlled plasmas in the fields of space technology as well as in plasma technology. Seddeek et al. [29] investigated the similarity solution in MHD flow and heat transfer over a wedge taking into account variable viscosity and thermal conductivities. Alam et al. [30] investigated the effects of variable suction and thermophoresis on steady MHD combined free-forced convective heat and mass transfer flow over a semi-infinite permeable inclined plate in the presence of thermal radiation. Aydin and Kaya [31] studied MHD mixed convection of a viscous dissipating fluid about a permeable vertical flat plate and found that the value of Richardson number determines the effect of the magnetic parameter on the momentum and heat transfer. Recently, Rahman and Salahuddin [32] investigated the effects of variable electric conductivity and viscosity on hydromagnetic heat and mass transfer flow along a radiated isothermal inclined permeable surface in a stationary fluid which includes internal heat generation.

The aim of the present study is to analyze steady, two-dimension, laminar MHD forced convection flow of alumina-water nanofluid on moving permeable flat plate with convective surface boundary condition. The similarity representation of the partial differential equations governing this problem is obtained. The motivation of this study is to explore the influence of nanofluid parameters with the effect of suction, convective heat transfer, and velocity parameter. The variation distribution of the shear stress and heat transfer rates (the physical quantities of interest in this study) with the parameters governing the problem are presented.

## 2. Formulation of the Problem

Consider a two-dimensional forced convective flow of water-based alumina nanoparticles over a moving permeable flat plate. A rectangular coordinate frame is selected in which the  $x$ -axis is vertical and  $y$ -axis is horizontal. A magnetic field of variable strength  $B(x)$  is applied perpendicular to the plate. The temperature of the plate on the top is held at a uniform temperature  $T_w$  which is assumed greater than the ambient temperature  $T_\infty$ . It will be further assumed that the bottom surface of the plate is heated by convection from a hot fluid of temperature  $T_f$ , and this generates a heat transfer coefficient  $h_f$  (see Aziz [33]). For the thermophysical properties of the alumina, see Oztop and Abu-Nada [34]. The flow configuration and the coordinate system are shown in Figure 1. Kinematic viscosity and thermal diffusivity are assumed constants. Particle coagulation, the magnetic Reynolds number, the electric field owing to the

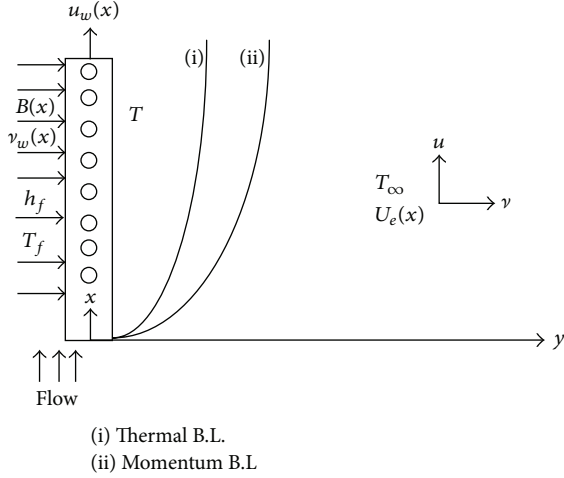


FIGURE 1: Flow configuration and coordinate system.

polarization of charges, viscous dissipation term, and Hall effects are assumed to be negligible. The field variables of this study are the velocity  $\vec{V} = (u, v)$  and the temperature  $T$ . Under the above assumptions, the boundary layer equations can be written in dimensional form as (see Schlichting and Gersten [35], Kays and Crawford [36])

$$\frac{\partial u}{\partial x} + \frac{\partial v}{\partial y} = 0, \quad (1)$$

$$\rho_{nf} \left( u \frac{\partial u}{\partial x} + v \frac{\partial u}{\partial y} \right) = -\frac{\partial p}{\partial x} + \mu_{nf} \frac{\partial^2 u}{\partial y^2} - \sigma B^2(x) u, \quad (2)$$

$$u \frac{\partial T}{\partial x} + v \frac{\partial T}{\partial y} = \alpha_{nf} \frac{\partial^2 T}{\partial y^2}. \quad (3)$$

The corresponding boundary conditions are

$$\begin{aligned} u &= u_w(x), & v &= -v_w(x), \\ -\kappa_{nf} \frac{\partial T}{\partial y} &= h_f [T_f - T_w] & \text{at } y &= 0, \\ u &\longrightarrow U_e(x), & T &\longrightarrow T_\infty, & C &\longrightarrow C_\infty & \text{as } y &\longrightarrow \infty. \end{aligned} \quad (4)$$

Here,  $p$  is the pressure,  $\sigma$  is the electric conductivity,  $U_e(x)$  is potential velocity,  $u_w(x)$  is the velocity of the moving plate,  $v_w(x)$  is the velocity normal to the plate with  $v_w(x) > 0$  for injection (blowing) and  $v_w(x) < 0$  for suction, and  $v_w(x) = 0$  corresponds to an impermeable sheet. As usual  $\mu_{nf}$  is the nanofluid viscosity,  $\rho_{nf}$  is the nanofluid density,  $\alpha_{nf}$  is the nanofluid thermal diffusivity and,  $\kappa_{nf}$  is the nanofluid thermal conductivity, which are given by

$$\begin{aligned} \mu_{nf} &= \frac{\mu_f}{(1-\phi)^{2.5}}, & \alpha_{nf} &= \frac{\kappa_{nf}}{(\rho C_p)_{nf}}, \\ (\rho C_p)_{nf} &= (1-\phi)(\rho C_p)_f + \phi(\rho C_p)_s, \end{aligned}$$

$$\begin{aligned} \rho_{nf} &= (1-\phi)\rho_f + \phi\rho_s, \\ \kappa_{nf} &= \frac{\kappa_f(\kappa_s + 2\kappa_f - 2\phi(\kappa_f - \kappa_s))}{(\kappa_s + 2\kappa_f + \phi(\kappa_f - \kappa_s))}, \end{aligned} \quad (5)$$

where  $\phi$  is the nanoparticle volume fraction,  $(\rho C_p)_{nf}$  is the nanofluid heat capacity,  $\kappa_f$  and  $\kappa_s$  are thermal conductivities of the fluid and of the solid fractions, respectively, and  $\rho_f$  and  $\rho_s$  are the densities of the fluid and of the solid fractions, respectively.

In the free stream,  $u = U_e(x)$ , and so (2) reduces to

$$U_e \frac{dU_e}{dx} = -\frac{1}{\rho_{nf}} \frac{\partial p}{\partial x} - \frac{\sigma B^2(x)}{\rho_{nf}} U_e(x). \quad (6)$$

Eliminating the pressure gradient term  $\partial p / \partial x$  between (2) and (6), we get

$$\begin{aligned} u \frac{\partial u}{\partial x} + v \frac{\partial u}{\partial y} &= U_e \frac{dU_e}{dx} \\ &+ \frac{1}{\rho_{nf}} \left[ \mu_{nf} \frac{\partial^2 u}{\partial y^2} - \sigma B^2(x)(u - U_e) \right]. \end{aligned} \quad (7)$$

By introducing stream function  $\psi$ , such that

$$u = \frac{\partial \psi}{\partial y}, \quad v = -\frac{\partial \psi}{\partial x}. \quad (8)$$

We also introduce the following dimensionless transformations:

$$\begin{aligned} \eta &= \frac{y}{x} \sqrt{n+1} \text{Re}_x^{1/2}, & \psi &= \frac{v_f}{\sqrt{n+1}} \text{Re}_x^{1/2} f(\eta), \\ \theta(\eta) &= \frac{T - T_\infty}{T_f - T_\infty}, & \text{Re}_x &= \frac{U_\infty x^{n+1}}{v_f}, \\ B(x) &= B_0 x^{(n-1)/2}, & u_w(x) &= u_0 x^n, \\ v_w(x) &= v_0 x^{(n-1)/2}, & U_e(x) &= U_\infty x^n, \end{aligned} \quad (9)$$

where  $B_0$ ,  $u_0$ ,  $v_0$ , and  $U_\infty$  are constants and where  $\text{Re}_x$  is the Reynolds number based on position  $x$  along the flow direction (see Hoernel [25]). Here,  $n$  (not necessarily an integer) is the power law exponent,  $u_0 > 0$  means that the plate is moving along the positive direction of  $x$ -axis, and  $u_0 < 0$  means that the plate is moving in the negative direction of  $x$ -axis. In our analysis, we choose  $u_0 > 0$ . The quantity  $v_0$  represents suction or injection,  $v_0 > 0$  represents suction, and  $v_0 < 0$  represents injection.

It is noticed that the continuity equation (1) is satisfied automatically and (3) and (7) yield

$$\frac{n+1}{(1-\phi)^{2.5}} f''' + \left(1 - \phi + \left(\frac{\rho_s}{\rho_f}\right)\phi\right) \times \left[\frac{n+1}{2} f f'' - n f'^2 + n\right] + M(f' - 1) = 0, \quad (10)$$

$$\frac{1}{Pr} \left(\frac{\kappa_{nf}}{\kappa_f}\right) \theta'' + \frac{1}{2} \left(1 - \phi + \frac{(\rho C_p)_s}{(\rho C_p)_f} \phi\right) f \theta' = 0, \quad (11)$$

where  $Pr = (\mu C_p)_f / \kappa_f$  is the Prandtl number and  $M = \sigma B_0^2 / (\rho_f u_\infty)$  is the magnetic parameter. Here, we assume that  $T_f > T_w > T_\infty$ .

The corresponding boundary conditions in (4) become

$$f'(0) = A, \quad f(0) = f_w, \quad \theta'(0) = -b \left(\frac{\kappa_f}{\kappa_{nf}}\right) [1 - \theta(0)], \quad f'(\infty) = 1, \quad \theta(\infty) = 0, \quad (12)$$

where  $A = u_0 / U_\infty$  is a constant and is considered as a velocity parameter and  $f_w = -2\nu_0 / \sqrt{\nu} U_\infty (n+1)$  is the suction parameter. The parameter  $A > 0$  means that the plate is moving in the same direction as the free stream velocity,  $A < 0$  means that the plate is moving in the opposite direction of the free steam, and  $A = 0$  stands for static plate.

The parameter  $b = (h_f / \kappa) \sqrt{\nu x} / U_e (n+1)$  is the convective heat transfer parameter, which should be constant. To fulfill this criterion, the coefficient of heat transfer  $h_f$  must be directly proportional to  $1/\sqrt{x}$ ; that is,  $h_f = c_1 / \sqrt{x}$ .

### 2.1. Particular Cases

- (i) Here, we should mention that if  $n = 0$  (the full stream velocity is constant),  $f_w = 0$  (the plate is impermeable),  $u_w = 0$  (the plate is stationary), and  $M = 0$  (absence of magnetic field), our system (10)–(12) reduces to that in Aziz [33].
- (ii) If  $f_w \neq 0$  (the plate is permeable),  $u_w = 0$ , and  $M = 0$ , our system (10)–(12) reduces to that in Ishak [37].

The parameters of engineering interest for the problem are the skin friction  $C_f$  and the local Nusselt number  $Nu$ , respectively. These physical quantities can be derived from the following definitions:

$$C_f = \frac{\mu_{nf}}{u_w^2 \rho_{nf}} \left(\frac{\partial u}{\partial y}\right)_{y=0}, \quad Nu = \frac{-x}{(T_f - T_\infty)} \left(\frac{\kappa_{nf}}{\kappa_f}\right) \left(\frac{\partial T}{\partial y}\right)_{y=0}. \quad (13)$$

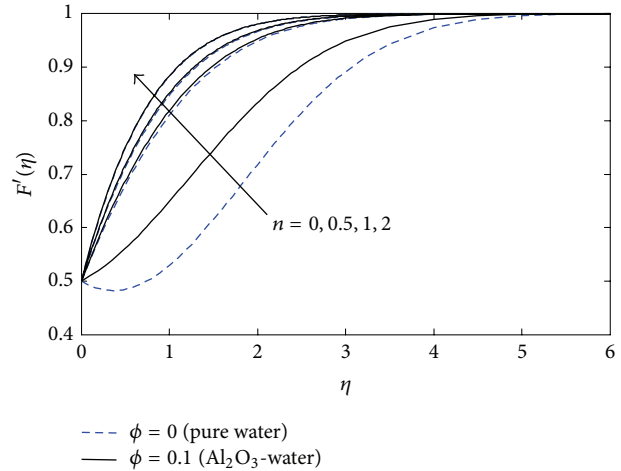


FIGURE 2:  $b = 0.5, f_w = 0.5, Pr = 6.2, M = 0.5,$  and  $A = 0.5$ .

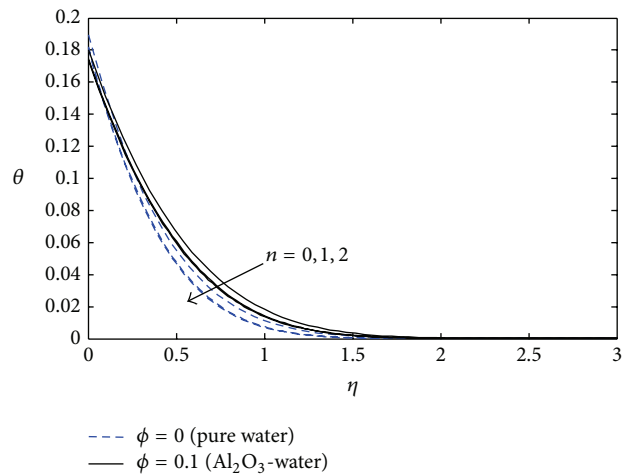


FIGURE 3:  $b = 0.5, f_w = 0.5, Pr = 6.2, M = 0.5,$  and  $A = 0.5$ .

By substituting from (8) and (12) into (13), we get

$$Re_x^{1/2} C_f = \frac{\sqrt{n+1}}{A^2 (1-\phi)^{2.5}} f''(0), \quad (14)$$

$$Re^{-1/2} Nu = -\sqrt{n+1} \frac{\kappa_{nf}}{\kappa_f} \theta'(0).$$

### 3. Results and Discussion

The transformed system of nonlinear ordinary differential equations (10) and (11) together with boundary conditions (12) containing various parameters, namely, the power law parameter  $n$ , magnetic parameter  $M$ , the Prandtl number  $Pr$ , the nanoparticles volume fraction  $\phi$  and convective heat transfer parameter  $b$ , suction parameter  $f_w$  and the velocity parameter  $A$ . Equations (10) and (11) together with boundary conditions given in (12) are solved numerically by an implicit finite difference method. To exhibit our results obtained by

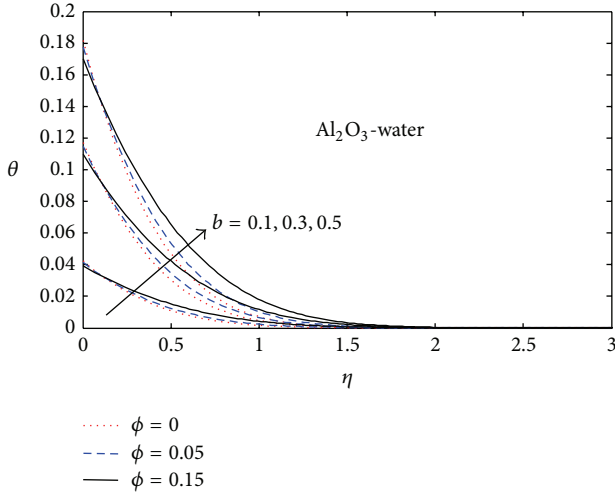


FIGURE 4:  $n = 2$ ,  $f_w = 0.5$ ,  $Pr = 6.2$ ,  $M = 0.5$ , and  $A = 0.5$ .

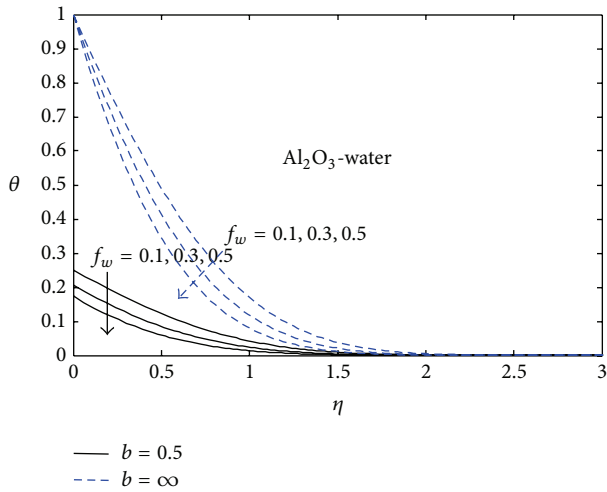


FIGURE 5:  $n = 2$ ,  $\phi = 0.1$ ,  $Pr = 6.2$ ,  $M = 0.5$ , and  $A = 0.5$ .

numerical computations, we plot the graphs given in Figures 2 to 10, respectively.

To exhibit the effects of various values of the power law exponent  $n$  on velocity  $F'(\eta)$  and temperature  $\theta(\eta)$  for two values of the nanoparticles volume fraction  $\phi$ , which are  $\phi = 0$  (pure water) and  $\phi \neq 0$  ( $=0.1$ ) ( $Al_2O_3$ -water), keeping the other parameters fixed ( $Pr = 6.2$ ,  $M = 0.5$ ,  $b = 0.5$ ,  $f_w = 0.5$ , and  $A = 0.5$ ), we plot Figures 2 and 3, respectively. It is clear from Figure 2 that the increased power law exponent increases the velocity. Also, it is clear that the presence of alumina nanoparticles reduces the momentum boundary layer thickness and increases the velocity. However, from Figure 3, it is seen that the increased power law exponent decreases the temperature and the existence of alumina nanoparticles increases the thermal boundary layer thickness. This is because the thermal conductivity of alumina is higher than that of water.

Figure 4 displays the influence of various values of the convective heat transfer parameter  $b$  and the nanoparticles volume fractions  $\phi$  on temperature distribution. We have

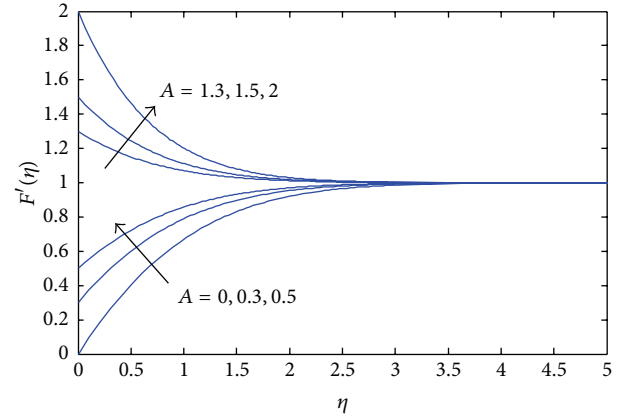


FIGURE 6:  $b = 0.1$ ,  $f_w = 0.1$ ,  $Pr = 6.2$ ,  $M = 0.5$ ,  $n = 2$ , and  $\phi = 0.1$ .

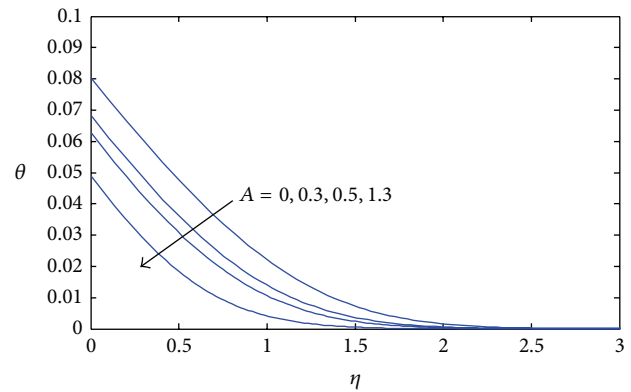


FIGURE 7:  $b = 0.1$ ,  $f_w = 0.1$ ,  $Pr = 6.2$ ,  $M = 0.5$ ,  $n = 2$ , and  $\phi = 0.1$ .

noted that the thermal boundary layer thickness increases when  $n$  or  $\phi$  increases. This agrees with the physical behavior that, when the convective heat transfer increases, the hot fluid side convection resistance decreases, and, consequently, the surface temperature increases (see Ishak [37]); because of this, the thermal boundary layer thickness increases, and because also alumina has high thermal conductivity, then the thickness increases more for alumina-water nanofluid.

Figure 5 shows the effect of the variation of suction parameter  $f_w$  on temperature for two cases of convective heat transfer parameter  $b$ , first when  $b = 0.5$  (convective boundary condition) and second when  $b = \infty$  (neglect convective condition, i.e., back to normal condition  $\theta(0) = 1$ ). All other parameters are nonzero. It can be seen that the thickness of the thermal boundary layer reduces with increasing values of  $f_w$  for the two cases of  $b$ .

Effects of the velocity parameter  $A$  on the velocity and temperature are shown in Figures 6 and 7, respectively. We have observed from Figure 6 that the velocity increases when  $A$  increases. We have noticed also that for each  $A < 1$  ( $u_0 < U_\infty$ ), the velocity increases till it becomes 1 and, for each  $A > 1$  ( $u_0 > U_\infty$ ) the velocity decreases till it becomes 1 while, from Figure 7, it is noted that the temperature decreases when  $A$  increases and the wall temperature also decreases when  $A$  increases.

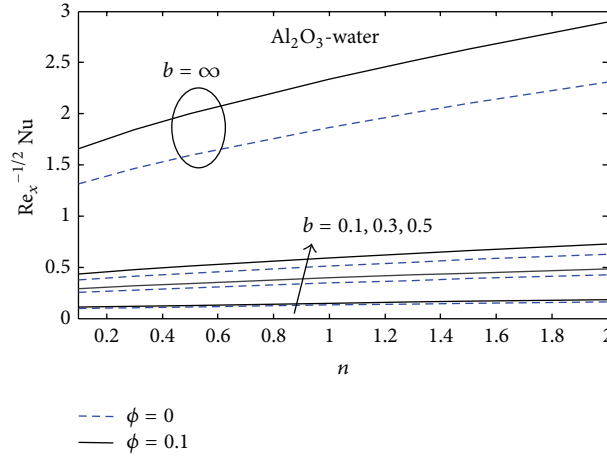


FIGURE 8:  $Pr = 6.2$ ,  $M = 0.5$ ,  $A = 0.5$ , and  $f_w = 0.1$ .

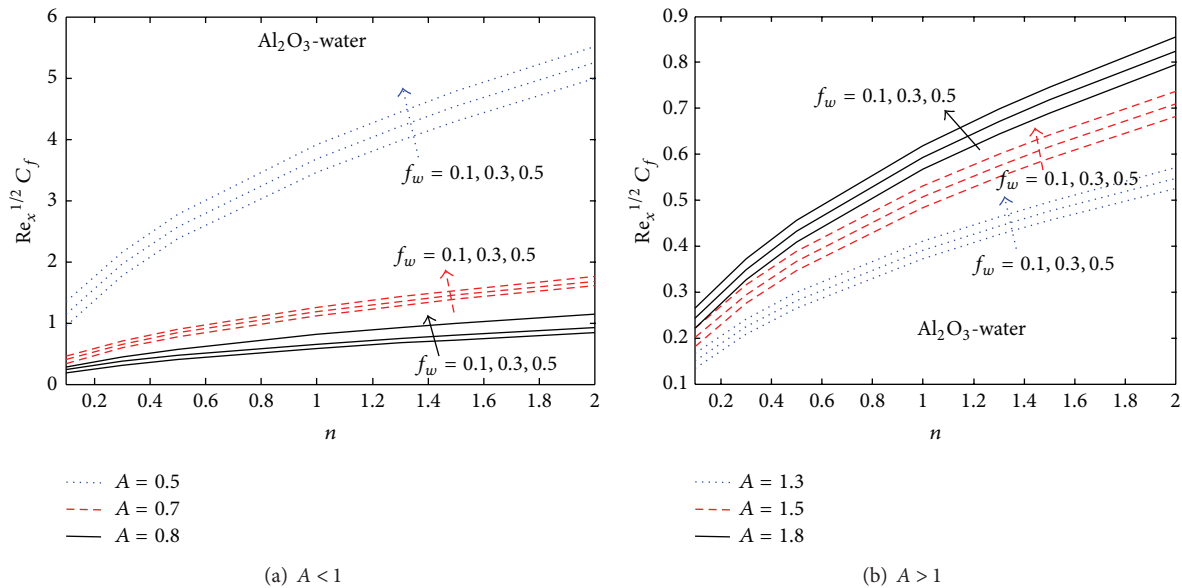


FIGURE 9:  $Pr = 6.2$ ,  $M = 0.5$ ,  $b = 0.5$ , and  $\phi = 0.1$ .

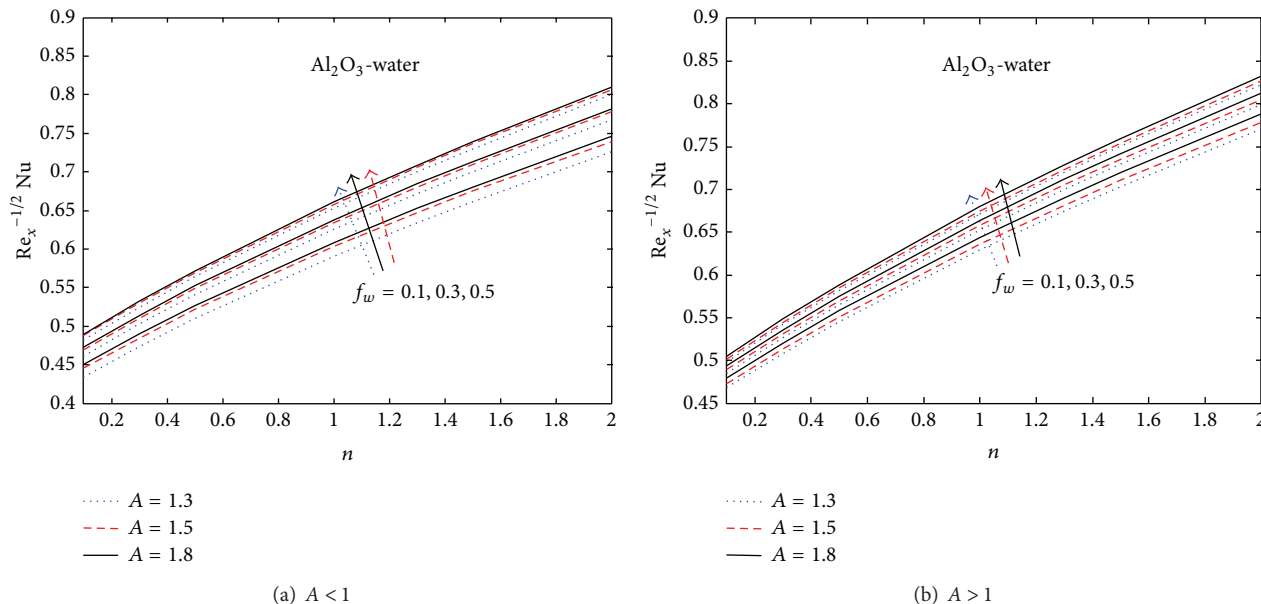
Figure 8 shows the effects of  $b$  on the shear stress versus the parameter  $n$  for pure water and alumina-water nanofluid ( $\phi \neq 0$  ( $=0.1$ )). It is clear that the value of shear stress without considering the convective boundary condition ( $b = \infty$ ) is greater than when considering the convective boundary condition for both  $\phi = 0$  and  $\phi \neq 0$ , also for the nanofluid the shear stress is greater more than for pure water. It is also noticed that increasing parameter  $n$  leads to increasing the shear stress, as well as at each value of  $n$ , the shear stress be higher for higher value of  $b$  both  $\phi = 0$  and  $\phi \neq 0$ .

Figures 9 and 10 show the effect of suction parameter  $f_w$  and the velocity parameter  $A$  on the shear stress and rate of heat transfer versus  $n$ , respectively. From Figure 9, we have seen that the shear stress increases when  $f_w$  increases. For  $A < 1$  as in Figure 9(a), we have noted that the shear stress decreases when  $A$  increases, but, for  $A > 1$  as in Figure 9(b), the shear stress increases with the increased  $A$ . However, from Figures 10(a) and 10(b), it is observed that

the rate of heat transfer increases with the increasing value of suction parameter  $f_w$  or the increasing value of the power law parameter  $n$ .

#### 4. Conclusion

In this paper, we have studied the problem of heat transfer in MHD forced convection flow of alumina-water nanofluid over moving permeable vertical flat plate with convective surface boundary condition. New similarity transformations have been presented and solved numerically. It was found that alumina nanoparticles when suspended in a fluid are capable of increasing the heat transfer capability of the base fluid. The shear stress as well as heat transfer rate increases with nanoparticle volume fraction. Thermal boundary layer thickness as well as heat transfer rate increases when the convective heat transfer parameter  $b$  increases. Thermal boundary layer thickness decreases while both shear stress

FIGURE 10:  $Pr = 6.2$ ,  $M = 0.5$ ,  $b = 0.5$ , and  $\phi = 0.1$ .

and heat transfer rate increase with the increase of suction parameter. Temperature and wall temperature decrease while velocity and heat transfer rate increase when the velocity parameter  $A$  increases.

## References

- [1] P. M. Congedo, S. Collura, and P. M. Congedo, "Modeling and analysis of natural convection heat transfer in nanofluids," in *Proceedings of the ASME Summer Heat Transfer Conference (HT '09)*, vol. 3, pp. 569–579, August 2009.
- [2] B. Ghasemi and S. M. Aminossadati, "Natural convection heat transfer in an inclined enclosure filled with a water-Cuo nanofluid," *Numerical Heat Transfer A*, vol. 55, no. 8, pp. 807–823, 2009.
- [3] C. J. Ho, M. W. Chen, and Z. W. Li, "Effect on natural convection heat transfer of nanofluid in an enclosure due to uncertainties of viscosity and thermal conductivity," in *Proceedings of the ASME/JSME Thermal Engineering Summer Heat Transfer Conference (HT '07)*, vol. 1, pp. 833–841, July 2007.
- [4] C. J. Ho, M. W. Chen, and Z. W. Li, "Numerical simulation of natural convection of nanofluid in a square enclosure: effects due to uncertainties of viscosity and thermal conductivity," *International Journal of Heat and Mass Transfer*, vol. 51, no. 17-18, pp. 4506–4516, 2008.
- [5] M. A. A. Hamad, I. Pop, and A. I. Md Ismail, "Magnetic field effects on free convection flow of a nanofluid past a vertical semi-infinite flat plate," *Nonlinear Analysis: Real World Applications*, vol. 12, no. 3, pp. 1338–1346, 2011.
- [6] M. A. A. Hamad and I. Pop, "Scaling transformations for boundary layer stagnation-point flow towards a heated permeable stretching sheet in a porous medium saturated with a nanofluid and heat absorption/generation effects," *Transport in Porous Media*, vol. 87, no. 1, pp. 25–39, 2011.
- [7] M. A. A. Hamad, "Analytical solution of natural convection flow of a nanofluid over a linearly stretching sheet in the presence of magnetic field," *International Communications in Heat and Mass Transfer*, vol. 38, no. 4, pp. 487–492, 2011.
- [8] E. Abu-Nada and A. J. Chamkha, "Effect of nanofluid variable properties on natural convection in enclosures filled with a CuO-EG-Water nanofluid," *International Journal of Thermal Sciences*, vol. 49, no. 12, pp. 2339–2352, 2010.
- [9] T. Teng, Y. Hung, T. Teng, H. Mo, and H. Hsu, "The effect of alumina/water nanofluid particle size on thermal conductivity," *Applied Thermal Engineering*, vol. 30, no. 14-15, pp. 2213–2218, 2010.
- [10] C. J. Ho, W. K. Liu, Y. S. Chang, and C. C. Lin, "Natural convection heat transfer of alumina-water nanofluid in vertical square enclosures: an experimental study," *International Journal of Thermal Sciences*, vol. 49, no. 8, pp. 1345–1353, 2010.
- [11] N. Bachok, A. Ishak, and I. Pop, "Boundary-layer flow of nanofluids over a moving surface in a flowing fluid," *International Journal of Thermal Sciences*, vol. 49, no. 9, pp. 1663–1668, 2010.
- [12] F. M. Hady, F. S. Ibrahim, S. M. Abdel-Gaied, and M. R. Eid, "Effect of heat generation/absorption on natural convective boundary-layer flow from a vertical cone embedded in a porous medium filled with a non-Newtonian nanofluid," *International Communications in Heat and Mass Transfer*, vol. 38, no. 10, pp. 1414–1420, 2011.
- [13] D. Lelea, "The performance evaluation of  $Al_2O_3$ /water nanofluid flow and heat transfer in microchannel heat sink," *International Journal of Heat and Mass Transfer*, vol. 54, no. 17-18, pp. 3891–3899, 2011.
- [14] S. K. Nandy and T. R. Mahapatra, "Effects of slip and heat generation/absorption on MHD stagnation flow of nanofluid past a stretching/shrinking surface with convective boundary conditions," *International Journal of Heat and Mass Transfer*, vol. 64, pp. 1091–1100, 2013.
- [15] D. Pal, G. Mandal, and K. Vajravelu, "MHD convection-dissipation heat transfer over a non-linear stretching and

- shrinking sheets in nanofluids with thermal radiation,” *International Journal of Heat and Mass Transfer*, vol. 65, pp. 481–490, 2013.
- [16] A. M. Rohni, S. Ahmad, and I. Pop, “Boundary layer flow over a moving surface in a nanofluid beneath a uniform free stream,” *International Journal of Numerical Methods for Heat and Fluid Flow*, vol. 21, no. 7, pp. 828–846, 2011.
- [17] S. K. Das, S. U. S. Choi, W. Yu, and T. Pradeep, *Nanofluids: Science and Technology*, Wiley, Hoboken, NJ, USA, 2007.
- [18] X. Wang and A. S. Mujumdar, “Heat transfer characteristics of nanofluids: a review,” *International Journal of Thermal Sciences*, vol. 46, no. 1, pp. 1–19, 2007.
- [19] X. Wang and A. S. Mujumdar, “A review on nanofluids, part I: theoretical and numerical investigations,” *Brazilian Journal of Chemical Engineering*, vol. 25, no. 4, pp. 613–630, 2008.
- [20] X. Wang and A. S. Mujumdar, “A review on nanofluids, part II: experiments and applications,” *Brazilian Journal of Chemical Engineering*, vol. 25, no. 4, pp. 631–648, 2008.
- [21] S. Kakaç and A. Pramuanjaroenkij, “Review of convective heat transfer enhancement with nanofluids,” *International Journal of Heat and Mass Transfer*, vol. 52, no. 13–14, pp. 3187–3196, 2009.
- [22] M. E. Ali, “The effect of variable viscosity on mixed convection heat transfer along a vertical moving surface,” *International Journal of Thermal Sciences*, vol. 45, no. 1, pp. 60–69, 2006.
- [23] A. Ishak, R. Nazar, and I. Pop, “Boundary layer on a moving wall with suction and injection,” *Chinese Physics Letters*, vol. 24, no. 8, pp. 2274–2276, 2007.
- [24] E. Magyari, “The moving plate thermometer,” *International Journal of Thermal Sciences*, vol. 47, no. 11, pp. 1436–1441, 2008.
- [25] J. Hoernel, “On the similarity solutions for a steady MHD equation,” *Communications in Nonlinear Science and Numerical Simulation*, vol. 13, no. 7, pp. 1353–1360, 2008.
- [26] D. Pal and H. Mondal, “Influence of temperature-dependent viscosity and thermal radiation on MHD forced convection over a non-isothermal wedge,” *Applied Mathematics and Computation*, vol. 212, no. 1, pp. 194–208, 2008.
- [27] R. Kandasamy and I. Muhaimin, “Scaling transformation for the effect of temperature-dependent fluid viscosity with thermophoresis particle deposition on MHD-free convective heat and mass transfer over a porous stretching surface,” *Transport in Porous Media*, vol. 84, no. 2, pp. 549–568, 2010.
- [28] G. Herdricha, M. Auweter-Kurtza, M. Fertiga, A. Nawaza, and D. Petkowa, “MHD flow control for plasma technology applications,” *Vacuum*, vol. 80, pp. 1167–1173, 2006.
- [29] M. A. Seddeek, A. A. Afify, and M. A. Hanaya, “Similarity solutions for steady MHD Falkner-Skan flow and heat transfer over a wedge by considering the effect of variable viscosity and thermal conductivity,” *Applications and Applied Mathematics*, vol. 4, pp. 301–313, 2009.
- [30] M. S. Alam, M. M. Rahman, and M. A. Sattar, “Effects of variable suction and thermophoresis on steady MHD combined free-forced convective heat and mass transfer flow over a semi-infinite permeable inclined plate in the presence of thermal radiation,” *International Journal of Thermal Sciences*, vol. 47, no. 6, pp. 758–765, 2008.
- [31] O. Aydin and A. Kaya, “MHD mixed convection of a viscous dissipating fluid about a permeable vertical flat plate,” *Applied Mathematical Modelling*, vol. 33, no. 11, pp. 4086–4096, 2009.
- [32] M. M. Rahman and K. M. Salahuddin, “Study of hydromagnetic heat and mass transfer flow over an inclined heated surface with variable viscosity and electric conductivity,” *Communications in Nonlinear Science and Numerical Simulation*, vol. 15, no. 8, pp. 2073–2085, 2010.
- [33] A. Aziz, “A similarity solution for laminar thermal boundary layer over a flat plate with a convective surface boundary condition,” *Communications in Nonlinear Science and Numerical Simulation*, vol. 14, no. 4, pp. 1064–1068, 2009.
- [34] H. F. Oztop and E. Abu-Nada, “Numerical study of natural convection in partially heated rectangular enclosures filled with nanofluids,” *International Journal of Heat and Fluid Flow*, vol. 29, no. 5, pp. 1326–1336, 2008.
- [35] H. Schlichting and K. Gersten, *Boundary Layer Theory*, McGraw-Hill, New York, NY, USA, 8th edition, 2000.
- [36] W. M. Kays and M. E. Crawford, *Convective Heat and Mass Transfer*, McGraw Hill, New York, NY, USA, 4th edition, 2005.
- [37] A. Ishak, “Similarity solutions for flow and heat transfer over a permeable surface with convective boundary condition,” *Applied Mathematics and Computation*, vol. 217, no. 2, pp. 837–842, 2010.

## Research Article

# Simulation of Evacuation Characteristics Using a 2-Dimensional Cellular Automata Model for Pedestrian Dynamics

**Liqiang Ji, Yongsheng Qian, Junwei Zeng, Min Wang, Dejie Xu, Yan Yan, and Shuo Feng**

*School of Traffic and Transportation, Lanzhou JiaoTong University, Lanzhou, Gansu 730070, China*

Correspondence should be addressed to Yongsheng Qian; [qianyongsheng@mail.lzjtu.cn](mailto:qianyongsheng@mail.lzjtu.cn)

Received 3 June 2013; Revised 4 August 2013; Accepted 4 August 2013

Academic Editor: Mohamed Fathy El-Amin

Copyright © 2013 Liqiang Ji et al. This is an open access article distributed under the Creative Commons Attribution License, which permits unrestricted use, distribution, and reproduction in any medium, provided the original work is properly cited.

In public places, the high pedestrian density is one of the direct causes leading to crowding and trample disaster, so it is very necessary to investigate the collective and evacuation characteristics for pedestrian movement. In the occupants' evacuation process, the people-people interaction and the people-environment interaction are sufficiently considered in this paper, which have been divided into the exit attraction, the repulsion force between people, the friction between people, the repulsion force between human and barrier, and the attraction of surrounding people. Through analyzing the existing models, a new occupant evacuation cellular automata (CA) model based on the social force model is presented, which overcomes the shortage of the high density crowd simulation and combines the advantages that CA has sample rules and faster calculating speed. The simulating result shows a great applicability for evacuation under the high density crowd condition, and the segregation phenomena have also been found in the bidirectional pedestrian flow. Besides these, setting isolated belt near the exit or entrance of underpass not only remarkably decreases the density and the risk of trample disaster but also increases the evacuation efficiency, so it provides a new idea for infrastructure design about the exits and entrances.

## 1. Introduction

In recent years, the large public activities have become very common, especially the large public collection that leads to severe clogging and crowding, which brings high risk of happening trample incidents and may result in huge casualty and property losses. According to the statistics, too many large-scale crowd trample disasters had happened constantly in the global range, such as the accident in the Beijing MiHong park in 2004 that led to 37 people dead and 15 people being injured, about 362 dead in the Hajj in 2006; in 2008, a temple of Indian Rajasthan happened trample tragedy, 147 dead and 55 being injured; in the electronic music carnival of the German city of Duisburg, about 21 dead and 500 being injured in 2010. The appearance of these calamities has made people pay more attention to the safety of public activities. Presently, China is in the period of society crisis: the population of city increases rapidly, the social activities' organizations are frequent, and the safety problems are urgently needed to be solved for the development of cities.

Accordingly, it is a critical subject to grasp the characteristics of occupant's crowding and evacuation and to find a more scientific people evacuation mode, which can help us seek new approaches of reducing the risk of emergency.

The pedestrian movement is more complex than vehicular flow for the reason that people are more flexible and intelligent than cars. Without the limit of "lanes," pedestrian movement is loose and free. Furthermore, the walkers are easily affected by others as well as the environment around, so the mutual interactions between people in the public places are regular, and they include homoplasmy and repulsion [1]. Take the following action of pedestrian as an example: it means that the latter pedestrian walks following the former one with a uniform speed and route. When a person walks in a crowd, he must keep a sufferable distance from surrounding people as much as possible in order to avoid mutual impact because it makes people psychologically uncomfortable and makes the walking speed slower. The differences between people and cars are that people's collisions are permissible and vehicles' are not. In addition, the movement of people

is also influenced by surrounding environment, lanes' conditions, and emergencies. All of these local and individual interactions, environmental and lanes' factors, and personal properties codetermine the pedestrian flow.

Recently, considerable research has been done on the study of pedestrian flow and has achieved a lot of constructive inclusions. The existing models studying human movement, including pedestrian flow and occupant evacuation, can be classified into two categories.

One is the microcosmic discrete model based on the traffic flow. The most widely used discrete models are CA and Gas-kinetic models [2, 3]. In [4–7], Nagatani et al. used Gas-kinetic model for some certain building structures like the large hall, bottleneck channel, and T-shaped channel to study how the structures influence the evacuation efficiency. Schadschneider et al. [8] provide an extensive overview of various aspects of pedestrian dynamics, focusing on evacuation processes, which reviews empirical results, discusses many modeling especially on cellular automata models, and presents some specific applications to safety analysis in public buildings. Reference [9] puts forward a new CA model which introduced the friction, and the repulsion considering the mutual function of people-people and people-environment. The authors of [10] only defined a probability function for route selecting and analyzed them, but the detailed mathematic equation of attraction and repulsion and their coefficients were not given. In [9], the attraction, the friction and the repulsion were added in their model, while the attraction produced by the motion directions of the ambient walkers was not considered, and the applicability for the high density crowding needs to be discussed since the walkers' routes selecting is not determined by individual's will but depends on the direction of pedestrian flows. Kirchner and Schadschneider [11] present simulations of evacuation processes using a recently introduced cellular automaton model for pedestrian dynamics which applies a bionics approach to describe the interaction between the pedestrians using ideas from chemotaxis. Helbing et al. [12] performed experiments for corridors, bottleneck areas, and intersections to test simulation models of pedestrian flows, and the result shows that the geometric boundary conditions are not only relevant for the capacity of the elements of pedestrian facilities but they also influence the time gap distribution of pedestrians, indicating the existence of self-organization phenomena.

While the other continuous flow model is based on the fluid dynamics, the most famous continuous model is the social forces model which is proposed by Helbing et al. [13, 14] and focused on the interaction of people-people and people-environment. Yang et al. [10, 15] present an occupant evacuation and movement CA model and study the self-organization phenomena and phase transition. Burstedde et al. [16] propose a two-dimensional cellular automaton model to simulate pedestrian traffic and show that the introduction of such a floor field is sufficient to model collective effects and self-organization encountered in pedestrian dynamics, for example, lane formation in counter flow through a large corridor. Wen et al. [17] proposed a pedestrian evacuation model which combined the motion mode of the robot and the theory of CA. A modified dynamic cellular automata model

is proposed to simulate the evacuation of occupants from a room with obstacles which takes into account some factors that play an important role in an evacuation process, such as human emotions and crowd density around the exits [18]. Cao and Shan [19] propose a new method to estimate the stock return and use boredom distribution to denote the final stock return which can reflect the features of technical patterns and investors' heterogeneity simultaneously. Gauthier [20] introduces a new class of derivative products that can hedge this risk which considers the hedging of the risk related to the cost of suboptimal entry or exit.

In a word, most of the research made use of the social forces model and the CA model separately. Although [9, 10] integrated the advantages of the two kinds of models, it was not perfect to some extent. In this paper, we introduce a new CA model for pedestrian evacuation and simulate the evacuation process of a plaza with one exit and a bidirectional channel, and we also presume that a trample accident happens in the process when the density of crowd is in a high level. After setting the isolated belt in the exit and the entrances of the channel, the causality in the accident sharply decreases.

## 2. Establishment of the CA Model

*2.1. Hypothesis.* The model in this paper is described in the two-dimensional plane system. The underlying structure is a  $L \times L$  cell grid, where  $L$  is the system size. Each cell can either be empty or occupied by exactly one pedestrian. The size of a cell corresponds to approximately  $1/3 \text{ m} \times 1/3 \text{ m}$ . This space takes the applicability of the model for the high density crowd seriously. According to [19], the human's body can show the deformation and compression because of the pressure; the density of the crowd is likely to reach 8 persons per square meter in limited cases. In [20], the most tolerable density of our country's crowd is 9 persons per square meter at an extreme situation after a precise calculation. That is the reason why most models do not accurately simulate the evacuation process.

The neighborhood selection of CA is pivotal as each cell's state depends on other cells in its field. The Moore type neighborhood is adapted in our model and its radius is two cells. The motion direction of pedestrian in Figure 1 shows that there are forward walkers moving from their own cells to the upper cells, the top right walkers moving to top right cells, and so on. Empirically, the average velocity of a forward pedestrian is about  $1 \text{ m/s}$ ; the speed of the right and left walkers is also  $1 \text{ m/s}$  while the backward walkers' is  $1 \text{ m/s}$  and the others' is  $\sqrt{2} \text{ m/s}$ .

*2.2. Update Rules.* The update is synchronous for all pedestrians; each pedestrian can move only one cell per time-step. In the update, two problems, that is, the route choice and the conflict occurring when more than one pedestrian vies for a cell, will be solved. Our model has presumed that a cell must be occupied by one person, so we adopt roulette choosing method to confirm who can move to the aim cell, and others stay in their own primary cells.

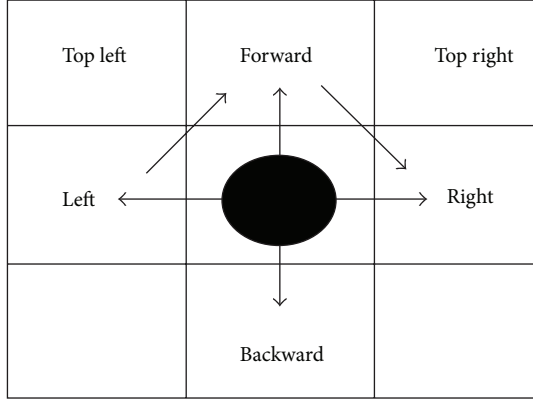


FIGURE 1: The motion direction of walkers.

The route choice is a significant issue, in our model, we introduce the approximate concept of the social forces and take the exit attraction, the repulsion, the friction, the repulsion force between human and barrier, and the attraction of surrounding people as objects codetermin the route choice. The definitions are as follows.

Firstly, the concept of the “floor field” is described to show the exit attraction, that is, each occupant is given a grid map, on which each cell has a degree of attractive force. For example, the exits have the greatest degree of attractive force during emergency evacuation. The math expression below is defined:

$$E = \begin{cases} E_0 & \exp \left\{ -\min \left[ \sqrt{(x_i - x_0^m)^2} + \sqrt{(y_i - y_0^m)^2} \right] \right\}, \\ (x_i, y_i) & \text{is not barrier} \\ 0, & \text{is barrier,} \end{cases} \quad (1)$$

where  $E_0$  is the maximum of the attraction,  $(x_{ij}, y_{ij})$  expresses the coordinates of the cell  $(i, j)$ ,  $(x_0^m, y_0^m)$  is the coordinates of exits, and the total number of exits is  $m$ .

The repulsive force between people-people and people-barrier is introduced when the distance of people-people or people-barrier (like wall) reaches a little value; at this time, in order to avoid the collision and have a enough free space, walkers stay away from other walkers and barriers. The formula of the repulsions is

$$R_{ij}(t) = A \exp \left[ \frac{r_{ij} - d_{ij}}{B} \right], \quad (2)$$

where  $A$  indicates the interactive intensity,  $B$  expresses the range of repulsion,  $r_{ij}$  denotes the radius sum of two people and  $d_{ij}$  shows the distance between two people or people-barrier. Besides, we define a repulsive coefficient to embody the different collision effects since the dissimilar collision can result in a different damage. That is,

$$P_r = \frac{1 - e^{-\alpha}}{1 + e^{-\alpha}}, \quad (3)$$

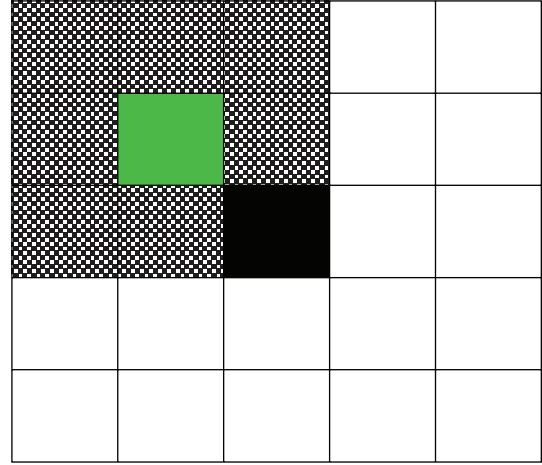


FIGURE 2: The possible calculating neighbors of an occupant.

where  $\alpha \in [0, \infty]$  is rigidity coefficient indicating the hurt degree caused by barriers and people.

The friction between two occupants or between occupant and barrier is considered when the distance between them is too small because the influence of friction is often much stronger than the repulsive forces' in a high density. The simple equation is given as

$$F_{ij(z)} = k\theta\varphi(z), \quad (4)$$

where  $k$  is a constant and  $\alpha$  is rigidity coefficient; consider the following:

$$\varphi(z) = \begin{cases} z, & z \geq 0, \\ 0, & z < 0, \end{cases} \quad \text{if } z \geq 0, \quad (5)$$

that is to say, the sum distance between two occupants is larger than the sum radius between them, and two occupants collide, if  $z < 0$ , that is the value is zero;  $\theta$  is friction coefficient according to the impacted objects' roughness.

The occupant-direction-attractive force  $D_{ij}$ : in the process of evacuation, the “follow” phenomena are often observed, which means that occupants tend to follow the movement of the majority.  $D_{ij}$  describes the influence of the direction that most occupants have taken around the cell. In the model, the walkers may choose the same moving direction as most people have taken, this force is defined as

$$D_{ij} = \beta N^2, \quad (6)$$

where  $\beta$  is the influencing factor and  $N$  is the total number of people within his neighborhood who choose the same moving direction.

Through analyzing the forces, the final following expression is defined to identify the occupant route choice:

$$T_{ij} = \exp(-R_{ij}) \exp(-F_{ij}) \exp(D_{ij}) E. \quad (7)$$

Considering that the friction and the repulsion have a hindering effect to walker's movement, while the exit

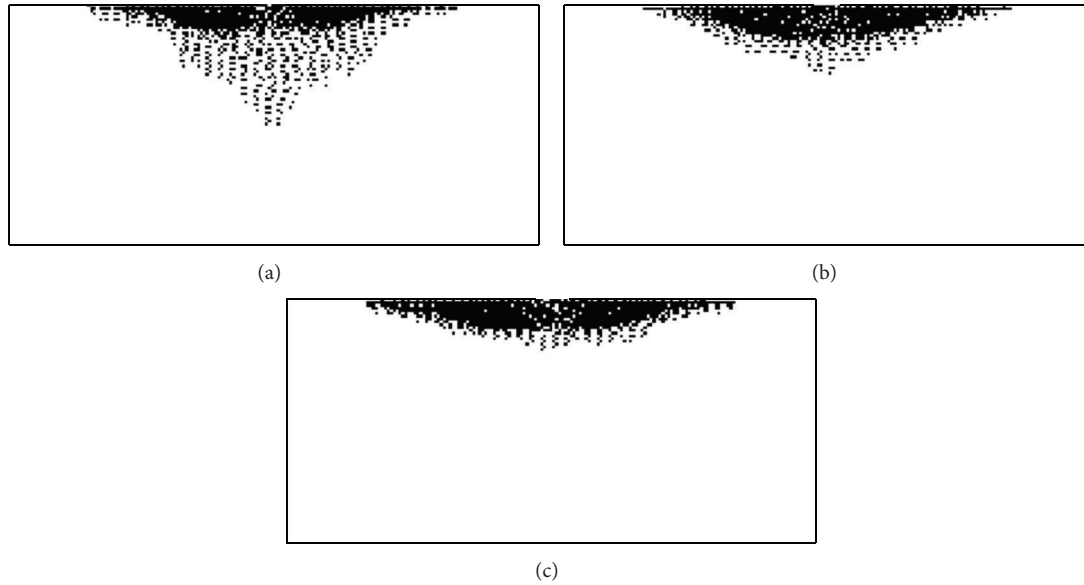


FIGURE 3: Simulations of evacuation in a stadium.

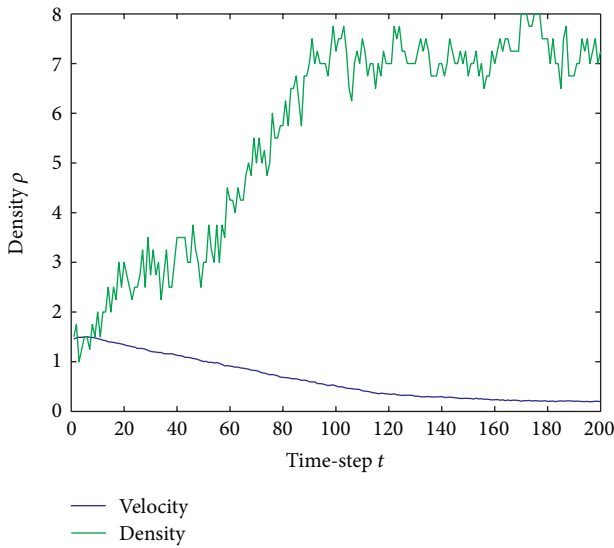


FIGURE 4: Velocity-time relation and density-time relation.

attraction and the occupant-direction- attractive force are beneficial to movement,  $R_{ij}$  and  $F_{ij}$  are negative and  $D_{ij}$  and  $E$  are positive. When a man chooses his route, the adjacent grid with a maximum attraction  $T_{ij}$  is selected as his next time-step aim grid because it is the most favorable one for him.

Figure 2 shows the potential aim grids and calculating neighbors; the black grid indicates a man, the green grid is one of his possible aim grids for next time-step; if it is unoccupied, we view it as the core and calculate its attraction value  $T_{ij}$  according to his seven neighbors except the black; otherwise, the value  $T_{ij}$  equals zero. If a possible grid's value  $T_{ij}$  is a maximum compared with other possible neighbors described in Figure 1, it is chosen as its aim grid.

In a word, the update rules are summarized as follows:

- (1) each occupant chooses another cell near him as his aim grid, according to the state of his neighborhood and the route-choice rules;
- (2) because one cell can only be occupied by one person at a time-step in our model, the conflict occurs when more than one person vies for a cell. In this situation, we adopt roulette choosing method to confirm who can move to the aim cell. The others have to stay at their origin position;
- (3) after arriving at aim cell, the occupant will identify a new attractive-force-degree distribution on his map based on new environment and select his next aim cell;
- (4) the update is synchronous for all occupants, when all updates end and turn to (1) for the next update.

### 3. Simulations and Results

**3.1. The Simulation of Evacuation for a Stadium.** In the simulations, we assume a rectangular stadium with a sole exit, and its size is 60 m × 30 m; the width of the exit is 2.7 m. The rigidity coefficient  $\alpha = 1$  (repulsion between people-people),  $\alpha = 2$  (repulsion between people-barrier), the friction coefficient  $\theta = 0.1$  (friction between people-people), and  $\theta = 0.5$  (friction between people-barrier). There are 1200 initial walkers in the stadium, and they are distributed randomly on the square lattice. Figure 3 shows the simulations of the occupant evacuation process.

Figure 3 shows the typical process of evacuation, and their separate corresponding time-steps is  $t = 100, 150$ , and  $200$ ; the practical corresponding time is  $t = 33$  s,  $20$  s, and  $67$  s. We can clearly observe the basic evacuation dynamics phenomena from the plots, including arching and stagnation

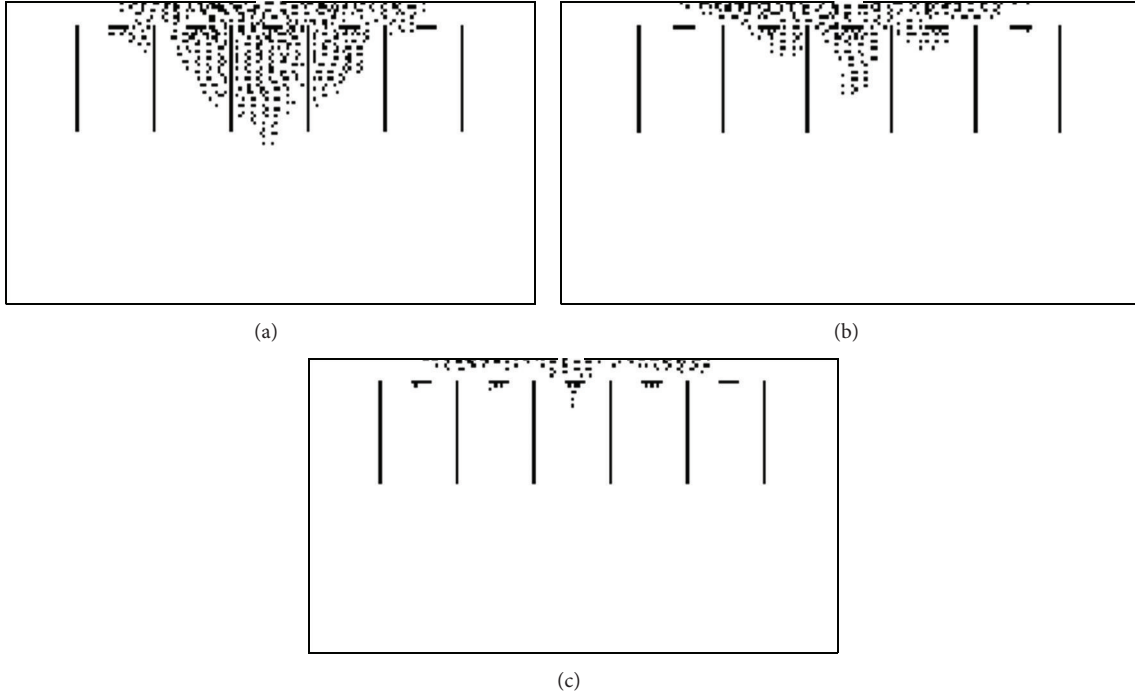


FIGURE 5: The simulation of evacuation process for a stadium setting the isolated belts.

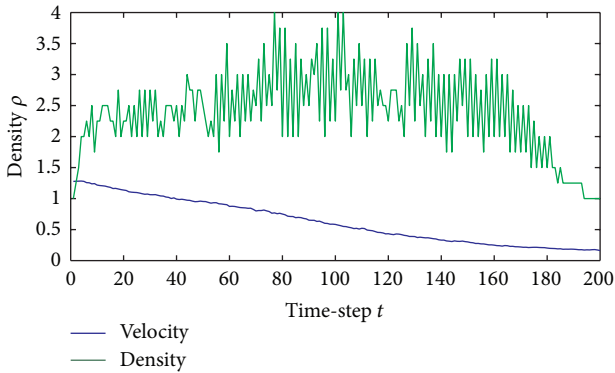


FIGURE 6: Velocity-time relation and density-time relation.

phenomenon; too many people assemble close to the door and form a serious blocking state, and there is too little space to move or even no free space to move, of course these are tallied with the actual situation.

Figure 4 shows the relation between walking velocity and time-steps and the relation between density and time-steps. The velocity is the average value that is calculated by the sum velocity of walkers in the range of  $4\text{ m}^2$  nearby the exit. In Figure 4, at the starting moment, the average speed approaches the maximum  $1.41\text{ m/s}$ ; the density of crowd has a small value which is about  $1.5\text{ m}^2/\text{per man}$ , so there is a large free space for pedestrians to walk. After a brief time, the density becomes higher and higher with the passage of time, which increases from about  $0.67\text{ people/m}^2$  to about

$7\text{ people/m}^2$ , while, at this stage, the moving speed decreases gradually from the maximum to about  $0.2\text{ m/s}$ , so we can conclude that the moving speed of a crowd depends on the crowd density, but not the individual speed, the higher crowd density, and the slower moving speed; when the density comes to the limit value (here it is 7 or 8 people per square meter), the moving speed comes to zero; this inclusion is consistent with [21].

In the above simulations, we find that the crowd density reaches  $7\text{ people/m}^2$ , and its moving speed reaches  $0.2\text{ m/s}$ . If people stay for a long time in a higher density crowd which will induce some physiological uncomfortableness, such as dyspnea, hypoxia of the heart and brain, and crowd panic, this uncomfortableness is easy to induce the trample disaster; therefore, we assume that a trample disaster happens nearby the exit once the density of crowd is over 6 people per square meter and the number of fatalities is noted at the same time. Through simulating the above evacuation using the same parameters, we get that the total number of casualties is 28 people at 100 time-steps, 71 people at 150 time-steps, and 122 people at 200 time-steps. According to this circumstance, some isolated belts are set to prevent the emergencies happening. The results are as follows.

Figure 5 shows the typical process of evacuation process, and their separate corresponding time-steps is similar to Figure 3. The isolated belts setting shows in the graphs, the distance between two vertical belts is  $8\text{ m}$ , and the distance between vertical belts and transverse belts is  $2\text{ m}$  of walking. In Figure 5, we can also observe the arching phenomena, but there are some differences compared with Figure 4; obviously, the number of the rest of evacuation pedestrians is palpable

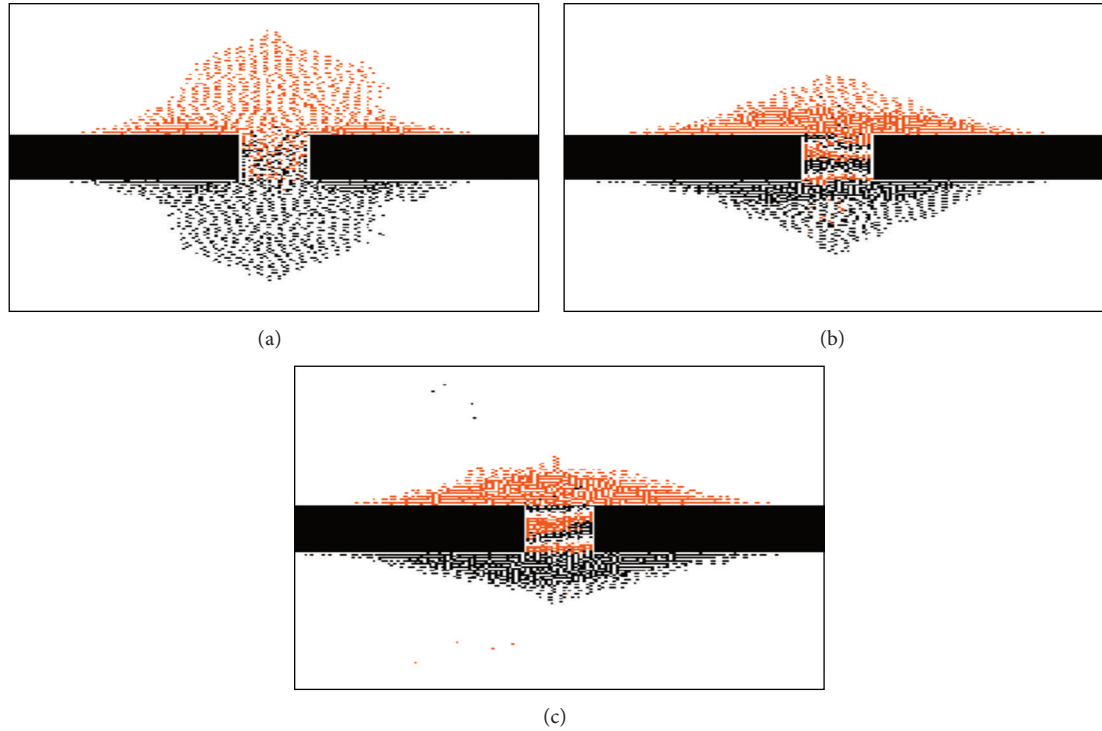


FIGURE 7: Simulations of evacuation for a bidirectional underpass.

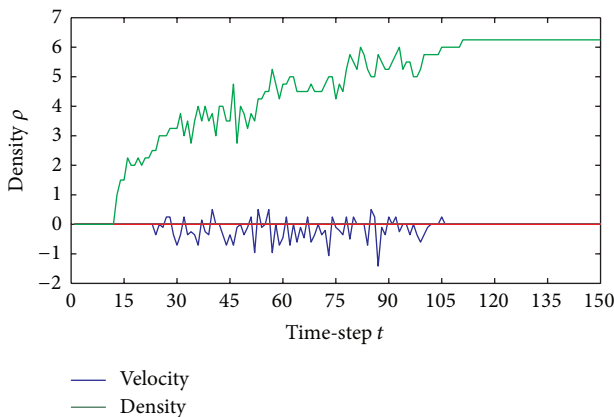


FIGURE 8: Velocity-time relation and density-time relation of simulation for the underpass.

fewer than that in Figure 3 at the same simulation time-steps, this sufficient improves that the moving speed is more faster.

Figure 6 shows the relation between walking velocity and time-steps and the relation between density and time-steps. In the graph, the density of crowd increases rapidly to 2–2.5 people/m<sup>2</sup> with the passage of time, and the speed gradually decreases to 1.3 m/s. With the further passage of time, the density does not increase greatly and its value stays at 3 people/m<sup>2</sup> for a long time until 180 time-steps; from then on, the density starts to decrease because most people have evacuated and the people in the density statistical area descend. Form the analysis, we know that setting isolated

belts can advance the evacuation efficiency substantially and decrease the crowd density, so the risk of accident happening is weakened to a great extent.

*3.2. The Simulation of Evacuation for a Bidirectional Underpass.* This paper also simulates an evacuation process for a bidirectional underpass whose length is 10 m and width is 8 m. At the initial moment, there are 1200 pedestrians distributed randomly on the bilateral 2-dimensional planes of the underpass.

Figure 7 shows the simulations of evacuation process for a bidirectional underpass, and their separate corresponding time-steps are  $t = 50, 100$ , and  $150$ ; the red grid points represent walkers who pass through the underpass from upper plane to under plane, while the black ones are just contrary. In Figure 7(a), pedestrians move to the entrances of the underpass at start evacuation moment, and form a typical arching, in Figure 7(b), the crowd density ascends furthermore, and “segregation phenomena” appears, and a steady jam phase forms inside the underpass. We can see that people separate into three blocking layers, and a few people in the heterogeneous directional crowd have passed the underpass. The reasons of the “segregation phenomena” have two aspects, one is that the heterogeneous pedestrians have no consciousness to prevent collisions between other people; another is the following action which incurs more people to join the clogging. In Figure 7(c), the layer phenomenon is more obvious, and the more density of the crowd is, the more congestion is produced.

Figure 8 shows the velocity-relation and density-time relation of simulations for the underpass. At the start moment

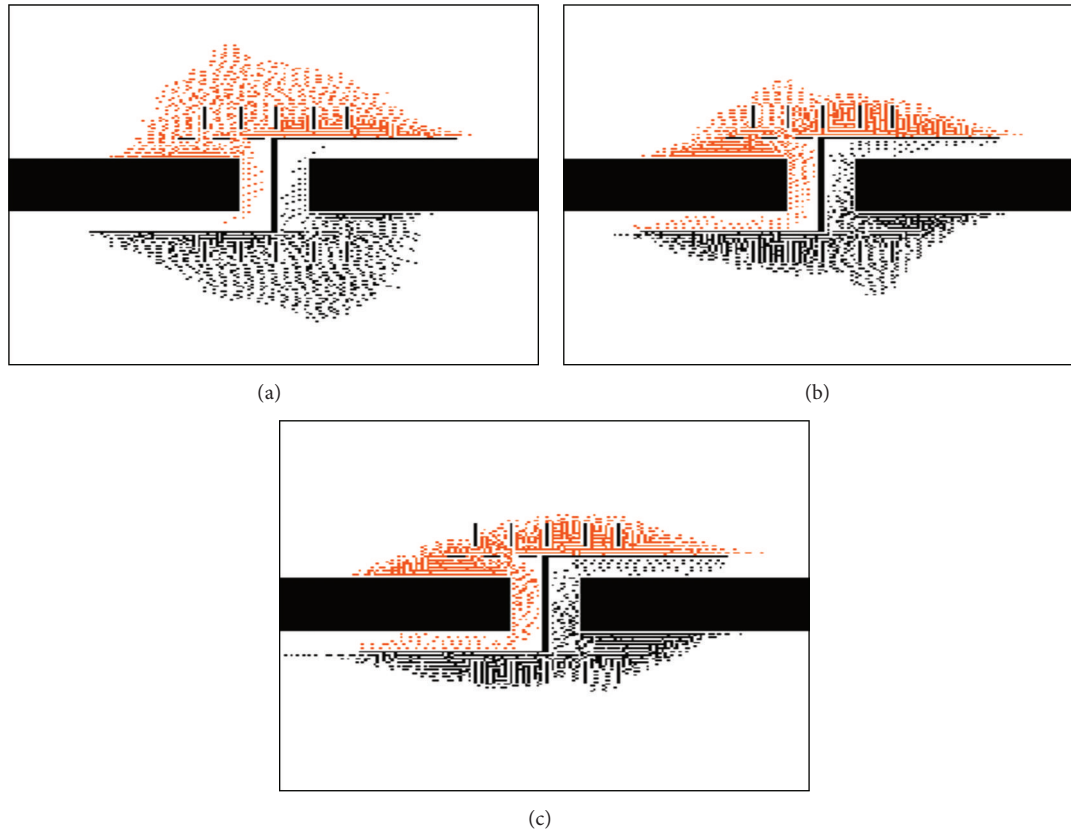


FIGURE 9: Simulations of evacuation for a bidirectional underpass after setting isolated belts.

of simulations, the density and the speed of crowd inside the underpass are zero, because the initial conditions assume that there are no pedestrians in the underpass. After a period, walkers move into the underpass, and the density of crowd ascends gradually; at the moment of 110 time-steps, the density stays at  $6.2 \text{ people/m}^2$  and stays in this value for the rest of the time. The coming of this state is there is a steady “layer blocking” has formed and the walkers have to stay in their original positions. We see from Figure 8 that the density increases with the increase of time-step, and the velocity has the same trend. However, the variation of speed at the density of  $4.5 \text{ people/m}^2$  is larger, which will increase the risk of conflict and interference between pedestrians. So, in the simulation, we presume that a crowding accident happens when the density is over  $4.5 \text{ people/m}^2$ ; the number of casualties are 0, 3; and 4 people at the time-steps 50, 100, and 150. We assume that the walkers’ speed of red grid points is negative, while the walkers’ speed of black ones is positive, so the sum of these two speeds counteracts each other and very small. At the start moment, the speed is zero because there is no one in the underpass. After a period, the walkers move into the underpass, but the density is still very small, and the summary speed counteracts to zero. When the density increases to about  $2 \text{ people/m}^2$ , the heterogeneous directional walkers start to interact and the mutual avoiding actions and surpassing actions appear,

which lead to the speed fluctuated at zero. After the time-steps of 110, the speed stays at zero because of the blocking phase. The tramper disaster happened in the electronic music carnival of the German city of Duisburg which was similar to our simulations.

In order to prevent the occurrence of blocking phrase, we also set the isolated belts at the entrances of the underpass.

Figure 9 shows the pedestrians’ evacuation process of the bidirectional underpass; the parameters are similar to the above instance. The setting of isolated belts displays in the plots; the full isolated belt is placed at the center of the tunnel; we design that all pedestrians walk by the right then turn right after passing the underpass and leave the system. In the figures, we can see a lower density outside the tunnel compared with Figure 7 as the isolated belts restrict the movements of walkers; the density of people inside the tunnel is more lower and there is no disturbance for bidirectional walkers; therefore, the number of walkers passing the tunnel is much more than the number of isolated belts, and the evacuation efficiency is advanced greatly.

#### 4. Conclusions

In this paper, a cellular automata model is presented to simulate the two-dimensional pedestrian movement. Based on the characteristic of pedestrian movement and the social

forces model, we have established a set of rules for route choice in pedestrian movement. The differences compared with previous research are that five kinds of “forces” are introduced to describe these effects, and the detailed expressions are given as well, analyzing the evacuation characteristics results of entrance and exit with isolated belts and without isolated belts. Using these behavioral rules and artificial instances, evacuation simulations is operated and emergency accidents are studied in our research. These simulations have improved the good applicability of our model and recurred the evacuation processes including crowding, blocking, and arching phenomena. In the simulations for a bidirectional underpass, the “layer blocking” phenomenon is found; it is a very important factor for crowding and clogging.

Besides, in order to prevent the occurrence of emergency for a high density crowd, we set the isolated belts for the exits and the entrances of the underpass and simulate the same instances; the results reveal that the setting of isolated belts can decrease the density of crowd and increase the evacuation efficiency remarkably. These conclusions are hopeful to monish the risk of crowd tramper disaster and prove some references for designer.

## Acknowledgments

The authors wish to thank the references for his helpful comments and suggestions for improvement. This paper is supported by the Chinese State Social Science Fund Project (11CJY067), Chinese Ministry of Education Humanities and Social Sciences project (10YJA630126), and Natural Science Foundation of Gansu province (1107RJYA070, 1208RJZA164).

## References

- [1] J. J. Fruin, *Pedestrian Planning and Design*, Elevator World Inc., Mobile, Ala, USA, 2nd edition, 1987.
- [2] V. J. Blue and J. L. Adler, “Cellular automata microsimulation for modeling bi-directional pedestrian walkways,” *Transportation Research B*, vol. 35, no. 3, pp. 293–312, 2001.
- [3] S. Hoogendoorn and P. H. L. Bovy, “Gas-kinetic modeling and simulation of pedestrian flows,” *Transportation Research Record*, vol. 1710, pp. 28–36, 2000.
- [4] Y. Tajima and T. Nagatani, “Clogging transition of pedestrian flow in T-shaped channel,” *Physica A*, vol. 303, no. 1-2, pp. 239–250, 2002.
- [5] Y. Tajima, K. Takimoto, and T. Nagatani, “Scaling of pedestrian channel flow with a bottleneck,” *Physica A*, vol. 294, no. 1-2, pp. 257–268, 2001.
- [6] T. Nagatani, “Jamming transition in the traffic-flow model with two-level crossings,” *Physical Review E*, vol. 48, no. 5, pp. 3290–3294, 1993.
- [7] T. Nagatani, “Dynamical transition and scaling in a mean-field model of pedestrian flow at a bottleneck,” *Physica A*, vol. 300, no. 3-4, pp. 558–566, 2001.
- [8] A. Schadschneider, W. Klingsch, H. Klupfel, T. Kretz, C. Rogsch, and A. Seyfried, “Evacuation dynamics: empirical results, modeling and applications,” in *Encyclopedia of Complexity and Systems Science*, pp. 3142–3176, Springer, Berlin, Germany, 2009.
- [9] A. Kirchner, K. Nishinari, and A. Schadschneider, “Friction effects and clogging in a cellular automaton model for pedestrian dynamics,” *Physical Review E*, vol. 67, no. 5, Article ID 056122, 10 pages, 2003.
- [10] L. Yang, J. Li, D. Zhao, W. Fang, and W. Fan, “A microcosmic discrete occupant evacuation model based on individual characteristics,” *Science in China. Series E*, vol. 47, no. 5, pp. 608–615, 2004.
- [11] A. Kirchner and A. Schadschneider, “Simulation of evacuation processes using a bionics-inspired cellular automaton model for pedestrian dynamics,” *Physica A*, vol. 312, no. 1-2, pp. 260–276, 2002.
- [12] D. Helbing, L. Buzna, A. Johansson, and T. Werner, “Self-organized pedestrian crowd dynamics: experiments, simulations, and design solutions,” *Transportation Science*, vol. 39, no. 1, pp. 1–24, 2005.
- [13] D. Helbing and P. Molnár, “Social force model for pedestrian dynamics,” *Physical Review E*, vol. 51, no. 5, pp. 4282–4286, 1995.
- [14] D. Helbing, I. Farkas, and T. Vicsek, “Simulating dynamical features of escape panic,” *Nature*, vol. 407, no. 6803, pp. 487–490, 2000.
- [15] L. Yang, W. Fang, J. Li, R. Huang, and W. Fan, “Cellular automata pedestrian movement model considering human behavior,” *Chinese Science Bulletin*, vol. 48, no. 16, pp. 1695–1699, 2003.
- [16] C. Burstedde, K. Klauck, A. Schadschneider, and J. Zittartz, “Simulation of pedestrian dynamics using a two-dimensional cellular automaton,” *Physica A*, vol. 295, no. 3-4, pp. 507–525, 2001.
- [17] W. G. Wen, H. Y. Yuan, and W. C. Fan, “A cellular automaton model for pedestrian dynamics based on the behavior of robot,” *Chinese Science Bulletin*, vol. 51, no. 23, pp. 2818–2822, 2006.
- [18] L. E. Aik and T. W. Choon, “Simulating evacuations with obstacles using a modified dynamic cellular automata model,” *Journal of Applied Mathematics*, vol. 2012, Article ID 765270, 17 pages, 2012.
- [19] G. Cao and D. Shan, “The effect of exit strategy on optimal portfolio selection with birandom returns,” *Journal of Applied Mathematics*, vol. 2013, Article ID 236579, 6 pages, 2013.
- [20] L. Gauthier, “Hedging entry and exit decisions: activating and deactivating barrier options,” *Journal of Applied Mathematics and Decision Sciences*, vol. 6, no. 1, pp. 51–70, 2002.
- [21] Q. M. Hu, W. N. Fang, and Y. Q. Jia, “The simulation of crowding and clogging for pedestrian crowd dynamics,” *Science in China. Series E*, vol. 39, pp. 1034–1038, 2009.

## Research Article

# Study on the Convective Term Discretized by Strong Conservation and Weak Conservation Schemes for Incompressible Fluid Flow and Heat Transfer

Peng Wang, Bo Yu, Jianyu Xie, Yu Zhao, Jingfa Li, and Qianqian Shao

National Engineering Laboratory for Pipeline Safety, Beijing Key Laboratory of Urban Oil and Gas Distribution Technology, China University of Petroleum, Beijing 102249, China

Correspondence should be addressed to Bo Yu; yubobox@vip.163.com

Received 25 March 2013; Accepted 11 August 2013

Academic Editor: Shuyu Sun

Copyright © 2013 Peng Wang et al. This is an open access article distributed under the Creative Commons Attribution License, which permits unrestricted use, distribution, and reproduction in any medium, provided the original work is properly cited.

When the conservative governing equation of incompressible fluid flow and heat transfer is discretized by the finite volume method, there are various schemes to deal with the convective term. In this paper, studies on the convective term discretized by two different schemes, named strong and weak conservation schemes, respectively, are presented in detail. With weak conservation scheme, the convective flux at interface is obtained by respective interpolation and subsequent product of primitive variables. With strong conservation scheme, the convective flux is treated as single physical variable for interpolation. The numerical results of two convection heat transfer cases indicate that under the same computation conditions, discretizing the convective term by strong conservation scheme would not only obtain a more accurate solution, but also guarantee the stability of computation and the clear physical meaning of the solution. Especially in the computation regions with sharp gradients, the advantages of strong conservation scheme become more apparent.

## 1. Introduction

In the 1980s, the conservation form and nonconservation form of the governing equation formally existed in the literature [1, 2]. Since then, the governing equations are clearly classified into these two different forms, and for the control volume, the different characteristics of these two forms of equations gradually drew the attention of researchers. Based on previous studies, the conservation form of the governing equation is superior to the non-conservation form in many aspects, for example: (1) in the control volume of limited size, only the conservation form could ensure that the conservation principles of variables are satisfied [3–5]; (2) in the calculation of flow problem involving shock wave, the obtained flow field is usually smooth and stable, employing the conservation form of the governing equation; while using the non-conservation equation might lead to unsatisfactory spatial oscillations in the upstream and downstream regions of the shock wave [6–8]; (3) when the conservation equation

is used in a body-fitted coordinate system, the conservative-ness of the governing equation can still be satisfied [9, 10]. More related research and applications are presented in the literature [11–18].

As a result, the conservation form of governing equation has been widely applied in the fields of computational fluid dynamics (CFD) and numerical heat transfer (NHT). In the compressible flow problems of aerodynamics, especially the flow containing shock wave, the conservation governing equation is usually expressed by first-order derivative equation system of the flux column vector, which is called strong conservation equation [1]. The convective flux in the strong conservation equation is regarded as a conservative variable. However, in the conservation equation employed in the incompressible fluid flow and heat transfer, the convective flux is the multiplication of primitive variables. In the aerodynamics field, when the governing equation is discretized by the finite volume method, strong conservation scheme is usually employed to deal with the convective flux

TABLE 1: Discretized expressions of the convective flux at the interface  $(\rho Au\phi)_e$ .

Discrete format	Weak conservation scheme	Strong conservation scheme	Condition
FUD	$\rho_e A_e u_e \phi_P$	$(\rho Au\phi)_P$	$u_e \geq 0$
	$\rho_e A_e u_e \phi_E$	$(\rho Au\phi)_E$	$u_e < 0$
SUD	$\rho_e A_e u_e \frac{3\phi_P - \phi_W}{2}$	$\frac{3(\rho Au\phi)_P - (\rho Au\phi)_W}{2}$	$u_e \geq 0$
	$\rho_e A_e u_e \frac{3\phi_E - \phi_{EE}}{2}$	$\frac{3(\rho Au\phi)_E - (\rho Au\phi)_{EE}}{2}$	$u_e < 0$
CD	$\rho_e A_e u_e \frac{\phi_P + \phi_E}{2}$	$\frac{(\rho Au\phi)_P + (\rho Au\phi)_E}{2}$	—
QUICK	$\rho_e A_e u_e \frac{3\phi_E + 6\phi_P - \phi_W}{8}$	$\frac{(3\rho Au\phi)_E + 6(\rho Au\phi)_P - (\rho Au\phi)_W}{8}$	$u_e \geq 0$
	$\rho_e A_e u_e \frac{3\phi_P + 6\phi_E - \phi_{EE}}{8}$	$\frac{(3\rho Au\phi)_P + 6(\rho Au\phi)_E - (\rho Au\phi)_{EE}}{8}$	$u_e < 0$

at interface as a whole, in order to guarantee the physical meaning of the numerical solution. While in the incompressible fluid flow and heat transfer field, the convective flux at interface is obtained by respective interpolation and subsequent product of relevant variables, which is called weak conservation scheme, correspondingly. The employment of weak conservation scheme is quite common in solving the incompressible fluid flow and heat transfer problems, and nevertheless, the applications of strong conservation scheme are rarely presented in the literature.

In order to yield a more reasonable discrete scheme of the convective term in the numerical computation of incompressible fluid flow and heat transfer, two common categories of the convection heat transfer problem are studied in this paper. Based on the discretization equation obtained by the finite volume method, the convective flux is discretized by strong and weak conservation schemes, respectively, and through the numerical results of cases, the advantages and disadvantages of these two different schemes are compared comprehensively and systematically in terms of accuracy, stability, and so on.

## 2. Numerical Method

It is noteworthy that the two discrete schemes of the convective term are derived from the finite volume method of the conservation governing equation, and thus, in the following text, the governing equations are all conservative and the discrete methods are all finite volume methods.

For the convenience of comparison and analysis without losing generality, the present paper takes the one-dimensional convection heat transfer problem as an example, and the governing equation of this problem can be written as follows:

$$\frac{\partial(\rho\phi)}{\partial t} + \frac{1}{A} \frac{\partial(\rho Au\phi)}{\partial x} = \frac{1}{A} \frac{\partial}{\partial x} \left( \Gamma A \frac{\partial\phi}{\partial x} \right), \quad (1)$$

where the second term on the left-hand side  $(1/A)(\partial(\rho Au\phi)/\partial x)$  is the convective term and its discretization is one critical

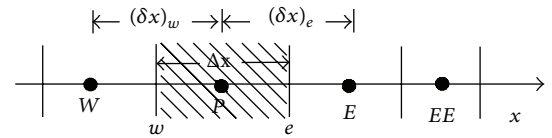


FIGURE 1: Sketch map of discrete grid.

key of the numerical computation. As mentioned above, in the numerical calculation of aerodynamics, strong conservation scheme is broadly employed to treat the convective flux  $\rho Au\phi$  as a conservative variable. On the other hand, in the calculation of incompressible fluid flow and heat transfer, using weak conservation scheme, the primitive variables  $\rho$ ,  $A$ ,  $u$ , and  $\phi$  are often discretized first and multiplied together to get the discretized convective term. For the sketch map of the discrete grid, the common expressions of the convective flux  $(\rho Au\phi)_e$  at the interface  $e$  with two different discrete schemes are shown in Table 1.

Through Table 1, with strong conservation scheme, the variable values of the convective flux at the interface are stored in the grid nodes rather than interpolate primitive variables at the interface. In the actual computation, this operation not only reduces the workload of interpolation to diminish the interpolation error, but also reduces the interface information storage to save memory.

In addition, the strong conservation scheme of the one-dimensional problem is also suitable for multidimensional issues. It is well known that in the field of CFD and NHT, the general governing equation can be expressed as follows:

$$\frac{\partial(\rho\phi)}{\partial t} + \text{div}(\rho\mathbf{U}\phi) = \text{div}(\Gamma_\phi \text{grad}\phi) + S_\phi. \quad (2)$$

When the convective term  $\text{div}(\rho\mathbf{U}\phi)$  is discretized by strong and weak conservation schemes, respectively, the discrete expressions in the  $x$  direction of the Cartesian coordinate system are the same with that in Table 1. And it needs to be noted that  $A_e = 1$ .

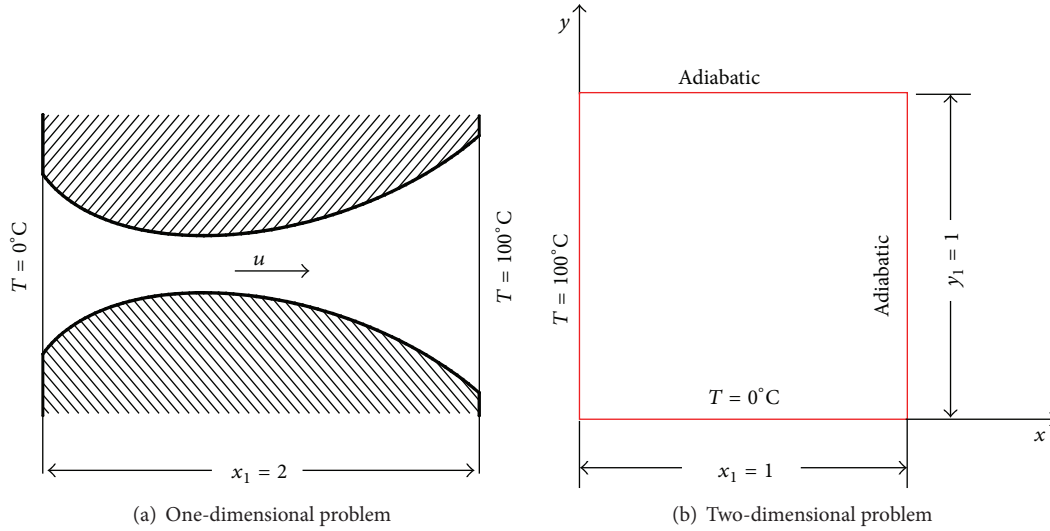


FIGURE 2: Boundary conditions of two categories of the problem.

### 3. Results and Analyses

In order to compare the differences between the two conservation schemes in terms of computation accuracy and stability, the present paper first compares the numerical results of two categories of convection-diffusion cases: (1) the one-dimensional convection heat transfer problem; (2) the two-dimensional convection heat transfer problem with constant cross-section. Subsequently, Taylor series are used to analyze the truncation errors of the discretization equation with the convective term discretized by strong and weak conservation schemes, respectively. Finally, the deviations of the numerical solutions are presented to compare the computation accuracy of these two schemes.

**3.1. Case Descriptions.** The physical model of the one-dimensional convection heat transfer problem (called “one-dimensional problem” for short, hereinafter) is shown in Figure 2(a). The cases of this category, CASE 1 and CASE 2 (the governing equations are shown as (1)), correspond to two situations which have large gradient and relatively small gradient of primitive variables, respectively. Similarly, the physical model of the two-dimensional convection heat transfer problem with constant cross-section (called “two-dimensional problem” for short, hereinafter) is shown in Figure 2(b). The cases of this category, CASE 3 and CASE 4 (the governing equations are shown as (2)), correspond to two situations which have large gradient and relatively small gradient of primitive variables, respectively.

The detailed boundary conditions of these two categories of the problem are presented in Figure 2, in which the left and right boundaries of the one-dimensional problem are of the first boundary condition, and the left and bottom boundaries of the two-dimensional problem are of the first boundary condition; meanwhile, the upper and right boundaries are of the second boundary condition. Table 2 shows the expressions of flow area and velocity distribution of the

TABLE 2: Flow area and velocity expressions of the one-dimensional problem.

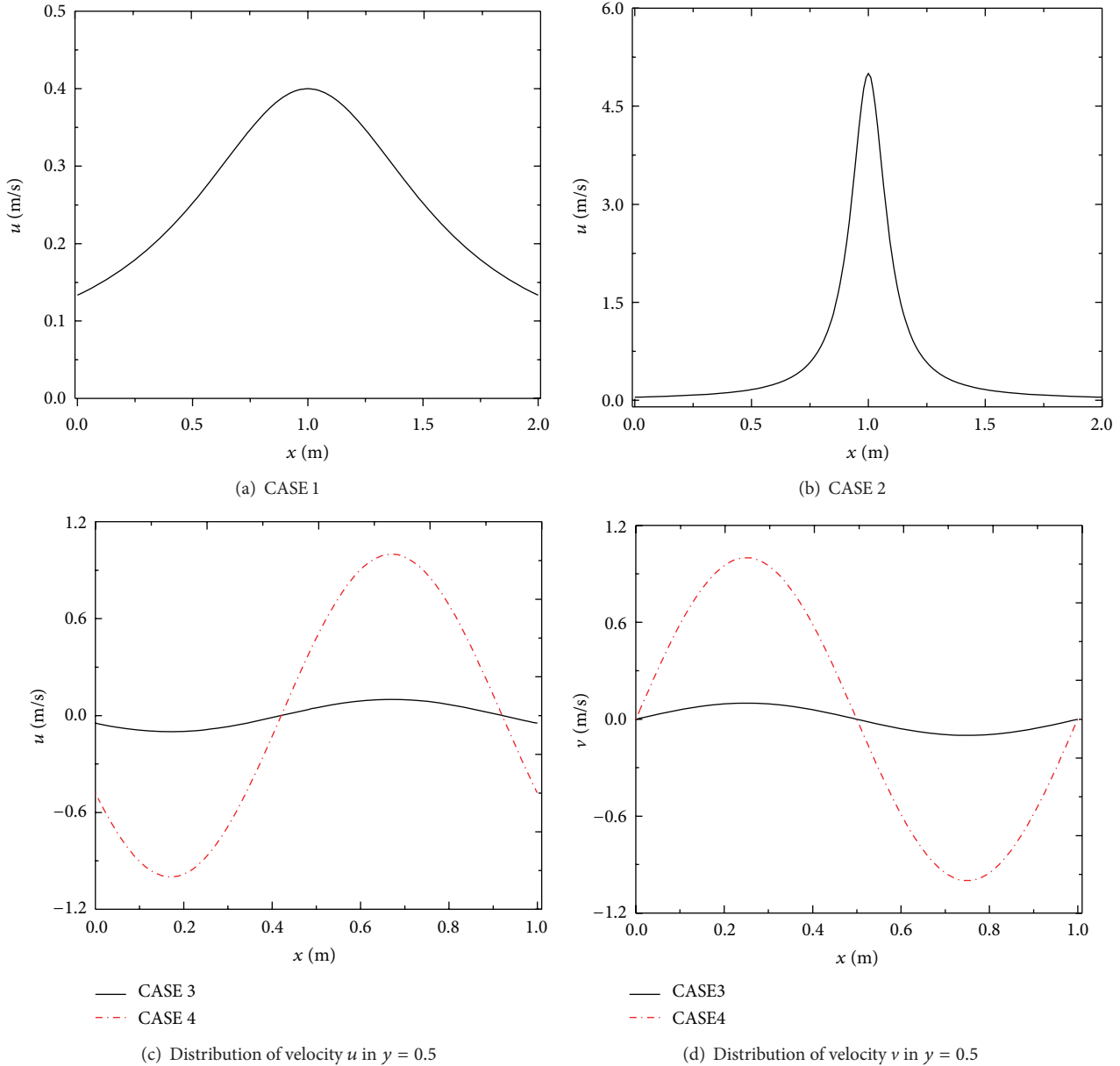
	Flow area	Velocity $u$
CASE 1	$A = -\sin(\pi x/2) + 1.5$	$u = 0.2/(-\sin(\pi x/2) + 1.5)$
CASE 2	$A = 4(-\sin(\pi x/2) + 1.01)$	$u = 0.05/(-\sin(\pi x/2) + 1.01)$

TABLE 3: Velocity expressions of the two-dimensional problem.

	Velocity $u$	Velocity $v$
CASE 3	$u = 0.1 \sin(2\pi(x + y))$	$v = -0.1 \sin(2\pi(x + y))$
CASE 4	$u = \sin(2\pi(x + y))$	$v = -\sin(2\pi(x + y))$

two one-dimensional cases. And the velocity profiles in the  $x$  direction of the two one-dimensional cases are given in Figures 3(a) and 3(b). In Table 3, there are the expressions of velocity distribution of the two two-dimensional cases. For direct display of the velocity distribution, Figures 3(c) and 3(d) depict the  $u$  and  $v$  velocity distributions in the position of  $y = 0.5$  along the  $x$  direction. It is noteworthy that in the four cases, densities and thermal conductivities are all set to be  $\rho = 1000 \text{ (kg/m}^3\text{)}$  and  $\Gamma = 100 \text{ W/(m} \cdot \text{°C)}$ , respectively.

Different kinds of uniform mesh are utilized for these four cases, and the grid number of CASE 3 and CASE 4 in the  $x$  and  $y$  directions is the same, that is,  $N_x = N_y$ . The convective term is discretized by weak conservation scheme and strong conservation scheme, respectively, and in the following text, these two schemes are referred to as Scheme 1 and Scheme 2. CD and QUICK formats are also employed to discretize the governing equation. The stable field of variable  $\phi$  is obtained by solving the discretized equation with explicit time marching method. And the numerical results indicate that all four cases achieve the grid-independent solutions when the grid number satisfies  $N_x = 200$ .

FIGURE 3: Velocity distribution along the  $x$  direction.

3.2. *Numerical Results.* As shown in Figure 4, the present paper first compares the solution of the two schemes on the sparse grid ( $N_x = 7$  for the one-dimensional problem and  $N_x = 30$  for the two-dimensional problem) with the grid-independent solution.

In Figure 4, Figures 4(a) to 4(d) show the temperature distribution along the  $x$  coordinate in CASE 1 and CASE 2 with CD and QUICK formats, and Figures 4(e) to 4(h) present the contour map of temperature field in CASE 3 and CASE 4 with CD and QUICK formats. It is found that on the sparse grid when the gradient of variables is relatively small, the solutions of these two schemes agree with the grid-independent solution very well. However, when the gradient becomes relatively large, the solution with strong

conservation scheme is obviously better than that with weak conservation scheme. It can be seen from Figures 4(b) and 4(d) that in CASE 2, when the convective term is discretized by weak conservation scheme, the solution would overshoot in the position of  $x = 1.0$ , and with the CD format, the oscillations are even more severe. In contrast, the solution of clear physical meaning can be obtained with strong conservation scheme. As shown in Figures 4(f) and 4(h), in the top right corner of the temperature contour map, the solution with weak conservation scheme deviates greatly from the grid-independent solution.

Through the above analyses, under the same computation conditions, when the primitive variables change slightly, the difference between the solutions of the two schemes is very

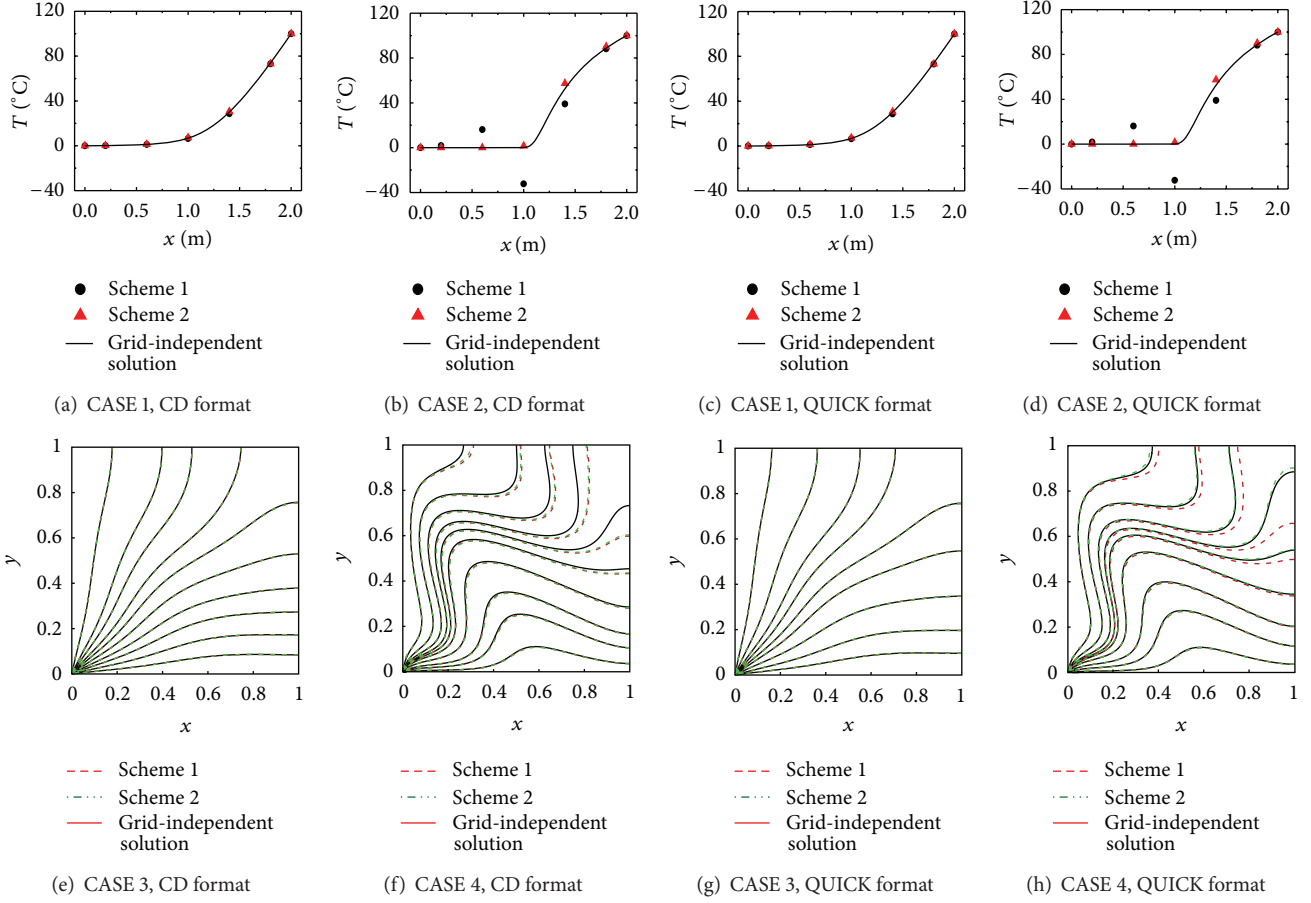


FIGURE 4: Comparison of different evaluations of the convective term.

small, but when there are sharp changes of variables, the superiority of high accuracy and stability with strong conservation scheme is apparently shown, and the corresponding solution is more likely to have clear physical meaning.

3.3. Accuracy Analysis. In order to further compare the accuracy difference of the numerical solutions with strong and weak conservation schemes, the present paper introduces Taylor series to analyze the truncation error of the same computation form obtained by discretizing the convective term with two different schemes. Taking the CD format of CASE 1 and CASE 2 as an example to explain the following.

Scheme 1:

$$\begin{aligned} & \frac{\rho_P + \rho_E}{2} \frac{A_P + A_E}{2} \frac{u_P + u_E}{2} \frac{T_P + T_E}{2} \\ &= \rho_e A_e u_e T_e + \rho_e A_e T_e \frac{1}{8} \frac{\partial^2 u}{\partial x^2} \Big|_e \Delta x^2 \\ & \quad + \rho_e u_e T_e \frac{1}{8} \frac{\partial^2 A}{\partial x^2} \Big|_e \Delta x^2 \\ & \quad + \rho_e A_e u_e \frac{1}{8} \frac{\partial^2 T}{\partial x^2} \Big|_e \Delta x^2 + o(\Delta x^3). \end{aligned} \quad (3)$$

Scheme 2:

$$\begin{aligned} \frac{(\rho AuT)_P + (\rho AuT)_E}{2} &= (\rho AuT)_e \\ & \quad + \frac{1}{8} \frac{\partial^2 (\rho AuT)}{\partial x^2} \Big|_e \Delta x^2 + o(\Delta x^3). \end{aligned} \quad (4)$$

The truncation errors of CD format obtained by the two schemes can be expressed as:

$$\begin{aligned} \epsilon^1 &= \rho_e A_e T_e \frac{1}{8} \frac{\partial^2 u}{\partial x^2} \Big|_e \Delta x^2 + \rho_e u_e T_e \frac{1}{8} \frac{\partial^2 A}{\partial x^2} \Big|_e \Delta x^2 \\ & \quad + \rho_e A_e u_e \frac{1}{8} \frac{\partial^2 T}{\partial x^2} \Big|_e \Delta x^2 + o(\Delta x^3), \end{aligned} \quad (5)$$

$$\epsilon^2 = \frac{1}{8} \frac{\partial^2 (\rho AuT)}{\partial x^2} \Big|_e \Delta x^2 + o(\Delta x^3). \quad (6)$$

Since the incompressible fluid flow satisfies the continuity equation, (6) can be further written as follows:

$$\epsilon^2 = (\rho Au)_e \frac{1}{8} \frac{\partial^2 T}{\partial x^2} \Big|_e \Delta x^2 + o(\Delta x^3). \quad (7)$$

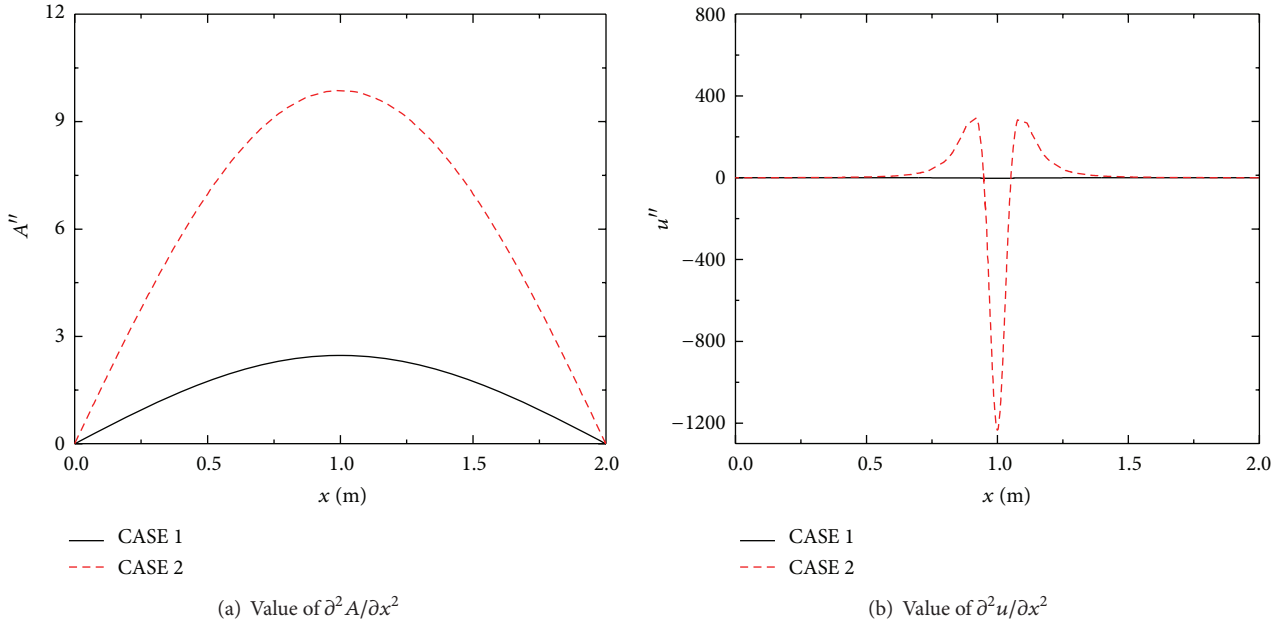


FIGURE 5: Values of  $\partial^2 A / \partial x^2$  and  $\partial^2 u / \partial x^2$  in CASE 1 and CASE 2.

Through comparing (5) and (6), the truncation error of weak conservation scheme contains  $\partial^2 A / \partial x^2$  and  $\partial^2 u / \partial x^2$ , while these two terms, respectively, reflect the changing degree of flow area and velocity. In order to further analyze the influence of  $\partial^2 A / \partial x^2$  and  $\partial^2 u / \partial x^2$  on the errors  $\varepsilon^1$  and  $\varepsilon^2$ , the values of  $\partial^2 A / \partial x^2$  and  $\partial^2 u / \partial x^2$  in one-dimensional cases are shown in Figure 5.

From Figure 5, the values of  $\partial^2 A / \partial x^2$  and  $\partial^2 u / \partial x^2$  in CASE 2 fluctuate more acutely than those in CASE 1, especially in the position of  $x = 1.0$ . The absolute value of  $\partial^2 u / \partial x^2$  in CASE 2 reaches as great as 1200, which is far larger than that in CASE 1. Correspondingly, comparing Figures 4(b) and 4(d), we can see that the abrupt change of velocity in CASE 2 with Scheme 1 appears exactly in the position of  $x = 1.0$ , and in the same position, the computation results of CASE 2 overshoot to make the solution not conform to the physical meaning. Hence, it is reasonable to conclude that in some cases, the values of  $\partial^2 A / \partial x^2$  and  $\partial^2 u / \partial x^2$  with weak conservation scheme have a serious effect on the numerical errors; however, there is no such problem with strong conservation scheme.

Based on the above analysis, the derivative of primitive variable is very small when the changing gradient is relatively small. When the values of the first two terms in (5) can be neglected compared with that of the third term, the truncation errors of the two different schemes are almost the same, and the two numerical solutions have no obvious difference. However, when the changing gradient is very large, the derivative of primitive variable becomes large, correspondingly. If the values of the first two terms in (5) are equal to or even greater than the value of the third term, it is obvious that  $\varepsilon^1 > \varepsilon^2$  and that there is a big difference between the numerical solutions of the two schemes.

Last but not least, in order to compare the calculation accuracy of the two different schemes quantitatively, the present paper defines the average absolute error and maximum absolute error as follows:

$$\text{average absolute error: } \varepsilon_a = \frac{1}{N_{\text{Grid}}} \sum_{n=1}^{N_{\text{Grid}}} |T_c - T_b|, \quad (8)$$

$$\text{maximum absolute error: } \varepsilon_m = \max(|T_c - T_b|).$$

Through (8), the average and maximum absolute errors of the four cases on different kinds of uniform mesh, in which the largest grid number is  $N_x = 200$  and the smallest one is  $N_x = 10$ , are calculated. And the numerical solutions on the grid  $N_x = 1000$  and  $N_x = 500$  are, respectively, regarded as the benchmark solutions of the one-dimensional and two-dimensional problems. It is worth pointing out that the grid number of the benchmark solution taken in this paper is much larger than the required grid number of obtaining the grid-independent solution; thus, it is feasible to use these numerical solutions to evaluate the average and maximum absolute errors of the two different schemes with grid numbers ranging from  $N_x = 10$  to  $N_x = 200$ . Additionally, the same conclusion can be obtained using CD or QUICK formats; thus, only the average and maximum absolute errors of the numerical solution employing QUICK format (as shown in Figures 6 and 7, resp.) are given to evaluate the computation accuracy. Furthermore, the ratios of the average absolute errors and those of the maximum absolute errors of the four cases employing QUICK format are presented in Figure 8.

From Figure 6, it is easily found that on the same grid, the average absolute errors of the numerical solutions with

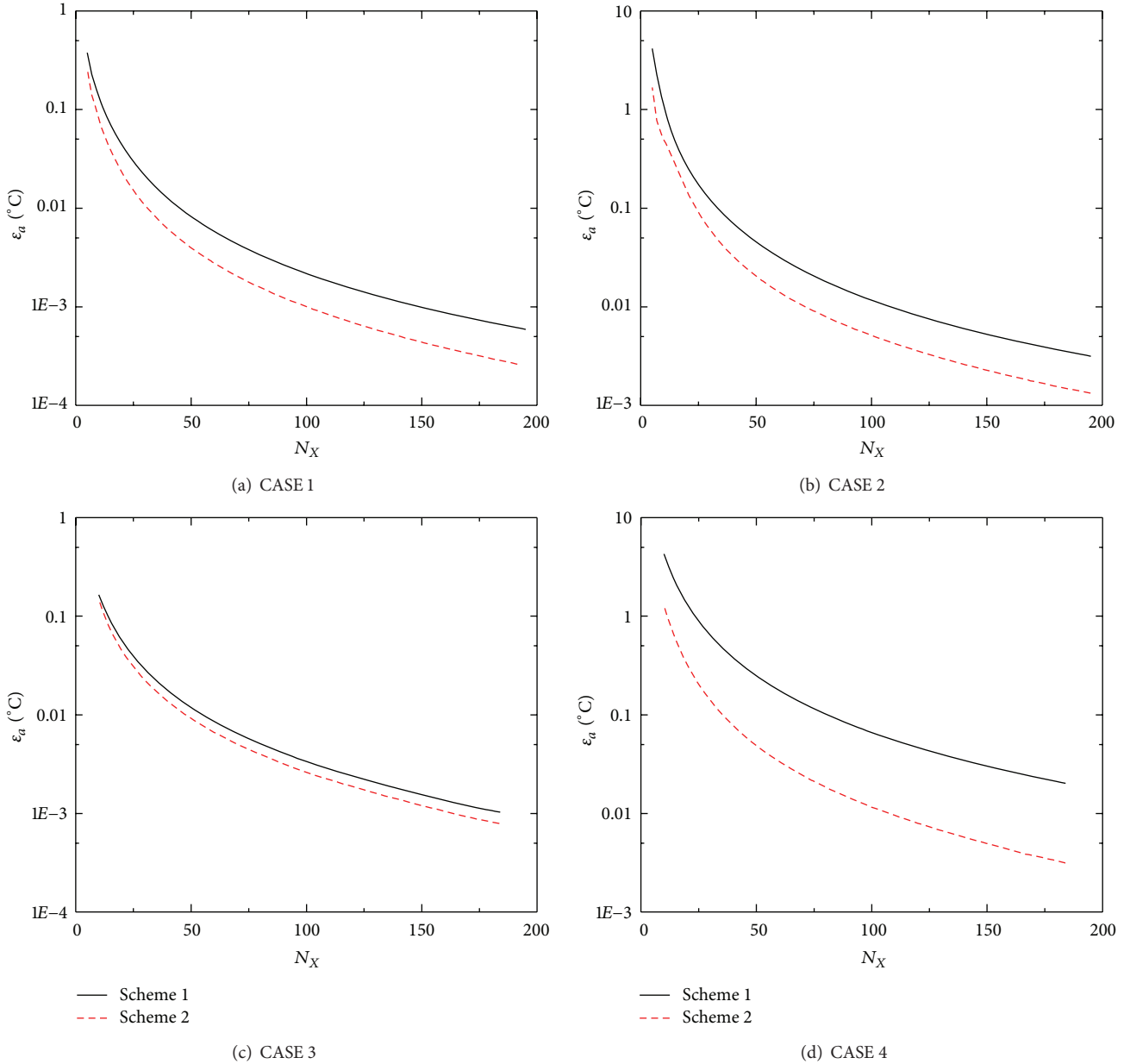


FIGURE 6: Average absolute error.

strong conservation scheme are all less than those with weak conservation scheme in the four cases.

As shown in Figure 7, when it comes to dealing with the one-dimensional problem, Scheme 2 is superior to Scheme 1, while in solving the two-dimensional problem, the performances of the two different schemes are basically the same. The reason why the results of CASE 3 and CASE 4 are not desirable lies in the consideration of the second boundary condition in CASE 3 and CASE 4. For the strong and weak conservation schemes, the maximum error usually occurs in the boundary adjacent nodes. Due to the fact that the effective treatment method of boundary condition has not been found so far, strong conservation scheme did not have an obvious advantage over weak conservation scheme in

CASE 3 and CASE 4. Comparing Figures 7(a), 7(b), 7(c), and 7(d), at the same time, it shows that when the gradient of variables is relatively large, in terms of average and maximum absolute errors, the solution with Scheme 2 enjoys higher accuracy than that with Scheme 1. That is because more interface interpolations are involved in Scheme 1, which might lead to error accumulation. Thus, under the same computation conditions, the solution with Scheme 1 is not as accurate as that with Scheme 2, and the larger the gradient of primitive variables is, the greater the errors due to interface interpolations are, along with the more obvious difference between the solutions of the two schemes.

Through Figure 8, the two kinds of ratio, average absolute error and maximum absolute error, with the two different

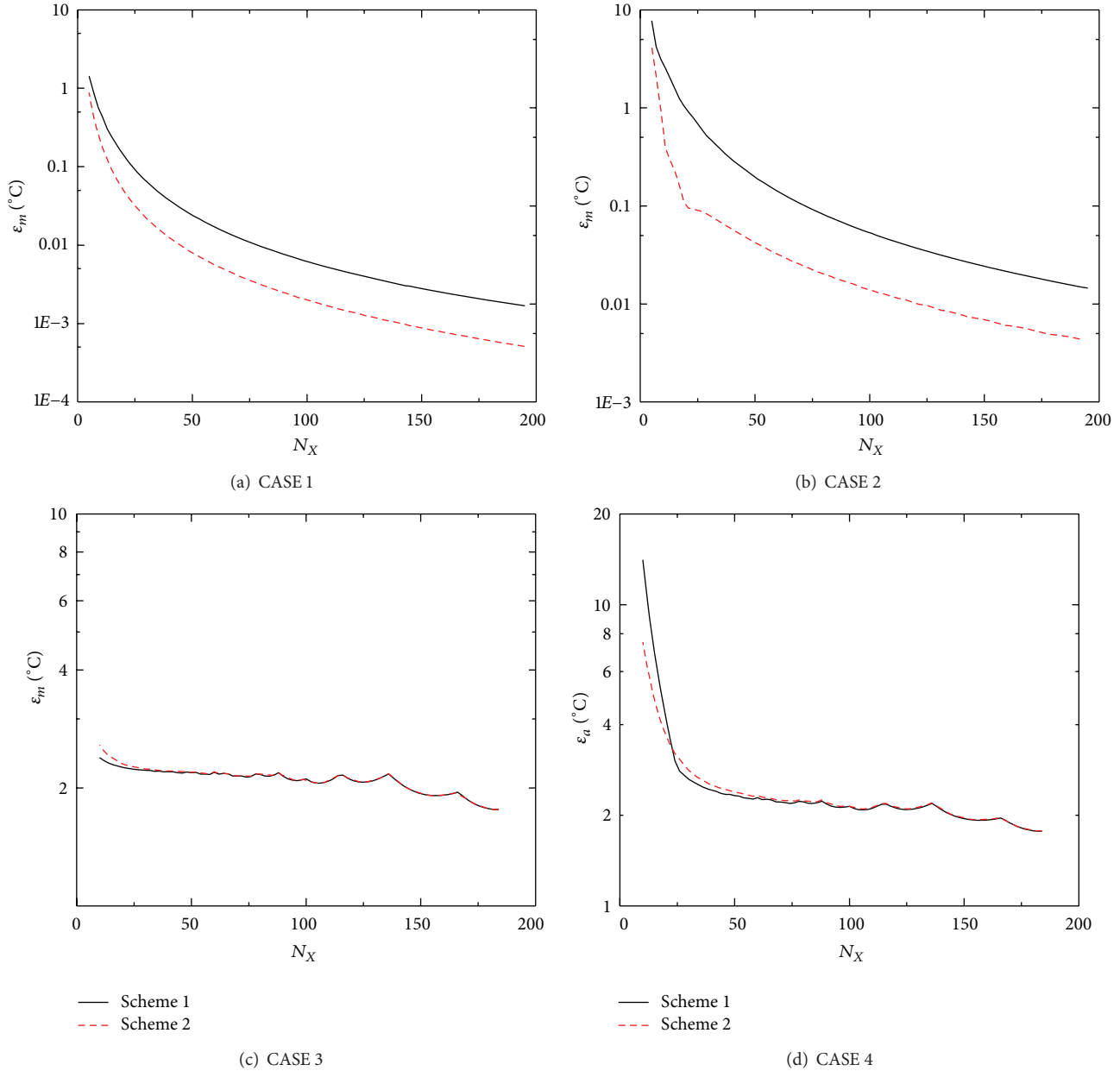


FIGURE 7: Maximum absolute error.

schemes are basically larger than 1. Notice specifically, from Figure 8(a) that the ratios of average absolute errors with the two schemes in solving the one-dimensional problem are presented basically to be 2, while in CASE 4 of the two-dimensional problem, the ratios of average absolute errors can be as large as 4–7. Moreover, from Figure 8(b), in solving the one-dimensional problem, the maximum absolute error with Scheme 1 is almost three times greater than that with Scheme 2.

In short, under the same computation conditions, when the gradient of primitive variables is relatively large, the numerical solution with Scheme 2 is more accurate than that with Scheme 1.

#### 4. Conclusions

In the incompressible fluid flow and heat transfer, when the conservation governing equation is discretized by the finite volume method, the convective flux at the interface can be obtained by strong conservation scheme and weak conservation scheme. The present paper studies the influences of these two different schemes on the numerical solution with various typical cases. The results of the numerical cases indicate the following:

- (1) under the same computation conditions and on the sparse grid, when the gradient of primitive variables is relatively small, the numerical solutions with

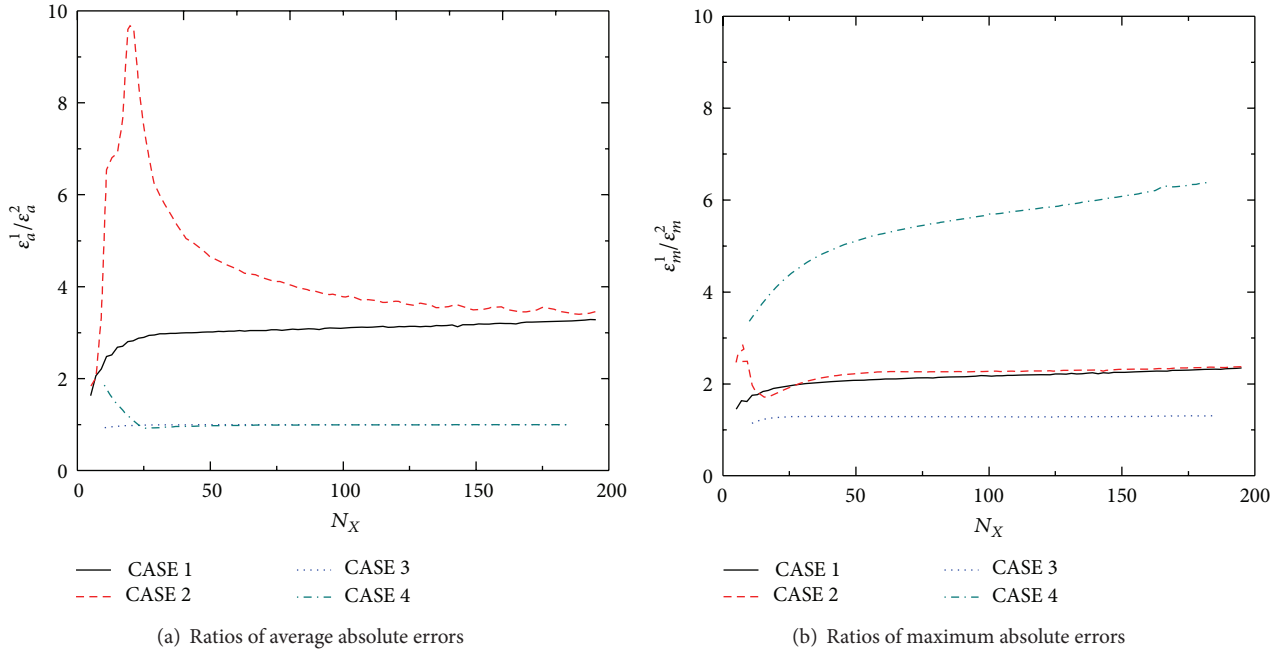


FIGURE 8: Ratios of errors.

the two schemes are close to each other and all could match the grid-independent solution quite well. When the gradient becomes sharp, the solution with weak conservation scheme deviates greatly from the benchmark solution: even oscillation or solution without physical meaning occurs. On the other hand, the solution with strong conservation scheme still matches the grid-independent solution well;

- (2) through calculating average absolute error and maximum absolute error, it is found that even when the gradient of primitive variables is small, strong conservation scheme still has advantage over weak conservation scheme.

In conclusion, treating the convective flux as single physical variable and discretizing the convective term by strong conservation scheme is a more effective way in the numerical computation of incompressible fluid flow and heat transfer.

## Nomenclatures

$t$ :	Time, s
$u, v$ :	Velocities, m/s
$u''$ :	Second partial derivative of velocity $u, u'' = \partial^2 u / \partial x^2$
$x, y$ :	Spatial coordinates, m
$\mathbf{U}$ :	Velocity vector
$A$ :	Flow area, $m^2$
$A''$ :	Second partial derivative of flow area $A, A'' = \partial^2 A / \partial x^2$
$N_x, N_y$ :	Grid numbers in the $x$ and $y$ coordinates
$N_{\text{Grid}}$ :	Total grid number
$S_\phi$ :	Heat source, $W/m^3$ .

## Greek Symbols

$\Delta x$ :	Width of control volume in the $x$ direction, m
$\delta x$ :	Distance between adjacent nodes, m
$\rho$ :	Density, $kg/m^3$
$\phi$ :	General variable
$\epsilon$ :	Numerical error
$\Gamma_\phi$ :	General diffusion coefficient, $W/(m \cdot ^\circ C)$
$\Gamma$ :	Thermal conductivity, $W/(m \cdot ^\circ C)$ .

## Superscripts

- 1: Scheme 1, weak conservation scheme  
2: Scheme 2, strong conservation scheme.

## Subscripts

$a$ :	Average error
$b$ :	Benchmark solution
$c$ :	Calculation solution
$l$ :	Computational domain
$m$ :	Maximum error
$e, w$ :	Interfaces of the control volume $P$ as shown in Figure 1
$P, W, E, EE$ :	Grid nodes as shown in Figure 1.

## Acknowledgment

This study is supported by the National Science Foundation of China (nos. 51134006, 51276198, and 51176204).

## References

- [1] J. D. Anderson, *Computational Fluid Dynamics-the Basics with Applications*, McGraw-Hill, New York, NY, USA, 1st edition, 1995.
- [2] P. J. Roache, *Computational Fluid Dynamics*, Hermosa, 3rd edition, 1976.
- [3] W. Q. Tao, *Numerical Heat Transfer*, Xi'an Jiaotong University Press, 2nd edition, 2002.
- [4] W. Q. Tao, *Advances in Computational Heat Transfer*, Science Press, 2nd edition, 2000.
- [5] H. K. Versteeg and W. Malalasekera, *An Introduction to Computational Fluid Dynamics: The Finite Volume Method*, Prentice Hall, 2nd edition, 2007.
- [6] P. D. Lax, "Weak solutions of nonlinear hyperbolic equations and their numerical computation," *Communications on Pure and Applied Mathematics*, vol. 7, pp. 159–193, 1954.
- [7] P. Lax and B. Wendroff, "Systems of conservation laws," *Communications on Pure and Applied Mathematics*, vol. 13, no. 2, pp. 217–237, 1960.
- [8] A. Jameson, "Transonic potential flow calculations using conservation form," in *Proceedings of the Computational Fluid Dynamics Conference*, 75A34193, pp. 148–161, Hartford, Conn, USA, 1975.
- [9] M. Vinokur, "Conservation equations of gasdynamics in curvilinear coordinate systems," *Journal of Computational Physics*, vol. 14, pp. 105–125, 1974.
- [10] T. J. Bridges, "Conservation laws in curvilinear coordinates: a short proof of Vinokur's theorem using differential forms," *Applied Mathematics and Computation*, vol. 202, no. 2, pp. 882–885, 2008.
- [11] R. J. DiPerna, "Decay of solutions of hyperbolic systems of conservation laws with a convex extension," *Archive for Rational Mechanics and Analysis*, vol. 64, no. 1, pp. 1–46, 1977.
- [12] A. Bressan, "Hyperbolic systems of conservation laws," *Revista Matemática Complutense*, vol. 12, no. 1, pp. 135–200, 1999.
- [13] R. K. S. Hankin, "The Euler equations for multiphase compressible flow in conservation form-Simulation of shock-bubble interactions," *Journal of Computational Physics*, vol. 172, no. 2, pp. 808–826, 2001.
- [14] C. Lai, R. A. Baltzer, and R. W. Schaffranek, "Conservation-form equations of unsteady open-channel flow," *Journal of Hydraulic Research*, vol. 40, no. 5, pp. 567–578, 2002.
- [15] L. M. Gao, K. T. Li, B. Liu, and Su J, "General integral conservation form of Navier-Stokes equations and numerical application," *Chinese Journal of Computational Physics*, vol. 25, no. 2, pp. 172–178, 2008.
- [16] S. H. Sohrab, "Derivation of invariant forms of conservation equations from the invariant Boltzmann equation," in *Proceedings of the 5th International Conference on Fluid Mechanics*, pp. 27–35, Acapulco, Mexico, 2008.
- [17] S.-F. Li, P. Zhang, and S. C. Wong, "Conservation form of Helbing's fluid dynamic traffic flow model," *Applied Mathematics and Mechanics*, vol. 32, no. 9, pp. 1109–1118, 2011.
- [18] R. C. Martineau, R. A. Berry, A. Esteve et al., "Comparison of natural convection flows under VHTR type conditions modeled by both the conservation and incompressible forms of the Navier-Stokes equations," *Nuclear Engineering and Design*, vol. 240, no. 6, pp. 1371–1385, 2010.

## Research Article

# Mathematical Analysis of Casson Fluid Model for Blood Rheology in Stenosed Narrow Arteries

J. Venkatesan,<sup>1</sup> D. S. Sankar,<sup>2</sup> K. Hemalatha,<sup>3</sup> and Yazariah Yatim<sup>4</sup>

<sup>1</sup> Department of Mathematics, Rajalakshmi Engineering College, Thandalam, Chennai 602 105, India

<sup>2</sup> Division of Mathematics, School of Advanced Sciences, VIT University, Chennai Campus, Chennai 600 127, India

<sup>3</sup> Department of Mathematics, Anna University, Chennai 600 025, India

<sup>4</sup> School of Mathematical Sciences, Universiti Sains Malaysia, 11800 Penang, Malaysia

Correspondence should be addressed to D. S. Sankar; [sankar\\_ds@yahoo.co.in](mailto:sankar_ds@yahoo.co.in)

Received 1 April 2013; Accepted 14 July 2013

Academic Editor: Mohamed Fathy El-Amin

Copyright © 2013 J. Venkatesan et al. This is an open access article distributed under the Creative Commons Attribution License, which permits unrestricted use, distribution, and reproduction in any medium, provided the original work is properly cited.

The flow of blood through a narrow artery with bell-shaped stenosis is investigated, treating blood as Casson fluid. Present results are compared with the results of the Herschel-Bulkley fluid model obtained by Misra and Shit (2006) for the same geometry. Resistance to flow and skin friction are normalized in two different ways such as (i) with respect to the same non-Newtonian fluid in a normal artery which gives the effect of a stenosis and (ii) with respect to the Newtonian fluid in the stenosed artery which spells out the non-Newtonian effects of the fluid. It is found that the resistance to flow and skin friction increase with the increase of maximum depth of the stenosis, but these flow quantities (when normalized with non-Newtonian fluid in normal artery) decrease with the increase of the yield stress, as obtained by Misra and Shit (2006). It is also noticed that the resistance to flow and skin friction increase (when normalized with Newtonian fluid in stenosed artery) with the increase of the yield stress.

## 1. Introduction

The study of the fluid dynamical aspects of blood flow through a stenosed artery is useful for the fundamental understanding of circulatory disorders. Stenosis in an artery is the narrowing of the blood flow area in the artery by the development of arteriosclerosis plaques due to the deposits of fats, cholesterol, and so forth on the inner wall of the artery. This leads to an increase in the resistance to flow and associated reduction in blood supply in the downstream which leads to serious cardiovascular diseases such as myocardial infarction and cerebral strokes [1–3].

Blood shows Newtonian fluid's character when it flows through larger diameter arteries at high shear rates, but it exhibits a remarkable non-Newtonian behavior when it flows through small diameter arteries at low shear rates [4, 5]. Moreover, there is an increase in viscosity of blood at low rates of shear as the red blood cells tend to aggregate into the Rouleaux form [6]. Rouleaux form behaves as a semi-solid along the center forming a plug flow region. In the plug flow region, we have a flattened parabolic velocity profile rather

than the parabolic velocity profile of a Newtonian fluid. This behavior can be modeled by the concept of yield stress. The yield stress for blood depends strongly on fibrinogen concentration and is also dependent on the hematocrit. The yield stress values for normal human blood is between 0.01 and 0.06 dyn/cm<sup>2</sup> [7].

Casson fluid model is a non-Newtonian fluid with yield stress which is widely used for modeling blood flow in narrow arteries. Many researchers have used the Casson fluid model for mathematical modeling of blood flow in narrow arteries at low shear rates. It has been demonstrated by Blair [8] and Copley [9] that the Casson fluid model is adequate for the representation of the simple shear behavior of blood in narrow arteries. Casson [10] examined the validity of Casson fluid model in his studies pertaining to the flow characteristics of blood and reported that at low shear rates the yield stress for blood is nonzero. It has been established by Merrill et al. [11] that the Casson fluid model predicts satisfactorily the flow behaviors of blood in tubes with the diameter of 130–1000  $\mu\text{m}$ .

Charm and Kurland [12] pointed out in their experimental findings that the Casson fluid model could be the best representative of blood when it flows through narrow arteries at low shear rates and that it could be applied to human blood at a wide range of hematocrit and shear rates. Blair and Spanner [13] reported that blood behaves like a Casson fluid in the case of moderate shear rate flows, and it is appropriate to assume blood as a Casson fluid. Aroesty and Gross [14] have developed a Casson fluid theory for pulsatile blood flow through narrow uniform arteries. Chaturani and Samy [15] analyzed the pulsatile flow of Casson fluid through stenosed arteries using the perturbation method.

Herschel-Bulkley fluid is also a non-Newtonian fluid with yield stress which is more general in the sense that it contains two parameters such as the yield stress and power law index, whereas the Casson fluid has only one parameter which is the yield stress. Herschel-Bulkley fluid's constitutive equation can be reduced to the constitutive equations of Newtonian, Power law, and Bingham fluid models by taking appropriate values to the parameters. Chaturani and Ponnalagar Samy [16] analyzed the steady flow of Herschel-Bulkley fluid for blood flow through cosine-shaped stenosed arteries.

Misra and Shit [17] analyzed the steady flow of Herschel-Bulkley fluid for blood flow in narrow arteries with bell-shaped mild stenosis. The mathematical modeling of Casson fluid model for steady flow of blood in narrow arteries with bell-shaped mild stenosis was not studied by anyone so far, according to the knowledge of the authors. Hence, in the present study, a mathematical model is developed to analyze the blood flow at low shear rates in narrow arteries with mild bell-shaped stenosis, treating blood as Casson fluid model. The results of the present study are compared with the results of Misra and Shit [17], and Chaturani and Ponnalagar Samy [16] and some possible clinical applications to the present study are also given.

## 2. Formulation

Let us consider an axially symmetric, laminar, steady, and fully developed flow of a non-Newtonian incompressible viscous fluid (blood) in the axial direction ( $z$ ) through a circular artery with bell-shaped mild stenosis. The non-Newtonian behavior of the flowing blood is characterized by Casson fluid model. The artery wall is assumed to be rigid (due to the presence of the stenosis) and the artery is assumed to be long enough so that the entrance and end effects can be neglected in the arterial segment under study. A cylindrical polar coordinate system ( $r, \psi, z$ ) is used to analyze the blood flow, where  $r$  and  $z$  are the variables taken in the radial and axial directions, respectively, and  $\psi$  is the azimuthal angle. The geometry of the arterial segment with mild constriction is shown in Figure 1.

Since the blood flow in narrow arteries is slow, the magnitude of the inertial forces is negligibly small, and thus the inertial terms in the momentum equations are neglected. Since the considered flow is unidirectional and is in the axial direction, the radial component of the momentum equation

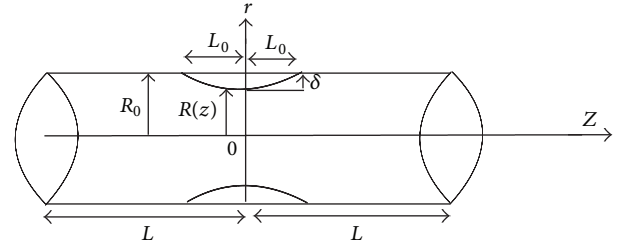


FIGURE 1: Geometry of the arterial segment with stenosis.

is ignored. The axial component of the momentum equation is simplified to the following:

$$-\frac{dp}{dz} = \frac{1}{r} \frac{d(r\tau)}{dr}, \quad (1)$$

where  $\tau$  is the shear stress and  $p$  is the pressure. The constitutive equation (relationship between the shear stress and strain rate) of Casson fluid model is defined as follows:

$$-\frac{du}{dr} = f(\tau) = \begin{cases} \frac{1}{k} (\sqrt{\tau} - \sqrt{\tau_c})^2, & \tau \geq \tau_c, \\ 0, & \tau \leq \tau_c, \end{cases} \quad (2)$$

where  $u$  is the velocity of blood in the axial direction,  $\tau_c$  is the yield stress, and  $k$  is the viscosity coefficient of Casson fluid.

The geometry of the segment of the narrow artery with mild bell-shaped stenosis is mathematically defined as follows:

$$R(z) = R_0 \left[ 1 - \frac{\delta}{R_0} e^{-m^2 \epsilon^2 z^2 / R_0^2} \right], \quad (3)$$

where  $R_0$  is the radius of the normal artery,  $R(z)$  is the radius of the artery in the stenosis region,  $\delta$  is the depth of the stenosis at its throat,  $m$  is a parametric constant, and  $\epsilon$  characterizes the relative length of the constriction, defined as  $\epsilon = R_0/L_0$ .

Equation (3) can be rewritten as

$$\frac{R(z)}{R_0} = 1 - ae^{-bz^2}, \quad (4)$$

where  $a = \delta/R_0$  and  $b = m^2 \epsilon^2 / R_0^2$ . Note that  $a$  and  $b$  are the parameters in the nondimensional form corresponding to the maximum projection of the stenosis at its throat and variable length of the stenosis in the segment of the narrow artery under study, respectively. Equation (3) spells out that the bell-shaped geometry has the advantage of having two parameters such as  $a$  and  $b$  compared to cosine-curve shaped geometry which has only one parameter, namely, the maximum depth of the stenosis [15]. In the bell-shaped stenosis geometry, by keeping  $b$  as variable and  $a$  as constant, one can generate arteries with different stenosis lengths with the same maximum depth of the stenosis  $a$ , and also by keeping  $a$  as variable and  $b$  as constant one can generate arteries with different maximum depths with the same length of the stenosis. The different stenosis shapes obtained by varying the stenosis height  $a$  with 30% stenosis that is,  $L_0 = 1.5$ , are shown in

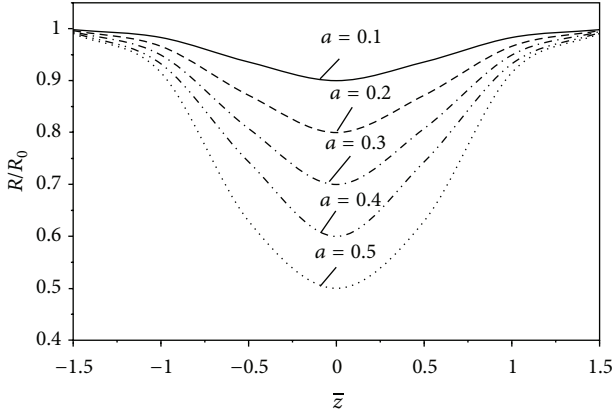


FIGURE 2: Stenosis geometries for different values of stenosis height  $a$ .

Figure 2. The percentage of stenosis is given by  $L_0/L \times 100$ . In the present study, we have taken  $L = 5$  cm and  $m = 2$  as taken by Misra and Shit [17].

Figure 3(a) depicts the shapes of stenoses with different lengths by fixing  $a = 0.2$  and keeping  $b$  as variable (for different values of stenosis the length  $L_0$  with fixed value of  $m = 2$ ). Figure 3(b) shows the shapes of stenoses with different lengths by fixing  $a = 0.2$  and varying the values of  $b$  (for different values of  $m$  and with a fixed value of  $L_0 = 1.5$ ). It is noticed that the width of the stenosis decreases with the increase in the values of  $m$ .

Equations (1) and (2) have to be solved with the help of the following no slip boundary condition:

$$u = 0 \quad \text{at } r = R(z), \tag{5}$$

and the regularity condition

$$\tau \text{ is finite at } r = 0. \tag{6}$$

### 3. Method of Solution

Integrating (1) and then using (6), we get

$$\tau = -\frac{r}{2} \frac{dp}{dz}. \tag{7}$$

From (7), the skin friction  $\tau_R$  is obtained as

$$\tau_R = -\frac{R}{2} \frac{dp}{dz}, \tag{8}$$

where  $R = R(z)$ .

The volumetric flow rate  $Q$  is as follows:

$$Q = \frac{\pi R^3}{\tau_R^3} \int_0^{\tau_R} \tau^2 f(\tau) d\tau, \tag{9}$$

where  $\tau$  and  $\tau_R$  are given by (7) and (8), respectively.

Substituting (2) into (9), we get

$$Q = \frac{\pi R^3}{\tau_R^3} \int_{\tau_c}^{\tau_R} \tau^2 \frac{1}{k} (\sqrt{\tau} - \sqrt{\tau_c})^2 d\tau. \tag{10}$$

Integrating (10) and then simplifying, one can get

$$Q = \frac{\pi R^3}{4k} \tau_R \left\{ 1 - \frac{16}{7} \left( \frac{\tau_c}{\tau_R} \right)^{1/2} + \frac{4}{3} \left( \frac{\tau_c}{\tau_R} \right) - \frac{1}{21} \left( \frac{\tau_c}{\tau_R} \right)^4 \right\}. \tag{11}$$

Since  $\tau_c/\tau_R \ll 1$ , neglecting the term involving  $(\tau_c/\tau_R)^4$  in (11), we get the expression for flow rate as

$$Q = \frac{\pi R^3}{4k} \tau_R \left\{ 1 - \frac{16}{7} \left( \frac{\tau_c}{\tau_R} \right)^{1/2} + \frac{4}{3} \left( \frac{\tau_c}{\tau_R} \right) \right\}. \tag{12}$$

Using (8) in (12), we get

$$-\frac{dp}{dz} = \frac{128\tau_c}{49R} + \frac{8}{R} \left( \frac{Qk}{\pi R^3} - \frac{\tau_c}{147} \right) + \frac{64}{7R} \sqrt{\frac{kQ\tau_c}{\pi R^3} - \frac{\tau_c^2}{147}}. \tag{13}$$

Neglecting the term involving  $\tau_c^2$  in (13), we get

$$-\frac{dp}{dz} = \frac{128\tau_c}{49R} + \frac{8Qk}{\pi R^4} + \frac{64}{7R} \sqrt{\frac{kQ\tau_c}{\pi R^3}}. \tag{14}$$

Integrating (14) along the length of the artery and using the conditions that  $p = p_1$  at  $z = -L$  and  $p = p_2$  at  $z = L$ , we obtain

$$p_1 - p_2 = \frac{128\tau_c}{49R_0} \int_{-L}^L \frac{dz}{(R/R_0)} + \frac{8Qk}{\pi R_0^4} \int_{-L}^L \frac{dz}{(R/R_0)^4} + \frac{64}{7} \sqrt{\frac{Qk\tau_c}{\pi R_0^5}} \int_{-L}^L \frac{dz}{(R/R_0)^{5/2}}. \tag{15}$$

Simplifying (15), one can obtain the following expression for pressure drop:

$$p_1 - p_2 = \frac{256}{49} \frac{\tau_c}{R_0} \left\{ (L - L_0) + \int_0^{L_0} \frac{dz}{(R/R_0)} \right\} + \frac{16Qk}{\pi R_0^4} \left\{ (L - L_0) + \int_0^{L_0} \frac{dz}{(R/R_0)^4} \right\} + \frac{128}{7} \sqrt{\frac{Qk\tau_c}{\pi R_0^5}} \left\{ (L - L_0) + \int_0^{L_0} \frac{dz}{(R/R_0)^{5/2}} \right\}. \tag{16}$$

3.1. Resistance to Flow. The resistance to flow  $\lambda$  is defined as follows:

$$\lambda = \frac{p_1 - p_2}{Q}. \tag{17}$$

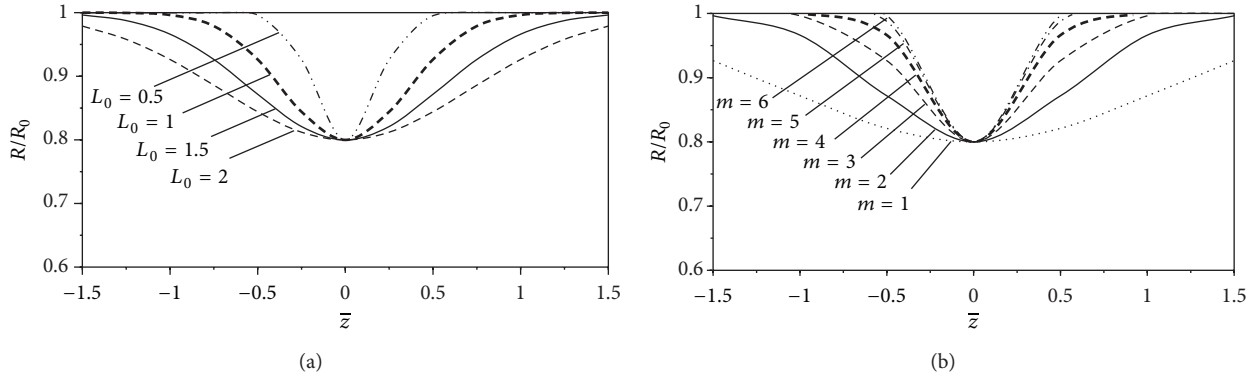


FIGURE 3: (a) Shapes of the arterial stenosis for different values of the stenosis length  $L_0$ . (b) Shapes of the arterial stenosis for different values of the stenosis shape parameter  $m$ .

The resistance to flow for Casson fluid in a stenosed artery is obtained as follows:

$$\begin{aligned} \lambda = & \frac{256\tau_c}{49QR_0} \left\{ (L - L_0) + \int_0^{L_0} \frac{dz}{(R/R_0)} \right\} \\ & + \frac{16k}{\pi R_0^4} \left\{ (L - L_0) + \int_0^{L_0} \frac{dz}{(R/R_0)^4} \right\} \\ & + \frac{128}{7} \sqrt{\frac{k\tau_c}{\pi QR_0^5}} \left\{ (L - L_0) + \int_0^{L_0} \frac{dz}{(R/R_0)^{5/2}} \right\}. \end{aligned} \quad (18)$$

In the absence of any constriction ( $\delta = 0$  and  $R = R_0$ ), the resistance to flow (in the normal artery)  $\lambda_N$  is given by the following:

$$\lambda_N = \frac{16L}{R_0} \left\{ \frac{k}{\pi R_0^3} + \frac{16\tau_c}{49Q} + \frac{8}{7} \sqrt{\frac{k\tau_c}{\pi QR_0^3}} \right\}. \quad (19)$$

The expression for resistance to flow in the dimensionless form is obtained as follows:

$$\bar{\lambda}_1 = \frac{\lambda}{\lambda_N} = 1 - \frac{L_0}{L} + \frac{1}{L} \left( \frac{(16\tau_c/49Q) I_1 + (k/\pi R_0^3) I_2 + (8/7) \sqrt{(k\tau_c/\pi QR_0^3)} I_3}{(16\tau_c/49Q) + (k/\pi R_0^3) + (8/7) \sqrt{k\tau_c/\pi QR_0^3}} \right), \quad (20)$$

where  $I_1 = \int_0^{L_0} (dz/(R/R_0))$ ,  $I_2 = \int_0^{L_0} (dz/(R/R_0)^4)$ , and  $I_3 = \int_0^{L_0} dz/(R/R_0)^{5/2}$ .

It is noted that  $\bar{\lambda}_1$  measures the relative resistance in a stenosed artery compared to normal artery. Substituting the expression for  $R/R_0$  from (4), the integrals  $I_1$ ,  $I_2$ , and  $I_3$  are reduced to the following:

$$\begin{aligned} I_1 = & \int_0^{L_0} \frac{dz}{(1 - ae^{-bz^2})}, \\ I_2 = & \int_0^{L_0} \frac{dz}{(1 - ae^{-bz^2})^4}, \\ I_3 = & \int_0^{L_0} \frac{dz}{(1 - ae^{-bz^2})^{5/2}}. \end{aligned} \quad (21)$$

Using a two-point Gauss quadrature formula, the integrals in (21) are evaluated as follows:

$$\begin{aligned} I_1 = & \frac{L_0}{2} \left[ \frac{1}{(1 - ae^{-(bL_0^2/12)(4+2\sqrt{3})})} \right. \\ & \left. + \frac{1}{(1 - ae^{-(bL_0^2/12)(4-2\sqrt{3})})} \right], \\ I_2 = & \frac{L_0}{2} \left[ \frac{1}{(1 - ae^{-(bL_0^2/12)(4+2\sqrt{3})})^4} \right. \\ & \left. + \frac{1}{(1 - ae^{-(bL_0^2/12)(4-2\sqrt{3})})^4} \right], \end{aligned}$$

$$I_3 = \frac{L_0}{2} \left[ \frac{1}{(1 - ae^{-(bL_0^2/12)(4+2\sqrt{3})})^{5/2}} + \frac{1}{(1 - ae^{-(bL_0^2/12)(4-2\sqrt{3})})^{5/2}} \right]. \tag{22}$$

If we want to compare the resistance to flow for different fluid models, we have to normalize it with respect to resistance to flow  $\lambda_{N_e}$  of Newtonian fluid in normal artery, and the respective expression for Casson fluid model is obtained as follows:

$$\begin{aligned} \bar{\lambda}_2 &= \frac{\lambda}{\lambda_{N_e}} \\ &= \left( 1 + \frac{16}{49} \left( \frac{\pi\tau_C R_0^3}{Qk} \right) + \frac{8}{7} \sqrt{\frac{\pi\tau_C R_0^3}{Qk}} \right) \\ &\times \left( 1 - \frac{L_0}{L} \right) + \frac{1}{L} \left( \frac{16}{49} \left( \frac{\pi\tau_C R_0^3}{Qk} \right) I_1 \right. \\ &\quad \left. + I_2 + \frac{8}{7} \sqrt{\frac{\pi\tau_C R_0^3}{Qk}} I_3 \right), \end{aligned} \tag{23}$$

where

$$\lambda_{N_e} = \frac{16kL}{\pi R_0^4}, \tag{24}$$

which is obtained from (18) with  $\delta = 0$ ,  $R(z) = R_0$ , and  $\tau_c = 0$ .

**3.2. Skin Friction.** From (8) and (14), the expression for the skin friction is obtained as follows:

$$\tau_R = -\frac{R}{2} \cdot \frac{dp}{dz} = \frac{64}{49} \tau_c + \frac{4Qk}{\pi R^3} + \frac{32}{7} \sqrt{\frac{kQ\tau_c}{\pi R^3}}. \tag{25}$$

In the absence of any constriction when  $(R(z) = R_0)$ , the expression for the skin friction becomes the following:

$$\tau_N = \frac{64}{49} \tau_c + \frac{4Qk}{\pi R_0^3} + \frac{32}{7} \sqrt{\frac{kQ\tau_c}{\pi R_0^3}}. \tag{26}$$

The nondimensional form of skin friction with effects on stenosis is defined as the ratio between the skin friction in the stenosed artery and skin friction in the normal artery. From (25) and (26), the skin friction with effects on stenosis is obtained as

$$\bar{\tau}_1 = \frac{\tau_R}{\tau_N} = \frac{4Qk + (32/7) (Qk\tau_c\pi R_0^3)^{1/2} (R/R_0)^{3/2} + (64/49) \tau_c\pi R_0^3 (R/R_0)^3}{(R/R_0)^3 \{4Qk + (32/7) (Qk\tau_c\pi R_0^3)^{1/2} + (64/49) \tau_c\pi R_0^3\}}. \tag{27}$$

The nondimensional form of skin friction with effects on the non-Newtonian behavior of blood is defined as the ratio between the skin friction of the non-Newtonian fluid in the stenosed artery and the skin friction of the Newtonian fluid in the same stenosed artery. The expression for skin friction with effects on the non-Newtonian behavior of blood is obtained as follows:

$$\begin{aligned} \bar{\tau}_2 &= \frac{\tau_R}{\tau_{N_e}} = \frac{1}{(R/R_0)^3} + \frac{16}{49} \left( \frac{\pi R_0^3 \tau_C}{Qk} \right) \\ &\quad + \frac{8}{7} \frac{1}{(R/R_0)^{3/2}} \sqrt{\frac{\pi R_0^3 \tau_C}{Qk}}, \end{aligned} \tag{28}$$

where

$$\tau_{N_e} = \frac{4kQ}{\pi R_0^3}. \tag{29}$$

#### 4. Numerical Simulations of the Results

The objective of this study is to discuss the effects of various parameters on the physiologically important flow quantities

such as skin friction, resistance to flow, and flow rate. The following parameters with their ranges mentioned as  $Q$ : 0–1,  $k$ : 2.0–7.0 (CP)<sup>n</sup>/sec<sup>n-1</sup>,  $\tau_c$ : 0.0–0.5 dyne/cm<sup>2</sup>,  $m = 2$ ,  $L = 5$  cm, and  $R_0 = 0.40$  are used to evaluate the expressions of these flow quantities and get data for plotting the graphs.

##### 4.1. Skin-Friction

**4.1.1. Effects of Stenosis on Skin-Friction.** The variation of skin friction  $\bar{\tau}_1$  with axial distance for different values of  $L_0/L$  and yield stress  $\tau_c$  with  $k = 4$  is shown in Figure 4. It is observed that the skin friction increases considerably with the increase in the stenosis length for a given value of yield stress  $\tau_c$ , but it decreases very slightly when the yield stress increases for the fixed value of  $L_0/L$ . The same observations were recorded by Misra and Shit [17] for the Herschel-Bulkley fluid.

The variations of skin friction  $\bar{\tau}_1$  at the midpoint of the stenosis with stenosis height  $\delta/R_0$  for different values of the yield stress  $\tau_c$  with  $k = 7$  and  $L_0/L = 0.3$  are sketched in Figure 5. It is noted that the skin friction decreases marginally as the yield stress increases.

The estimates of skin friction  $\bar{\tau}_1$  for different values of axial variable  $z$  and viscosity coefficient  $k$  with  $\tau_c = 0.05$  and

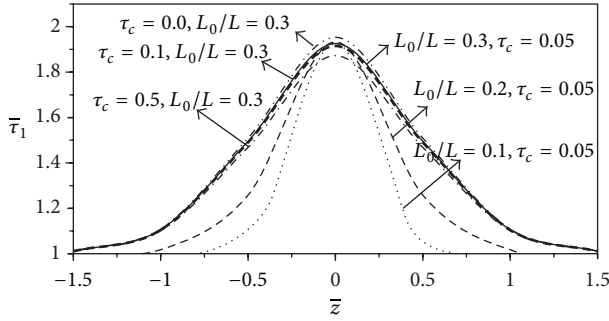


FIGURE 4: Variations of skin friction  $\bar{\tau}_1$  with axial distance for different percentages of stenosis  $L_0/L$  and yield stress  $\tau_c$ .

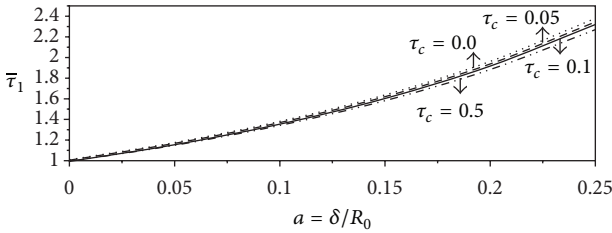


FIGURE 5: Variations of skin friction  $\bar{\tau}_1$  with stenosis height  $a$  for different values of yield stress  $\tau_c$ .

30% stenosis are computed in Table 1. It is observed that the skin friction increases very slightly with the increase of the viscosity coefficient.

In order to compare our results with those of Misra and Shit [17], the variations of skin friction  $\bar{\tau}_1$  with axial distance for different fluids are shown in Figure 6 for 30% of stenosis with  $k = 4$  and  $\tau_c = 0.05$ . It is observed that the plot of the skin friction of Casson fluid model lies between those of the Herschel-Bulkley fluid model with  $n = 1$  and  $n = 1.05$ . Here, the skin friction is normalized with respect to the normal artery with the same fluid, as was done by Misra and Shit [17].

The mathematical form of cosine curve-shaped geometry for stenosis given by Chaturani and Ponnalagar Samy [16] is reproduced as follows:

$$\frac{R(z)}{R_0} = 1 - \frac{\delta}{2R_0} \left[ 1 + \cos \frac{2\pi}{L_0} \left( z - d - \frac{L_0}{2} \right) \right], \quad (30)$$

$$d \leq z \leq d + L_0.$$

For computation, values of the parameters are taken as  $L = 10$ ,  $d = 3.5$ , and  $L_0 = 3$ .

The variations of skin friction  $\bar{\tau}_1$  with axial distance for Casson fluid model with cosine- and bell-shaped stenosis geometries with 30% stenosis and with  $k = 4$  and  $\tau_c = 0.05$  are shown in Figure 7 (the data for plotting the graph is computed from (27)). It is found that the skin friction in cosine curve-shaped stenosed arteries is considerably higher than that in bell-shaped stenosed arteries.

**4.1.2. Effects of Non-Newtonian Behavior on Skin-Friction.** We can study the effects of different non-Newtonian fluids if we normalize it with respect to Newtonian fluid as done

TABLE 1: Variations of the skin friction  $\bar{\tau}_1$  with axial distance for different values of viscosity with  $\tau_c = 0.05$  and  $L_0/L = 0.3$ .

$z$	$\bar{\tau}$		
	$k = 2$	$k = 4$	$k = 7$
-1.5	1.01069	1.010799	1.010864
-1	1.104858	1.105946	1.106599
-0.5	1.490229	1.495693	1.49897
0	1.915269	1.926048	1.932516
0.5	1.490229	1.495693	1.49897
1	1.104858	1.105946	1.106599
1.5	1.01069	1.010799	1.010864

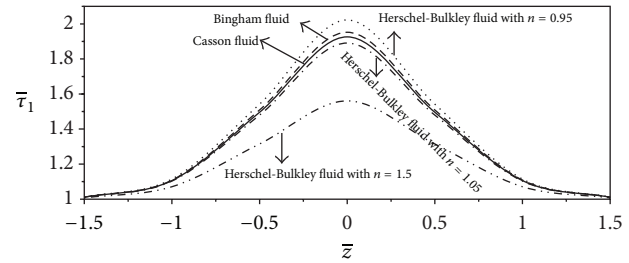


FIGURE 6: Variations of skin friction  $\bar{\tau}_1$  with axial distance for different fluids.

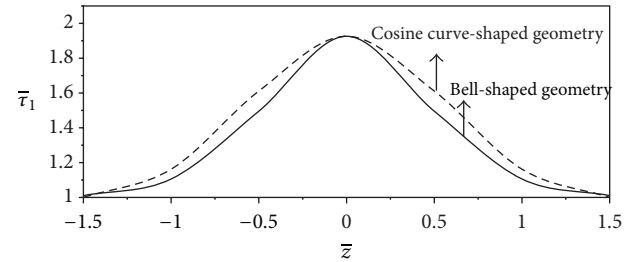


FIGURE 7: Variations of skin friction  $\bar{\tau}_1$  for Casson fluid with axial distance for different arterial geometries.

by [15, 16, 18–20]. In this case, the following results are in agreement with the results given by these authors but are opposite in nature to those given in Section 4.1.1 except for the variations of skin friction with axial distance for different values of stenosis length as given in Figure 8.

The variations of skin friction  $\bar{\tau}_2$  with axial distance for different values of  $L_0/L$  and for a given  $k = 4$  and  $\tau_c = 0.05$  are illustrated in Figure 9. It is observed that the skin friction increases considerably with the increase in the stenosis length.

Figure 10 sketches the variations of skin friction  $\bar{\tau}_2$  with axial distance for different values of yield stress with  $k = 4$  and  $L_0/L = 0.3$ . It is observed that the skin friction increases marginally with the increase in the yield stress  $\tau_c$  of the fluid.

The variations of skin friction  $\bar{\tau}_2$  at the midpoint of the stenosis with stenosis height  $\delta/R_0$  for different values of the yield stress  $\tau_c$  with  $k = 4$  and  $L_0/L = 0.3$  are shown in

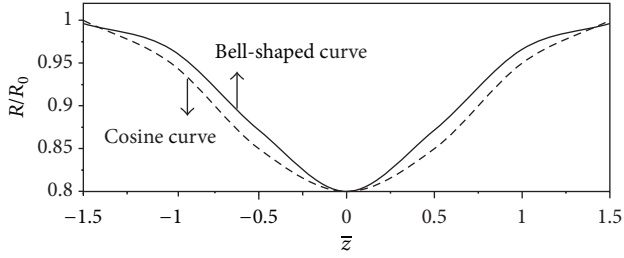


FIGURE 8: Comparison of cosine- and bell-shaped stenosis shapes.

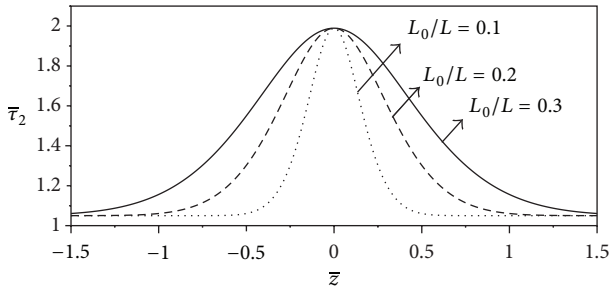


FIGURE 9: Variations of skin friction  $\bar{\tau}_2$  with axial distance for different values of stenosis size  $L_0/L$ .

Figure 11. It is clear that the skin friction increases marginally when the yield stress increases.

Figure 12 depicts the variations of skin friction  $\bar{\tau}_2$  with axial distance for different values of viscosity coefficient  $k$  for  $\tau_c = 0.05$  and 30% of stenosis. One can notice that the skin friction decreases slightly as viscosity increases.

Figure 13 shows the variations of skin friction  $\bar{\tau}_2$  with axial distance for different fluid models using cosine-shaped stenosis with 30% of stenosis, yield stress  $\tau_c = 0.05$ , and  $k = 4$ . It is observed that the skin friction of Casson fluid model lies between those of the Herschel-Bulkley fluid model with  $n = 0.95$  and  $n = 1$ .

The variations of skin friction  $\bar{\tau}_2$  with axial distance for different fluid models using bell-shaped stenosis with 30% of stenosis, yield stress  $\tau_c = 0.05$ , and  $k = 4$  are shown in Figure 14. It is observed that the skin friction of Casson fluid model lies between those of the Herschel-Bulkley fluid model with  $n = 0.95$  and  $n = 1$ .

Figure 15 shows the variations of skin friction  $\bar{\tau}_2$  with axial distance for Casson fluid model with cosine- and bell-shaped geometries with 30% stenosis,  $k = 4$ , and  $\tau_c = 0.05$  (data computed using (28)). It is seen that the cosine-shaped stenosis has a greater width than that of bell-shaped stenosis as depicted in Figure 8.

Misra and Shit [17] have analyzed the variations of skin friction with axial distance for different values of power law index and yield stress and reported that the skin friction decreases with increase in yield stress. If normalized with Newtonian fluid, the skin friction increases considerably when the yield stress increases with axial distance for 30% stenosis,  $k = 4$  as displayed in Figure 16.

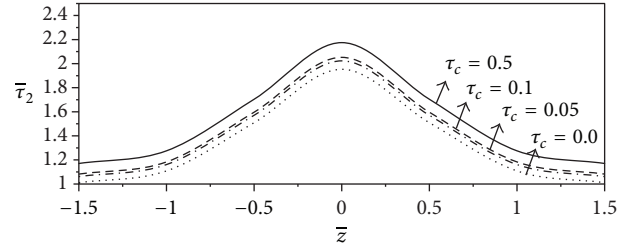


FIGURE 10: Variations of skin friction  $\bar{\tau}_2$  with axial distance for different values of yield stress  $\tau_c$ .

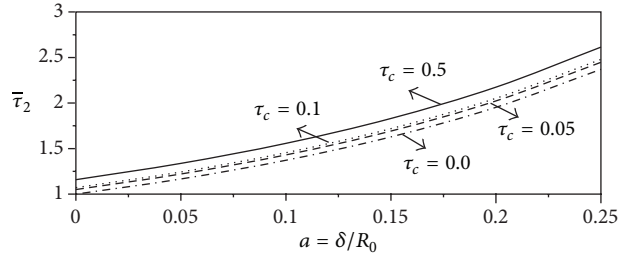


FIGURE 11: Variations of skin friction  $\bar{\tau}_2$  with stenosis height  $\delta/R_0$  for different values of yield stress  $\tau_c$ .

4.2. Resistance to Flow. The variations of resistance to flow  $\bar{\lambda}_1$  with the height of the stenosis  $\delta/R_0$  for different values of stenosis length  $L_0/L$  with viscosity coefficient  $k = 4$  and yield stress  $\tau_c = 0.05$  are shown in Figure 17. It is found that the flow resistance increases nonlinearly with the increase in the stenosis size.

Using the result (23), the variations of resistance to flow  $\bar{\lambda}_2$  with stenosis height for different values of stenosis length, for the given  $k = 4$  and  $\tau_c = 0.05$  are shown in Figure 18. It is observed that the flow resistance decreases considerably when the length of the stenosis increases. Also, the variations of resistance to flow  $\bar{\lambda}_2$  with stenosis height for different values of yield stress and for  $k = 4$  and  $L_0/L = 0.3$  is shown in Figure 19. It is clear that the resistance to flow increases significantly with the increase in the yield stress.

4.3. Flow Rate. Figure 20 depicts the variation of flow rate with axial distance for different values of viscosity coefficient  $k$  and yield stress  $\tau_c$  with 30% of stenosis. One can notice that the flow rate decreases significantly with the increase of either the viscosity coefficient or the yield stress. It is also observed that the flow rate decreases very significantly (nonlinearly) at the throat of the stenosis for lower values of either the yield stress or viscosity coefficient and slowly (almost linearly) for higher values of either the yield stress or viscosity coefficient.

4.4. Physiological Application. To highlight some possible clinical applications of the present study, the data used by Sankar [21] (the radii of different arteries and flow rate) are used to compute the physiologically important flow quantities such as resistance to flow and skin friction. The values of the parameters are taken as  $k = 3.5$  and  $\tau_c = 0.04$ . The dimensionless resistance to flow  $\bar{\lambda}_2$  and skin friction  $\bar{\tau}_2$  are

TABLE 2: Estimates of resistance to flow  $\bar{\lambda}_2$  and skin friction (dimensionless)  $\bar{\tau}_2$  in arteries with different radii with  $L_0/L = 1$ .

Blood vessels		$a = 0.10$		$a = 0.15$	
Radius $R_0$ (cm)	$\tau'_c$	$\bar{\lambda}$	$\bar{\tau}$	$\bar{\lambda}$	$\bar{\tau}$
Flow rate $Q$ ( $\text{cm}^3 \text{s}^{-1}$ )					
Aorta (1, 71.67)	$1.529080 \times 10^{-2}$	1.567142	1.722748	1.745439	2.008973
Femoral (0.5, 19.63)	$5.718029 \times 10^{-3}$	1.429659	1.581644	1.598551	1.856356
Carotid (0.4, 12.57)	$4.571948 \times 10^{-3}$	1.407374	1.558726	1.574716	1.831521
Coronary (0.15, 3.47)	$8.733753 \times 10^{-4}$	1.303768	1.451998	1.463802	1.715671
Arteriole (0.008, 0.00008)	$5.629388 \times 10^{-3}$	1.428014	1.579953	1.596792	1.854524

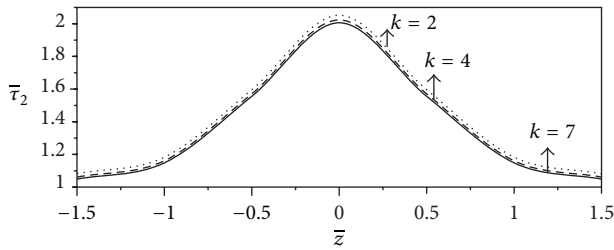


FIGURE 12: Variations of skin friction  $\bar{\tau}_2$  with axial distance for different values of viscosity  $k$ .

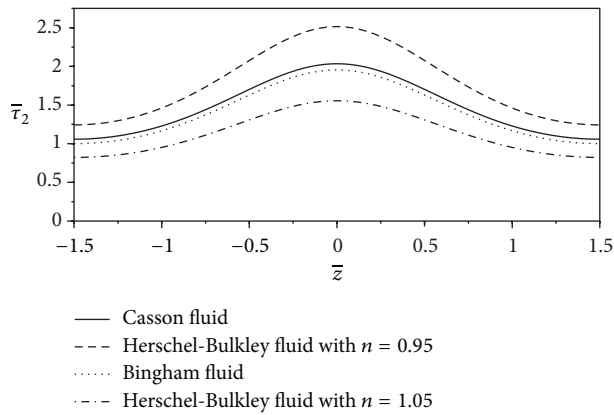


FIGURE 13: Variations of skin friction  $\bar{\tau}_2$  with axial distance for different fluid models with cosine-shaped stenosis.

computed for arteries with different radii and with  $m = 2$  and  $L_0/L = 1$  from (23) and (28) (normalized with Newtonian fluid in stenosed artery) and are presented in Table 2. It is noted that the resistance to flow increases, considerably when the stenosis height increases and skin friction significantly increases with the increase of stenosis height.

The percentages of increase in resistance to flow and skin friction over that for uniform diameter tube (no stenosis) and for arteries with different radii are computed in Table 3. One can observe that the percentages of increase in resistance

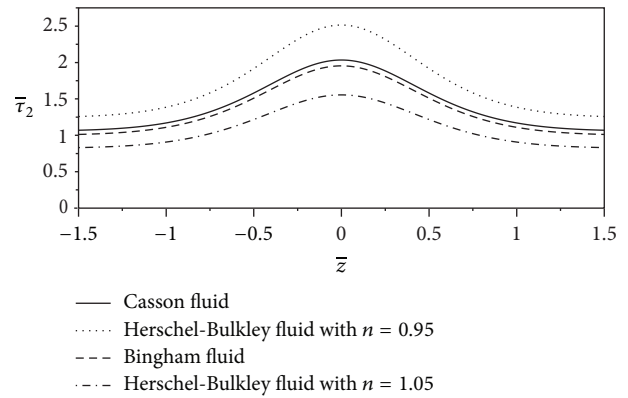


FIGURE 14: Variations of skin friction  $\bar{\tau}_2$  with axial distance for different fluid models with bell-shaped stenosis.

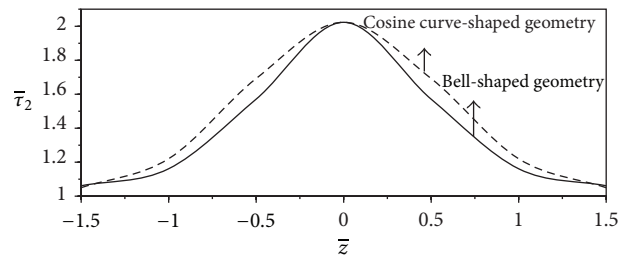


FIGURE 15: Variations of skin friction  $\bar{\tau}_2$  of Casson fluid model with axial distance for different geometries.

to flow and skin friction increase significantly when stenosis height increases. Comparisons of resistance to flow ( $\bar{\lambda}_2$ ) in bell-shaped stenosed arteries and cosine curve-shaped stenosed arteries with different values of stenosis size parameters  $a$ ,  $L_0$ , and  $m$  are given in Table 4. It is recorded that the resistance to flow in bell-shaped stenosed artery increases considerably when the length of the stenosis increases, and also it significantly increases when stenosis height increases. But it marginally decreases with the increase of the stenosis length parameter  $m$ . It is also found that for

TABLE 3: Estimates of the percentage of increase in resistance to flow  $\bar{\lambda}_2$  and skin friction  $\bar{\tau}_2$  for arteries with different radii with  $L_0/L = 1$  and  $\tau_c = 0.04 \text{ dyn cm}^{-2}$ .

Blood vessels	$\tau'_c$	$a = 0.10$		$a = 0.15$	
		$\bar{\lambda}$ (%)	$\bar{\tau}$ (%)	$\bar{\lambda}$ (%)	$\bar{\tau}$ (%)
Aorta	$1.529080 \times 10^{-2}$	20.31	32.25	34.00	54.23
Femoral	$5.718029 \times 10^{-3}$	21.13	34.00	35.44	57.28
Carotid	$4.571948 \times 10^{-3}$	21.27	34.31	35.69	57.82
Coronary	$8.733753 \times 10^{-4}$	22.00	35.86	36.97	60.53
Arteriole	$5.629388 \times 10^{-3}$	21.14	34.03	35.45	57.32

TABLE 4: Estimates of percentage of increase in resistance to flow  $\bar{\lambda}_2$  for arteries with different radii and with (i) bell-shaped stenosis (ii) cosine curve-shaped stenosis.

Blood vessels	Bell-shaped stenosis					Cosine curve-shaped stenosis	
			$\bar{\lambda}_2$ (%)			$\bar{\lambda}_2$ (%)	
	$a = 0.1$	$a = 0.1$	$a = 0.1$	$a = 0.2$	$a = 0.2$	$a = 0.1$	$a = 0.2$
	$m = 2$	$m = 2$	$m = 3$	$m = 3$	$m = 2$	$L_0 = 1.0$	$L_0 = 1.5$
	$L_0 = 1.0$	$L_0 = 1.5$	$L_0 = 1.5$	$L_0 = 1.5$	$L_0 = 1.5$	$L_0 = 1.0$	$L_0 = 1.5$
Aorta	4.06	6.09	4.33	10.42	15.31	4.28	15.79
Femoral	4.23	6.34	4.50	10.87	15.99	4.45	16.78
Carotid	4.25	6.38	4.53	10.95	16.11	4.50	16.96
Coronary	4.40	6.60	4.68	11.35	16.72	4.71	17.86
Arteriole	4.23	6.34	4.50	10.88	16.00	4.47	16.79

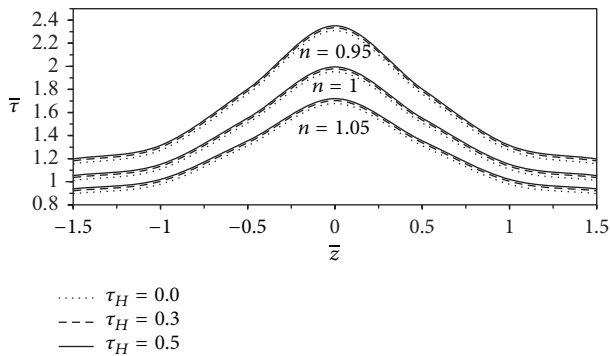


FIGURE 16: Variations of skin friction with axial distance for different values of power index and yield stress  $\tau_H$ .

a given set of values of the parameters, the percentage of increase in resistance to flow in the case of bell-shaped stenosed artery is slightly lower than that of cosine curve-shaped stenosed artery. This is physically verified with the depth of the stenosis for cosine-shaped stenosis (shown in Figure 8) being more; the resistance to flow is higher in this type of stenosis geometry compared to the bell-shaped stenosis geometry.

### 5. Conclusion

The present study analyzed the steady flow of blood in a narrow artery with bell-shaped mild stenosis, treating blood as Casson fluid, and the results are compared with the results of Misra and Shit for, Herschel-Bulkley fluid model [17] and also

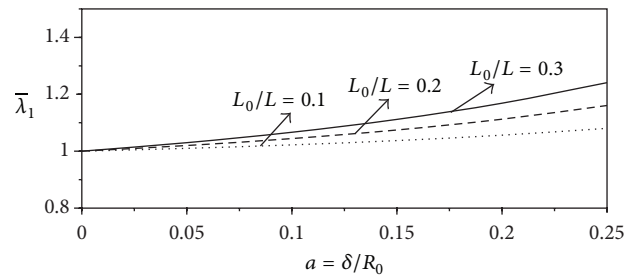


FIGURE 17: Variations of flow resistance  $\bar{\lambda}_1$  with stenosis height  $\delta/R_0$  for different values of stenosis length  $L_0/L$ .

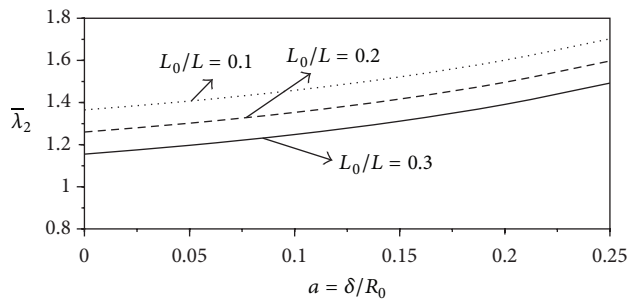


FIGURE 18: Variations of flow resistance  $\bar{\lambda}_2$  with stenosis height  $\delta/R_0$  for different values of stenosis length  $L_0/L$ .

with the results of Chaturani and Ponnalagar Samy [16] (for blood flow in cosine curve-shaped stenosed arteries, treating blood as Herschel-Bulkley fluid model). The main findings of the present mathematical analysis are as follows:

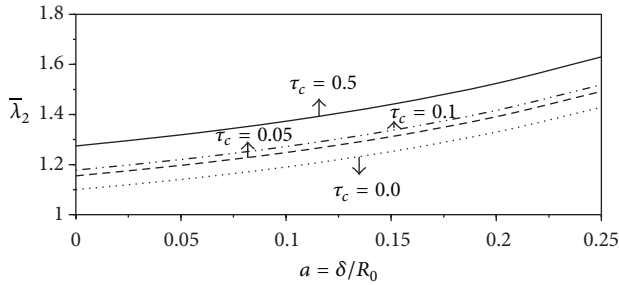


FIGURE 19: Variations of flow resistance  $\bar{\lambda}_2$  with stenosis height  $\delta/R_0$  for different values of yield stress  $\tau_c$ .

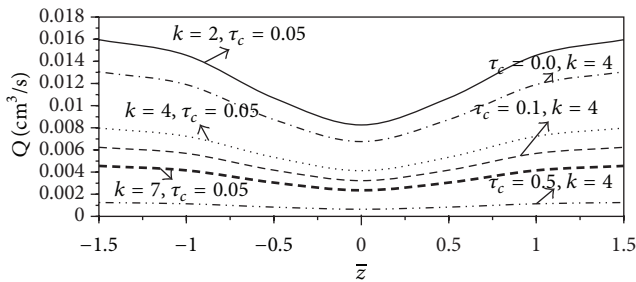


FIGURE 20: Variations of the rate of flow with axial distance for different values of viscosity  $k$  and yield stress  $\tau_c$ .

(i) Whether normalized with respect to non-Newtonian or Newtonian fluid in normal artery (i.e., in both cases of the effect of stenosis and the effect of non-Newtonian fluid) we notice the following.

- (1) Skin friction increases with the increase of depth and length of the stenosis.
- (2) Skin friction of Casson fluid model is significantly lower than that of the Herschel-Bulkley fluid model.
- (3) Skin friction in bell-shaped stenosed artery is considerably lower than that in the cosine curve-shaped stenosed artery.

(ii) The effect of stenosis on blood flow is that the resistance to flow increases when either the stenosis length or depth increases.

(iii) The effect of non-Newtonian fluid on blood flow is that the resistance to flow increases significantly with the increase of yield stress, but it decreases when either the stenosis length or depth increases.

(iv) The percentage of increase in resistance to flow in the case of bell-shaped stenosed artery is slightly lower than that of the cosine curve-shaped stenosed artery in the case of normalization with respect to Newtonian fluid.

(v) Flow rate decreases with the increase of the yield stress and viscosity coefficient.

Hence, in view of the results obtained, we conclude that the present study may be considered as an improvement in

the studies of the mathematical modeling of blood flow in narrow arteries with mild stenosis.

## Nomenclature

$\tau$ :	Shear stress
$\tau_c$ :	Yield stress for Casson fluid
$\tau_R$ :	Skin friction in stenosed artery
$\bar{\tau}_1$ :	Nondimensional skin friction normalized with non-Newtonian fluid
$\bar{\tau}_2$ :	Nondimensional skin friction normalized with Newtonian fluid
$\tau_N$ :	Skin friction in normal artery normalized with non-Newtonian fluid
$\tau_{N_e}$ :	Skin friction in normal artery normalized with Newtonian fluid
$\delta$ :	Stenosis height
$\lambda$ :	Flow resistance
$\bar{\lambda}_1$ :	Nondimensional flow resistance normalized with non-Newtonian fluid
$\bar{\lambda}_2$ :	Nondimensional flow resistance normalized with Newtonian fluid
$\bar{\lambda}_N$ :	Flow resistance in normal artery normalized with non-Newtonian fluid
$\bar{\lambda}_{N_e}$ :	Flow resistance in normal artery normalized with Newtonian fluid
$Q$ :	Volumetric flow rate
$r$ :	Radial coordinate
$z$ :	Axial coordinate
$u$ :	Radial velocity
$R_0$ :	Radius of the normal artery
$R(z)$ :	Radius of the artery in the stenosed portion
$L$ :	Half-length of segment of the narrow artery
$L_0$ :	Half-length of the stenosis
$p$ :	Pressure
$k$ :	Viscosity coefficient.

## Acknowledgments

The authors thank S. V. Subhashini, Assistant Professor (SG), Department of Mathematics, Anna University, Chennai, for her useful suggestions and timely help for improving the quality of the paper. The research work is supported by the Research University grant of the Universiti Sains Malaysia, Malaysia. RU Grant no. 1001/PMATHS/811177.

## References

- [1] M. E. Clark, J. M. Robertson, and L. C. Cheng, "Stenosis severity effects for unbalanced simple-pulsatile bifurcation flow," *Journal of Biomechanics*, vol. 16, no. 11, pp. 895–906, 1983.
- [2] D. Liepsch, M. Singh, and M. Lee, "Experimental analysis of the influence of stenotic geometry on steady flow," *Biorheology*, vol. 29, no. 4, pp. 419–431, 1992.
- [3] S. Cavalcanti, "Hemodynamics of an artery with mild stenosis," *Journal of Biomechanics*, vol. 28, no. 4, pp. 387–399, 1995.
- [4] V. P. Rathod and S. Tanveer, "Pulsatile flow of couple stress fluid through a porous medium with periodic body acceleration and

- magnetic field," *Bulletin of the Malaysian Mathematical Sciences Society*, vol. 32, no. 2, pp. 245–259, 2009.
- [5] G. R. Cokelet, "The rheology of human blood," in *Biomechanics*, Y. C. Fung et al., Ed., p. 63, Prentice-hall, Englewood Cliffs, NJ, USA, 1972.
- [6] W. Boyd, *Text Book of Pathology: Structure and Functions in Diseases*, Lea and Febiger, Philadelphia, Pa, USA, 1963.
- [7] B. C. Krishnan, S. E. Rittgers, and A. P. Yoganathan, *Bioid Mechanics: The Human Circulation*, Taylor and Francis, New York, NY, USA, 2012.
- [8] G. W. S. Blair, "An equation for the flow of blood, plasma and serum through glass capillaries," *Nature*, vol. 183, no. 4661, pp. 613–614, 1959.
- [9] A. L. Copley, "Apparent viscosity and wall adherence of blood systems," in *Flow Properties of Blood and Other Biological Systems*, A. L. Copley and G. Stainsly, Eds., Pergamon Press, Oxford, UK, 1960.
- [10] N. Casson, "Rheology of disperse systems," in *Flow Equation for Pigment Oil Suspensions of the Printing Ink Type. Rheology of Disperse Systems*, C. C. Mill, Ed., pp. 84–102, Pergamon Press, London, UK, 1959.
- [11] E. W. Merrill, A. M. Benis, E. R. Gilliland, T. K. Sherwood, and E. W. Salzman, "Pressure-flow relations of human blood in hollow fibers at low flow rates," *Journal of Applied Physiology*, vol. 20, no. 5, pp. 954–967, 1965.
- [12] S. Charm and G. Kurland, "Viscometry of human blood for shear rates of  $0-100,000 \text{ sec}^{-1}$ ," *Nature*, vol. 206, no. 4984, pp. 617–618, 1965.
- [13] G. W. S. Blair and D. C. Spanner, *An Introduction to Biorheology*, Elsevier Scientific, Oxford, UK, 1974.
- [14] J. Aroesty and J. F. Gross, "Pulsatile flow in small blood vessels. I. Casson theory," *Biorheology*, vol. 9, no. 1, pp. 33–43, 1972.
- [15] P. Chaturani and R. P. Samy, "Pulsatile flow of Casson's fluid through stenosed arteries with applications to blood flow," *Biorheology*, vol. 23, no. 5, pp. 499–511, 1986.
- [16] P. Chaturani and V. R. Ponnalagar Samy, "A study of non-Newtonian aspects of blood flow through stenosed arteries and its applications in arterial diseases," *Biorheology*, vol. 22, no. 6, pp. 521–531, 1985.
- [17] J. C. Misra and G. C. Shit, "Blood flow through arteries in a pathological state: a theoretical study," *International Journal of Engineering Science*, vol. 44, no. 10, pp. 662–671, 2006.
- [18] D. S. Sankar, "Two-fluid nonlinear mathematical model for pulsatile blood flow through stenosed arteries," *Bulletin of the Malaysian Mathematical Sciences Society*, vol. 35, no. 2A, pp. 487–498, 2012.
- [19] D. S. Sankar and K. Hemalatha, "Pulsatile flow of Herschel-Bulkley fluid through stenosed arteries—a mathematical model," *International Journal of Non-Linear Mechanics*, vol. 41, no. 8, pp. 979–990, 2006.
- [20] S. U. Siddiqui, N. K. Verma, and R. S. Gupta, "A mathematical model for pulsatile flow of Herschel-Bulkley fluid through stenosed arteries," *Journal of Electronic Science and Technology*, vol. 4, pp. 49–466, 2010.
- [21] D. S. Sankar, "Perturbation analysis for blood flow in stenosed arteries under body acceleration," *International Journal of Non-linear Sciences and Numerical Simulation*, vol. 11, no. 8, pp. 631–653, 2010.

## Research Article

# Optimized Weighted Essentially Nonoscillatory Third-Order Schemes for Hyperbolic Conservation Laws

A. R. Appadu<sup>1</sup> and A. A. I. Peer<sup>2</sup>

<sup>1</sup> Department of Mathematics and Applied Mathematics, University of Pretoria, Pretoria 0002, South Africa

<sup>2</sup> Department of Applied Mathematical Sciences, University of Technology, Mauritius, La Tour Koenig, Pointe-aux-Sables, Mauritius

Correspondence should be addressed to A. R. Appadu; rao.appadu@up.ac.za

Received 12 April 2013; Revised 25 June 2013; Accepted 25 June 2013

Academic Editor: Mohamed Fathy El-Amin

Copyright © 2013 A. R. Appadu and A. A. I. Peer. This is an open access article distributed under the Creative Commons Attribution License, which permits unrestricted use, distribution, and reproduction in any medium, provided the original work is properly cited.

We describe briefly how a third-order Weighted Essentially Nonoscillatory (WENO) scheme is derived by coupling a WENO spatial discretization scheme with a temporal integration scheme. The scheme is termed WENO3. We perform a spectral analysis of its dispersive and dissipative properties when used to approximate the 1D linear advection equation and use a technique of optimisation to find the optimal cfl number of the scheme. We carry out some numerical experiments dealing with wave propagation based on the 1D linear advection and 1D Burger's equation at some different cfl numbers and show that the optimal cfl does indeed cause less dispersion, less dissipation, and lower  $L_1$  errors. Lastly, we test numerically the order of convergence of the WENO3 scheme.

## 1. Introduction

Spatial discretization methods in order to solve partial differential equations can be broadly classified as finite difference, finite volume, finite element, and spectral methods. All these methods combined with explicit or implicit time integration schemes can be effectively applied to solve partial differential equations.

Computational dispersion arises from space differencing and must not be confused with instability [1]. A noisy solution is not necessarily unstable. Both dispersion and instability can lead to noise. In the case of dispersion, the waves do not grow in amplitude but become separated from one another, each at its own speed [1]. Computational dispersion causes waves of different wavelengths to travel at different speeds.

One of the most common ways of measuring the relative merit of a numerical scheme for advection is to consider the scheme's dispersion and dissipation [2]. All linear numerical schemes are either dispersive or dissipative [3]. We now briefly survey some techniques implemented to minimise dispersion and/or dissipation, in regions of shocks.

Antidiffusion has been proposed in order to improve the resolving power of dissipative schemes [4]. Antidiffusion does well with shock-type discontinuities, but at the same time, distortions are produced in smooth regions. Artificial viscosity does work to suppress oscillations and capture shock waves [5]. However, it ruins the resolution of numerical schemes in recognising shock waves. Filters are also used to control computational noise. The Galerkin finite element methods are useful to solve the advection equation [6]. However, they generate a great deal of computational noise in highly steep gradients. An iteration smoothing process was proposed by Forester [7] in order to smooth the computational values from the results of the Galerkin finite element method.

The concept of limiters was introduced by Boris and Book [8] and van Leer [9]. The approach of flux-corrected transport is an early version of the concept of limiters [10]. Boris and Book [8] introduced a flux-corrected method which improves the accuracy of a variety of finite difference algorithms. The second version of limiters is geometric limiters [10]. One example is van Leer's scheme which blends

Fromm's method with a geometric limiter [9]. The scheme naturally detects a discontinuity and changes its behaviour accordingly.

Essentially Nonoscillatory (ENO) and WENO schemes have been developed to capture shocks efficiently [11]. These are high-order accurate finite difference schemes designed for problems with piecewise smooth solutions containing discontinuities. The fundamental notion resides at the approximation level, where a nonlinear adaptive procedure is used to choose the locally smoothest stencil, thus avoiding crossing discontinuities in the interpolation procedure as much as possible. WENO methods suffer from a tendency for the weights of the various stencils to revert quite slowly to the underlying high-order method as the numerical resolution of a smooth function improves.

The effects of dispersion terms on numerical solutions have been done since a long time [5]. However, it is only since the last two decades that extensive studies on the dispersion-controlled dissipative scheme were reported. Work on scheme dispersion reduction was first reported by Fromm [12]. Fromm's scheme in 1D is made up of a linear combination of Lax-Wendroff and the Beam-Warming second-order upwind schemes as these two dispersive schemes have phase errors in opposite directions. We can also combine dispersive and dissipative schemes to obtain composite schemes. This idea was implemented in meteorological codes which compose the oscillatory second-order Leap-Frog scheme with the dissipative backward Euler scheme [4].

Kasahara and Washington [13] use a three-level Leap-Frog scheme for 50 time steps which is inherently unstable followed by one cycle of the Lax-Wendroff scheme. The Leap-Frog scheme when applied for 50 time steps is unstable. The Lax-Wendroff scheme is essentially dispersive but does possess some damping property. The damping properties of Lax-Wendroff render the combined procedure of the application of 50 time steps of the three-level Leap-Frog scheme and one cycle of Lax-Wendroff scheme stable. Shchepetkin and McWilliams [14] have combined the Leap-Frog scheme with the Trapezoidal Rule. Liska and Wendroff [4] have obtained a composite scheme which comprises Lax-Wendroff as the dispersive scheme and the two-step Lax-Friedrichs scheme as the dissipative scheme to obtain the Lax-Wendroff/Lax-Friedrichs scheme.

The paper is organised as follows. In Sections 2 and 3, we construct the WENO reconstruction and the time integration schemes. The originality in this work resides in the fact that expressions for the amplification factor and the relative phase error have been obtained for the WENO3 scheme discretizing the 1D linear advection equation. Very few papers have examined these properties for WENO schemes as it is cumbersome to obtain the expression for the amplification factor of WENO schemes in general. Spectral analysis of the WENO3 scheme is discussed in Section 4. In Section 5, we compute the optimal cfl number of the WENO3 scheme by using a technique of optimisation that minimizes both the dispersion and dissipation errors. Such an optimal cfl number is important as the cfl number is chosen quite arbitrarily for WENO schemes, and, hence, the efficient shock-capturing properties of WENO methods

are not exploited. Section 7 gives a description of how to quantify errors from numerical results into dispersion and dissipation. Some numerical experiments are performed in Section 8 and errors are compared at different cfl numbers. Section 9 highlights the salient features of the paper.

## 2. WENO Spatial Reconstructions

WENO schemes are commonly used for the solution of hyperbolic conservation laws of the form

$$u_t + f_x(u) = 0, \quad (1)$$

where  $u$  is the conserved variable and  $f$  is the flux function.

Integrating (1) over the cell  $I_x = \{\xi : |\xi - x| \leq h/2\}$  and denoting its cell average by  $\bar{u}(x, t)$ , we get the equation

$$\bar{u}_t(x, t) = -\frac{1}{h} \left[ f\left(u\left(x + \frac{h}{2}, t\right)\right) - f\left(u\left(x - \frac{h}{2}, t\right)\right) \right]. \quad (2)$$

Upwind schemes sample the solution at the cell centres  $x = x_j$ , and in this case we can write (2) in the semidiscrete form as follows:

$$\frac{d\bar{u}_j(t)}{dt} = -\frac{1}{h} [\hat{f}_{j+1/2} - \hat{f}_{j-1/2}], \quad (3)$$

where the exact flux is  $\hat{f}_{j+1/2} \equiv f(u(x_{j+1/2}, t))$ . Since the flux is required on cell boundaries, the discontinuities which may be present prevent the use of a quadrature formula to integrate in time. A Riemann solver is needed to identify the direction of propagation of the waves, and then an ODE solver is applied to advance (3) in time.

The relation (3) requires a reconstruction to recover the approximation of point values  $u(x_{j+1/2}, t)$ . Assuming that the cell averages  $\bar{u}_j^n$  are known, the following piecewise polynomial reconstruction is done:

$$u^n(x) = \sum_j p_j(x) \chi_j(x), \quad (4)$$

where  $\chi_j$  is the characteristic function of the cell  $I_j$ . Denoting the order of accuracy by  $k$ ,  $p_j(x)$  is a polynomial of degree at most  $k - 1$  on the cell  $I_j$ , such that

$$p_j(x) = u(x, t^n) + O(h^k), \quad x \in I_j, \quad (5)$$

and maintains conservation; that is,

$$\frac{1}{h} \int_{I_j} p_j(x) dx = \bar{u}_j^n. \quad (6)$$

The approximations at the cell boundaries for the semi-discrete upwind scheme (3) are given by  $u_{j+1/2}^- = p_j(x_{j+1/2})$  and  $u_{j+1/2}^+ = p_{j+1}(x_{j+1/2})$ . The evolution step consists of approximating the point values  $u(x_{j+1/2}, t)$  from  $u_{j+1/2}^-$  and  $u_{j+1/2}^+$ , by identifying the waves according to their direction of propagation, and to find the numerical flux,

$\widehat{f}_{j+1/2} = h(u_{j+1/2}^-, u_{j+1/2}^+)$ . Here we consider the monotone Lax-Friedrichs flux which is given by

$$h(a, b) = \frac{1}{2} [f(a) + f(b) - \alpha(b - a)], \quad \alpha = \max_u |f'(u)|. \quad (7)$$

A WENO reconstruction consists of associating a weight to all of the candidate stencils of an Essentially Nonoscillatory (ENO) reconstruction. All the possible approximations at cell boundaries  $u_{j+1/2}^{-(r)}$  for  $r = 0, \dots, k-1$  are evaluated using  $p_j(x)$ , and then

$$u_{j+1/2}^- = \sum_{r=0}^{k-1} \omega_r u_{j+1/2}^{-(r)}, \quad (8)$$

where the weights satisfy

$$\omega_r \geq 0, \quad \sum_{r=0}^{k-1} \omega_r = 1. \quad (9)$$

If  $u(x, t)$  is smooth over all the candidate stencils, then some linear weights  $d_r$  are used, such that

$$u_{j+1/2}^- = \sum_{r=0}^{k-1} d_r u_{j+1/2}^{-(r)} = u(x_{j+1/2}) + O(h^{2k-1}). \quad (10)$$

The linear weights  $d_r$  for  $r = 0, \dots, k-1$  are found by carrying out a Taylor series expansion of (10).

In case there is a discontinuity present in one of the candidate stencils, its corresponding weight turns to be nearly 0, such that only a smooth approximation is considered. The weights are given by

$$\omega_r = \frac{\alpha_r}{\sum_{s=0}^{k-1} \alpha_s}, \quad (11)$$

where

$$\alpha_r = \frac{d_r}{(\epsilon + \beta_r)^2}, \quad r = 0, \dots, k-1. \quad (12)$$

The parameter  $\epsilon$  in (12) is used to avoid divisions by zeros during computations, and as per the majority of literature in the field we will take  $\epsilon$  as  $10^{-6}$ .

The parameters  $\beta_r$  are called the smoothness indicators of the candidate stencils. They make the weights of smooth stencils dominant over those of discontinuous stencils. The smoothness indicators are measures of the  $L^2$ -norms of the derivatives of  $p_j(x)$ ; that is,

$$\beta_r = \sum_{l=1}^{k-1} \int_{I_j} h^{2l-1} \left( \frac{\partial^l p_r(x)}{\partial x^l} \right)^2 dx. \quad (13)$$

If a stencil is smooth then its corresponding smoothness indicator  $\beta_r = O(h^2)$ , but if the stencil contains a discontinuity then  $\beta_r = O(1)$ . This strategy reduces the contribution of nonsmooth stencils.

Similarly, the WENO principle is used for  $u_{j-1/2}^+$ , where

$$u_{j-1/2}^+ = \sum_{r=0}^{k-1} \tilde{\omega}_r u_{j-1/2}^{+(r)}, \quad \tilde{\omega}_r = \frac{\tilde{\alpha}_r}{\sum_{s=0}^{k-1} \tilde{\alpha}_s}, \quad (14)$$

$$\tilde{\alpha}_r = \frac{\tilde{d}_r}{(\epsilon + \beta_r)^2},$$

for  $r = 0, \dots, k-1$ , and the terms  $\tilde{d}_r$  satisfy  $\tilde{d}_r = d_{k-1-r}$ .

### 3. Time Integration Schemes

In this section, we describe some time integration schemes to advance the solution of (2) in time. The time step is taken as

$$\Delta t = \frac{c}{\max_j |f'(u_j)|} h, \quad (15)$$

where the CFL number  $c$  is necessary for stability.

Let  $L(u)$  be an approximation to the spatial derivative  $-f(u)_x$  and consider the semidiscrete formulation (3) as a system of initial value problem of ODE

$$u_t = L(u). \quad (16)$$

We mention a result that motivates the use of high-order Strong Stability-Preserving (SSP) Runge-Kutta (RK) methods in time. If the first-order forward Euler time stepping method

$$u^{n+1} = u^n + \Delta t L(u^n) \quad (17)$$

is SSP, that is,

$$\|u^{n+1}\| \leq \|u^n\|, \quad (18)$$

for  $\Delta t \leq \Delta t_{FE}$ , then the same strong stability is preserved for higher order SSPRK methods under the restriction

$$\Delta t \leq c \Delta t_{FE}, \quad (19)$$

where  $c$  is the CFL coefficient for the high-order time integration.

The explicit  $\nu$  stage Runge-Kutta method has the general form

$$u^{(i)} = \sum_{k=0}^{i-1} (\alpha_{i,k} u^{(k)} + \Delta t \beta_{i,k} L(u^{(k)})), \quad i = 1, \dots, \nu, \quad (20)$$

$$u^{(0)} = u^n, \quad u^{(\nu)} = u^{n+1}.$$

For nonnegative coefficients  $\alpha_{i,k} \geq 0$  and  $\beta_{i,k} \geq 0$ , the Runge-Kutta method (20) is a convex combination of Euler forward schemes. The scheme should satisfy  $\sum_{k=0}^{i-1} \alpha_{i,k} = 1$ .

**Lemma 1.** *If the forward Euler method (17) is strongly stable under the CFL restriction  $\Delta t \leq \Delta t_{FE}$ ,  $\|u^n + \Delta t L(u^n)\| \leq \|u^n\|$ , then the Runge-Kutta method (20) with  $\beta_{i,k} \geq 0$  is SSP provided the following CFL restriction (19) is fulfilled:*

$$\Delta t \leq c \Delta t_{FE}, \quad c = \min_{i,k} \frac{\alpha_{i,k}}{\beta_{i,k}}. \quad (21)$$

For the special class of optimal  $\nu$  stage  $\nu$ th-order SSPRK schemes, the CFL coefficient is maximized according to Lemma 1. Optimal second-order and third-order SSPRK schemes are, respectively, given by

$$\begin{aligned} u^{(1)} &= u^n + \Delta t L(u^n), \\ u^{n+1} &= \frac{1}{2}u^n + \frac{1}{2}u^{(1)} + \frac{1}{2}\Delta t L(u^{(1)}), \\ u^{(1)} &= u^n + \Delta t L(u^n), \\ u^{(2)} &= \frac{3}{4}u^n + \frac{1}{4}u^{(1)} + \frac{1}{4}\Delta t L(u^{(1)}), \\ u^{n+1} &= \frac{1}{3}u^n + \frac{2}{3}u^{(2)} + \frac{2}{3}\Delta t L(u^{(2)}). \end{aligned} \quad (22)$$

#### 4. Spectral Analysis of WENO3

In this paper, we focus on third-order WENO3 reconstruction. Setting  $k = 2$  in (8), we get

$$u_{j+1/2}^- = \omega_0 u_{j+1/2}^{-(0)} + \omega_1 u_{j+1/2}^{-(1)}, \quad (23)$$

where

$$\begin{aligned} u_{j+1/2}^{-(0)} &= \frac{1}{2}\bar{u}_j + \frac{1}{2}\bar{u}_{j+1}, \\ u_{j+1/2}^{-(1)} &= -\frac{1}{2}\bar{u}_{j-1} + \frac{3}{2}\bar{u}_j. \end{aligned} \quad (24)$$

The smoothness indicators (13) of the nonlinear weights (11) and (12) turn out to be

$$\begin{aligned} \beta_0 &= (\bar{u}_{j+1} - \bar{u}_j)^2, \\ \beta_1 &= (\bar{u}_j - \bar{u}_{j-1})^2, \end{aligned} \quad (25)$$

with linear coefficients  $d_0 = 2/3$  and  $d_1 = 1/3$ .

For the sake of finding amplification factors of numerical schemes, we consider the linear advection case  $f(u) = au$  into (1), where  $a$  is a constant. This results in the numerical flux (7) simplifying to

$$\hat{f}_{j+1/2} = \frac{a}{6}(-u_{j-1} + 5u_j + 2u_{j+1}), \quad (26)$$

and, therefore, (16) is approximated by

$$L(v_j) = -\frac{a}{6h}(v_{j-2} - 6v_{j-1} + 3v_j + 2v_{j+1}). \quad (27)$$

The fully discretized method is given by

$$\begin{aligned} u_i^{n+1} &= -\frac{1}{1296}c^3 u_{i-6}^n + \frac{1}{72}c^3 u_{i-5}^n \\ &+ \frac{1}{144}(2 - 13c)c^2 u_{i-4}^n \\ &+ \frac{1}{216}c^2(-36 + 53c)u_{i-3}^n \\ &- \frac{1}{144}c(24 - 84c + 31c^2)u_{i-2}^n \\ &- \frac{1}{72}c(-72 + 32c + 5c^2)u_{i-1}^n \\ &+ \frac{1}{432}(432 - 216c - 90c^2 + 59c^3)u_i^n \\ &+ \frac{1}{72}c(-24 + 12c + c^2)u_{j+1}^n \\ &- \frac{1}{36}(-2 + c)c^2 u_{i+2}^n - \frac{1}{162}c^3 u_{i+3}^n, \end{aligned} \quad (28)$$

where  $c = a\Delta t/h$ .

On substituting  $u_i^n$  by  $\xi^n \exp(I\theta ih)$  where  $\xi$  is the amplification factor,  $I = \sqrt{-1}$ , and  $\theta h$  is the phase angle, we obtain the amplification factor as

$$\begin{aligned} \xi &= -\frac{1}{1296}c^3 \exp(-6Iw) + \frac{1}{72}c^3 \exp(-5Iw) \\ &+ \frac{1}{144}(2 - 13c)r^2 \exp(-4Iw) \\ &+ \frac{1}{216}c^2(-36 + 53c) \exp(-3Iw) \\ &- \frac{1}{144}c(24 - 84c + 31c^2) \exp(-2Iw) \\ &- \frac{1}{72}c(-72 + 32c + 5c^2) \exp(-Iw) \\ &+ \frac{1}{432}(432 - 216c - 90c^2 + 59c^3) \\ &+ \frac{1}{72}c(-24 + 12c + c^2) \exp(Iw) \\ &- \frac{1}{36}(-2 + c)c^2 \exp(2Iw) \\ &- \frac{1}{162}c^3 \exp(3Iw), \end{aligned} \quad (29)$$

where  $w = \theta h$ .

The real and imaginary parts of  $\xi$  are given by

$$\begin{aligned} \Re(\xi) &= \left(1 - \frac{1}{2}c - \frac{5}{24}c^2 + \frac{59}{432}c^3\right) \\ &+ \left(\frac{2}{3}c - \frac{5}{18}c^2 - \frac{1}{18}c^3\right) \cos(w) \\ &\times \left(-\frac{1}{6}c + \frac{23}{36}c^2 - \frac{35}{144}c^3\right) \cos(2w) \\ &+ \left(-\frac{1}{6}c^2 + \frac{155}{648}c^3\right) \cos(3w) \\ &+ \frac{1}{144}c^2(2 - 13c) \cos(4w) \\ &+ \frac{1}{72}c^3 \cos(5w) - \frac{1}{1296}c^3 \cos(6w), \quad (30) \\ \Im(\xi) &= \left(-\frac{4}{3}c + \frac{11}{18}c^2 + \frac{1}{12}c^3\right) \sin(w) \\ &+ \left(\frac{1}{6}c - \frac{19}{6}c^2 + \frac{3}{16}c^3\right) \sin(2w) \\ &+ \left(-\frac{1}{6}c^2 + \frac{163}{648}c^3\right) \sin(3w) \\ &- \frac{1}{144}c^2(2 - 13c) \sin(4w) \\ &- \frac{1}{72}c^3 \sin(5w) + \frac{1}{1296}c^3 \sin(6w), \end{aligned}$$

respectively.

The modulus of the amplification factor, AFM, is computed as

$$AFM = \sqrt{(\Re(\xi))^2 + (\Im(\xi))^2}, \quad (31)$$

and the region of stability is obtained as  $0 \leq c \leq 1.48$  as depicted in Figure 1.

The relative phase error, RPE, is obtained as

$$RPE = -\frac{1}{cw} \tan^{-1} \left( \frac{\Im(\xi)}{\Re(\xi)} \right). \quad (32)$$

Plots of the AFM versus the phase angle at six different cfl numbers, namely, 0.25, 0.5, 0.75, 1.0, 1.25, and 1.47, are shown in Figure 2. The scheme is least dissipative at cfl = 0.25. At low cfl numbers, the scheme is less dissipative especially for phase angles,  $w \in [0, 1]$ . Plots of the RPE versus phase angle at the six different cfl numbers are shown in Figure 3. There is no big change in the dispersive character at cfl 0.25, 0.5, 0.75, and 1.0, and at these cfl numbers, phase lag behaviour is exhibited at all phase angles,  $w \in [0, \pi]$ . At phase angles greater than 0.5, phase lead behaviour is exhibited at cfl = 1.47.

The modified equation of WENO3 when discretized by the 1D linear advection equation is given by

$$u_t + au_x + \left(\frac{1}{12}a\Delta t h^3 + \frac{1}{24}(a\Delta t)^4\right)u_{xxxx} + \dots = 0, \quad (33)$$

indicating that the scheme is third-order accurate in space and essentially dissipative in nature.

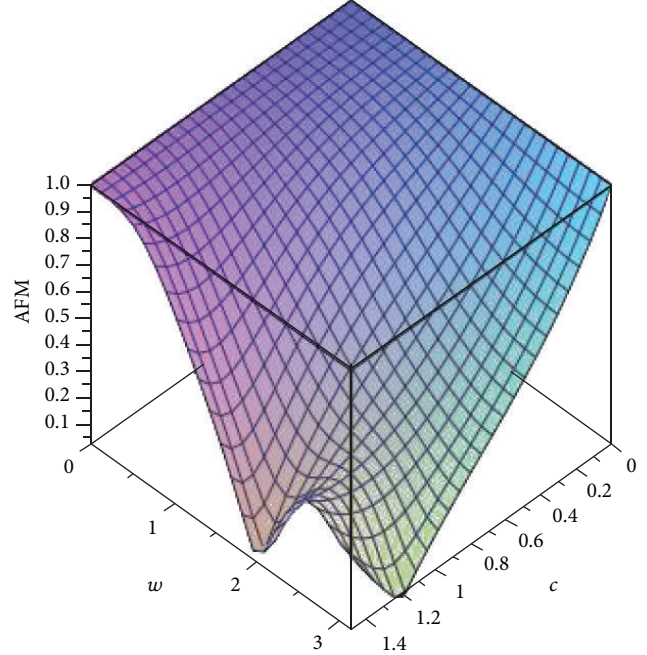


FIGURE 1: Plot of modulus of amplification factor versus phase angle versus cfl number for the WENO3 scheme.

### 5. Optimisation of WENO3 Scheme Discretizing the 1D Linear Advection Equation

The technique of Minimized Integrated Exponential Error for Low Dispersion and Low Dissipation (MIEELDL) has been introduced in Appadu and Dauhoo (2011). It basically enables us to choose the optimal parameters from two conditions; namely,

- (i) small amounts of dissipation when added can help to curb numerical dispersion [4];
- (ii) the dissipation and dispersion errors must both be small in a numerical scheme to yield efficient shock-capturing properties.

We now describe the technique of minimized integrated exponential error for low dispersion and low dissipation (MIEELDL). Suppose that the amplification factor of the numerical scheme when applied to the 1D linear advection equation, given by

$$u_t + au_x = 0, \quad (34)$$

is

$$\xi = \Re(\xi) + I\Im(\xi). \quad (35)$$

The quantities  $|1 - RPE|$  and  $(1 - AFM)$  measure the dispersion and dissipation errors, respectively. For a numerical scheme to have low dispersion and low dissipation, we require

$$|1 - RPE| + (1 - AFM) \rightarrow 0. \quad (36)$$

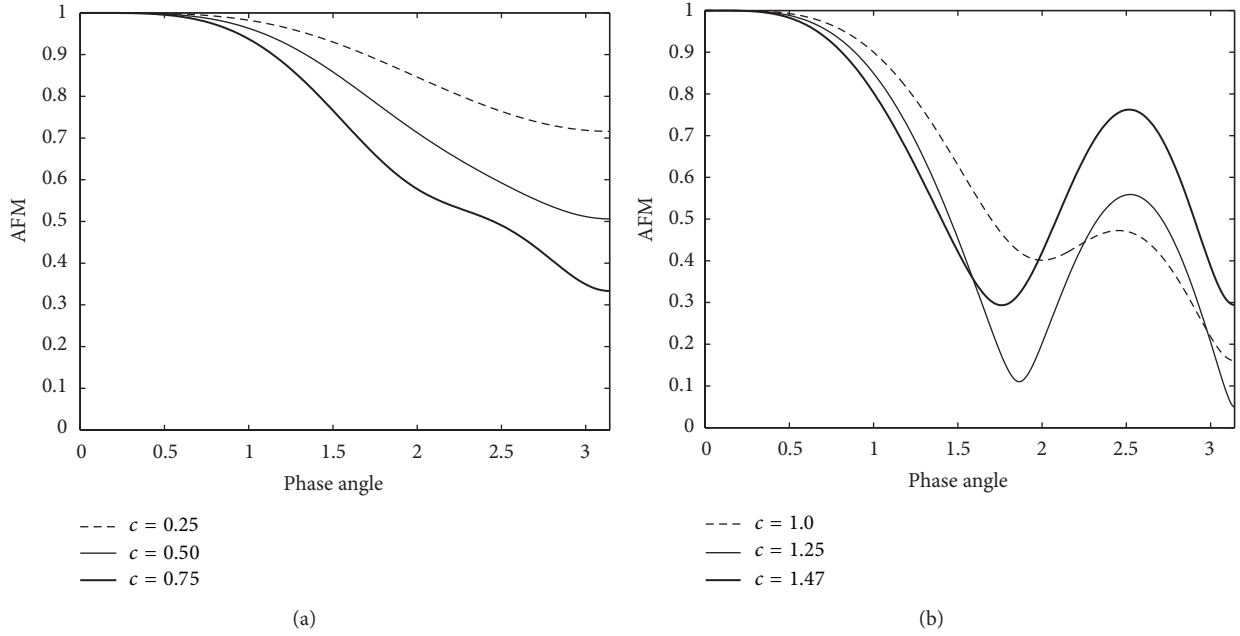


FIGURE 2: Plots of AFM versus phase angle at some cfl numbers for the WENO3 scheme.

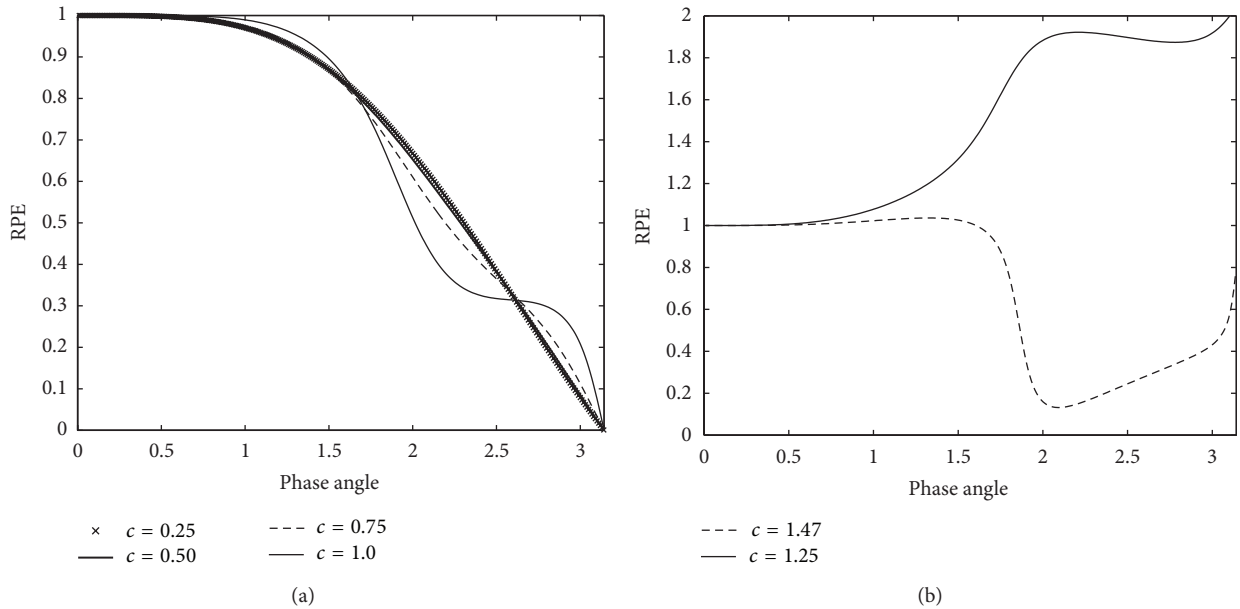


FIGURE 3: Plots of RPE versus phase angle at some cfl numbers for the WENO3 scheme.

Also when dissipation neutralises dispersion optimally, we have

$$||1 - RPE| - (1 - AFM)| \rightarrow 0. \quad (37)$$

Thus on combining these two conditions, we get the following condition necessary for dissipation to neutralise dispersion

and for low dispersion and low dissipation character to be satisfied:

$$\begin{aligned} \text{eldld} &= ||1 - RPE| - (1 - AFM)| \\ &+ (|1 - RPE| + (1 - AFM)) \rightarrow 0, \end{aligned} \quad (38)$$

where eldld denotes error for low dispersion and low dissipation.

If we plot the quantity,  $e_{ldld}$  versus RPE versus AFM, as done in [15], we can see that  $e_{ldld} = 0$  when  $RPE = 1$  (no dispersion) and  $AFM = 1$  (no dissipation), and this makes sense. However, the  $e_{ldld}$  takes a constant value of 2 when  $RPE = 2$  independent of the value of the AFM, and this presents a drawback of the measure. Therefore, we have presented a modification to the quantity,  $e_{ldld}$ , which is

$$e_{ldld} = \exp(|1 - RPE| - (1 - AFM)) + \exp(|1 - RPE| + (1 - AFM)) - 2 \rightarrow 0, \quad (39)$$

and this quantity goes to zero when  $|1 - RPE| \rightarrow 0$  and  $(1 - AFM) \rightarrow 0$ .

The  $e_{ldld}$  denotes exponential error for low dispersion and low dissipation [15, 16].

**5.1. Only One Parameter Involved.** If the cfl number is the only parameter, we compute the integrated error for low dispersion and low dissipation,  $IEELDL$ ,

$$\int_0^{w_1} e_{ldld} dw, \quad (40)$$

for a range of  $w \in [0, w_1]$ , and this integral will be a function of  $c$ . The optimal cfl is the one at which the integral quantity is closest to zero.

**5.2. Two Parameters Are Involved.** Suppose that we now have two parameters, say  $\lambda$  and  $c$ . In that case, we can compute

$$\int_0^{c_1} \int_0^{w_1} e_{ldld} dw dc, \quad (41)$$

and this integral will be a function of  $\lambda$  and we can obtain the optimal value of  $\lambda$ .

We can also compute

$$\int_0^{w_1} e_{ldld} dw, \quad (42)$$

and this integral will consist of  $\lambda$  and  $c$ . From there, we can obtain the optimal values of both  $\lambda$  and  $c$ .

Considerable and extensive work on the technique of minimised integrated exponential error for low dispersion and low dissipation has been carried out in [15–17]. In [15], we have obtained the optimal cfl of some explicit methods like Lax-Wendroff, Beam-Warming, and Upwind Leap-Frog when applied to the 1D advection equation. In [17], we use the technique to understand why not all composite methods can be effective to control dispersion and dissipation in regions of shocks. In [16], we consider the family of third-order methods proposed by Takacs [2] where we optimize two parameters, namely, the cfl number and another variable which also controls dispersion and dissipation.

In this work, we use the technique,  $MIEELDL$ , to compute the optimal cfl number of the WENO3 scheme. The plots of the integrated error versus cfl number are shown in Figure 4, which indicates that the optimal cfl is close to zero.

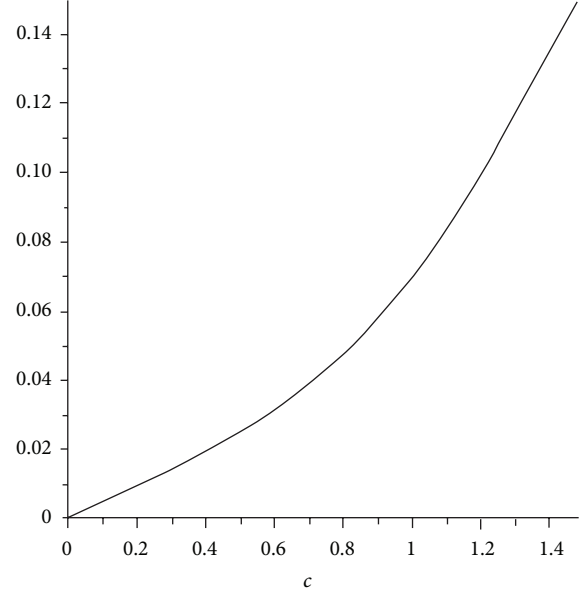


FIGURE 4: Plot of  $IEELDL$  versus cfl number for the WENO3 scheme.

## 6. Optimisation of WENO3 Scheme Discretizing the 1D Burgers' Equation

Ascher and McLachlan [18] have obtained the dispersion relation for the equation

$$u_t = 2\alpha uu_x + \rho u_x + \mu u_{xxx}. \quad (43)$$

They considered the linearized version of (43) which is

$$u_t = \rho u_x + \mu u_{xxx}. \quad (44)$$

By considering a plane wave solution of the form  $u(x, t) = \exp(I((\theta/h)x + (\omega_1/\Delta t)t))$ , where  $\theta$  and  $\omega_1$  are the wavenumber and dispersion relation, respectively, the exact dispersion relation is

$$\omega_1 = \rho \frac{\Delta t}{h} \theta - \frac{\nu \Delta t}{h^3} \theta^3. \quad (45)$$

The exact phase velocity can then be deduced. A numerical scheme can then be used to discretize (44), and, thus, the numerical phase velocity can be obtained. The relative phase error is then computed as the ratio of the numerical phase velocity to the exact phase velocity.

Since a linearised version of the 1D Burgers' equation,

$$u_t + \left(\frac{1}{2}u^2\right)_x = 0, \quad (46)$$

is not possible, we cannot obtain the relative phase error, and thus it is not possible to obtain the variation of the quantity,  $IEELDL$ , versus  $c$  to deduce the optimal cfl number. To estimate the optimal cfl number, we can run our numerical experiment at some cfl numbers, compute the  $L_1$  error, dispersion, dissipation errors, and  $e_{ldld}$ , and then guess the optimal cfl number. This approach has been done in Section 8.3.

## 7. Quantification of Errors from Numerical Results [2, 15, 16]

In this section, we describe how Takacs [2] quantifies errors from numerical results into dispersion and dissipation errors.

The Total Mean Square Error is calculated as

$$\frac{1}{N} \sum_{i=1}^N (u_i - v_i)^2, \quad (47)$$

where  $u_i$  represents the analytical solution and  $v_i$  is the numerical (discrete) solution at a given grid point,  $i$ .

The Total Mean Square Error can be expressed as

$$\frac{1}{N} \sum_{i=1}^N (u_i - v_i)^2 = \frac{1}{N} \sum_{i=1}^N (u_i)^2 + \frac{1}{N} \sum_{i=1}^N (v_i)^2 - \frac{2}{N} \sum_{i=1}^N u_i v_i. \quad (48)$$

Next,

$$\frac{1}{N} \sum_{i=1}^N (u_i - \bar{u}_i)^2 = \frac{1}{N} \sum_{i=1}^N ((u_i)^2 - 2u_i \bar{u}_i + (\bar{u}_i)^2), \quad (49)$$

$$\frac{1}{N} \sum_{i=1}^N (v_i - \bar{v}_i)^2 = \frac{1}{N} \sum_{i=1}^N ((v_i)^2 - 2v_i \bar{v}_i + (\bar{v}_i)^2).$$

The Total Mean Square Error can be further expressed as

$$\begin{aligned} & \frac{1}{N} \sum_{i=1}^N (u_i - \bar{u}_i)^2 + \frac{1}{N} \sum_{i=1}^N (v_i - \bar{v}_i)^2 + \frac{2}{N} \sum_{i=1}^N u_i \bar{u}_i \\ & + \frac{2}{N} \sum_{i=1}^N v_i \bar{v}_i - \frac{1}{N} \sum_{i=1}^N (\bar{u}_i)^2 - \frac{1}{N} \sum_{i=1}^N (\bar{v}_i)^2 - \frac{2}{N} \sum_{i=1}^N u_i v_i. \end{aligned} \quad (50)$$

The expression in (50) can be rewritten as

$$\sigma^2(u) + \sigma^2(v) + 2(\bar{u})^2 + 2(\bar{v})^2 - (\bar{u})^2 - (\bar{v})^2 - \frac{2}{N} \sum_{i=1}^N u_i v_i, \quad (51)$$

where  $\sigma^2(u)$  and  $\sigma^2(v)$  denote the variance of  $u$  and  $v$ , respectively, and  $\bar{u}$  and  $\bar{v}$ , denote the mean values of  $u$  and  $v$  respectively.

Thus, the Total Mean Square Error is given by

$$\sigma^2(u) + \sigma^2(v) + ((\bar{u})^2 - 2\bar{u}\bar{v} + (\bar{v})^2) + \left(2\bar{u}\bar{v} - \frac{2}{N} \sum_{i=1}^N u_i v_i\right), \quad (52)$$

which on further simplification yields

$$\sigma^2(u) + \sigma^2(v) + (\bar{u} - \bar{v})^2 - 2 \left( \frac{1}{N} \sum_{i=1}^N u_i v_i - \bar{u} \bar{v} \right). \quad (53)$$

Thus, we have

$$\frac{1}{N} \sum_{i=1}^N (u_i - v_i)^2 = \sigma^2(u) + \sigma^2(v) + (\bar{u} - \bar{v})^2 - 2 \text{Cov}(u, v). \quad (54)$$

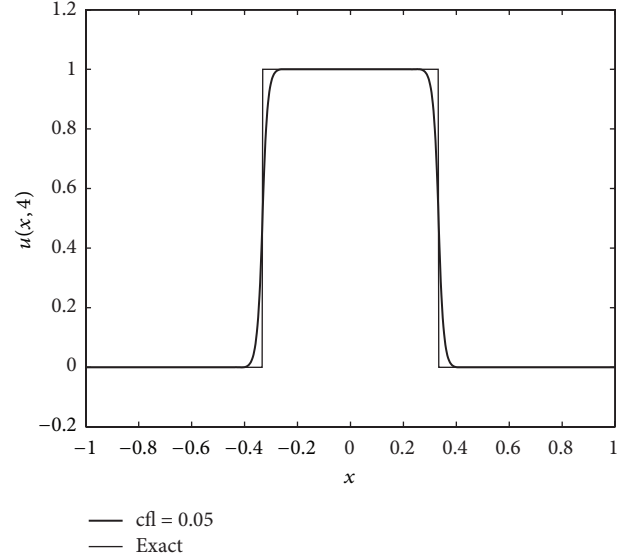


FIGURE 5: Results of Problem II at cfl number 0.05 with number of spatial steps,  $N = 800$ .

But the correlation coefficient,  $\rho$ , is given by  $\text{Cov}(u, v) / \sigma(u)\sigma(v)$ . Hence, the Total Mean Square Error can be written as

$$\frac{1}{N} \sum_{i=1}^N (u_i - v_i)^2 = \sigma^2(u) + \sigma^2(v) + (\bar{u} - \bar{v})^2 - 2\rho\sigma(u)\sigma(v), \quad (55)$$

which simplifies to

$$\begin{aligned} & \frac{1}{N} \sum_{i=1}^N (u_i - v_i)^2 \\ & = (\sigma(u) - \sigma(v))^2 + (\bar{u} - \bar{v})^2 + 2(1 - \rho)\sigma(u)\sigma(v). \end{aligned} \quad (56)$$

On putting  $\rho = 1$ , we get  $2(1 - \rho)\sigma(u)\sigma(v) = 0$ . Thus, we define  $2(1 - \rho)\sigma(u)\sigma(v)$  as the dispersion error as correlation coefficient in statistics is analogous with phase lag or phase lead in Computational Fluid Dynamics.

Consequently,  $(\sigma(u) - \sigma(v))^2 + (\bar{u} - \bar{v})^2$  measures the dissipation error. The total error is defined as the sum of the dissipation and dispersion errors.

Since our domain  $x \in [0, 1]$ , the  $L_1$  error is calculated as

$$h \sum_{i=1}^N |u_i - v_i|, \quad (57)$$

where  $u_i$  and  $v_i$  are the computed and exact values, respectively, and  $h$  and  $N$  are the step length and number of cells, respectively.

## 8. Numerical Experiments

8.1. Problem I. We solve  $u_t + u_x = 0$  with the initial conditions  $u(x, 0) = \sin(\pi x)$  for  $x \in [0, 1]$ . We display the errors

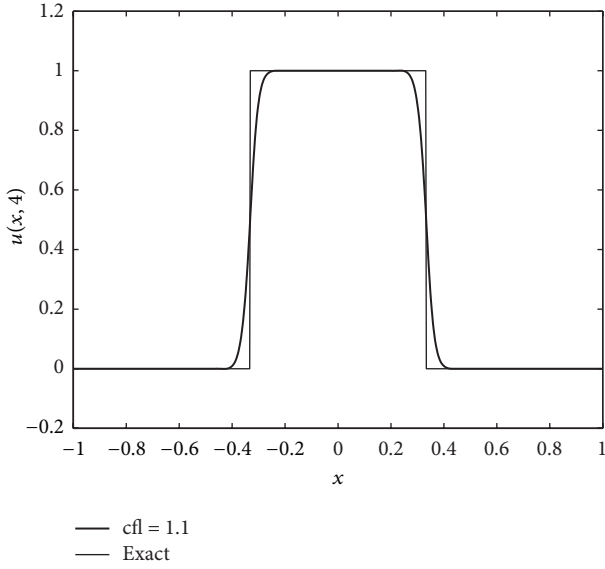


FIGURE 6: Results of Problem II at cfl number 1.1 with number of spatial steps,  $N = 800$ .

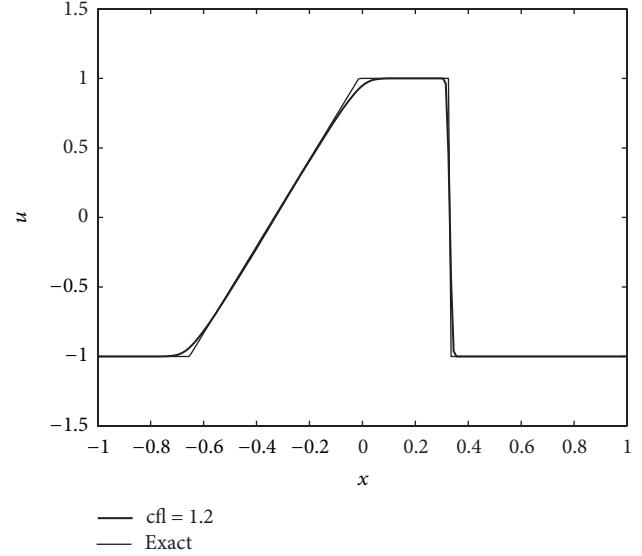


FIGURE 8: Solutions for Problem III with 200 cells at  $T = 0.32$  using WENO3 scheme at cfl number 1.3.

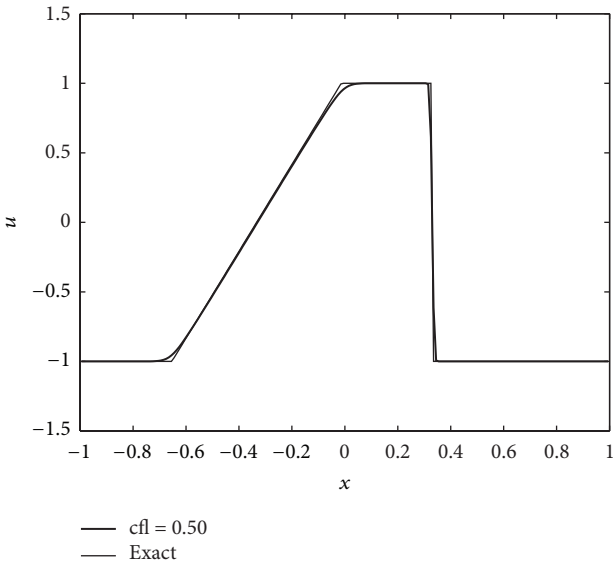


FIGURE 7: Solutions for Problem III with 200 cells at  $T = 0.32$  using WENO3 scheme at cfl number 0.50.

and convergence rates at time  $T = 1.0$  at some different cfl numbers, namely, 0.05, 0.1, 0.25, 0.5, 1.0, 1.25, and 25/17 in Tables 1, 2, 3, 4, 5, 6, and 7. The order of convergence obtained numerically at the seven values of cfl is approximately equal to 3. At low cfl numbers, the order is in general closer to 3. This shows that the choice of the cfl number affects to a certain extent the order of convergence.

8.2. *Problem II.* We solve  $u_t + u_x = 0$  with the initial condition being  $u(x, 0) = 1$  for  $|x| < 1/3$  and  $u(x, 0) = 0$  elsewhere [19]. We use some different values of cfl and cells,  $N$ . We use  $N = 800$ . The various types of errors, namely, dissipation error and

TABLE 1: Errors for Problem I at time  $T = 10$  and cfl = 0.05.

$N$	$L_1$ error	$L_1$ order
40	$1.269805 \times 10^{-2}$	—
80	$1.658269 \times 10^{-3}$	3.40
160	$1.576016 \times 10^{-4}$	2.94

TABLE 2: Errors for Problem I at time  $T = 10$  and cfl = 0.1.

$N$	$L_1$ error	$L_1$ order
40	$1.272504 \times 10^{-2}$	—
80	$1.695274 \times 10^{-3}$	2.91
160	$2.510625 \times 10^{-4}$	2.76

TABLE 3: Errors for Problem I at time  $T = 10$  and cfl = 0.25.

$N$	$L_1$ error	$L_1$ order
40	$1.283696 \times 10^{-2}$	—
80	$1.729243 \times 10^{-3}$	2.89
160	$2.96433 \times 10^{-4}$	2.54

TABLE 4: Errors for Problem I at time  $T = 10$  and cfl = 0.5.

$N$	$L_1$ error	$L_1$ order
40	$1.354268 \times 10^{-2}$	—
80	$1.821605 \times 10^{-3}$	2.89
160	$3.15924 \times 10^{-4}$	2.53

dispersion error, are tabulated for some values of cfl numbers in Table 8. It can be seen clearly that the cfl number influences the shock-capturing property of the scheme to a great extent. Results are depicted in Figures 5 and 6.

Table 8 shows the dissipation, dispersion, total errors, and eeldld at some values of cfl. We observe that the total error

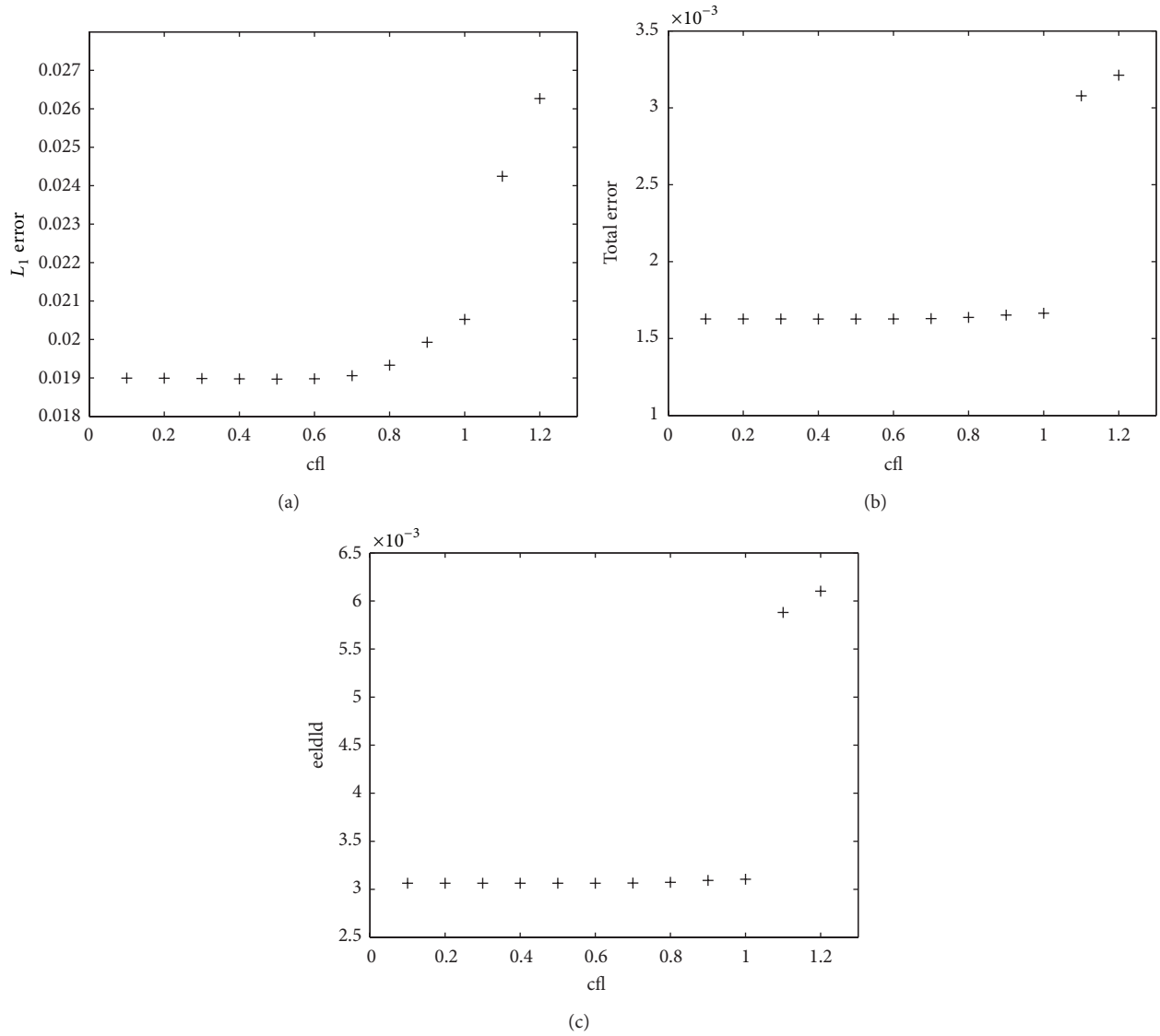


FIGURE 9: Plots of errors versus cfl number using WENO3 scheme for Problem III.

TABLE 5: Errors for Problem I at time  $T = 10$  and  $cfl = 1.0$ .

$N$	$L_1$ error	$L_1$ order
40	$1.903424 \times 10^{-2}$	—
80	$2.509531 \times 10^{-3}$	2.92
160	$4.216578 \times 10^{-4}$	2.57

TABLE 7: Errors for Problem I at time  $T = 10$  and  $cfl = 25/17$ .

$N$	$L_1$ error	$L_1$ order
40	$3.2771865 \times 10^{-2}$	—
80	$4.213891 \times 10^{-3}$	2.96
160	$6.46257 \times 10^{-4}$	2.70

TABLE 6: Errors for Problem I at time  $T = 10$  and  $cfl = 1.25$ .

$N$	$L_1$ error	$L_1$ order
40	$2.500545 \times 10^{-2}$	—
80	$3.255547 \times 10^{-3}$	2.94
160	$5.197687 \times 10^{-4}$	2.65

8.3. *Problem III.* We solve Burger' equation

$$u_t + \left(\frac{1}{2}u^2\right)_x = 0, \tag{58}$$

with initial conditions being

$$u(x, 0) = 1 \quad \text{for } |x| < \frac{1}{3}, \quad u(x, 0) = -1 \quad \text{elsewhere.} \tag{59}$$

The time  $T = 0.32$ . We perform the experiment using WENO3 over 200 cells at some cfl numbers. The  $L_1$  errors,

and ceidd are least at low cfl numbers. These two quantities increase monotonically as the cfl number increases.

TABLE 8: Errors for Problem II at time  $T = 4.0$ .

cfl	Dissipation error	Dispersion error	Total error	eeldld
0.05	$1.226025 \times 10^{-4}$	$3.662431 \times 10^{-3}$	$3.785033 \times 10^{-3}$	$7.338306 \times 10^{-3}$
0.1	$1.225995 \times 10^{-4}$	$3.662445 \times 10^{-3}$	$3.785045 \times 10^{-3}$	$7.338335 \times 10^{-3}$
0.2	$1.225756 \times 10^{-4}$	$3.662562 \times 10^{-3}$	$3.785137 \times 10^{-3}$	$7.338569 \times 10^{-3}$
0.3	$1.225113 \times 10^{-4}$	$3.662889 \times 10^{-3}$	$3.785400 \times 10^{-3}$	$7.339226 \times 10^{-3}$
0.4	$1.223875 \times 10^{-4}$	$3.663557 \times 10^{-3}$	$3.785945 \times 10^{-3}$	$7.340568 \times 10^{-3}$
0.5	$1.221869 \times 10^{-4}$	$3.664757 \times 10^{-3}$	$3.786944 \times 10^{-3}$	$7.342976 \times 10^{-3}$
0.6	$1.218963 \times 10^{-4}$	$3.666677 \times 10^{-3}$	$3.788573 \times 10^{-3}$	$7.346830 \times 10^{-3}$
0.7	$1.215076 \times 10^{-4}$	$3.669750 \times 10^{-3}$	$3.791257 \times 10^{-3}$	$7.352998 \times 10^{-3}$
0.8	$1.210324 \times 10^{-4}$	$3.674625 \times 10^{-3}$	$3.795657 \times 10^{-3}$	$7.362783 \times 10^{-3}$
0.9	$1.218720 \times 10^{-4}$	$3.702746 \times 10^{-3}$	$3.824618 \times 10^{-3}$	$7.419234 \times 10^{-3}$
1.0	$1.325062 \times 10^{-4}$	$3.886192 \times 10^{-3}$	$4.018698 \times 10^{-3}$	$7.787523 \times 10^{-3}$
1.1	$2.664458 \times 10^{-4}$	$5.697562 \times 10^{-3}$	$5.9640074 \times 10^{-3}$	$1.1427719 \times 10^{-2}$
1.2	$4.998687 \times 10^{-3}$	$2.152228 \times 10^{-3}$	$2.6520962 \times 10^{-3}$	$4.353663 \times 10^{-2}$

TABLE 9: Errors for Problem III at time  $T = 0.32$ .

cfl	$L_1$ error	Dissipation error	Dispersion error	Total error	eeldld
0.1	$1.899421 \times 10^{-2}$	$9.6601082 \times 10^{-5}$	$1.53065207 \times 10^{-3}$	$1.6272532 \times 10^{-3}$	$3.063658 \times 10^{-3}$
0.2	$1.899205 \times 10^{-2}$	$9.656411 \times 10^{-5}$	$1.530635 \times 10^{-3}$	$1.627199 \times 10^{-3}$	$3.063623 \times 10^{-3}$
0.3	$1.898594 \times 10^{-2}$	$9.646438 \times 10^{-5}$	$1.530581 \times 10^{-3}$	$1.627045 \times 10^{-3}$	$3.063515 \times 10^{-3}$
0.4	$1.897550 \times 10^{-2}$	$9.630490 \times 10^{-5}$	$1.530486 \times 10^{-3}$	$1.626791 \times 10^{-3}$	$3.063324 \times 10^{-3}$
0.5	$1.896950 \times 10^{-2}$	$9.625772 \times 10^{-5}$	$1.530438 \times 10^{-3}$	$1.626696 \times 10^{-3}$	$3.06229 \times 10^{-3}$
0.6	$1.897802 \times 10^{-2}$	$9.652521 \times 10^{-5}$	$1.530544 \times 10^{-3}$	$1.627069 \times 10^{-3}$	$3.063441 \times 10^{-3}$
0.7	$1.905973 \times 10^{-2}$	$9.798369 \times 10^{-5}$	$1.531593 \times 10^{-3}$	$1.629577 \times 10^{-3}$	$3.065543 \times 10^{-3}$
0.8	$1.933042 \times 10^{-2}$	$1.019279 \times 10^{-4}$	$1.535211 \times 10^{-3}$	$1.637139 \times 10^{-3}$	$3.072791 \times 10^{-3}$
0.9	$1.992670 \times 10^{-2}$	$1.076351 \times 10^{-4}$	$1.545164 \times 10^{-3}$	$1.652799 \times 10^{-3}$	$3.092728 \times 10^{-3}$
1.0	$2.052249 \times 10^{-2}$	$1.133164 \times 10^{-4}$	$1.551133 \times 10^{-3}$	$1.664449 \times 10^{-3}$	$3.104686 \times 10^{-3}$
1.1	$2.424540 \times 10^{-2}$	$1.417231 \times 10^{-4}$	$2.936234 \times 10^{-3}$	$3.077957 \times 10^{-3}$	$5.881118 \times 10^{-3}$
1.2	$2.626771 \times 10^{-2}$	$1.655616 \times 10^{-4}$	$3.046531 \times 10^{-3}$	$3.212092 \times 10^{-3}$	$6.102380 \times 10^{-3}$

dispersion errors, and dissipation errors are shown in Table 9. Results are shown in Figures 7 and 8.

We observe that the errors are least at cfl 0.50 and greatest at cfl 1.2. Figure 9 shows the plots of  $L_1$  error, and total error and eeldld, all versus the cfl number. These three errors are least at low cfl numbers.

## 9. Conclusion

In this work, we study the spectral analysis of the dissipation and dispersion errors of the WENO3 scheme at some different cfl numbers and verify numerically the order of convergence of the WENO3 scheme. It is observed that low cfl numbers are preferred to minimise the  $L_1$  error, dispersion and dissipation errors, and eeldld. An extension of this work is to obtain the optimal cfl of some WENO schemes discretizing some 1D nonlinear equations such as Korteweg-de-Vries and also 2D equations such as scalar advection, convection-diffusion, and Korteweg-de-Vries equations.

## Nomenclature

$I = \sqrt{-1}$   
 $\Delta t$ : Time step  
 $h$ : Spatial step  
 $n$ : Time level  
 $a$ : Advection velocity  
 $c$ : cfl/Courant number  
 $c = a\Delta t/h$   
 $w$ : Phase angle in 1D  
 $w = \theta h$   
RPE: Relative phase error per unit time step  
AF: Amplification factor  
AFM =  $|AF|$ .

## Acknowledgments

The authors thank the anonymous referees whose comments helped to improve the work and the presentation of this paper. This work was initiated when Dr. Appadu was on a research

visit at the University of Technology which was funded by the Research Development Programme (RDP) of the University of Pretoria. The period of support for the RDP funds is from January 2012 to January 2014.

## References

- [1] D. A. Randall, "An introduction to atmospheric modeling," Tech. Rep., 2007.
- [2] L. L. Takacs, "A two-step scheme for the advection equation with minimized dissipation and dispersion errors," *Monthly Weather Review*, vol. 113, no. 6, pp. 1050–1065, 1985.
- [3] H. Trac and U.-L. Pen, "A primer on eulerian computational fluid dynamics for astrophysics," *Publications of the Astronomical Society of the Pacific*, vol. 115, no. 805, pp. 303–321, 2003.
- [4] R. Liska and B. Wendroff, "Composite schemes for conservation laws," *SIAM Journal on Numerical Analysis*, vol. 35, no. 6, pp. 2250–2271, 1998.
- [5] Z. Jiang, "On dispersion-controlled principles for non-oscillatory shock-capturing schemes," *Acta Mechanica Sinica*, vol. 20, no. 1, pp. 1–15, 2004.
- [6] S. Okamoto, K. Hara, A. Takei, and F. Masuda, "A study on numerical methods for air quality simulation," *Tokyo University of Information Sciences*, vol. 5, no. 1, pp. 65–72, 2001.
- [7] C. K. Forester, "Higher order monotonic convective difference schemes," *Journal of Computational Physics*, vol. 23, no. 1, pp. 1–22, 1977.
- [8] J. P. Boris and D. L. Book, "Flux-corrected transport. I. SHASTA, a fluid transport algorithm that works," *Journal of Computational Physics*, vol. 11, no. 1, pp. 38–69, 1973.
- [9] B. van Leer, "Towards the ultimate conservative difference scheme. II. Monotonicity and conservation combined in a second-order scheme," *Journal of Computational Physics*, vol. 14, no. 4, pp. 361–370, 1974.
- [10] P. Colella and E. Puckett, "Modern methods for fluid flow," Tech. Rep., 1994.
- [11] X.-D. Liu, S. Osher, and T. Chan, "Weighted essentially non-oscillatory schemes," *Journal of Computational Physics*, vol. 115, no. 1, pp. 200–212, 1994.
- [12] J. E. Fromm, "A method for reducing dispersion in convective difference schemes," *Journal of Computational Physics*, vol. 3, no. 2, pp. 176–189, 1968.
- [13] A. Kasahara and W. M. Washington, "Thermal and dynamical effects of orography on the general circulation of the atmosphere," in *Proceedings of the WMO/IUGG Symposium on Numerical Weather Prediction*, pp. 47–56, Tokyo, Japan, November-December 1968.
- [14] A. F. Shchepetkin and J. C. McWilliams, "Quasi-monotone advection schemes based on explicit locally adaptive dissipation," *Monthly Weather Review*, vol. 126, no. 6, pp. 1541–1580, 1998.
- [15] A. R. Appadu and M. Z. Dauhoo, "The concept of minimized integrated exponential error for low dispersion and low dissipation schemes," *International Journal for Numerical Methods in Fluids*, vol. 65, no. 5, pp. 578–601, 2011.
- [16] A. R. Appadu, "Some applications of the concept of minimized integrated exponential error for low dispersion and low dissipation," *International Journal for Numerical Methods in Fluids*, vol. 68, no. 2, pp. 244–268, 2012.
- [17] A. R. Appadu, "Investigating the shock-capturing properties of some composite numerical schemes for the 1-D linear advection equation," *International Journal of Computer Applications in Technology*, vol. 43, no. 2, pp. 79–92, 2012.
- [18] U. M. Ascher and R. I. McLachlan, "Multisymplectic box schemes and the Korteweg-de Vries equation," *Applied Numerical Mathematics*, vol. 48, no. 3-4, pp. 255–269, 2004.
- [19] A. A. I. Peer, M. Z. Dauhoo, A. Gopaul, and M. Bhuruth, "A weighted ENO-flux limiter scheme for hyperbolic conservation laws," *International Journal of Computer Mathematics*, vol. 87, no. 15, pp. 3467–3488, 2010.

## Research Article

# The Fractal Dimension of River Length Based on the Observed Data

Ni Zhihui,<sup>1,2</sup> Wu Lichun,<sup>3</sup> Wang Ming-hui,<sup>1</sup> Yi Jing,<sup>1</sup> and Zeng Qiang<sup>1</sup>

<sup>1</sup> Key Laboratory of Hydraulic and Waterway Engineering, The Ministry of Education and National Engineering Research Center for Inland Waterway Regulation, Chongqing Jiaotong University, Chongqing 400074, China

<sup>2</sup> Southwestern Research Institute of Water Transportation Engineering, Chongqing Jiaotong University, Chongqing 400016, China

<sup>3</sup> Chongqing Education College, Chongqing 400067, China

Correspondence should be addressed to Ni Zhihui; benny251@163.com

Received 20 May 2013; Accepted 27 June 2013

Academic Editor: Shuyu Sun

Copyright © 2013 Ni Zhihui et al. This is an open access article distributed under the Creative Commons Attribution License, which permits unrestricted use, distribution, and reproduction in any medium, provided the original work is properly cited.

Although the phenomenon that strictly meets the constant dimension fractal form in the nature does not exist, fractal theory provides a new way and means for the study of complex natural phenomena. Therefore, we use some variable dimension fractal analysis methods to study river flow discharge. On the basis of the flood flow corresponding to the waterline length, the river of the overall and partial dimensions are calculated and the relationships between the overall and partial dimensions are discussed. The law of the length in section of Chongqing city of Yangtze River is calibrated by using of variable fractal dimension. The results conclude that it does express a second-order accumulated variable-dimensional fractal phenomenon, and the dimension can reflect the degree of the river; the greater dimension, the more the river bend. It has different dimensions at a different location in the same river. In the same river, the larger dimension, the worse flow discharge capacity of the river and the more obvious of the flood will be on the performance.

## 1. Introduction

A fractal dimension is a ratio providing a statistical index of complexity comparing how detail in a pattern changes with the scale at which it is measured. It has also been characterized as a measure of the space-filling capacity of a pattern that tells how a fractal scales differently than the space it is embedded in; a fractal dimension does not have to be an integer.

Fractals have been introduced in order to quantify the self-similarity observed in nature while at the same time to make the study of nondifferentiable processes possible. Given that this self-similar behavior has often a “local” character, the theory of fractals was generalized to multifractals, enabling the description of more complex phenomena with varying fractal properties. Examples of processes that have been thus treated are the energy dissipation in turbulence and the price increments in finance. In the field of geophysics and atmospheric physics, fractal and multifractal analyses have been extensively applied [1], since self-similarity is present in a wide variety of such phenomena, from the distribution of

earthquake epicenters [2–4] and hypocenters [5] to climate change [6] and atmospheric turbulence [7, 8]. In the same field of research, fractal and multifractal methods have been used both to characterize the long-term behavior of related signals and to indicate possible precursors in experimental time series of their records, yielding very promising results [9–12].

Fractal processes have become one of the most widely used modeling tools in science and engineering, with diverse applications in finance, physics, network traffic, and recently geography sciences. In the study of geometric properties of dynamical systems or fractal measures, one is often interested in the asymptotic behaviour of local quantities associated with the underlying dynamical or geometric structure. For example, one is often interested in the ergodic average of a continuous function, the local entropy or the local Lyapunov exponent, or the local dimension of a measure. These quantities provide a description of various aspects of measures or dynamical systems, for example, chaoticity, sensitive dependence, and so forth. All these quantities provide important information about the underlying geometric or

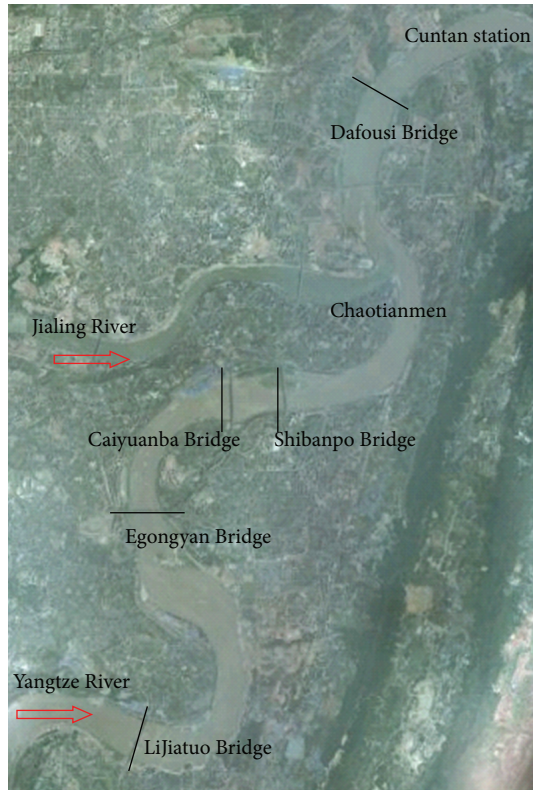


FIGURE 1: The plan of Chongqing city of Yangtze River.

dynamical structure [13]. The mixing length based on fractal theory has been calculated and analyzed [14]. Jou et al. [15] by assuming a self-similar structure for the Kelvin waves along vortex loops with successive smaller scale features model the fractal dimension of a super fluid vortex tangle in the zero temperature limits. Their model assumes that at each step the total energy of the vortices is conserved but the total length can change. They obtain a relation between the fractal dimension and the exponent describing how the vortex energy per unit length changes with the length scale. In addition, many scholars have also concerned about relationship between the fractal theory and river systems [16–22].

The analysis of river flows has a long history; nevertheless some important issues have been lost. Many scholars use some fractal analysis methods to study river flow fluctuations. Sadegh Movahed and Hermanis [23] have studied one component of the climate system, the river flux, by using the novel approach in the fractal analysis like detrended fluctuation analysis, fourier-detrended fluctuation analysis and scaled windowed variance analysis methods. The statistical and fractal analysis of river flows should be an important issue in the geophysics and hydrological systems to recognize the influence of environmental conditions and to detect the relative effects. A set of most important results which can be given by using statistical tools are as follows: a concept of scale self-similarity for the topography of Earth's surface [24], the hydraulic-geometric similarity of river system and

floods forced by the heavy rain [25], and so forth. Already more than half a century ago the engineer Hurst found that runoff records from various rivers exhibit “long-range statistical dependencies.” Later, such long-term correlated fluctuation behavior has also been reported for many other geophysical records including precipitation data. These original approaches exclusively focused on the absolute values or the variances of the full distribution of the fluctuations, which can be regarded as the first and second moments of detrended fluctuation analysis [24, 26]. In the last decade it has been realized that a multifractal description is required for a full characterization of the runoff records [27]. This multifractal description of the records can be regarded as a “fingerprint” for each station or river, which, among other things, can serve as an efficient nontrivial test bed for the state-of-the-art precipitation-runoff models.

In this work, the fractal dimension of the river (hereinafter referred to as dimension) is generated by studying characteristics of fractal structure. The dimension of the river is divided into river length and river network, to explore the fractal dimension from the view of the entire river length, to be called the unitary dimensions of river length. However, it has different dimensions at a different location in the same river. Meandering is different, so the dimension of rivers length (hereinafter referred to as part dimension) is, even vary considerably.

Chongqing is an oversize industrial city and the water-land transport hub that developed relying on the Yangtze River and Jialing River. The main section of Chongqing city is from Daduko to Tongluoxia; tributary section is from Jingkou of Jialing River to Chaotianmen. The total length of it is about 60 km. The section of Chongqing city of Yangtze River is located in the southeastern edge of Sichuan basin; the section of river is the lotus root shape. Because the river is affected by geological structure and its lithology changes, the longitudinal profile along the higher ups and downs changes greatly, and the river boundary conditions are very complicated as the section of Yangtze River is located in fluctuating backwater area of Three Gorges Project. Based on statistic water surface profile when flow discharge is  $58000 \text{ m}^3/\text{s}$  of Cuntan station, the average river width of Jiulongpo and Caiyuanba is more than 900 m, the total length of the two sections is about 6 km, and the length of narrow reach which is below 600 m is 1.7 km. The reach in the section of Chongqing city performance is of continuous and irregular curve shape, which has 6 continuous bends. These curves are slowly bending  $150^\circ$  and  $90^\circ$  elbow. Chongqing section of the Yangtze River in 2007 is shown in Figure 1.

At present, the research on the fractal characteristics of river length in section of Chongqing city of Yangtze River is few, and it is still in the theoretical exploration and analysis phase. Chongqing is located in the upper reaches of the Yangtze River, is an important strategic position, and is the largest port city in the upper reaches of the Yangtze River. Therefore, measurement on fractal dimension of river length in section of Chongqing city of Yangtze River can give full play to the effect of golden waterway in Yangtze River. It will play a leading role in water transport of Chongqing,

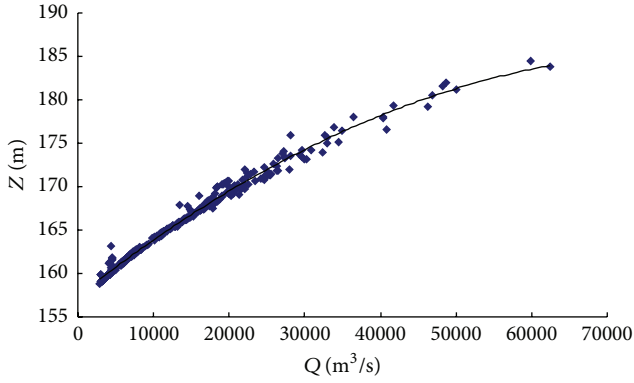


FIGURE 2: Discharge and water level relationship curve.

and provide better services for the upper reaches of Yangtze River and the western region. Thus, the study of the fractal dimension of river length in section of Chongqing city of Yangtze River is of great significance. In this paper, in the view of river length, the fractal dimension and its relationship with floods will be studied.

## 2. Methods

**2.1. Building of 1D Model Program.** The former USSR, North America, Western Europe, and China have carried out research and application of hydrodynamic, sediment transport model since the 1950s. A one-dimensional mathematical model of water flow has been more mature after several decades' development and application.

This research is studied through one-dimensional flow mathematical model. In view of the constant flow calculation which has been more mature, a one-dimensional constant flow mathematical model is taken to the whole river.

**2.1.1. Basic Equations.** Here is a 1D water movement and continuity equation:

$$\begin{aligned} \frac{\partial A}{\partial t} + \frac{\partial Q}{\partial x} &= 0, \\ \frac{\partial Q}{\partial t} + \frac{\partial UQ}{\partial x} + gA \frac{\partial Z}{\partial x} &= -\frac{B}{\rho} \tau_b, \end{aligned} \tag{1}$$

where  $A$  is cross-section area,  $Q$  is flow discharge,  $U$  is section average flow velocity,  $Z$  is water level,  $B$  is river width,  $x$  is horizontal direction,  $t$  is time,  $\rho$  is water density, and  $\tau_b$  is shear stress of river bottom.

Simplified equations is used in the calculation process, and water movement is changed to

$$\begin{aligned} \frac{\partial Q}{\partial x} &= 0, \\ Z_2 + \frac{\alpha_2 V_2^2}{2g} &= Z_1 + \frac{\alpha_1 V_1^2}{2g} + h_f + h_j, \end{aligned} \tag{2}$$

where  $Z_1$  is downstream section level,  $Z_2$  is upstream section level,  $V_1$  is downstream section average velocity,  $V_2$  is

upstream section average velocity,  $\alpha_1$  is downstream section kinetic energy correction factor,  $\alpha_2$  is upstream section kinetic energy correction factor,  $h_f$  is frictional head loss, and  $h_j$  is local head loss.

**2.1.2. Boundary Condition.** Control conditions of this model are the flow discharge of upstream and water level of downstream. Stage-discharge data of Cuntan station is the boundary condition of downstream. According to the hydrological data in 2011 and 2012 of Cuntan station, stage-discharge relation of Cuntan station is shown in Figure 2 and Table 1.

**2.1.3. Model Verification.** Roughness is vital to the calculation of water surface profile. Roughness must adjust and revise repeatedly until to the deviation between calculated value and measured value. Finally, the ideal roughness is 0.036.

There is water level date from May 1, 2009, to October 17 of the section of Chongqing city. When water level of downstream is 161.66 m, flow discharge of Cuntan station is 6320 m<sup>3</sup>/s. The water level of calculation and observation is shown in Table 2.

From Table 2 the following can be seen. The calculation water level of the section of Chongqing city is similar to the observe water level. The result of calculation is reasonable.

In this work, 1D model program mentioned above is used to calculate the length of waterline ( $L$ ) corresponding to 25 class flow discharge ( $Q$ ).

**2.2. Building of Fractal Dimension.** According to the definition of Mandelbrot, fractal refers to the body that the part is similar to the whole in some way. Mandelbrot (1967) put forward the formula of a statistical fractal dimension estimated for the self-similar fractal case:

$$L = AQ^{-D}, \tag{3}$$

where  $L$  is Euclidean length (waterline),  $Q$  is the measured size (flow discharge),  $D$  is the fractal dimension, and  $A$  is a proportion constant.

Take the natural logarithm to (3), then get it as follows:

$$\ln L = \ln A - D \ln Q. \tag{4}$$

And then paint  $\ln L$  and  $\ln Q$  on the coordinates of  $y$ -axis and  $x$ -axis, respectively, and last, use the least square method to fit the straight line and its slope is  $-D$ . We can derive its fractal dimension.

If the fractal dimension is calculated as a constant, it is simple fractal dimension, and if not, it needs to be described as variable fractal dimension [28]. In fact, the phenomenon of strictly meet the simple fractal dimension form does not exist in nature, a large number of complex phenomena need to use variable fractal dimension to describe.

In this thesis, fractal theory of cumulative sum sequence is used for calculation.

This specific method steps are as follows.

- (1) Determine the raw data  $(L_i, Q_i)$ , where  $Q_i$  orders from small to large,  $i = 1, 2, \dots, n$ . There are some data

TABLE 1: The water level-discharge line in Chongqing Cuntan station (Yellow Sea Elevation).

Z (m)	158.784	159.125	159.464	159.801	160.136	160.469	160.8	161.129	161.456	161.781	162.104	162.425	162.744
Q (m <sup>3</sup> /s)	2000	2500	3000	3500	4000	4500	5000	5500	6000	6500	7000	7500	8000
Z (m)	163.061	163.376	163.689	164	167	169.8	172.4	174.8	177	179	180.8	182.4	183.8
Q (m <sup>3</sup> /s)	8500	9000	9500	10000	15000	20000	25000	30000	35000	40000	45000	50000	55000

TABLE 2: The water level of calculate and observation.

Section	Observation	Calculation	Deviation
Dafousi	162.11	162.204	0.094
Hudie Dam	164.86	164.80	-0.060

points in log-log coordinates. And then calculate the slope  $l_{i,i+1}$  of two adjacent points by the use of (5); the sub variable fractal dimension is  $D_{i,i+1} = -l_{i,i+1}$ . In general, the fractal dimensions change much and there is no law:

$$D_{i,i+1} = \frac{\ln(L_i/L_{i+1})}{\ln(Q_{i+1}/Q_i)}. \quad (5)$$

- (2) Construct the accumulated sum of a total order, and  $(L_1, L_2, L_3, \dots)$  is the basic sequence. Then it is constructed by following the rules:

$$\{S1_i\} = \{L_1, L_1 + L_2, L_1 + L_2 + L_3, \dots\}, \quad i = 1, 2, \dots, n, \quad (6)$$

$$\{S2_i\} = \{S1_1, S1_1 + S1_2, S1_1 + S1_2 + S1_3, \dots\}, \quad i = 1, 2, \dots, n, \quad (7)$$

$$\{S3_i\} = \{S2_1, S2_1 + S2_2, S2_1 + S2_2 + S2_3, \dots\}, \quad i = 1, 2, \dots, n, \quad (8)$$

where  $S1, S2, S3, \dots$  are the accumulated sum of first order, second order, and third order,  $N = 1, 2, 3, \dots$

- (3) Establish variable fractal dimension model of the accumulated sum of a total order, taking the first order as an example, and the variable fractal dimension is the opposite slope of data points calculated by (6) in the log-log coordinates.

According to the data of  $n$ , fractal dimensions of  $n - 1$  are obtained, known as the fractal dimension sequence.  $DN_{i,i+1}$  is variable fractal dimension sequence of the accumulated sum of a total order,  $N = 1, 2, \dots; i = 1, 2, \dots, n - 1$ .

- (4) Determine the better order of the accumulated sum, and identify the corresponding fractal dimension.

### 3. Data and Results

Based on the field observations of topographic map in the Chongqing section of the Yangtze River in 2007 (Figure 1),

a valuable data and analysis results by (4) are given. In this paper, the results are shown in Figure 3.

From the double logarithmic coordinates it can be seen that (Figure 3) the data point is clearly not a straight line. From the analysis of it, the relationship that the river length of Chongqing section of the Yangtze River was able to meet the variable fractal dimension should be applicable to sub-dimensional variable fractal model. Therefore, we have adopted variable fractal model to calculate the fractal dimension. The calculation result of the fractal dimension during median flood period on the left bank  $D2$  is  $-0.3321$ , the correlation coefficient  $R$  is  $0.9855$ ; the fractal dimension on the right bank  $D2$  is  $-0.3323$ , the correlation coefficient  $R$  is  $0.9854$ . The calculation result of the fractal dimension during flood period on the left bank  $D2$  is  $-1.6844$ , and the correlation coefficient  $R$  is  $0.9834$ ; the fractal dimension on the right bank  $D2$  is  $-1.6859$ , and the correlation coefficient  $R$  is  $0.9834$  (Tables 3 and 4).

From Figure 4 it can be seen that, after the transformation of second-order accumulated and variable dimensional fractal, the data points fit better to a straight line, which means that the river length in section of Chongqing city of Yangtze River has the characteristics of second-order accumulated variable dimensional fractal. Thus, the river length in the section of Chongqing city of Yangtze River has characteristics of second-order fractal dimension.

### 4. Analysis and Discussion

The fractal dimension of the river length reflects the degree of bending of the river. It is shown that the greater the fractal dimension of the river length, the more tortuous of the river. On the contrary, the river is straighter. It has different dimensions of the river length and the degree of bending at a different location in the same river. In terms of the flood, the possibility and intensity of flooding in a different reach are different. Thus, calculating the fractal dimension values of the whole river length has little significance. The river segmentation being carried out, which calculated the value of the fractal dimension in different sections, found out the correlation between the fractal dimension of each reach and flood.

From the qualitative analysis of the possibility of flood and its fractal dimension on various river reaches, it is shown that there are some relationships between them. The greater fractal dimensions of the river length, the more tortuous of the river. The worse flood carrying capacity of the rivers, the more obvious the flood will be on the performance. However, from quantitative analysis, what kind of relationship exists between the fractal dimension of river length and the flood? Based on Chongqing city segments of Yangtze River, the

TABLE 3: Result of subdimensional fractal dimension of Chongqing city of Yangtze River left bank.

	Q (m <sup>3</sup> /s)	L <sub>i</sub> /m	D <sub>i,i+1</sub>	S <sub>1<sub>i</sub></sub>	D1 <sub>i,i+1</sub>	S <sub>2<sub>i</sub></sub>	D2 <sub>i,i+1</sub>
Median flood	2000	29743.12	—	29743.12	—	29743.12	—
	2500	29725.56	504.65	59468.68	-0.44	89211.80	-0.29
	3000	29708.00	401.50	89176.68	-0.64	178388.48	-0.39
	3500	29712.25	-1371.56	118888.93	-0.77	297277.41	-0.46
	4000	29716.51	-1167.50	148605.44	-0.86	445882.85	-0.51
	4500	29720.76	-1014.47	178326.21	-0.93	624209.06	-0.55
	5000	29725.02	-895.65	208051.22	-0.98	832260.28	-0.58
	5500	29728.44	-995.69	237779.66	-1.03	1070039.95	-0.61
	6000	29731.86	-899.53	267511.53	-1.06	1337551.47	-0.63
	6500	29735.28	-819.68	297246.81	-1.09	1634798.28	-0.65
	7000	29738.71	-752.37	326985.52	-1.12	1961783.80	-0.66
	7500	29678.17	39.23	356663.68	-1.14	2318447.48	-0.68
	8000	29617.63	36.34	386281.31	-1.16	2704728.79	-0.69
	8500	29557.09	33.83	415838.40	-1.18	3120567.19	-0.70
	9000	29496.55	31.62	445334.95	-1.19	3565902.15	-0.71
	9500	29456.19	44.50	474791.14	-1.21	4040693.29	-0.72
Flood	10000	29415.83	—	474750.79	—	4040652.93	—
	15000	29274.54	92.04	504025.33	-9.43	4544678.26	-5.60
	20000	29133.25	62.65	533158.58	-6.90	5077836.83	-4.09
	25000	29105.34	238.94	562263.91	-5.54	5640100.75	-3.29
	30000	29077.42	191.15	591341.34	-4.69	6231442.09	-2.79
	35000	29079.26	-2412.46	620420.60	-4.12	6851862.69	-2.45
	40000	29081.10	-2061.36	649501.70	-3.70	7501364.39	-2.21
	45000	29602.35	-6.40	679104.05	-3.32	8180468.44	-2.02
	50000	29123.60	6.17	708227.65	-3.13	8888696.09	-1.88
	55000	29144.84	-123.62	737372.49	-2.93	9626068.58	-1.77

TABLE 4: The second-order accumulated fractal dimension of the measured.

Station	Linear correlation equation	Dimension D2	Relative number R <sup>2</sup>
The left bank (median flood)	y = 0.3321x + 4.0393	-0.3321	0.9855
The left bank (flood)	y = 1.6884x - 16.166	-1.6884	0.9834
The right bank (median flood)	y = 0.3323x + 4.0518	-0.3323	0.9854
The right bank (flood)	y = 1.6859x - 16.047	-1.6859	0.9834

relationship between them is explored by using quantitative calculation and measured data.

4.1. *Calculation of Local Fractal Dimension.* The section of Chongqing city of Yangtze River is divided into six sections. So we can calculate the fractal dimension of each reach and the correlation coefficient by the left and right sides separately, and the concrete results were shown in Tables 5 and 6.

From Tables 5 and 6 it can be seen that the correlation coefficient on the fractal dimension of the length for each reach in section of Chongqing city of the Yangtze River is more than 98%. It is shown that the length has good characteristics of fractal dimension, and it can reflect the characteristics of it.

In Table 5, the fractal dimensions during flood period on the left bank of river length for the three reaches of

Lijiatuo Bridge to Egongyan Bridge, Egongyan Bridge to Caiyuanba Bridge, and Caiyuanba Bridge to Shibampo Bridge are -1.7203, -1.6844, and -1.6776, respectively. In Table 6, the fractal dimensions on the right bank of river length are -1.7071, -1.6805, and -1.6736, respectively. And the dimension can reflect the degree of bending of the river; the greater dimension, the more tortuous of the river. So we can get that the bending degree of the four reaches of Caiyuanba Bridge to Shibampo Bridge, Egongyan Bridge to Caiyuanba Bridge, and Lijiatuo Bridge to Egongyan Bridge is more and more big.

4.2. *The Local Fractal Dimension and Overall Fractal Dimension.* The arithmetic average of river length does not mean the overall fractal dimension values (see Table 7). In order to further reveal the existence of the law, the situation of the level with the left bank in section of Chongqing city of the Yangtze

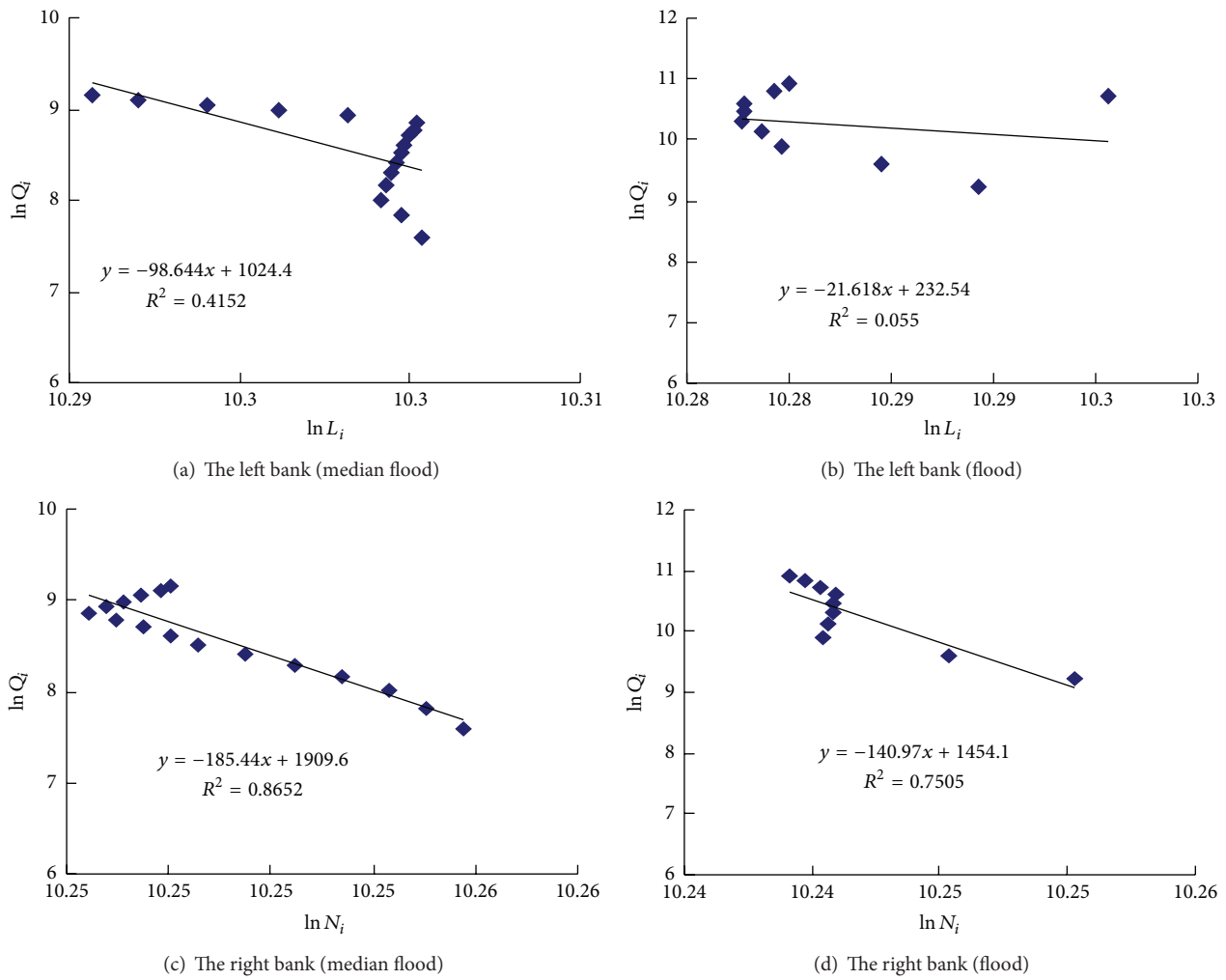


FIGURE 3: The original subdimensional fractal sequence of Chongqing city of Yangtze River.

TABLE 5: The result of second-order accumulated variable-dimensional fractal sequence of Chongqing city of Yangtze River left bank.

	Station	Linear correlation equation	Dimension $D_2$	Relative number $R^2$
Median flood	The upper reaches of the Yangtze River to Lijiatuo bridge	$y = 0.3318x + 4.8736$	-0.3318	0.9855
	Lijiatuo bridge to Ergongyan Yangtze River bridge	$y = 0.3327x + 4.4858$	-0.3327	0.9853
	Ergongyan bridge to Caiyuanba Yangtze River bridge	$y = 0.3328x + 4.6929$	-0.3328	0.9853
	Caiyuanba bridge to Shibampo Yangtze River bridge	$y = 0.3316x + 5.0926$	-0.3216	0.9859
	Shibampo bridge to the Big Temple Yangtze River bridge	$y = 0.3315x + 4.4454$	-0.3315	0.9856
	The Big Temple bridge to the lower reaches of the Yangtze River	$y = 0.3318x + 4.6043$	-0.3318	0.9855
Flood	The upper reaches of the Yangtze River to Lijiatuo bridge	$y = 1.6705x - 11.711$	-1.6705	0.9831
	Lijiatuo bridge to Ergongyan Yangtze River bridge	$y = 1.7203x - 14.294$	-1.7203	0.9839
	Ergongyan bridge to Caiyuanba Yangtze River bridge	$y = 1.6844x - 12.606$	-1.6844	0.9831
	Caiyuanba bridge to Shibampo Yangtze River bridge	$y = 1.6776x - 10.838$	-1.6776	0.9836
	Shibampo bridge to the Big Temple Yangtze River bridge	$y = 1.6822x - 14.053$	-1.6822	0.9833
	The Big Temple bridge to the lower reaches of the Yangtze River	$y = 1.6766x - 13.155$	-1.6766	0.9832

Where  $y = \ln(Q_i)$ ,  $x = \ln(S_2)$ .

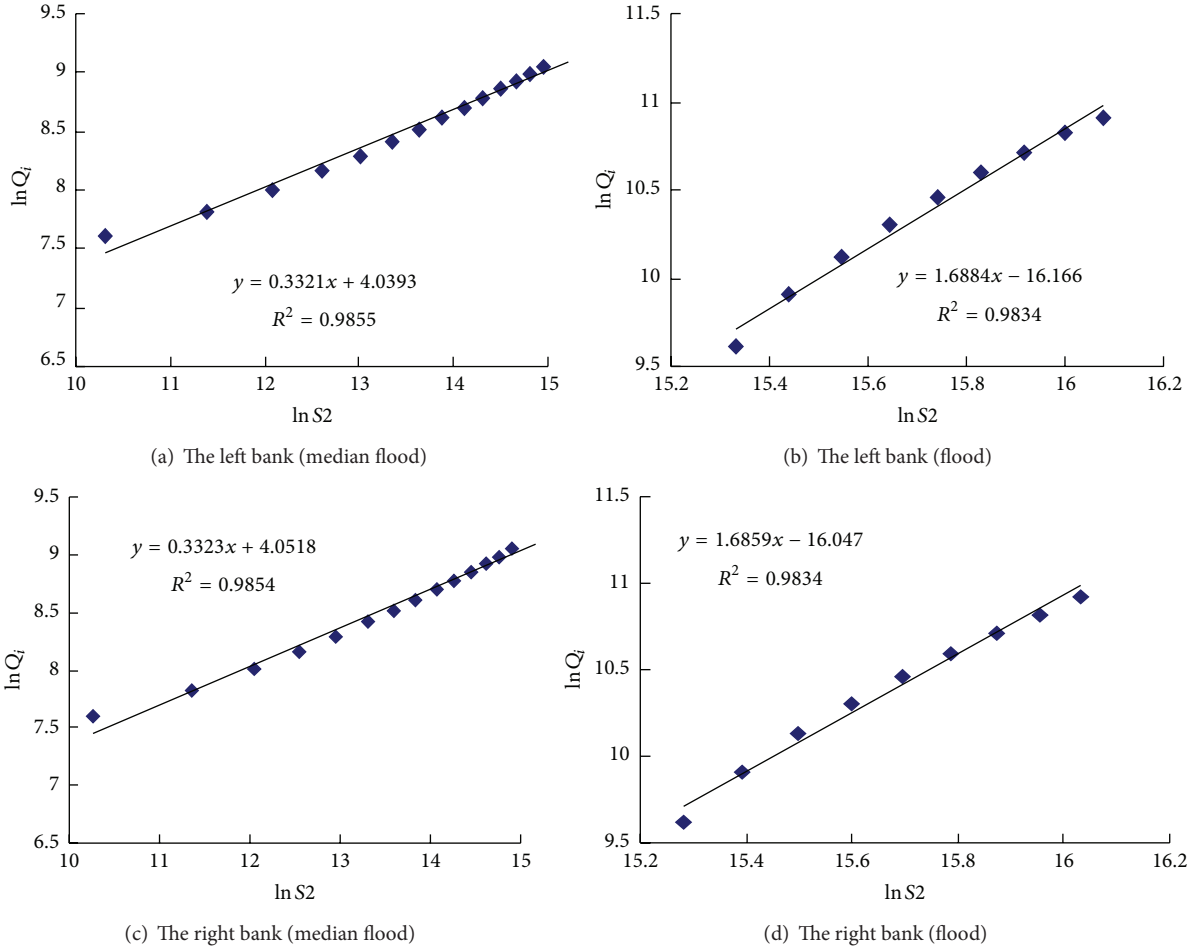


FIGURE 4: Second-order accumulated variable-dimensional fractal sequence of Chongqing city of Yangtze River.

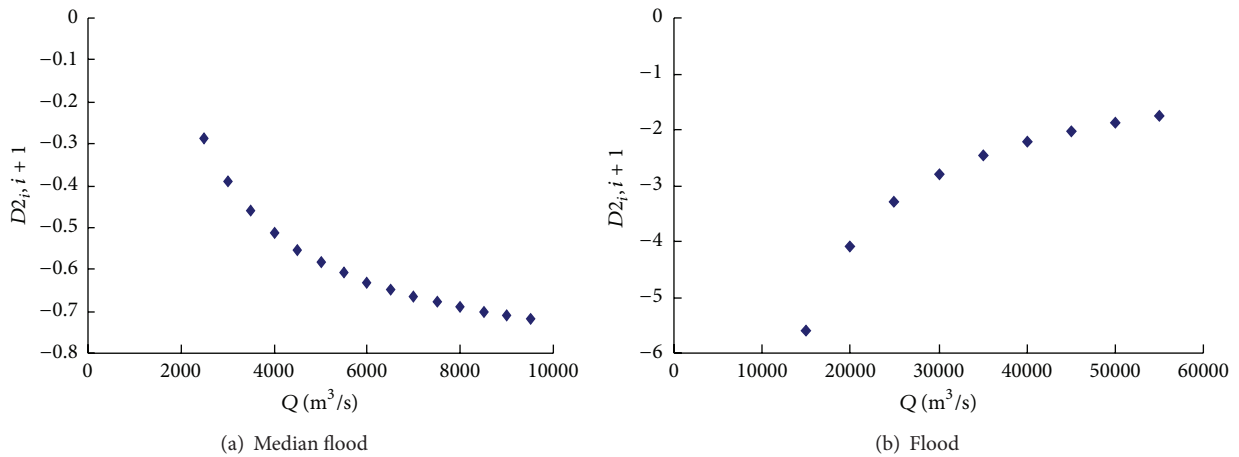


FIGURE 5: Second-order accumulated variable-dimensional fractal-flow discharge of Chongqing city of Yangtze River left bank.

River is calculated. The fractal dimensions with the upper reaches of the Yangtze River to Lijiatuo bridge and Lijiatuo bridge to Egongyan bridge are  $-0.3318$ ,  $-0.3327$ , respectively. From the upper reaches of the Yangtze River to Egongyan bridge, the arithmetic mean is  $-0.3322$ , and it is not equal

to fractal dimension  $-0.3325$  (Table 5). The results are also consistent with other reaches of the river and the right bank. So, it can be found that the fractal dimension of length in section of Chongqing city of the Yangtze River is not equal to its part fractal dimension of the arithmetic mean.

TABLE 6: The result of second-order accumulated variable-dimensional fractal sequence of Chongqing city of Yangtze River right bank.

	Station	Linear correlation equation	Dimension $D_2$	Relative number $R^2$
Median flood	The upper reaches of the Yangtze River to Lijiatuo bridge	$y = 0.3326x + 4.873$	-0.3326	0.9853
	Lijiatuo bridge to Ergongyan Yangtze River bridge	$y = 0.332x + 4.4746$	-0.3320	0.9855
	Ergongyan bridge to Caiyuanba Yangtze River bridge	$y = 0.3286x + 4.7992$	-0.3286	0.9852
	Caiyuanba bridge to Shibampo Yangtze River bridge	$y = 0.332x + 5.0899$	-0.3320	0.9855
	Shibampo bridge to the Big Temple Yangtze River bridge	$y = 0.3319x + 4.4296$	-0.3319	0.9855
	The Big Temple bridge to the lower reaches of the Yangtze River	$y = 0.3328x + 4.6864$	-0.3328	0.9853
Flood	The upper reaches of the Yangtze River to Lijiatuo bridge	$y = 1.7111x - 12.181$	-1.7111	0.9839
	Lijiatuo bridge to Ergongyan Yangtze River bridge	$y = 1.7071x - 13.804$	-1.7071	0.9832
	Ergongyan bridge to Caiyuanba Yangtze River bridge	$y = 1.6805x - 12.625$	-1.6805	0.9835
	Caiyuanba bridge to Shibampo Yangtze River bridge	$y = 1.6736x - 10.772$	-1.6736	0.9832
	Shibampo bridge to the Big Temple Yangtze River bridge	$y = 1.6802x - 14.081$	-1.6802	0.9833
	The Big Temple bridge to the lower reaches of the Yangtze River	$y = 1.6931x - 12.889$	-1.6931	0.9834

Where  $y = \ln(Q_t)$ ,  $x = \ln(S_2)$ .

TABLE 7: The result of average arithmetic dimension to overall and partial fractal of Chongqing city of Yangtze River.

Fractal dimension	Left bank (median flood/flood)	Right bank (median flood/flood)
The average arithmetic partial dimension	-0.3304/-1.6853	-0.3317/-1.6909
Overall dimension	-0.3321/-1.6884	-0.3323/-1.6859

4.3. *The Relationship between Fractal Dimension and the Flow Discharge.* In general, from Tables 5 and 6 and Figure 5, the dimension during median flood period is smaller than the dimension during flood period in the same observation station. And the absolute value of dimension during median flood period is inversely proportional to the flow discharge.

Some theory can be derived from the relationship between stage and discharge at the customs of Chongqing Cuntan hydrological station (Table 1); the larger flow, the higher level in the same observation station. Conversely, the greater dimension, the higher flow and the more obvious the flood will be on the performance. This just confirms the relationship between the possibility of flood and fractal dimension: the greater dimension, the more the river bend, and the larger dimension, the worse flow discharge capacity of the river and the more obvious the flood will be on the performance.

### 5. Conclusions

In this paper, taking the measured data in section of Chongqing city of Yangtze River as an example explored the fractal characteristics from the perspective of fractal scale. Through analysis, comparison, and discussion in this paper, it draws the following conclusions.

- (1) The phenomenon of variable dimension fractal, with second-order fractal dimension, exists on the main reaches in section of Chongqing city of the Yangtze River. The fractal dimension value during median flood period of the left bank is -0.3321, the right bank is -0.3323, the fractal dimension value during flood

period of the left bank is -1.6884, and the right bank is -1.6859.

- (2) The dimension can reflect the degree of bending of the river; the greater dimension, the more tortuous of the river. It can be got that the bending degree of the three reaches of Caiyuanba Bridge to Shibampo Bridge, Egongyan Bridge to Caiyuanba Bridge, and Lijiatuo Bridge to Egongyan Bridge is more and more big.
- (3) The fractal dimension of length in section of Chongqing city of the Yangtze River is not equal to its part fractal dimension of the arithmetic mean.
- (4) In the same river, the larger dimension, the more obvious the flood will be on the performance. Therefore, the fractal dimension of the river can be used as a quantitative indicator of flood forecasting. The larger fractal dimensions, the worse capacity of flood carrying. However, due to the impact of floods produced by many factors, such as water level and sediment, the fractal dimension of the river can only be one of the indicators as forecasting floods. Considered, we should identify more predictors of faster, more accurate prediction of flood.

### Acknowledgments

The study was supported by the Natural Science Foundation Project of CQ CSTC (Grant no. cstc2012jjA30002), the Science and Technology Project of Chongqing Education Committee (Grants no. KJ110409, no. KJ111501), the National

Engineering Research Center for Inland Waterway Regulation Program (Grant no. SLK2012A02), and the National Key Technology R&D Program (Grant no. 2012BAB05B03).

## References

- [1] S. Lovejoy and D. Schertzer, "Scale invariance, symmetries, fractals and stochastic simulations of atmospheric phenomena," *Bulletin of the American Meteorological Society*, vol. 67, no. 1, pp. 21–32, 1986.
- [2] Y. Y. Kagan and L. Knopoff, "Stochastic synthesis of earthquake catalogs," *Journal of Geophysical Research*, vol. 86, no. B4, pp. 2853–2862, 1981.
- [3] D. Marsan, C. J. Bean, S. Steacy, and J. McCloskey, "Spatio-temporal analysis of stress diffusion in a mining-induced seismicity system," *Geophysical Research Letters*, vol. 26, no. 24, pp. 3697–3700, 1999.
- [4] D. Kiyashchenko, N. Smirnova, V. Troyan, and F. Vallianatos, "Dynamics of multifractal and correlation characteristics of the spatio-temporal distribution of regional seismicity before the strong earthquakes," *Natural Hazards and Earth System Science*, vol. 3, no. 3–4, pp. 285–298, 2003.
- [5] M. C. Robertson, C. G. Sammis, M. Sahimi, and A. J. Martin, "Fractal analysis of three-dimensional spatial distributions of earthquakes with a percolation interpretation," *Journal of Geophysical Research*, vol. 100, no. B1, pp. 609–620, 1995.
- [6] Y. Ashkenazy, D. R. Baker, H. Gildor, and S. Havlin, "Nonlinearity and multifractality of climate change in the past 420,000 years," *Geophysical Research Letters*, vol. 30, no. 22, 2003.
- [7] D. Schertzer, S. Lovejoy, F. Schmitt, Y. Chigirinskaya, and D. Marsan, "Multifractal cascade dynamics and turbulent intermittency," *Fractals*, vol. 5, no. 3, pp. 427–471, 1997.
- [8] P. Hubert, Y. Tessier, S. Lovejoy et al., "Multifractals and extreme rainfall events," *Geophysical Research Letters*, vol. 20, no. 10, pp. 931–934, 1993.
- [9] P. A. Varotsos, N. V. Sarlis, E. S. Skordas, and M. S. Lazaridou, "Fluctuations, under time reversal, of the natural time and the entropy distinguish similar looking electric signals of different dynamics," *Journal of Applied Physics*, vol. 103, no. 1, Article ID 014906, 2008.
- [10] N. Scafetta and B. J. West, "Phenomenological reconstructions of the solar signature in the Northern Hemisphere surface temperature records since 1600," *Journal of Geophysical Research*, vol. 112, no. D24, 2007.
- [11] Y. Ida, M. Hayakawa, A. Adalev, and K. Gotoh, "Multifractal analysis for the ULF geomagnetic data during the 1993 Guam earthquake," *Nonlinear Processes in Geophysics*, vol. 12, no. 2, pp. 157–162, 2005.
- [12] P. A. Varotsos, N. V. Sarlis, E. S. Skordas, H. K. Tanaka, and M. S. Lazaridou, "Attempt to distinguish long-range temporal correlations from the statistics of the increments by natural time analysis," *Physical Review E*, vol. 74, no. 2, Article ID 021123, 2006.
- [13] L. Olsen, "Multifractal analysis of divergence points of deformed measure theoretical Birkhoff averages. IV. Divergence points and packing dimension," *Bulletin des Sciences Mathématiques*, vol. 132, no. 8, pp. 650–678, 2008.
- [14] Z. H. Ni, X. J. Zhang, and R. S. Xu, "Fractal study on the vertical concentration distribution of sediment flow in Yangtze River and Yellow River," *Yangtze River*, vol. 42, no. 19, pp. 73–76, 2011 (Chinese).
- [15] D. Jou, M. S. Mongiov, M. Sciacca, and C. F. Barenghi, "Vortex length, vortex energy and fractal dimension of superfluid turbulence at very low temperature," *Journal of Physics A*, vol. 43, no. 20, Article ID 205501, pp. 1–10, 2010.
- [16] V. I. Nikora, "Fractal structures of river plan forms," *Water Resources Research*, vol. 27, no. 6, pp. 1327–1333, 1991.
- [17] P. La Barbera and R. Rosso, "On the fractal dimension of stream networks," *Water Resources Research*, vol. 25, no. 4, pp. 735–741, 1989.
- [18] V. K. Gupta and E. Waymire, "Statistical self-similarity in river networks parameterized by elevation," *Water Resources Research*, vol. 25, no. 3, pp. 463–476, 1989.
- [19] A. Robert and A. G. Roy, "On the fractal interpretation of the mainstream length-drainage area relationship," *Water Resources Research*, vol. 26, no. 5, pp. 839–842, 1990.
- [20] D. G. Tarboton, R. L. Bras, and I. Rodriguez-Iturbe, "A physical basis for drainage density," *Geomorphology*, vol. 5, no. 1–2, pp. 59–76, 1992.
- [21] Z. H. Ni, Z. Y. Song, X. J. Zhang, L. C. Wu, and J. Yi, "A modification to vertical distribution of tidal flow Reynolds stress in shallow sea," *China Ocean Engineering*, vol. 26, no. 3, pp. 431–442, 2012.
- [22] W. Kinsner, "A unified approach to fractal dimensions," *International Journal of Cognitive Informatics and Natural Intelligence*, vol. 1, no. 4, pp. 26–46, 2007.
- [23] M. Sadegh Movahed and E. Hermanis, "Fractal analysis of river flow fluctuations," *Physica A*, vol. 387, no. 4, pp. 915–932, 2008.
- [24] B. B. Mandelbrot and J. R. Wallis, "Some long-run properties of geophysical records," *Water Resources Research*, vol. 5, no. 2, pp. 321–340, 1969.
- [25] P. Burlando and R. Rosso, "Scaling and multiscaling models of depth-duration-frequency curves for storm precipitation," *Journal of Hydrology*, vol. 187, no. 1–2, pp. 45–64, 1996.
- [26] C. Matsoukas, S. Islam, and I. Rodriguez-Iturbe, "Detrended fluctuation analysis of rainfall and streamflow time series," *Journal of Geophysical Research*, vol. 105, no. D23, pp. 29165–29172, 2000.
- [27] G. Pandey, S. Lovejoy, and D. Schertzer, "Multifractal analysis of daily river flows including extremes for basins of five to two million square kilometres, one day to 75 years," *Journal of Hydrology*, vol. 208, no. 1–2, pp. 62–81, 1998.
- [28] Y. H. Fu, "Fractal dimension and fractals in ocean engineering," *China Ocean Engineering*, vol. 8, no. 3, pp. 285–292, 1994.

## Research Article

# Simulation of Stress Distribution near Weld Line in the Viscoelastic Melt Mold Filling Process

Binxin Yang,<sup>1</sup> Jie Ouyang,<sup>2</sup> and Fang Wang<sup>1</sup>

<sup>1</sup> School of Applied Sciences, Taiyuan University of Science and Technology, Taiyuan, Shanxi 030024, China

<sup>2</sup> School of Science, Northwestern Polytechnical University, Xi'an, Shaanxi 710072, China

Correspondence should be addressed to Jie Ouyang; jieouyang@nwpu.edu.cn

Received 20 April 2013; Revised 31 May 2013; Accepted 18 June 2013

Academic Editor: Bo Yu

Copyright © 2013 Binxin Yang et al. This is an open access article distributed under the Creative Commons Attribution License, which permits unrestricted use, distribution, and reproduction in any medium, provided the original work is properly cited.

Simulations of interface evolution and stress distribution near weld line in the viscoelastic melt mold filling process are achieved according to the viscoelastic-Newtonian two-phase model. The finite volume methods on nonstaggered grids are used to solve the model. The level set method is used to capture the melt interface. The interface evolution of the viscoelastic melt in the mold filling process with an insert is captured accurately and compared with the result obtained in the experiment. Numerical results show that the stress distribution is anisotropic near the weld line district and the stress distribution varies greatly at different positions of the weld line district due to the complicated flow behavior after the two streams of melt meet. The stress increases quickly near the weld line district and then decreases gradually until reaching the tail of the mold cavity. The maximum value of the stress appears at some point after the insert.

## 1. Introduction

The plastic mold filling process produces large numbers of parts of high quality. Plastic material in the form of granules is melted until it is soft enough to be injected under pressure to fill a mold. Early simulations of mold filling process mostly used the Hele-Shaw model coupled with the finite element method, which is based on the creeping flow lubrication model [1–4]. With the development of computer hardware, 3D simulations of mold filling process have been realized by using Navier-Stokes equations and different numerical methods [5–10]. The papers mentioned above studied the mold filling process without the consideration of the interface motion. The development of the interface capturing or tracking techniques, such as volume of fluid method (VOF) and the level set method has propelled greatly the development of mold filling simulation techniques. Many papers studying mold filling process coupled with interface tracking techniques can be found [11–20]. In these papers, the viscoelastic properties of materials were ignored. However, the melt for mold filling process is often viscoelastic materials. Some papers made a study on mold filling problems with viscoelastic free surfaces [21, 22]. However, these papers

studied the problem with only viscoelastic fluid phase considered and the gas phase in the cavity ignored, in which case complex boundary conditions must be properly dealt with. Yang et al. [23] proposed a model for mold filling process in which the governing equations for the viscoelastic fluid (melt phase) and the Newtonian fluid (gas phase) are successfully united into a system of generalized Navier-Stokes equations, avoiding dealing with complex boundary conditions.

The viscoelastic behaviour in mold filling process has been tested in [23], in which the die swelling phenomenon and the influences of elasticity and viscosity on velocity, stresses, pressure, stretch, and the first normal-stress difference have been discussed in detail. However, it is well known that weld line is unavoidable in most products of even moderate complexity by mold filling process and influences weightily the quality of the products and the stress distribution near the weld line influences the mechanical property of the products greatly. This paper uses the viscoelastic-Newtonian two-phase flow model established in [23] and finite volume method on nonstaggered grids to study the mold filling process with an insert in the cavity and analyze the stress distribution near the weld line. The comparison

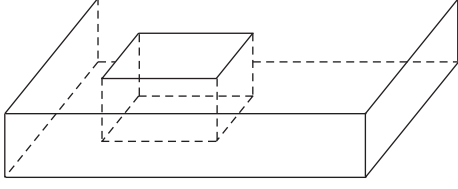


FIGURE 1: Sketch map of the mold with an insert in.

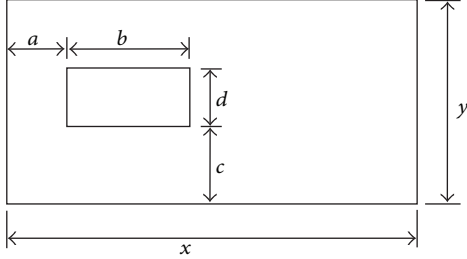


FIGURE 2: Computational domain of the mold.

between the numerical results and those obtained from experiments shows the correctness of the model and the numerical methods.

## 2. Mathematical Model (see [23])

**2.1. Interface Capturing Equations.** We use the corrected level set method proposed by Sussman et al. [27] to capture the interface. The level set and its reinitialization equations are described as follows:

$$\frac{\partial \varphi}{\partial t} + \mathbf{u} \cdot \nabla \varphi = 0 \quad (1)$$

$$\frac{\partial \varphi}{\partial t_r} + \text{sign}(\varphi_0) (|\nabla \varphi| - 1) = \omega \delta_\varepsilon(\varphi) |\nabla \varphi|, \quad (2)$$

$$\varphi(x, y, 0) = \varphi_0(x, y),$$

where  $\varphi$  is the interface,  $\mathbf{u} = (u, v)$  is the velocity vector of the melt,  $t$  is the time,  $\omega$  is the weight coefficient,  $t_r$  is a pseudo time, and  $\text{sign}(\varphi_0)$  is the sign function of  $\varphi$  which is defined as

$$\text{sign}(\varphi_0) = \frac{\varphi_0}{\sqrt{\varphi_0^2 + [\min(\Delta x, \Delta y)]^2}}. \quad (3)$$

Here,  $\Delta x$  and  $\Delta y$  are the grid widths along  $x$  and  $y$  direction, respectively, and  $[\min(\Delta x, \Delta y)]^2$  is used to avoid denominator's dividing by zero.  $\delta_\varepsilon(\varphi)$  is the Dirac function defined as

$$\delta_\varepsilon(\varphi) = \begin{cases} \frac{1}{2\varepsilon} \left( 1 + \cos\left(\frac{\pi\varphi}{\varepsilon}\right) \right) & |\varphi| < \varepsilon, \\ 0 & \text{otherwise.} \end{cases} \quad (4)$$

Here,  $\varepsilon$  is a small positive number about a grid width. See Sussman et al. [27] for more details.

**2.2. Governing Equations for Flow Field.** The governing equations for the flow field with the consideration of fibers are given as follows.

Continuity

$$\frac{\partial \rho}{\partial t} + \frac{\partial u}{\partial x} + \frac{\partial v}{\partial y} = 0, \quad (5)$$

$u$ -momentum

$$\begin{aligned} & \frac{\partial(\rho u)}{\partial t} + \frac{\partial(\rho u u)}{\partial x} + \frac{\partial(\rho v u)}{\partial y} - \frac{1}{\text{Re}} \left( \frac{\partial^2(\mu u)}{\partial x^2} + \frac{\partial^2(\mu u)}{\partial y^2} \right) \\ &= -\frac{\partial p}{\partial x} H_\varepsilon(\varphi) + \frac{(\beta - 1)}{\text{Re}} \left( \frac{\partial^2(\mu u)}{\partial x^2} + \frac{\partial^2(\mu u)}{\partial y^2} \right) H_\varepsilon(\varphi) \\ &+ \frac{1}{\text{Re}} \frac{\partial \tau_{xx}}{\partial x} H_\varepsilon(\varphi) + \frac{1}{\text{Re}} \frac{\partial \tau_{xy}}{\partial y} H_\varepsilon(\varphi), \end{aligned} \quad (6)$$

$v$ -momentum

$$\begin{aligned} & \frac{\partial(\rho v)}{\partial t} + \frac{\partial(\rho u v)}{\partial x} + \frac{\partial(\rho v v)}{\partial y} - \frac{1}{\text{Re}} \left( \frac{\partial^2(\mu v)}{\partial x^2} + \frac{\partial^2(\mu v)}{\partial y^2} \right) \\ &= -\frac{\partial p}{\partial y} H_\varepsilon(\varphi) + \frac{(\beta - 1)}{\text{Re}} \left( \frac{\partial^2(\mu v)}{\partial x^2} + \frac{\partial^2(\mu v)}{\partial y^2} \right) H_\varepsilon(\varphi) \\ &+ \frac{1}{\text{Re}} \frac{\partial \tau_{yx}}{\partial x} H_\varepsilon(\varphi) + \frac{1}{\text{Re}} \frac{\partial \tau_{yy}}{\partial y} H_\varepsilon(\varphi), \end{aligned} \quad (7)$$

where the Reynolds number  $\text{Re} = \rho_l L U / \mu_l$ ,  $\rho(\varphi) = \xi + (1 - \xi) H_\varepsilon(\varphi)$ ,  $\mu(\varphi) = \eta + (1 - \eta) H_\varepsilon(\varphi)$ ,  $\xi = \rho_g / \rho_l$ ,  $\eta = \mu_g / \mu_l$ ,  $\beta$  is the ratio of the Newtonian viscosity and the total viscosity. Since isothermal mold filling process is considered here,  $\beta$  is a constant. The subscripts  $l$  and  $g$  denote the liquid phase and the gas phase, respectively, and  $L$  and  $U$  are parameters for nondimensionalization.

Constitutive

$$\omega \frac{\partial \psi}{\partial t} + \nabla \cdot (\omega \mathbf{u} \psi) - \nabla \cdot (\Lambda \nabla \psi) = S_\psi. \quad (8)$$

Here, the extended Pom-Pom (XPP) constitutive equation developed by Verbeeten et al. [28] is used as the constitutive relationship. The constants and functions in (8) are defined in Table 1 [24, 25], where  $f(\lambda, \boldsymbol{\tau}) = 2\lambda_{ob}/\lambda_{os} e^{\nu(\lambda-1)}(1-1/\lambda) + 1/\lambda^2[1 - \alpha \mathbf{I}_{\boldsymbol{\tau}\boldsymbol{\tau}}/3G_0^2]$ ,  $\lambda = \sqrt{1 + |\mathbf{I}_{\boldsymbol{\tau}}|/3G_0}$ ,  $\nu = 2/q$ , and the Weissenberg number is defined as  $\text{We} = \lambda_{ob} U / L$ . Here  $\lambda$  is the backbone stretch used to represent the stretched degree of the polymer molecule,  $\lambda_{ob}$  and  $\lambda_{os}$  denote the orientation and backbone stretch relaxation time scales of the polymer chains, respectively,  $G_0$  is the linear relaxation modulus,  $\alpha$  is an adjustable parameter, which controls the anisotropic drag,  $\mathbf{I}$  is the identity tensor,  $q$  is the number of arms of polymer

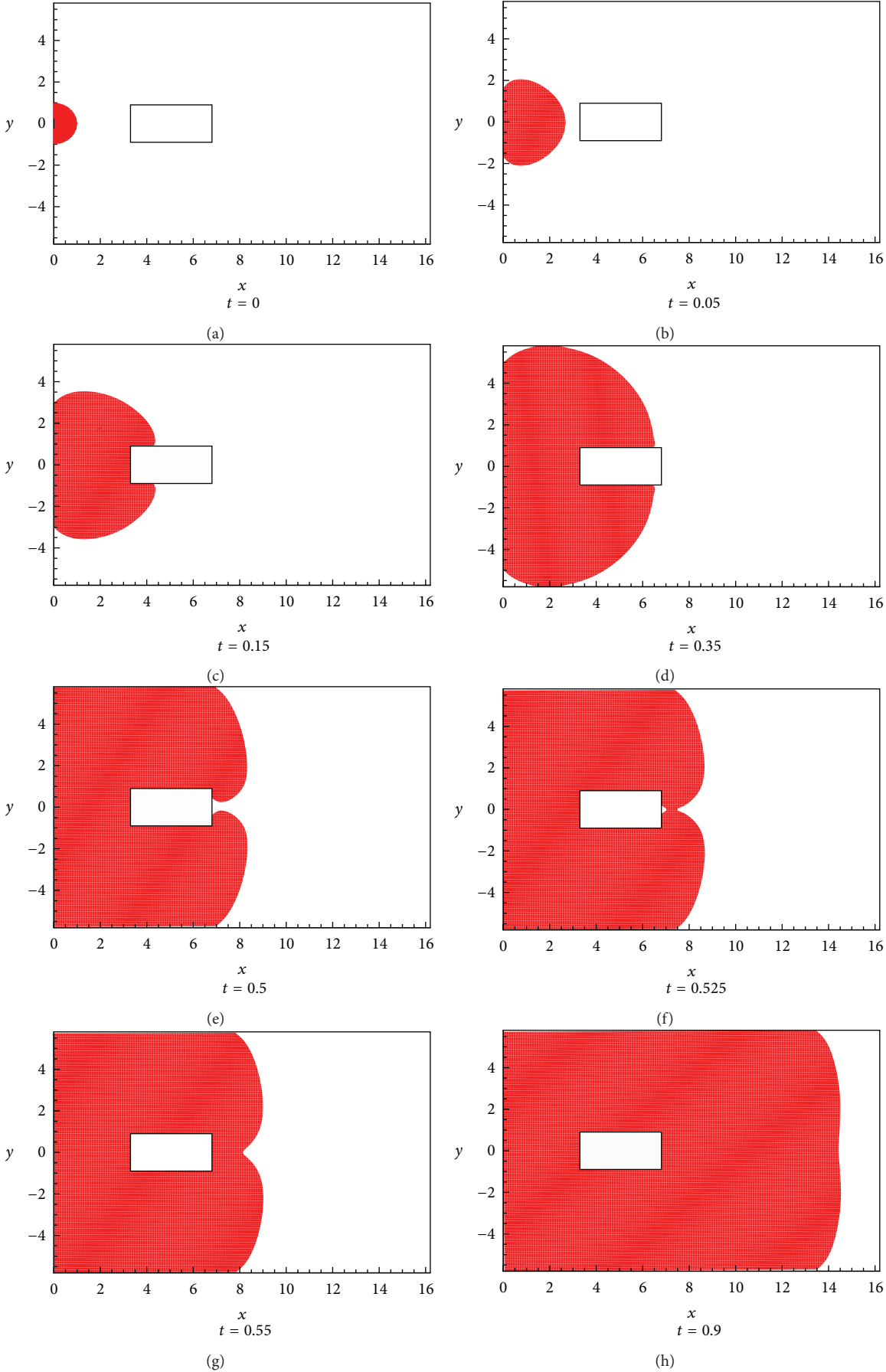


FIGURE 3: Continued.

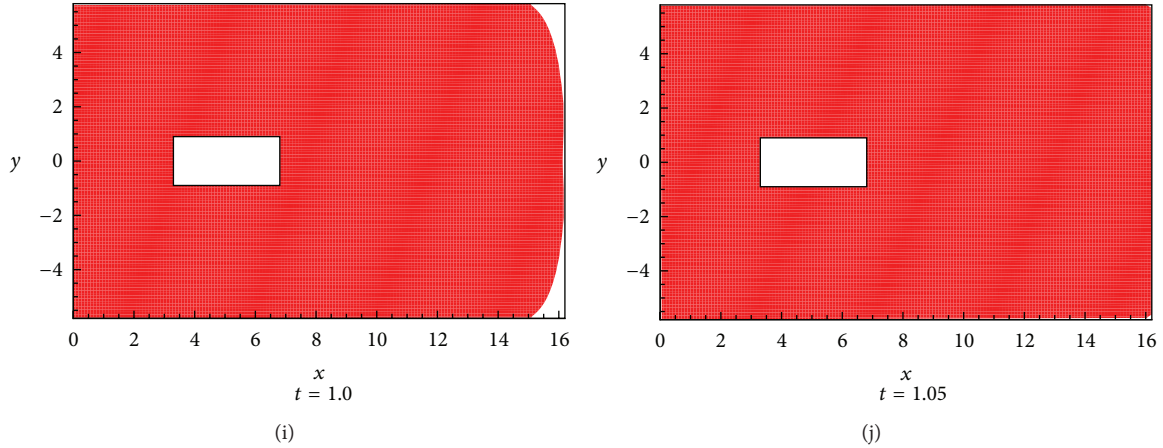


FIGURE 3: Melt positions at different time in the mold filling process.

chains and  $\mathbf{d}$  is the strain tensor. Some hints on choosing meaningful values of the parameters in XPP model can be found in [25]; in this paper, we take  $\beta = 1.0/9.0$ ,  $\alpha = 0.15$ ,  $q = 2.0$ ,  $\varepsilon = 1.0/3.0$ .

**2.3. Boundary Conditions.** Proper boundary conditions must be posed on the solid walls of the cavity. In this paper, no-slip boundary conditions are used for the velocities, that is,  $u = v = 0$ . As for the pressure boundary conditions, for the air in the cavity, we use no-slip boundary conditions, that is,  $p = 0$ , while for the melt in the cavity, no-penetration boundary conditions are used, that is,  $\partial p / \partial \mathbf{n} = 0$ .

### 3. Numerical Methods

Level set evolution equation (1) and the reinitialization equation (2) are solved by the finite difference method on a rectangular grid. The spatial derivatives are discretized by the 5th-order weighted essentially non-oscillatory (WENO) scheme [29, 30] and the temporal derivatives are discretized by the 3rd-order total variation diminishing Runge-Kutta (TVD-R-K) scheme [31].

The finite volume SIMPLE methods on a nonstaggered grid are used to solve the governing equations (5)–(8).

The validity of the methods has been verified in [23].

### 4. Numerical Results and Analysis

**4.1. Mold Filling Process.** Figure 1 shows the sketch map of the mold with an insert in. Figure 2 gives the top view of the mold, which also represents the computational area. In this paper, we take  $x = 16.2$ ,  $y = 11.6$ ,  $a = 3.3$ ,  $b = 3.4$ ,  $c = 4.9$ ,  $d = 1.8$ , which are the same as those in [26]. The inlet lies in the middle of the left wall of the computational area. The grid number is  $200 \times 120$ .

Figure 3 gives the melt interface positions at different times in mold filling process.

From Figure 3 we can see that the melt is divided into two streams when it reaches the insert. The two streams move

forward until they pass the insert; then they begin to move toward each other until they meet at some point behind the insert, from where the weld line begins to form, and a hole appears between the insert and the meet point of the two streams of melt. After meeting, the melt moves toward two opposite directions. One direction is moving forward and the other direction is moving backward to fill in the hole formed between the insert and the meeting point. The hole is finally filled with melt and two streams of melt reunion into one stream and move forward. Figure 4 gives the comparison between the interface evolution after the insert and that obtained in the experiment [26]. The well agreement shows the validity of our model and method.

**4.2. Distribution of the Stress Birefringence.** In order to get the stress distribution and make a comparison with the experimental results given by the stress birefringence distribution, we use the formula in [32] to compute the numerical stress birefringence, which is given as follows:

$$\Delta n = C \left[ (\tau_{xx} - \tau_{yy})^2 + 4\tau_{xy}^2 \right]^{1/2}. \quad (9)$$

Here,  $\Delta n$  is the stress birefringence.  $C$  is the stress-optical coefficient, which is a constant for linear stress-optical principle, and we take  $C = 1$ .

Figure 5 shows the distribution of the stress birefringence at  $t = 1.05$  in the simulation. We can see that the stress birefringence distribution is anisotropic near the weld line district and varies greatly at different positions of the weld line district. This phenomenon is induced by the complicated flow behavior after the two streams of melt meet. Since the melt moves toward two opposite directions, the stress birefringence distribution decreases progressively along the two opposite directions. The stress distribution birefringence obtained in experiment after the product is completely produced is given in Figure 6 [26]. Since only the mold filling process is considered in the simulation, while the birefringence is obtained after the cooling stage, some difference exists between the numerical and experimental

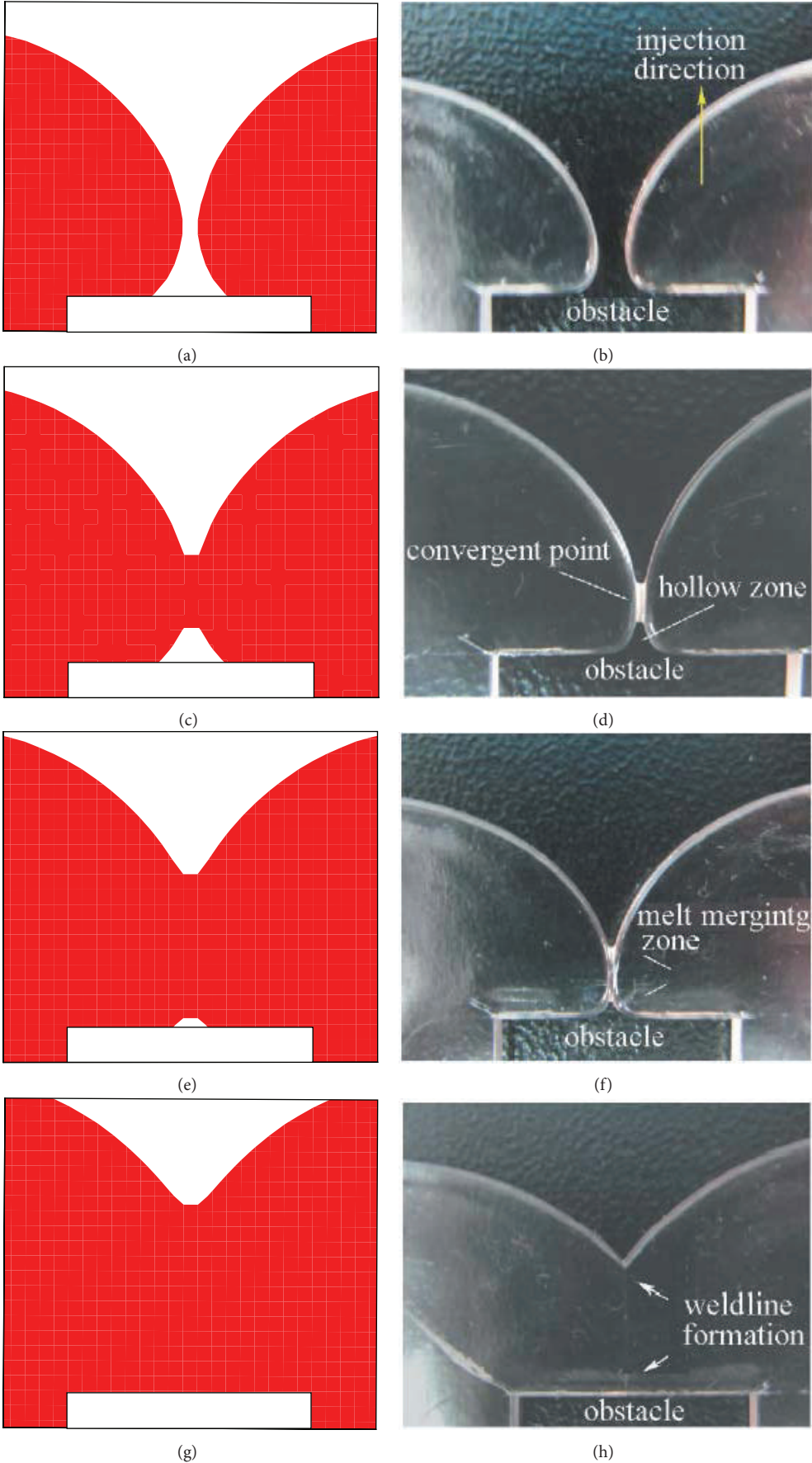


FIGURE 4: Comparison between the interface evolution after the insert and that obtained in experiment.

TABLE 1: Definition of the constants and functions in the constitutive equation [24, 25].

Equation	$\omega$	$\psi$	$\Lambda$	$S_\psi$
$\tau_{xx}$ normal stress	We	$\tau_{xx}$	0	$2(1-\beta)\frac{\partial u}{\partial x} + 2We\tau_{xx}\frac{\partial u}{\partial x} + 2We\tau_{xy}\frac{\partial u}{\partial y} - f(\lambda, \tau)\tau_{xx}$ $- [f(\lambda, \tau) - 1]\frac{1-\beta}{We} - \alpha\frac{We}{1-\beta}(\tau_{xx}^2 + \tau_{xy}^2)$
$\tau_{xy}$ shear stress	We	$\tau_{xy}$	0	$(1-\beta)\left(\frac{\partial v}{\partial x} + \frac{\partial u}{\partial y}\right) + We\tau_{xx}\frac{\partial v}{\partial x} + We\tau_{yy}\frac{\partial u}{\partial y}$ $- f(\lambda, \tau)\tau_{xy} - \alpha\frac{We}{1-\beta}\tau_{xy}(\tau_{xx} + \tau_{yy})$
$\tau_{yy}$ normal stress	We	$\tau_{yy}$	0	$2(1-\beta)\frac{\partial v}{\partial y} + 2We\tau_{yy}\frac{\partial v}{\partial y} + 2We\tau_{xy}\frac{\partial v}{\partial x} - f(\lambda, \tau)\tau_{yy}$ $- [f(\lambda, \tau) - 1]\frac{1-\beta}{We} - \alpha\frac{We}{1-\beta}(\tau_{yy}^2 + \tau_{xy}^2)$
$\tau_{zz}$ stress	We	$\tau_{zz}$	0	$-f(\lambda, \tau)\tau_{zz} - [f(\lambda, \tau) - 1]\frac{1-\beta}{We} - \alpha\frac{We}{1-\beta}\tau_{zz}^2$

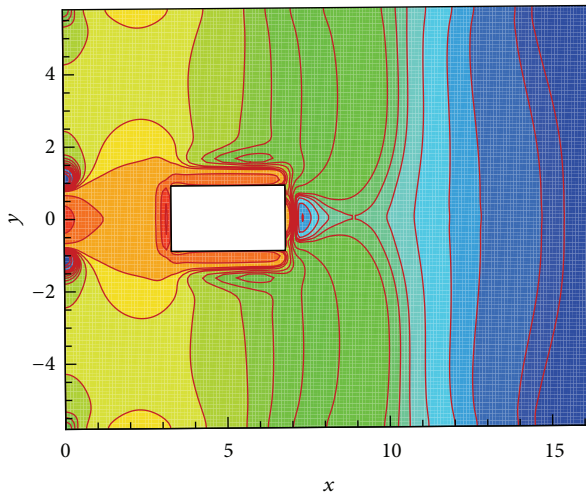
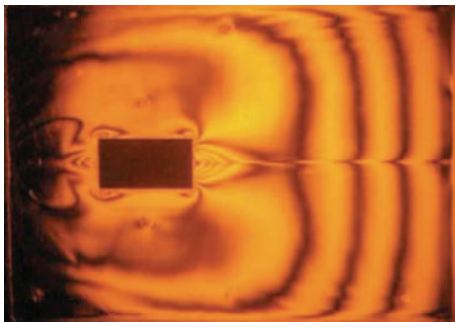
FIGURE 5: The distribution of the stress birefringence at  $t = 1.05$  in the simulation.

FIGURE 6: The stress distribution birefringence obtained in experiment [26] after the product is completely produced.

results. However, both the numerical and the experimental results are qualitative agreeable.

Figure 7 gives the change of the stress birefringence from the tail of the insert until the end of the cavity, which is in accordance qualitatively with the experiment in [26], that

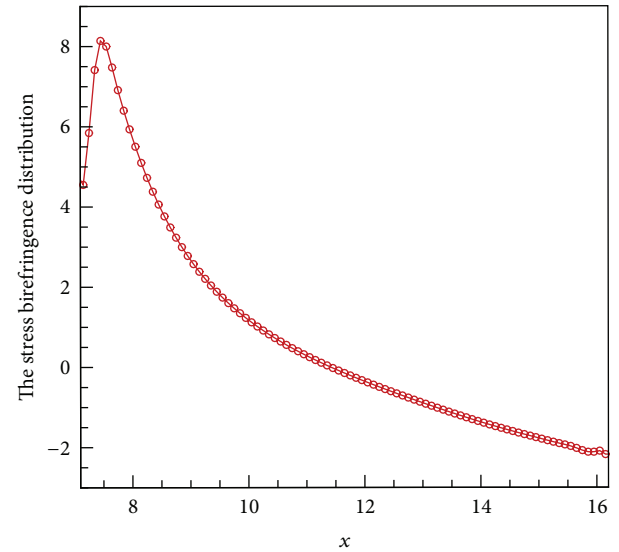


FIGURE 7: The change of the stress birefringence from the tail of the insert until the end of the cavity.

is, the stress birefringence increases quickly near the weld line district and then decreases gradually until reaching the tail of the mold cavity. The maximum value of the stress birefringence appears at some point after the insert.

## 5. Conclusion

In this paper, simulations of interface evolution and stress distribution near weld line in the viscoelastic melt mold filling process are achieved according to the viscoelastic-Newtonian two-phase model established by Yang et al. [23]. The interface evolution of the viscoelastic melt in the mold filling process with an insert in is captured accurately. The distribution of the stress birefringence is qualitative agreeable with that of experiment. The stress increases quickly near the weld line district and then decreases gradually until reaching the

tail of the mold cavity. The maximum value of the stress birefringence appears at some point after the insert.

## Acknowledgments

All the authors would like to acknowledge the National Natural Science Foundation of China (10871159), National Natural Science Foundation of Shanxi (2012011019-2), and Doctoral Foundation of Taiyuan University of Science and Technology (20112011).

## References

- [1] V. W. Wang, C. A. Hieber, and K. K. Wang, "Dynamic simulation and graphics for the injection-molding of 3-dimensional thin parts," *Journal of Polymer Engineering*, vol. 7, no. 1, pp. 21–45, 1986.
- [2] H. H. Chiang, C. A. Hieber, and K. K. Wang, "A unified simulation of the filling and post filling stages in injection molding. Part I. Formulation," *Polymer Engineering and Science*, vol. 31, no. 2, pp. 116–123, 1991.
- [3] K. K. Kabanemi, H. Vaillancourt, H. Wang, and G. Salloum, "Residual stresses, shrinkage, and warpage of complex injection molded products: numerical simulation and experimental validation," *Polymer Engineering and Science*, vol. 38, no. 1, pp. 21–37, 1998.
- [4] D. E. Smith, D. A. Tortorelli, and C. L. Tucker III, "Analysis and sensitivity analysis for polymer injection and compression molding," *Computer Methods in Applied Mechanics and Engineering*, vol. 167, no. 3-4, pp. 325–344, 1998.
- [5] J. F. Hétu, D. M. Gao, A. Garcia-Rejon, and G. Salloum, "3D finite element method for the simulation of the filling stage in injection molding," *Polymer Engineering and Science*, vol. 38, no. 2, pp. 223–236, 1998.
- [6] E. Pichelin and T. Coupez, "Finite element solution of the 3D mold filling problem for viscous incompressible fluid," *Computer Methods in Applied Mechanics and Engineering*, vol. 163, no. 1-4, pp. 359–371, 1998.
- [7] S. W. Kim and L. S. Turng, "Three-dimensional numerical simulation of injection molding filling of optical lens and multiscale geometry using finite element method," *Polymer Engineering and Science*, vol. 46, no. 9, pp. 1263–1274, 2006.
- [8] H. M. Zhou, T. Geng, and D. Q. Li, "Numerical filling simulation of injection molding based on 3D finite element model," *Journal of Reinforced Plastics and Composites*, vol. 24, no. 8, pp. 823–830, 2005.
- [9] R. Y. Chang and W. H. Yang, "Numerical simulation of mold filling in injection molding using a three-dimensional finite volume approach," *International Journal for Numerical Methods in Fluids*, vol. 37, no. 2, pp. 125–148, 2001.
- [10] J. Zhou and L. S. Turng, "Three-dimensional numerical simulation of injection mold filling with a finite-volume method and parallel computing," *Advances in Polymer Technology*, vol. 25, no. 4, pp. 247–258, 2006.
- [11] B. X. Yang, J. Ouyang, C. T. Liu, and Q. Li, "Simulation of non-isothermal injection molding for a non-newtonian fluid by Level Set method," *Chinese Journal of Chemical Engineering*, vol. 18, no. 4, pp. 600–608, 2010.
- [12] E. J. Holm and H. P. Langtangen, "A unified finite element model for the injection molding process," *Computer Methods in Applied Mechanics and Engineering*, vol. 178, no. 3-4, pp. 413–429, 1999.
- [13] J. A. Luoma and V. R. Voller, "An explicit scheme for tracking the filling front during polymer mold filling," *Applied Mathematical Modelling*, vol. 24, no. 8-9, pp. 575–590, 2000.
- [14] S. Soukane and F. Trochu, "Application of the level set method to the simulation of resin transfer molding," *Composites Science and Technology*, vol. 66, no. 7-8, pp. 1067–1080, 2006.
- [15] R. Ayad and A. Rigolot, "The VOF-G/FEV model for tracking a polymer-air interface in the injection moulding process," *Journal of Mechanical Design*, vol. 124, no. 4, pp. 813–821, 2002.
- [16] G. Tie, L. Dequn, and Z. Huamin, "Three-dimensional finite element method for the filling simulation of injection molding," *Engineering with Computers*, vol. 21, no. 4, pp. 289–295, 2006.
- [17] M. S. Kim, J. S. Park, and W. I. Lee, "A new VOF-based numerical scheme for the simulation of fluid flow with free surface. Part II: application to the cavity filling and sloshing problems," *International Journal for Numerical Methods in Fluids*, vol. 42, no. 7, pp. 791–812, 2003.
- [18] H. M. Zhou, B. Yan, and Y. Zhang, "3D filling simulation of injection molding based on the PG method," *Journal of Materials Processing Technology*, vol. 204, no. 1-3, pp. 475–480, 2008.
- [19] C. K. Au, "A geometric approach for injection mould filling simulation," *International Journal of Machine Tools and Manufacture*, vol. 45, no. 1, pp. 115–124, 2005.
- [20] B. X. Yang, J. Ouyang, S. P. Zheng, Q. Li, and W. Zhou, "Simulation of polymer molding filling process with an adaptive weld line capturing algorithm," *International Journal of Material Forming*, vol. 5, no. 1, pp. 25–37, 2012.
- [21] A. Bonito, M. Picasso, and M. Laso, "Numerical simulation of 3D viscoelastic flows with free surfaces," *Journal of Computational Physics*, vol. 215, no. 2, pp. 691–716, 2006.
- [22] M. F. Tomé, A. Castelo, J. Murakami et al., "Numerical simulation of axisymmetric free surface flows," *Journal of Computational Physics*, vol. 157, no. 2, pp. 441–472, 2000.
- [23] B. X. Yang, J. Ouyang, Q. Li, Z. F. Zhao, and C. T. Liu, "Modeling and simulation of the viscoelastic fluid mold filling process by level set method," *Journal of Non-Newtonian Fluid Mechanics*, vol. 165, no. 19-20, pp. 1275–1293, 2010.
- [24] M. Aboubacar, J. P. Aguayo, P. M. Phillips et al., "Modelling Pom-Pom type models with high-order finite volume schemes," *Journal of Non-Newtonian Fluid Mechanics*, vol. 126, no. 2-3, pp. 207–220, 2005.
- [25] M. G. H. M. Baltussen, W. M. H. Verbeeten, A. C. B. Bogaerds, M. A. Hulsen, and G. W. M. Peters, "Anisotropy parameter restrictions for the eXtended Pom-Pom model," *Journal of Non-Newtonian Fluid Mechanics*, vol. 165, no. 19-20, pp. 1047–1054, 2010.
- [26] J. Han, C. Y. Shen, C. T. Liu, S. J. Wang, and J. B. Chen, "Flow induced birefringence of weldline region in polystyrene injection molding," *CIESC Journal*, vol. 59, no. 5, pp. 1305–1309, 2008.
- [27] M. Sussman, E. Fatemi, P. Smereka, and S. Osher, "An improved level set method for incompressible two-phase flows," *Computers and Fluids*, vol. 27, no. 5-6, pp. 663–680, 1998.
- [28] W. M. H. Verbeeten, G. W. M. Peters, and F. P. T. Baaijens, "Differential constitutive equations for polymer melts: the extended Pom-Pom model," *Journal of Rheology*, vol. 45, no. 4, pp. 823–843, 2001.

- [29] G. S. Jiang and D. P. Peng, “Weighted ENO schemes for Hamilton—Jacobi equations,” *SIAM Journal on Scientific Computing*, vol. 21, no. 6, pp. 2126–2143, 2002.
- [30] S. Osher and C. W. Shu, “High-order essentially non-oscillatory schemes for Hamilton-Jacobi equations,” *SIAM Journal on Numerical Analysis*, vol. 28, no. 4, pp. 907–922, 1991.
- [31] C. W. Shu and S. Osher, “Efficient implementation of essentially non-oscillatory shock-capturing schemes II,” *Journal of Computational Physics*, vol. 83, no. 1, pp. 32–78, 1989.
- [32] A. I. Isayev, G. D. Shyu, and C. T. Li, “Residual stresses and birefringence in injection molding of amorphous polymers: simulation and comparison with experiment,” *Journal of Polymer Science B*, vol. 44, no. 3, pp. 622–639, 2006.

## Research Article

# Comparison Study on the Performances of Finite Volume Method and Finite Difference Method

Renwei Liu,<sup>1</sup> Dongjie Wang,<sup>1</sup> Xinyu Zhang,<sup>1</sup> Wang Li,<sup>1,2</sup> and Bo Yu<sup>1</sup>

<sup>1</sup> National Engineering Laboratory for Pipeline Safety and Beijing Key Laboratory of Urban Oil and Gas Distribution Technology, China University of Petroleum, Beijing 102249, China

<sup>2</sup> PetroChina Southwest Pipeline Company, Chengdu 610041, China

Correspondence should be addressed to Bo Yu; yubobox@vip.163.com

Received 26 March 2013; Revised 9 June 2013; Accepted 9 June 2013

Academic Editor: Shuyu Sun

Copyright © 2013 Renwei Liu et al. This is an open access article distributed under the Creative Commons Attribution License, which permits unrestricted use, distribution, and reproduction in any medium, provided the original work is properly cited.

Vorticity-stream function method and MAC algorithm are adopted to systemically compare the finite volume method (FVM) and finite difference method (FDM) in this paper. Two typical problems—lid-driven flow and natural convection flow in a square cavity—are taken as examples to compare and analyze the calculation performances of FVM and FDM with variant mesh densities, discrete forms, and treatments of boundary condition. It is indicated that FVM is superior to FDM from the perspective of accuracy, stability of convection term, robustness, and calculation efficiency. Particularly, when the mesh is coarse and taken as  $20 \times 20$ , the results of FDM suffer severe oscillation and even lose physical meaning.

## 1. Introduction

In the numerical solution of flow and heat transfer problems, the concepts of conservative and nonconservative equations were firstly proposed in [1, 2] in the 1980s. It is noteworthy that, from the perspective of differential unit, the conservative and nonconservative equations are equivalent, which are both the mathematical expression of physical conservation law. Nevertheless, the numerical calculation is implemented on the calculation unit of finite size, for which the two forms of equations are of different characteristics. Practical calculation process shows that the influence of differences between conservative and nonconservative forms on accuracy, stability, and efficiency of numerical calculation is significant.

Conservative governing equation and the corresponding discrete form show some advantages; for example, in the control volume with finite size, only the conservative equation can guarantee that the conservation law of the problem studied is satisfied [3–5]. The result obtained by the conservative equation is of higher accuracy generally. In the calculation of flow problem involving shock wave, the obtained flow field is usually smooth and stable employing the conservation form of governing equation, while using the non-conservation

equation might lead to unsatisfactory spatial oscillations in the upstream and downstream regions of the shock wave [6–8]. Moreover, when the conservation equation is used to a body-fitted coordinate system, the conservativeness of governing equation can still be satisfied [9, 10]. More related researches and applications are presented in the literature [11–15]. Hence, the conservation property of discretized equations is desirable in engineering calculation. Based on this, it is of great significance to investigate the influence from conservation property on the calculation performances and provide guidance for the better implementation of it. The present paper compares the calculation performances by analyzing the finite volume method which is conservative and finite difference method which is nonconservative.

Some researchers made comparisons of the two methods. Patankar [16] and West and Fuller [17] pointed out that the results obtained in the situation that grids numbers decrease and mass conservation is rigorously controlled lose its physical meaning. Leonard [18] made a comparison of the accuracy of truncation error of the convection term in FVM and FDM. By theoretical derivation, he indicated that the truncation error of FVM is smaller than that of FDM in second-order central difference and second-order upwind difference. Botte et al. [19] made comparison of the accuracy,

mass conservation, and computation time. It was validated by examples that FDM cannot ensure mass conservation while FVM can. Meanwhile, the influence of boundary conditions on the accuracy of algorithm was taken into consideration.

Previous researchers mainly focused on the comparison of accuracy. There are few systemic studies on the stability, robustness, and computation efficiency. This paper compared the calculation performances of FVM and FDM based on previous research. Comprehensive comparison of accuracy, stability of convection term, robustness, and calculation efficiency was performed. The results obtained may enrich the study on the calculation performances of conservative and nonconservative methods, which are expected to provide some reference for the practical calculation.

## 2. Physical Problem

To make the study possess general significance, it is necessary to analyze the calculation performances of the two methods based on variant problems. Lid-driven flow and natural convection flow in a square cavity which are both typical problems in computational fluid mechanics and numerical heat transfer are solved in this paper to make a systemic analysis on the subject.

As Figure 1(a) shows, in the lid-driven flow the lid moves horizontally at a constant velocity  $u_{top}$  while the other three boundaries keep still. The Reynolds number, Re (Reynolds number) adopted in this paper, is 1000.

Figure 1(b) shows the schematic of natural convection flow in a square cavity. The left and right boundaries are the first boundary conditions, between which the temperature on the left boundary is higher. The other two boundaries are adiabatic ones. In calculation, Pr (Prandtl number) is taken as 0.71 and Ra (Rayleigh number) is taken as  $10^6$ .

## 3. Numerical Method

Considering that the calculation approach is influential to the calculation, in order to compare the difference of calculation performances between FVM and FDM, this paper adopts both primitive variable method and nonprimitive variable method to solve the governing equations. For primitive variable method, MAC algorithm is adopted, and for nonprimitive variable method, the generally used vorticity-stream function algorithm is adopted. The conservation property generally refers to the convection term, and thus only the difference of convective term between conservative and nonconservative forms is compared. MAC method is characterized by the direct solving of velocity and pressure. The key point of this method is to obtain a nondivergent velocity field in every time step or iteration step. That is, the velocity field of every time layer or iteration layer should satisfy the continuity equation and pressure, and the velocity is decoupled by solving Poisson equation which is relevant to pressure.

**3.1. Governing Equation.** In primitive variable method, pressure and velocity are directly used as variables to solve the

TABLE 1: Parameters of equations for MAC of lid-driven flow.

Name of variables	$\Phi$	$\Gamma_\phi$	$S_\phi$
X direction	$U$	$\frac{1}{Re}$	$-\frac{\partial P}{\partial X}$
Y direction	$V$	$\frac{1}{Re}$	$-\frac{\partial P}{\partial Y}$

TABLE 2: Parameters of equations for MAC of natural convection flow.

Name of variables	$\Phi$	$\Gamma_\phi$	$S_\phi$
X direction	$U$	1	$-\frac{\partial P}{\partial X}$
Y direction	$V$	1	$\frac{Ra\Theta}{Pr} - \frac{\partial P}{\partial Y}$
Temperature	$\Theta$	$\frac{1}{Pr}$	0

equations. As to the incompressible fluid, the dimensionless unsteady-state conservative and nonconservative equations can be written as respectively,

$$\frac{\partial \Phi}{\partial \tau} + \frac{\partial (U\Phi)}{\partial X} + \frac{\partial (V\Phi)}{\partial Y} = \Gamma_\phi \left( \frac{\partial^2 \Phi}{\partial X^2} + \frac{\partial^2 \Phi}{\partial Y^2} \right) + S_\phi, \quad (1)$$

$$\frac{\partial \Phi}{\partial \tau} + U \frac{\partial \Phi}{\partial X} + V \frac{\partial \Phi}{\partial Y} = \Gamma_\phi \left( \frac{\partial^2 \Phi}{\partial X^2} + \frac{\partial^2 \Phi}{\partial Y^2} \right) + S_\phi, \quad (2)$$

where the values of  $\Phi$ ,  $\Gamma_\phi$ , and  $S_\phi$  for lid-driven flow and natural convection flow are shown in Table 1 and Table 2, respectively. From (1) and (2) we can see that the convection term of conservative equation is given in the form of divergence while that in nonconservative equation is not, where the nondimensional excessive temperature can be described as  $\Theta = (T - T_l)/(T_h - T_l)$  and  $U, V$  are defined as nondimensional velocities in separate directions ( $X$  direction or  $Y$  direction). Governing equations of conservative and nonconservative equations of primitive variable method are given before. In the calculation process, MAC algorithm is adopted to obtain the result in steady state by unsteady calculation over enough time. The result of steady state is analyzed as follows from the angle of primitive variable method. Taking the vorticity-stream function method as example, the governing equations of conservative form and nonconservative form can be written as respectively,

$$a_\phi \left( \frac{\partial (U\Phi)}{\partial X} + \frac{\partial (V\Phi)}{\partial Y} \right) = \Gamma_\phi \left( \frac{\partial^2 \Phi}{\partial X^2} + \frac{\partial^2 \Phi}{\partial Y^2} \right) + S_\phi, \quad (3)$$

$$a_\phi \left( U \frac{\partial \Phi}{\partial X} + V \frac{\partial \Phi}{\partial Y} \right) = \Gamma_\phi \left( \frac{\partial^2 \Phi}{\partial X^2} + \frac{\partial^2 \Phi}{\partial Y^2} \right) + S_\phi. \quad (4)$$

As to the vorticity-stream function method, only the lid-driven flow is studied in this paper. Values of  $\Phi$ ,  $a_\phi$ ,  $\Gamma_\phi$ , and  $S_\phi$  are shown in Table 3. where “ $\omega$ ” stands for vorticity and “ $\psi$ ” stands for stream function.

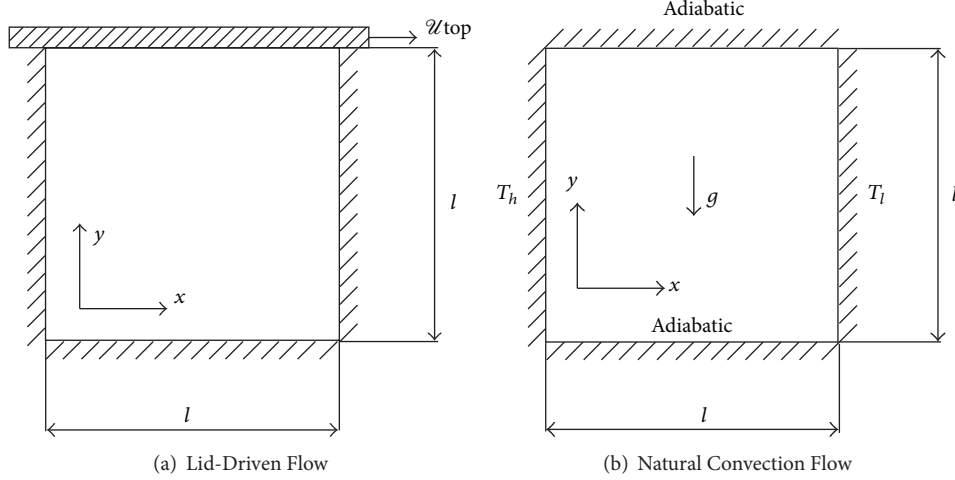


FIGURE 1: Schematic of different physical problem in a square cavity.

TABLE 3: Parameters of equations for vorticity-stream function algorithm of lid-driven flow.

Name of variables	$\Phi$	$a_\phi$	$\Gamma_\phi$	$S_\phi$
Vorticity equation	$\omega$	1	$\frac{1}{Re}$	0
Stream function equation	$\psi$	0	1	$-\omega$

where “ $\omega$ ” stands for vorticity, and “ $\psi$ ” stands for stream function.

**3.2. Discretization of Equations.** Uniform mesh is adopted in this paper. In order to compare the calculation performances of FVM and FDM with variant discretized schemes, central difference and second-order upwind scheme are adopted. As to FVM, taking  $e$  interface on  $X$  direction as example, the expressions can be written as,

$$\Phi_e^+ = \Phi_e^- = \frac{\Phi_P + \Phi_E}{2}, \quad (5)$$

$$\Phi_e^+ = 1.5\Phi_P - 0.5\Phi_W, \quad U_e \geq 0 \quad (6a)$$

$$\Phi_e^- = 1.5\Phi_E - 0.5\Phi_{EE}, \quad U_e < 0, \quad (6b)$$

where “ $e$ ” stands for the east interface between two nodes; “ $E$ ” stands for east node and “ $W$ ” means west node; and “ $EE$ ” can be defined as the east node of “ $E$ ” node.

As to FDM, taking node  $P$  as example, the expressions can be written as

$$\frac{\partial \Phi}{\partial X} \Big|_P^+ = \frac{\partial \Phi}{\partial X} \Big|_P^- = \frac{\Phi_E - 2\Phi_P + \Phi_W}{2\Delta X}, \quad (7)$$

$$\frac{\partial \Phi}{\partial X} \Big|_P^+ = \frac{3\Phi_P - 4\Phi_W + \Phi_{WW}}{2\Delta X}, \quad U_P \geq 0 \quad (8a)$$

$$\frac{\partial \Phi}{\partial X} \Big|_P^- = \frac{-3\Phi_P + 4\Phi_E - \Phi_{EE}}{2\Delta X}, \quad U_P < 0. \quad (8b)$$

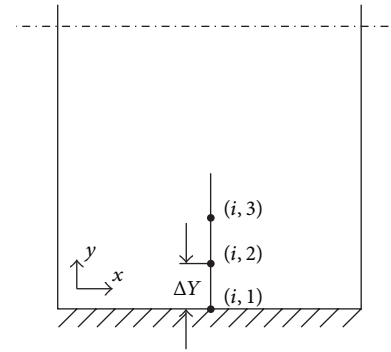


FIGURE 2: Schematic of the treatment for boundary conditions of vorticity-stream function method.

**3.3. Treatment of the Boundary Condition of Vorticity.** Since the influence from boundary condition of vorticity on the solution of equations is significant, in this section, the calculation performances of FVM and FDM with variant treatments of the boundary condition for vorticity are studied.

Three boundary conditions of vorticity are compared and studied. In the boundary as shown in Figure 2, their expressions, Thom equation [20], Woods equation [21], and Jensen equation [22], as well as corresponding accuracy are shown in (9)–(11);

Thom equation:

$$\omega_{i,1} = \frac{2(\psi_{i,2} - \psi_{i,1})}{\delta Y^2} + O(\Delta Y), \quad (9)$$

Woods equation:

$$\omega_{i,1} = \frac{3(\psi_{i,2} - \psi_{i,1})}{\Delta Y^2} - \frac{1}{2}\omega_{i,2} + O(\Delta Y^2), \quad (10)$$

Jensen equation:

$$\omega_{i,1} = \frac{-7\psi_{i,1} + 8\psi_{i,2} - \psi_{i,3}}{2\Delta Y^2} + O(\Delta Y^2). \quad (11)$$

3.4. *Deferred Correction.* When MAC is adopted, momentum and energy equations are both solved in explicit scheme while in vorticity-stream function method, the convection term is treated in implicit scheme by deferred correction, which can guarantee the main-diagonal domination of the solving matrix and thus guarantee the calculation stability. As to FVM, taking  $\Phi_e$  as example, the expressions of deferred correction are as follows:

$$\begin{aligned} \text{when } U_e \geq 0 \quad \Phi_e &= \Phi_P + (\Phi_e^+ - \Phi_P)^*, \\ \text{when } U_e < 0 \quad \Phi_e &= \Phi_E + (\Phi_e^- - \Phi_E)^*, \end{aligned} \quad (12)$$

where “\*” in these equations stands for the former calculation step.

As to FDM, similarly to the treatment of  $\Phi_e$  in FVM, the deferred correction for node  $P$  can be written as the sum of first-order upwind gradient and correction gradient which is shown as follows:

$$\begin{aligned} \text{when } U_P \geq 0 \quad U_P \frac{\partial \Phi}{\partial X} \Big|_P^+ &= U_P \left( \frac{\Phi_P - \Phi_W}{\Delta X} \right) \\ &+ \left[ U_P \left( \frac{\partial \Phi}{\partial X} \Big|_P^+ - \frac{\Phi_P - \Phi_W}{\Delta X} \right) \right]^*, \end{aligned} \quad (13)$$

$$\begin{aligned} \text{when } U_P < 0 \quad U_P \frac{\partial \Phi}{\partial X} \Big|_P^- &= U_P \left( \frac{\Phi_E - \Phi_P}{\Delta X} \right) \\ &+ \left[ U_P \left( \frac{\partial \Phi}{\partial X} \Big|_P^- - \frac{\Phi_E - \Phi_P}{\Delta X} \right) \right]^*. \end{aligned} \quad (14)$$

The first terms in the right side of (12)–(14) are all first-order upwind term. The second terms are incorporated into the source term as the form of correction term. The discretized equation is solved by G-S solver with underrelaxation, of which the discrete expression is shown as (15) and the discretized equations of FVM and FDM are shown in (16a), (16b), (17a), and (17b), respectively:

$$a_P \Phi_P = a_E \Phi_E + a_W \Phi_W + a_N \Phi_N + a_S \Phi_S + b, \quad (15)$$

$$\begin{aligned} a_E &= \frac{\max(-U_e, 0)}{\Delta X} + \frac{1}{\text{Re } \Delta X^2}, \\ a_W &= \frac{\max(U_w, 0)}{\Delta X} + \frac{1}{\text{Re } \Delta X^2}, \\ a_N &= \frac{\max(-V_n, 0)}{\Delta Y} + \frac{1}{\text{Re } \Delta Y^2}, \\ a_S &= \frac{\max(V_s, 0)}{\Delta Y} + \frac{1}{\text{Re } \Delta Y^2}, \\ a_P &= \frac{\max(U_e, 0)}{\Delta X} + \frac{\max(-U_w, 0)}{\Delta X} + \frac{\max(V_n, 0)}{\Delta Y} \\ &+ \frac{\max(-V_s, 0)}{\Delta Y} + \frac{2}{\text{Re } \Delta X^2} + \frac{2}{\text{Re } \Delta Y^2}, \end{aligned} \quad (16a)$$

$$\begin{aligned} b &= -\max(U_e, 0) \left[ \frac{\Phi_e^+ - \Phi_P}{\Delta X} \right] + \max(-U_e, 0) \left[ \frac{\Phi_e^- - \Phi_E}{\Delta X} \right] \\ &+ \max(U_w, 0) \left[ \frac{\Phi_w^+ - \Phi_W}{\Delta X} \right] - \max(-U_w, 0) \left[ \frac{\Phi_w^- - \Phi_P}{\Delta X} \right] \\ &- \max(V_n, 0) \left[ \frac{\Phi_n^+ - \Phi_P}{\Delta Y} \right] + \max(-V_n, 0) \left[ \frac{\Phi_n^- - \Phi_N}{\Delta Y} \right] \\ &+ \max(V_s, 0) \left[ \frac{\Phi_s^+ - \Phi_S}{\Delta Y} \right] - \max(-V_s, 0) \left[ \frac{\Phi_s^- - \Phi_P}{\Delta Y} \right], \end{aligned} \quad (16b)$$

$$\begin{aligned} a_E &= \frac{\max(-U_P, 0)}{\Delta X} + \frac{1}{\text{Re } \Delta X^2}, \\ a_W &= \frac{\max(U_P, 0)}{\Delta X} + \frac{1}{\text{Re } \Delta X^2}, \\ a_N &= \frac{\max(-V_P, 0)}{\Delta Y} + \frac{1}{\text{Re } \Delta Y^2}, \\ a_S &= \frac{\max(V_P, 0)}{\Delta Y} + \frac{1}{\text{Re } \Delta Y^2}, \end{aligned} \quad (17a)$$

$$\begin{aligned} a_P &= \frac{\max(-U_P, 0)}{\Delta X} + \frac{\max(U_P, 0)}{\Delta X} + \frac{\max(-V_P, 0)}{\Delta Y} \\ &+ \frac{\max(V_P, 0)}{\Delta Y} + \frac{2}{\text{Re } \Delta X^2} + \frac{2}{\text{Re } \Delta Y^2}, \end{aligned}$$

$$\begin{aligned} b &= -\max(U_P, 0) \left[ \frac{\partial \Phi}{\partial X} \Big|_P^+ - \frac{\Phi_P - \Phi_W}{\Delta X} \right] \\ &+ \max(-U_P, 0) \left[ \frac{\partial \Phi}{\partial X} \Big|_P^- - \frac{\Phi_E - \Phi_P}{\Delta X} \right] \\ &- \max(V_P, 0) \left[ \frac{\partial \Phi}{\partial Y} \Big|_P^+ - \frac{\Phi_P - \Phi_S}{\Delta Y} \right] \\ &+ \max(-V_P, 0) \left[ \frac{\partial \Phi}{\partial Y} \Big|_P^- - \frac{\Phi_N - \Phi_P}{\Delta X} \right], \end{aligned} \quad (17b)$$

where  $a_N$ ,  $a_P$ ,  $a_E$ ,  $a_W$ , and  $a_S$  are coefficients in discretized equations and  $b$  is the source term in discretized equations.

## 4. Results Comparison and Analysis

In this section, the accuracy, stability of convection term, robustness and calculation efficiency of variant algorithms, schemes, and treatments of boundary condition which have been discussed previously are systemically compared and analyzed based on the calculation results of lid-driven flow and natural convection flow in a square cavity.

4.1. *Accuracy.* Firstly, the accuracy of FVM and FDM is evaluated by comparing bench mark solution with the results

TABLE 4: Truncation error of FVM and FDM governing equations for vorticity-stream function algorithm of lid driven flow in a square cavity.

	Convection item	Diffusion item
FVM (format)	$\frac{\Phi_e}{\Delta X} - \frac{\Phi_w}{\Delta X}$	$\frac{1}{\Delta X} \frac{\partial \Phi}{\partial x} \Big _e - \frac{1}{\Delta X} \frac{\partial \Phi}{\partial x} \Big _w$
FVM (TE)	$-\frac{\Delta X^2}{8} \Phi_p''' - \frac{\Delta X^4}{128} \Phi_p^{(5)} - \dots$	$-\frac{\Delta X^2}{24} \Phi_p^{(4)} - 13 \frac{\Delta X^4}{5760} \Phi_p^{(6)} - \dots$
FDM (format)	$\frac{\partial \Phi}{\partial X} \Big _p$	$\frac{\partial^2 \Phi}{\partial X^2} \Big _p$
FDM (TE)	$-\frac{\Delta X^2}{6} \Phi_p''' - \frac{\Delta X^4}{120} \Phi_p^{(5)} - \dots$	$-\frac{\Delta X^2}{12} \Phi_p^{(4)} - \frac{\Delta X^4}{360} \Phi_p^{(6)} - \dots$

obtained from variant mesh density, discrete schemes, and boundary conditions. Through precision analysis, FVM and FDM are, respectively, adopted with the Taylor expansion commenced at midpoint ( $P$  node), and their respective truncation error (TE) is just as shown Table 4 [19]. The truncation errors of FVM are obviously less than the FDM's.

**4.1.1. Influence of Mesh Density.** In [4], it is indicated that the conservative property can affect the accuracy while the nonconservative FDM loses its conservative property in the situation when the grid is too small. To make further analysis, the calculation results obtained by FVM and FDM with variant mesh densities are compared. The results of the velocity along the horizontal central axis  $V$  and velocity along the vertical central axis  $U$  obtained by FDM and FVM with central difference scheme of MAC algorithm are compared and illustrated in Figure 3.

From Figure 3 we can see that, when the mesh density is taken as  $80 \times 80$ , the results obtained by FVM and FDM both agree well with the benchmark solution. When the mesh density is reduced to  $40 \times 40$ , the results obtained by FVM are closer to the benchmark solution and if the mesh density is further reduced to  $20 \times 20$ , the results obtained by FDM differ from the benchmark solution greatly, in which FVM shows its advantage in accuracy. This phenomenon is in good agreement with the theoretical analysis in [18]; that is, the conservative property of FVM better ensures the accuracy of calculation. Therefore, whether the conservative property can be realized is of much significance to the accuracy of the obtained result.

**4.1.2. Influence of Boundary Condition.** In the following section, FVM and FDM with variant boundary conditions are compared from the perspective of accuracy by vorticity-stream function method. The results of the velocity along the horizontal central axis  $V$  and velocity along the vertical central axis  $U$  obtained by FDM and FVM with central difference scheme are compared and illustrated in Figure 4, and the influence of boundary condition of vorticity is also given. From Figure 4 we can see that no matter which treatment of boundary condition is adopted the accuracy of FVM is higher than that of FDM in vorticity-stream function method.

**4.1.3. Influence of Discrete Scheme.** The selection of discrete forms is also influential to the accuracy. Thus the results obtained with variant discrete forms are studied. Taking the vorticity-stream function with boundary condition treated by first-order Thom equation as example, the results of the velocity along the horizontal central axis  $V$  and velocity along the vertical central axis  $U$  obtained by FDM and FVM with variant discrete schemes are compared and illustrated in Figure 5, from which we can see that, whether second-order central difference or second-order upwind scheme is adopted, the accuracy of FVM is higher than that of FDM, the comparison between (a) and (b) indicates that second-order upwind difference possesses higher accuracy than second-order central difference.

**4.1.4. Influence of Physical Problem.** Finally, two methods in variant physical problems are compared from the perspective of accuracy based on the convection flow in a square cavity. Taking the result obtained by MAC algorithm as example, Figure 6 shows the comparison of results of the velocity along the horizontal central axis  $V$  and velocity along the vertical central axis  $U$  obtained by FDM and FVM. Temperature fields obtained by FVM and FDM are compared with the grid-independent solution (obtained with grid of  $256 \times 256$ ) as Figure 7 shows.

From the comparison in Figure 6 and Figure 7 we can see that, based on the results obtained by MAC of natural convection flow in a square cavity, the accuracy of FVM is generally superior to that of FDM. Thus, it is indicated by comparison that, no matter which mesh density, scheme, and treatment of boundary condition is adopted, FVM shows better accuracy than FDM.

**4.2. Stability of Convection Term.** Stability of mathematical meaning can only ensure that the oscillation of solution is controlled within a range but cannot eliminate the absence of oscillation. The amplification of oscillation may result in divergence. Stability of convection term originates from varied difference schemes for convective item and is independent of the introducing of rounding error in the calculation. This stability is the key point to obtain a solution with physical meaning. It is concluded that all the unstable schemes will result in the oscillation of solution. Stability condition of

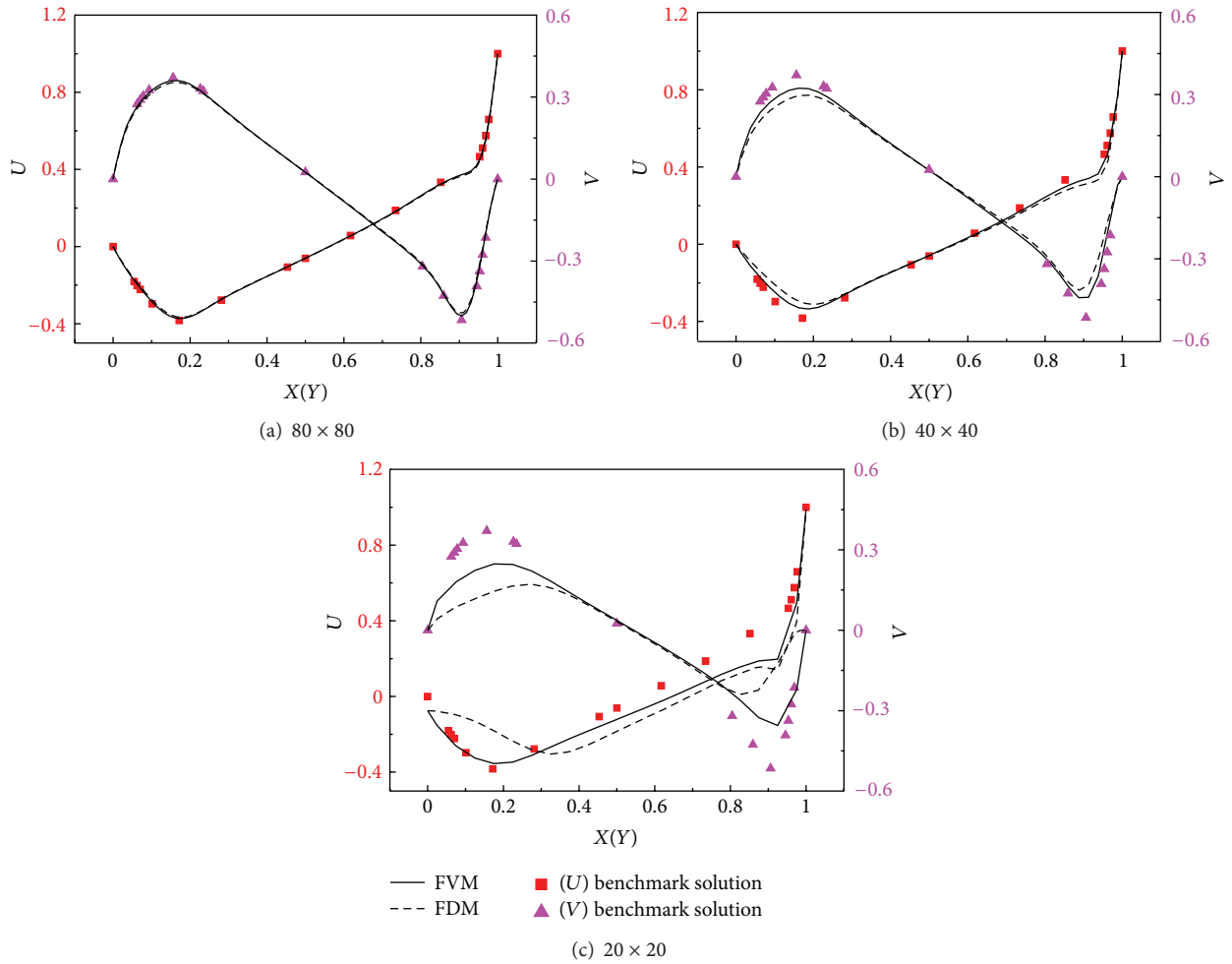


FIGURE 3: Velocity on the central axis of lid-driven flow obtained by MAC with variant mesh densities.

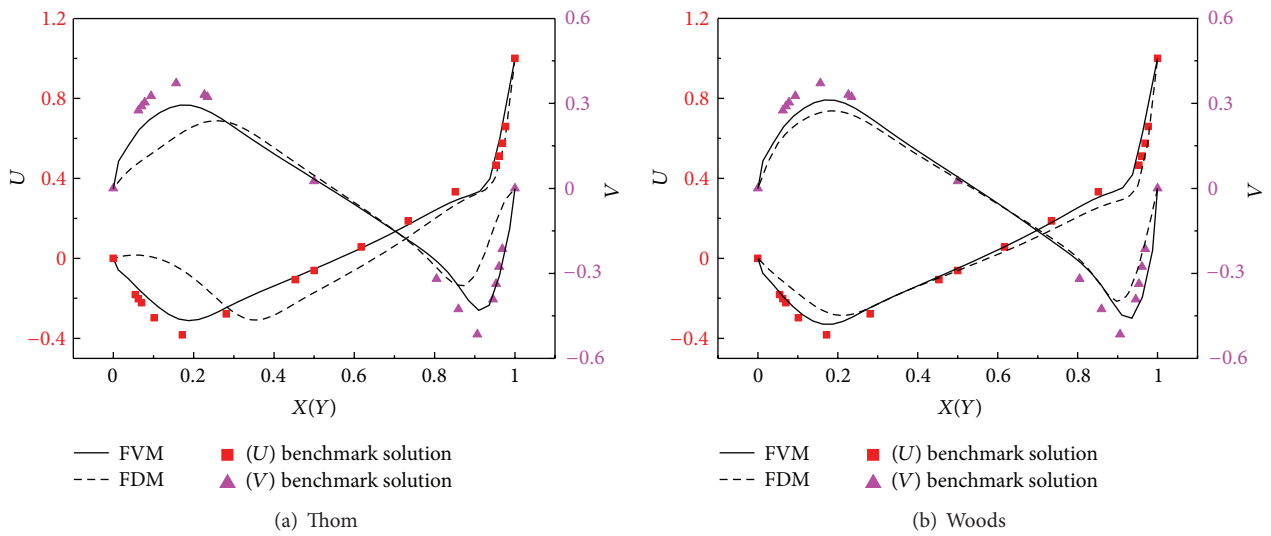


FIGURE 4: Velocity along the central axis obtained by second-order central difference scheme with two treatments of boundary condition when the mesh density is  $40 \times 40$ .

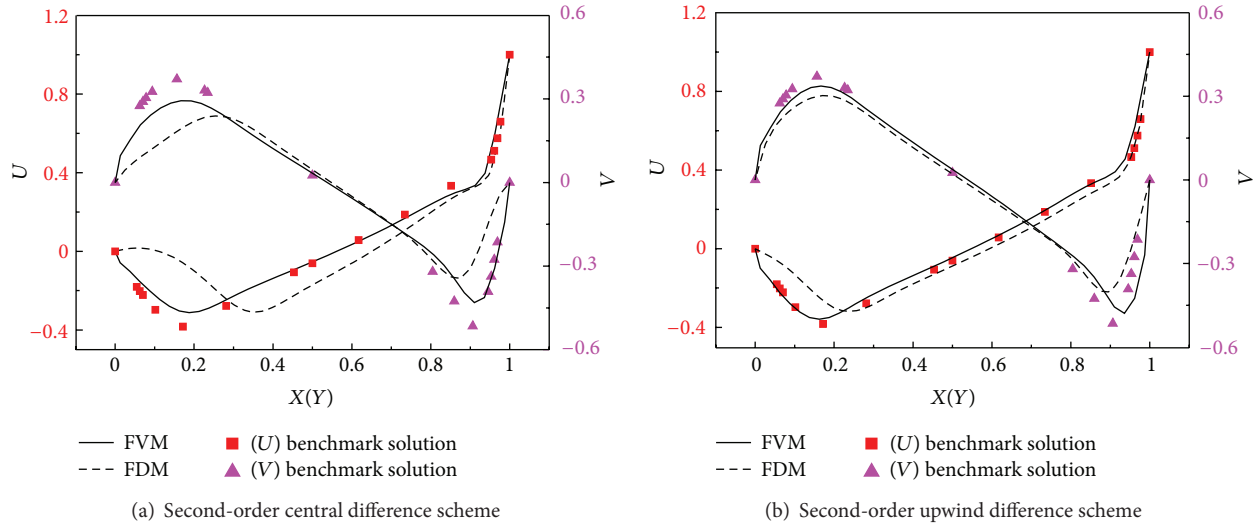


FIGURE 5: Velocity along the central axis obtained by vorticity-stream function method for lid-driven flow with different schemes when the mesh density is  $40 \times 40$ .

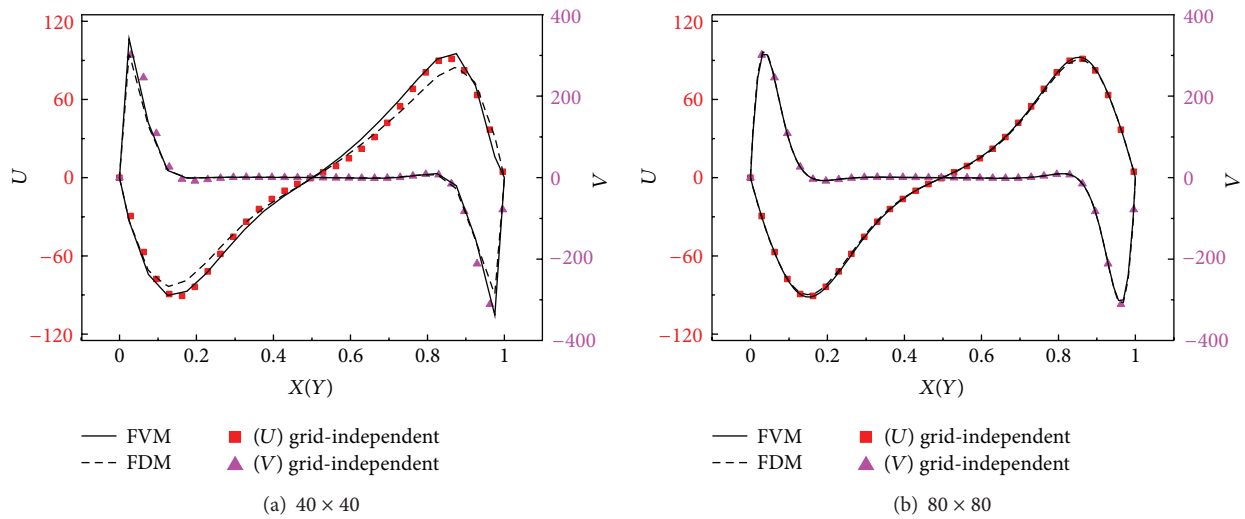


FIGURE 6: Velocity along the central axis of convection flow in a square cavity with variant grid densities.

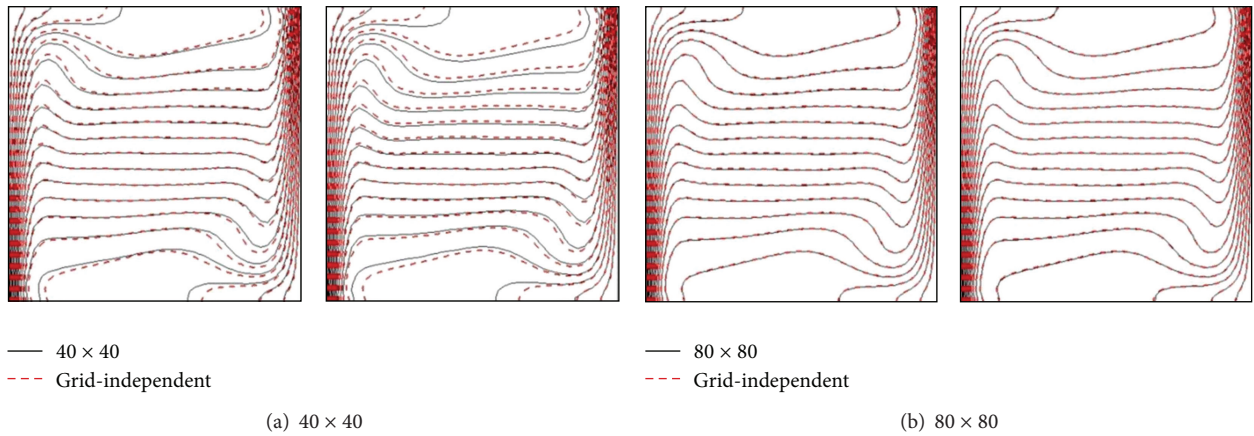


FIGURE 7: Comparison of temperature contours of natural convection flow in a square cavity with variant mesh densities (FVM in the left column and FDM in the right column).

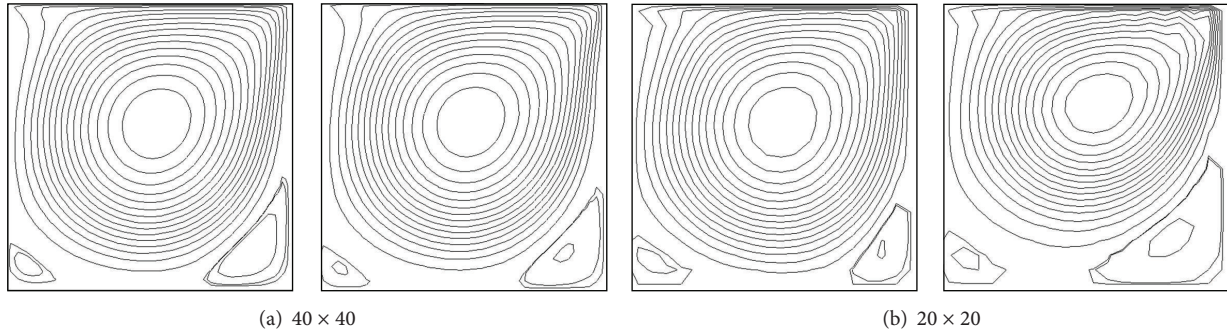


FIGURE 8: Comparison of stream lines in lid-driven flow with variant mesh densities (FVM in the left column and FDM in the right column).

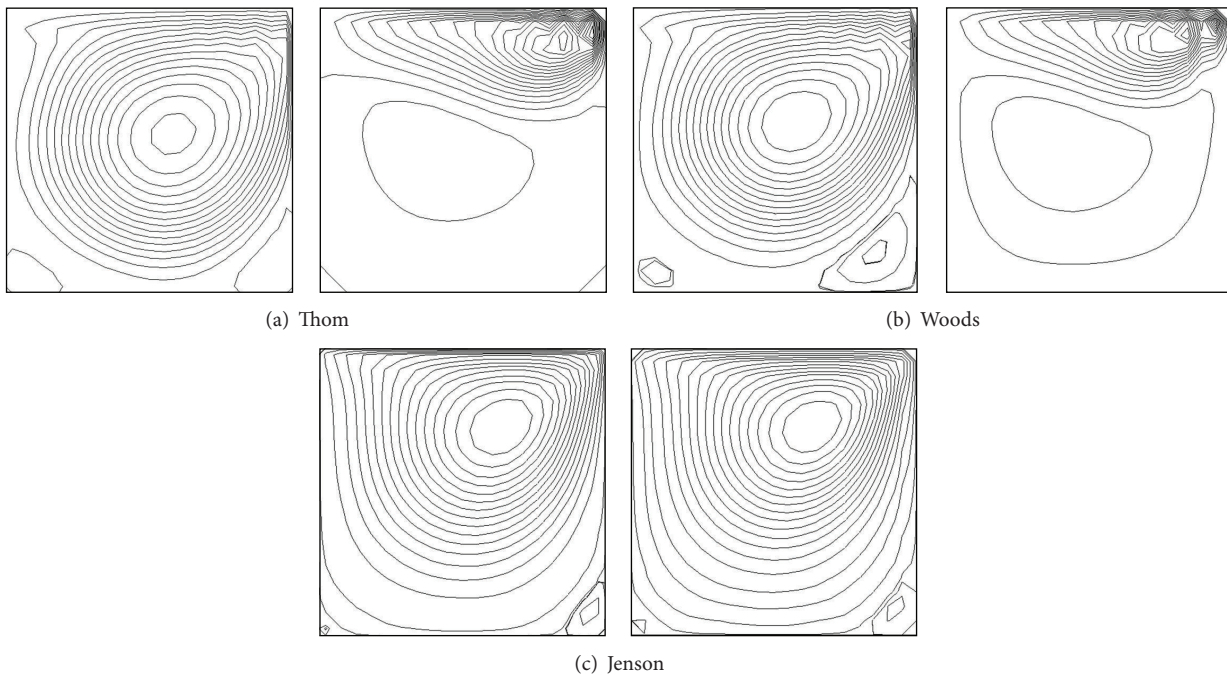


FIGURE 9: Stream functions of lid-driven flow under variant boundary treatments with the grid of  $20 \times 20$  (FVM in the left column and FDM in the right column).

the convection item (Mesh Peclet number) is affected by the following factors such as mesh density and boundary condition. Taking lid-driven flow as example, the stability of convection term of FVM and FDM with variant mesh densities treatments of boundary condition is compared.

**4.2.1. Influence of Mesh Density.** Figure 8 shows the comparison of stream lines between FVM and FDM with variant mesh densities. With the grid of  $40 \times 40$ , the two methods both can capture the structure of primary vortex and secondary vortex as Figure 8(a) shows. It is seen in Figure 8(b) that, when the mesh of  $20 \times 20$  is adopted, concussion phenomenon appears, which is more serious in FDM, and the location of the vortex center obviously moves upward.

**4.2.2. Influence of Boundary Condition.** Similarly to the accuracy analysis, the results obtained by variant treatments for

vorticity of wall boundary are compared as Figure 9 shows. Three treatments, Thom, Woods, and Jenson, are analyzed. From Figure 9 we can see that, only when Jenson equation is adopted, the results obtained by FVM and FDM are relatively close, while when Thom and Woods are adopted, FVM shows better results than FDM. The results obtained by FDM suffer severe oscillation and even lack physical meaning. It is clear that, based on the lid-driven flow, stability of convection term of FVM is superior to that of FDM. The influence from the same boundary error (truncation error and rounding error) on difference solving methods is illustrated in Figure 9. With the treatment of boundary condition with the same truncation error or rounding error, the stability of FVM is better than that of FDM, especially in the situation with boundary treatment of (a) and (b) with relatively low precision truncation error; FDM is very unstable and very easy to slip into oscillation.

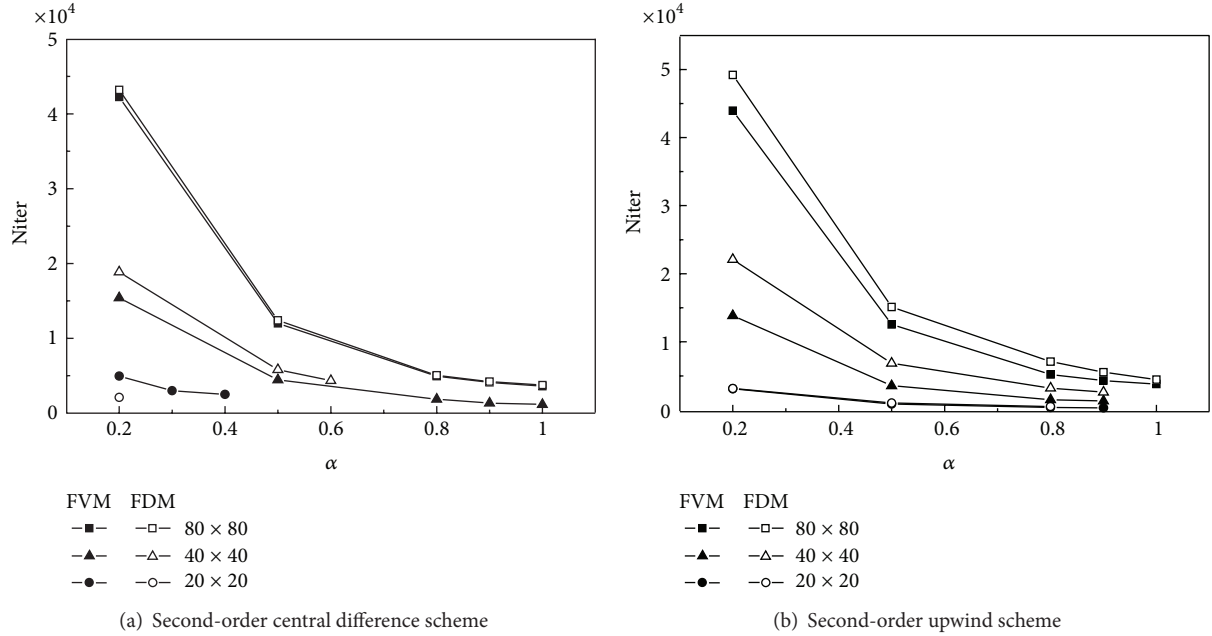


FIGURE 10: Comparison of the robustness of lid-driven flow with variant schemes.

**4.3. Robustness.** Robustness is a very critical index to evaluate the numerical approaches. In this section, the robustness of FVM and FDM is compared based on the lid-driven flow problem, which is solved by vorticity-stream function. Grids of  $20 \times 20$ ,  $40 \times 40$ , and  $80 \times 80$  are adopted, respectively, in the calculation. Relaxation factor is tentatively taken up from 0.2 to the maximum which can ensure the convergence of calculation. Iterations are correspondingly recorded as well.

It is shown in Figure 10 when the whether the central difference scheme or second-order upwind scheme is adopted, with the refining of calculation grids, the maximum relaxation factor ( $\alpha$ ) increases in both FVM and FDM, the robustness is enhanced, and the iterations (Niter) correspondingly decrease as well.

As Figure 10(a) shows, in the situation that central difference scheme is adopted, with the grid of  $20 \times 20$  and  $40 \times 40$ , the maximum relaxation factor of FVM is bigger than that of FDM while with the grid of  $80 \times 80$ , the relaxation factor can be taken as 1.0 in both methods. Similarly, as Figure 10(b) shows, generally speaking, when second-order upwind difference scheme is adopted, the maximum relaxation factor is bigger than that of FDM. Based on the result of lid-driven flow, the conservative FVM is superior to the nonconservative FDM from the perspective of numerical robustness.

In the numerical simulation of complex flow field, calculation efficiency is another critical index, on which this paper makes analysis. From Figure 10 we can see that, with the increasing of relaxation factor, the iterations of two methods both decrease generally. What needs to be notified is that the iterations of FVM are smaller than those of FDM.

**4.4. Efficiency.** In the numerical simulation of complex flow field, calculation efficiency is another critical index, on which this paper makes analysis.

As is shown in Table 5, although the calculation time required by every iteration step in FVM and FDM is almost the same, with the increasing of mesh numbers, calculation time required by FVM slightly decreases. Thus, total calculation time of FVM is much smaller than that of FDM. That is, FVM is much more efficient than FDM. Thus, it is validated that the efficiency of FVM is better than that of FDM in the same calculation condition.

## 5. Conclusions

Based on vorticity-stream function and MAC algorithm, lid-driven flow and natural convection in a square cavity are calculated. The accuracy, stability of convective term, robustness of FVM and FDM with variant mesh densities, discrete forms, and treatments of boundary condition are compared. The following conclusions are drawn.

- (1) No matter which algorithm, discrete form, or treatment of boundary condition is adopted, the results obtained by conservative FVM are closer to benchmark solution than those obtained by FDM. The accuracy of FVM is higher than FDM, especially when the mesh density is relatively small.
- (2) The results of lid-driven flow indicate that the results obtained by FDM show more serious oscillation and the results obtained even lose physical meaning. Thus, the stability of convection term of FVM is superior than that of FDM.
- (3) As to the lid-driven flow, it is indicated that, when vorticity-stream function method is adopted, the relaxation factor of conservative method is bigger than that of the nonconservative one while the iterations are less, which shows that the robustness

TABLE 5: Computation iterations and time of FVM and FDM in second-order central difference scheme for vorticity-stream function algorithm of lid driven flow.

Mesh	$\alpha$	FVM			FDM		
		Iterations	Time(s)	Time of each iteration	Iterations	Time(s)	Time of each iteration
20	0.2	4950	73.8	0.015	2100	30.7	0.015
20	0.1	10500	154.4	0.015	4300	61.6	0.014
40	0.6	3250	151.9	0.047	4350	199.3	0.046
40	0.5	4450	203.5	0.046	5800	262.9	0.045
40	0.4	6300	296.3	0.047	7950	369.3	0.046
80	0.8	4950	822.3	0.166	5050	858.4	0.170
80	0.6	8500	1413.4	0.166	9000	1539.5	0.171
80	0.4	17250	2969.4	0.172	17750	3242.0	0.183

and calculation efficiency of conservative method are better than those of the nonconservative method.

- (4) In the lid-driven flow, with vorticity-stream function method, the calculation time required by every iteration step of FVM is slightly smaller than that of FDM. Together with the smaller total iteration steps, FVM is more efficient than FDM.

## Acknowledgment

The study is supported by the National Science Foundation of China (nos. 51134006, 51176204, and 51276198).

## References

- [1] J. D. Anderson Jr., *Computational Fluid Dynamics: The Basics With Applications*, McGraw-Hill, 1995.
- [2] P. J. Roache, *Computational Fluid Dynamics*, Hermosa, 1976.
- [3] W. Q. Tao, *Heat Transfer*, Science Press, 2001.
- [4] W. Q. Tao, *Advances in Computational Heat Transfer*, Science Press, 2000.
- [5] Y. Jaluria and K. E. Torrance, *Computational Heat Transfer*, Hemisphere Publishing Corporation, 1986.
- [6] P. D. Lax, "Weak solutions of nonlinear hyperbolic equations and their numerical computation," *Communications on Pure and Applied Mathematics*, vol. 7, pp. 159–193, 1954.
- [7] P. Lax and B. Wendroff, "Systems of conservation laws," *Communications on Pure and Applied Mathematics*, vol. 13, no. 2, pp. 217–237, 1960.
- [8] A. Jameson, "Transonic potential flow calculations using conservation form," in *Proceedings of the Computational fluid dynamics conference*, pp. 148–161, Hartford, Conn, USA, 1975.
- [9] M. Vinokur, "Conservation equations of gasdynamics in curvilinear coordinate systems," *Journal of Computational Physics*, vol. 14, pp. 105–125, 1974.
- [10] T. J. Bridges, "Conservation laws in curvilinear coordinates: a short proof of Vinokur's theorem using differential forms," *Applied Mathematics and Computation*, vol. 202, no. 2, pp. 882–885, 2008.
- [11] R. J. DiPerna, "Decay of solutions of hyperbolic systems of conservation laws with a convex extension," *Archive for Rational Mechanics and Analysis*, vol. 64, no. 1, pp. 1–46, 1977.
- [12] A. Bressan, "Hyperbolic systems of conservation laws," *Revista Matemática Complutense*, vol. 12, no. 1, pp. 135–198, 1999.
- [13] R. K. S. Hankin, "The Euler equations for multiphase compressible flow in conservation form-Simulation of shock-bubble interactions," *Journal of Computational Physics*, vol. 172, no. 2, pp. 808–826, 2001.
- [14] C. Lai, R. A. Baltzer, and R. W. Schaffranek, "Conservation-form equations of unsteady open-channel flow," *Journal of Hydraulic Research*, vol. 40, no. 5, pp. 567–578, 2002.
- [15] L. M. Gao, K. T. Li, B. Liu, and J. Su, "General integral conservation form of Navier-Stokes equations and numerical application," *Chinese Journal of Computational Physics*, vol. 25, no. 2, pp. 172–178, 2008.
- [16] S. Patankar, *Numerical Heat Transfer and Fluid Flow*, Hemisphere Publishing, 1980.
- [17] A. West and T. Fuller, "Influence of rib spacing in proton-exchange membrane electrode assemblies," *Journal of Applied Electrochemistry*, vol. 26, no. 6, pp. 557–565, 1996.
- [18] B. P. Leonard, "Comparison of truncation error of finite-difference and finite-volume formulations of convection terms," *Applied Mathematical Modelling*, vol. 18, no. 1, pp. 46–50, 1994.
- [19] G. G. Botte, J. A. Ritter, and R. E. White, "Comparison of finite difference and control volume methods for solving differential equations," *Computers and Chemical Engineering*, vol. 24, no. 12, pp. 2633–2654, 2000.
- [20] A. Thom, "The flow past cylinders at low speeds," *Proceedings of the Royal Society A*, vol. 141, pp. 651–659, 1993.
- [21] L. C. Woods, "A note on the numerical solution of fourth order differential equations," vol. 5, pp. 176–182, 1954.
- [22] V. G. Jenson, "Viscous flow round a sphere at low Reynolds numbers ( $Re \leq 40$ )," *Proceedings of the Royal Society A*, vol. 249, pp. 346–366, 1959.

## Research Article

# Numerical Simulation on Flow Field of Oilfield Three-Phase Separator

Yong-tu Liang,<sup>1</sup> Sheng-qiu Zhao,<sup>1,2</sup> Xia-xue Jiang,<sup>1</sup> Xian-qi Jia,<sup>1</sup> and Wang Li<sup>1</sup>

<sup>1</sup> Beijing Key Laboratory of Urban Oil and Gas Distribution Technology, China University of Petroleum, Beijing 102249, China

<sup>2</sup> Trans-Asia Gas Pipeline Company Limited, Beijing 100007, China

Correspondence should be addressed to Yong-tu Liang; [liangyt21st@163.com](mailto:liangyt21st@163.com)

Received 26 March 2013; Accepted 13 April 2013

Academic Editor: Bo Yu

Copyright © 2013 Yong-tu Liang et al. This is an open access article distributed under the Creative Commons Attribution License, which permits unrestricted use, distribution, and reproduction in any medium, provided the original work is properly cited.

The conventional measurement method can no longer guarantee the accuracy requirement after the oilfield development entering high water cut stage, due to the water content and gas phase in the flow. In order to overcome the impact of measurement deviation the oilfield production management, the flow field of three-phase separator is studied numerically in this paper using Fluent 6.3.26. Taking into consideration the production situation of PetroChina Huabei Oilfield and the characteristics of three-phase separator, the effect of internal flow status as well as other factors such as varying flow rate, gas fraction, and water content on the separation efficiency is analyzed. The results show that the separation efficiencies under all operation conditions are larger than 95%, which satisfy the accuracy requirement and also provide the theoretical foundation for the application of three-phase separators at oilfields.

## 1. Introduction

The rapid development of national economy has greatly increased the consumption of petroleum of China. Since China became net importer of petroleum in 1993, the import dependence has raised from 6% to 55.2% in 2010 [1–3]. The pressing demand for oil has led to the consecutive production of China's interior oilfield during high water cut stage. In the daily operation management of oilfields, the accurate and timely measurement of well fluids is very important, which would become the significant basis for the supervision of operation, the analysis of reservoir change, and the establishment of production decisions. Up to now, the measurement method for wells at PetroChina Huabei Oilfield is sampling. This kind of traditional measurement method can no longer guarantee the precision during high water cut stage due to the extensive variation of water content and gas-oil ratio, bringing much inconvenience to the operation management. In order to overcome this, it is necessary to select a three-phase separate measurement system, which could provide the accurate measurement as well as the automatic control of well fluids.

The former numerical studies of interior flow field of separator concentrate on gravity separator and centrifugal separator, and a great many of them focus on specific work conditions. The physical model and calculation method will vary the work conditions.

Yang et al. [4] conducted the numerical simulation of gravity separator by CFD method, analyzed the influence of separation factors on separating efficiency, and believed the most important factors are that diameter of gas particles and liquid viscosity, followed by gas content and throughput. Luo et al. [5] introduced RSM model to obtain the velocity, pressure, and concentration distribution of the [gas-liquid measure cyclone], which provided basis for the improvement and optimization of separator structure. Zhou and Xia [6] analyzed the impact of centrifugal force as well as the collision process of air stream at the wall on separation effectiveness and proposed a remodel design scheme based on this gas-liquid two-phase simulation. Du [7] increased the measuring precision of crude oil (and associated water) and associated gas to 0.5% and 5%, respectively, by adopting new measuring technology which included the combined application of mass flow meter, intelligent gas flow meter, and microcomputer.

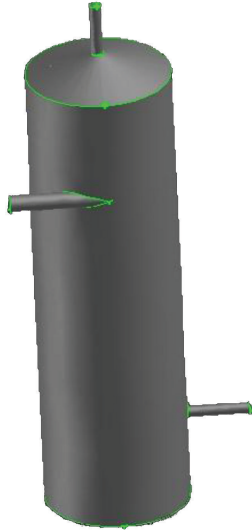


FIGURE 1: Model of three-phase separator.

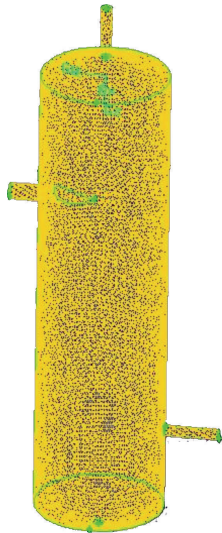


FIGURE 2: Mesh system.

Based on low permeability oilfield development and production situation, Pan et al. [8] designed an XYD oil-gas-water three-phase automatic metering unit which could realize the automatic online consecutive metering of oil-gas-water [and the gas production, well production of a single well.] Pang et al. [9] combined cyclone separator and horizontal separator together, manufacturing an XJ oil-gas-water three-phase metering unit especially for high water cut oilfields, which is able to improve the gas-liquid separation effectively. Qu and Ma [10] employed cyclone separator and stabilization tank simultaneously for separation and designed a skid-mounted three-phase separating and metering unit. Oil-gas-water three-phase metering is achieved by the joint use of mass flow meter and gas vortex precession flow meter. This unit is portable, effective, and compact and is suitable for single well metering and calibration.

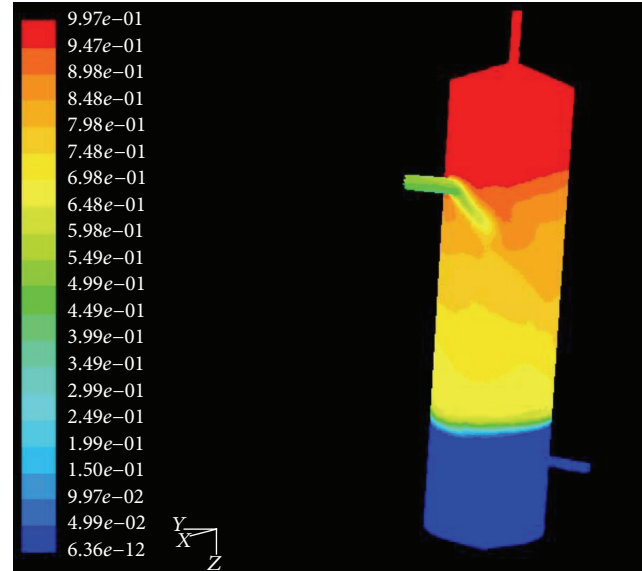


FIGURE 3: Distribution of volume fraction of gas.

In this paper, the process of oil-gas-water three-phase separation by gravity vertical metering separator is numerically simulated by CFD methods. Internal flow status and the effect of factors such as varying flow rate, gas ratio, and water ratio on the separation efficiency are analyzed, which may provide the theoretical foundation for the application of three-phase separators at oilfields.

## 2. Methodology

**2.1. Physical Model.** The three-phase separator calculated in this study is 4.4 m high, the diameter of which is 1.2 m. The inlet diameter is 0.159 m and the inlet is 0.8 m below the top. The diameters of gas outlet and liquid outlet are both 0.1 m. Liquid outlet is 0.6 m above the bottom. As shown in Figure 1, the geometric model of this separator is achieved by Gambit. The inlet of separator is at the tangential, which means that it is spiral-flow-type inlet diverter. Mesh is generated by Tex/Hybrid scheme, the interval size of which is 0.5. Total amount of grid number is 260,000. The multiphase flow model employed in this paper is VOF, while RNG  $k-\epsilon$  model is adopted for the calculation of turbulent flow.

### 2.2. Boundary Conditions and Parameters

**2.2.1. Inlet Boundary.** Normally, there are three kinds of inlet boundary conditions, which are mass inlet, pressure inlet, and velocity inlet. Mass inlet and velocity inlet show no difference for incompressible fluids. When inlet velocity or flow rate is unknown, pressure inlet should be employed by giving gross pressure and static pressure.

The velocity boundary is adopted. The flow rate, water content, and gas content are considered as variables since the incoming fluid is unstable at the metering station.

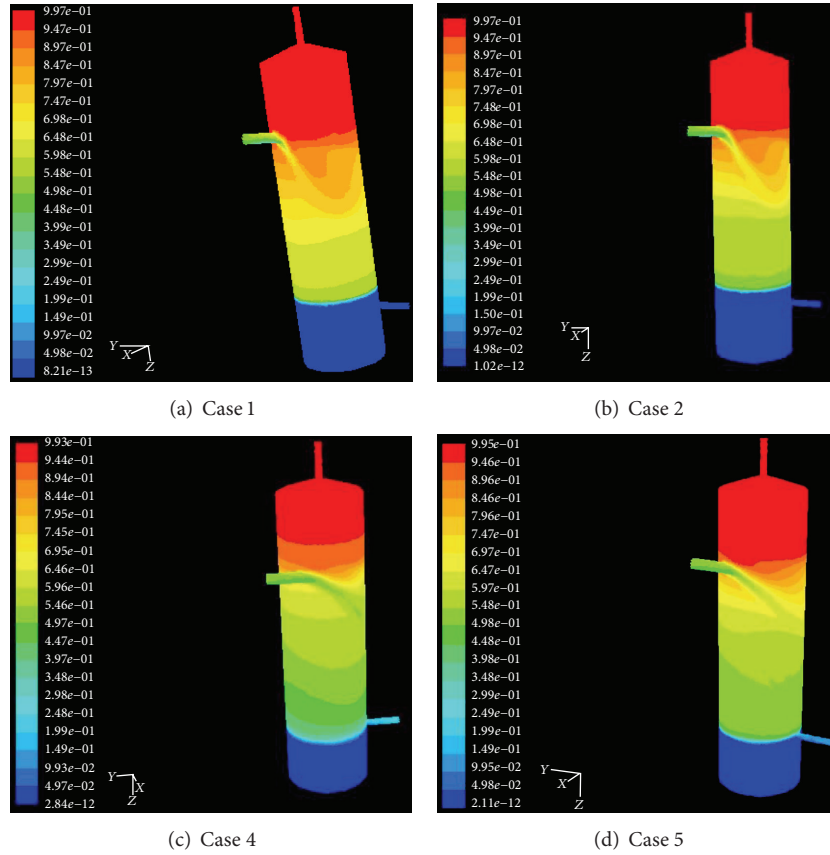


FIGURE 4: Results of flow distribution under different flow rates.

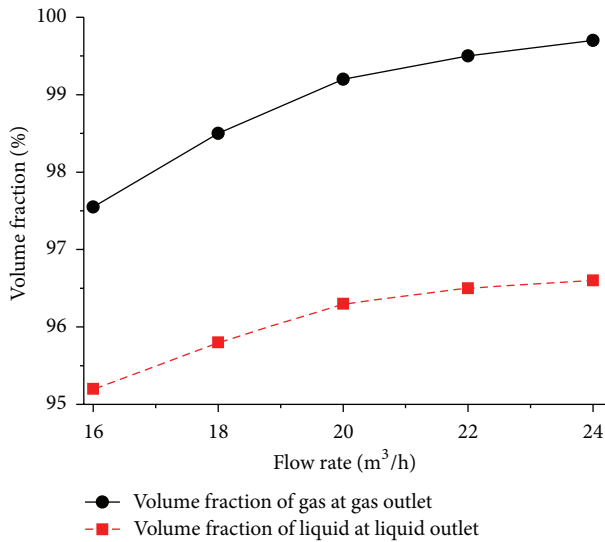


FIGURE 5: Impact of flow rate on the separation efficiency.

2.2.2. *Outlet Boundary.* There are many kinds of outlet boundary conditions, among which flow rate and pressure condition are the most commonly used. The outlet boundary condition cannot be chosen well, but should be set according

to the inlet. In this case, the outlet velocity is calculated by continuity equation by considering inlet flow rate.

2.2.3. *Wall Interface.* In the condition of this study, the wall of the separator is set, and the medium inside is viscous, making it a nonslip boundary condition. Besides this, other parameters such as roughness, thermal property, and permeability property are all defined as default in Fluent.

2.2.4. *Parameters.* The densities of crude oil, water, and natural gas are 890 kg/m<sup>3</sup>, 1000 kg/m<sup>3</sup>, and 0.6679 kg/m<sup>3</sup>, respectively, and the kinetic viscosities of them are 0.093 kg/(m·s), 0.001 kg/(m·s), and 12.28 × 10<sup>-5</sup> kg/(m·s), respectively. The diameter of droplet is 100 μm. The operation pressure and temperature are 0.3 MPa and 48°C.

### 3. Results and Analyses

After numerical calculation of oil-gas-water three-phase separator, the internal flow status and the impact of varying flow rate, gas ratio, and water ratio are analyzed, so as to figure out the feasibility of this kind of separator for PetroChina Huabei Oilfield.

3.1. *Flow Field.* It is the turbulent multiphase flow at the inlet of the separator. In this case, the flow rate is 20 m<sup>3</sup>/h with

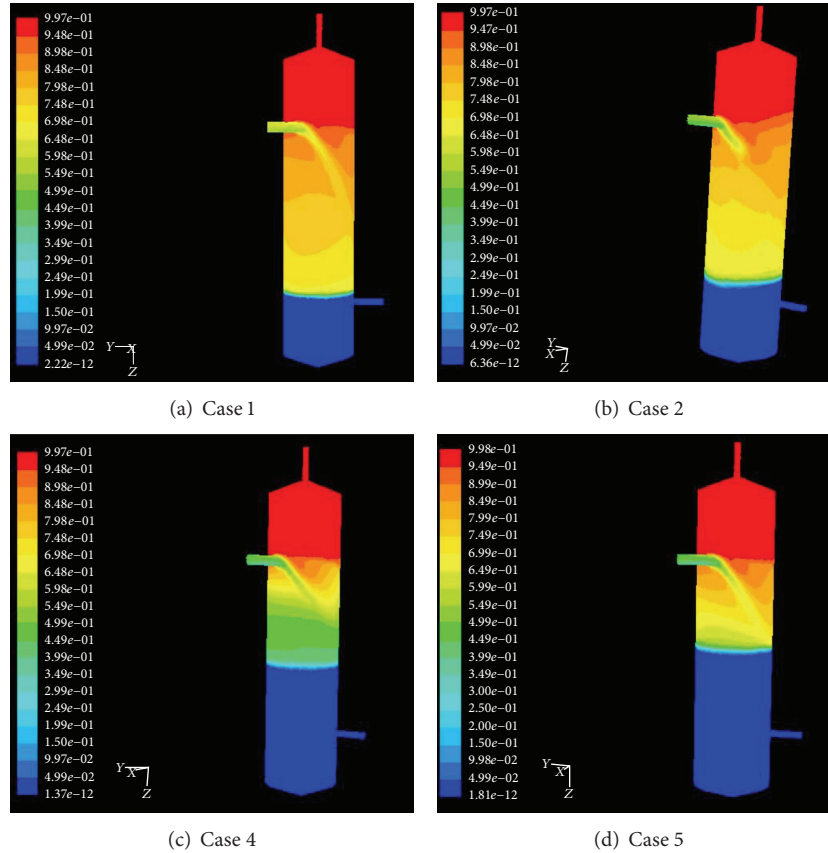


FIGURE 6: Results of flow distribution under different gas volume fractions.

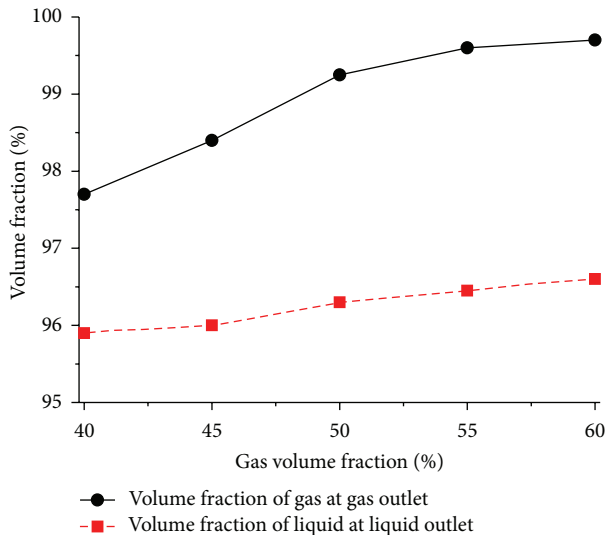


FIGURE 7: Impact of gas volume fraction on the separation efficiency.

the water and gas contents of 80% and 50%. The result is shown as follows.

As Figure 3 shows, fluids flow down rotationally due to the kinetic energy and gravity. The separation is proceeded in the separation region, in which the gas fraction is

TABLE 1: Flow rate of different cases.

Case	1	2	3	4	5
Flow rate ( $\text{m}^3/\text{h}$ )	16	18	20	22	24

50%–80%, apparently displaying gradient along the gravity direction. Gas fraction at the liquid-phase region is below 5%. Oppositely, it is above 95% at the gas-phase region, indicating the effectiveness of separation. This result matches the actual operational condition well, illustrating the viability of selected algorithm, multiphase flow model, and turbulent model.

The separation efficiency is represented by the gas fraction at the gas outlet and the liquid fraction at the liquid outlet. The higher the gas fraction at the gas outlet, the less liquid brought by gas, the better the efficiency and, vice versa.

**3.2. Impact of Flow Rate.** Flow rate changes frequently in the actual working condition of oil and gas gathering system, which may significantly affect the internal flow distribution of the separator. Meanwhile, the spiral-flow-type inlet diverter makes separation efficiency quite sensitive to the inlet flow rate. In this numerical study, the gas volume fraction and water content are fixed to 50% and 80%, respectively, while flow rate is changed as Table 1 shows to demonstrate the impact of flow rate.

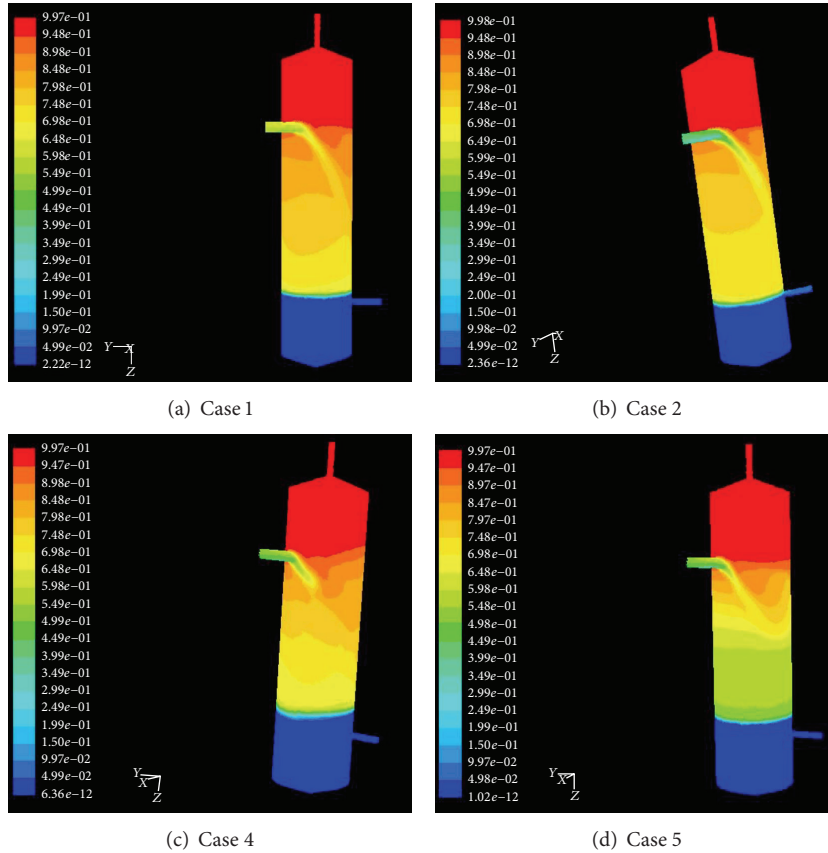


FIGURE 8: Results of flow distribution under different water contents.

TABLE 2: Gas volume fraction of different cases.

Case	1	2	3	4	5
Gas volume fraction (%)	40	45	50	55	60

TABLE 3: Water content of different cases.

Case	1	2	3	4	5
Water content (%)	64	72	80	88	96

From the results shown in Figures 3 and 4, the stream line tends to be gentle after fluids entered the separator. And it can be seen that the larger variation of gas volume fraction along the gradient direction in the gas-liquid separation region, the faster the separation. The trends of gas fraction and liquid fraction at the outlet are shown in Figure 5.

Figure 5 shows that, in the actual working load of oilfield production, gas volume fraction at gas outlet and liquid volume fraction at liquid outlet can remain above 97% and 96%. And the separation efficiency would be even larger with the increased flow rate. That is because the inlet of the separator is tangent with the main body, and the mixture will be separated by self-rotary motion. The higher the flow rate, the larger the centrifugal force, the better separation effect.

**3.3. Impact of Gas Volume Fraction.** Another factor that may remarkably affect the separation is gas volume fraction. Considering the lease operation condition, the flow rate and water content are fixed to 20 m<sup>3</sup>/h and 80%, respectively, while the gas volume fraction is changed as Table 2 shows.

As can be seen from Figure 6, with the increase of gas volume fraction, the gas-liquid separation region is getting smaller. Moreover, the separation process will be accelerated if there is large gas volume fraction gradient along the vertical direction.

Figure 7 indicates that gas volume fraction at gas outlet and liquid volume fraction at liquid outlet can remain above 97% and 96%, and they will increase with the gas volume fraction. This can demonstrate that spiral-flow separator is more suitable for the separation of mixture with large gas-oil ratio.

**3.4. Impact of Water Content.** PetroChina Huabei Oilfield is in the high water cut stage, while water flooding is adopted, making the water fraction high among well fluids. The variation of water will have an impact on the viscosity and density of well fluids mixture, thus affecting the flow condition in the metering separator, further influencing the separation efficiency. In this part, the flow rate is set to 20 m<sup>3</sup>/h and gas volume fraction is 50%, with the water content varying as Table 3 shows.

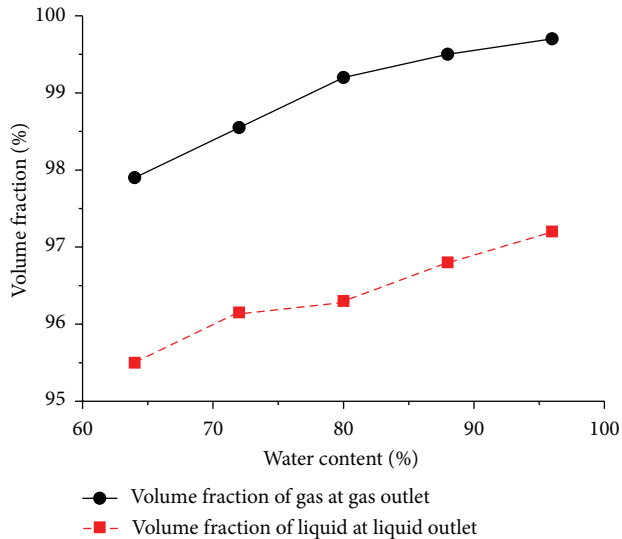


FIGURE 9: Impact of water content on the separation efficiency.

It can be easily seen from Figure 8, with the increasing water content, in the gas-liquid separation region, that gas volume fraction gradient along the vertical direction becomes larger, indicating better separation effect.

The impact of water content on the separation efficiency is shown in Figure 9. With the gas volume fraction at gas outlet and the liquid volume fraction at liquid outlet remaining above 97% and 95%, the separation efficiency would increase with higher water content. The reason for this phenomenon is that increasing water content leads to the decrease of mixture viscosity, which is beneficial to the flow of mixture in the separator. Besides, larger water content gives smaller ratio of crude oil, making it easier for natural gas to separate.

#### 4. Conclusions

Based on the previous results and analyses, it is reasonable to conclude that

- (1) confined to the production flow rate range of oilfield, the efficiency of metering separator would increase with the augmentation of well fluids flow rate;
- (2) spiral-flow diverter is propitious to large gas-oil ratio mixture, and large gas volume fraction would contribute to the separation efficiency;
- (3) the increasing water content would significantly reduce the viscosity of mixture, so as to promote the separation, and meanwhile, the natural gas could be easier to separate since the oil ratio decreased.

After the analyses of factors such as varying flow rate, gas fraction, and water content to the separation efficiency, the gas volume fraction at gas outlet and the liquid volume fraction at liquid outlet can remain above 97% and 95%, respectively, providing clear evidence of the feasibility of this kind of three-phase separate measurement system at PetroChina Huabei Oilfield.

#### Acknowledgment

The study is supported by the National Science Foundation of China (no. 51276198).

#### References

- [1] L. Zhang, Z. Yang, J. Liang, and Y. Cai, "Spatial variation and distribution of urban energy consumptions from cities in China," *Energies*, vol. 4, no. 1, pp. 26–38, 2011.
- [2] Q. Zhai, H. Cao, X. Zhao, and C. Yuan, "Cost benefit analysis of using clean energy supplies to reduce greenhouse gas emissions of global automotive manufacturing," *Energies*, vol. 4, no. 10, pp. 1478–1494, 2011.
- [3] X. Dong, Y. Zhang, W. Cui et al., "Energy-based adjustment of the agricultural structure in a low-carbon economy in Manas County of China," *Energies*, vol. 4, no. 9, pp. 1428–1442, 2011.
- [4] Q. Yang, J. Feng, H. B. Luo et al., "CFD simulation of the inner flow field of the gas-liquid gravity separator," *Mechanical Research & Application*, vol. 20, no. 2, pp. 72–74, 2007.
- [5] H. B. Luo, J. Feng, Q. Yang et al., "CFD simulation of the inner flow field of the gas-liquid measure cyclones," *Mechanical Engineer*, vol. 1, pp. 74–76, 2007.
- [6] H. Zhou and N. Xia, "Numerical simulation on the gas-liquid flows inside the oil-gas Separators," *Chinese Journal of Computational Mechanics*, vol. 23, no. 6, pp. 766–771, 2006.
- [7] H. Du, "Research and application of the measurement technology about the three-phase fluid about oil well," *Fault-Block Oil & Gas Field*, vol. 12, no. 4, pp. 54–55, 2005.
- [8] M. Y. Pan, Y. J. Geng, B. H. Huang et al., "Application of XDY oil-gas-water three-phase metering unit," *Oil-Gasfield Surface Engineering*, vol. 26, no. 11, pp. 38–39, 2007.
- [9] H. Pang, Y. J. Wang, B. H. Huang et al., "YJ oil-gas-water three-phase metering unit," *Oil-Gasfield Surface Engineering*, vol. 28, no. 5, pp. 91–92, 2009.
- [10] X. J. Qu and C. J. Ma, "Design of a skid-mounted three-phase separating and metering unit," *Automation in Petro-Chemical Industry*, vol. 2, pp. 58–60, 2009.

## Research Article

# Mixed Platoon Flow Dispersion Model Based on Speed-Truncated Gaussian Mixture Distribution

Weitiao Wu, Wenzhou Jin, and Luou Shen

*School of Civil and Transportation Engineering, South China University of Technology, Guangzhou 510641, China*

Correspondence should be addressed to Luou Shen; [ctwshen@163.com](mailto:ctwshen@163.com)

Received 13 March 2013; Revised 11 May 2013; Accepted 11 May 2013

Academic Editor: Shuyu Sun

Copyright © 2013 Weitiao Wu et al. This is an open access article distributed under the Creative Commons Attribution License, which permits unrestricted use, distribution, and reproduction in any medium, provided the original work is properly cited.

A mixed traffic flow feature is presented on urban arterials in China due to a large amount of buses. Based on field data, a macroscopic mixed platoon flow dispersion model (MPFDM) was proposed to simulate the platoon dispersion process along the road section between two adjacent intersections from the flow view. More close to field observation, truncated Gaussian mixture distribution was adopted as the speed density distribution for mixed platoon. Expectation maximum (EM) algorithm was used for parameters estimation. The relationship between the arriving flow distribution at downstream intersection and the departing flow distribution at upstream intersection was investigated using the proposed model. Comparison analysis using virtual flow data was performed between the Robertson model and the MPFDM. The results confirmed the validity of the proposed model.

## 1. Introduction

Traffic flow in urban areas presents interrupted flow features. Due to the compression and splitting by signal lights, traffic flow is separated into series and moves downstream in platoons. Vehicles in platoon travel at different speeds because of the diverse behaviors of drivers and maneuvering characteristics of vehicles. While moving downstream, the platoon starts spreading in a longer segment which is called platoon dispersion. Platoon dispersion modeling is one of the key aspects in intelligent transportation system (ITS) area, which provides theoretical support for signal coordination control.

Many researchers have worked on the platoon dispersion topic. Pacey [1] first studied the diffusion problem and proposed a model assuming that the speed follows normal distribution ranging from negative to positive infinity. Grace and Potts [2] further investigated Pacey's model from the density view. Robertson [3], using data collected by Hillier and Rothery [4], developed a recurrent dispersion model that is widely used in signal coordination optimization and control systems such as TRANSYT [5], SCOOT [6], SATURN [7], and TRAFLO [8]. Seddon [9] found that Robertson's model

was based on travel time shifted geometric distribution. Tracz [10] and Polus [11] have shown that vehicular travel time distribution is not necessarily a shifted geometric distribution as in Robertson's model and is more consistent with a normal, lognormal or a gamma distribution. Liu and Yang [12–14] studied Grace's model using field data collected in Shanghai, China, proposed a method to correct the vehicle startup time loss, and analyzed the problem of the front and rear of the platoon. Wang et al. [15, 16] developed a platoon dispersion model under the assumption that the travel time follows normal distribution and found it to be a better-fitted field data than Pacey's assumption. Wei et al. [17] proposed a platoon dispersion model for cars from the density view assuming speed following truncated normal distribution.

Robertson's model in TRANSYT implies dispersion by the platoon dispersion factor for three external friction levels. Manar and Baass [18] demonstrate that platoon dispersion depends not only on external friction but also on internal friction measured by volume and density and developed mathematical models relating platoon dispersion to internal and external frictions. G. C. K. Wong and S. C. Wong [19] developed a multiclass traffic flow model as an extension of the LWR model, which considered the heterogeneous

drivers. Bonneson et al. [20] developed a procedure for prediction of the arrival flow profile for an intersection approach considering platoon decay due to mid-segment driveway access and egress, which tends to have a significant impact on the arrival flow profile. In a recent study, Cheng [21] found that the traffic flow on China urban roads presents a characteristic of mixed vehicle speed distributions. Chen et al. [22] analyzed the bus-car mixed traffic, and results show that the bus ration has significant impact on the speed distribution.

The literature review shows that researchers have doubted the distribution assumptions of both Pacey's and Robertson's models. However, due to the simplicity of Robertson's recurrent equation, it has received the most popularity. Meanwhile, very few studies tried to develop a new dispersion model. Recent researches present a trend investigating the impact of heterogeneity, mixed flow, and internal frictions on platoon dispersion.

The traffic on urban arterials in China presents a mixed flow feature due to the large amount of buses. Typically, buses run on three types of facilities: normal lanes with mixed traffic, dedicated bus lanes, and bus rapid traffic (BRT) lanes.

Dedicated bus lanes and BRT lanes are special lanes separated from other traffic by road markings or physical barriers, which present unique operational features. However, urban arterials in China mostly belong to the first class, which present mixed traffic flow.

Generally, the percentage of buses in mixed traffic flow varies from 10% to 25% during peak periods. Mixed platoon presents special characteristics compared to car platoon because of the lesser maneuverability of buses and the running speed constrained by scheduled stops. Previous research has not been done on bus platoon dispersion modeling, and no car and bus mixed platoon dispersion model has been developed either. The investigation of the mixed platoon dispersion problem will provide theoretical support for signal coordination and bus priority control.

## 2. Model Development

**2.1. Speed Density Distribution Assumption.** In Pacey's platoon dispersion model, the speed is assumed following normal distribution ranging from negative to positive infinity, which does not properly reflect the field situation. Because vehicles with speeds  $v < v_{\min}$  and  $v > v_{\max}$  ( $v_{\min}$  and  $v_{\max}$  denote minimum speed and maximum speed, resp.) are rarely observed in the actual world, which is confirmed by field data as shown in the data acquisition and analysis section given below, therefore, the assumed speed following truncated distribution ranging from  $v_{\min}$  to  $v_{\max}$  is more suitable. The distribution can be truncated normal distribution or other. In this study, due to the fact that the field data fits the truncated Gaussian mixture distribution (TGMD) better and its widely use with simple mathematic form, the TGMD is chosen to demonstrate the development of the mixed platoon dispersion model based on speed-truncated distribution.

By modifying Pacey's speed normal distribution, the proposed TGMD is shown in the following equation:

$$f(v) = \begin{cases} \sum_{j=1}^M \alpha_j p_j(v | \mu_j, \sigma_j) = c \sum_{j=1}^M \alpha_j \frac{1}{\sqrt{2\pi}\sigma_j} e^{-0.5((v-\mu_j)/\sigma_j)^2}, & v_{\min} \leq v \leq v_{\max}, \sum_{j=1}^M \alpha_j = 1, \\ 0, & \text{others,} \end{cases} \quad (1)$$

where,  $\alpha_j$ ,  $\mu_j$ , and  $\sigma_j$ ,  $j = 1, 2, \dots, M$ , are the parameters of Gaussian mixture distribution, which can be estimated by EM algorithm [23, 24],  $M$  is the number of mixed component, and  $c$  is a parameter ensuring that the accumulated probability of  $f(v)$  in range  $[v_{\min}, v_{\max}]$  equals 100%. As for  $v_{\min} \leq v \leq v_{\max}$ , because  $\int_{v_{\min}}^{v_{\max}} f(v) dv = 1$ , then  $c^{-1} = \sum_{j=1}^M \alpha_j [\Phi(v_{\max}/\sigma_j - \mu_j/\sigma_j) - \Phi(v_{\min}/\sigma_j - \mu_j/\sigma_j)]$ , where  $\Phi$  denotes the cumulative function of the standard normal distribution.

**2.2. Platoon Flow Dispersion Model.** Assuming the start time of the green phase of upstream signal  $t = 0$  and the stop bar location  $x = 0$ , then, the departing flow function when the upstream intersection signal turns to green is  $q'(x = 0, t)$ . For signal coordination control, the arriving flow distribution downstream is used to calculate parameters such as delay, stop, and queue length based on shock wave theory. Therefore, it is important to develop a model to predict the arriving flow function from the upstream departing flow function. The following section presents the model development process.

During time differential  $[T, T + dT]$ , the departing vehicles from the upstream intersection stop line are  $q'(x = 0, T)dT$ ; following speed-truncated distribution assumption, the vehicle flow  $q'(x = 0, T = t - x/v)f(v)dv$  leaving at time  $t - x/v$  from the upstream intersection stop line will arrive at the downstream intersection  $x$  ( $x > 0$ ) at time  $t$ , which is  $q'(x = 0, T)f(v)dv dT$ . Therefore, the number of vehicles arriving at downstream intersection during time differential  $[t, t + dt]$  can be expressed using the following integration equation:

$$q(x, t) dt = \int_{T_1=t-x/v_1}^{T_2=t-x/v_2} f(v) q'(x = 0, T = t - \frac{x}{v}) dv dT. \quad (2)$$

Then, after dividing by the time differential in both sides of (2), the arriving flow rate at downstream intersection becomes

$$q(x, t) = \int_{v_1}^{v_2} f(v) q(x = 0, T = t - \frac{x}{v}) dv, \quad (3)$$

where  $v_1$  and  $v_2$  represent the minimum and maximum speeds for those vehicles arriving at downstream location  $x$  at time  $t$ .

Without loss of generality, there are three typical departing flow patterns in the actual world: stable linear flow,

decreasing linear flow, and stable combined with decreasing linear flow as demonstrated in Figure 1. The following section will develop the arriving flow function at the downstream intersection based on speed TGMD assumption.

**2.2.1. Stable Linear Flow Pattern.** The departing flow function of the stable linear flow pattern at the upstream intersection stop line  $x = 0$  is  $q'(x = 0, T)$ , which can be expressed in the following equation:

$$q'(x = 0, T) = \begin{cases} q, & 0 < T \leq g \\ 0, & T > g, \end{cases} \quad (4)$$

where  $g$  is the duration of the green phase and  $q$  is the departing saturation flow rate.

Then, the arriving flow function at downstream intersection location  $x$  at time  $t$  can be expressed as the following piecewise function:

(a) when  $x/v_{\min} \leq x/v_{\max} + g$ ,

$$q(x, t) = \begin{cases} 0, & t < \frac{x}{v_{\max}} \cup t > \frac{x}{v_{\min}} + g \\ q \int_{x/t}^{v_{\max}} f(v) dv, & \frac{x}{v_{\max}} \leq t < \frac{x}{v_{\min}} \\ q \int_{x/t}^{v_{\max}} (v) dv, & \frac{x}{v_{\min}} \leq t \leq \frac{x}{v_{\max}} + g \\ q \int_{v_{\min}}^{x/(t-g)} f(v) dv, & \frac{x}{v_{\max}} + g < t \leq \frac{x}{v_{\min}} + g, \end{cases} \quad (5)$$

(b) when  $x/v_{\min} > x/v_{\max} + g$ ,

$$q(x, t) = \begin{cases} 0, & t < \frac{x}{v_{\max}} \cup t > \frac{x}{v_{\min}} + g \\ q \int_{x/t}^{v_{\max}} f(v) dv, & \frac{x}{v_{\max}} \leq t < \frac{x}{v_{\max}} + g \\ q \int_{x/t}^{x/(t-g)} f(v) dv, & \frac{x}{v_{\max}} + g \leq t \leq \frac{x}{v_{\min}} \\ q \int_{v_{\min}}^{x/(t-g)} f(v) dv, & \frac{x}{v_{\min}} < t \leq \frac{x}{v_{\min}} + g. \end{cases} \quad (6)$$

Let  $u = (v - \mu)/\sigma$  and the dispersion rate  $\alpha = \sigma/\mu$ , because

$$\begin{aligned} & \int_{v_1}^{v_2} f(v) dv \\ &= c \sum_{j=1}^M \alpha_j \int_{v_1}^{v_2} \frac{1}{\sqrt{2\pi}\sigma_j} e^{-0.5((v-\mu_j)/\sigma_j)^2} dv \\ &= c \sum_{j=1}^M \alpha_j \int_{(v_1-\mu_j)/\sigma_j}^{(v_2-\mu_j)/\sigma_j} \frac{1}{\sqrt{2\pi}} e^{-0.5u^2} du \\ &= c \sum_{j=1}^M \alpha_j \int_{(tv_1/\mu_j-t)/\alpha_j t}^{(tv_2/\mu_j-t)/\alpha_j t} \frac{1}{\sqrt{2\pi}} e^{-0.5u^2} du, \end{aligned}$$

$$\begin{aligned} &= \frac{c}{2} \sum_{j=1}^M \alpha_j \left( 2 \int_0^{(tv_2/\mu_j-t)/\sqrt{2}\alpha_j t} \frac{1}{\sqrt{2\pi}} e^{-0.5u^2} du \right. \\ &\quad \left. - 2 \int_0^{(tv_1/\mu_j-t)/\sqrt{2}\alpha_j t} \frac{1}{\sqrt{2\pi}} e^{-0.5u^2} du \right) \\ &= \frac{c}{2} \sum_{j=1}^M \alpha_j [\Phi(z)]_{z_{j,1}}^{z_{j,2}}, \end{aligned} \quad (7)$$

where  $z_{j,2} = (tv_2/\mu_j - t)/\sqrt{2}\alpha_j t$ ,  $z_{j,1} = (tv_1/\mu_j - t)/\sqrt{2}\alpha_j t$ , and  $v_1$  and  $v_2$  are constants, because  $\Phi(z) = 2 \int_0^{\sqrt{2}z} (1/\sqrt{2\pi}) e^{-0.5u^2} du = (2/\sqrt{\pi}) \int_0^z e^{-u^2} du$  is the accumulated probability function of standard normal distribution. Based on (5), (6), and (7),  $q(x, t)$  can be calculated using the following formula:

(a) when  $x/v_{\min} \leq x/v_{\max} + g$ ,

$$q(x, t) = \begin{cases} 0, & t > \frac{x}{v_{\max}} \cup t < \frac{x}{v_{\min}} + g \\ \frac{cq}{2} \sum_{j=1}^M \alpha_j [\Phi(z)]_{(x/\mu_j-t)/\sqrt{2}\alpha_j t}^{(tv_{\max}/\mu_j-t)/\sqrt{2}\alpha_j t}, & \frac{x}{v_{\max}} \leq t < \frac{x}{v_{\min}} \\ \frac{cq}{2} \sum_{j=1}^M \alpha_j [\Phi(z)]_{(tv_{\min}/\mu_j-t)/\sqrt{2}\alpha_j t}^{(tv_{\max}/\mu_j-t)/\sqrt{2}\alpha_j t}, & \frac{x}{v_{\min}} \leq t \leq \frac{x}{v_{\max}} + g \\ \frac{cq}{2} \sum_{j=1}^M \alpha_j [\Phi(z)]_{(tx/\mu_j(t-g)-t)/\sqrt{2}\alpha_j t}^{(tx/\mu_j(t-g)-t)/\sqrt{2}\alpha_j t}, & \frac{x}{v_{\max}} + g < t \leq \frac{x}{v_{\min}} + g, \end{cases} \quad (8)$$

(b) when  $x/v_{\min} > x/v_{\max} + g$ ,

$$q(x, t) = \begin{cases} 0, & t > \frac{x}{v_{\max}} \cup t < \frac{x}{v_{\min}} + g \\ \frac{cq}{2} \sum_{j=1}^M \alpha_j [\Phi(z)]_{(x/\mu_j-t)/\sqrt{2}\alpha_j t}^{(tv_{\max}/\mu_j-t)/\sqrt{2}\alpha_j t}, & \frac{x}{v_{\max}} \leq t < \frac{x}{v_{\max}} + g \\ \frac{cq}{2} \sum_{j=1}^M \alpha_j [\Phi(z)]_{(x/\mu_j-t)/\sqrt{2}\alpha_j t}^{(tx/\mu_j(t-g)-t)/\sqrt{2}\alpha_j t}, & \frac{x}{v_{\max}} + g \leq t \leq \frac{x}{v_{\min}} \\ \frac{cq}{2} \sum_{j=1}^M \alpha_j [\Phi(z)]_{(tv_{\min}/\mu_j-t)/\sqrt{2}\alpha_j t}^{(tx/\mu_j(t-g)-t)/\sqrt{2}\alpha_j t}, & \frac{x}{v_{\min}} < t \leq \frac{x}{v_{\min}} + g. \end{cases} \quad (9)$$

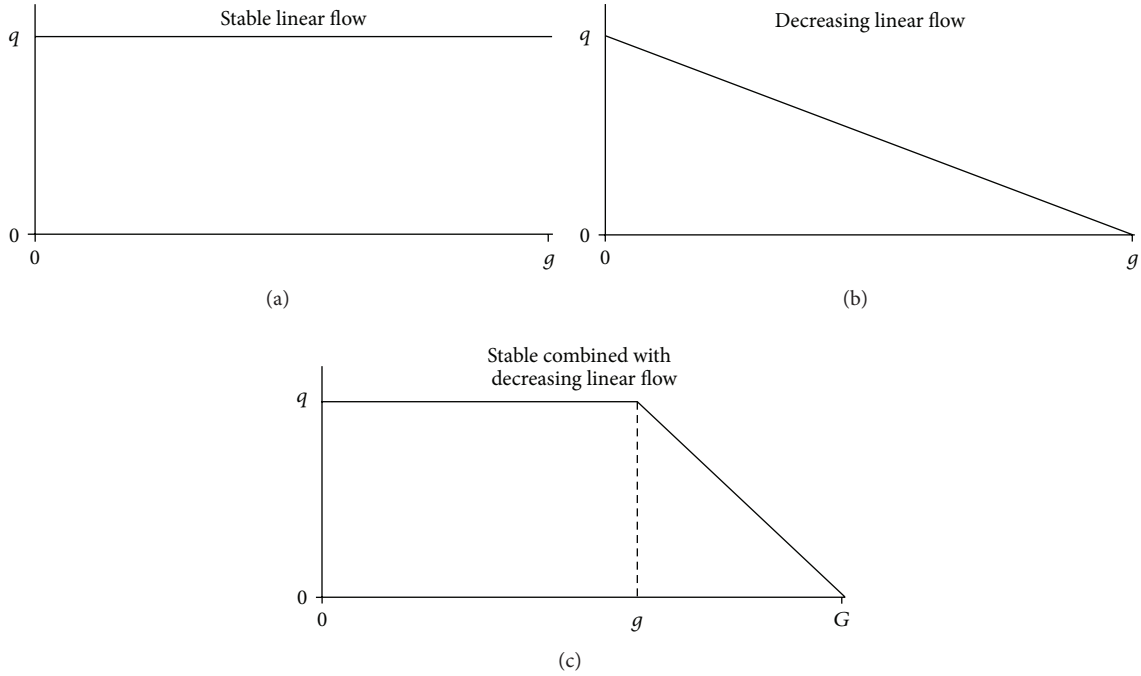


FIGURE 1: Three typical departing flow patterns.

2.2.2. *Decreasing Linear Flow Pattern.* The departing flow function of the decreasing linear flow pattern at the upstream intersection stop line  $x = 0$  during the green phase is  $q'(x = 0, T)$  as expressed in the following equation:

$$q'(x = 0, T) = \begin{cases} q - aT, & 0 < T \leq g \\ 0, & T > g, \end{cases} \quad (10)$$

where  $a = q/g$  is the linear decreasing rate.

Following the method for stable linear flow pattern, the arriving flow function at the downstream intersection location  $x$  at time  $t$  can be expressed as the following piecewise function:

(a) when  $x/v_{\min} \leq x/v_{\max} + g$ ,

$$q(x, t) = \begin{cases} 0, & t < \frac{x}{v_{\max}} \cup t > \frac{x}{v_{\min}} + g \\ (q - at) \int_{x/t}^{v_{\max}} f(v) dv - ax \int_{x/t}^{v_{\max}} \frac{f(v)}{v} dv, & \frac{x}{v_{\max}} \leq t < \frac{x}{v_{\min}} \\ (q - at) \int_{v_{\min}}^{v_{\max}} f(v) dv - ax \int_{v_{\min}}^{v_{\max}} \frac{f(v)}{v} dv, & \frac{x}{v_{\min}} \leq t \leq \frac{x}{v_{\max}} + g \\ (q - at) \int_{v_{\min}}^{x/(t-g)} f(v) dv - ax \int_{v_{\min}}^{x/(t-g)} \frac{f(v)}{v} dv, & \frac{x}{v_{\max}} + g < t \leq \frac{x}{v_{\min}} + g, \end{cases} \quad (11)$$

(b) when  $x/v_{\min} > x/v_{\max} + g$ ,

$$q(x, t) = \begin{cases} 0, & t > \frac{x}{v_{\max}} \cup t < \frac{x}{v_{\min}} + g \\ (q - at) \int_{x/t}^{v_{\max}} f(v) dv - ax \int_{x/t}^{v_{\max}} \frac{f(v)}{v} dv, & \frac{x}{v_{\max}} \leq t < \frac{x}{v_{\min}} + g \\ (q - at) \int_{x/t}^{x/(t-g)} f(v) dv - ax \int_{x/t}^{x/(t-g)} \frac{f(v)}{v} dv, & \frac{x}{v_{\max}} + g \leq t \leq \frac{x}{v_{\min}} \\ (q - at) \int_{v_{\min}}^{x/(t-g)} f(v) dv - ax \int_{v_{\min}}^{x/(t-g)} \frac{f(v)}{v} dv, & \frac{x}{v_{\min}} < t \leq \frac{x}{v_{\min}} + g. \end{cases} \quad (12)$$

Bases on (11), (12), and (7), the flow function  $q(x, t)$  can be revised as follows:

(a) when  $x/v_{\min} \leq x/v_{\max} + g$ ,

$$q(x, t) = \begin{cases} 0, & t > \frac{x}{v_{\max}} \cup t < \frac{x}{v_{\min}} + g \\ \frac{c(q-at)}{2} \sum_{j=1}^M \alpha_j [\Phi(z)]_{\frac{(x/\mu_j - t)/\sqrt{2}\alpha_j t}{(tv_{\max}/\mu_j - t)/\sqrt{2}\alpha_j t}}^{(tv_{\max}/\mu_j - t)/\sqrt{2}\alpha_j t} \\ -ax \int_{x/t}^{v_{\max}} \frac{f(v)}{v} dv, & \frac{x}{v_{\max}} \leq t < \frac{x}{v_{\min}} \\ \frac{c(q-at)}{2} \sum_{j=1}^M \alpha_j [\Phi(z)]_{\frac{(x/\mu_j - t)/\sqrt{2}\alpha_j t}{(tx/\mu_j(t-g) - t)/\sqrt{2}\alpha_j t}}^{(tx/\mu_j(t-g) - t)/\sqrt{2}\alpha_j t} \\ -ax \int_{x/t}^{x/(t-g)} \frac{f(v)}{v} dv, & \frac{x}{v_{\min}} \leq t \leq \frac{x}{v_{\max}} + g \\ \frac{c(q-at)}{2} \sum_{j=1}^M \alpha_j [\Phi(z)]_{\frac{(x/\mu_j - t)/\sqrt{2}\alpha_j t}{(tv_{\min}/\mu_j - t)/\sqrt{2}\alpha_j t}}^{(tx/\mu_j(t-g) - t)/\sqrt{2}\alpha_j t} \\ -ax \int_{v_{\min}}^{x/(t-g)} \frac{f(v)}{v} dv, & \frac{x}{v_{\max}} + g < t \leq \frac{x}{v_{\min}} + g, \end{cases} \quad (13)$$

(b) when  $x/v_{\min} > x/v_{\max} + g$ ,

$$q(x, t) = \begin{cases} 0, & t > \frac{x}{v_{\max}} \cup t < \frac{x}{v_{\min}} + g \\ \frac{c(q-at)}{2} \sum_{j=1}^M \alpha_j [\Phi(z)]_{\frac{(x/\mu_j - t)/\sqrt{2}\alpha_j t}{(tv_{\max}/\mu_j - t)/\sqrt{2}\alpha_j t}}^{(tv_{\max}/\mu_j - t)/\sqrt{2}\alpha_j t} \\ -ax \int_{x/t}^{v_{\max}} \frac{f(v)}{v} dv, & \frac{x}{v_{\max}} \leq t < \frac{x}{v_{\max}} + g \\ \frac{c(q-at)}{2} \sum_{j=1}^M \alpha_j [\Phi(z)]_{\frac{(x/\mu_j - t)/\sqrt{2}\alpha_j t}{(tx/\mu_j(t-g) - t)/\sqrt{2}\alpha_j t}}^{(tx/\mu_j(t-g) - t)/\sqrt{2}\alpha_j t} \\ -ax \int_{x/t}^{x/(t-g)} \frac{f(v)}{v} dv, & \frac{x}{v_{\max}} + g \leq t \leq \frac{x}{v_{\min}} \\ \frac{c(q-at)}{2} \sum_{j=1}^M \alpha_j [\Phi(z)]_{\frac{(x/\mu_j - t)/\sqrt{2}\alpha_j t}{(tv_{\min}/\mu_j - t)/\sqrt{2}\alpha_j t}}^{(tx/\mu_j(t-g) - t)/\sqrt{2}\alpha_j t} \\ -ax \int_{v_{\min}}^{x/(t-g)} \frac{f(v)}{v} dv, & \frac{x}{v_{\min}} < t \leq \frac{x}{v_{\min}} + g. \end{cases} \quad (14)$$

The first item in (13) and (14) can be calculated using the accumulated probability function of standard normal distribution; the second item cannot be computed by integration. Therefore, let  $u = (v - \mu)/\sigma$ , and the natural exponential

function can be expanded applying the Taylor series as shown in the following:

$$\begin{aligned} & \int_{v_1}^{v_2} \frac{f(v)}{v} dv \\ &= c \sum_{j=1}^M \alpha_j \int_{(v_1 - \mu_j)/\sigma_j}^{(v_2 - \mu_j)/\sigma_j} \frac{1}{\sqrt{2\pi}(u\sigma_j + \mu_j)} e^{-0.5u^2} du \\ &= c \sum_{j=1}^M \alpha_j \int_{(v_1 - \mu_j)/\sigma_j}^{(v_2 - \mu_j)/\sigma_j} \frac{1}{\sqrt{2\pi}(u\sigma_j + \mu_j)} \\ & \quad \times \left( 1 - \frac{u^2}{2} + \frac{u^4}{8} \cdots + (-1)^n \frac{u^{2n}}{n!2^n} \right) du. \end{aligned} \quad (15)$$

The expanded Taylor series can be computed by integration. As the Taylor series method is an approximation method, for application requiring high computation accuracy the numerical integration method is needed which can be easily obtained with the help of a modern computer.

**2.2.3. Stable Combined with Decreasing Linear Flow Pattern.** The departing flow function of the stable combined with decreasing linear flow pattern at the upstream intersection stop line  $x = 0$  during the green phase is  $q'(x = 0, T)$  as expressed in the following equation:

$$q'(x = 0, T) = \begin{cases} q, & 0 < T \leq g \\ q - a(T - g), & g < T \leq G, \end{cases} \quad (16)$$

where  $a = q/(G - g)$  is the linear decreasing rate.

Because different classes of flows are addable, the arriving flow function at downstream intersection for the stable combined with decreasing linear flow pattern can be expressed by adding the arriving flow of the stable linear flow pattern with the arriving flow of the decreasing linear flow pattern by shifting time  $g$ . The details of the calculation formula are not presented here.

The proposed MPFDM is developed as given in the previous section. If  $x$  is set as the downstream signal locations, the platoon dispersion process between the two signals can be quantitatively analyzed using the model. The results can be used to calculate signal timing parameters such as delay, stop, and queue length for signal coordination and bus priority control.

### 3. Data Acquisition and Analysis

Field data were collected for model development and validation. The surveyed road is a typical four-lane two-way urban arterial, Wushan Road, which normally operates at undersaturation traffic condition. Along this road, there are 14 bus lines, and the posted speed limit is 50 km/h (13.89 m/s). License plates were recorded by video cameras at two locations (650 m distance): one is right after the signals at Yuehan Road and the other is located right before the diverging points. Travel times were directly computed from video records, and the original speeds (journey speeds for

TABLE 1: Origin platoon journey speed data.

	Period 1 (7:45–8:25 am)			Period 2 (8:25–10:00 am)			Period 3 (10:00–10:40 am)		
	Car	Bus	Mixed	Car	Bus	Mixed	Car	Bus	Mixed
Length (m)		650			650			650	
Flow rate (veh/h)		1007			881			648	
Bus traffic (%)		13.1			10.8			11.8	
Sample size	617	88	705	1244	151	1395	410	51	461
Minimum speed (m/s)	8.67	5.65	5.65	7.74	5.37	5.37	7.22	6.13	6.13
Maximum speed (m/s)	20.97	14.44	20.97	21.67	12.50	21.67	20.96	13.27	20.96
Average speed (m/s)	13.52	7.80	12.85	13.62	8.14	13.23	13.97	8.10	13.31
Standard deviation	1.99	1.79	2.64	1.90	1.34	2.56	1.85	1.61	2.44

TABLE 2: Estimated parameter values of Gaussian mixture distribution based on EM algorithm.

	1st component			2nd component			Iteration times
	$\alpha_1$	$\mu_1$	$\sigma_1$	$\alpha_2$	$\mu_2$	$\sigma_2$	
Period 1	0.8290	13.6642	3.2344	0.1710	8.9297	4.0870	3
Period 2	0.9065	13.5757	4.1019	0.0935	7.6659	0.8087	22
Period 3	0.9004	13.9452	3.6320	0.0996	7.5916	0.4910	7

buses, running speed for cars) were derived from travel time and distance. The data was collected from 7:45 AM to 10:40 AM. Three time periods were apparently identified based on different traffic volume levels. A statistics summary of the original car and mixed platoon speed data for all time periods is presented in Table 1.

As shown in Table 1, the average speeds of the car platoon are slightly higher than those of mixed platoon for all time periods; the standard deviations of car platoon are lower than those of mixed platoon; the minimum speeds of car platoon are greater than those of mixed platoon; the maximum speeds of car platoon are the same as those of mixed platoon. All these are reasonable because buses have lower speed compared to cars presented in the mixed platoon.

The plots of the speed histogram and the fitted Gaussian mixture distribution curves are shown in Figure 2. From the plots, two humps were obviously identified from the speed data histogram of the mixed platoon, which represent car and bus groups, respectively. This confirmed the results of Cheng [21] and Chen et al. [22]. For this reason, some researchers [25, 26] have proposed to use compound distributions that use an appropriate combination of more than one distribution as a modeling tool, since the fitting of corresponding distributions is usually regarded as the “dissection” of a heterogeneous population into more homogeneous “parts.” Due to the fact that Gaussian mixture distribution can approximate any continuous distribution and its widely use with simple mathematic form composed of several weighted normal distributions, Gaussian mixture distribution is used in this paper. Let the number of mixed component  $M = 2$ , based on MATLAB software, and parameters for all time periods were obtained using EM algorithm as listed in Table 2. Because EM algorithm is widely known, its details are not presented here in order to keep conciseness.

Furthermore, performances of different distributions (including normal, lognormal, Weibull, and gamma) fitting for the mixed platoon speed data present K-S evaluation  $P$  values  $< 0.01$  with 0.05 of significance level due to different speed distribution characteristics of cars and buses in the mixed platoon. Nevertheless, Gaussian mixture distribution is the one with K-S evaluation  $P$  values  $> 0.15$  for all time periods. Because the speed of Gaussian mixture distribution spreads within a limited value range between minimum speed and maximum speed, we can accept the assumption that speed follows truncated Gaussian mixture distribution, which is composed of several components of truncated normal distribution with the same range limit [25, 26].

What is worth mentioning is that  $M$  is usually determined using the histogram observation method, whose detailed steps are to draw the envelope of sample data histogram and observe the number of curve peaks  $F$ , generally required  $F \leq M < 2F$ .

#### 4. Platoon Flow Dispersion Analysis

Because the MPFDM demonstrated here assumes the speed following TGMD, the parameters used in the model need to be transferred from the Gaussian mixture distribution. The TGMD statistics of the vehicle speed data and the parameters estimated by EM algorithm of period 1 are summarized in Table 3, which is used in this section to demonstrate the application of MPFDM in signal coordination analysis.

*4.1. Departing Flow Function at Upstream Intersection.* To compare the performance of the proposed model with the Robertson model, virtual departing flow distributions for mixed platoon from upstream intersection are assumed for

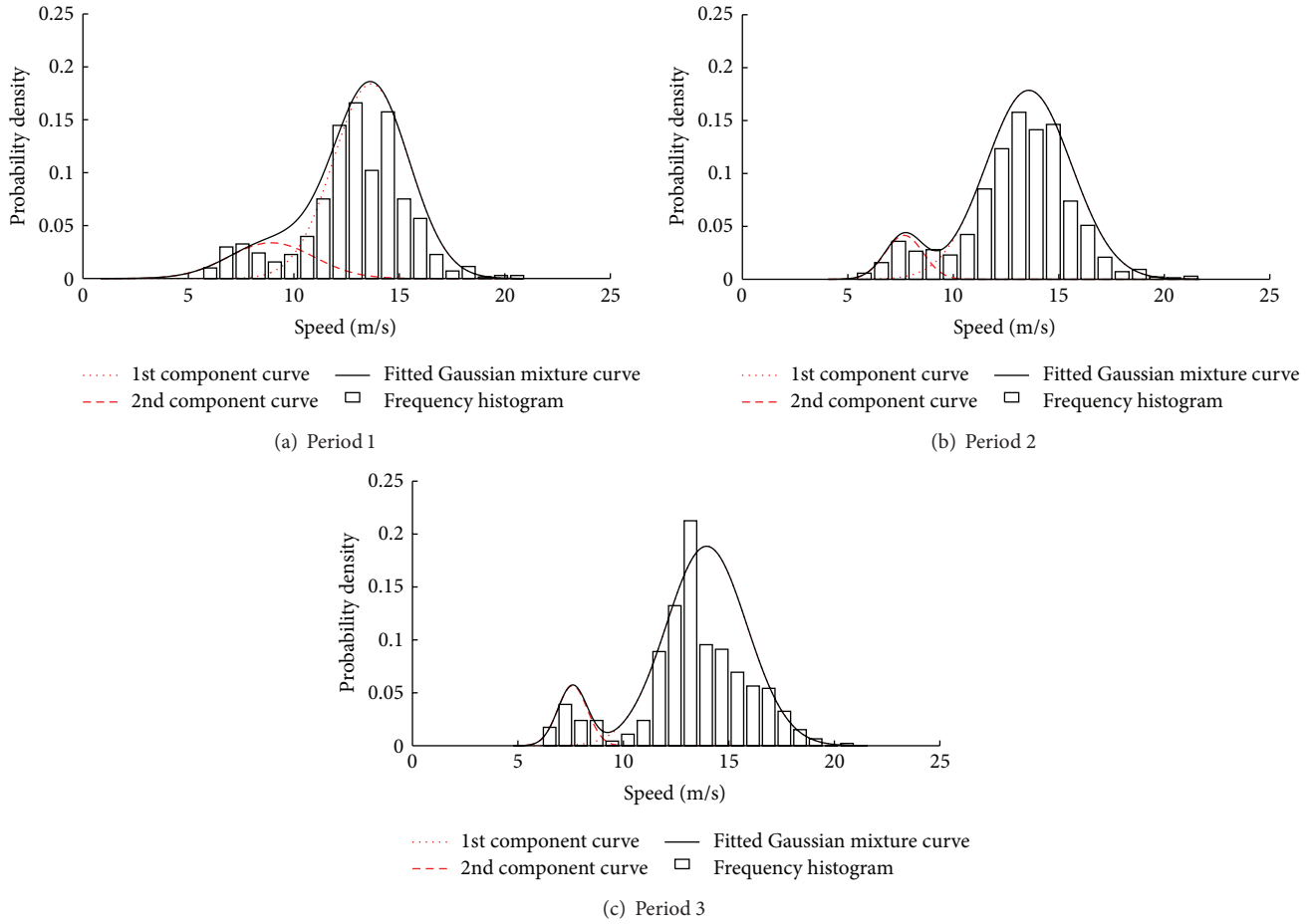


FIGURE 2: Speed distribution histogram and fitted Gaussian mixture distribution curve of the study segment.

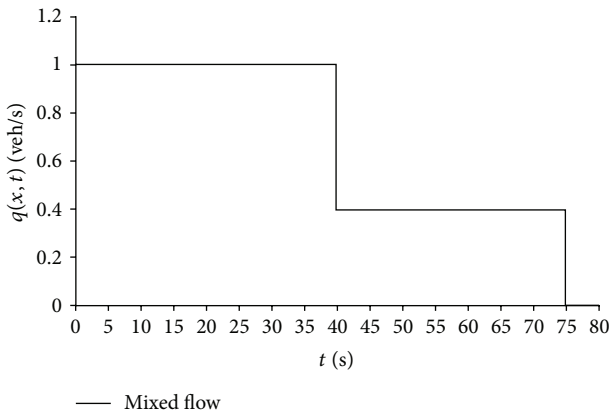


FIGURE 3: Departing flow distribution at upstream intersection.

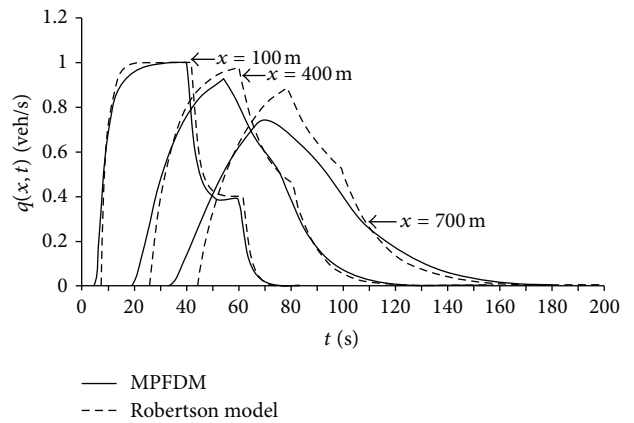


FIGURE 4: Comparison of arriving flow distribution between the proposed model and the Robertson model.

numeric analysis and are shown in Figure 3. The mixed flow is the sum of car and bus flows.

4.2. Arriving Flow Distribution at Downstream Intersection. The virtual downstream intersections are assumed at  $x_d = 100, 400, 700$  (m). The arriving flow distribution function  $q(x = x_d, t)$  is analyzed for mixed platoon. Because

the Robertson model is widely known, its details are not presented here.

The arriving flow distribution at downstream locations at  $x_d = 100, 400, 700$  (m) for mixed platoon using different modeling methods is presented in Figure 4.

Based on Figure 4, the following can be concluded regarding the model performance.

TABLE 3: Statistics of TGMD of Time Period 1.

	Symbol	Mixed platoon
TGMD coefficient	$c$	1.055
Minimum speed (m/s)	$v_{\min}$	5.65
Maximum speed (m/s)	$v_{\max}$	20.97
Parameters of Gaussian mixture distribution	$\alpha_1$	0.8290
	$\alpha_2$	0.1710
	$\mu_1$	13.6642
	$\mu_2$	8.9297
	$\sigma_1$	3.2344
	$\sigma_2$	4.0870

- (a) According to MPFDM, during time period  $\forall t \notin [x_d/v_{\max}, x_d/v_{\min} + g]$ , the flow rate  $q(x_d, t) = 0$ ; when  $x/v_{\min} \leq x/v_{\max} + g$ , during time period  $\forall t \in [x_d/v_{\max}, x_d/v_{\min} + g]$ , the flow rate  $q(x_d, t)$  increases as  $t$  increases; during time period  $\forall t \in [x_d/v_{\min}, x_d/v_{\min} + g]$ , the flow rate  $q(x_d, t)$  starts to decrease; when  $x/v_{\min} > x/v_{\max} + g$ , during time period  $\forall t \in [x_d/v_{\max}, x_d/v_{\min}]$ , the flow rate  $q(x_d, t)$  increases as  $t$  increases; during time period  $\forall t \in [x_d/v_{\min}, x_d/v_{\min} + g]$ , the flow rate  $q(x_d, t)$  starts to decrease. Furthermore, as  $x_d$  increases, the peak flow rate decreases, and it will take longer time  $x_d/v_{\min} + g - x_d/v_{\max}$  for all vehicles to pass the downstream intersection. This is as observed in the actual world. However, the Robertson model lacks the capability of modeling this phenomenon.
- (b) Compared to the Robertson model, vehicles at the front of the platoon reach the downstream intersection earlier and those at the rear of platoon spread in a shorter range for MPFDM. As the distance increases, the difference increases. This is because the platoon speed of MPFDM follows TGMD, which spreads in a narrower range in  $[v_{\min}, v_{\max}]$ .
- (c) Compared to the Robertson model, the peak of flow is lower and appears as a smooth hump for MPFDM, and the hump becomes flatter as the distance increases. This is due to faster vehicles presented in the Robertson model and the fact that the volume conservation rule cannot be violated.
- (d) Compared to the Robertson model, MPFDM presents the exact time the first vehicle and the last vehicle reaches the downstream intersection, which also reflects the fact in the field. However, vehicles travelling at a very small or even zero speed exist in the Robertson model.

## 5. Conclusion

Large percentage of bus flow in mixed flow affects the accuracy of platoon dispersion modeling in Pacey's model or the Robertson model, which does not discriminate between bus traffic and car traffic. Through speed TGMD assumption, the mixed flow can be modeled by combining bus platoon

with car platoon. Mixed platoon speed distribution will be influenced by the interaction between cars and buses, which is affected by flow rate, roadway function class, and percentage of buses. However, the interaction will eventually manifest a complicated speed distribution which cannot deal with simple distribution [27].

This strategy used here for mixed platoon modeling can be applied for all kinds of vehicle-type combination. For bus-car mixed traffic, only this mixed platoon dispersion model is needed; for multiple vehicle types, because platoon speed distribution can be fitted by adjusting the number of mixed components, the arriving mixed flow at the downstream intersection can be obtained. Therefore, the model has wide application value.

Vehicles with infinite speeds exist in both Pacey's model and Robertson model, which violate the speed distribution limits (minimum and maximum speeds) in the actual world. The proposed truncated distribution assumption fixes the defect of those models.

## Acknowledgments

This work was supported by the National Science Foundation of China under Contract no. 61174188. This support is gratefully acknowledged. The authors also thank Dr. Shen for his instructive advice and useful suggestion.

## References

- [1] G. M. Pacey, "The progress of a bunch of vehicles released from a traffic signal," Research Note No. RN/2665/GMP, Road Research Laboratory, Berkshire, UK, 1956.
- [2] M. J. Grace and R. B. Potts, "A theory of the diffusion of traffic platoons," *Operation Research*, vol. 12, pp. 255–275, 1964.
- [3] D. I. Robertson, "TRANSYT—a network study tool," RRL Report LR 253, Road Research Laboratory, Berkshire, UK, 1969.
- [4] J. A. Hillier and R. W. Rothery, "The synchronization of traffic signals for minimum delay," *Transportation Science*, vol. 1, pp. 81–93, 1967.
- [5] "TRANSYT-7F User's Manual Release 10 (TM)," 2006.
- [6] P. B. Hunt, F. I. Robertson, R. D. Bretherton, and R. I. Winton, "SCOOT—a traffic responsive method of coordinating signals, RRL tool," RRL Report LR 1041, Road Research Laboratory, Berkshire, UK, 1981.
- [7] M. D. Hall, D. van Vliet, and L. G. Willumsen, "SATURN—a simulation/assignment model for the evaluation of traffic management schemes," *Traffic Engineering and Control*, vol. 21, no. 4, pp. 168–176, 1980.
- [8] E. B. Lieberman and B. J. Andrews, "TRAFLO—a new tool to evaluate transportation management strategies," *Transportation Research Record*, vol. 772, pp. 9–15, 1980, TRB, National Research Council, Washington, DC, USA.
- [9] P. A. Seddon, "Another look at platoon dispersion: 3. The recurrence relationship," *Traffic Engineering and Control*, vol. 13, no. 10, pp. 442–444, 1972.
- [10] M. Tracz, "The prediction of platoon dispersion based on rectangular distribution of journey time," *Traffic Engineering and Control*, vol. 16, no. 11, pp. 490–492, 1975.
- [11] A. Polus, "A study of travel time and reliability on arterial routes," *Transportation*, vol. 8, no. 2, pp. 141–151, 1979.

- [12] C. Liu and P. Yang, "Diffusion models of traffic platoon on signal-intersection and control of coordinated signals," *Journal of Tongji University (Nature Science Edition)*, vol. 24, no. 6, pp. 636–641, 1996.
- [13] C. Q. Liu and P. K. Yang, "Diffusion model of density of traffic platoon and signal coordinated control," *China Journal of Highway and Transport*, vol. 14, no. 1, pp. 89–91, 2001.
- [14] C. Q. Liu and P. K. Yang, "Modification of Grace's density diffusion model and its application," *Journal of Highway and Transportation Research and Development*, vol. 18, no. 1, pp. 62–64, 2001.
- [15] D. H. Wang, F. Li, and X. M. Song, "A new platoon dispersion model and its application," *Journal of Jilin University (Engineering and Technology Edition)*, vol. 39, no. 4, pp. 891–896, 2009.
- [16] D. Wang, Y. Zhang, and Z. Wang, "Study of platoon dispersion models," in *Proceedings of the TRB Annual Meeting*, Washington, DC, USA, 2003.
- [17] M. Wei, W. Jin, and L. Shen, "A platoon dispersion model based on a truncated normal distribution of speed," *Journal of Applied Mathematics*, vol. 2012, Article ID 727839, 13 pages, 2012.
- [18] A. Manar and K. G. Baass, "Traffic platoon dispersion modeling on arterial streets," *Transportation Research Record*, vol. 1566, pp. 49–53, 1996.
- [19] G. C. K. Wong and S. C. Wong, "A multi-class traffic flow model—an extension of LWR model with heterogeneous drivers," *Transportation Research A*, vol. 36, no. 9, pp. 827–841, 2002.
- [20] J. A. Bonneson, M. P. Pratt, and M. A. Vandehey, "Predicting arrival flow profiles and platoon dispersion for urban street segments," *Transportation Research Record*, vol. 2173, pp. 28–35, 2010.
- [21] X. Cheng, "Distribution of vehicle free flow speeds based on Gaussian mixture model," *Journal of Highway and Transportation Research and Development*, vol. 29, no. 8, pp. 132–135, 2012.
- [22] J. Chen, T. Wang, C. Li, and C. Yuan, "Speed models of mixed traffic flow on bus-car and vehicle and analysis of traffic running state," *China Journal of Highway and Transport*, vol. 25, no. 1, 2012.
- [23] L. J. Yu, "Finite weibull mixture distribution model of VOT distribution forecasting," *China Journal of Highway and Transport*, vol. 22, no. 4, pp. 96–101, 2009.
- [24] P. Tao, D. Wang, and S. Jin, "Mixed distribution model of vehicle headway," *Journal of Southwest Jiaotong University*, vol. 46, no. 4, pp. 633–637, 2011.
- [25] A. D. May, *Traffic Flow Fundamentals*, Prentice Hall, New York, NY, USA, 1990.
- [26] N. H. Johnson and S. Kotz, *Continuous Univariate Distributions*, John Wiley & Sons, New York, NY, USA, 1970.
- [27] *Transit Capacity and Quality of Service Manual*, Transportation Research Board, Washington, DC, USA, 2nd edition, 2003.